

Alma Mater Studiorum - Università di Bologna

DOTTORATO DI RICERCA IN  
INGEGNERIA CIVILE, CHIMICA, AMBIENTALE E DEI MATERIALI

Ciclo 33

**Settore Concorsuale:** 08/A1 - IDRAULICA, IDROLOGIA, COSTRUZIONI IDRAULICHE E MARITTIME

**Settore Scientifico Disciplinare:** ICAR/02 - COSTRUZIONI IDRAULICHE E MARITTIME E IDROLOGIA

SUBMARINE LANDSLIDES IN THE CENTRAL MEDITERRANEAN: CAUSES AND RECURRENCES

**Presentata da:** Tugdual Trystan Nicolas Marie Gauchery

**Coordinatore Dottorato**

Prof. Luca Vittuari

**Supervisore**

Dr. Marzia Rovere (ISMAR-CNR)

**Co-supervisore**

Prof. Attilio Castellarin

Prof. Lisa Borgatti

Dr. Antonio Cattaneo (IFREMER)

**Esame finale anno 2021**



Alma Mater Studiorum - Università di Bologna

DOTTORATO DI RICERCA IN  
INGEGNERIA CIVILE, CHIMICA, AMBIENTALE E DEI MATERIALI

Ciclo 33

**Settore Concorsuale:** 08/A1 - IDRAULICA, IDROLOGIA, COSTRUZIONI IDRAULICHE E MARITTIME

**Settore Scientifico Disciplinare:** ICAR/02 - COSTRUZIONI IDRAULICHE E MARITTIME E IDROLOGIA

SUBMARINE LANDSLIDES IN THE CENTRAL MEDITERRANEAN: CAUSES AND RECURRENCES

**Presentata da:** Tugdual Trystan Nicolas Marie Gauchery

**Coordinatore Dottorato**

Prof. Luca Vittuari

**Supervisore**

Dr. Marzia Rovere (ISMAR-CNR)

**Co-supervisore**

Prof. Attilio Castellarin

Prof. Lisa Borgatti

Dr. Antonio Cattaneo (IFREMER)

**Esame finale anno 2021**



# Abstract

---

In the frame of a European Marie Skłodowska-Curie Actions Training Network program on Submarine Landslides and Their impact on European continental margins (SLATE), this research concentrated on submarine landslides in the central Mediterranean Sea. Commonly found in marine and lacustrine environments, submarine landslides represent one of the main mechanisms of sediment transport along continental margins, their volumes can be far larger than any terrestrial landslides and have potential to produce far-reaching tsunamis that can rival those produced by earthquakes. However, many uncertainties remain concerning their preconditioning factors, triggering mechanisms, return frequencies and relationship with climate change as well as their geohazard potential, which vary depending on their location.

Newly identified submarine landslides emplaced in the Gela Basin (GB; south of Sicily, central Mediterranean Sea) were investigated where the particular geodynamic and oceanographic context and the limited extent basin is ideal for submarine landslides research. The investigation through multiple data types including deep boreholes, multi-channel and sub-bottom seismic profiles, sediment cores and swath bathymetry revealed the emplacement of multiple submarine landslides during the margin outbuilding in the Pliocene-Quaternary with a drastic transition in their volumes and emplacement location at the Middle-Pleistocene Transition (MPT). This change, accompanied by an accelerated margin outbuilding from 150 to 900 m/kyr and growth of the contourite deposits, has been related to the decreasing tectonic activity at the southern front of the Maghrebian fold-and-thrust belt and the climatic changes linked to the switch to the 100-kyr Milankovitch cyclicity. Numerical in-house codes used for the reconstruction of two small-size MTDs located at the ends of the GB show similar potential of generating high-wave tsunamis that can impact the coasts of Malta and Sicily but different triggering mechanisms based on the stability analysis. A multiproxy approach made on the sediment cores revealed that strong bottom currents and very-high sedimentation rate fluctuations, associated with sea-level changes, affected the stability of contourite deposits and contributed to the recurrent emplacement of MTDs.

**Keywords:** Submarine landslides, preconditioning factors, triggering mechanisms, return frequencies, Gela Basin, Middle Pleistocene Transition, Milankovitch cyclicity, contourite deposits, very-high sedimentation rate



# Acknowledgments

---

I would like to use this opportunity to thank the reviewers of my thesis who accepted to read and revise it as well as many people who allowed me to realize it in the best conditions including:

My supervisors Profs. Luca Vittuari, Attilio Castelerin and Lisa Borgatti from the University of Bologna (Italy) who gave me the opportunity to be part of their PhD program in Civil, Chemical, Environmental and Materials Engineering in their prestigious university, the oldest in Europe.

Dr. Marzia Rovere as my main supervisor from ISMAR-CNR (Bologna) who gave me help, guidance and taught me scientific rigor in the publication of articles during my PhD. Dr. Claudio Pellegrini from the same facilities who was considered as my co-supervisor towards the end of the PhD due to its help and very good advice to keep me motivated when hard times were ahead. Dr Fabio Trincardi to let me access the facilities of ISMAR of Bologna and the few but very interesting discussion we had during the interpretation of the seismic profiles.

Dr. Antonio Cattaneo as my external co-supervisor from IFREMER (Brest, France) who, despite his busy planning, succeeded to find some time and discuss about sedimentology as well as many other topics, which I really enjoyed. Je me souviens particulièrement de ce déjeuner à la crêperie avec Germain Bayon et chez lui autour d'un super diner en compagnie de sa famille.

Dr. Francesca Zolezzi as my external co-supervisor from the industry (RINA-Genova-Italy) and his team for their help and sharing their data.

My SLATE project colleagues including all the early stage researchers and their principal investigators that I had the privilege to meet a few times a year and discuss about our projects.

My Ismar colleagues with whom I shared a part of my life with special thanks to Marco Taviani, Paolo Montana, Andrea Gallerani, Alessandra Asioli, Luigi Vigliotti, Giorgio Castellan, Tommaso Tesi, Federica Foglini, Annamaria Correggiari, Alessandra Mercorella, Andrea Argnani. Andrea Gallerani, grazie per tutti questi momenti di condivisione, aiuto e discussione, sia in laboratorio che in montagna. Marco Taviani, j'aimerais tellement te

## Acknowledgments

---

remercier comme il se doit pour tes conseils et m'avoir fait découvrir la ville, ses marchés, ses spécialités dont le vin et le fromage local avec Paolo Montagna, des moments extraordinaires qui resteront gravés dans ma mémoire!

My Ifremer colleagues with Dr. Samuel Toucanne for his advises and lectures on sortable silt and grain size, the technicians for the grain size analysis as well as many PhD students (Claire, Matthieu, Arthur, Shray, Thomas, etc.).

Hélène and her cousin Jena-Claude Capraix who gave me access to the doors of Ifremer and the world of marine geosciences.

My high-school (Le Likes, Quimper) science teachers Elisabeth Prat who gave me the taste for natural sciences, especially earth sciences and my English teacher Elise Thepaut for making me want to learn English, travel and live abroad.

Last but not least, all my friends from my bachelor (UniLaSalle Beauvais, France), master (University of Bremen, Germany), New Zealand trip and Bologna. I would like to give special thanks to my family including my parents, Ronan, Esther, Yoann, Mariette, Awen, Gael, Avel, Even, Jean, Marie-Laure, Alain, Tabou, Pierre and all the others for their continuous support during my life and long studies. Je pense tout particulièrement à mon papy qui appréciait les sciences naturelles et l'anglais et avec qui j'aurais tant aimé partager ces moments. C'est pourquoi je souhaiterais lui dédicacer cette thèse et j'espère qu'il aurait été fier de son petit-fils.



Michel Gauchery (1921 – 2009)

Without all these people, none of this would have been possible. Thank you!

# Table of Contents

---

Abstract.....	i
Acknowledgments .....	iii
Table of Contents.....	v
List of Figures.....	xi
List of Tables .....	xxv
List of Acronyms and Symbols .....	xxvii
Chapter 1. Introduction.....	1
1.1 Scientific Background: the ITN SLATE project.....	1
1.2 Submarine Landslides.....	2
<b>1.2.1 Definition, Classification and Lexicon.....</b>	<b>2</b>
<b>1.2.2 Spatial distribution of subaqueous landslides.....</b>	<b>7</b>
<b>1.2.3 Dimensions of subaqueous landslides .....</b>	<b>9</b>
<b>1.2.4 Pre-disposing factors and triggering mechanisms.....</b>	<b>10</b>
<b>1.2.5 Tsunamigenic potential .....</b>	<b>12</b>
<b>1.2.6 Economic and Social impact.....</b>	<b>14</b>
<b>1.2.7 Investigating Subaqueous Landslides.....</b>	<b>17</b>
1.3 Scientific objectives, approach .....	19
1.4 Thesis Outline .....	20
Chapter 2. Regional Setting.....	23
2.1 Geodynamic setting .....	23
2.2 Oceanography and Contourites .....	26
2.3 Geology and Climate .....	32
2.4 Geomorphology and Hydrology .....	38
Chapter 3. Study Area, Data and Methodology.....	43
3.1 Study Area .....	43
3.2 Overview and origin of the data .....	46
3.3 Data acquisition .....	46
3.4 Data definition and purpose.....	53

<b>3.4.1 Boreholes data</b> .....	<b>53</b>
<b>3.4.2 Multi-Channel Seismic</b> .....	<b>54</b>
<b>3.4.3 Sub-Bottom Seismic</b> .....	<b>54</b>
<b>3.4.4 Sediment cores</b> .....	<b>55</b>
<b>3.4.5 Swath bathymetry</b> .....	<b>55</b>
<b>3.5 Applied methods</b> .....	<b>56</b>
<b>3.5.1 Well data interpretation</b> .....	<b>56</b>
<b>3.5.2 Multi-channel Seismic profiles</b> .....	<b>57</b>
<b>3.5.3 Chirp-sonar seismic profiles</b> .....	<b>60</b>
<b>3.5.4 Sediment cores</b> .....	<b>62</b>
3.5.4.1 Magnetic susceptibility.....	64
3.5.4.2 X-ray fluorescence.....	65
3.5.4.3 X-ray images .....	66
3.5.4.4 Foraminifera assemblages .....	66
3.5.4.5 Radiocarbon AMS .....	67
3.5.4.6 Stable isotopic analysis ( $\delta^{18}\text{O}$ and $\delta^{13}\text{C}$ ) .....	68
3.5.4.7 Plant debris analysis .....	68
3.5.4.8 Grain-size distribution .....	69
<b>3.5.5 Bathymetry analysis</b> .....	<b>71</b>
<b>3.5.6 Paleo-current reconstruction</b> .....	<b>72</b>
<b>3.5.7 Tsunamigenic potential</b> .....	<b>73</b>
<b>Chapter 4. Factors controlling margin instability during the Plio-Quaternary in the Gela Basin</b> .....	<b>75</b>
1. Introduction .....	77
2. Background .....	78
<b>2.1 Geodynamic and tectonic setting of the Gela Basin</b> .....	<b>78</b>
<b>2.2 Oceanographic circulation</b> .....	<b>79</b>
<b>2.3 Stratigraphy and late Quaternary depositional sequences</b> .....	<b>80</b>
<b>2.4 Contourite deposits in the Gela Basin</b> .....	<b>80</b>
<b>2.5 Mass-transport deposits in the Gela Basin</b> .....	<b>80</b>
3. Material and methods .....	80
<b>3.1 Boreholes and sediment cores</b> .....	<b>80</b>
<b>3.2 Multi-channel seismic (MCS) reflection profiles</b> .....	<b>80</b>

<b>3.3 Sub-bottom seismic reflection (SBS) profiles</b> .....	<b>82</b>
<b>3.4 Bathymetric data</b> .....	<b>83</b>
<b>4. Results</b> .....	<b>83</b>
<b>4.1 Seismostratigraphic units</b> .....	<b>85</b>
4.1.1 Unit H (Base Pliocene – Upper Pliocene) .....	85
4.1.2 Unit G (Upper Pliocene – base Pleistocene) .....	85
4.1.3 Unit F (Base Pleistocene – Lower Pleistocene) .....	85
4.1.4 Unit E (Lower Pleistocene – MPT ~ 800 ka) .....	86
4.1.5 Unit D (MPT ~ 800 ka – ES5) .....	86
4.1.6 Unit C (ES5 – ES2) .....	87
4.1.7 Unit B (ES2 – ES1 ~ 30 ka) .....	87
4.1.8 Unit A (ES1 ~ 30 ka – present) .....	88
<b>4.2 Seafloor morphology and seismic facies</b> .....	<b>90</b>
<b>5. Discussion</b> .....	<b>91</b>
<b>5.1 The Pliocene–Quaternary stratigraphic architecture of the Gela Basin</b> .....	<b>91</b>
5.1.1 Progradational phase (Pliocene – MPT) .....	91
5.1.2 Progradational-aggradational (MPT – present) .....	92
5.1.3 Slope instability and different types of MTDs .....	93
<b>5.2 Contourite deposits as key markers of stratigraphic architecture</b> .....	<b>93</b>
5.2.1 Onset of contourite deposits .....	93
5.2.2 Evolution of contourite deposits.....	93
5.2.3 Bottom currents strength and sea level variations .....	93
5.2.4 Contourites and erosional surfaces as predisposing factors to margin instability .....	93
<b>5.3 Climate as main driver of clinothem architecture and margin instability after the MPT</b> .....	<b>94</b>
6. Conclusions.....	95
Take-Home Message.....	99
 Chapter 5. Tsunamis from submarine collapses along the eastern slope of the Gela Basin.....	 101
INTRODUCTION .....	103

THE GELA BASIN EASTERN SLOPE .....	105
<b>Geological Setting</b> .....	<b>105</b>
<b>Mass Failures Along the GBES</b> .....	<b>105</b>
NUMERICAL METHODS .....	105
<b>Landslide Dynamics</b> .....	<b>106</b>
<b>Tsunami Generation and Propagation</b> .....	<b>107</b>
BUILDING THE LANDSLIDE SCENARIOS AND THE TSUNAMI COMPUTATIONAL GRID .....	107
<b>Landslides Scenario for NTS</b> .....	<b>108</b>
<b>Landslide Scenario for SGBS</b> .....	<b>108</b>
<b>Tsunami Computational Grids</b> .....	<b>108</b>
LANDSLIDE SIMULATIONS .....	109
TSUNAMI PROPAGATION .....	111
CONCLUSIONS .....	114
Furthert Improvements and Perspectives.....	114
Take-Home Messages.....	119
 Chapter 6. Post-LGM multi-proxy sedimentary record of bottom- current variability and downslope sedimentary processes in a contourite drift of the Gela Basin .....	121
1. INTRODUCTION .....	123
2. BACKGROUND .....	124
<b>2.1 Geological setting</b> .....	<b>124</b>
<b>2.2 Oceanographic regime since Last Glacial Maximum</b> .....	<b>124</b>
<b>2.3 Contourite-derived mass-transport deposits</b> .....	<b>126</b>
3. MATERIALS, METHODS AND APPROACH .....	127
<b>3.1 Methods</b> .....	<b>127</b>
3.1.1 Hydroacoustic data .....	127
3.1.2 Sediment cores .....	127
<b>3.2 Laboratory Analysis on sediment cores</b> .....	<b>127</b>
<b>3.3 Data handling</b> .....	<b>127</b>
3.3.1 Paleo-flow speed reconstruction by sortable silt .....	127

3.3.2 Paleo-oceanographic reconstruction by sediment elemental ratios ....	130
3.3.3 Paleo-current and gravity flows identification by sedimentary facies .	130
4. RESULTS .....	130
<b>4.1 Seismic and sedimentary facies .....</b>	<b>130</b>
4.1.1 Core MS75 .....	130
4.1.2 Core MS72 .....	131
<b>4.2 Grain size distribution .....</b>	<b>131</b>
4.2.1 Core MS75 .....	131
4.2.2 Core MS72 .....	131
<b>4.3 Paleo-flow reconstruction .....</b>	<b>131</b>
<b>4.4 Oxygen and Carbon stable isotopes .....</b>	<b>131</b>
<b>4.5 Foraminifera assemblages and ecozones .....</b>	<b>133</b>
<b>4.6 Age-depth model .....</b>	<b>133</b>
<b>4.7 Sedimentation rates and age of emplacement of MTDs .....</b>	<b>135</b>
<b>4.8 Paleoenvironmental elemental proxies .....</b>	<b>135</b>
4.8.1 Core MS75 .....	135
4.8.2 Core MS72 .....	135
5. DISCUSSION .....	135
<b>5.1 Deciphering along-slope and downslope processes in sedimentary records</b> .....	<b>135</b>
<b>5.2 LIW intensity and interface variations in the Gela Basin during</b> <b>deglaciation .....</b>	<b>138</b>
<b>5.3 Predisposing conditions to slope instability .....</b>	<b>141</b>
6. CONCLUSIONS .....	142
Take-Home Messages.....	147
Chapter 7. Synthesis, Conclusions and Perspectives .....	149
7.1 Synthesis .....	149
<b>7.1.1 Tsunamigenic potential in the Gela Basin.....</b>	<b>155</b>
<b>7.1.2 Along- and down-slope processes in the Gela Basin.....</b>	<b>158</b>
7.2 Conclusions.....	164
7.3 Perspectives .....	166

Bibliography .....	167
Annexes .....	199
Annexe 1: List of secondments, research stays, courses and seminars, conferences and outreach attended .....	199
Annexe 2: Location of the data (seismic profiles and piston core) within the Gela Basin accessed and interpreted during this Phd .....	201
Annexe 3: High-resolution seismic image of the Gela Basin along-strike variability .....	203

# List of Figures

---

## Chapter 1

Figure 1.1: Schematic representation of the anatomy of a subaqueous landslide adapted and modified from Bull et al. (2009; Mountjoy and Micallef (2018); Steventon et al. (2019). 3

Figure 1.2: Schematic illustration of the major types of submarine gravity-driven depositional processes modified and adapted from Hugh et al. (2002); Harders et al. (2011).. 5

Figure 1.3: Schematic illustration of a complex subaqueous landslide transformed in terms of sediment concentration and mechanical behaviour as it moves downslope, modified from Shanmugam (2013). ..... 6

Figure 1.4: A) Compilation of worldwide location of mass-transport deposits (MTDs) in oceans, seas and lakes based on (Hühnerbach et al., 2004; Moscardelli and Wood, 2016; Sammartini et al., 2019). Black rectangle indicates the location of B. B) Typology and position of MTDs discovered in the Mediterranean Sea (Urgeles and Camerlenghi, 2013).. ..... 9

Figure 1.5: A) Histogram showing the number of slope failures and their estimated volumes worldwide (grey bars), in the western (black bars) and eastern North Atlantic (blue bars) (modified and adapted from Hühnerbach et al., 2004, Moscardelli and Wood, 2016) and B) in the Mediterranean Sea (after Urgeles and Camerlenghi, 2013). ..... 10

Figure 1.6: A) Representation to understand the role of pre-conditioning factors and B) triggering mechanisms in slope failures (pers. com. Angelo Camerlenghi). FS: factor of safety. C) Frequency of the slope failures in the Mediterranean Sea versus the major triggering mechanisms (Urgeles and Camerlenghi, 2013). In addition, the triggering mechanisms are separated according to those that increase the driving stress and those that reduce the shear strength. VD: volcano development, VU: volcano uplift, EQ: earthquake, TS: tectonic steepening, ST: steepening, ER: erosion, DC: differential compaction, DI: diapirism, AN: anthropic, HS: high sedimentation rates, FF: fluid flow, PP: pore pressure, GH: gas hydrates, GA: gas, SL: sea level. .... 12

Figure 1.7: Conceptual diagram showing the stages and mechanisms of a tsunami generation from a mass-transport deposit (MTD) with A) the pre-failure, B) the initial landslide dynamic, C) the positive and negative wave generation and D) the wave propagation and run-up (modified after Tappin, 2017; Pakoksung et al., 2019). ..... 14

Figure 1.8: Sketch representing the different marine geohazards present on a continental margin (modified from Camargo et al., 2019). ..... 17

## Chapter 2

Figure 2.1: Present day location of the plate tectonic setting in the Mediterranean from Faccenna et al. (2014). ..... 23

Figure 2.2: A) Paleogeographic Atlas illustrating the movement of the continents from the Early Jurassic with the rotation of Africa plate towards Eurasia plate, modified from Scotese (2001). B) Sketch showing the tectonic evolution of the western Mediterranean since the Early Jurassic and the slab rollback of the Apenninic back arc, modified after Fernández et al. (2019). C) Geodynamic evolution of the Mediterranean from 10 Ma to present days, modified after Jolivet et al. (2006). ..... 25

Figure 2.3: Relief and bathymetric map showing the modern emplacement of the Apenninic arc (Maghrebian fold and-thrust belt) in the Strait of Sicily as well as the location of the grabens, which represents the extensional rift system. PG = Pantelleria Graben, MG = Malta Graben, LG = Linosa Graben..... 26

Figure 2.4: A) Oceanographic circulation of the shallow (MAW), intermediate (LIW) and deep-water (WMDW and EMDW) masses in the Mediterranean Sea. The dotted black line indicates the profile location of B. The circles refers the formation sites of the LIW (in red) and the deep-water masses (in grey). B) Vertical distribution of the Mediterranean Sea water masses modified from GRID-Arendal (<http://www.grida.no/resources/5885>) based on Hopkins (1985) and Zavaterielli and Mellor (1995). MAW (blue arrows) = Modified Atlantic Water, LIW (red arrows) = Levantine Intermediate Water, WMDW (grey arrows) = Western Mediterranean Deep Water, EMDW (grey arrows) = Eastern Mediterranean Deep Water..... 29

Figure 2.5: Location of contourite deposits in the central Mediterranean Sea along the main bottom current path, modified after Cattaneo et al. (2017). Black rectangle indicates the location of B. B) Zoom on the water masses circulation and exchange in the Strait of Sicily The purple circles represent the locations and sizes of the previously studied contourite deposits. 8 = Micallef et al., 2013; 9 = Verdicchio and Trincardi, 2008; 10 = Martorelli et al., 2011; 11 = Marani et al., 1993..... 30

Figure 2.6: Morpho-bathymetric map of the Mediterranean Sea with the location of buried contourite deposits discovered along the present-day path of the LIW based on multiple references (Table 2.1)..... 31

Figure 2.7: A) Thickness map of Messinian evaporites deposited during the Messinian Salinity Crisis in the Mediterranean Sea from Haq et al., (2020). L-PB: Liguro-Provençal Basin, AB: Algerian Basin, IB: Ionian Basin, HB: Herodotus Basin, SB: Sirte Basin, LB: Levant Basin, and on the fringes of NC: the Nile Cone. B) Thickness map of the Plio-Quaternary sediments in the Mediterranean Sea modified from Capponi et al. (2020)..... 33

Figure 2.8: A) (a) 65°N summer solstice insolation. (b) Atmospheric CO<sub>2</sub> concentration, Allan Hills vertical error bars indicate 2σ spread with horizontal age uncertainty, (c) Global LR04 benthic stacked δ<sup>18</sup>O (blue) and ODP 1123 seawater δ<sup>18</sup>O (black). The MPT and the "typical 41 ka-world" intervals are highlighted in grey and yellow respectively, from Chalk et al. (2017). B) Correlation of the marine isotope stages (MIS) based on Lopes et al. (2014) with oxygen isotope curve (=ice volume) from Atlantic and Pacific Ocean cores from Lisiecki and Raymo (2009). The positioning of the sub-units of MIS 5 is based on Toucanne et al. (2012). C) δ<sup>18</sup>O of NGRIP ice core from Desprat et al. (2013) and sea-level curve from Lambeck et al. (2014). (GS-1: Glacial Stadial 1, GI-1: Glacial Interstadial 1, GS-2: Glacial Stadial 2)..... 36

Figure 2.9: A) Morpho-bathymetric map of the Mediterranean Sea with insets on specific areas characterized by different morphologies such as troughs, grabens, basins, plateaus, volcanic islands, submerged lands, canyons, depressions based on Palomino et al. (2011) and Del Bianco et al. (2014). B) 3D model showing the presence of excavated valleys at the present-day seafloor formed during the Messinian Salinity Crisis based on Urgeles et al. (2010) and adapted from Garcia-Castellanos (2011a). ..... 40

Figure 2.10: Morpho-bathymetric map of the Strait of Sicily. Location of the Imera Meridionale based on Verri et al. (2017). ..... 40

Figure 2.11: River discharge of freshwater into the Mediterranean Sea modified from GRID-Arendal (<http://www.grida.no/resources/5897>) based on Struglia et al. (2004) and Ludwig et al. (2009). ..... 42

## Chapter 3

Figure 3.1: Morpho-bathymetric map showing the location of mass-transport deposits (slide/slump and debris avalanche; Kuhlmann et al., 2017) and their headwalls, of contourite

deposits (Verdicchio and Trincardi, 2008) and earthquakes (INGV) previously studied along the eastern Gela Basin. ML: Magnitude Local. .... 45

Figure 3.2: A) Sketch representing the complexity of coring boreholes with a riser drilling where drilling mud containing the cuttings is collected onboard for analysis. B) Examples of different drill bits and core bits depending the substrate hardness and the type of samples desired to be recovered. C) Sketch showing the riserless drilling system where cuttings are not recovered. D) Sketch to show how cores samples are recovered from the substrate with drilling. E) Representation of coring with a Logging While Drilling (LWD) installed on top of the drill bit. All images are from JAMSTEC website (<https://www.jamstec.go.jp/cdex/e/operations/>)..... 48

Figure 3.3: A) Sketch representing the acquisition of multi-channel seismic profiles modified after Geostar Survey (2009). B) Pictures showing an example of air gun and multi-channel streamer used onboard a research vessel. C) Example of a multi-channel seismic profile after processing. .... 49

Figure 3.4: A) Schema representing the deployment of various shallow-water sub-bottom profiling systems from Stoker et al. (1997). B) Picture of a CHIRP sub-bottom profiler from WHOI (2020). C) Example of a CHIRP sonar seismic profile used in this research..... 50

Figure 3.5: A) Sketch representing the technic used to acquire the piston cores (WHOI, 2020). B) Photo of the Piston corer onboard the R/V Urania during Gela-05 mission in 2005 and C) during coring operation (Langone et al., 2005). D) Example of photos of piston core sections splitted and labelled..... 51

Figure 3.6: Core labelling scheme system used for the inscription of the piston core sections. Adapted and modified after Kopf et al. (2016). .... 52

Figure 3.7: A) Representation of how a multibeam echosounder system acquires high-resolution bathymetric data (Ifremer, 2020). B) Bathymetric map showing the surface mapped with the mutlibeam echosounder along the eastern Gela Basin (surrounded by a black dotted line). C) Bathymetric maps demonstrating the increase in resolution of the bathymetry with the use of a multibeam echosounder. Note that each parallel lines observed on the high-resolution bathymetry (NW-SE) represent a pass of the ship during the acquisition with the swath echosounder..... 53

Figure 3.8: Comparison of the resolution of the data used in this research adapted and modified from pers. com. Dr. Johnathan Ford. .... 56

Figure 3.9: A) Bathymetric map showing the location of the three selected deep boreholes and the multi-channel seismic (MCS) profile. B) Correlation of the key time intervals of the selected deep boreholes. C) Geochronology of a MSC profile by the deep borehole B1. Location of the MCS profile in Fig. 3.9A. .... 57

Figure 3.10: Identified geochronology of the selected MCS profiles based on profile 1 from Lower Pliocene to Pleistocene. Location of the MCS profiles on the map. Note the junction of all the MCS profiles. .... 58

Figure 3.11: Zoom on 2 selected MCS profiles to explain the methods for the identification of A) erosional surfaces (red lines) and B) mass transport deposits (MTDs) on seismic profiles. Location of the profiles in Fig. 3.10. .... 59

Figure 3.12: A) Sequence-stratigraphic interpretation of an acoustic sub-bottom profile from the northern Gela Basin correlated to long piston cores. Modified after Kuhlmann et al. (2015). B) Example of an interpreted sub-bottom profile studied in this thesis and based on the characteristics of the seismic units identified in Kuhlmann et al. (2015). C) Map showing the location of the sub-bottom profiles of A and B among all the sub-bottom profiles available in the study area. .... 61

Figure 3.13: Examples of sub-bottom seismic (SBS) profiles showing A) the clear evidence at the seafloor of a headwall and an erosional base and B) two MTDs characterized by different toe domains and separated by high-amplitude seismic reflectors. Note the reduced penetration of the acoustic signal below the MTDs. .... 62

Figure 3.14: A) Morpho-bathymetric map showing the location of the two piston cores studied in this research. B) Location and representation of the penetration depth of the piston cores on sub-bottom profiles. The different colours is used to indicate the changes of amplitude reflectors crossed by the cores. Red = high amplitude reflectors, blue = low amplitude reflectors. .... 63

Figure 3.15: Data example of core MS72 with a) a representation of the amplitude reflectors crossed by the piston corer, b) a photography of the core with the colour code, c) the magnetic susceptibility measured, d) an elemental ratio, e) the X-ray images and f) the foraminifera assemblages identified as well as the presence of other components (i.e. vegetal remains, oxidation, bioturbation, shell remains, etc.), and g) the position of the radiocarbon dating and h) the stable isotopic analysed. .... 65

Figure 3.16: A) Hjulström-Sundborg diagram and B) sediment percentage-flow speed relationship modified from McCave and Hall (2006). ..... 70

Figure 3.17: Example of grain distribution and frequency for core MS75. Note the changes from unimodal to bimodal distribution with an increase in the sortable silt fraction. 71

Figure 3.18: High-resolution bathymetric map showing the location of the MTDs and contourite moats identified with a geomorphometric approach compared to the position of the sediment cores recovered in the Gela Basin. .... 72

## Chapter 4

Figure 1: Relief and bathymetric map of the Strait of Sicily; red and blue arrows represent the Levantine Intermediate Water (LIW) and the Modified Atlantic Water (MAW) (adapted from Lermusiaux and Robinson, 2001). 1–4 = previously studied contourite deposits: 1 = Marani et al. (1993), 2 = Martorelli et al. (2011), 3 = Micallef et al. (2013) and 4 = Verdicchio and Trincardi (2008). AIS = Atlantic Ionian Stream, ATC = Atlantic Tunisian Current, PG = Pantelleria Graben, MG = Malta Graben, LG = Linosa Graben. Inset: general oceanographic circulation in the Mediterranean Sea. (For interpretation of the references to colour in this figure legend, the reader is referred to the Web version of this article.). ..... 78

Figure 2: A. The eastern Gela Basin bathymetric map showing the location of the MCS profiles (green lines), deep boreholes (circles) and piston cores (squares) used in this study. The deep boreholes cross section is on depositional strike, whether the piston core cross section is on depositional dip. NTS: Northern Twin Slide, STS: Southern Twin Slide, FS: Father Slide. B. Regional stratigraphic correlation between the boreholes B1–B3 and the piston cores M1–M3. See also Table 1. (For interpretation of the references to colour in this figure legend, the reader is referred to the Web version of this article.). ..... 79

Figure 3: A. Original seismic section and line drawing of MCS profile 1 crossing the borehole “Plinio Sud 001” (location in Fig. 2A). B. Enlargement of the prograding shelf-edge of MCS profile 1. C. Bathymetric map showing the location of B (black rectangle) and of SBS profile (white line) shown in D. D. Interpretation of SBS profile “HE81” showing the geometry of the seismic units A and B (Table 3) at the shelf edge. This profile was used to correlate the unconformity ES1 on MCS profile 1. .... 82

Figure 4: A. Original seismic section and line drawing of MCS profile 2 highlighting the initiation of contourite deposits during the Upper Pliocene and their evolution through time. B. Enlargement of the pro- grading shelf-edge of MCS profile 2. C. Bathymetric map showing the location of B (black rectangle) and of SBS profile (white line) shown in D. D. Interpretation of SBS “HE29” highlighting the timing of contourite growth in Sector 1. E. 3D bathymetric view of the area in C. See Fig. 3A and Table 3 for the description and interpretation of seismic units. ....83

Figure 5: A. Original seismic section and line drawing of MCS profile 3 showing the largest prograding set of the eastern Gela Basin. B. Bathymetric map showing the location of the enlarged area in Fig. 6A (black rectangle) and of SBS profile (white line) shown in C. C. Interpretation of SBS “MKR19” showing seismic units A, B and C (Table 3). D. Original seismic section and line drawing of MCS profile 4 showing oblique clinoforms during the Pliocene, top truncated strata and a net change in shelf aggradation after the MPT; same vertical and horizontal scales as in Fig. 5A. See Fig. 3A and Table 3 for the description and interpretation of the seismic units. ....84

Figure 6: A. Enlargement of the shelf-edge clinothem of MCS profile 3 of Fig. 5A bounded by the last eight erosional unconformities and highlighted by toplaps and onlaps (red arrows), showing a descending shelf-edge trajectory. B. Sea-level curve adapted from Spratt and Lisiecki (2006) with the corresponding rollover point for each erosional surface. Given the depth of rollover points (shoreline position) on the seismic profile, we estimated an average tectonic component of 0.1 mm/yr after the MPT, except for the last sea-level cycle when the tectonic vertical component is estimated at 2.5 mm/yr. (For interpretation of the references to colour in this figure legend, the reader is referred to the Web version of this article.). ....85

Figure 7: A. Original seismic section and line drawing of MCS profiles 5 and 6 showing the along-strike variability (NW–SE direction) of the Pliocene–Pleistocene succession. See Fig. 2A for location.....86

Figure 8: SBS profile “RSM” which shows the younger clinothem (units A and B) crossed by SBS profiles “HE122” and “MKR19” (NE–SW direction) to highlight the changes in clinothem thickness along the shelf and the overall along-strike variability of the margin. ....86

Figure 9: Isobath maps (A and B) of key stratigraphic horizons and isopach maps (C, D, E, F, G) of significant stratigraphic units in the study area. C shows evidence of three sub-basins in Sector 1. D shows that sediment deposition was limited to the shelf edge during the corresponding time interval. E represents the overall Plio-Quaternary deposition showing maximum thickness in Sector 1. F and G are the sedimentation thickness between ES2 and ES1 and between ES1 and the seabed. H represents the sediment accumulation since ES2 until today (seismostratigraphic units A + B, Table 3) where it concentrated mainly on the slope of sectors 1 and 3. ....87

Figure 10: A. SBS profile “MEDCORE-138” showing the internal structures of the most prominent contourite deposit in the upper slope of Sector 3. Seismic units A and B show that the deposition of the drift crests occurred mainly during MIS 5 (see also Table 3). B. SBS profile “MA87” showing the continuity of the contourite deposits along the shelf edge and upper slope. C. SBS “MA1” showing the presence of a buried drift developed on top of ES2. D. SBS “MA80” shows a moat and the Gela Drift Slide (GDS) gliding on top of the erosional surface ES2. E. Bathymetric map with location of the seismic profiles shown in A, B, C and D. F. 3D bathymetric view showing the GDS deposit located downslope the failed drift crests. Horizontal and vertical scales of SBS profiles are given in Fig. 10D. ....88

Figure 11: A. Shaded-relief map of the 25-m-resolution DTM of the eastern margin of the Gela Basin subdivided in three sectors and highlighting the mass-transport deposits (MTDs) described in previous studies (Northern Twin Slide–NTS and Southern Twin Slide–STS). B. Slope gradient map showing an average gradient of 2.1° and up to 32° at the shelf edge of sectors 1 and 3. C. Aspect map showing a southern direction in Sector 1 and an N–NW direction in sectors 2 and 3. D. Curvature map revealing hummocky surfaces corresponding to the MTDs discovered by this study (Southern Gela Basin Slide–SGBS and Gela Drift Slide–GDS). ....89

Figure 12: N–S oriented chronostratigraphic cross-section summarizing the evolution of the eastern Gela Basin since the Pliocene. The temporal distribution of the deposits is schematic. SAR: sediment accumulation rate. ....91

Figure 13: A. Recurrence time plotted against reconstructed volumes of mass-transport deposits (MTDs) and turbidite deposits mapped in the eastern Gela Basin since the Pliocene (see also Table 4). B. Time sketch of the eastern Gela shelf-edge margin growth (black lines) for the Pliocene to Quaternary along with the distribution of sedimentary bodies and MTDs. 92

Figure 14: Along-dip shelf stratigraphic reconstructions illustrating the changes in sediment deposition during the current Holocene highstand (A) and the Last Glacial Maximum (B). C. The occurrence of an elongated area of non-deposition adjacent to contourite deposits on the Malta Plateau indicates the path of bottom currents flowing at around 100 m w.d. ....94

## Chapter 5

Figure 1: (A) Simplified structural sketch of the Strait of Sicily and adjacent regions with the shelf-edge of the Gela Basin eastern slope (GBES) highlighted by the 200 m isobath (in light blue). Structural elements adapted from various sources (mainly Argnani et al., 1987; Argnani et al., 2012). Bathymetric data are from EMODnet (EMODnet Bathymetry Consortium, 2018). MTB = Maghrebian Thrust Belt, GN = Gela Nappe, HP = Hyblean Plateau. (B) Zoom on the north-eastern sector of the GBES, highlighting the Twin Slides complex and the different slide features. The black line marks the “Father Slide” headwall, the red and green ones are for the subsequent NIS and STS headwalls, respectively. At the toe of the scarps, the deposits of the two slides are shown with the red-dashed and green-dashed lines, respectively. (C) Zoom on the southern sector of the GBES. The blue line marks the SBGS headwall, at about 200 m depth, while the dashed-blue line delimits the slide deposit, at the toe of the slope. ....106

Figure 2: (A) Bathymetric map of the NTS scenario. The blue contour marks the initial slide boundary, the dashed-red one delimits the observed slide deposit. The green line denotes the whole slide boundary, one of the code inputs. The black line describes the predefined trajectory of the blocks’ CoM. The initial thickness is shown via the yellow-red-brown colour scale. (B) Landslide profile cut along the CoM path. The blue, red, and green lines mark the initial mass, the deposit, and the gliding surface profiles, respectively. The black-dashed line is for the present morphology. ....107

Figure 3: (A) Bathymetric map of the SGBS scenario, with the initial mass boundary marked in blue and observed deposit in dashed-red. The resulting initial slide thickness is marked by the yellow-red-brown colour scale. The other input for the simulation code, the lateral slide boundaries, and the CoM predefined trajectory, are reported in green and black respectively. (B) Morphological slice along the CoM path. In blue the initial slide profile, in red the observed deposit. The green line marks the undisturbed gliding surface, the black-dashed line the present bathymetry. ....108

Figure 4: Tsunami computational grids: the larger (G1) is characterized by a 250-m step, while the smaller ones (G2 and G3) have higher resolution (50-m spaced nodes) and are focused

on the SGBS and NTS areas, respectively. The propagation of the tsunami over domains with different spatial intervals is possible through the nested-grids technique. ....109

Figure 5: Landslide dynamics for NTS (left) and SGBS (right). (A) Mean velocity (red line) and individual CoM velocity (black dots) vs. time for the NTS scenario. (B) Analogous quantities for the SGBS scenario. (C) Mean thickness (red line) and individual block thickness (black dots) time history for the NTS case. (D) SGBS mean thickness (blue line) and block thickness (black dots). (E) Froude number vs. time for the NTS case. (F) Froude number vs. time for the SGBS scenario. ....110

Figure 6: Propagation sketches for the NTS-generated tsunami. The colour scale is saturated for values higher than 1 m and lower than -1 m for graphical reasons. The black contour marks the area swept by the slide. ....110

Figure 7: Propagation frames for the SGBS-generated tsunami. The colour scale spans the interval [-2;2] m and is saturated for values out of this range. The black contour delimits the SGBS area. ....111

Figure 8: Maximum water elevation for the two landslide scenarios, NTS (left) and SGBS (right). The black boundaries mark the area swept by the landslide motion. Notice that the colour scales cover different intervals for the two plots. ....112

Figure 9: (Upper panel) Map of the Sicily coast, with relevant coastal cities. The red and blue spots represent the NTS and SGBS, respectively. (Lower panel) Maximum water height associated with the two tsunami scenarios (NTS and SGBS, in red and blue respectively) along the coast of Sicily from west to east. The numbers and the dashed-purple lines refer to the toponyms reported in the upper panel. ....113

Figure 10: Maximum water elevation along the coast of the Malta archipelago, taken on the 20-m isobath, for the two tsunami scenarios: NTS on the left, SGBS on the right. The numbered dots mark the main toponyms. Notice the different range of the colour scales used for the two cases. ....114

## Chapter 6

Figure 1: A) Circulation of the surface (Modified Atlantic Water – MAW), intermediate (Levantine Intermediate Water – LIW) and deep-waters (Western and Eastern Mediterranean Deep Water – WMDP and EMDW) in the Mediterranean Sea (modified from Astraldi et al.,

2001; Millot, 1999; Millot and Taupier-Letage, 2005). The black circles indicate the location of the reference cores used in this study. B) Relief and bathymetric map of the Strait of Sicily area with superimposed the water mass circulation and the general tectonic framework. C) Relief and bathymetric map of the Gela Basin highlighting mass-transport deposits: Twin Slides (Minisini et al., 2007), Southern Gela Basin Slide (SGBS) and Gela Drift Slide (GDS) (Gauchery et al., 2021). White polygons indicate contourite deposits (Verdicchio and Trincardi, 2008; Gauchery et al., 2021). .....125

Figure 2: A) 2D and B) 3D bathymetric map with location of cores MS75 and MS72 (white stars). The black line indicates the sub-bottom seismic reflection profile shown in C; the red line outlines a contour-parallel moat located upslope of the mass-transport deposits Southern Gela Basin Slide (SGBS) and Gela Drift Slide (GDS). C) Sub-bottom seismic reflection profile showing the location of cores MS75 and MS72. ....126

Figure 3: A) Location of core MS75 in sub-bottom seismic reflection profile. Blue = low seismic amplitude (Units A and C), red = high seismic amplitude (Unit B). The Erosional Surface (ES1) is radiocarbon dated between the Last Glacial Maximum (LGM) and ~ 30 kyr cal. BP (Kuhlmann et al., 2015) and seismo-stratigraphically correlated in the study area. B) From left to right: seismic units, core photo and colour scale, X-ray core scan, grain-size frequency/distribution and  $\log_{10} \overline{SS}$ , magnetic susceptibility, Zr/Rb ratio. Zoom of X-ray photos: C) non-parallel lamination and moderate abundance of pyritized micro-burrows. D) Non-parallel lamination and increase in pyritized micro-burrows along with decrease in grain size. E) Non-parallel wavy curved lamination, bioturbation and pyritized micro-burrows. F) Pyritized micro-burrows and back-fill. ....128

Figure 4: A) Location of core MS72 in the sub-bottom seismic reflection profile. Blue = low seismic amplitude (Unit A), red = high seismic amplitude (Unit B). B) From left to right: seismic units, core photo and colour scale, X-ray core scan, grain-size frequency/distribution and  $\log_{10} \overline{SS}$ , magnetic susceptibility, Zr/Rb ratio. Zoom of X-ray photos: C) change from moderate/high bioturbation by shallow tier structures (pyritized micro-burrows) to macro ichnofacies. D) Intercalations of wavy laminations with low-angle cross-bedding laminations. E) Convolute laminations, load casting and flame structures. F) Lenticular beds characterized by erosional base and sharp contact at the top, close alternation of centimetric silty and muddy layers inside and escaping bioturbating macro fauna. ....129

Figure 5: Reliability tests of the downcore correlation coefficients on the 9-points window adapted from McCave and Andrews (2019). Plots of correlation vs slope identify the unreliable  $\overline{SS}$  data for cores: A) MS75 and B) MS72 when correlation is  $< 0.5$  and slope  $< 0.07$ . Plots of  $SS\%$  vs  $\overline{SS}$  to calculate: C) the initial correlation coefficient using all  $\overline{SS}$  data and D) the final correlation coefficient after rejection of unreliable data with their linear regressions. E) Pale blue bars indicate sediment samples where paleo bottom-currents are not the main active sediment-transport mechanism. ....132

Figure 6: Bulk composition (carbon/nitrogen ratio combined with stable carbon isotopes) of plant debris sampled in core MS72 (see Figs. 4B and 7 for location of the samples, “vr”). End-members  $\delta^{13}C$  values are from Vizzini et al. (2003) and DeLaune and Lindau (1987). ....133

Figure 7: A) Stratigraphic correlation of the  $\square^{18}O$  record of cores MS72 and MS75 compared with the reference cores from the Alborán Sea, Menorca Drift and Strait of Sicily (see references on top of each core). The stratigraphic position of the main foraminiferal bioevents is reported. The reference INTIMATE event stratigraphy is from Björck et al. (1998) and Blockley et al. (2012). The ages reported for the reference core MD04-2797CQ are calibrated (yr BP) according to Rouis-Zargouni et al. (2010). The data were not corrected for the ice volume effect. G.r. = Globigerinoides ruber, G.s. = Globorotalia scitula, G. tr. rc = Globorotalia truncatulinoides right coiling, GS = Greenland Stadial, GI = Greenland interstadial, HS = Heinrich Stadial, LGM = Last Glacial Maximum chronozone according to Mix et al. (2001). B) Micrographs of foraminifera assemblages and their ecozones: a & b) hemipelagic sample without terrigenous; c) foraminifera with terrigenous; d) cold-water planktonic foraminifera showing different test sizes (no hydraulic selection); e) abundant vegetal debris with fine terrigenous; f) foraminifera assemblage, including taxa typical of inner shelf (*Elphidium crispum*), with fine terrigenous. ....134

Figure 8: Linear sedimentation rates (LSR) of cores MS72 (A) and MS75 (B). Red dots indicate the  $^{14}C$  calibrated ages. Planktonic foraminifera ecozones and seismic units are displayed below the age-depth plot. The dashed vertical lines identify the estimated age of emplacement of mass-transport deposits GDS and SGBS. ....138

Figure 9: Isotopic stratigraphy ( $\square^{18}O$ ), geochemical element composition (S/Cl, Ca/Ti), sortable silt mean size ( $\overline{SS}$ ) and LSR of core MS75 displayed in age. Sea-level curve from Lambeck et al. (2014). Reworked foraminifera = black circles, pyrites = red triangles. GS-1 =

Glacial Stadial 1 (sky blue bar), GI-1 = Glacial Interstadial 1, HS1 = Heinrich Stadial 1 (dark blue bar), HE1 = Heinrich Event 1, LGM = Last Glacial Maximum. Pale blue rectangles on  $\overline{SS}$  data represent sediments unsorted by bottom currents. ....139

Figure 10: Isotopic stratigraphy ( $\delta^{18}O$ ), geochemical element composition (S/Cl, Ca/Ti, Ba/Ti), sortable silt mean size ( $\overline{SS}$ ), and LSR of core MS72 displayed in age. Sea-level curve from Lambeck et al. (2014). Reworked foraminifera = black circles, pyrites = black triangles, plant debris = blue diamonds. See Fig. 9 for other symbols and abbreviations. ....140

Figure 11: Basin-wide correlation of benthonic and planktonic  $\delta^{13}C$  and  $\delta^{18}O$  records of core MS72 and the reference cores of the Mediterranean. The ages are calibrated (yr BP). The yellow stripes represent the intervals with evidence of major reworking/displacement of foraminifera. See Fig. 7 for a detailed explanation of symbols and abbreviations. ....141

Figure 12: Sortable silt mean size ( $\overline{SS}$ ) in the Gela Basin (A and C) compared to the Corsica Trough (B and D) over the last 19 kyr BP. The green arrows indicate the increases and decreases in flow speed ( $cm\ s^{-1}$ ). The deepest cores (all but MS75) registered fluctuations of the intermediate water mass (LIW). The shallower core (MS75) shows contrasting values compared to the other cores, which possibly reflect changes in the depth of the upper boundary of the LIW due to sea-level rise pulses and the activity of the surface water (MAW) at the beginning of deglaciation. ....142

## Chapter 7

Figure 7.1: A) Bathymetric map showing the location of profiles 3 and 5. B) Isopach map representing the overall Pliocene-Quaternary deposition in the Gela Basin and showing the extension of the largest (north) and thickest (east) progradation sets highlighted by profiles 3 and 5. C) Interpreted multi-channel seismic profile 3 showing the largest progradation set of the Gela Basin and its increasing rate at the Middle-Pleistocene Transition (MPT). D) Interpreted multi-channel seismic profile 5 highlighting the thickest progradation set of the Gela Basin and the changes of the along-strike spatial distribution of the MTDs emplaced in the Gela Basin at the MPT. MSC: Messinian Salinity Crisis. .... 155

Figure 7.2: Bathymetric map showing the location of the North Twin Slide (NTS) and South Gela Basin Slide (SGBS) and the location of the recent seismic sequences registered near the Gela Basin as well as the positioning of the faults (CS\_1 and CS\_2) used in the stability analysis based on Antoncicchi et al. (2020). CS\_01 represents the offshore continuation of the

Scicli-Raguza fault where a few NE-SW small fault segments until 8 km were identified in the near offshore area (Azzaro and Barbono, 2000). CS\_2 is a normal fault offsetting the Meso-Cenozoic sedimentary succession until Top Messinian at the Gela Nappe front and possibly reactivated in compression. .... 157

Figure 7.3: CHIRP profiles highlighting A) the SGBS evacuated source area and B) the confined toe domain compared to C) the schematic drawing representing a frontally-confined mass flow from Sobiesiak et al. (2018). Note that no deformation are visible in front and within the toe domain of the SGBS. D) Bathymetric map with location of the CHIRP profiles shown in A, B and F. E) 3D bathymetric view showing the evacuated amphitheatre-like source area of the SGBS and its hummocky depositional area as well as the GDS deposit located downslope the failed drift crest. F) CHIRP profiles representing the GDS cross-section and showing the depletion near the headscarp as well as the concentrated accumulation at the toe domain with an emergent front inducing a backward rotation. G) Schematic drawing of the frontally-emergent mass flow from Sobiesiak et al. (2018) used to compare the GDS depositional area based on its morphology and internal structures. H) Enlargement of the GDS emergent front showing the possible presence of blocks and a basal erosion as represented in I) the cartoon modified after Sobiesiak et al. (2018) inducing no-slip flows. .... 161

Figure 7.4: Representation of the number of MTDs found in the Mediterranean Sea with respect to their age constrained plotted versus the sea level curve of the last 100 kyr. Figure modified from Urgeles and Camerlenghi (2013). .... 162

# List of Tables

---

## Chapter 2

Table 2.1: Buried contourite deposits identified in the Mediterranean Sea and along the northeastern Atlantic Ocean. ....	32
---	----

## Chapter 3

Table 3.1: Names, coordinates, mission, water depth and length of the piston cores recovered in the south-eastern Gela Basin. ....	63
--	----

Table 3.2: Overview of all the analysis made on the piston cores, their resolution and the material used. Examples of these analysis are given in figures 3.15 and 3.17. The “x” is used when there is no specific resolution applied and more details can be found for each analysis in the following sub-chapters. ....	64
---	----

Table 3.3: Grain size classification modified from Wentworth (1922).....	69
--	----

## Chapter 4

Table 1: Boreholes and sediment piston cores used in this study.....	81
--	----

Table 2: Seismic facies F1 to F5 observed in MCS profiles, complemented with illustrative images, sketches, facies descriptions and inferred sedimentary processes. ....	81
--	----

Table 3: Details of seismic units A to H identified in the seismic profiles and correlated with borehole and sediment core data. For the descriptions of seismic facies refer to Table 2. ....	90
--	----

Table 4: MTDs and turbidite deposits observed in the seismic profiles available in the study area, accompanied by their inferred recurrence times, dimensions, source directions, location along the margin sectors and likely controlling factors. ....	90
--	----

## Chapter 5

Table 1: List of submarine landslides with volumes comparable to the NTS and the SGBS whose tsunamigenic potential has been explored in literature. ....	104
--	-----

## Chapter 6

Table 1: AMS <sup>14</sup>C and calibrated ages based on monospecific and mixed foraminifera. Results are expressed as 2-sigma range. ....130

Table 2: Summary of the seismic and sedimentary proxies of cores MS72 and MS75. ....131

Table 3: Foraminifera ecozones and inferred paleoenvironments for cores MS72 and MS75 along with the corresponding time intervals/events to which the ecozones were equated. Bolded and underlined names define the abundant and common species, respectively. ....136

Table 4: Age-depth model adopted in this study. ....137

## **Chapter 7**

Table 7.1: List of proxies used to identify along- and down-slope processes based on literatures. .... 162

# List of Acronyms and Symbols

---

## Acronyms

AGIP = Azienda Generale Italiana Petroli

AHP = African Humid Period

AIS = Atlantic Ionian Stream

AMS = Accelerator Mass Spectrometry

ATC = Atlantic Tunisian Current

Be = Benthonic

CHIRP = Compressed High Intensity Radar Pulse

CNR = Consiglio Nazionale delle Ricerche

CoMs = Centre of Mass

CTD = Conductivity, Temperature, Depth

DICAM = Department of Civil, Chemical, Environmental and Materials Engineering

EMDW = Eastern Mediterranean Deep Water

EMODnet = European Marine Observation and Data Network

Eni S.p.A. = Ente Nazionale Idrocarburi

ES = Erosional Surface

ESRs = Early Stage Researchers

FS = Factor of Safety

GB = Gela Basin

GBES = Gela Basin eastern slope

GDS = Gela Drift Slide

GI-1 = Glacial Interstadial-1

GPS = Global Positioning System

GS = Gela Slide

GS-1 and -2 = Glacial Stadial-1 and -2

HE1 = Heinrich Event 1

INGV = Istituto Nazionale di Geofisica e Vulcanologia

ISMAR = Institute of Marine Sciences

LGM = Last Glacial Maximum

LIW = Levantine Intermediate Water

LWD = Logging While Drilling

MAW = Modified Atlantic Water

MCS = Multi-Channel Seismic

MIS = Marine Isotope Stage

MPI = Mediterranean Pliocene

MPT = Middle Pleistocene Transition

MSC = Mediterranean Salinity Crisis

MSCA-ITN = Marie Skłodowska-Curie Innovative Training Network

MTC = Mass-Transport Complex

MTD = Mass-Transport Deposit

MWP-1A and -1B = MeltWater Pulse-1A and -1B

NOSAMS = National Ocean Sciences Accelerator Mass Spectrometry

NTS = Northern Twin Slide

PG = Pantelleria Graben

PI = Planktonic

ROV = Remotely Operated Vehicles

SAR = Sediment Accumulation Rate

SBP = Sub-Bottom Profiler

SBS = Sub-Bottom Seismic

SBS = Sub-Bottom Seismic

SGBS = South Gela Basin Slide

SI = Système International d'unités (International System of Units)

SLATE = Submarine LANDslides and Their impacts on European continental margins

SPOT = Sismicità Potenzialmente innescabile Offshore e Tsunami

STS = Southern Twin Slide

SWE = Shallow-Water Equations

T IA and IB = Termination IA and IB

VPDB = Vienna Pee Dee Belemnite standard

w.d. = water depth

WHOI = Woods Hole Oceanographic Institution

WMDW = Western Mediterranean Deep Water

XRF = X-Ray Fluorescence

### Symbols

Kyr = Kiloyears, 1 Kyr = 1000 yrs

Ka = Kiloyears ago

Myr = Millions of years

Ma = Millions of years ago

Psu = Practical salinity unit

$\delta$  = delta

$\sigma$  = sigma

$\delta^{18}\text{O} = {}^{18}\text{O}/{}^{16}\text{O}$  = ratio of stable isotopes oxygen-18 and oxygen-16

${}^{14}\text{C}$  = radiocarbon, radioactive isotope of carbon

$\text{CO}_2$  = Carbone dioxide

$\mu\text{m}$  = micrometres

kV = Kilovolt

$\text{CaCO}_3$  = Calcium Carbonate

## List of Acronyms and Symbols

---

$\delta^{13}\text{C} = {}^{13}\text{C}/{}^{12}\text{C}$  = ratio of stable isotopes carbon-13 and carbon-12

$\overline{SS}$  = sortable silt mean size

SS% = sortable silt percentage

Al = Aluminium

B = Boron

Ba = Barium

Ca = Calcium

Cl = Chlorine

Fe = Iron

H = Hydrogen

Mn = Manganese

N = Nitrogen

Rb = Rubidium

S = Sulfur

Ti = Titanium

Zr = Zirconium

M1 to 3 = long piston core names

B1 to 3 = Borehole names

Cd = drag parameter

Cf = frontal drag

$\sqrt{gh}$  = wave phase speed

g = gravity acceleration

h = local sea depth

Fr = Froude number

$\mu\text{A}$  = microampere

# Chapter 1. Introduction

---

## 1.1 Scientific Background: the ITN SLATE project

This Ph.D. thesis is the result of the activities carried out during the H2020 research project “SLATE” (Submarine **L**Andslides and **T**heir impacts on **E**uropean continental margins) funded by the Marie Skłodowska-Curie Innovative Training Network (MSCA-ITN). The project sponsored my research grant (September 2017-September 2020) and gave me the opportunity to participate into an European project, working in collaboration with institutions from academia and industry located in multiple European countries, participating and presenting research work at national and international conferences and workshops. The project saw the participation of 15 early stage researchers (ESRs) employed by a partnership of leading European institutes and universities in the field of marine and earth sciences. I was one of the ESRs employed by the Institute of Marine Sciences (ISMAR) of the Consiglio Nazionale delle Ricerche (CNR), enrolled in the XXXIII PhD programme of the Department of Civil, Chemical, Environmental and Materials Engineering (DICAM) of Alma Mater, University of Bologna, Italy.

The scientific objectives of the SLATE project were to better understand the pre-conditioning and triggering factors of subaqueous landslides, their motion and evolution of the failed material, and their deriving hazards on coastal and marine infrastructures along European margins. The project integrated a broad range of scientific expertise (e.g. geochemistry, geophysics, numerical modelling, geotechnical studies etc.), including the private sector (FugroGeoConsulting, RINA, GEOMAR and DEA Deutsche Erdoel AG), to train and co-supervise the ESRs. The ESRs were provided background data, technology and knowledge to acquire, treat, analyse and interpret various geoscientific datasets. Each ESR was affiliated to at least two European institutions to develop, via multiple visits (secondments), different laboratory/software skills. At the project website (<https://www.itn-slate.eu/>) each ESR was able to share their project aims as well as the conferences/workshops/courses/outreach experienced.

This thesis develops around submarine landslides emplaced in the Gela Basin which is located in the Strait of Sicily (central Mediterranean Sea) and was supported by the close and fruitful collaboration with public research institutes such as Ifremer in France and private companies such as RINA Consulting S.p.A. and Eni S.p.A. in Italy. During my PhD time, several visits were conducted to these institutions in order to access, analyse, discuss and

interpret the data. The research stays, training courses, seminars and conferences were a great way to show my work as well as to meet and discuss with experts from the research and industry communities. A summary of the secondments/research stays/courses and seminars/conferences are given in Annexe 1.

## 1.2 Submarine Landslides

### 1.2.1 Definition, Classification and Lexicon

Submarine landslides are an important and very efficient process in the transport of sediments from continental shelf and the upper-slope into deep ocean basins where they are represented by sedimentary bodies and characterize high-environmental stresses (Hampton et al., 1996; Mulder and Cochonat 1996). Similar processes are present in fresh-water as well (lakes; e.g. Sammartini et al., 2019 and references therein), and in order to include both environments, oceans and lakes, when introducing the process they are called “subaqueous landslides”.

The sediment flux transported by rivers to ocean/lakes creates the ocean’s largest sediment repository along the coast forming sedimentary strata that dip seaward, which represent an important record of Earth history (Kennet, 1982). Sediments go through diagenesis during the margin outbuilding, but failure of unconsolidated materials can occur on a variety of environments which are governed by specific natural processes leading to sediment redistribution through subaqueous landslides and in turn, modifying the sedimentary records in the deep-sea (Masson et al., 2006). Submarine landslides can occur with different failure mechanisms from mud-flows to blocky slides depending mostly on the source sediment composition, leading to the emplacement of complex structure deposits. The failures induce the downslope movement of sediments generating surface geomorphic features at the seafloor classified into source and depositional areas (Fig. 1.1). The source area defines the zone where sediments failed along a basal shear surface from the preserved slope which is generally highlighted by a sharp contact at the head scarp and at the lateral scarps (Bull et al., 2009). The scarps can reach more than 100 m height (Urgeles and Camerlenghi, 2013 and references therein) and in some cases, features including blocks and minor debris can be left stranded during the mass-movement in the source area (Fig. 1.1). The geomorphometric analysis of the seafloor usually reveals smooth surface in the case the mass-movement evacuated the landslide scarp and concave downslope steps created by the blocks that remained at the source area (Fig. 1.1). The depositional area is often characterized by a frontal ramp where the mass-movement

motion ceased and by internal and surface deformation (Bull et al., 2009; Fig. 1.1). Overall, these sedimentary bodies are termed “mass-transport deposit”- MTD. Three internal domains characterize MTDs including normal faults in the extensional domain (source area), chaotic structures in the translational domain (evacuation area) and folds and thrusts faults in the contractional domain (depositional area) (Steventon et al., 2019; Fig. 1.1). In the latter, the internal structure is reflected on the surface of the MTD by convex downslope ridges perpendicular to the direction of movement (Bull et al., 2009).

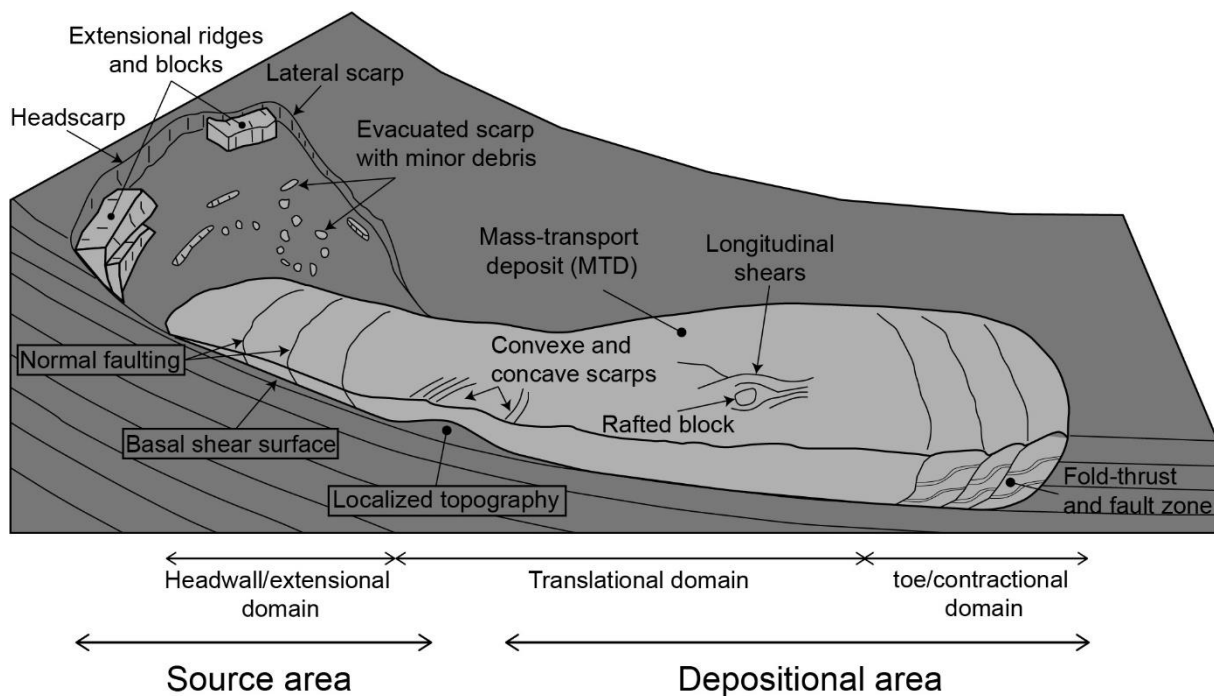


Figure 1.1: Schematic representation of the anatomy of a subaqueous landslide adapted and modified from Bull et al. (2009; Mountjoy and Micallef (2018); Steventon et al. (2019).

Submarine landslide is a general term to designate all the different types of the subaqueous high-density flows (e.g. slides, debris slide, slumps, and debris flow) that are driven by gravity (Hampton et al., 1996; Masson et al., 2006). The diverse gravity-driven depositional processes depends on the type of material transported/failed (rocks, soils, mud, or a mixture of all of them) and the sediment concentration leading to different mechanical behaviour (deformation) during the sliding motion (Dott, 1963). MTDs can be characterized by brittle deformation (e.g. slide block, debris slide) or plastic deformation/laminar flow (e.g. slump, debris flow) (McHugh et al., 2002) leading to different internal structures, which inform on the type of movements and the material transported. A rigid and internally undeformed MTD is described as slide (e.g. translational and rotational slides) while an MTD characterized by the prevalence of viscous fluids is described as mass flow (e.g. debris Flow) and characterized by

a high and a low sediment concentration, respectively (Lee et al., 2007). Combined, the two terms allow the classification in sub-categories below (Fig. 1.2):

- A) Block slide (or translational slide) characterizes the movement of blocks/units moving downslope with a relatively coherent mass/strata parallel (no internal deformation) due to gravitational instability along a planar glide plane (e.g. Harders et al., 2011; Sammartini et al., 2018).
- B) Debris Slide (or debris avalanche) is a mass movement in which fragmentation has reduced the landslide mass to individual rock fragments, blocks and clasts in a cohesionless slump during sudden, catastrophic failures. They commonly have a well-defined amphitheatre-like source area, while blocks create a hummocky terrain on top of the MTD (e.g. Bell et al., 2013; Masson et al., 2002).
- C) Slump (or rotational slide) is a coherent mass of sediments with the rotational movement of blocks in response to gravitational instability on a curved and concaved rupture surface along a discrete glide plane (e.g. Perissoratis and Papadopoulos, 1999). The rotational shear-surface movements cause internal deformation and are capable of transporting gravel and coarse-grained sediment. Slumps can be recognized by their chaotic seismic facies in seismic reflection profiles (e.g. Martinsen, 1989; Shanmugam, 2006).
- D) Debris flow is a heterogeneous and cohesionless sedimentary body composed of large clasts supported and carried along the slope by a sediment-water mixture (e.g. Masson et al., 1997; Talling et al., 2007). The flow has a plastic rheology with minimum sediment concentration (mud-rich or sand-rich) capable of transporting clasts, gravels and coarse-grained materials by inherent strength (e.g. Gee et al., 1999; Lastras et al., 2002).
- E) Creep is the slow downslope movement of sediments resulting in its deformation and generating compressional ridges due to rotational movement of strata (Hill et al., 1982; e.g. Li et al., 2016). There is no head or lateral scarp or exposed shear surface in this type of mass-movement.

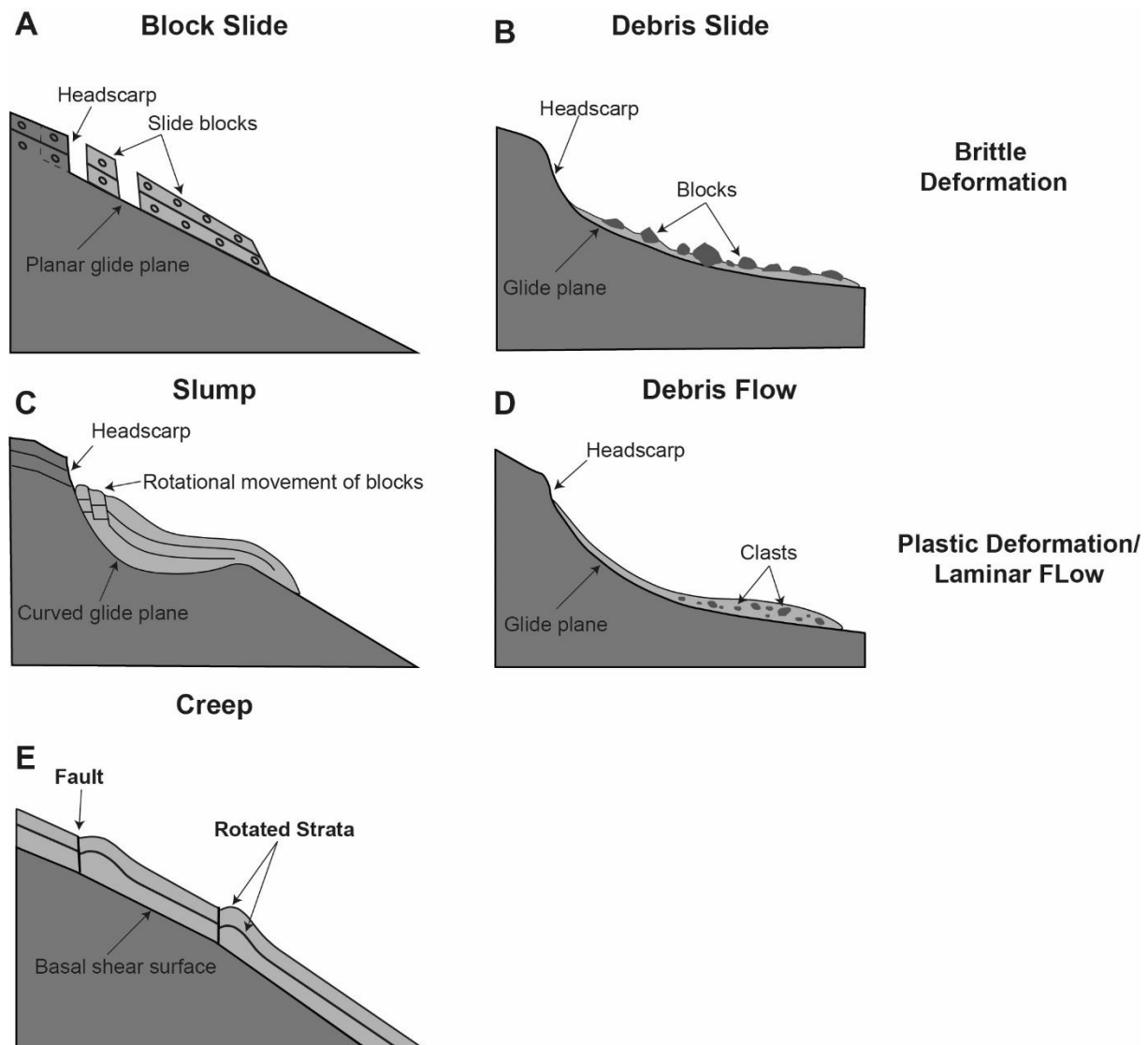


Figure 1.2: Schematic illustration of the major types of submarine gravity-driven depositional processes modified and adapted from Hugh *et al.* (2002); Harders *et al.* (2011).

However, landslides are not restricted to only one of these sub-categories but can be the combination of two or more of the above processes with flow transformations and superposition of different bodies. When this happens they are called “complex landslides” or “mass-transport complexes” (MTCs) (Fisher, 1983; Fig. 1.3). The long-runout distance tends to play a role in the flow transformation of the MTD (e.g. MTD offshore northwest Africa, Talling *et al.*, 2007). In fact, submarine landslides can extend from a few tens to hundreds of kilometres (e.g. Storegga Slide, Bugge *et al.*, 1987; Canary Debris Flow, Masson *et al.*, 1997; Urgeles and Camerlenghi, 2013 and reference therein). The long-runout distances can increase the fluid content (or flow state) during the mass-movement and form a distal end member taking the form of one of the MTD sub-categories or as a turbidity current (Fisher, 1983). Turbidity current is one of the sediment flow type with debris flow (Middleton and Hampton,

1973; Haughton et al., 2009; e.g. Piper et al., 1999) but is not considered as a mass-transport processes according to Dott's (1963) classification due to the very low sediment concentration. A turbidity current is a dilute flow driven by a low sediment concentration ( $< 23\%$ , see fig. 3) under the influence of gravity and supported by fluid turbulence where deposition occurs through settling (Sanders, 1965; Mulder and Alexander, 2001). Turbidity currents are considered Newtonian flows due to the lack of inherent strength leading to unsteady and non-uniform behaviour the moment a shear stress is applied. Turbidity currents can be the end member of a debris flow as suggested in figure 1.3 (e.g. Sohn et al., 2002; Felix and Peakall, 2006) as well as other sediment transport processes (e.g. Strachan, 2008).

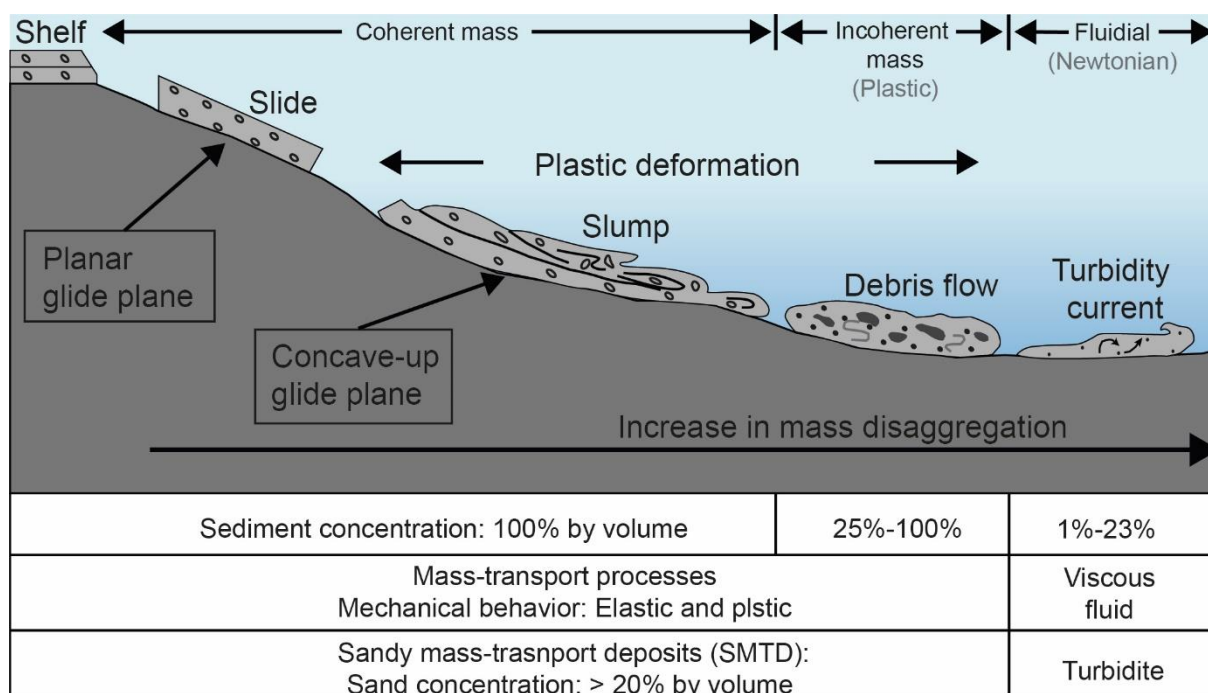


Figure 1.3: Schematic illustration of a complex subaqueous landslide transformed in terms of sediment concentration and mechanical behaviour as it moves downslope, modified from Shanmugam (2013).

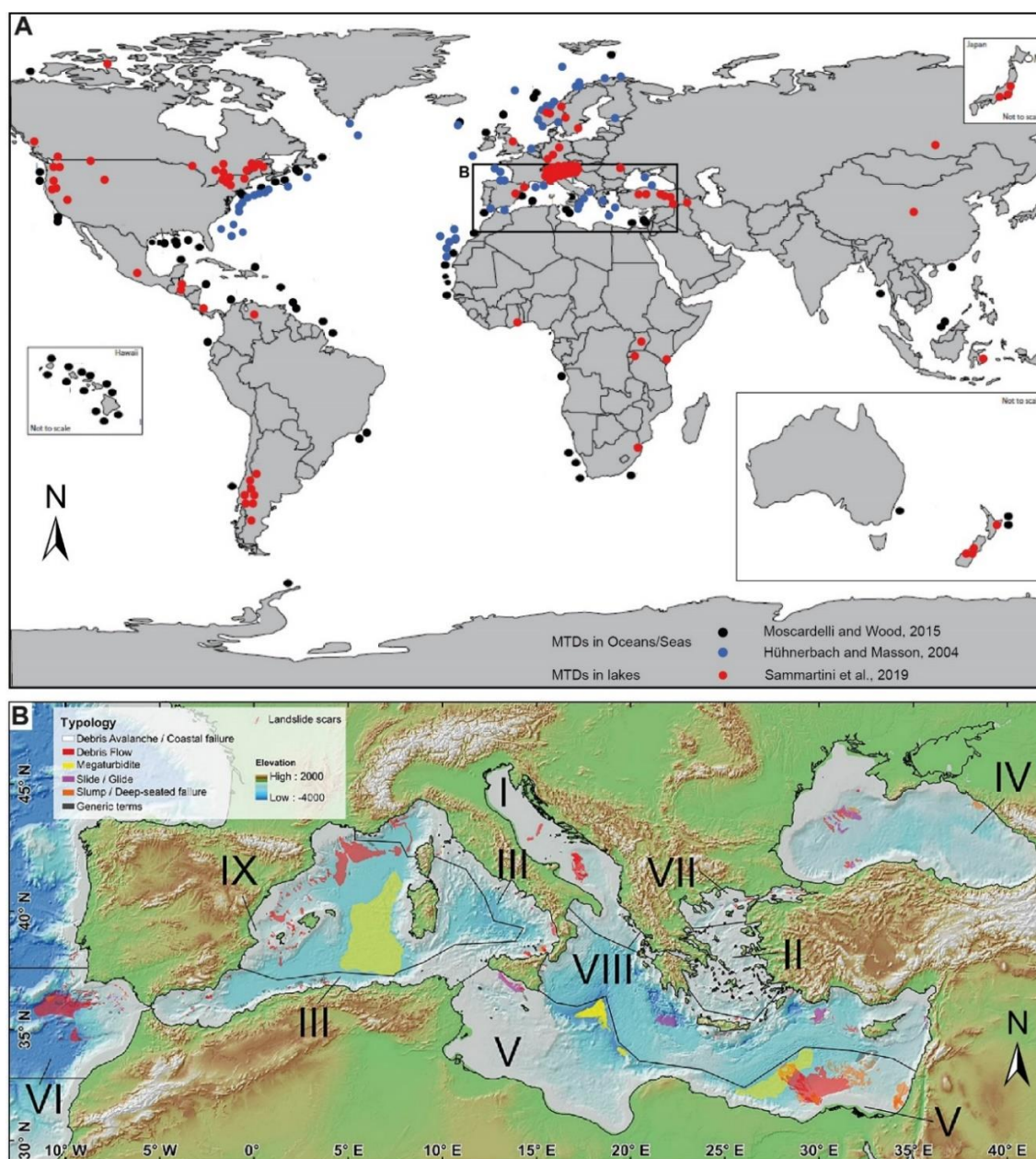
Thus, sediment concentration, which is much higher in submarine landslides (25 to 100% by volume) compared to turbidity currents ( $< 23\%$  by volume) governs also the efficiency of the mass-transport (Shanmugam, 2012). The flows transformation during the downslope motion can drastically increase the MTD in size and speed eroding sediments from the substrate (Piper et al., 1997). Turbidity currents are estimated to be capable of reaching velocities up to 67 km/h (Piper et al., 1988). The velocities are subjective as velocity meters are commonly destroyed during direct measurements due to the destructive potential of sediment transport processes such as the mass flow in the case of submarine landslides or the high erosion and knickpoint migration along channels in turbidity systems (Heijnen et al.,

2018). For examples, direct measurement of turbidity currents could be made when lower velocity was recorded at 5.4 km/h (Hage et al., 2019) and 26 km/h (Paull et al., 2018). In this latter case, the turbidity current was capable of carrying an 800 kg frame on a few kilometres' runout (up to 4.2 km) and at a speed of up to 14.4 km/h despite a rather low velocity (Paull et al., 2018). There is no record of direct measurement of flow velocities from MTDs and cannot be reconstructed after deposition due to the non-proportional relationship with grain-size and the impossibility to know if the MTDs have experienced flow transformation during their transport from the source area (Shanmugam, 2013).

### 1.2.2 Spatial distribution of subaqueous landslides

Subaqueous landslides are globally distributed in oceans, seas and lakes along continental margins from active to passive margins and from glaciated to non-glaciated margins where slopes are present (Moscardelli and Wood, 2016; Hühnerbach et al., 2004; Urgeles and Camerlenghi, 2013; Sammartini et al., 2019; Mountjoy and Micallef, 2018 and references therein; Mienert et al., 2002 and reference therein; Fig. 1.4A). However, they tend to be more present in certain geological settings and occur preferentially in fjords, active river deltas, submarine canyon-fan systems, volcanic island flanks (Moscardelli and Wood, 2016; Hühnerbach et al., 2004). Some features as steep slopes and conditions as rapid deposition of sediments were thought to favour their emplacements (Korup et al., 2007), but most of the submarine landslides occurred on very low slope angles,  $\sim 5^\circ$  in the Atlantic (Hühnerbach et al., 2004) and  $< 2^\circ$  in the Mediterranean Sea (Urgeles and Camerlenghi, 2013). In addition, very low slope angles ( $< 2^\circ$ ) tend to cause the emplacement of the largest submarine landslides (Hühnerbach et al., 2004; Urlaub et al., 2015). The water depth interval of where submarine landslides initiates (source area) is rather wide (200 to 1,500 m w.d.) but tend to be deeper in the Atlantic (between 500-1,500 m; Hühnerbach et al., 2004) compared to the Mediterranean Sea (200 to 600 m; Urgeles and Camerlenghi, 2013). Subsequent retrogressive erosion may extend the failure upslope towards the shelf edge (Masson et al., 2010). The water depths of the MTDs depositional areas vary depending on the runout (i.e. distance run by the MTD from the source area). The runout depends essentially on the type of material and the type of movement (section 2.1) but does not depend of the slope angle as longest runout are found on the lowest slope angles (McAdoo et al., 2000). Steeper slopes tend to involve less disintegrative materials (slide and slump) while larger failures occurring on low slope angle tend to consist of softer and more mobile sediments (debris flow and turbidity current) (Hühnerbach et al., 2004). In the Mediterranean Sea, MTDs are frequently observed near and/or within the source

areas (Urgeles and Camerlenghi, 2013). Multiple factors play a role in determining the type of sediment transport processes and the slope angle of a margin (Shanmugam, 2000), which can be characterized by steep (e.g. Rhone-Ebro margins) and gentle slope (e.g. The Nile delta). One of the major sediment load contributing to the margin outbuilding is the fluvial transport of sediment (Milliman and Meade, 1983) where a relationship between the distance travelled by the sediments (erosion and hydro-selection) and the various continental margin growth (Bouma, 2000) may explain the different types of sediment transport processes reported in the Mediterranean Sea (Fig. 1.4B). To resume, a multitude of subaqueous landslides were mapped worldwide where slopes are present and still the maps show many other submarine slopes that could have experienced MTDs.



(caption on next page)

*Figure 1.4: A) Compilation of worldwide location of mass-transport deposits (MTDs) in oceans, seas and lakes based on (Hühnerbach et al., 2004; Moscardelli and Wood, 2016; Sammartini et al., 2019). Black rectangle indicates the location of B. B) Typology and position of MTDs discovered in the Mediterranean Sea (Urgeles and Camerlenghi, 2013).*

---

### 1.2.3 Dimensions of subaqueous landslides

Subaqueous landslides may have a wide range of volumes and areas (Urgeles and Camerlenghi 2013; Sammartini et al., 2019). The largest known MTD affected an area of nearly 80,000 km<sup>2</sup> characterized by a volume of more than 20,000 km<sup>3</sup> off the southeast coast of Africa, the “Agulhas Slump” (Dingle, 1977). This volume would be sufficient to cover entirely France with more than 30 m of sediments. Another very large subaqueous landslide is the “Chamais Slump” close to the Agulhas Slump covering an area up to 68,700 km<sup>2</sup> and a volume of 17,433 km<sup>3</sup> (Dingle, 1980). Apart from these two exceptionally large submarine landslides, most of them involve volumes of several 100 km<sup>3</sup> worldwide (Moscardelli and Wood, 2016; Fig. 1.5A). Among the largest are the Storegga Slide offshore Norway (3500 km<sup>3</sup>; Bryn et al., 2005; Haflidason et al., 2005), the Western MTD at the Amazon Fan (2000 km<sup>3</sup>; Piper et al., 1997); the Isular Slope Slide (1500 km<sup>3</sup>; Schwab et al., 1993) and the Brunei Slide in Indonesia (1200 km<sup>3</sup>; Gee et al., 2007). Some of these large submarine landslides occurred along passive margins (e.g. Storegga Slide) while failures of large landslides tend to have a lower frequency along active margins (Scarselli, 2020 and reference therein) explained by the seismic loading of low peak ground acceleration (Strozyk et al., 2010) and the lack of available sediments (Tappin et al., 2007). Fluvial transport represents a major sediment load for continental margins (Milliman and Meade, 1983) where numerous landslides have been reported (e.g. Coleman et al., 1998; Loncke et al., 2009; L’Heureux et al., 2010) but the lack of major sediment input do not necessarily impede the failure of large MTDs (Urlaub et al., 2015 and reference therein). Surprisingly, very large submarine landslides tend to occur on remarkably low gradients (Urlaub et al., 2015) and transport intact blocks from tens to hundreds of meters (Shanmugam and Wang, 2015). The correlation complexity between size and frequency of the subaqueous landslides with slope gradient was found in the northern Atlantic. Hühnerbach et al. (2004) indicate that failures are more frequent but significantly smaller (median volume equal to 1.4 km<sup>3</sup>) on a stronger slope gradient (4.5°) and fewer but much larger (median volume equal to 30 km<sup>3</sup>) on a weaker slope gradient (2.2°).

In the Mediterranean Sea, Urgeles and Camerlenghi (2013) reported 696 submarine landslides covering 18% of the seafloor. The MTDs are mainly characterized by volume of less than 50 km<sup>3</sup> (Fig. 1.5B) and areas up to 100 km<sup>2</sup>. A massive Mediterranean example is the

Gela Slide in the Gela Basin (central Mediterranean Sea, Trincardi and Argnani, 1990) with a volume estimated of  $630 \text{ km}^3$  for an area of more than  $1500 \text{ km}^2$  (Mueller et al., 2020). However, more than half of submarine landslides reported in the Mediterranean Sea range with much smaller volumes and area sizes, from  $0.1$  to  $10 \text{ km}^3$  (380/696) and from  $1$  to  $100 \text{ km}^2$  (419/696) (Urgeles and Camerlenghi, 2013; Fig. 1.5B). All the submarine landslides are present around the Mediterranean Sea where most of them initiated on slopes characterized by low gradients ( $1$  to  $2^\circ$ ; Urgeles and Camerlenghi, 2013).

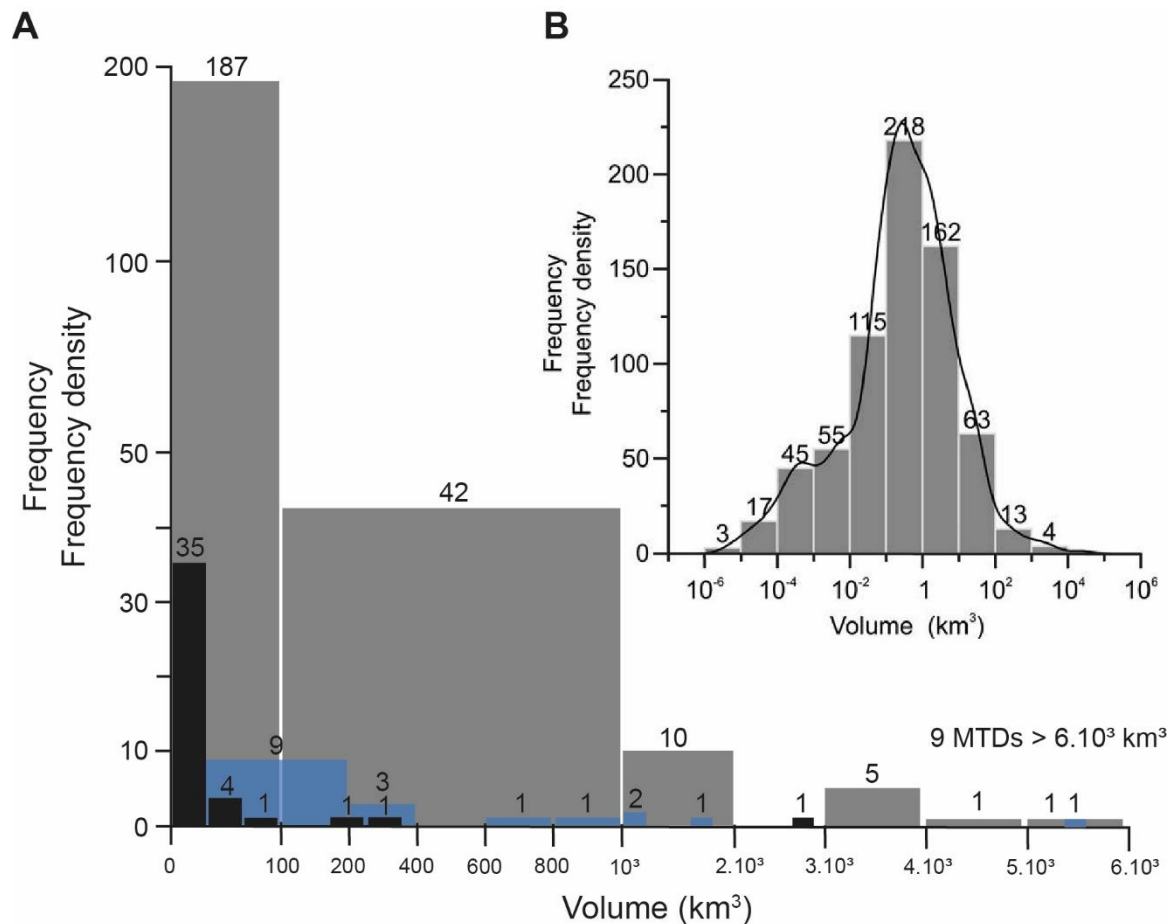


Figure 1.5: A) Histogram showing the number of slope failures and their estimated volumes worldwide (grey bars), in the western (black bars) and eastern North Atlantic (blue bars) (modified and adapted from Hühnerbach et al., 2004, Moscardelli and Wood, 2016) and B) in the Mediterranean Sea (after Urgeles and Camerlenghi, 2013).

#### 1.2.4 Pre-disposing factors and triggering mechanisms

Subaqueous landslides are the result of rapid changes within the sedimentary environment controlled by gravity, the material type, grain size distribution, the weight (e.g. compaction), the slope angle and the pore-water pressure. Along continental margins and lakes, slopes are considered stable as long as the forces that act to resist deformation in the sediments

(shear strength) are greater than gravity (shear stress). A limit equilibrium calculation between these two forces generates a factor of safety (FS) indicating stability if the shear strength is higher than the shear stress ( $FS > 1$ ; Fig. 1.6A) or instability if the shear stress is equal of superior to the shear strength ( $FS \leq 1$ ; Fig. 1.6B) (Strasser et al., 2007 and reference therein). In order for a slope to become unstable and being involved in sediment failure, various pre-conditioning factors and triggering mechanisms can decrease and lose the shear strength and/or increase the shear stress (Masson et al., 2006; Talling et al., 2013; Urgeles and Camerlenghi, 2013; Fig. 1.6C). These mechanisms can vary in time and act on both the shear strength and the shear stress within a few minutes (e.g. earthquakes, Fine et al., 2005) or may take a few hundreds of thousands of years (e.g. climate forcing, Talling et al., 2014). They can change the physical, chemical, and geotechnical properties of the sediments leading to changes in excess pore pressure, which contribute to bring instability and/or participate in sediment failure (Flemings et al., 2008; Urgeles and Camerlenghi, 2013; Wiemer et al., 2015). The excess pore pressure is proposed to explain the long-runout of submarine landslides (Gee et al., 1999) and these mechanisms include seismic/volcanic activity (e.g. Masson et al., 2002; Mountjoy et al., 2018; Roland et al., 2020), slope oversteepening due to contourite deposition (Miramontes et al., 2018) and diapirism (Tripsanas et al., 2003), increased and high sedimentation rates (Laberg and Camerlenghi, 2008; Leynaud et al., 2007; Sawyer et al., 2017), deposition of weak layers providing potential glide planes (e.g. Harders et al., 2010; Locat et al., 2014), the alteration of clay (Wiemer et al., 2015), gas discharge (Sultan et al., 2004), diagenesis (Davies and Clark, 2006), fluid flow (Greene et al., 2002; Huhn et al., 2006), and human activity (e.g. Dan et al., 2007). A more complete list of trigger mechanisms is available in Urgeles and Camerlenghi (2013) showing those capable of decreasing the shear strength (e.g. fluid flow, gas dissociation) and those increasing the shear stress (e.g. seismic loading over-steepening) (Fig. 1.6C). However, in some context such as active margins, repeated earthquake loading can lead to dissipation of the pore-pressure excess and increase the sediment strength (Sawyer and DeVore, 2015; Ten Brick et al., 2016).

Overall, many “natural” processes have the potential to affect submarine slopes and contribute to failures in some cases. The variety of pre-disposing and triggering factors indicate the importance to clearly identify these processes beyond the triggering factor often related to seismic shaking.

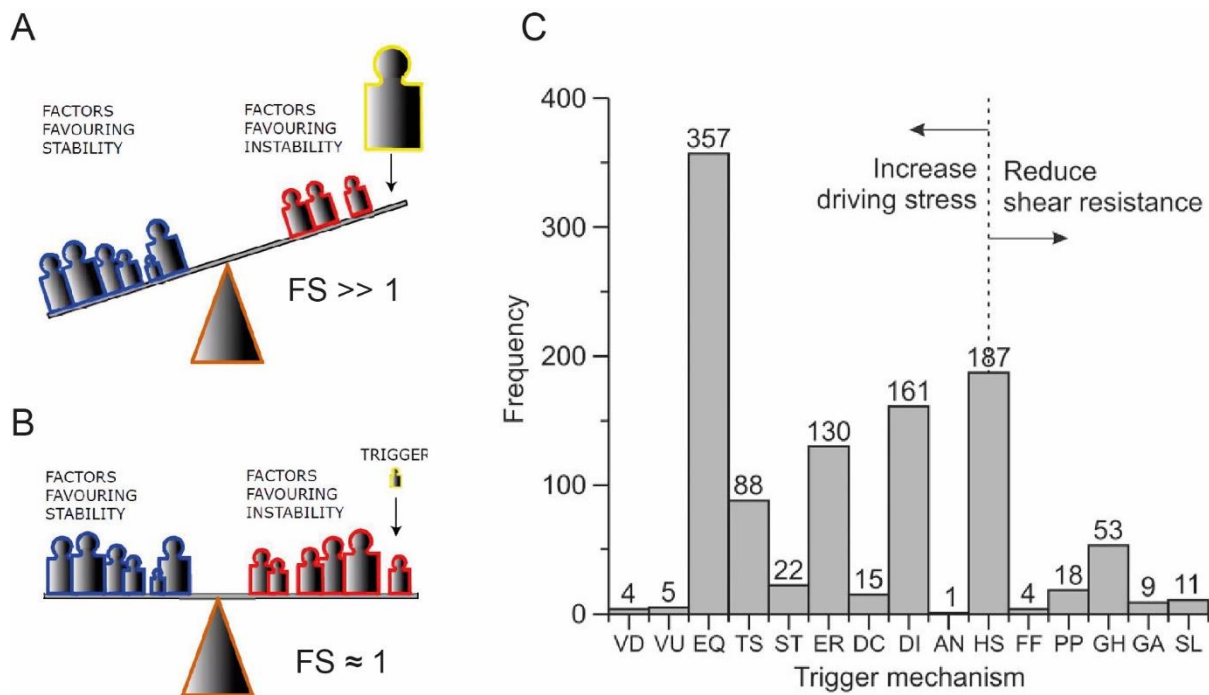


Figure 1.6: A) Representation to understand the role of pre-conditioning factors and B) triggering mechanisms in slope failures (pers. com. Dr. Angelo Camerlenghi). FS: factor of safety. C) Frequency of the slope failures in the Mediterranean Sea versus the major triggering mechanisms (Urgeles and Camerlenghi, 2013). In addition, the triggering mechanisms are separated according to those that increase the driving stress and those that reduce the shear strength. VD: volcano development, VU: volcano uplift, EQ: earthquake, TS: tectonic steepening, ST: steepening, ER: erosion, DC: differential compaction, DI: diapirism, AN: anthropic, HS: high sedimentation rates, FF: fluid flow, PP: pore pressure, GH: gas hydrates, GA: gas, SL: sea level.

Also, anthropogenic activities may impact slope stability, as in the case of the 1979's landslide which occurred during the works for expanding offshore Nice airport (see Dan et al., 2007). Preceding the failure, multiple failures and collapses (> 100) were reported on the airport. These indicators were precursors of an unstable slope due to an increasing weight of sediments during the construction and the important pluviometry preceding the failure, which increased drastically the pore pressure in the aquifer leading to the failure of the slope (Dan et al., 2007). Failure tend to occur between two different sediment layers inducing that changes of physical/mechanical/chemical properties can generate weak surfaces favouring slope failure (e.g. Kvaslstad et al., 2005; Kuhlmann et al., 2017; Miramontes et al., 2018).

### 1.2.5 Tsunamigenic potential

Subaqueous landslides have the similar potential to generate tsunamis (e.g. Sawyer et al., 2017; Strupler et al., 2018) as earthquakes (e.g. Kanamori and Kikuchi, 1993), volcanic eruptions (e.g. Yegorov, 2007), meteorological (e.g. Bechle and Wu, 2014) and meteorite

impacts (e.g. Smit, 1996). The rapid movement of a sediment mass (landslide dynamic) creates water displacement in front and behind the failed mass inducing impulsive vertical displacement of the water towards the sea surface referred as energy transfer from landslide to the water column (Tinti and Bortolucci, 2000; Tappin, 2017; Fig. 1.7A and B). This energy transfer generates (Fig. 1.7C) and propagates a water wave or series of waves (called “tsunamis”) characterized by long wavelength and long periods (wave propagation) that may impact the coastline with a certain vertical run-up (Tinti and Bortolucci, 2000; Fig. 1.7D). However, not all subaqueous landslides generate tsunami waves as the energy transfer into wave energy is determined by multiple factors such as the water depth of the landslide, its volume and the slope gradient which directly influence the initial acceleration and maximum velocity (Harbitz et al., 2006; Ward, 2001; Løvholt et al., 2005; Zengaffinen et al., 2020). Since 1950, 64 tsunamis were caused by landslides worldwide, which represent around 8% of all tsunamis registered at the global scale (NTL website: [www.tsun.sccc.ru/nh/tsunami.php](http://www.tsun.sccc.ru/nh/tsunami.php)). Subaqueous landslides-triggered tsunamis tend to reach higher run-ups locally with shorter wavelengths but their propagation efficiency is reduced compared to earthquakes-triggered tsunamis (Okal and Synolakis, 2003). Overall, the result of the total tsunami energy generated by subaqueous landslide and earthquakes is equivalent (Ruff, 2003) but earthquakes-triggered tsunamis represent 73% of all tsunamis source worldwide (NTL website: [www.tsun.sccc.ru/nh/tsunami.php](http://www.tsun.sccc.ru/nh/tsunami.php)). The threat of a tsunami comes from the fact that the propagation of a tsunami do not move water but carries energy traveling through water (energy transfer). The length of the MTD, its thickness and its initial acceleration dictates the size of the tsunami (surface elevation) while its wave speed depends on the water depth of the seafloor (Harbitz et al., 2006). Therefore, larger submarine landslides should trigger higher surface elevation with devastating effects on adjacent coastal areas (e.g. Fine et al., 2005), however simulations of a few "small" MTDs ( $\sim 1 \text{ km}^3$ ) cases in the Mediterranean Sea demonstrate that can produce tsunami sufficiently high to cause damages to the coastal areas (e.g. Ceramicola et al., 2014; Harbitz et al., 2014; Macías et al., 2015). In particular, their suddenness tend to generate tsunamis more dangerous than tsunamis from relatively larger but slower landslides (Discroll et al., 2000). In the Mediterranean Sea, there is a recurrence of around one submarine landslide every year and every thousand years for volumes superior at  $0.001 \text{ km}^3$  and at  $10 \text{ km}^3$ , respectively (Urgeles and Camerlenghi, 2013). This work of simulation of past subaqueous landslides and the estimation of their potential geohazards is used to better prepare coastal cities as well as offshore infrastructures for possible future tsunamis. To do so, the most representative

submarine landslides in terms of volume and water depth are used in numerical simulations because they are the most probable event to occur again.

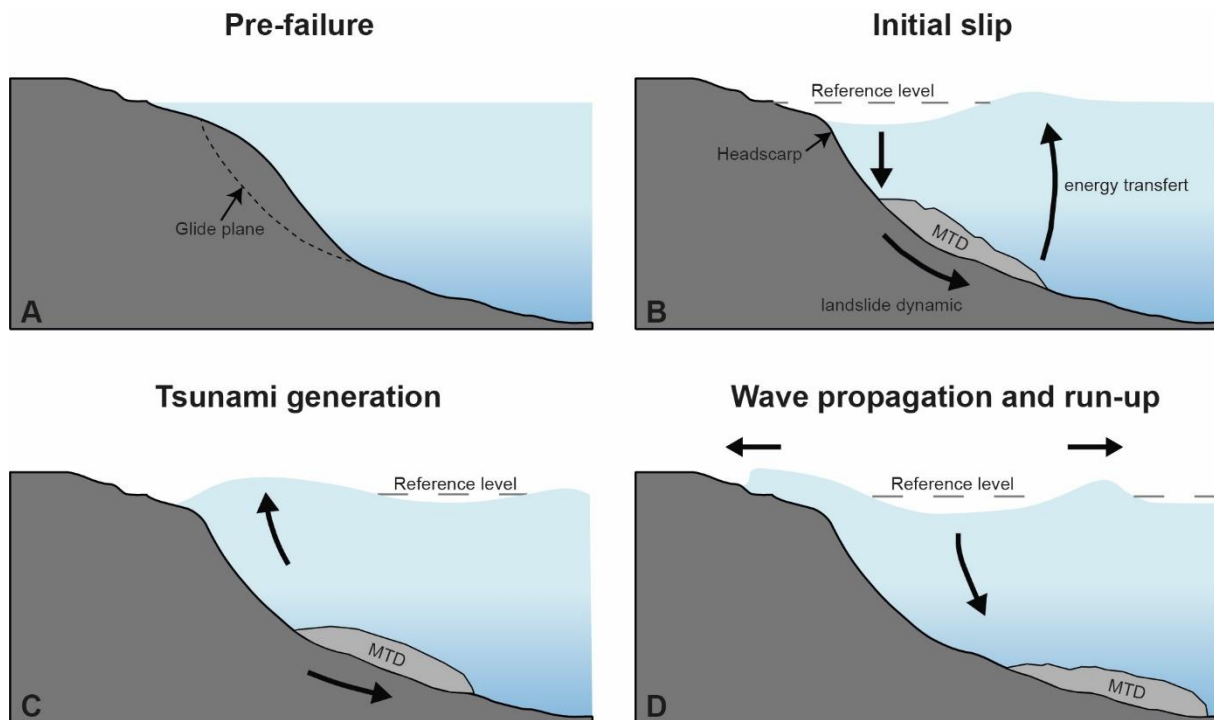


Figure 1.7: Conceptual diagram showing the stages and mechanisms of a tsunami generation from a mass-transport deposit (MTD) with A) the pre-failure, B) the initial landslide dynamic, C) the positive and negative wave generation and D) the wave propagation and run-up (modified after Tappin, 2017; Pakoksung et al., 2019).

### 1.2.6 Economic and Social impact

Subaqueous landslides represent a major marine geohazard with destructive capability in both subaerial (Glade et al., 2005; Jakob and Hungr, 2005; Kirchbaum et al., 2010; e.g. Geertsema et al., 2009) and subaqueous environments (Piper et al., 1999; Talling et al., 2014; Pope et al., 2017). Compared to subaerial environments, subaqueous environments are characterized by additional stresses such as water hydrostatic pressure and oceanographic currents. This type of environment induce water-saturated sediments, potentially charged in dissolved gas, favouring the occurrence of MTDs on very low slope gradient ( $1^{\circ}$ - $5^{\circ}$ ) (Hühnerbach et al., 2004) while terrestrial landslides are almost always stable at comparable slope angles (Ohlmacher, 2001; Donnarumma et al., 2013). Despite their ubiquitous occurrence on subaqueous and subaerial slopes in very different environments, they tend to form analogous features inducing similar behaviour (Shanmugam, 2013; Shanmugam and Wang, 2015). However, subaqueous MTDs can be a few orders of magnitude larger than their terrestrial counterparts (Masson et al, 1992; Hampton et al., 1996; Korup, 2012; Lamarche et al., 2016).

For example, the world's largest subaqueous MTD (20,331 km<sup>3</sup>; Dingle, 1977) is a thousand times volumetrically larger than the world's largest subaerial MTD (20 km<sup>3</sup>; Harrison and Falcon, 1938). Subaqueous landslides are not only larger in size than terrestrial landslides, but also have longer runout distances for similar volumes (Urgeles and Camerlenghi, 2013). The longer runout in subaqueous environments over low slope angles have been attributed to several mechanisms such as flow transformation (Talling et al., 2007), hydroplaning effect and sustained high pore pressure (Urgeles and Camerlenghi, 2013 and reference therein). In subaerial environments, the landslide velocity directly controls the number of casualties (up to thousands) and damages to infrastructures that can reach billion in monetary losses annually (Froude and Petley, 2018; e.g. Tilling et al., 1990). Subaerial landslide activity can be extensively studied using high-resolution satellite and remote sensing mapping, real-time monitoring tools, news reports, social media, which help to operate a comprehensive forecast system. On the contrary, although subaqueous landslides play a hazard potential, our understanding and capability of monitoring is limited compared to subaerial landslides (Talling et al., 2014). In fact, they may cause extensive damages, especially since the increasing number of modern coastal and offshore infrastructures related to the growing economic interest of the seabed for energy (oil, gas; Pinder, 2001), communications (Carter et al., 2009) and mineral resources (Heffernan, 2019; e.g. Lusty et al., 2019) due to a rising demand.

Therefore, numerous geohazards both subaqueous (Camargo et al., 2019) and subaerial (see Mateos et al., 2017) pose a potential threat to coastal areas and populations and maritime activities. Marine geohazards include: 1. slope failures (landslides), earthquakes (faults), volcanism (submarine eruptions and flank collapse from submarine volcanoes) that can cause tsunamis. 2. positive (mounds, ridges, seamount, volcanic highs) and negative reliefs (canyons, slope-channels, gullies, escarpments) that may obstacle navigation. 3. migrating bedforms (e.g. sandwaves), fluid flow (mud volcanoes, gas hydrate, free gas accumulation), bottom currents (contourite deposits) that may pose a risk to offshore installations. 4. subsidence, coastal erosion, and sea-level change that harm the wealth of coastal environments (Fig. 1.8).

As said, sediment transport processes pose a threat to offshore platforms (e.g. Hooper and Suhayda, 2005), coastal infrastructure (L'Heureux et al., 2012) and communication cables (e.g. Carter et al., 2012; Kopf et al., 2010). The different dominant flow regimes have an implication on the runout distance exercising pressure on seafloor infrastructures. For example, mudflows triggered by large hurricanes destroyed offshore platforms due to seafloor collapses

in the Mississippi delta (Hooper and Suhayda, 2005). Sediment transport processes may break or damage submarine communication cables, which represent a critical asset as they carry 95% of the transoceanic data traffic including the internet and financial markets (Carter et al., 2012; Talling et al., 2014). From 1995 to 2015, Pope et al. (2017) reported 113 cable breaks caused by individual earthquakes during which mass-flows may have been involved. Modification in slope gradient may also be induced by erosion during knickpoint migration in slope channels (Heijnen et al., 2020) that can remove the sediment supporting the communication cable and lead to its breaking (pers. com. Maarten Heijnen). On the other hand, subaqueous failures can directly affect population both on the long-term (e.g. sub-seafloor methane gas exposure and release; Urgeles et al., 2007) and on the short-term with the possible generation of tsunamis (e.g. Tappin et al., 2001; 2014; Fine et al., 2005). Additionally, subaqueous landslides play a role also in the formation of gas and hydrocarbon reservoirs dictating the location, geometry and facies distributions by developing stratigraphic traps (Lamarche et al., 2016; e.g. Portnov et al., 2019; Solheim et al., 2005). The rapid transport of clay-poor and sand-rich sediments by any sediment transport processes (e.g. slide, slump, debris flow) into deep-water environments can develop thick and isolated petroleum reservoirs in deep-water environments (Shanmugam et al., 2009; e.g. Alves and Cartwright, 2010; Beaubouef and Abreu, 2010). Therefore, subaqueous landslides represent a potential hazard, especially since the urbanisation of coastlines in certain European regions, notably in the very densely populated Mediterranean region. The Mediterranean population (120 million inhabitants) is overwhelmed by 135 million visitors each year on only 46,000 km of coastline. A full and integrated marine geohazard assessment, including submarine landslides, is a prerequisite to undertake successful risk management of coastal and deep sea areas by identifying, mapping, and characterizing geohazards occurrence, their parameters and the processes that regulate their occurrence.

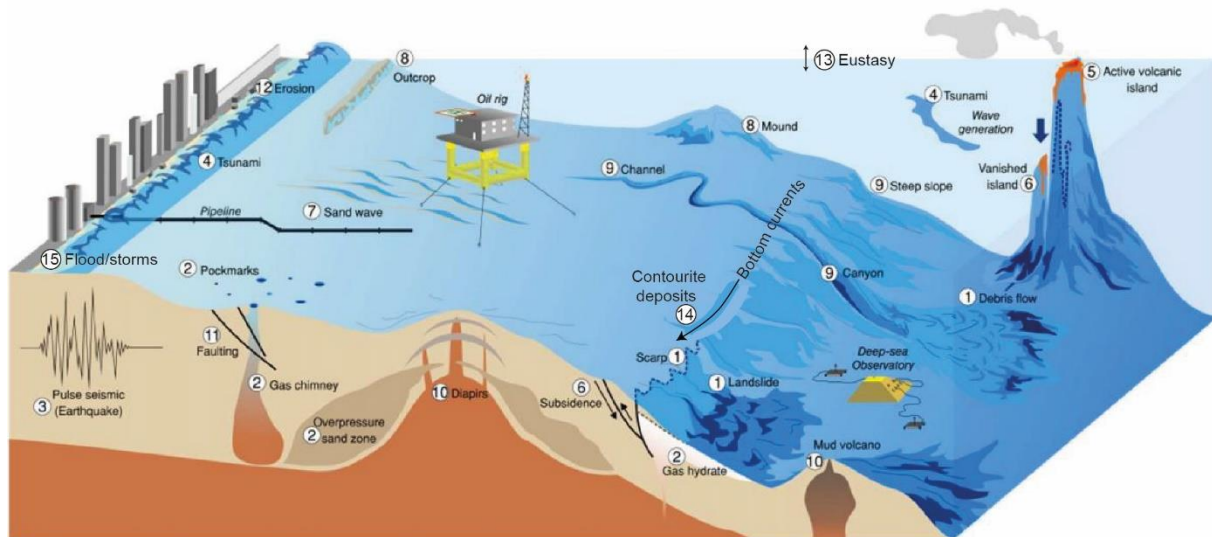


Figure 1.8: Sketch representing the different marine geohazards present on a continental margin (modified from Camargo et al., 2019).

### 1.2.7 Investigating Subaqueous Landslides

The study and detailed analysis of subaqueous landslides and their failure mechanisms in marine realms can turn out to be remote leading to challenging and possible expensive missions (Talling et al., 2013; Kelley et al., 2014). The high cost explains the limited number of missions operated offshore and that only 20% of the seafloor has been mapped with a 100 m resolution compared to 100% of the Moon and Mars with the same resolution (Amos, 2020). However, the recovery and analysis of thousands upon thousands of rock and sediment samples from the seafloor give a far better idea about the geology. Despite the considerable improvements in our understanding of subaqueous environments and their relative landslides in the last decades from Prior et al. (1982) and Bugge et al. (1987) to Locat et al. (1999) and Roland et al. (2020), technological issues still remain in the data positioning and resolution (Clarke, 2012). However, it is probable that a certain number of small and mid-size MTDs will be discovered in the near future alongside the increasing resolution of geophysical technologies for sub-seafloor and seafloor mapping (Casas et al., 2016; Posamentier et al., 2007). Already, the advancement of geophysical technologies permitted the recognition of an increasing number of MTCs (e.g. Gamberi, 2011; Moscardelli 2006; Dalla Valle 2013; Georgiopoulou 2018).

Subaqueous landslides and their deposits are recognized based on multiple criteria (Bull et al., 2009 and references therein), which are established from numerous previous studies (see Embley and Jacobi, 1977; Prior et al., 1982; McAdoo et al., 2000; Locat and Lee, 2002).

MTDs can be investigated through direct observations (submergence vehicle, remotely operated vehicles-ROVs), sampling (e.g. sediment cores, piston cores, drilling cores), indirect velocity estimate (communication cables break), geophysical surveys (seafloor mapping and seismic-reflection profiling), laboratory experiments (e.g. Triaxial stress test, tank experiments), and analogue and numerical modelling. Direct observations of MTDs with submergence vehicle and/or ROVs allow the photographic and video documentation of subaqueous landslides but this method is limited in time and space (e.g. Green et al., 2006). The breaking of communication cables by subaqueous landslides has been used as an indirect measurement tool to estimate their occurrence and flow velocity from the cable-break time lapse (e.g. Piper et al., 1988; Hage et al., 2019; Paull et al., 2018). Geophysical surveys through acoustic signals can acquire surface expression and morphology (seafloor mapping) and/or internal acoustic character and geometry (seismic-reflection profiling) of MTDs (Gamberi et al., 2019). Seafloor mapping has been developed since the 1950s with significant progress in the efficiency of mapping seafloor faster (multibeam mapping systems, 27700 km<sup>2</sup>/day; Shanmugam, 2012) and in its resolution (up to few centimetres) to recognize the morphological characteristics of MTDs (e.g. Casalbore et al., 2019). Seismic reflection profiling allow obtaining cross-section profiles of the seafloor and sub-seafloor with different degree of resolution: from very high resolution (e.g. sub-bottom profilers) to very high-penetration systems (e.g. multi-channel systems). They provide information on the first dozens of meters (sub-bottom) to kilometres (multi-channel) of the sub-seafloor. However, these approaches are limited to identify subtle sedimentological and structural internal features of the MTDs, which require direct sampling of sediments and/or higher resolution techniques such as 3D-seismics (Frey-Martinez et al., 2005 and references therein; Waage et al., 2019). The 3D-seismic technology remains poorly used due to the industry-scale higher costs compared to more conventional techniques that are accessible to the academic and research sectors. The study of submarine MTDs can be useful for comparing with ancient systems that are outcropping onshore (e.g. Festa et al., 2016 and references therein). The analysis of ancient outcropping MTD examples can advance the understanding of the internal structures of MTDs, including the glide plane and sliding mechanism, and estimating the age of the MTDs. In addition, sediment samples from both subaqueous and fossil MTDs can be tested in laboratory to evaluate their shear strength (e.g. Hsu et al., 2018) and improve the numerical models (e.g. Dey et al., 2016). Indeed, in the last decades, significant progress has been made to increase our understanding of subaqueous landslides and the factors that govern their onsets and evolution

through interdisciplinary studies (e.g. L'Heureux et al., 2010; Henkel et al., 2011, Clare et al., 2018; Badhani et al., 2020a; Gatter et al., 2020).

### 1.3 Scientific objectives, approach

Even though submarine landslides have been the subject of a wealth of studies worldwide, still many aspects remain poorly understood such as their preconditioning and triggering mechanisms, their frequency and relationship to climate/sea level, and their dynamics and interplays with other geological processes in the marine environment. As seen, submarine landslides represent an important geohazard for coastal and offshore infrastructures, especially in the Mediterranean Sea, characterized by densely populated coastlines, where most of continental slopes experienced or are susceptible to experience slope failures (Urgeles and Camerlenghi, 2013). The study of newly identified submarine landslides in the Gela Basin (central Mediterranean Sea) represents an opportunity to improve our understanding of submarine landslides and of the evolution of the Gela Basin by addressing the following scientific questions:

- What are the pre-conditioning and triggering factors responsible for the emplacement of submarine landslides in the Gela Basin?
- How frequency and size of the submarine landslides emplaced in the Gela Basin evolved through the Pliocene-Pleistocene?
- What were the key time intervals for the emplacement of submarine landslides and their relationship with climate and/or sea-level change?
- What threat pose submarine landslides on the offshore and coastal infrastructures around the Gela Basin?

The objectives of this thesis are to use a multidisciplinary approach and analytical techniques for slope instability in order to identify the variety of factors and drastic shifts in sedimentary regime responsible for submarine landslides in the Gela Basin, which could also be applicable for the entire Mediterranean basin. This approach includes a complete geological analysis considering tectonic evolution and seismicity, sediment provenance and dispersal, the architectural development of the margin and its relation to the oceanographic setting, and detailed stratigraphic analysis of available sediment cores.

## 1.4 Thesis Outline

This PhD thesis is organised in 7 Chapters.

**Chapter 1** introduces the H2020 ITN project, which underlies this research study, and contains the scientific background on subaqueous landslides as well as scientific questions and objectives of the thesis.

**Chapter 2** presents the regional setting of the study area with a literature review of the geodynamic, oceanographic, geological and geomorphological settings from the Mediterranean to the Gela Basin scale.

**Chapter 3** resumes previous researches made on submarine landslides in the Gela Basin and illustrates the data and methodology used in this study with a detailed description of the different data types (well data, multi-channel and sub-bottom seismic profiles, piston cores and multibeam bathymetry), their provenance, acquisition techniques, purpose and applications.

**Chapter 4** documents the last 5 Ma evolution of the Gela Basin using multi-channel and single-channel seismic profiles and boreholes. The data indicate a complete re-organisation of the margin outbuilding at the mid-Pleistocene transition (0.8 Ma) with drastic changes in the cyclicity of the margin instability and in the volumes displaced. This chapter has been published as:

Gauchery, T., Rovere, M., Pellegrini, C., Cattaneo, A., Campiani, E., Trincardi, F., 2021. Factors controlling margin instability during the Plio-Quaternary in the Gela Basin (Strait of Sicily, Mediterranean Sea). *Marine Petroleum Geology* 123, 104767. <https://doi.org/10.1016/j.marpetgeo.2020.104767>

**Chapter 5** evaluates the geohazard potential of two similar-size MTDs discharged in the northern and southern Gela Basin based on bathymetric and seismic data as input to numerical models which define the tsunami-landslides scenarios. This chapter has been published as:

Zaniboni, F., Pagnoni, G., Paparo, M.A., Gauchery, T., Rovere, M., Argnani, A., Armigliato, A., Tinti, S., 2021. Tsunamis From Submarine Collapses Along the Eastern Slope of the Gela Basin (Strait of Sicily). *Frontiers Earth Sciences* 8, 644. <https://doi.org/10.3389/feart.2020.602171>

**Chapter 6** analyse in detail the variability and interplay of sedimentary processes and climate/oceanographic forcing during the last 20 ka that favoured the deposition of MTDs in the southern Gela Basin, of which Chapter 5 has defined the geohazard potential, by applying a multi-proxy approach on sedimentary records acquired through long piston sediment cores. This chapter has been published as:

Gauchery, T., Rovere, M., Pellegrini, C., Asioli, A., Tommaso, T., Cattaneo, A., Trincardi, F., 2021. Post-LGM multi-proxy sedimentary records of bottom-current variability and downslope sedimentary processes in a contourite drift of the Gela Basin (Strait of Sicily). *Marine Geology* 439, 106564. <https://doi.org/10.1016/j.margeo.2021.106564>

**Chapter 7** synthesizes the outcomes of the three manuscripts, highlighting their limits and main implication.



# Chapter 2. Regional Setting

## 2.1 Geodynamic setting

The Mediterranean basin develops at the plate boundary between the African in the south and the Eurasian plates in the north, and the Arabian plate, further east (Figure 2.1). The numerous continental blocks, mountain ranges, volcanic arcs (modern and ancient) and oceanic basins (including several back-arc basins) bear witness of the long history of collision. The current kinematic movements between the continental blocks, characterized by subduction and collision processes, generate deformation zones and consequently seismicity (Dilek, 2006; Fig. 2.1).

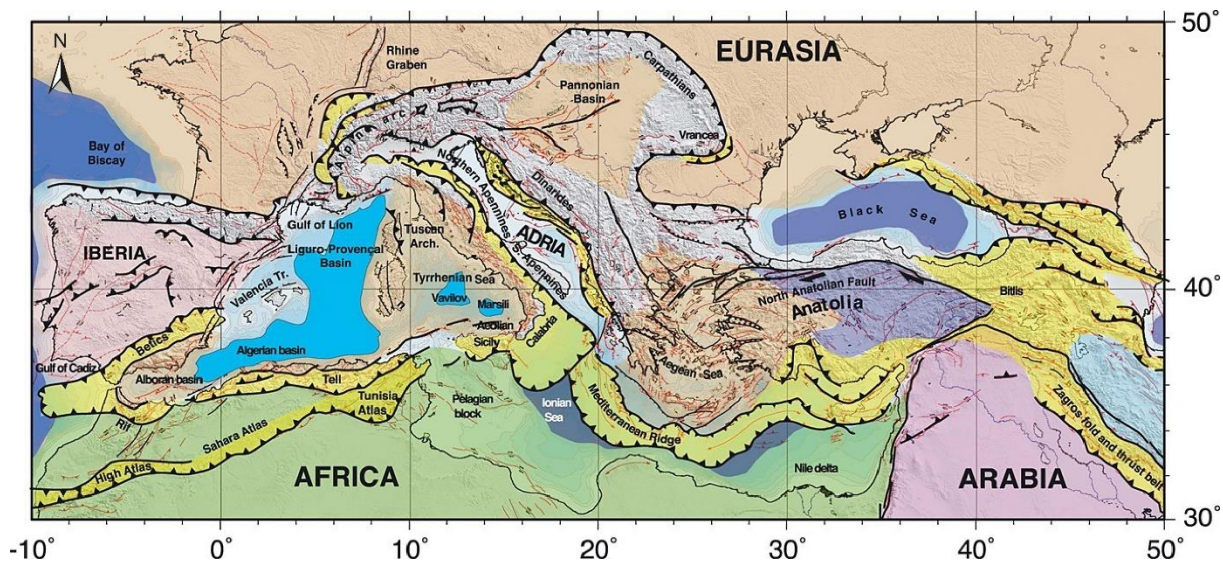


Figure 2.1: Present day location of the plate tectonic setting in the Mediterranean from Faccenna et al. (2014).

The Mediterranean Sea is the last remnant of a large ocean (the Tethys Ocean) located between the Gondwana and Laurasia supercontinents where its extent encompassed more than half of the circumference of the Earth until its closure during the Oligocene-Miocene (~23 Ma; Torfstein and Steinberg, 2020; Fig. 2.2A). The closure of the Tethys Ocean, due to the counterclockwise rotation of Africa towards Eurasia (Faccenna et al., 2001 and references therein), formed an enclosed basin reducing the connection with the surrounding oceans (Fig. 2.1A). The opening of the Ionian Basin and the eastern Mediterranean is thought to have started in the Triassic-Jurassic (Frizon de Lamotte, et al., 2011) and continued during the rotation of Africa towards Europe during the Upper Cretaceous (84 Ma - Figure 2.2A and B) (Rosenbaum,

et al., 2002). On the western edge of the Ionian Basin, the Malta Plateau is thought to be the expression of a transforming margin that developed during the rifting of the northern margin of Gondwana (Jurassic to early Cretaceous; Frizon de Lamotte, et al., 2011).

During the Tertiary and Quaternary, the geodynamic evolution of the Mediterranean is mainly controlled by the African-Eurasian convergence with the northward subduction of the African plate and the retreat of the Tethysian subducting plate and the opening of several back-arc basins (Jolivet and Faccenna, 2000; Fig. 2.2B and C). The Central and Western Mediterranean was controlled by a NW subduction-collisional boundary between the African and European plates position (the Appenninic back-arc) and by its southward retreat (slab rollback) until its present-day position expressed in the north of the Strait of Sicily (Jolivet and Faccenna, 2000; Faccenna et al., 2001; Figs. 2.2B). The slab rollback becoming predominant resulted in the opening of the Liguro-Provençal basin with the rotation of the Corso-Sardinian block during Oligocene to early Miocene (Malinverno and Ryan, 1986; Faccenna, et al., 2011; Fig. 2.2B). Then, from Middle Miocene (12 Ma) to today, the similar episode of retreat with the migration of the Calabro-Sicilian arc to the south-east induced the opening of the Tyrrhenian Sea (Faccenna et al., 2011; Fig. 2.2C). These geodynamic episodes led to the formation of four basins: the Alboran Sea, the Liguro-Provençal basin, the Tyrrhenian Sea and the Aegan Sea (Jolivet et al., 2006).

The convergence of the tectonic plates (tectonic uplift) contributed to the closure of the Strait of Gibraltar leading to the onset of the Mediterranean Salinity Crisis (MSC) 5.59 Ma (Garcia-Castellanos and Villaseñor, 2011b; Govers, 2009; Krijgsman et al., 1999; Fig. 2.2C). The MSC lasted around 260 kyr before Atlantic water (re)connected the Mediterranean Sea (Krijgsman et al., 1999; Garcia-Castellanos et al., 2009; 2020; Madof et al., 2019). The re-opening, which occurred around 5.33 Ma (Krijgsman et al., 1999), was first explained by the regressive fluvial erosion leading to a drastic intensification of the continental erosion during the MSC (Loget and Van Den Driessche, 2006) until a rollback and steepening of the lithospheric slab was proposed by Govers (2009). It may be considered that both processes participated in re-instating the oceanographic connection of the Mediterranean Sea with the Atlantic Ocean.

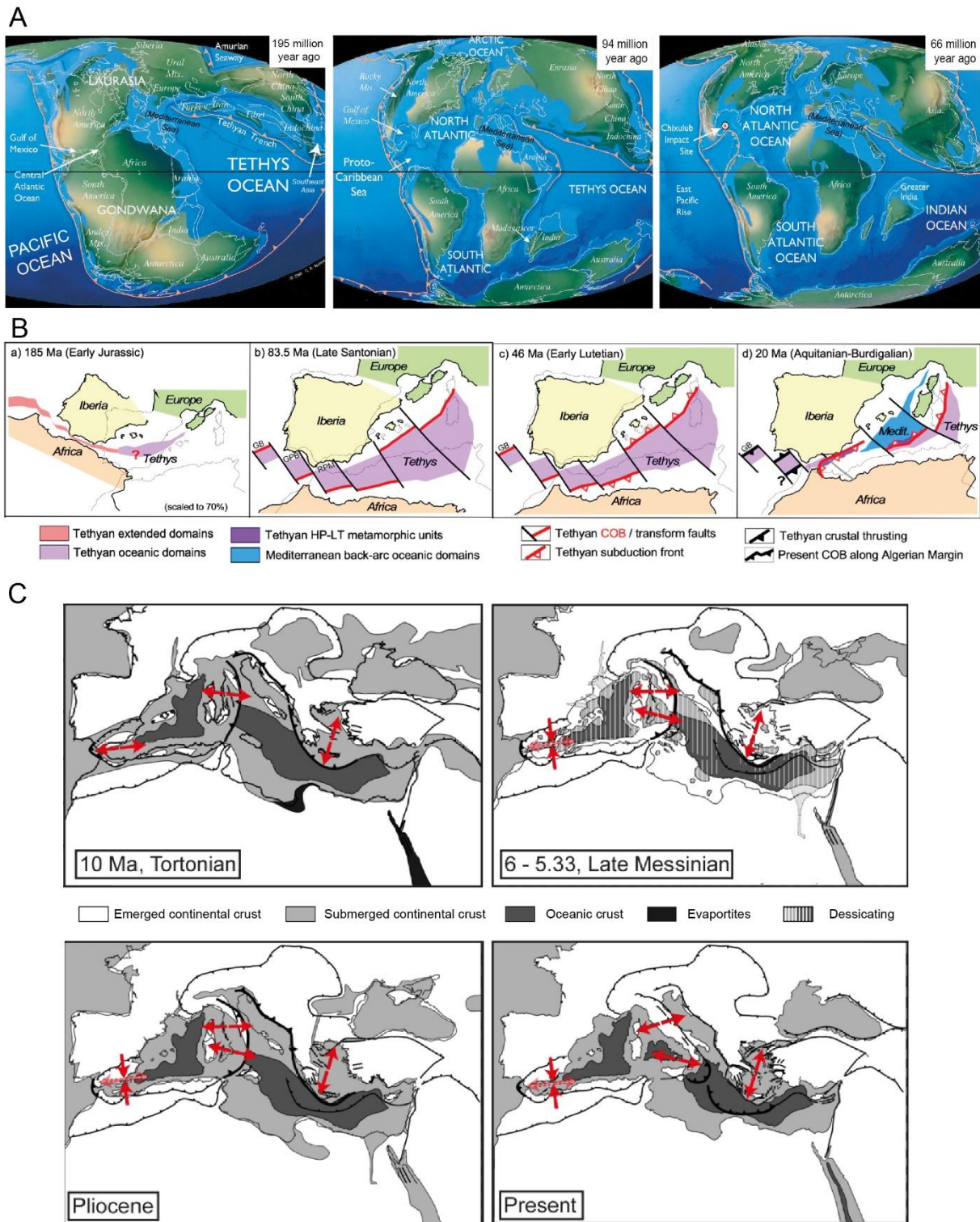


Figure 2.2: A) Paleogeographic Atlas illustrating the movement of the continents from the Early Jurassic with the rotation of Africa plate towards Eurasia plate, modified from Scotese (2001). B) Sketch showing the tectonic evolution of the western Mediterranean since the Early Jurassic and the slab rollback of the Appenninic back arc, modified after Fernàndez et al. (2019). C) Geodynamic evolution of the Mediterranean from 10 Ma to present days, modified after Jolivet et al. (2006).

The Mediterranean Sea experiences compressional as well as extensional movements (rifts) where the lithosphere is being pulled apart such as the rifting phase in the Strait of Sicily (central Mediterranean Sea). This rift initiated soon after the end of the MSC (~ 5.3 Ma) resulting in the formation of relatively deep grabens (Pantelleria, Malta and Linosa Grabens) south of the Gela Basin (Colantoni, 1975; Finetti, 1984; Fig. 2.3). In addition, the early Pliocene represents the initial formation of the Gela Basin as a foredeep depocentre due to the overthrust and S/SE migration of the contractional front (Gela Nappe) of the African/European plates boundary (Maghrebian fold-and-thrust belt) (Ghielmi et al., 2012; Fig. 2.3). The movements of the Gela Nappe resulted in the increasing depth of the foredeep, and therefore slope gradient, which may have played a role in the increasing of slope instability in the Gela foredeep (Trincardi and Argnani, 1990).

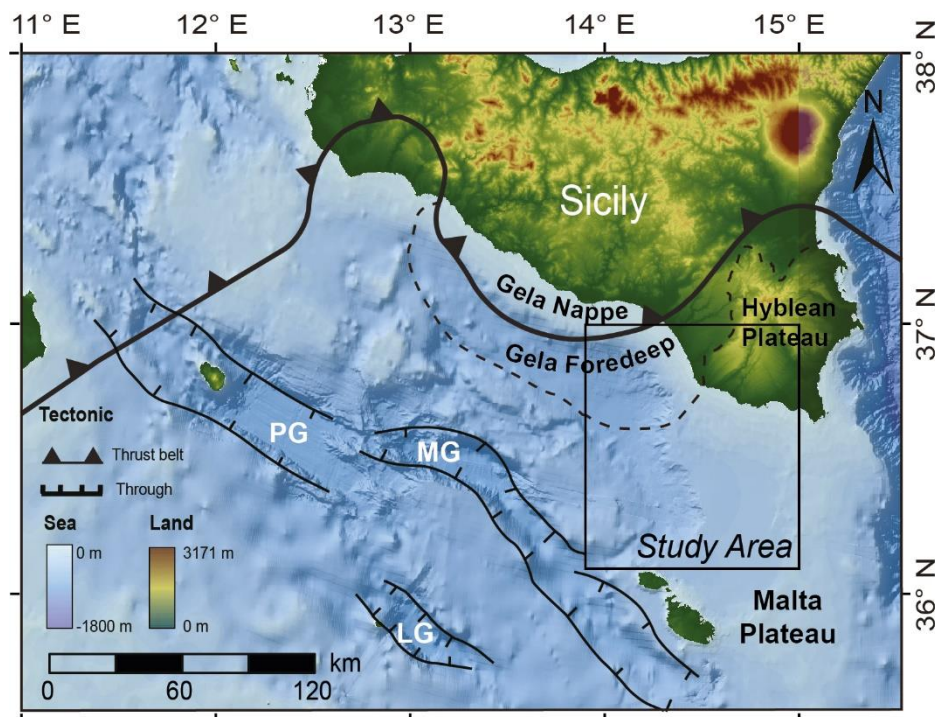


Figure 2.3: Relief and bathymetric map showing the modern emplacement of the Apennic arc (Maghrebian fold and-thrust belt) in the Strait of Sicily as well as the location of the grabens, which represents the extensional rift system. PG = Pantelleria Graben, MG = Malta Graben, LG = Linosa Graben.

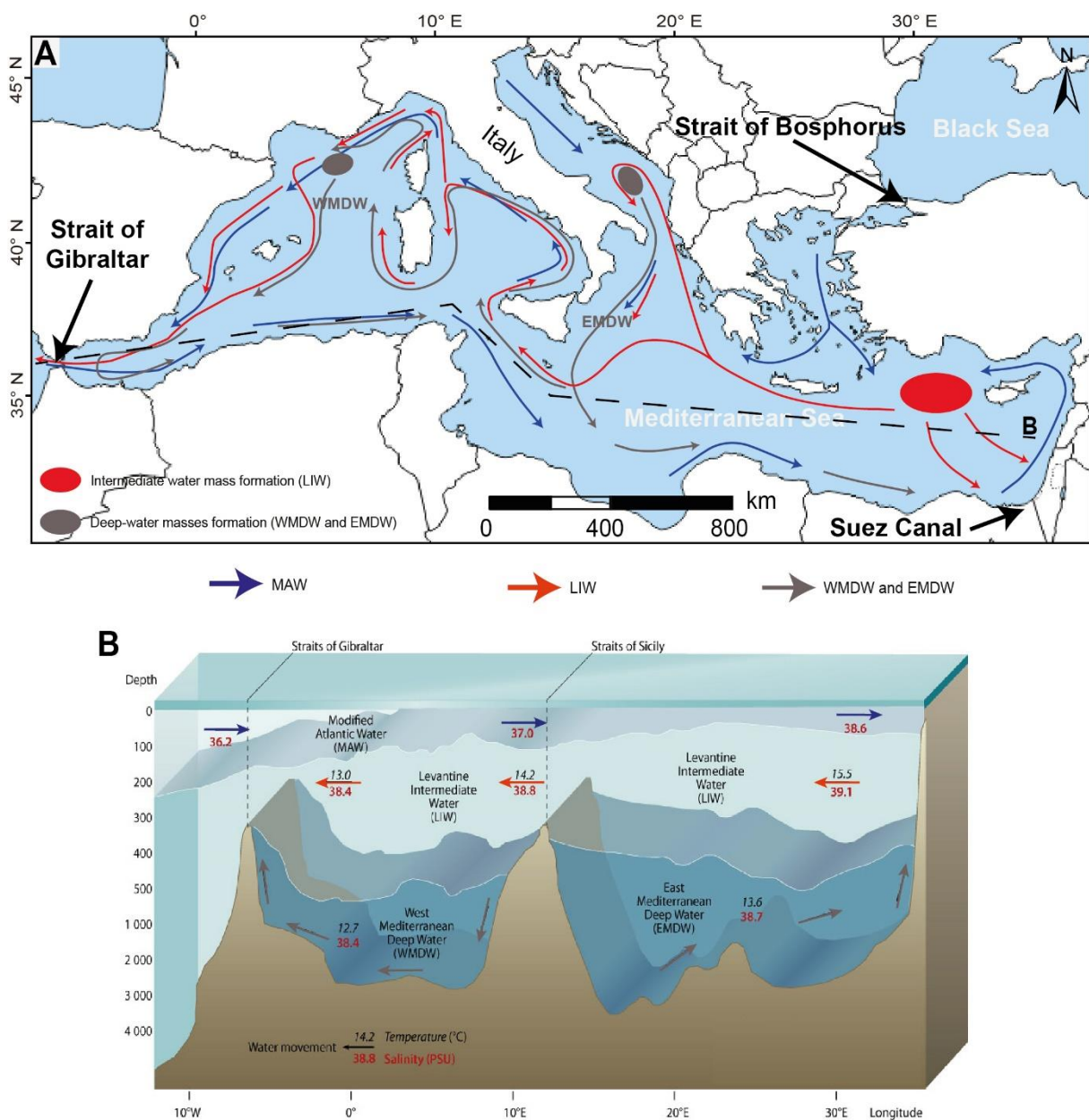
## 2.2 Oceanography and Contourites

Following major geodynamic movements of the Earth's plates, the newly formed Mediterranean Sea is characterized as a semi-enclosed basin between the African and the European continents over 2.5 million km<sup>2</sup>, which still represents less than 1% of the global ocean surface. The Mediterranean Sea is connected to the Atlantic Ocean via the Strait of

Gibraltar, the Black Sea via the Strait of Bosphorus and the Red Sea via the Suez Canal (Fig. 2.4A). The particular location of the enclosed Mediterranean Sea between latitudes 30° and 46°N results in an intense evaporation of the sea explaining the higher salinity content compared to the Atlantic Ocean ( $\geq 38$  psu in the Mediterranean Sea and  $\leq 37$  psu in the Atlantic Ocean; Skliris et al., 2018; Fig. 2.4B). The closure of the Strait of Gibraltar during the MSC, which resulted in a drastic decrease of the sea level of the Mediterranean Sea, demonstrated the importance of the Atlantic Ocean connection to the Mediterranean Sea. In fact, climate induces stronger evaporation compared to what the Mediterranean receives from river run-off and rainfall (Ducrocq et al., 2016). The remarkable water loss by evaporation during the MSC had to eventually be released through precipitation but was insufficient to compensate the disconnection from the Atlantic Ocean (Govers, 2009; Garcia-Castellanos and Villasenor, 2011b). This is deduced from the very high evaporation in the present days, which is estimated to be more than 7 times the total riverine freshwater flux in the Mediterranean Sea (Zavaterielli and Mellor, 1995; Ludwig et al., 2009 and references therein).

In the present-days, the strong exchange of water with variable densities drive the thermohaline circulation in the Mediterranean Sea including the presence of very active shallow, intermediate and deep-water masses (Millot and Taupier-Letage, 2005; Astraldi et al., 2001; Millot, 1999; Fig. 2.4A). The connection via marine gateways control the exchange flows and influence water circulation. The Strait of Gibraltar connects the Atlantic Ocean to the Mediterranean Sea and allows the entrance of fresher waters (less saline and colder) at the surface of the southwestern Mediterranean Sea (called the Modified Atlantic Water-MAW; Fig. 2.4A and B). As the MAW flows towards the eastern basin between 100 m and 200 m, the dry and warm climate enhances the evaporation resulting in the increasing of its salinity and temperature (Millot and Taupier-Letage, 2005). Overall, the net evaporation of the eastern Mediterranean Sea is about three times the net evaporation of the western Mediterranean Sea (Shaltout and Omstedt, 2015). The MAW continues its course flowing along the northern coast of Sicily or circulates towards the Levantine Basin via the Strait of Sicily where the MAW mass sinks to form the Levantine Intermediate Water (LIW) (Millot and Taupier-Letage, 2005; Fig. 2.4A). The formation of the LIW in the Levantine Basin is due to strong and cold winds in winter coming from northern Europe that cool off the warm and saline MAW resulting in the increase of its density and a decrease of its temperature (Millot and Taupier-Letage, 2005). The denser and cooler LIW circulates from the eastern to the western basin and along the northern coast of the Mediterranean Sea via the Strait of Sicily between 200 m and 600 m

(Millot and Taupier-Letage, 2005; Sammari et al., 1999; Fig. 2.4A and B). Similarly, the LIW, relatively warm and light, transforms into colder and denser deep water during winter cooling in the Adriatic Sea and in the Gulf of Lions to form the Eastern Mediterranean Deep-Water (EMDW) and the Western Mediterranean Deep Water (WMDW), respectively (Astraldi et al., 2001; Millot, 1999). The EMDW and WMDW circulate clockwise in their respective basins, only part of the EMDW circulates through the Strait of Sicily and access the western Mediterranean Sea (Astraldi et al., 2001; Fig. 2.4A). The shallow depths of the Strait of Gibraltar and the Strait of Sicily allow the circulation of the shallow and intermediate water masses (Fig. 2.4B).



(caption on next page)

Figure 2.4: A) Oceanographic circulation of the shallow (MAW), intermediate (LIW) and deep-water (WMDW and EMDW) masses in the Mediterranean Sea. The dotted black line indicates the profile location of B. The circles refer to the formation sites of the LIW (in red) and the deep-water masses (in grey). B) Vertical distribution of the Mediterranean Sea water masses modified from GRID-Arendal (<http://www.grida.no/resources/5885>) based on Hopkins (1985) and Zavaterielli and Mellor (1995). MAW (blue arrows) = Modified Atlantic Water, LIW (red arrows) = Levantine Intermediate Water, WMDW (grey arrows) = Western Mediterranean Deep Water, EMDW (grey arrows) = Eastern Mediterranean Deep Water.

---

Oceanographic currents, present in oceans and seas, can rework/transport sediments due to differences in density and temperature of the water column (Heezen and Hollister, 1964). These oceanographic currents circulating close to the seafloor are called “bottom currents” and, depending on their velocities, can erode and/or settle sediments (Faugères et al., 1993a). Different velocities characterize the MAW and the LIW in the Strait of Sicily (Lermusiaux and Robinson, 2001). Their velocity is controlled by the seafloor morphology (Rovere et al., 2019) and the climate (e.g. Hernández-Molina et al., 2003), which regulates the evaporation (Millot and Taupier-Letage, 2005), controls the wind temperature and its direction (Astraldi et al., 2001). The seafloor morphology can be characterized by radical transition in the seafloor depth inducing modification of the bottom currents velocities (e.g. Breitzke et al., 2017). Similar process is observed on mountain ledges where the ground relief intensifies the action of wind and forms snowdrift (Schweizer et al., 2003). The submarine process is due to the increasing pressure of an incompressible fluid (i.e. water) resulting in the intensification of the bottom currents when they are constrained in smaller areas and in the displacing/reworking of sediments. The high-velocity thermohaline circulation resulted in the formation of contourite deposits along the main bottom current path (Cattaneo et al., 2017 and references therein; Fig. 2.5A) and within Straits (e.g. Martorelli et al., 2011; Verdicchio and Trincardi, 2008; Ercilla et al., 2016; Hernández-Molina et al., 2016a; Fig. 2.5B).

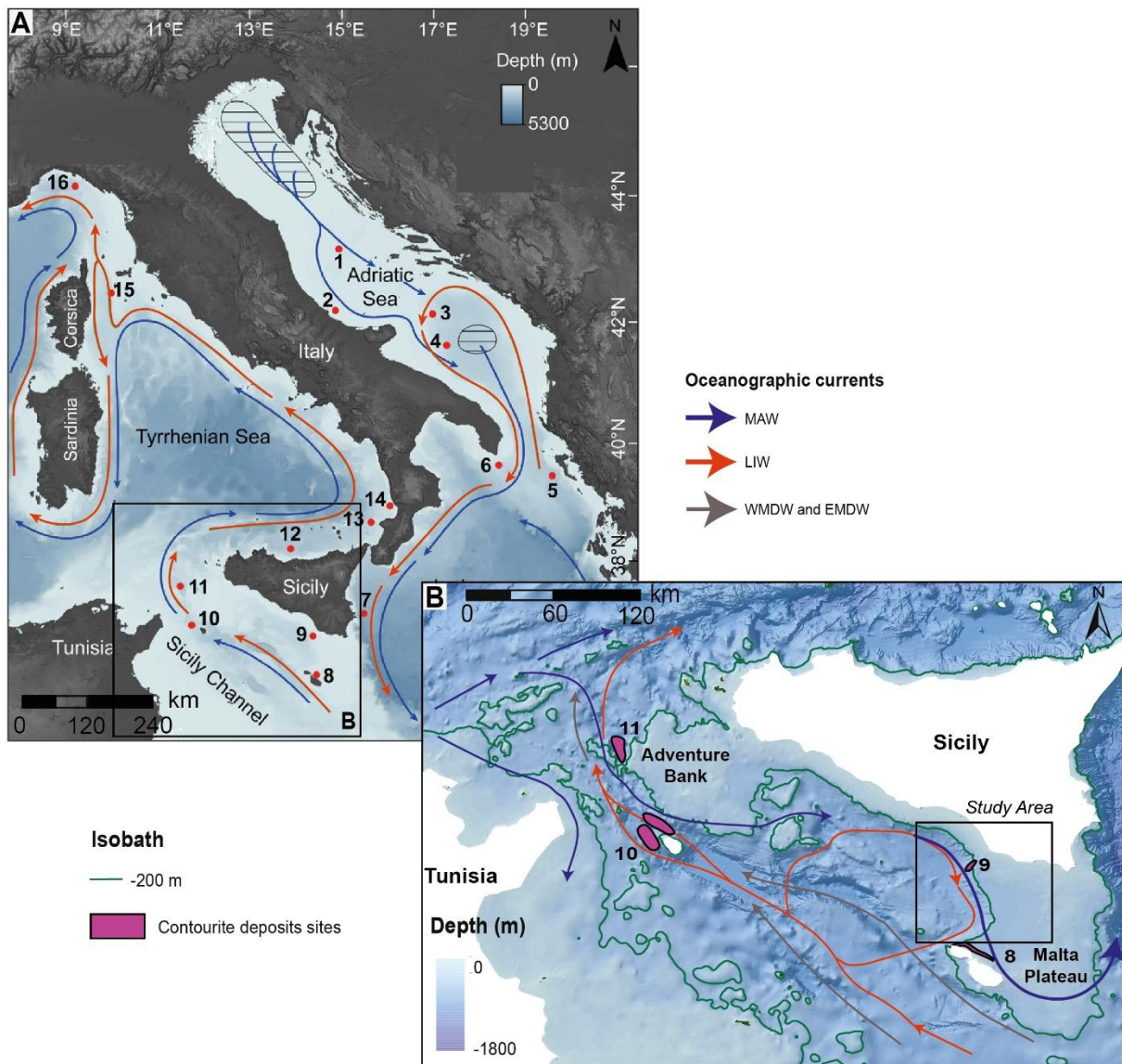


Figure 2.5: Location of contourite deposits in the central Mediterranean Sea along the main bottom current path, modified after Cattaneo et al. (2017). Black rectangle indicates the location of B. B) Zoom on the water masses circulation and exchange in the Strait of Sicily. The purple circles represent the locations and sizes of the previously studied contourite deposits. 8 = Micallef et al., 2013; 9 = Verdicchio and Trincardi, 2008; 10 = Martorelli et al., 2011; 11 = Marani et al., 1993.

Vestiges of ancient formation of contourite deposits were identified in the Mediterranean Sea and in the Atlantic Ocean (e.g. Van Rooij et al., 2010; Pellegrini et al., 2016) (Fig. 2.6; Table 2.1). Their deposition in the stratigraphic record helped our comprehension of bottom currents history including their initiation (from Early Pliocene to Mid-Pleistocene Transition-MPT) and their paleo-velocities (Table 2.1). Interestingly, all the buried contourite deposits are present along the present-day path inferring a similar bottom current path of the bottom currents. Furthermore, most of the buried contourite deposits indicate an acceleration of the thermohaline circulation around the MPT. The growth of

contourite deposits seems to be related to a key moment in the climate history that impacted the bottom currents velocities. The MPT represents the transition to stronger changes in the amount of ice on the continents resulting in stronger amplification of the sea level fluctuations (from 60 to 120 m) (Rohling et al., 2014). In addition, the stronger amplification was accompanied by a shift from mostly symmetric 41-ka to strongly asymmetric 100-ka cycles (Clark et al., 2006). These changes modified the bottom currents velocities as well as the sedimentation along continental margins (Somoza et al., 1997).

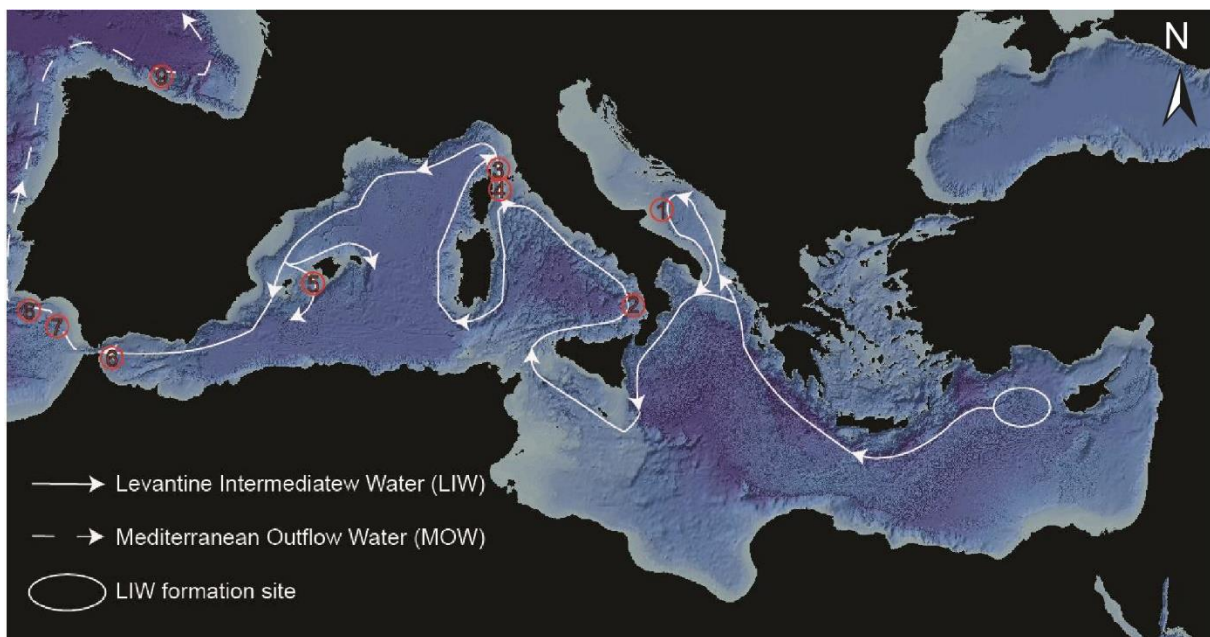


Figure 2.6: Morpho-bathymetric map of the Mediterranean Sea with the location of buried contourite deposits discovered along the present-day path of the LIW based on multiple references (Table 2.1).

Table 2.1: Buried contourite deposits identified in the Mediterranean Sea and along the northeastern Atlantic Ocean.

N°	Water-depth (m)	Contourite deposits		Location/characteristics	References
		Onset	Growth		
1	460-660	Pliocene	MPT	Flank of the anticline	Pellegrini et al., 2016
2	>240	MPT		Morpho-structural high	Amelio and Martorelli, 2008
3	300-600	Mid-Late Pliocene		Topographic restriction/gateway	Roveri, 2002
4	175-850	Mid-Late Pliocene	MPT	Gateway	Miramontes et al., 2016
5	150-275	Early Pliocene		Fault-generated seafloor relief	Vandorpe et al., 2011
6	200-700	Early Pliocene		Topographic barriers	Ercilla et al., 2002
7	530-830	Mid-Pliocene	Late Pliocene to Early Quaternary	Gateway	Hernández-Molina, 2014
8	500-700	Early Pliocene	MPT	Inherited seafloor topography	Roque et al., 2012
9	600-1550	Early Pliocene	Upper Pliocene to MPT	Paleobasins (intraslope basin)	Van Rooij et al., 2010

## 2.3 Geology and Climate

The geological complexity of the Mediterranean Sea is due to multiple events experienced since the closure of the Tethys Ocean to the present-days including the desiccation of the Mediterranean Sea and the climatic and geologic events, in which all contributed to the deposition of a variety of rocks and strata to form the present-day seafloor.

During the closure of the Tethyan Ocean, its location near the equator and the shallow depth resulted in tropical marine environment leading to the dominant deposition of limestone characterised by very rich and abundant fauna (Tang, 2018). In the present-days, only the Eastern Mediterranean Sea conserve remnants of the southern margin of the Tethys Ocean (Dannowski et al., 2019; Dellong et al., 2018). In contrast, the slab rollback in the Western Mediterranean Sea resulted in a younger basin. The intense evaporation of the Mediterranean Sea during the isolation from the Atlantic Ocean led to a large decrease of the sea level and the rapid precipitation and accumulation of evaporites (salt) at abyssal depths (Hsü et al., 1973; Ryan, 1973; Haq et al., 2020). The precipitated evaporites accumulation reaches more than 1 000 000 km<sup>3</sup> and > 3 km in some basins (Sonnenfeld and Finetti, 1985; Fig. 2.7A).

Following the desiccation of the Mediterranean Sea, all the basins experienced a sedimentation at different rates as the thickness of the Pliocene-Quaternary can vary from 0 to 4500 m in some areas (Capponi et al., 2020; Gennesseaux et al., 1998; Fig. 2.7B). The Pliocene-Quaternary unit evolved according to the local sediment supply, tectonic and bottom current activity, and relative sea-level variations, which can result in sedimentation and/or erosion of the continental margin (e.g. Gerber et al., 2009; Roque et al., 2012). The controlling factors can drive seaward (i.e. aggradational) or landward (i.e. retrogradational) the outbuilding of the margin (Patruno and Helland-Hansen, 2018). The margin is composed of sediment blocks (i.e. clinothems) recording the history of the basin and can be made of pelagites, hemipelagites, sapropels and tephras.

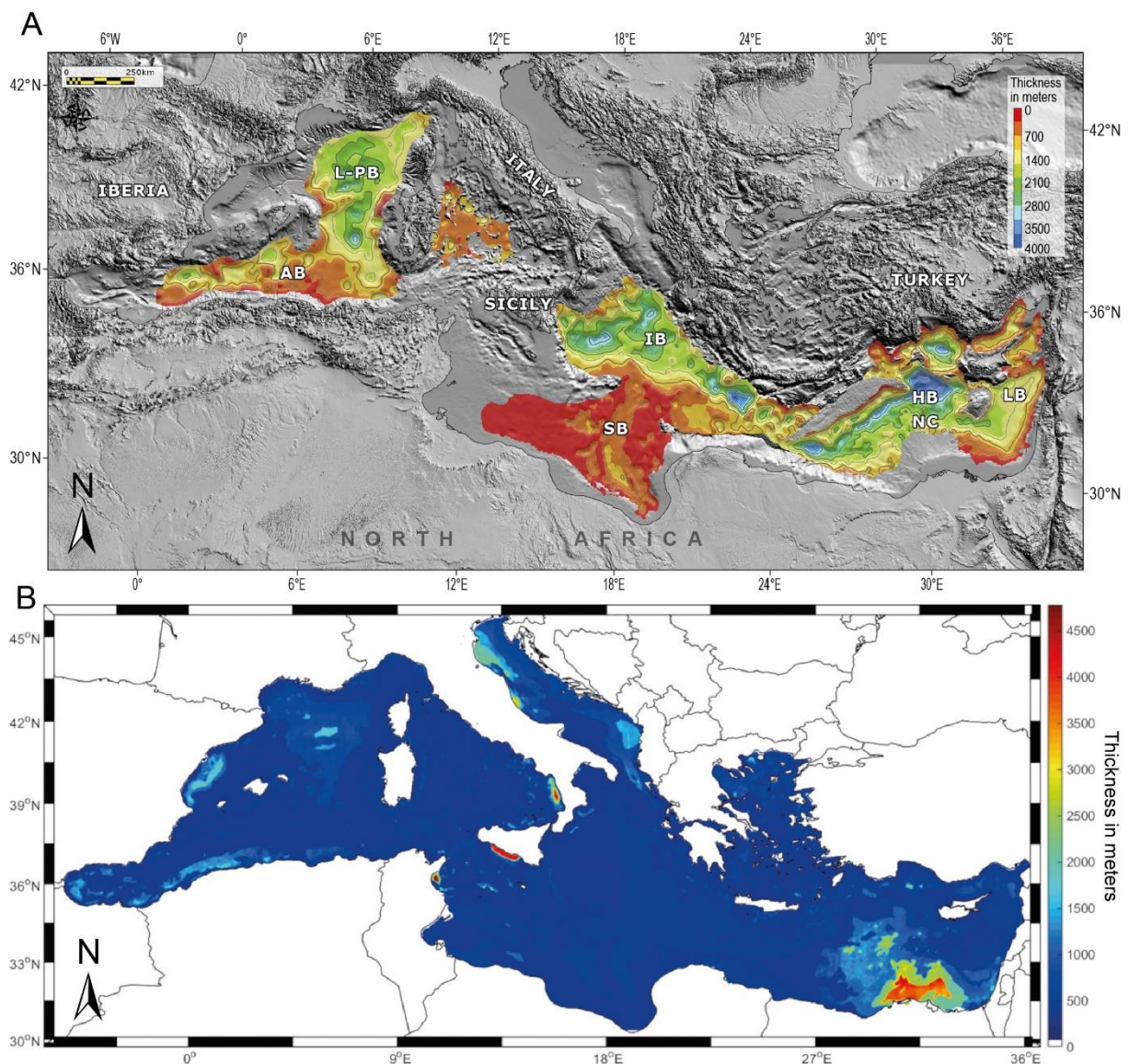


Figure 2.7: A) Thickness map of Messinian evaporites deposited during the Messinian Salinity Crisis in the Mediterranean Sea from Haq et al., (2020). L-PB: Liguro-Provençal Basin, AB: Algerian

*Basin, IB: Ionian Basin, HB: Herodotus Basin, SB: Sirte Basin, LB: Levant Basin, and on the fringes of NC: the Nile Cone. B) Thickness map of the Plio-Quaternary sediments in the Mediterranean Sea modified from Capponi et al. (2020).*

Pelagites are by definition sediments constituted of microscopic remains of either calcareous and/or siliceous debris organisms (biogenic material) and a fraction of very fine detritus (terrigenous material), dominantly clays, that accumulates in the deepest and most remote areas of the ocean (Stow et al., 1996). The percentage of biogenic and terrestrial material can vary between regions and reach > 70% of biogenic material in pelagic oozes or > 70% of terrigenous material in Red and brown clays (Rothwell, 2005; Hüneke and Mulder, 2011). Pelagic sedimentation occur through the very slow (< 1 cm/kyr) settling of particles on the seafloor. In the Mediterranean Sea, two types of pelagic deposits can be distinguished: hemipelagic deposits and deposits of sapropels.

Hemipelagic sediments are fine-grained sediments composed of biogenic (pelagic > 10%) and terrigenous materials (>10%), with more than 40% of silt size or greater (> 4  $\mu\text{m}$ ) (Stow and Tabrez, 1998 and references therein). Most common along and near continental margins and oceanic islands (as far as 300 km) in shallow and deep-water settings (Stow and Tabrez, 1998), their significant proportion of fraction coarser than 4  $\mu\text{m}$  often mislead them with other processes (i.e. gravity and along-slope processes). Hemipelagic sedimentation occur through the combination of pelagic settling (vertical settling) and detritus of various origin (lateral advection) resulting in various sedimentation rates (usually between < 5 to > 20 cm/ka and exceptionally > 100 cm/ka) and in poorly grain size distribution (Stow et al., 1996; Stow and Tabrez, 1998). Terrigenous materials are generally composed of minerals of continental origin (quartz, feldspars and clays) depending on the nature of the supply pathway (i.e. fluvial, Aeolian, glacial or volcanic) and therefore on the oceanographic and tectonic setting (Stow and Tabrez, 1998). In the Strait of Sicily, the hemipelagic sediments are generally rich in calcium due the high concentration of micro-fossils (Reeder et al., 2002). Hemipelagites, being non-reworked, are ideal for isotope analysis and radiocarbon dating (i.e.  $\delta^{18}\text{O}$  and  $^{14}\text{C}$ ), which allows the study of sediment provenance and climatic change.

Sapropels are dark (black or very dark green) pelagic sediments found at different stratigraphic levels in the Mediterranean Sea (Kidd et al., 1978; Emeis and Weissert, 2009). Identified only in the Eastern Mediterranean Sea, they are rich levels in organic matter and generally contain planktonic foraminifera (micro-organisms that live suspended in the water column) and plant debris but no benthonic foraminifera (micro-organisms that live on the

seafloor). The absence of benthonic foraminifera and the preservation of organic matter was explained by the depletion of dissolved oxygen (hypoxia or anoxic). This depletion in oxygen is still debated but would be due to an increase in fluvial input (i.e. African monsoon) and/or temperature rises (i.e. ice melting, sea level rise) leading to a stratification of the water column, an increase in export production (Grant et al., 2016 and references therein).

These different types of deposition in the Mediterranean Sea are directly related to climatic changes, which varied since the re-initiation of sediment deposition in the early Pliocene. In the last million years, the geographic position of the Mediterranean Sea led to climate variability and diversity resulting in heat transfer between two distinct atmospheric fronts from the equator and the high latitudes generating climatic contrasts. The climatic changes are principally due to variations of the Earth's movements along its axis (axial tilt), in its direction of rotation (axial precession) and around the sun (orbital eccentricity) inducing variation in solar radiation of the Earth (Milankovitch, 1930). The eccentricity regulates the length of the seasons (from circular to elliptical), the obliquity controls the intensity of the seasons (stronger obliquity = stronger seasons) and the precession makes the seasonal contrast between the Northern and the Southern Hemisphere. These changes are reflected as long-term decrease/increase of the icecaps resulting in the alternation of glacial and interglacial periods in the last million years (Fig. 2.8A). A significant change in frequency occurred between 1.25 Ma and 0.7 Ma, called the Mid-Pleistocene Transition (MPT), modifying the Earth's climate cycles from 41 to 100 kyr and increasing its intensity (Chalk et al., 2017; Bol'shakov, 2015; Fig. 2.8A).

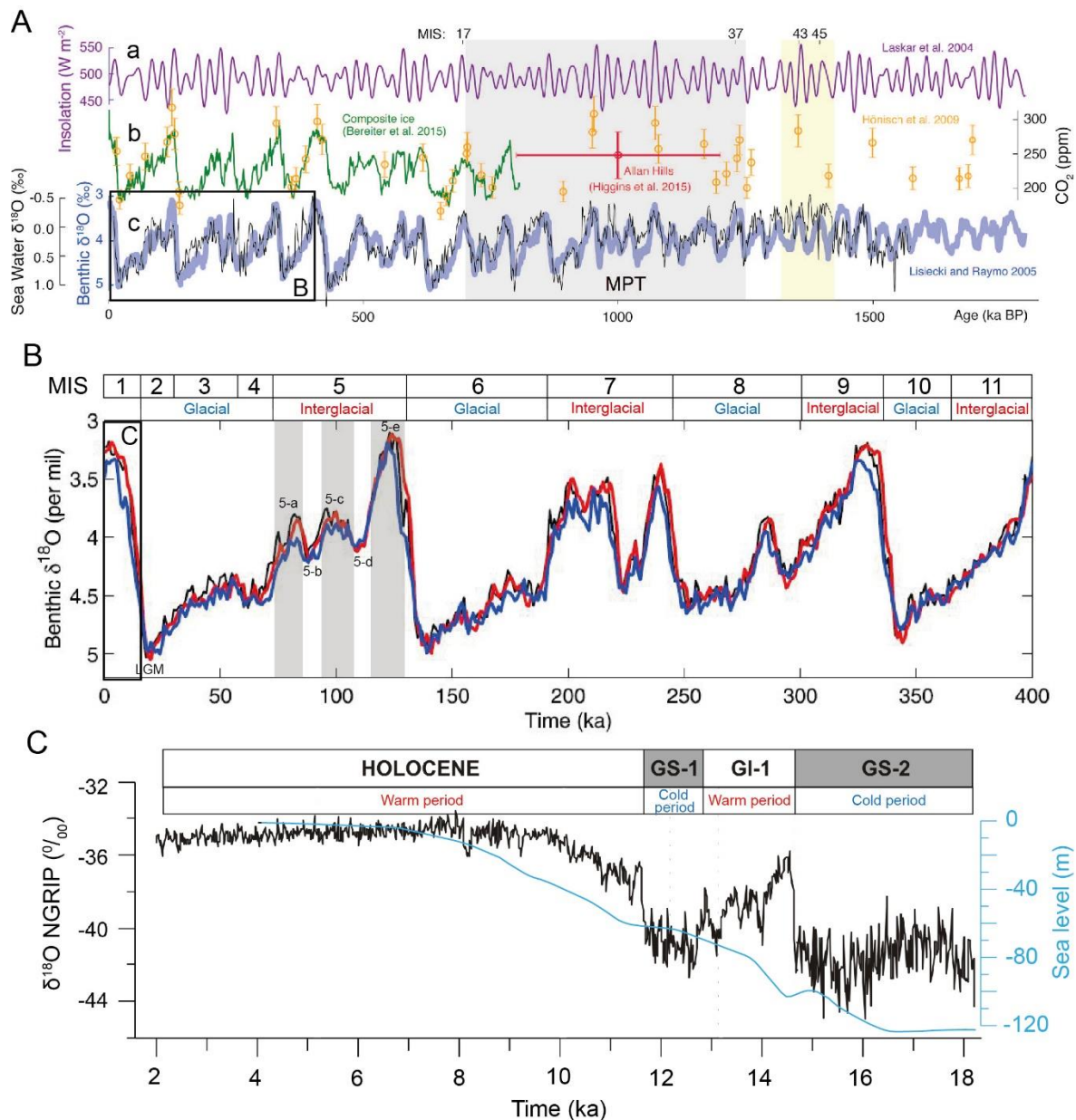


Figure 2.8: A) (a) 65°N summer solstice insolation. (b) Atmospheric CO<sub>2</sub> concentration, Allan Hills vertical error bars indicate 2σ spread with horizontal age uncertainty, (c) Global LR04 benthic stacked δ<sup>18</sup>O (blue) and ODP 1123 seawater δ<sup>18</sup>O (black). The MPT and the "typical 41 ka-world" intervals are highlighted in grey and yellow respectively, from Chalk et al. (2017). B) Correlation of the marine isotope stages (MIS) based on Lopes et al. (2014) with oxygen isotope curve (=ice volume) from Atlantic and Pacific Ocean cores from Lisiecki and Raymo (2009). The positioning of the sub-units of MIS 5 is based on Toucanne et al. (2012). C) δ<sup>18</sup>O of NGRIP ice core from Desprat et al. (2013) and sea-level curve from Lambeck et al. (2014). (GS-1: Glacial Stadial 1, GI-1: Glacial Interstadial 1, GS-2: Glacial Stadial 2).

The intensified and longer glacial-interglacial cycles after the MPT modified the climate and resulted in stronger variations of the sea level, which can be reconstructed from various proxies such as foraminifera assemblages and the study of oxygen isotopes (e.g. Rouis-Zargouni et al., 2010; Shackelton et al., 2003). These variations are expressed in Marine

Isotopic Stages and Substages (MIS) from  $\delta^{18}\text{O}$  records and can be identified in many sedimentary records (Lobo and Ridente, 2014 and references therein; Fig. 2.8B). The Last Glacial Maximum (LGM; 23-19 ka) corresponds to the maximum extent of the global ice masses and associated to the lowest global eustatic sea level (Hughes et al., 2013). The  $\delta^{18}\text{O}$  records of the last 18 kyr show that this period experienced multiple climatic changes from the end of the LGM to the actual interglacial period explaining the un-continuous sea-level rise (Fig. 2.8C). This information and others (i.e. water temperature, salinity, bottom current) are recorded by different species of foraminifera and clearly indicate a period of cooling as well as a reduction in salinity of the surface Mediterranean Sea due to icecap melting (Heinrich Event-HE1, 16 ka, Sierro et al., 2005) until 15 ka. Following this period of cooling and reduced sea surface salinity, the increase in temperature and sea level reflect the global warming and therefore, the re-entry into the current interglacial period (Fig. 2.8C). However, this period did not occur progressively and has experienced abrupt climatic changes including the Bølling-Allerød warm period (or GI-1, 15-12.8 ka, Desprat et al., 2013) associated with a fast sea-level rise, a short cooling period (GS-1, 12.8-11.5 ka, Cacho et al., 2001) and a gradual warm Holocene. The transition to warmer conditions was accompanied by an enhanced runoff of Nile river from 10.8 to 6.8 ka and the deposition of Sapropel S1 in the Eastern Mediterranean Sea (Rohling et al., 2015).

In addition to climatic changes inducing the deposition of various types of sediments, another type of deposit can be found in the sub-seafloor called “Tephra”. This deposit is the result of volcanic eruption that are ejected in the atmosphere and may fallout in the ocean, eventually settling on the seafloor. These volcanic particles can be transported by the wind and oceanographic currents and contain volcanic material (pumice and/or volcanic glass). Tephra layers have been found in the Mediterranean Sea, in particular in the central and eastern Mediterranean seas, as marked by several volcanic regions with high volcanic activity during the Quaternary (Sulpizio et al., 2014; Satow et al., 2015; Narcisi and Vezzoli, 1999). The geochemical analysis of the tephra layers allows the identification of the type of volcanic eruption and the particular volcano associated (e.g. Kuhlmann et al., 2017).

The Gela Basin, which is the study area of this thesis, has been filled with 2.5 km of marine sediments since the end of the MSC (Colantoni et al., 1975). The marine sediments consists in majority of clays until the Early Pleistocene when thin-bedded fine-grained sands intercalated the clays (ca. 1.5 Ma to 0.8 Ma; Ghielmi et al., 2012). These sand layers were

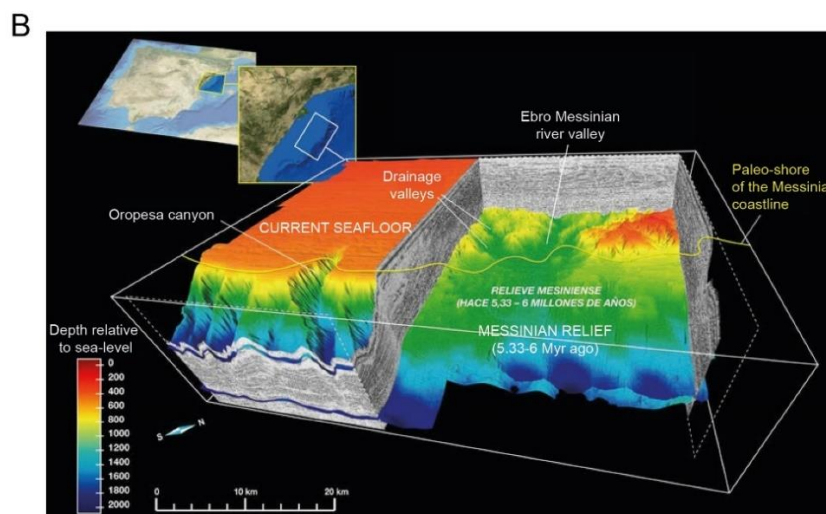
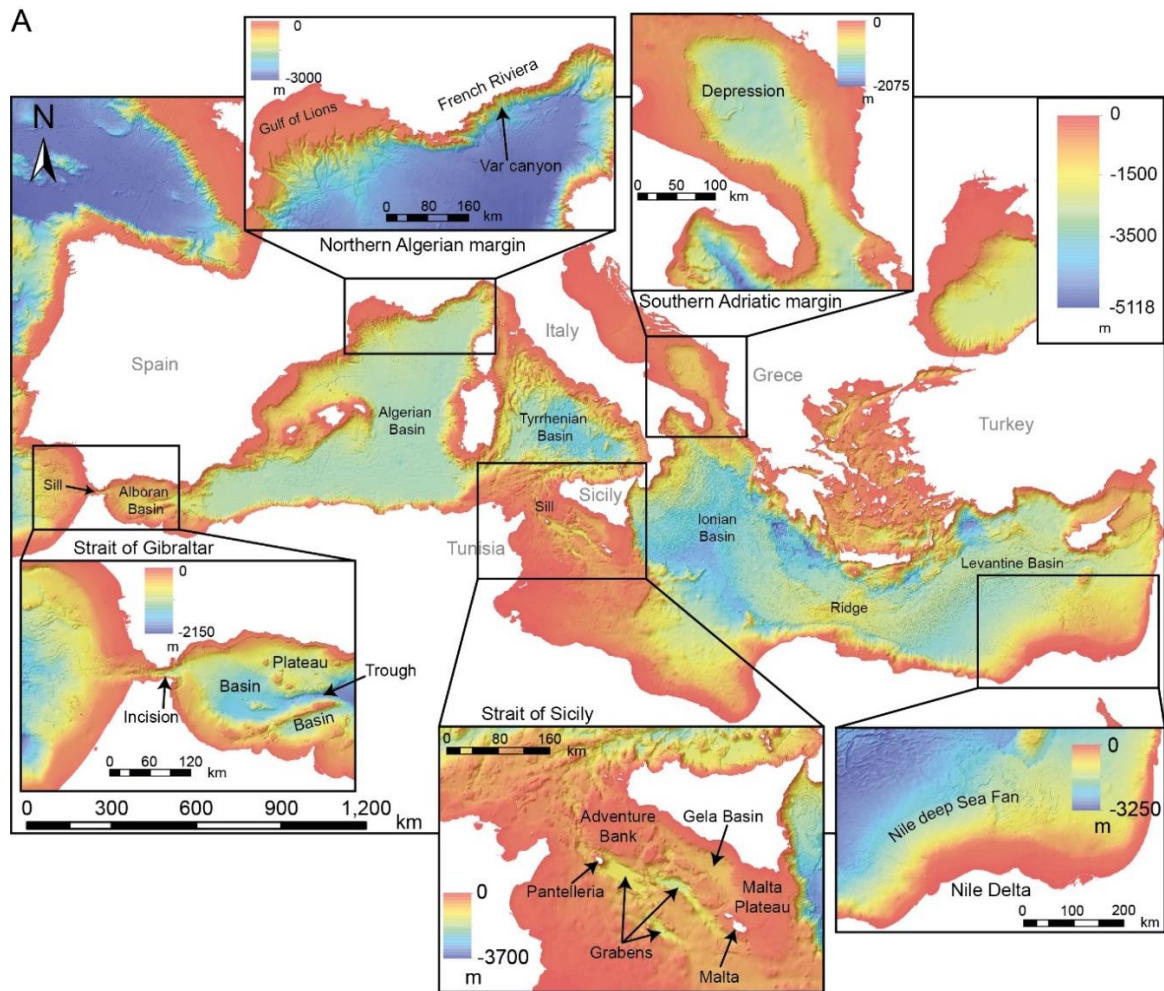
deposited by turbidity currents and their increase in thickness and grain size in the northeast of the Gela Basin indicate a main entry point of the turbidity system near the city of Gela (Ghielmi et al., 2012; Fig. 8). The Gela Nappe, north of the study area, consists of marls and shales of the foredeep basin while the Malta Plateau is made of a thick carbonate succession superposed by marls and silty-clays (Ghielmi et al., 2012; Schramm and Livraga, 1986).

## 2.4 Geomorphology and Hydrology

The Mediterranean Sea is about 4000 km long from the Strait of Gibraltar to the coast of the eastern Levantine Sea and is divided between Sicily and Tunisia by a submarine sill (the Strait of Sicily) separating the western from the eastern Mediterranean Sea (Fig. 2.9A). The formation and extension of the western Mediterranean Sea led in turn to its subdivision into the Alboran, Algerian and Tyrrhenian Basins. Together, the Alboran and Algerian Basins constitutes the western basin (Fig. 2.9A). The eastern Mediterranean Sea is sub-divided into the Ionian and the Levantine Basin by a submarine ridge present south of Crete (Fig. 2.9A). The Ionian Basin represents the deepest basin (4,900 m) of the Mediterranean Sea. The submarine sills, such as the Strait of Gibraltar and Strait of Sicily, represent shallow and narrow passages compared to the basins (13 km for the Strait of Gibraltar and 140 km for the Strait of Sicily). In addition, the complex tectonic and geodynamic history of the Mediterranean, superimposed to the convergence between Africa and Eurasia, resulted in the formation of volcanic islands (e.g. Pantelleria Island), basins (e.g. Gela Basin) and land submergence (Malta Island) (Fig. 2.9A). Several Mediterranean continental margins are characterized by deep canyons down to 2,500 m (e.g. Var Canyon; Barber, 1981; Clauzon, 1978; Fig. 2.9A). The sea level drop in the Mediterranean Sea caused the incision of deep canyons during the Messinian Salinity crisis due river discharge into the sea (e.g. Messinian incisions in the Nile Delta Barber, 1981; Clauzon, 1978; Gargani et al., 2010; Fig. 2.9A). The megaflood of the Mediterranean Sea after the MSC resulted in the excavation of Miocene sediment and bedrock within the Strait of Gibraltar, which is characterized in the present days by a very large ramp (390 km long) slowly dipping (slope gradient =  $3.6^\circ$ ) towards the Mediterranean Sea (Garcia-Castellanos et al., 2009; 2020; Fig. 2.9A). The flooding resulted in several hundred meters deep incisions (Fig. 2.9A) due to the huge discharge of about  $10^8 \text{ m}^3 \text{ s}^{-1}$  (three orders of magnitude larger than the present Amazon River) estimating an erosional rate of 0.4 m per day and the excavation of  $1000 \text{ km}^3$  into the Alboran Sea (Garcia-Castellanos et al., 2009; 2020). The presence of submarine canyons at the present-days Mediterranean seafloor indicate their survival despite

long-term outbuilding of the continental margins since their formation during the MSC (Amblas et al., 2012; Fig. 2.9B).

The width of the Mediterranean continental shelves can vary rapidly from very wide (e.g. Gulf of Lions) to very narrow (e.g. French Riviera) (Fig. 2.9A).



(caption on next page)

Figure 2.9: A) Morpho-bathymetric map of the Mediterranean Sea with insets on specific areas characterized by different morphologies such as troughs, grabens, basins, plateaus, volcanic islands, submerged lands, canyons, depressions based on Palomino et al. (2011) and Del Bianco et al. (2014). B) 3D model showing the presence of excavated valleys at the present-day seafloor formed during the Messinian Salinity Crisis based on Urgeles et al. (2010) and adapted from Garcia-Castellanos (2011a).

In the Strait of Sicily, the continental shelf is rather narrow along the southern coast of Sicily (14 km) but increases to several tens of kilometres towards the Malta Islands (Malta Plateau). Shallow-water plateau and bank (100-150 m w.d.) characterize areas off the southeast and southwest of Sicily (Malta Plateau and Adventure Bank; Bishop and Debono, 1996; Maurizio et al., 2015; Fig. 2.10). Deep grabens formed during the Miocene-Pleistocene rifting phase, reaching down to 1731 m w.d. on a W-E axis direction (Maurizio et al., 2015) (Fig. 2.10). In the south of Sicily, the Gela Basin, constrained between Malta and Sicily in an N-S direction, is 85 km long and reaches a maximum water depth of 936 m in the north of the basin (2.10). The slope gradient of the eastern Gela Basin is rather low (1.5 to 4.5°) with values around 20° in the headwalls of submarine landslides (Minisini et al., 2007; Kuhlmann et al., 2014).

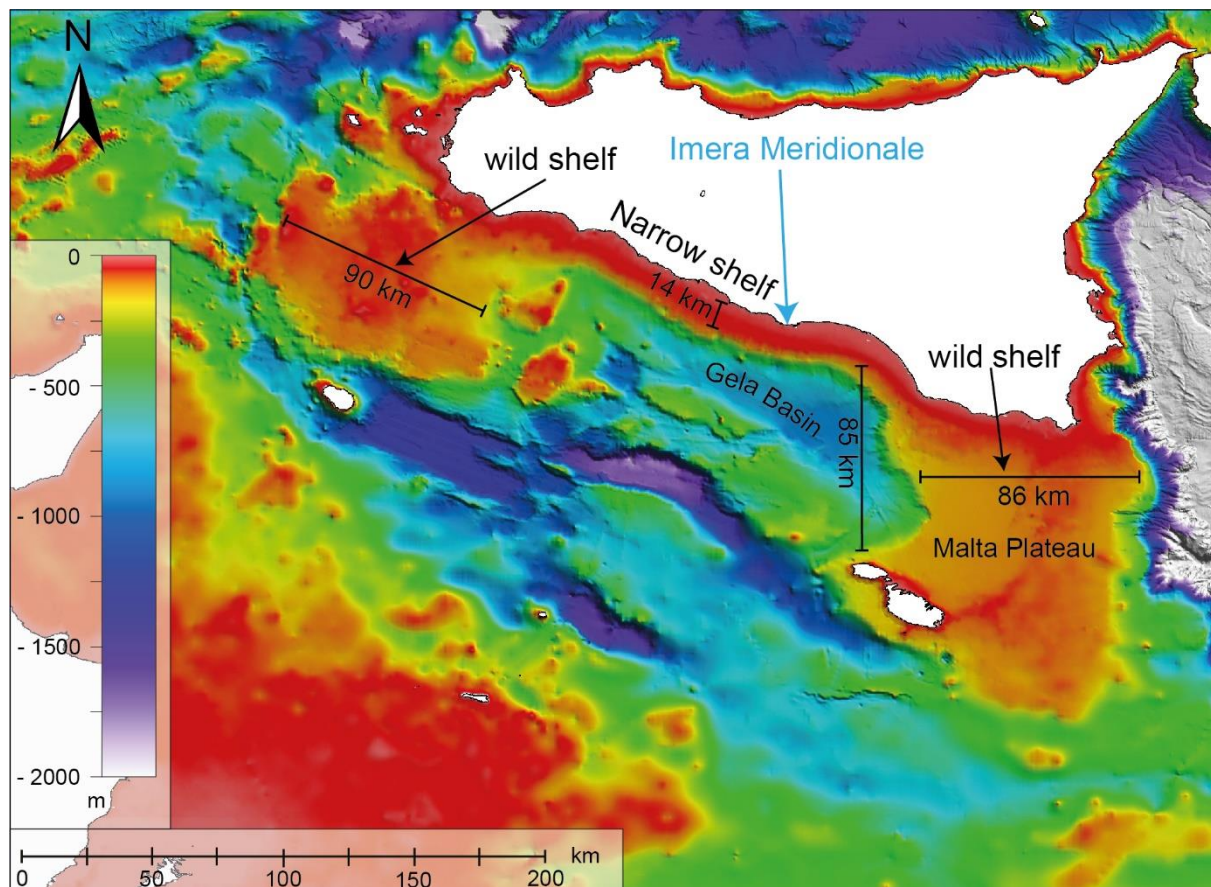


Figure 2.10: Morpho-bathymetric map of the Strait of Sicily. Location of the Imera Meridionale mouth based on Verri et al. (2017).

The river discharge play a role in i) shaping part of the Mediterranean morphology (Gargani et al., 2010) and ii) driving changes in the oceanographic circulation (Verri et al., 2017). The river discharge is the amount of water that flows into the sea/ocean and is called freshwater flux. It takes into account the precipitation and evaporation within the catchment area. The total freshwater flux of the Mediterranean Sea is estimated between 400 and 569 km<sup>3</sup> yr<sup>-1</sup>. In order of declining importance: the Rhone (53 km<sup>3</sup> yr<sup>-1</sup>), Po (50 km<sup>3</sup> yr<sup>-1</sup>), Nile, Ebro (13 km<sup>3</sup> yr<sup>-1</sup>), Tiber (6.8 km<sup>3</sup> yr<sup>-1</sup>), Adige (6.3 km<sup>3</sup> yr<sup>-1</sup>) basins (Ludwig et al., 2009; Shaltout and Omstedt, 2015; Struglia et al., 2004; Wang and Polcher, 2019; Fig. 2.11). The Nile drainage system contributes to more than half of the Mediterranean freshwater input but loses more than half since the construction of the Aswan dam in 1964 (Shaltout and Omstedt, 2012) and through ground-water infiltration and evaporation (Ludwig et al., 2009). The reduced freshwater income increases further the salinity of the Mediterranean Sea ( $\geq 38$  psu; Skliris et al., 2018) but is well compensated by the high fresher water input from the Atlantic ( $\leq 37$ ; 25000 km<sup>3</sup> yr<sup>-1</sup>, Soto-Navarro et al., 2010; Skliris et al., 2018). The Black Sea represents another source of low saline water (18 psu; Ünlülata et al., 1990) into the Mediterranean Sea ( $< 400$  km<sup>3</sup> yr<sup>-1</sup>; Ludwig et al., 2009; Wang and Polcher, 2019) but decreased in the last decades due to lower river discharge into the Black Sea (Shaltout and Omstedt, 2012).

The central Mediterranean Sea, including the southern Sicilian and Libyan drainage basins, has the weakest average freshwater flux (4 km<sup>3</sup> yr<sup>-1</sup>; Ludwig et al., 2009). The calculated 0.4 km<sup>3</sup> yr<sup>-1</sup> annual discharge of Sicilian rivers based on Verri et al. (2017) indicates that the Sicilian drainage basins represent only 10% of the central region freshwater flux. The main freshwater source in the study area come from the Imera Meridionale (0.13 km<sup>3</sup> yr<sup>-1</sup>, west of the Gela Basin, Verri et al., 2017; Fig. 2.10) but is still one of the weakest freshwater discharge in the central Mediterranean Sea. These values show that Sicily has the weakest annual freshwater flux in the Mediterranean Sea.

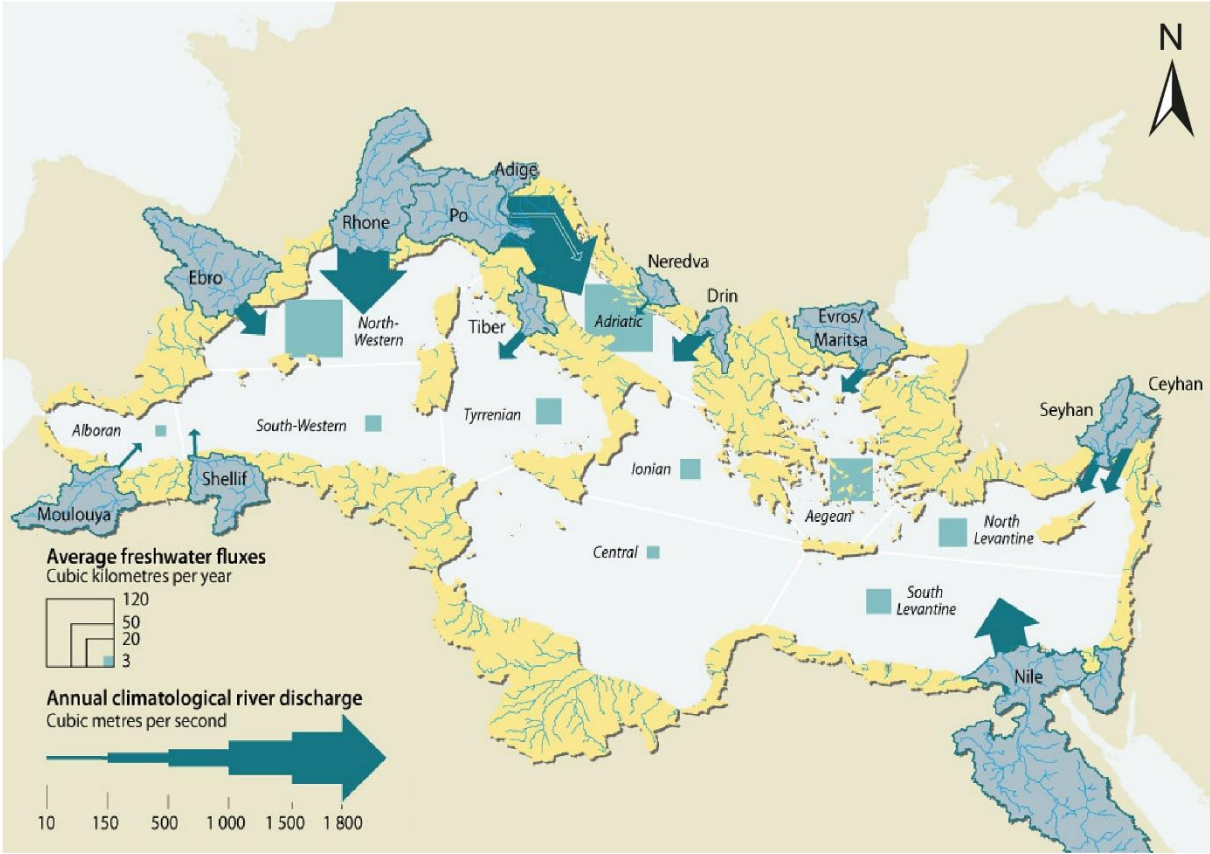


Figure 2.11: River discharge of freshwater into the Mediterranean Sea modified from GRID-Arendal (<http://www.grida.no/resources/5897>) based on Struglia et al. (2004) and Ludwig et al. (2009).

# Chapter 3. Study Area, Data and Methodology

---

## 3.1 Study Area

The Gela Basin, located in Strait of Sicily, is under the influence of geodynamic movements and water masses exchange from the western and eastern Mediterranean Sea. The geodynamic movements, including the southward migration of the Maghrebian fold-and-thrust belt in the north and the extensional rift system in the south, constrain the Gela Basin inducing the reactivation of high-angle fault system within the carbonate substratum (Ghielmi et al., 2012) where seismic activities have been monitored since 1985 (INGV - Istituto Nazionale di Geofisica e Vulcanologia; Fig. 3.1). The loading at the front of the Gela Nappe, which moved S-SE, bended the carbonate platform affecting the Gela Basin with subsidence and therefore, increased its slope gradient, which in turn may have played a role in the rising of slope instabilities in the Gela foredeep (Trincardi and Argnani, 1990). The Strait of Sicily, including the Gela Basin, experiences stronger water flow exchanges at the surface (1.4 times) than the Strait of Gibraltar due to higher evaporation in the eastern Mediterranean Sea and a wider extent (11 times wider than the Strait of Gibraltar) (Shaltout and Omstedt, 2015).

The oceanographic circulation and the geodynamic activity influenced the outbuilding of the Gela Basin, which resulted in the emplacement of multiple exposed, partially overlapping and stacked MTDs documenting a frequent return (~10 kyr) in sediment instability in the area (Minisini et al., 2009; Kuhlmann et al., 2017; Fig. 3.1). The emplacement of various types of MTDs (Fig. 3.1) involving different volumes of sediments, from very large (Gela Slide, 630 km<sup>3</sup>; Mueller et al., 2020) to < 1 km<sup>3</sup> (multiple debris flow deposits; Minisini et al., 2007), informs on the variety of pre-conditioning factors and triggering mechanisms. The Gela Slide, involving as much as 700 m of the sedimentary sequence without significant internal deformation (plane-parallel and continuous reflectors) with a relatively short-distance runout of 1-3 km, occurred on a 90 km along-strike inclined planar and sub-horizontal surface characterized by a maximum slope gradient of 10-15° (Trincardi and Argnani, 1990). Its emplacement, estimated at 600 ka (Di Stefano et al., 1993), was probably related to the latest Gela Nappe movements (Trincardi and Argnani, 1990). In more recent research, Minisini et al. (2007) discovered 30 km east to the Gela Slide the presence of relatively small seafloor-exposed landslides (< 1 km<sup>3</sup>) with variable MTDs morphologies in the lower slope and prominent headwalls ( $\leq 32^\circ$ ;  $\geq 250$  m) as well as remnants of old and partially buried headscarp in the

upper-slope (Kuhlmann et al., 2014). High-resolution seismic revealed a very complex sliding sequence of stacked MTDs with multistage failure of the most recent landslides, called Southern and Northern Twin Slide (STS and NTS) (Kuhlmann et al., 2017). The detail analyses of new long cores recovered close to the landslides permitted the sequence stratigraphic reconstruction and, together with high-resolution seismic profiles, emit multiple mechanisms that might control the depositional variability and explain the sliding sequence. The core-seismic correlation unravelled the stratigraphic architecture of the area indicating the impact of sea level cycles on the shelf sedimentary units with clear evidence of erosional surfaces, which reflect subaerial exposures during sea level fall and lowstand (Kuhlmann et al., 2015). The repeated failures, estimated every 10 kyr, increased sedimentation rate, which reached 200 cm/kyr based on the cores, and therefore, suggest an increase in pore pressure and fluid escape favouring further failures (Minisini and Trincardi, 2009; Kuhlmann et al., 2015). In addition, cores indicate abrupt physical changes in lithology and mechanical properties along sub-vertical normal faults and sub-horizontal strata where failures predominantly took place (Kuhlmann et al., 2017), which confirm the presence of faults and weak layers in the headwalls as suggested by Minisini et al. (2007). The abnormal fast sedimentation rate and tectonic activity recorded in the northern Gela Basin played a role in the failure mechanisms of the MTDs (Trincardi and Argani, 1990; Minisini and Trincardi, 2009; Kuhlmann et al., 2015). The abnormal fast sedimentation rate calculated during sea level rise was explained either by an intensification of the LIW during the drowning of the shelf (Verdicchio and Trincardi, 2008) or by hyperpycnal plumes due to extreme precipitations during arid conditions (Kuhlmann et al., 2015). The intensification of the LIW was inferred from the presence of contourite deposits near the shelf-edge while the hyperpycnal flows were inferred by the presence of sediment undulations but could also be explained by the action of internal waves (Kuhlmann et al., 2015; Fig. 3.1).

The last failures, the NTS and STS, initiated at around 200 m w.d., have similar runout, were emplaced in the lower slope (500 – 700 m w.d.) and are characterized by evacuated headwalls (Minisini et al., 2007). The presence of individual terraces within the headwalls of both landslides suggest a multi-stages failure, which involve a debris avalanche and a successive slide/slump and therefore, indicate the potential presence of multiple weak layers and a recurrent trigger mechanism (Minisini and Trincardi, 2009; Kuhlmann et al., 2014; Fig. 3.1). Kuhlmann et al. (2017) estimated that rather weak earthquakes (4 to 4.8 on Richter scale) were sufficient to trigger the Twin Slides and therefore, suggest it as a potential trigger mechanism.

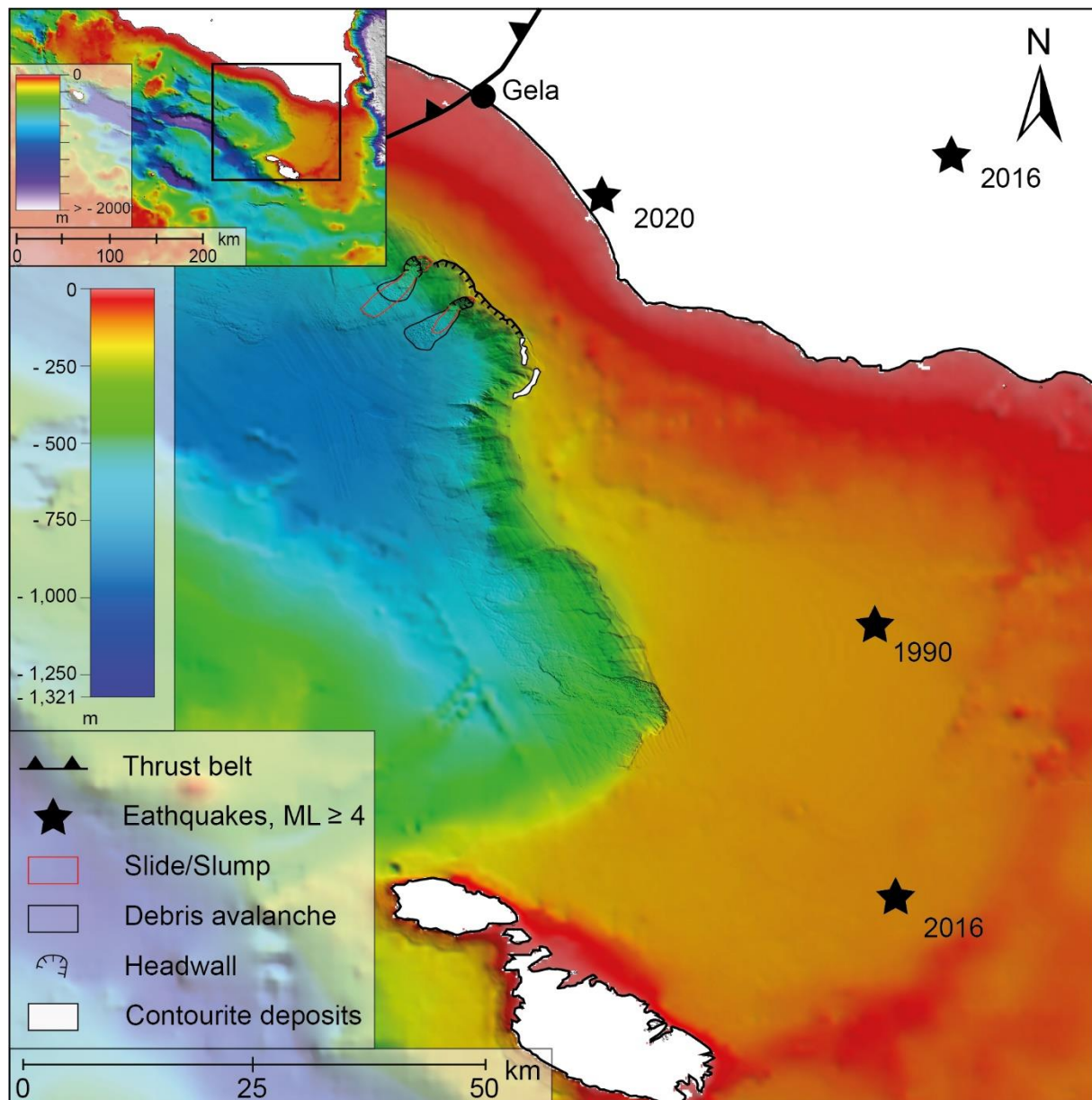


Figure 3.1: Morpho-bathymetric map showing the location of mass-transport deposits (slide/slump and debris avalanche; Kuhlmann *et al.*, 2017) and their headwalls, of contourite deposits (Verdicchio and Trincardi, 2008) and earthquakes (INGV) previously studied along the eastern Gela Basin. *ML*: Magnitude Local.

However, doubts remains on a single type of mechanism to explain the emplacement of the MTDs since the discovery of MTDs in the southern Gela Basin near Malta, which suggest different pre-conditioning and triggering mechanisms. The acquisition of new dataset permitted the discovery of instabilities along the entire eastern margin and new materials and methods to better comprehend of the overall mechanisms of failures in the Gela Basin.

## 3.2 Overview and origin of the data

The objectives of this thesis were addressed with multiple types of datasets and accessed in order to identify and study submarine landslides in the Gela Basin at the seafloor and sub-seafloor. The datasets consist of geophysical data (seismic and bathymetric data) and sediment samples (boreholes and piston cores) belonging to the industry and Institute of Marine Sciences (ISMAR) Bologna.

AGIP (General Italian Oil Company) and ELF (French oil company) drilled deep boreholes in the northern Gela Basin in the early 1970's and 1980's. These companies are today subsidiaries of Eni S.p.A. and Total, respectively. The total drilling depth of the boreholes reached down to 4.5 km below the seafloor. All the data recovered during the drilling were registered in borehole logs, which are today available online via the videpi website (<http://www.videpi.com/videpi/progetto.asp>).

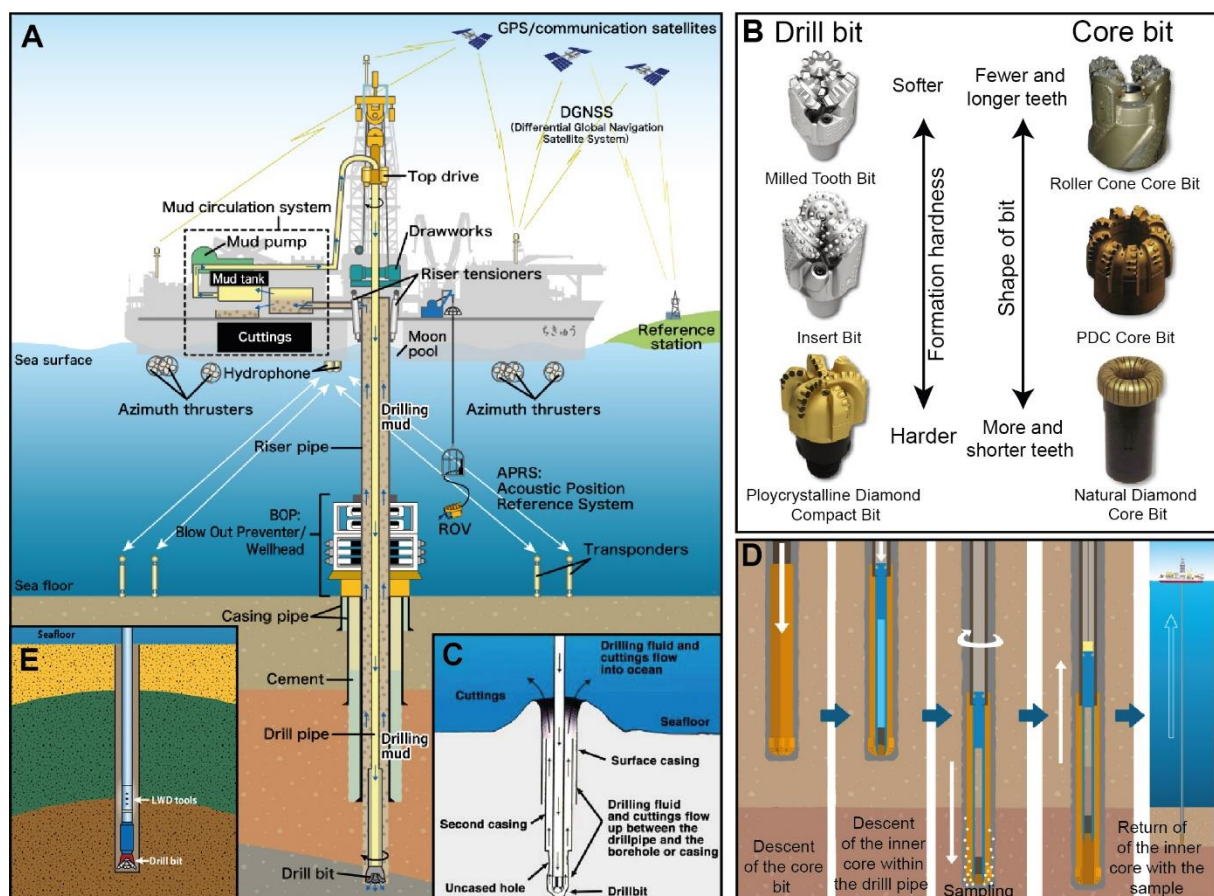
Eni S.p.A. participated as well in the acquisition of geophysical data in the Gela Basin by collecting multi-channel seismic (MCS) profiles (deep seismic) in the 1990's over the Gela Basin and Malta Plateau. Unfortunately, the location of the MCS profiles cannot be shown due to confidential issues. The MCS profiles were made exceptionally available for my PhD at their premise in Milan (Italy) and a few of the profiles were authorized to be published (Annexe 2).

The Institute of Marine Sciences (ISMAR) of Bologna collected multiple datasets along the eastern slope of the Gela Basin during several surveys on board R/V Urania between 2005 and 2009. A dense network of shallow seismic reflection data (sub-bottom seismic profiles; Annexe 2) was collected as well as long sediment cores with variable recovery length (up to 11.61 m) and high-resolution bathymetric data (down to 20 m resolution).

## 3.3 Data acquisition

Boreholes are narrow holes in the seafloor drilled with a rotary drilling system from a ship, or a semi-submersible, or a jackup depending on the water depth (Fig. 3.2A). They are used to collect sediment and rock samples deep below the seafloor for geological research. All information acquired during and after the drilling are reported in a borehole log. A drilling system is composed of a drill pipe and drill bit hanged from the derrick of the ship/ semi-submersible/jackup (Fig. 3.2A). The drill bit is used for drilling a borehole and can have different shapes depending on the hardness of the sediments/rocks encountered (Fig. 3.2B).

The combined rotation and the weight of the drill pipe upon the drill bit allow to penetrate the substrate over several kilometres of depth. During the drilling, mud (water-based or oil-based or foam) is injected in the borehole to lubricate, cool the drill bit and clear out the hole of the cuttings. The cuttings can be pumped out onto the seafloor with the mud in the case of a riserless drilling (Fig. 3.2C) or recovered in riser drilling and be used as geological samples (Fig. 3.2A). In order to take core samples, the drill bit is substituted with a core bit, which is characterized by a central opening around which the drill bit cuts the borehole (Fig. 3.2B). As the core bit drilled down the seafloor, the inner core barrel collects the core sample until the entire barrel is full (9.5 m long) (Fig. 3.2D). The inner core barrel with the core sample is recovered onboard with wireline through the drill pipe (Fig. 3.2D). Additional data are collected from the boreholes during drilling (logging while drilling-LWD; Fig. 3.2E) or once the drilling has stopped (wireline logging). Various tools and sensors can measure valuable information including a wide variety of geological information (e.g. resistivity, density, porosity) by direct measurements inside the borehole (wireline logging), or by carefully monitoring the drilling mud (mud logging). This geological information reported in the borehole log help to constrain its lithology and the changing depths of facies.



(caption on next page)

*Figure 3.2: A) Sketch representing the complexity of coring boreholes with a riser drilling where drilling mud containing the cuttings is collected onboard for analysis. B) Examples of different drill bits and core bits depending the substrate hardness and the type of samples desired to be recovered. C) Sketch showing the riserless drilling system where cuttings are not recovered. D) Sketch to show how cores samples are recovered from the substrate with drilling. E) Representation of coring with a Logging While Drilling (LWD) installed on top of the drill bit. All images are from JAMSTEC website (<https://www.jamstec.go.jp/cdex/e/operations/>).*

---

Multi-channel seismic profiles are vertical images of the deep sub-seafloor containing geophysical information which allow to study the sub-surface changes in lithology and structure. These profiles are the result of seismic waves diffused from a controlled source bouncing off the seafloor and deeper sediment layers (according to their density) before to be received by multiple channels (Fig. 3.3A). The controlled source (e.g. air gun) is dragged behind the stern of the research vessel and can emit different frequencies (Fig. 3.3B). The frequencies used to acquire MCS profiles defines their penetration depth and resolution. The different density of the material controls the velocity at which the sound travels through this material (acoustic impedance; Stoker et al., 1997). The receivers of the seismic waves are hydrophones connected via one seismic streamer where the information is relayed to the vessel to be treated (Fig. 3.3B). The length of the streamer allows “tardive” reflected waves that may have travelled further down into the sub-seafloor to be intercepted. The length of the streamer can reach a few kilometres in order to receive seismic waves from 5 to 10 km deep (penetration depth in the seafloor). The use of these methods depends on the water depth of the study area and the objectives of the research. The analogue data received by the streamer are then converted into digital data by a digital convertor in order to be processed with specific software (Fig. 3.3C).

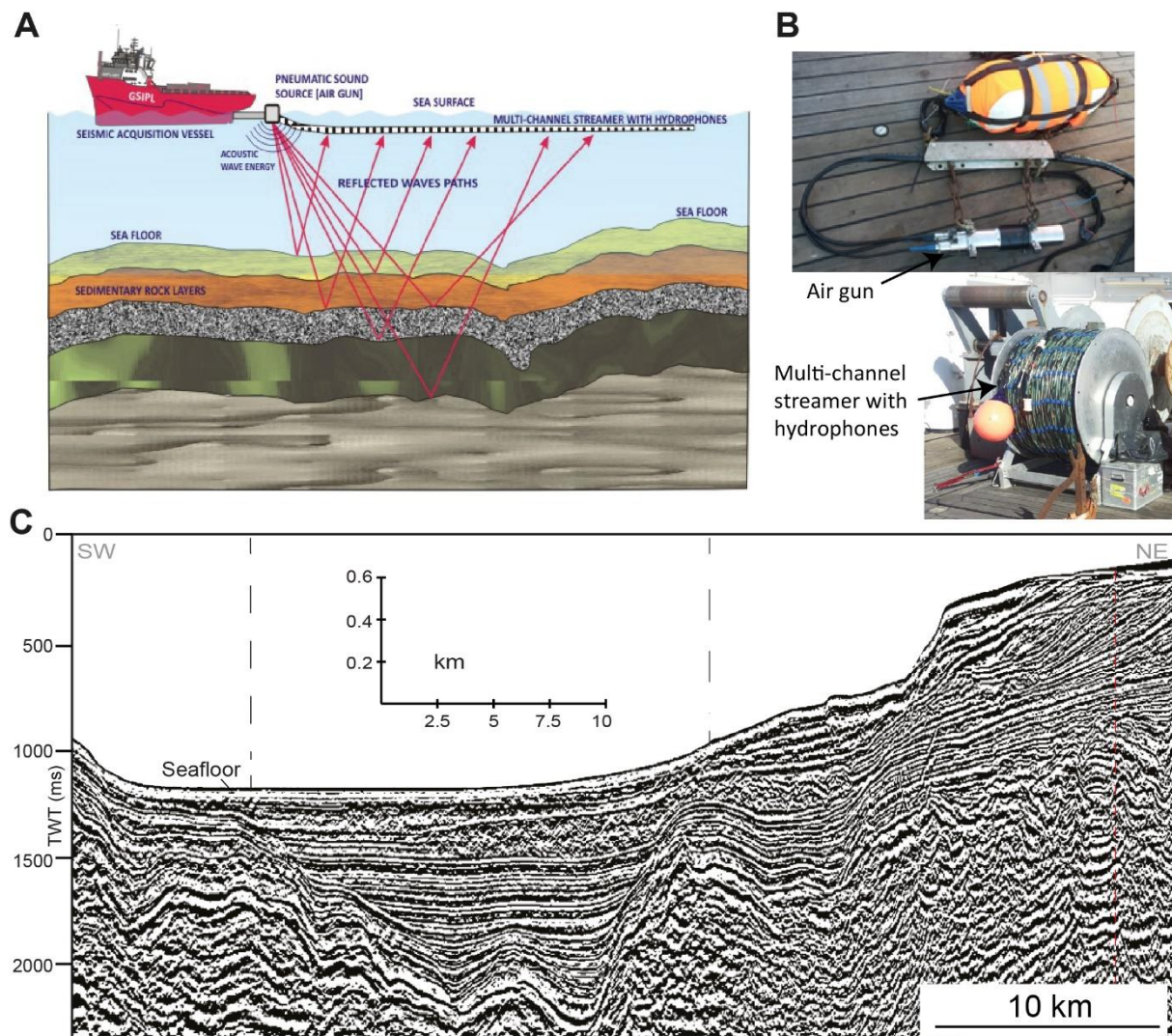


Figure 3.3: A) Sketch representing the acquisition of multi-channel seismic profiles modified after Geostar Survey (2009). B) Pictures showing an example of air gun and multi-channel streamer used onboard a research vessel. C) Example of a multi-channel seismic profile after processing.

Sub-bottom CHIRP-sonar seismic profiles are acquired with a Compressed High Intensity Radar Pulse (CHIRP) system, which represents one of the shallow Sub-Bottom Profiler (SBP) systems commonly used in marine surveys (Stoker et al., 1997; Tóth, 2011 and references therein; Fig. 3.4A). The SBP systems use various types of sound sources and frequencies resulting in different seafloor penetration (from a few meters to more than 50 m) and vertical resolution (from a few meters down to 0.05 m). The use of these different SBP systems depend on the water depth and the objectives of the study where each of the systems has their advantages and disadvantages (Tóth, 2011). The CHIRP sub-bottom profiler use sweep signals to generate pressure waves with high frequency range (up to 25 kHz) (Fig. 3.4B). The CHIRP profiles used in this thesis were acquired with a 2-7 kHz sweep-modulated band width, equivalent to a 3.5 kHz profiler fired from 16 transducers (Langone et al., 2005). The

recording length was 500-2000 ms (Langone et al., 2005). The high-frequency range allows a resolution down to 0.05 m and a penetration depth < 100 m in the soft sediments (Fig. 3.4C).

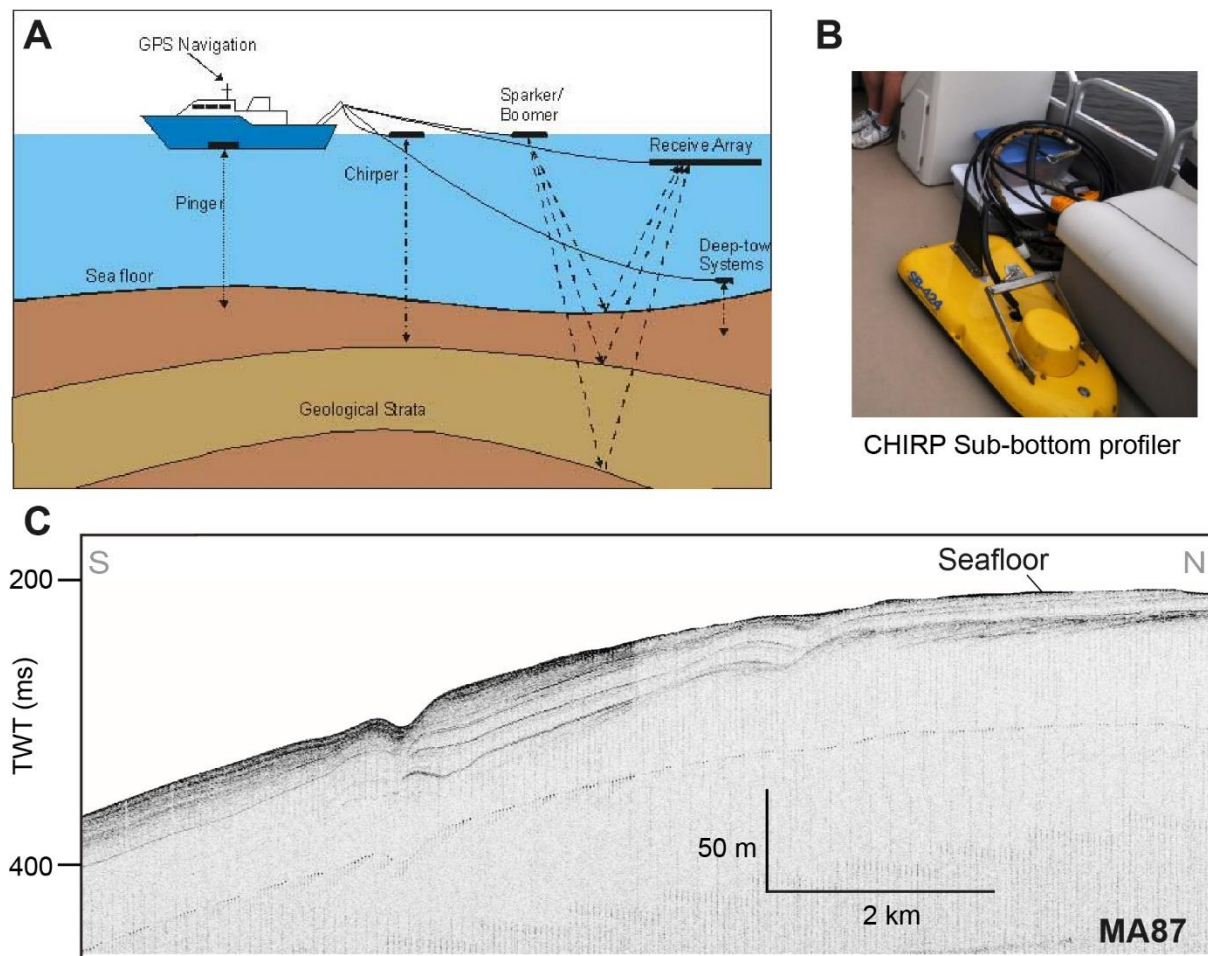


Figure 3.4: A) Schema representing the deployment of various shallow-water sub-bottom profiling systems from Stoker et al. (1997). B) Picture of a CHIRP sub-bottom profiler from WHOI (2020). C) Example of a CHIRP sonar seismic profile used in this research.

In order to recover sediment cores, a piston core system was used on board R/V Urania during mission MARCOS07 in 2007 (Fig. 3.5A and B). The piston corer system is composed of a nose cone (to penetrate the sediments), a tube (contain the sediments during the sampling), a weight (on top of the tube), a piston inside the tube and a small gravity corer attached to a tripping arm above the weight of the piston corer (Fig. 3.5C). The piston corer, attached to the vessel with a wire, is lowered towards the sea floor preceded by the small gravity core during the descent phase (Fig. 3.5C). The contact of the gravity corer with the sea floor opens the tripping arm releasing the piston corer on a fast free-fall (free fall phase; Fig. 3.5C). The weight and nose cone help to penetrate the sediments. During the penetration of the piston corer within the sea floor, the piston stops at the sediment surface (sampling phase; 3.5C). The pressure

differential applied by the piston on the sediment surface allows the entrance of soft material without disruption and retain the sediments during the retrieval of the piston corer. The piston corer is preferably used in soft sediment (e.g. clays) and normally allows to sample longer and relatively undisturbed cores. The tube containing the sediments can recover sediments down to few meters below the seafloor. After acquisition and once recovered on board, the cores are cut into sections 1 m long, closed with caps on both ends and labelled according to a standard scheme (Fig. 3.6). Once back to the laboratory, analyses are run on complete and split sections of the cores. One half of each sections are retained as an archive half to ensure that there will always be material to work on/refer to in the future. The other half (a.k.a. the “working half”) can be visually logged throughout and sub-sampled for various analyses.

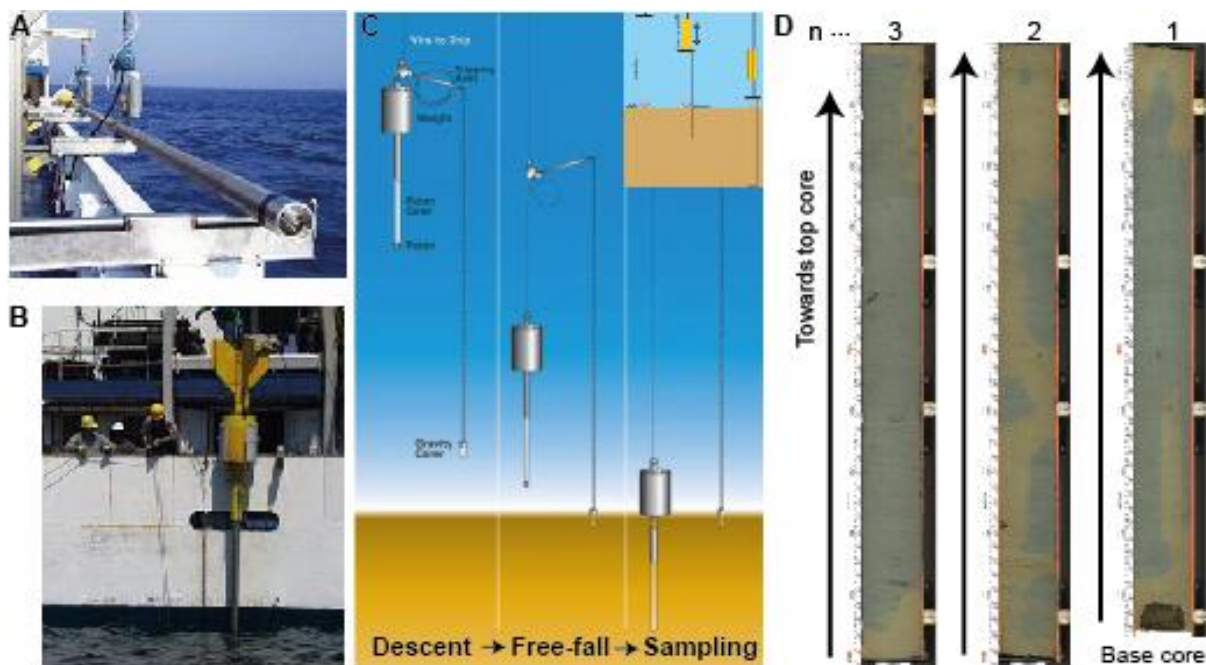


Figure 3.5: A) Sketch representing the technic used to acquire the piston cores (WHOI, 2020). B) Photo of the Piston corer onboard the R/V Urania during Gela-05 mission in 2005 and C) during coring operation (Langone et al., 2005). D) Example of photos of piston core sections splitted and labelled.

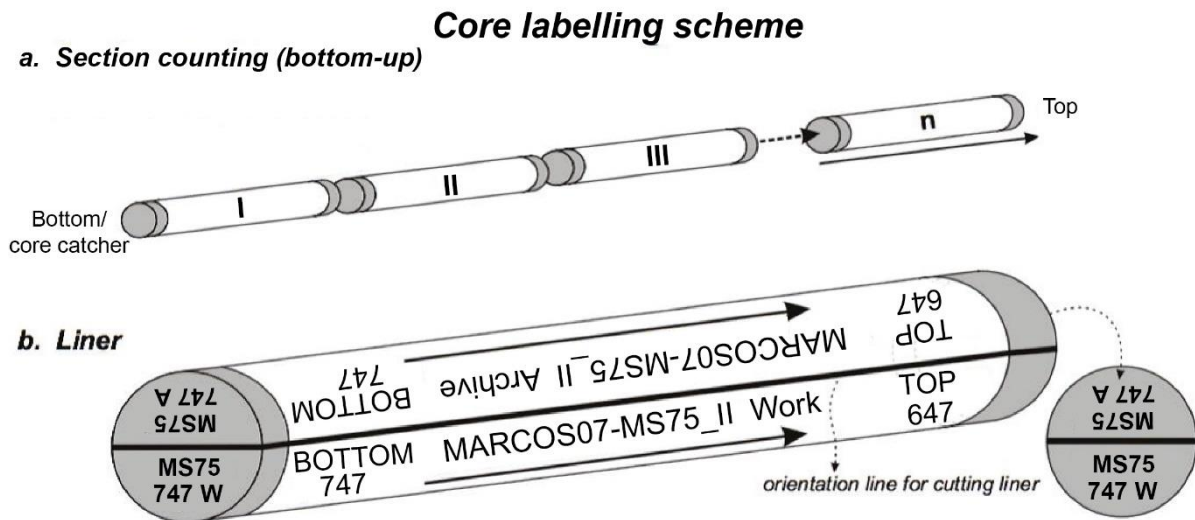


Figure 3.6: Core labelling scheme system used for the inscription of the piston core sections. Adapted and modified after Kopf et al. (2016).

High-resolution swath bathymetry is acquired by hull-mounted sonar arrays that collect bathymetric soundings from below the ship (Fig. 3.5A). First adopted in the 1990s, the sonar is composed of a transmit and a receiver array. Sound waves (or beams) are emitted from the transmit array through a fan shape, which sends out the sound waves with different angles (Fig. 3.5A). The time for the emitted sound waves to be reflected by the seafloor and return to the receiver array determine the water depth of the seafloor. The received angle and two-way travel time for sound give the exact position of the beams and their water depths, if the speed of sound is known for the entire water column. In fact, changes in temperature and salinity affect the speed of sound by  $4.5 \text{ m s}^{-1}$  per each degree Celsius increase in temperature and  $1.3 \text{ m s}^{-1}$  per each 1psu increase in salinity (Byrne et al., 2020). In order to estimate the speed of sound in the water for multibeam calibration, a CTD (Conductivity, Temperature, Density) probe measures at multiple stations continuous profiles of temperature, salinity, dissolved oxygen, fluorescence and light transmittance (Langone et al., 2005). The determined ship's position with a Global Positioning System (GPS) permit the acquisition of the data with an accuracy of  $\sim 1 \text{ m}$  and a depth resolution of 50 cm. A 30 kHz Kongsberg EM-300 multi-beam system was used to map over  $1400 \text{ km}^2$  of the eastern Gela Basin (Fig. 3.5B) while other sectors were obtained with a 50 kHz Reson Seabat 8160. This method allowed a drastic increase of the bathymetric resolution from  $\sim 100 \times 100 \text{ m}$  resolution from EMODnet (EMODnet Bathymetry Consortium, 2016) to a  $20 \times 20 \text{ m}$  resolution with the swath multibeam echosounder (Fig. 3.5C).

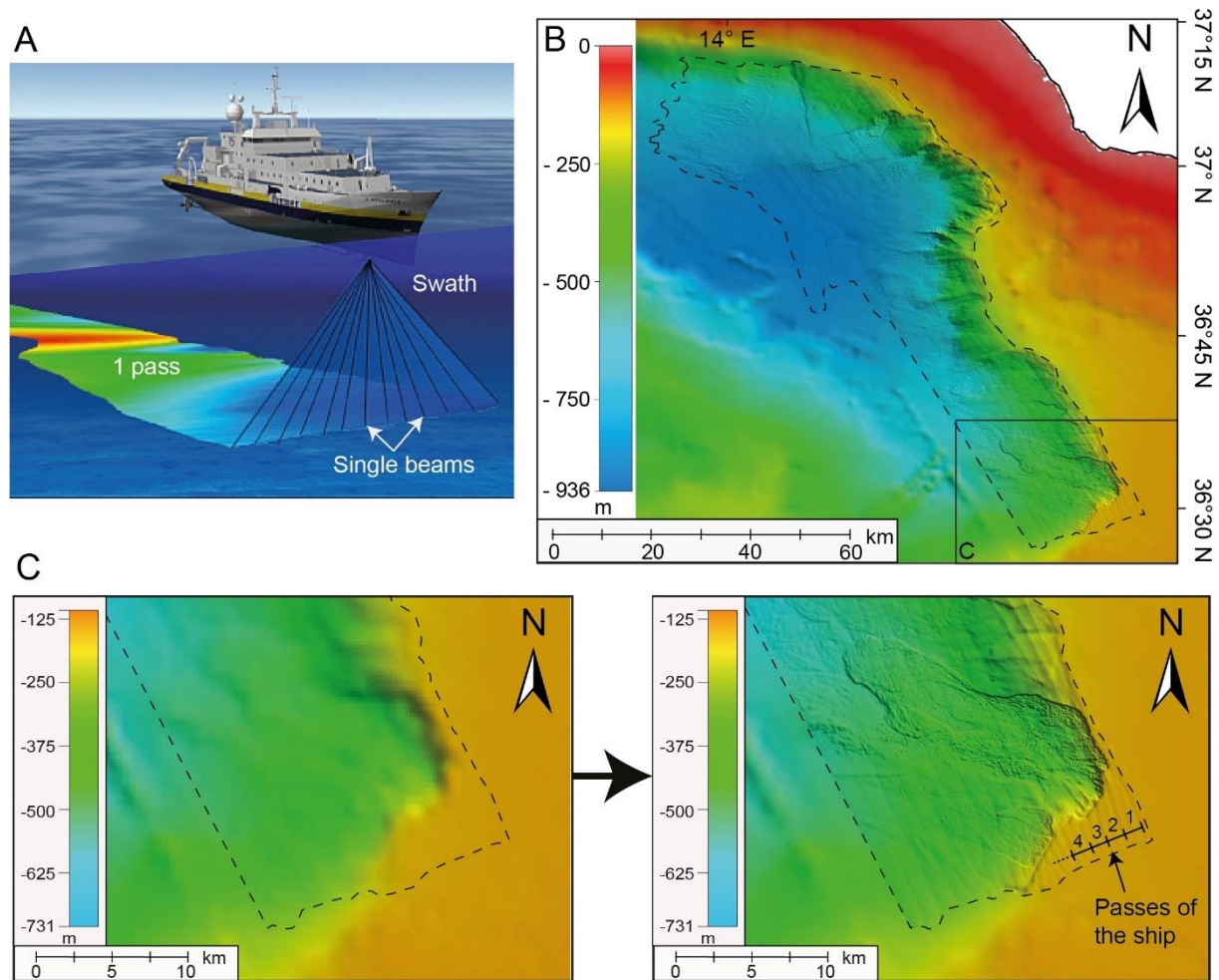


Figure 3.7: A) Representation of how a multibeam echosounder system acquires high-resolution bathymetric data (Ifremer, 2020). B) Bathymetric map showing the surface mapped with the multibeam echosounder along the eastern Gela Basin (surrounded by a black dotted line). C) Bathymetric maps demonstrating the increase in resolution of the bathymetry with the use of a multibeam echosounder. Note that each parallel lines observed on the high-resolution bathymetry (NW-SE) represent a pass of the ship during the acquisition with the swath echosounder.

### 3.4 Data definition and purpose

#### 3.4.1 Boreholes data

Data acquired during and/or after the drilling of the boreholes can contain multiple information based on the cuttings, in-situ measurements and/or the study of cores. The data measured down borehole in the Gela Basin were: the spontaneous potential of the different rock formation, their resistances, and their sonic transit time completed by analyses of the cores including their stratigraphic formation and the foraminifera assemblage content. Together, the information permitted to characterize the type of rock formation, to define the true vertical depth of each stratigraphic formations and estimate their age of deposition.

In this study, the information from a few boreholes drilled in the northern Gela Basin were used to identify the different types of rock formation on a small lateral but long vertical scale (Fig. 3.8). The interpretation and correlation of multiple boreholes allows an increasing of the lateral resolution in order to observe the changes in depth of the rock formations identified in each of them. Additionally, the resolution of the changing depth in the rock formation could be extended and increased by being correlated to multi-channel seismic (MCS) profiles. However, the interpretation of MCS profiles is limited by the depth and resolution of the boreholes.

### 3.4.2 Multi-Channel Seismic

MCS consists of vertical seismic images of the sub-seafloor where the reflected energy of each shot is recorded by multiple detectors. The vertical profiles are represented by high/low amplitude reflectors that can be parallel, discontinuous, mounded and/or chaotic.

MCS gives the advantages of multifold imaging of the same location enhancing the signal/noise ratio of the seismic profile through stacking and the possibility to estimate seismic velocity from the recorded data (Tóth, 2011). It has been used for the identification of deeply buried features (e.g. MTDs and contourite deposits) thanks to the extended lateral and vertical resolution scale (Fig. 3.8). MCS profiles permitted the identification and extension of key time reflectors over 5,000 km<sup>2</sup> where the ages were constrained by the borehole logs.

In addition, the correlation between the MCS profiles permitted the realisation of surface maps of key seismic reflectors representing specific times in order to evaluate the morphology of seafloor and its evolution. Then, thickness maps could be made based on the difference between the surface maps to show the changes in sedimentation of the Gela Basin over time.

### 3.4.3 Sub-Bottom Seismic

Chirp-sonar seismic consists of the same source of imaging than MCS but results in a different penetration depth and resolution of seismic profiles (Fig. 3.8). The higher frequencies used by the Chirp-sonar seismic ensures a maximum resolution but a lower penetration depth due to quicker attenuation.

The chirp-sonar seismic profiles were used for their acoustic values in imaging sediments buried at shallow depth with very high vertical resolution and are particularly good

to use in shallow water environments (e.g. Plets et al., 2009; Baltzer et al., 2014). The resolution allowed the investigation of present-day to Quaternary sedimentary structures and processes (e.g. Menier et al., 2006; Baltzer et al., 2014). They tend to be particularly useful for delineating shallow features such as gas accumulations, buried channels, pockmarks, and characterize the geomorphology and stratigraphy along the eastern Gela Basin. They permitted to localize and analyse MTDs, define a chronology and constrain their time of deposition.

#### **3.4.4 Sediment cores**

Sediment cores are cylindrical samples that are recovered from the seabed and filled with sediments. The recovered cores can have different lengths according to the type of devices (i.e. gravity coring, piston coring) used to extract a portion of the seafloor and the type of sediments composing the seafloor. The sediment composition can vary from clay to gravel depending on the location of the cores, the water depth and the distance from the coast.

Similar to deep boreholes, piston coring system is economically more accessible than boreholes, allows the extraction of sediments without significant disturbance but is limited in depth (Fig. 3.8). The sediments extracted with a piston corer preserve the depositional sequence of the stratigraphic layers (WHOI, 2020). This technic is the closest to in-situ data and allows the recover longer core samples compared to gravity cores. The cores are like time capsules in which scientists can study the changes in grain-size/composition of the sediments, the fluids and gas compositions, the foraminifera assemblages, the plant debris and the internal structures over time. For example, the recognition of hemipelagic deposits is made via grain-size analysis and geochemistry depending on the location. These changes in the cores indicate modification of the climate, the oceanographic circulation, seafloor stability and sediment sources. Depending on the location and the penetration of the core in the seafloor, the time span recorded can vary significantly.

#### **3.4.5 Swath bathymetry**

Swath bathymetry is the measurement of the water depth in the oceans, seas and lakes with a multibeam echosounder, a type of sonar that produces a swath of depth information compared to a singlebeam echosounder system that sends out one sound wave at a time to find the depth directly under the ship. This method is usually used as a first tool for seafloor exploration to map and investigate the morphologic expression of the seafloor over large areas. In addition, the high resolution (20 to 50 m; Fig. 3.8), depending on the water depth, allows

the identification of large features (e.g. contourite and mass transport deposits). The analysis of high resolution bathymetric maps can be done by making gradient, direction and curvature maps. This information were used to define the geohazard of downslope and along-slope processes in this research.

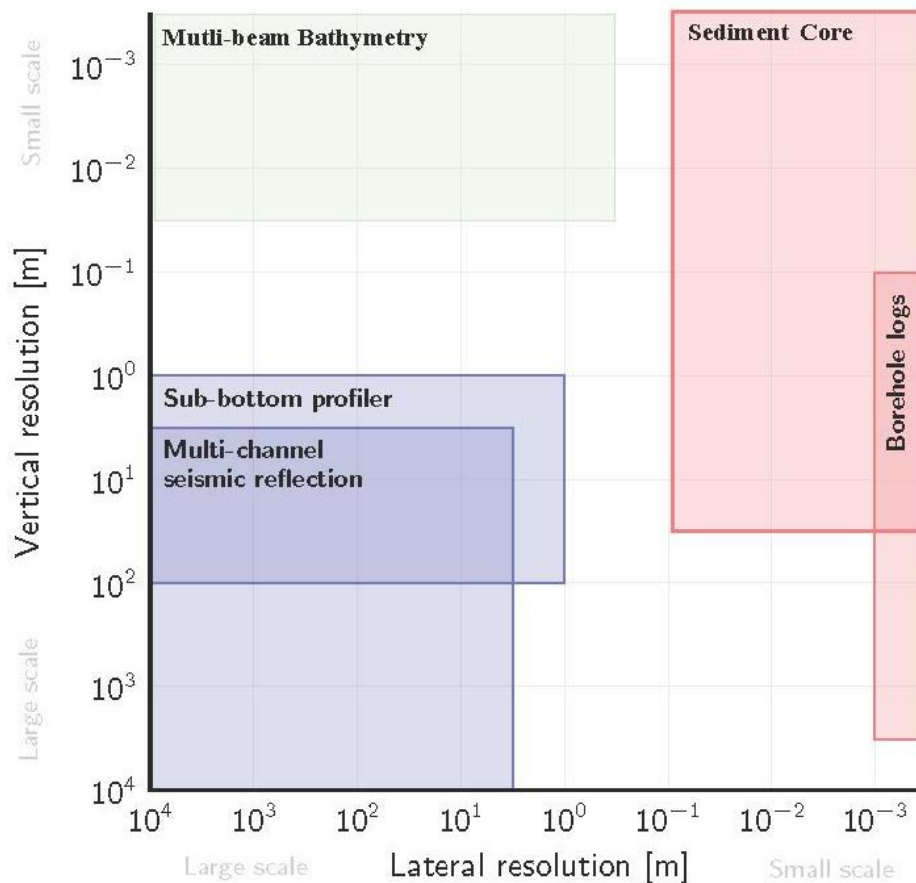


Figure 3.8: Comparison of the resolution of the data used in this research adapted and modified from pers. com. Dr. Johnathan Ford.

## 3.5 Applied methods

### 3.5.1 Well data interpretation

Deep boreholes recovered along the shelf of the Gela Basin were selected for this research for their total drilling depth and their location (Fig. 3.9A). The deep boreholes were drilled deep enough to identify the entire Pliocene-Quaternary but characterized by too low resolution to recognise the different stages of the Quaternary. In total, three boreholes were selected and correlated by the key time intervals identified in the well data (Fig. 3.9B). The key time intervals identified in one the deep borehole (B1) were correlated to one of the MCS

profiles (Fig. 3.9C). This correlation allowed a geochronology of the sediments in depth along the MCS profile characterized by changes in lithology.

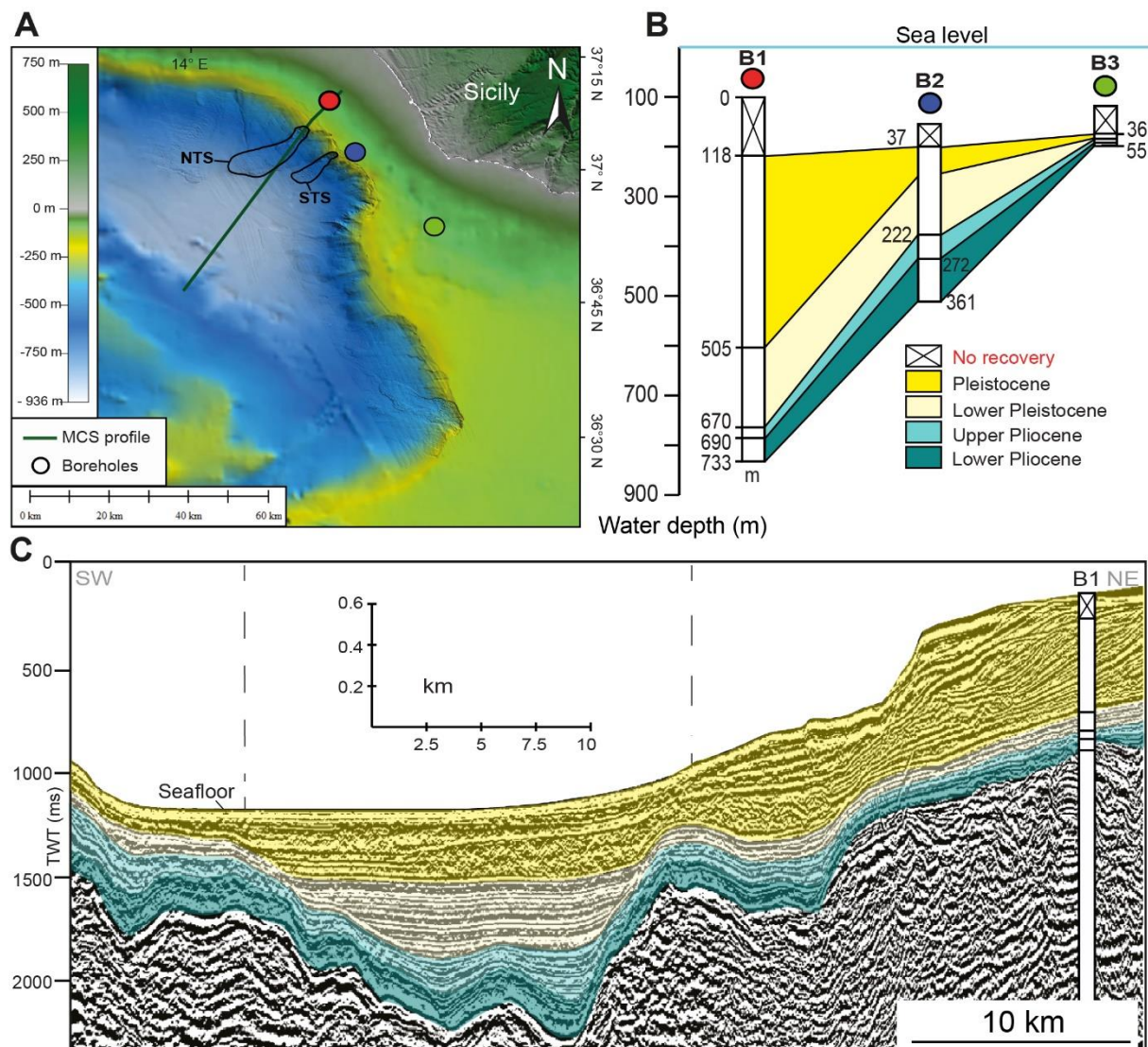


Figure 3.9: A) Bathymetric map showing the location of the three selected deep boreholes and the multi-channel seismic (MCS) profile. B) Correlation of the key time intervals of the selected deep boreholes. C) Geochronology of a MSC profile by the deep borehole B1. Location of the MCS profile in Fig. 3.9A.

### 3.5.2 Multi-channel Seismic profiles

All MCS profiles acquired in the Gela Basin were correlated with profile 1. Surface (isobaths) and thickness (isopach) maps of key seismic reflectors were generated. Each isobath map represents a paleo-seafloor and their comparison allow an analysis of the seafloor morphology over time. Isopach maps represent the difference between two isobath maps in order to analyse the depositional evolution of the basin.

Few MCS profiles were selected based on their resolution, penetration depth, location and their intersections, in order to analyse the main changes in the margin outbuilding of the Gela Basin (Fig. 3.10).

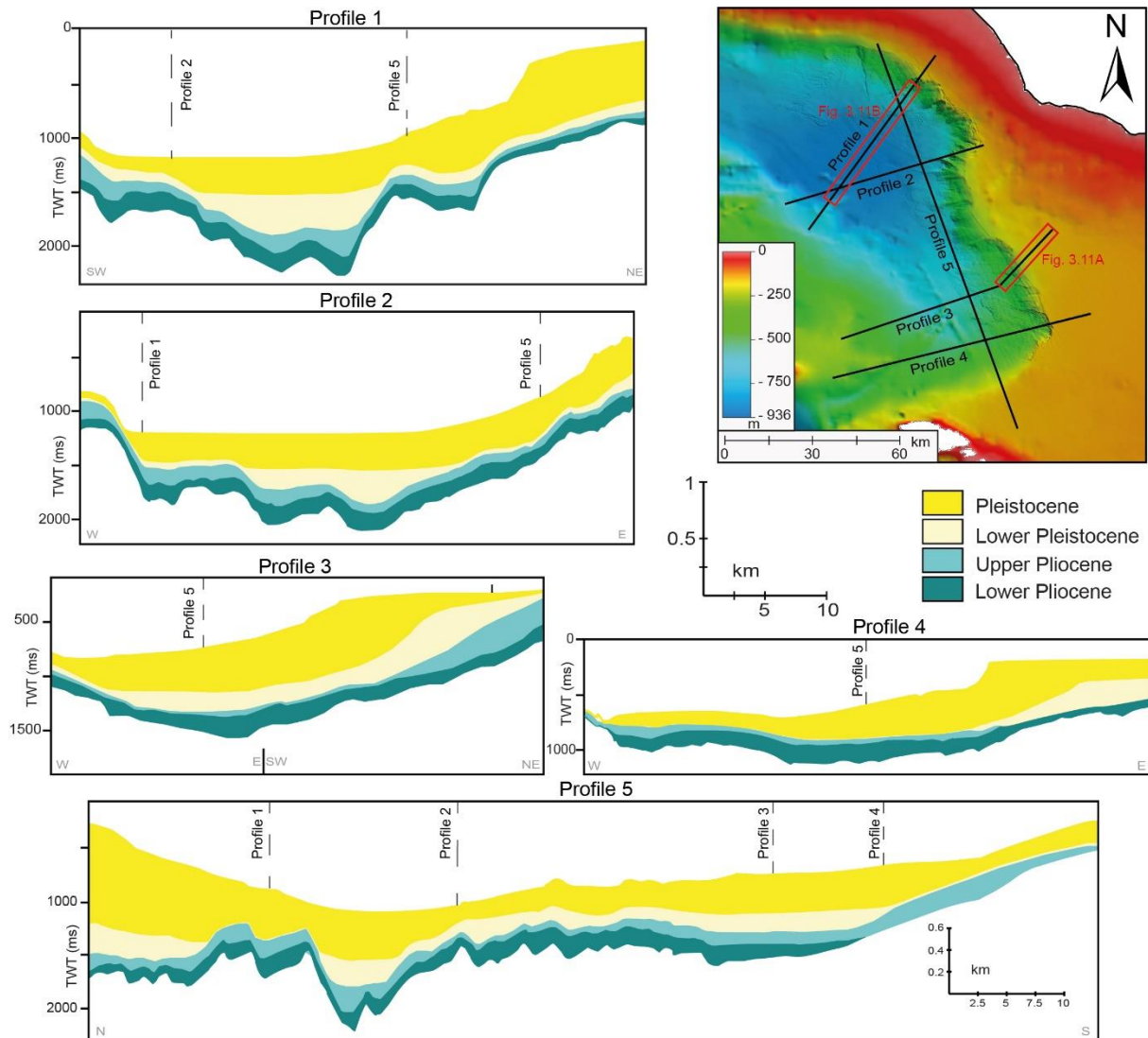


Figure 3.10: Identified geochronology of the selected MCS profiles based on profile 1 from Lower Pliocene to Pleistocene. Location of the MCS profiles on the map. Note the junction of all the MCS profiles.

Different seismic facies could be identified and described. Chaotic, low and high amplitude reflectors, typical of MTDs, were found on the slope and in the basin. On the shelf, seismic reflectors were characterized by an erosional character with top-lapping reflections (erosional surfaces). In total, up to 8 erosional surfaces (ESs) were identified in the MCS profiles (Figs 3.11A). A few of these erosional surfaces could be correlated and/or dated with reflectors identified in other MCS profiles in previous research. The two shallowest ESs coincided with ES1 and ES2 identified and dated by Kuhlmann et al. (2015). The last erosional

surface (ES8) identified in profile 3 corresponds to the MPT horizon studied and dated at 800 ka by Di Stefano et al. (1993). Another reflector, characterized by an erosional character at the shelf, could be identified and traced in all the MCS profiles and coincided with the top reflector of the first large MTD emplaced after the MPT (Fig. 3.11B). This reflector was estimated to be age of around 450 ka. The estimated dating of this reflector permitted to better constrain the age by reducing the time interval during which the MTDs were emplaced (Fig. 3.11B).

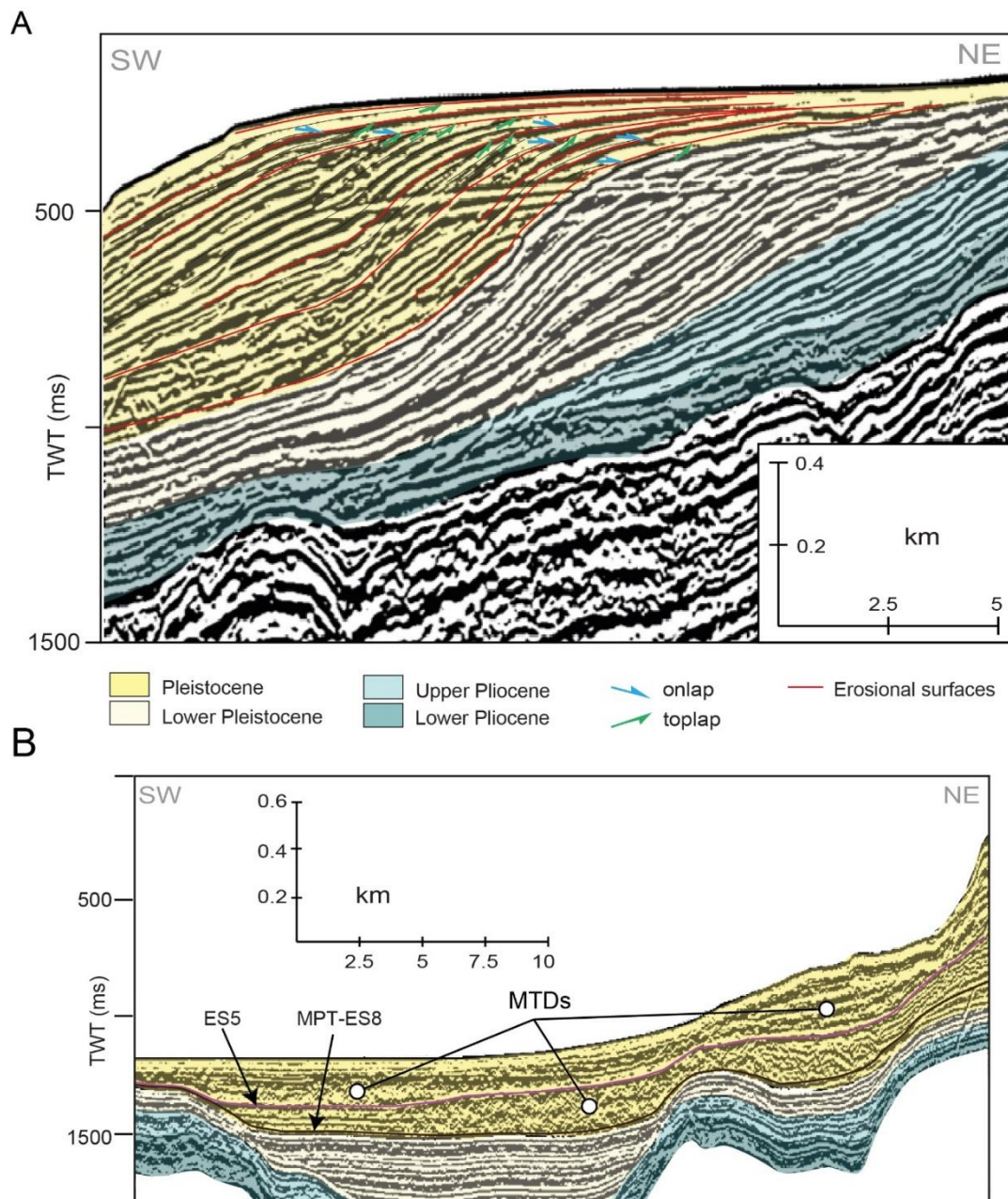


Figure 3.11: Zoom on 2 selected MCS profiles to explain the methods for the identification of A) erosional surfaces (red lines) and B) mass transport deposits (MTDs) on seismic profiles. Location of the profiles in Fig. 3.10.

### 3.5.3 Chirp-sonar seismic profiles

Seismic units were previously identified in sub-bottom seismic (SBS) reflections profiles thanks to the age dating of deep cores (> 50 m) recovered in the northern Gela Basin (Kuhlmann et al., 2015; Fig. 3.12A). The chronostratigraphy of the last five Marine Isotope Stages (MIS) was used in the interpretation of the sequence stratigraphic architecture of the shelf and slope. The different characteristics of deposition of the MIS units were used to recognize them in other sub-bottom profiles along the study area when correlation was not possible. In fact, despite a concentrated grid of sub-bottom profiles acquired along the eastern Gela Basin from shelf to basin (Annexe 3), the high-resolution but low penetration of the SBSs did not always permitted to correlate all the MISs units identified in the northern Gela Basin to the south. For example, MIS 5 (71-130 ka; Lisiecki and Stern, 2016) was recognized as sediment layers draping the margin from shelf to slope (Fig. 3.12A) during the last sea-level highstand (Benjamin et al., 2017). Additionally, MIS 5 is characterized on SBS profiles by toplaps on the shelf due to sea-level fall (Kuhlmann et al., 2015, Figs. 3.12A and B). Sea-level fall induced toplaps and forced downlap deposition of MIS 4 and 3 (71-29 ka) on the slope (Figs. 3.12A and B). The toplaps of the most recent MIS units (5, 4 and 3) indicate the emplacement of the shallowly-buried unconformity (ES1) identified and dated at 30 kyr BP by Kuhlmann et al. (2015) (Figs. 3.12A and B). Similar to other areas of the Mediterranean, the unconformity overlaid by onlapping or draping of sediment units indicates a region affected by sea-level lowstand. The last two MIS (1 and 2; 29 ka to present) drape ES1 from slope to shelf as deposition occurred during sea-level rise and current high-stand (Fig. 3.12A and B).

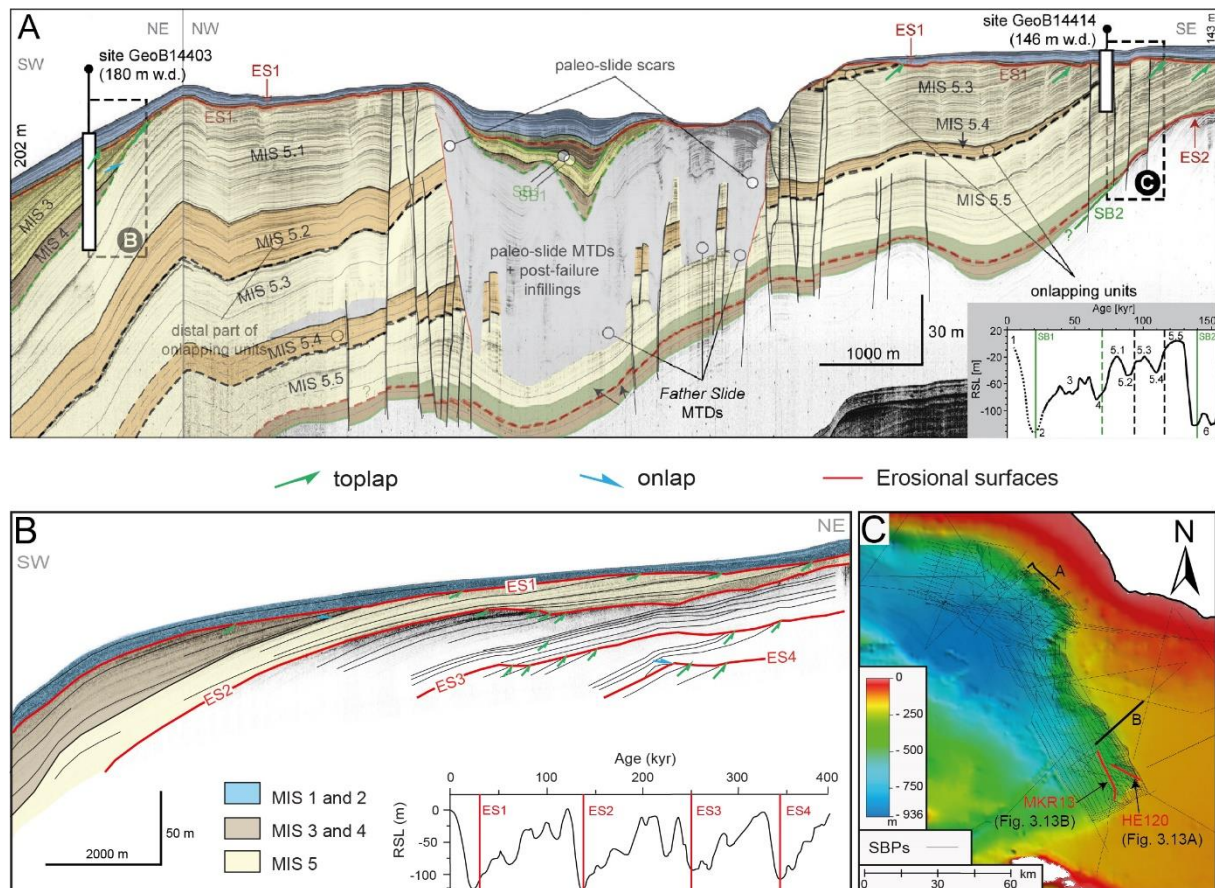


Figure 3.12: A) Sequence-stratigraphic interpretation of an acoustic sub-bottom profile from the northern Gela Basin correlated to long piston cores. Modified after Kuhlmann et al. (2015). B) Example of an interpreted sub-bottom profile studied in this thesis and based on the characteristics of the seismic units identified in Kuhlmann et al. (2015). C) Map showing the location of the sub-bottom profiles of A and B among all the sub-bottom profiles available in the study area.

In addition to the presence of unconformities, the high-resolution of sub-bottom profiles permitted to unravel the presence of MTDs that are characterized by acoustically transparent or chaotic seismic facies (Fig. 3.13; Annexe 3), erosional bases, localized hyperbolic diffractions and steep headwalls (Fig. 3.13A). The MTDs can be separated laterally by continuous high-amplitude reflectors and characterized by blocky areas, confined and emergent front (Figs. 3.13A and B).

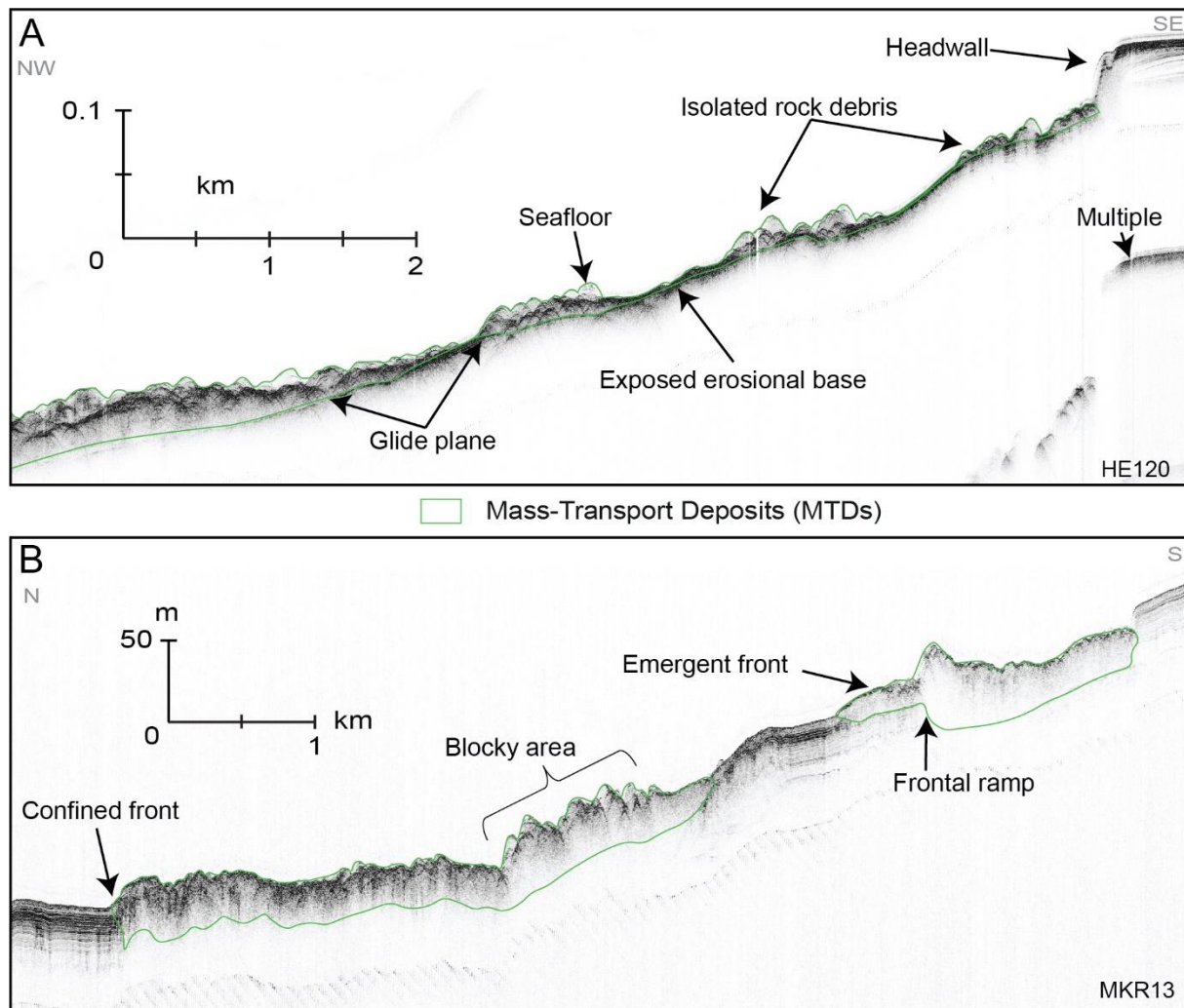


Figure 3.13: Examples of sub-bottom seismic (SBS) profiles showing A) the clear evidence at the seafloor of a headwall and an erosional base and B) two MTDs characterized by different toe domains and separated by high-amplitude seismic reflectors. Note the reduced penetration of the acoustic signal below the MTDs.

### 3.5.4 Sediment cores

Two piston cores were recovered in the southern Gela Basin on the lower (MS72) and upper slope (MS75) (Fig. 3.14A; Tab. 3.1). The recovery sites of the deepest and shallowest cores are located near the toe domain of an MTD and the southern headwall of another MTD, respectively (Fig. 3.14A). The SBS profiles indicate that both cores penetrated sediment units characterized by undisturbed sediments and composed of the most recent sediment units draping the last unconformity ES1 (Fig. 3.14B).

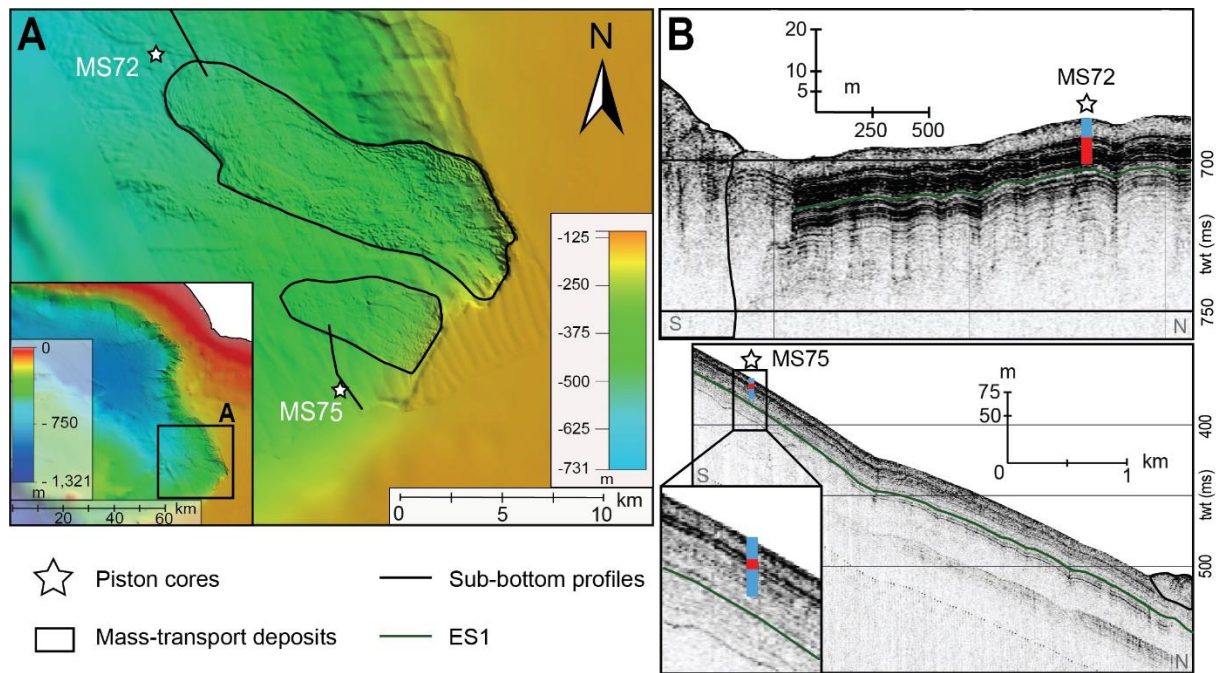


Figure 3.14: A) Morpho-bathymetric map showing the location of the two piston cores studied in this research. B) Location and representation of the penetration depth of the piston cores on sub-bottom profiles. The different colours is used to indicate the changes of amplitude reflectors crossed by the cores. Red = high amplitude reflectors, blue = low amplitude reflectors.

Table 3.1: Names, coordinates, mission, water depth and length of the piston cores recovered in the south-eastern Gela Basin.

Core Name	Coordinates		Mission #	Water depth (m)	Length (cm)
	Latitude	Longitude			
MARCOS07-MS72	36°21.925'N	14°21.395'E	MARCOS 2007	550	1078.5
MARCOS07-MS75	36°13.2'N	14°26.757'E	MARCOS 2007	280	842.5

Multiple analysis were applied to the sealed cores, to half cores and to samples from the piston cores (Table 3.2). A multi-analysis approach was key for a better chronostratigraphic reconstruction of paleo oceanographic and climate conditions (e.g. Martinez-Ruiz et al., 2015; Nieto-Moreno et al., 2011).

Table 3.2: Overview of all the analysis made on the piston cores, their resolution and the material used. Examples of these analysis are given in figures 3.15 and 3.17. The “x” is used when there is no specific resolution applied and more details can be found for each analysis in the following sub-chapters.

Cores	AMS 14C dating (samples)	Magnetic Susceptibility (sealed cores)	XRF (half-core)	X-ray (half-core)	Stable isotopes (samples)	Plant Debris (samples)	Grain size (samples)
MS72	x (Mixed material)	2 cm	1 cm	x	X ( <i>G. bulloides</i> + <i>B. marginata</i> )	x	5 cm
MS75	x (Mixed material)	2 cm	1 cm	x	X( <i>B. marginata</i> )	x	5 cm

#### 3.5.4.1 Magnetic susceptibility

The magnetic susceptibility measured on the sealed cores was used to quantify the amount of magnetic material. The magnetic material was identified by a Bartington system from ISMAR, which consists of generating a magnetic field on the sealed cores in order to measure the quantity of material that can become magnetized. This method is non-destructive and runs automatically. The amount of magnetic minerals can indicate for example the presence of volcanoclastic material (tephras) deposited during volcanic eruptions, and broadly differentiate marine sedimentation from terrigenous input (Vigliotti et al., 2008; example in Fig. 3.15c).

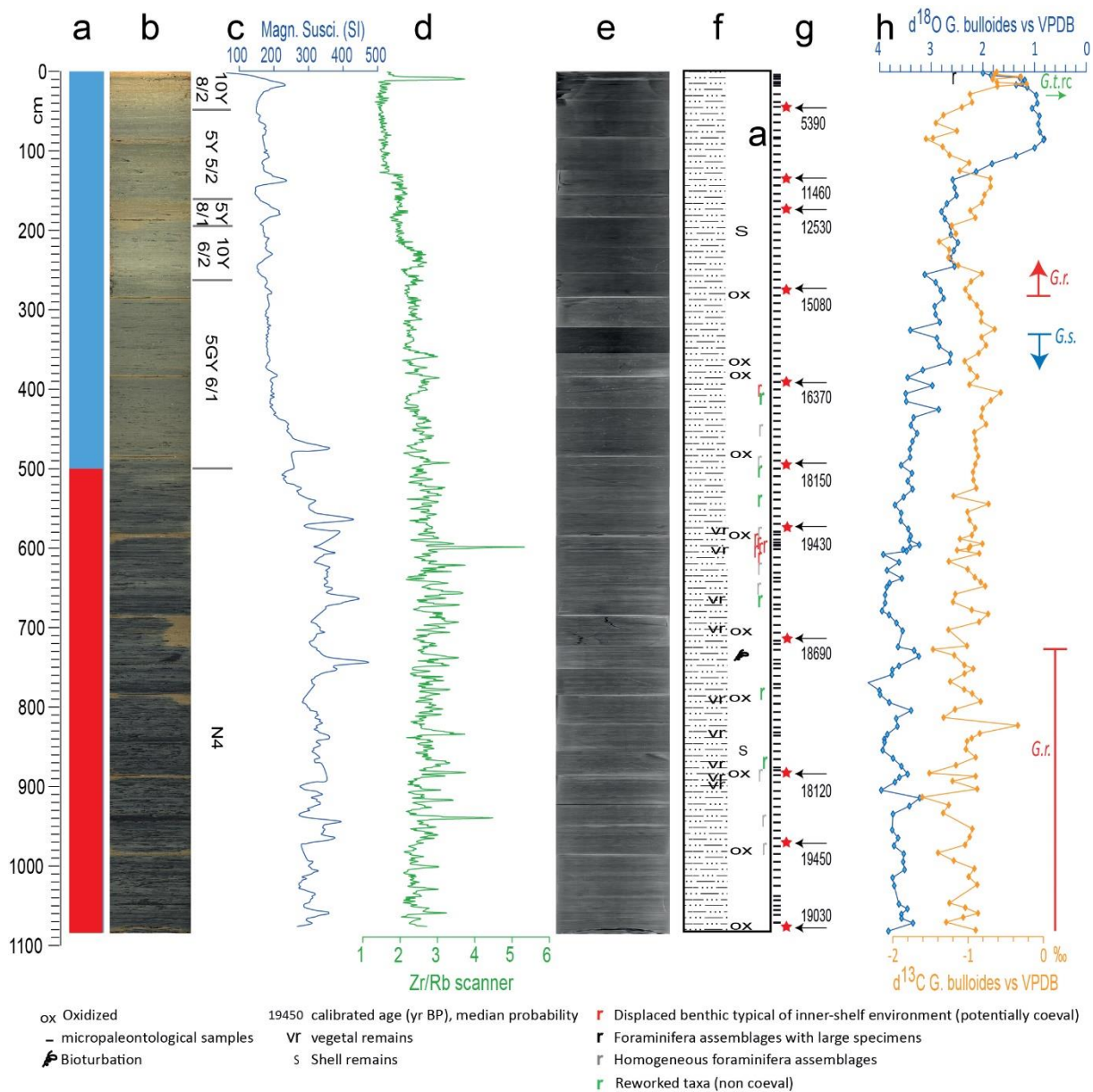


Figure 3.15: Data example of core MS72 with a) a representation of the amplitude reflectors crossed by the piston corer, b) a photography of the core with the colour code, c) the magnetic susceptibility measured, d) an elemental ratio, e) the X-ray images and f) the foraminifera assemblages identified as well as the presence of other components (i.e. vegetal remains, oxidation, bioturbation, shell remains, etc.), and g) the position of the radiocarbon dating and h) the stable isotopic analysed.

### 3.5.4.2 X-ray fluorescence

The X-ray fluorescence (XRF) is used to qualitatively and semi-quantitatively analyse the major and trace elements in the surface sediment of the split cores. The elements were measured by an AVAATECH core scanner at ISMAR in Bologna. This non-destructive method consists of bombarding the sediment every 1 cm with different X-rays energy (10, 30 and 50 kV) to destabilise the atoms. Their destabilization creates displacements of electrons

(ionic displacements) to re-stabilize the atoms. The energy released during the ionic displacements is measured allowing to identify the elements present thanks to typical energy signatures. The results converted to elemental count were used to identify the changes in elemental composition along the cores, which can inform on various paleo-environmental changes in the water column and at the seafloor such as grain size, productivity, oxygenation, sediment source, etc. (Martinez-Ruiz et al., 2015; Piva et al., 2008; Jaccard et al., 2010; Govin et al., 2012; Bahr et al., 2014; Revel et al., 2015). An example of an element ratio (Zr/Rb) used to reconstruct the grain size is given in figure 3.15d.

#### 3.5.4.3 X-ray images

X-ray images are two dimensional radiological images (projected X-ray) acquired by generating X-ray on top of the core towards the half sections of the cores. X-ray passes through the sediments where they are partly absorbed and the quantity of radiation that passes through the sediments usually vary along the core depending on the heterogeneity. This method was initially developed for medical purpose before used in palaeontology and then on sediment (Bouma, 1964 and references therein). The quantity of X-ray absorption depends on the density and structural composition (Bouma, 1964). The images acquired along all sections of both piston cores were used to identify the presence of sediment structures and/or bioturbation (Fig. 3.15e). The identification of sediment structures (e.g. wavy laminations, flame structures, erosional base) and bioturbation (e.g. pyritized micro-burrows) contributes in turn to decipher sediments reworked by bottom currents or from gravity-driven processes and reconstruct the paleoceanographic condition present at the seafloor during sediment deposition (e.g. Martín-Chivelet et al., 2008; Petrovic et al., 2019; Stow and Smillie, 2020).

#### 3.5.4.4 Foraminifera assemblages

Foraminifera assemblages consists of single-cell microorganisms (<1 mm) that can live in the water column (Planktonic) or at the seafloor (Benthonic) and produce an external shell made of calcium carbonate (CaCO<sub>3</sub>) or mineral grains or other particles glued together to protect themselves (World Foraminifera Database). They inhabit all marine environments from brackish to hypersaline waters, from marsh to deep ocean floor, from poles to the tropics. Many parameters influence the foraminifera assemblages, among which the oxygen content and the food availability (organic matter flux). After the death of the organisms, the hard shells are deposited at the seafloor and buried with the sediments where they can be easily preserved due to their small size and hardness. Their quality of preservation make them abundant in the

sediments and are easily recognizable thanks to the complex and specific morphology of the shells for each species. Over 40,000 fossil species have been reported in World Foraminifera Database and characterized by occurrence and disappearance helping in turn the fossil record to estimate the age of sediments/rocks. The occurrence/disappearance of foraminifera species has been driven by changes in the oceans (i.e. salinity, temperature, bottom current velocity, oxygenation, nutrient content) (e.g. Lirer et al., 2019).

219 sediment samples were taken from the piston cores at regular and close intervals (every 5 to 10 cm) in order to identify the occurrence and/or disappearance of the maximum number of foraminifera species. This method was used to reconstruct the bioecozones of the cores, which consist of inferring the environment in a restricted space interval of the cores by grouping all the species present and their tendency to appear or disappear. The foraminifera were extracted from the sediments through wet sieving and identified using an optical microscope, which is time-consuming but essential for their recognition and the reconstruction of the environment of deposition (e.g. Capotondi et al., 1999). Multiple foraminifera assemblages could be recognized and classified into sub-categories such as displaced, reworked, homogeneous and large specimens (Fig. 3.15f).

#### 3.5.4.5 Radiocarbon AMS

Radiocarbon AMS (Accelerator Mass Spectrometry) is a carbon dating method that can be applied on foraminifera species but is time consuming and not always possible when there is low abundance in the sediment. The radiocarbon AMS consists of accelerating the ions contained in the shells to extraordinary high kinetic energy allowing the counting of carbon 14 atoms that are present in the sample (mass analysis). However, foraminifera shells contain typically only a few micrograms of carbon and therefore, laboratories requires a minimum weight of 8-10 mg for each single shells in order to contain sufficiently enough carbon in their shells to be detected for the carbon dating (Beta Analytic, 2021). The selection of the shells is done with a microscope to identify clean and representative specimens with a minimum size for each samples. This phase of selection is crucial for an effective and accurate measurement of the carbon dating to narrow down the age of marine sediments (Colman et al., 2002; example in figure 3.15g) previously initiated by the bioecozones or assess radiocarbon reservoir ages (Broecker et al., 1984; Patterson et al., 1995; Siani et al., 2010). The carbon dating of data points with the bioecozones was used to estimate the age-depth relationship where limited amount of absolute chronological information is available. In addition, the sedimentation rate

could be calculated between data points with chronological information by measuring the thickness of sediments accumulated in a given time.

#### 3.5.4.6 Stable isotopic analysis ( $\delta^{18}\text{O}$ and $\delta^{13}\text{C}$ )

The analysis of stable isotopes informs on paleoceanographic conditions as foraminifera shells incorporate oxygen and precipitate carbon from the ocean during their growth. Isotopes are atomic nuclei containing same number of protons but a different number of neutrons resulting in different physical behaviours (related to diffusion, solubility, boiling point, etc.). Many elements have several isotopes (stable or unstable) with different portions (nuclear weight, e.g.  $^{11/10}\text{B}$ ,  $^{13/12}\text{C}$ ,  $^{15/14}\text{N}$ ,  $^{18/17/16}\text{O}$ ,  $^{36/34/33/32}\text{S}$ , etc.). The abundance of isotopes with even number of neutrons is higher than those with “odd” numbers and tend to be more stable. The isotopes are created by the fractioning of elements between two substances or two phases (gaseous, liquid, solid) of the same substance with different isotopic ratio (Kendal and Caldwell, 1998). One of the fractioning processes is the kinetic effects, which is due to the higher mobility of the lighter isotopes associated for example with evaporation and precipitation (Kendal and Caldwell, 1998). Lighter isotopes (e.g.  $\text{H}_2^{16}\text{O}$ ) will evaporate while heavier isotopes (e.g.  $\text{H}_2^{18}\text{O}$ ) will precipitate more easily. The  $^{18}\text{O}/^{16}\text{O}$  ratio ( $\delta^{18}\text{O}$ ) of the shell depends on the temperature and salinity of the water in which the foraminifera develop. The different isotopic abundance is preserved in the foraminifera shells, which do not decay radioactively, and inform us on the paleo-temperature in the water column (planktonic species) and at the seafloor (benthonic species) (e.g. Cacho et al., 2001; Sicre et al., 2013). The information retrieved from the stable isotopes helped us to reinforce the age model of the cores by comparing the values with other study areas. An example of  $\delta^{18}\text{O}$  and  $\delta^{13}\text{C}$  from *G. bulloides* is given in figure 3.15h.

#### 3.5.4.7 Plant debris analysis

Plant debris analysis refers to the study of vegetation fragments (i.e. wood, marshes) stranded in sediment cores collected in marine environments, where they were transported by rivers and/or oceanographic currents and/or submarine landslides. Paleo-vegetation grew similarly to plants in modern conditions on land and in shallow water environments and the photosynthesis regulated absorption and exchange of gases (i.e. oxygen, carbon) which remain stored in the debris.

Plant debris were only found in one core (MS72, Fig. 3.15f) during the sieving of sediment samples for the separation of the foraminifera. The handpicked samples went through the elemental analyser-ratio mass spectrometry analysis to estimate the organic carbon, total nitrogen and isotopic carbon ( $\delta^{13}\text{C}_{\text{oc}}$ ). The isotopic composition allowed us to identify their origins (source) and therefore infer their mode of transport (e.g. Tesi et al., 2007).

#### 3.5.4.8 Grain-size distribution

Grain-size distribution is the grain-size analysis of sediment deposited/transported at the seafloor and collected by the sediment cores. Sediment grain-size can vary from clay (< 0.0039 mm) to gravel (> 2 mm) and be classified from very fine to very coarse in each of the classes (Table 3.3).

Table 3.3: Grain size classification modified from Wentworth (1922).

Particles diameter ( $\mu\text{m}$ )		Wentworth classification		Correspondence with simplified logs of cores	
Minimum	Maximum				
1000	2000	very coarse	Sand		
500	1000	coarse		coarse	
250	500	medium		medium	
125	250	fine		fine	
63	125	very fine		Very fine	
31	63	coarse	Silt	silt	Sortable Silt
15.6	31	medium		silty-clay	
7.8	15.6	fine			
3.9	7.8	very fine			
< 3.9	3.9	clay	Clay	clay	

In marine environments, some specific grain-size fractions have been used to diagnose high current speed (e.g. Lonsdale and Malfait 1974; Ledbetter, 1979; Ledbetter and Balsam 1985; McCave and Hall, 2006). Water velocity was correlated to grain size in Hjulström-Sundborg diagram and to its concentration (McCave and Hall, 2006) (Fig. 3.16). The Hjulström-Sundborg diagram has been particularly used in hydrology as it shows the relationships between erosion, transportation and deposition. The diagram highlights the frictional resistance as the dominant force to prevent erosion for sediment superior > 0.01 mm (10  $\mu\text{m}$ ) (Fig. 3.16A). The particle size < 10  $\mu\text{m}$  is characterized by cohesive behaviour therefore erosion velocity increases with decreasing grain size. McCave and Hall (2006) discovered by opposing sortable silt (10-63  $\mu\text{m}$  - SS) to mean silt grain size (4-63 $\mu\text{m}$ ) that the fraction < 10  $\mu\text{m}$  exhibit a cohesive behaviour, which can affect the sensitivity of mean silt

grain size to bottom currents strength. The boundary defined between 8 and 10  $\mu\text{m}$  by McCave et al. (1995) was confirmed through experimentation by Mehta and Letter (2013). However, the SS fraction remains exclusively used for low to average flow velocity (up to 25 cm/s) and when sand concentration is less than 50% (Fig. 3.16B).

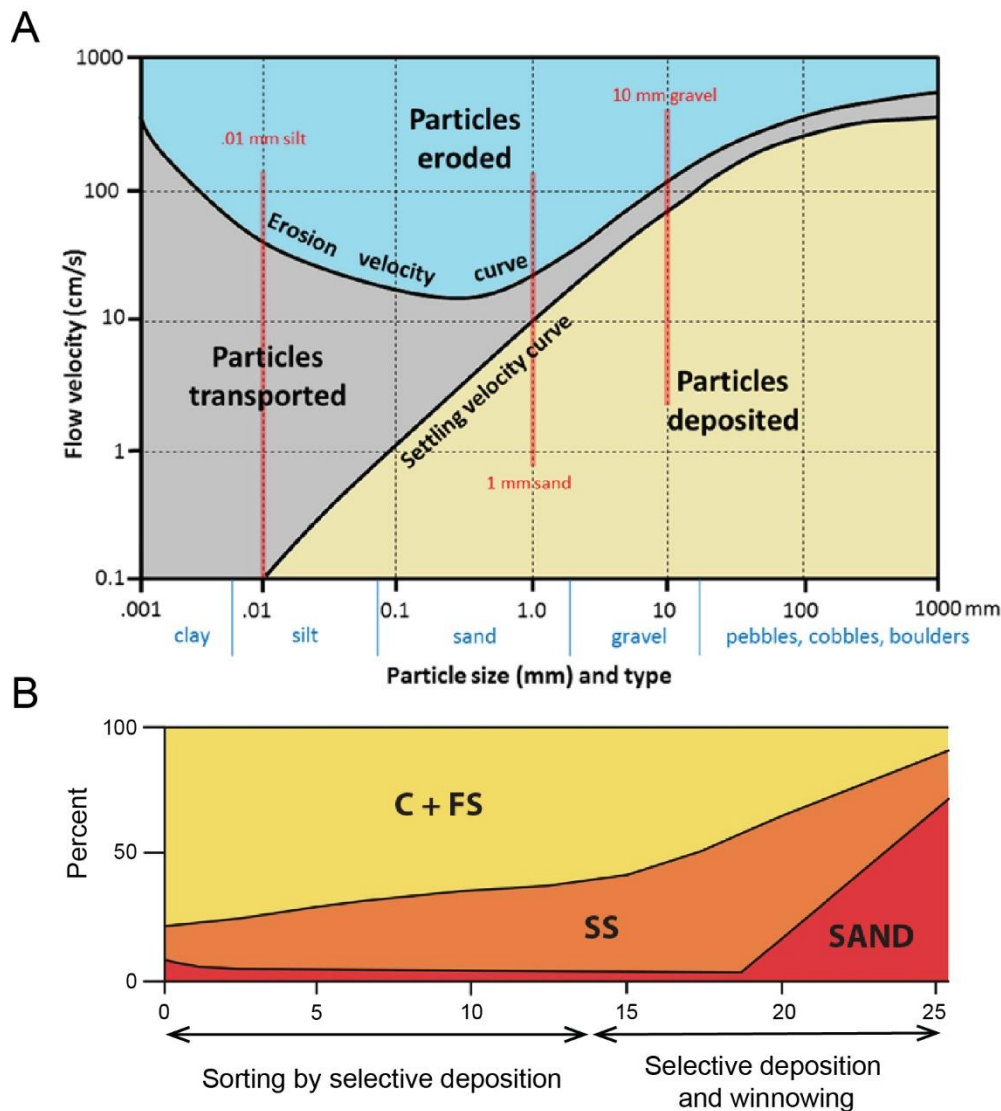


Figure 3.16: A) Hjulström-Sundborg diagram and B) sediment percentage-flow speed relationship modified from McCave and Hall (2006).

The piston cores were sampled at regular intervals (every 5 cm) for grain-size analysis in order to obtain a continuous and high-resolution reconstruction of textural changes. The 291 sediment samples were washed with hydrochloric acid to perform the grain-size analysis on the carbonate-free fraction of the sediment. A Malver Mastersizer 3000 was used at Ifremer in Brest (France) to measure the size and concentration of the sediment. The grain-size analysis

was used to identify the sorting and distribution of the sediments via its grain-size concentration, an indicator of sediment deposition influenced by bottom-currents (Fig. 3.17).

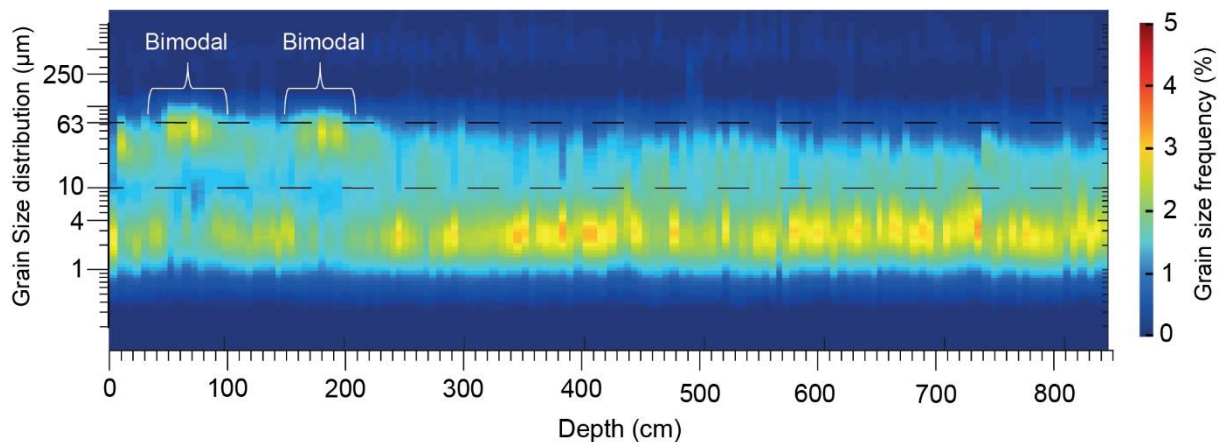


Figure 3.17: Example of grain distribution and frequency for core MS75. Note the changes from unimodal to bimodal distribution with an increase in the sortable silt fraction.

### 3.5.5 Bathymetry analysis

Bathymetric data acquired along the eastern margin of the Gela Basin were analysed with a geomorphometric approach (a feature-based quantitative representation). Maps representing the shaded relief, slope gradient, aspect and curvature of the seafloor were generated. These maps, obtained with the ESRI ArcGIS software, allowed a new approach to recognize: i) steep and narrow slope gradient near the shelf edge typical of headwalls of MTDs, ii) preferential flow directions and iii) isolated upwardly concave and convex structures. The interpretation of these maps allow the identification of 16 MTDs and two sites of contourite deposits exposed at the seafloor (Fig. 3.18).

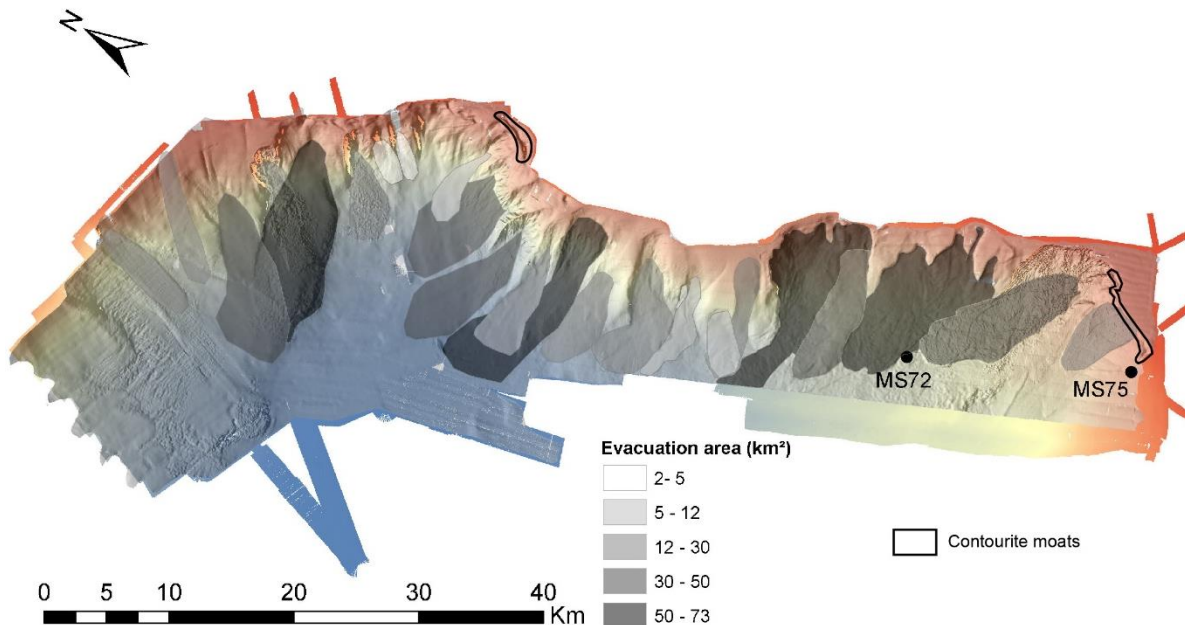


Figure 3.18: High-resolution bathymetric map showing the location of the MTDs and contourite moats identified with a geomorphometric approach compared to the position of the sediment cores recovered in the Gela Basin.

### 3.5.6 Paleo-current reconstruction

The paleo-current reconstruction was achieved through the combination of multiple analyses (foraminifera, element and isotopes composition, X-ray and grain size). The presence of reworked and hydraulic selection/sorting foraminifera, high oxygen content (isotope composition, element ratio Mn/Ti), laminae structures (X-ray) and high sortable silt mean size (grain-size) indicated a strengthening of the bottom currents, while higher productivity (element ratio Ba/Ti), low oxygen content, presence of authigenic pyrite, enhanced water mass stratification and low sortable silt mean size a weakening of bottom currents.

Sortable silt mean size represents one of the most important tools to deduce the flow energy and calculate its velocity (McCave et al., 2017). Major changes in ocean circulation that accompanied glacial to interglacial climate shifts induced changes in the SS demonstrating the use of grain size in inferring the magnitude of bottom current flow speed changes (McCave et al., 2017). Compared to sand, sortable silt allows a continuous record in most of the sediment cores. The sortable silt mean size ( $\overline{SS}$ ) was calculated to estimate the magnitude of absolute flow speed changes based on McCave and Andrews (2019) method. The  $\overline{SS}$  was obtained by calculating the exponential of the sum-product function of the bins and divided by the percentage of the sortable silt fraction:

$$Exp = \left( \frac{\text{sum-product}}{\%10-63 \mu m} \right)$$

Where:

$$\text{Sum-product} = \left( \frac{\text{percentage of each bin}}{\text{natural log of the bins' mid-point}} \right)$$

The accuracy of the paleo-velocity calculation was estimated by the correlation coefficient ( $r$ ) measuring the linear relationship between  $\overline{SS}$  of all samples versus their abundance percentage in sortable silt (SS%). The closer the ( $r$ ) is to 1 more confidently sediments can be interpreted as current-sorted and reliable to provide a flow history (McCave et al., 1995; McCave and Hall, 2006). SS% was calculated by dividing the percentage of the sortable silt fraction by the percentage of the grain-size fraction below 63  $\mu m$ :

$$SS\% = \left( \frac{\%10-63 \mu m}{<63 \mu m} \right)$$

In the study area, mass-transport deposits are present in close proximity to bottom current deposits. Therefore, to differentiate along-slope from downslope sedimentary processes, we used the 9 points correlation method proposed by McCave and Andrews (2019). The method uses the Correl function in Microsoft Excel to evaluate the correlation among nine values of SS% versus  $\overline{SS}$ . In addition, Correl was combined with Microsoft Excel Linest function (the mean values of the slope on the same nine values) to determine the correlation coefficients for each sample.

### 3.5.7 Tsunamigenic potential

In the research of the tsunamigenic potential for the eastern Gela Basin, an assessment of the potential hazard to trigger a tsunami was based on the volumes of the MTDs identified in the study area. The two largest and most recent MTDs were selected in order to reconstruct the landslide and tsunami scenarios. Further numerical techniques were used to assess the stability of the MTDs under seismic load (i.e. different earthquakes intensities), simulate the landslide dynamics and evaluate the tsunami generation and impact on the coasts of Sicily and Malta.

The pre-failure margin morphology (correlate the isolines) was reconstructed in order to get the initial sliding surface. The difference in the headwalls between the post-failure isolines and pre-failure isolines (initial sliding surface) permitted, by extrapolation, to calculate the initial volumes of the MTDs and comparing them with the emplaced volumes. Once the

parameters of the initial slide were obtained (undisturbed sliding surface, top initial surface, predefined centre of mass), the landslide motion could be computed by the in-house code “UBO-BLOCK1” which adopts a Lagrangian approach, and splits the slide body into interactive portions that can change shape but conserve their volumes (e.g. Zaniboni et al., 2016). The computed sliding motions provided the velocity of the slides including the accelerations and decelerations that are necessary for the tsunami simulation. At the same time, a stability analysis was made along profiles across the initial sliding mass by applying different peak ground accelerations (earthquakes intensity) to assess the safety factor  $F$ . The safety factor was calculated through an in-house numerical code (Paparo and Tinti, 2017). Finally, the tsunami simulation was computed with an algorithm developed by Tinti and Tonini (2013), to estimate the size, speed and propagation of the tsunamis generated by the sliding motions as well as their impacts on the coasts of Sicily and Malta.

# Chapter 4. Factors controlling margin instability during the Plio-Quaternary in the Gela Basin

---

“Factors controlling margin instability during the Plio-Quaternary in the Gela Basin

(Strait of Sicily, Mediterranean Sea)”

- Authors:
- Tugdual Gauchery (University of Bologna, Italy; *Istituto di Scienze Marine, CNR di Bologna, Italy*)
  - Marzia Rovere (*Istituto di Scienze Marine, CNR di Bologna, Italy*)
  - Claudio Pellegrini (*Istituto di Scienze Marine, CNR di Bologna, Italy*)
  - Antonio Cattaneo (*Ifremer, Géosciences Marines, Plouzané, France*)
  - Elisabetta Campiani (*Istituto di Scienze Marine, CNR di Bologna, Italy*)
  - Fabio Trincardi (*Istituto di Scienze Marine, CNR, Bologna, Italy*)

- Objectives:
- Determine when and where MTDs were emplaced
  - Understand their relationship with tectonic activity, climate change and shifts in the oceanographic currents
  - Define the predominant predisposing factors during the evolution of the Gela Basin

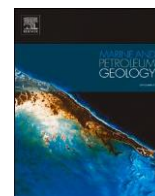




ELSEVIER

Contents lists available at ScienceDirect

## Marine and Petroleum Geology

journal homepage: [www.elsevier.com/locate/marpetgeo](http://www.elsevier.com/locate/marpetgeo)

Research paper

## Factors controlling margin instability during the Plio-Quaternary in the Gela Basin (Strait of Sicily, Mediterranean Sea)

Tugdual Gauchery <sup>a</sup>, Marzia Rovere <sup>a,\*</sup>, Claudio Pellegrini <sup>a</sup>, Antonio Cattaneo <sup>b</sup>,  
Elisabetta Campiani <sup>a</sup>, Fabio Trincardi <sup>a</sup>

<sup>a</sup> Istituto di Scienze Marine, National Research Council, Via P. Gobetti 101, 40129, Bologna, Italy

<sup>b</sup> IFREMER, Géosciences Marines, Z.I Pointe du Diable, BP70, Plouzané, France

## ARTICLE INFO

## Keywords:

Stratigraphy  
Middle Pleistocene Transition  
Plio-Quaternary  
Contourites  
Climothems  
Mass-transport deposits  
Continental margin evolution  
Glacio-eustatic variations

## ABSTRACT

This study presents novel findings on the Pliocene and Quaternary evolution of the Gela Basin (Strait of Sicily, Mediterranean Sea), an area recording the interaction between tectonics, climate change at Milankovitch and sub-Milankovitch timescales, and dynamic water masses exchange between the eastern and western Mediterranean Sea. The calibration of seismic profiles with exploration boreholes allowed for the refining of the chronostratigraphic framework of the Gela Basin and highlighted the main phases of margin growth. Since the Pliocene, the margin has recorded the deposition of 100 m high shelf-edge clinothems, accompanied by sediment drifts on the slope and mass-transport deposits (MTDs), possibly triggered by seismic activity. Through the Plio-Quaternary the locus of deposition of sediment drifts migrated upslope due to a progressive shift of bottom currents. After the Middle Pleistocene Transition (MPT) the margin experienced an accelerated outbuilding with the deposition of a 700 m thick succession in only 0.8 Myr. At this time, a marked change in sedimentary architecture reflects the growth of shelf-edge clinothems and associated MTDs on the slope, and the spreading of contourite deposits over a broader and generally shallower area. Sediment flux to the basin and the intensity of bottom currents appear both paced at 100 kyr eccentricity orbital cycles. The growth of bottom current deposits on a large portion of the upper slope and outer shelf likely reflects constraints to the bottom current flow by the margin morphology, inherited from Miocene and Pliocene tectonics. Overall, a combination of long-term tectonic activity, climate change and shifts in oceanographic regime resulted in a complex along-strike variability of the margin morphology and stratigraphic architecture and affected where and when MTDs were emplaced. These conclusions show how climate cyclicity influence sediment supply which combined with margin morphology can promote slope instability in continental margins.

### 1. Introduction

Continental margins preserve a unique long-term sedimentary record that offers the opportunity to study changes in eustasy (Tziperman and Gildor, 2003), modified by local tectonic-driven uplift/tilting/subsidence of the margin, sediment supply (Llave et al., 2011) and oceanographic regime (Thiéblemont et al., 2019). Stratigraphic successions therefore reflect a combination of changing climate, oceanographic regime and tectonic conditions (e.g. Gong et al., 2018; Pellegrini et al., 2020; Steckler et al., 1998). Stratigraphic successions represent ideal archives to solve: i) variation in strata geometries as physical expressions of long-term climatic components; ii) relation between climate regime, tectonic activity and fluctuations in sediment flux from

catchment(s) to the basin; iii) impact of glacio-eustatic cycles on the processes that govern how the sediment is delivered, transported, deposited and ultimately remobilized into the basin.

A variety of sedimentary bodies may deposit and coexist along a continental margin, including clinothems, turbidite, mass-transport (MTDs) and contourite deposits (e.g. Anell and Midtkandal, 2017; Faugères et al., 1999; Johannessen and Steel, 2005; Paumard et al., 2019). The Pliocene and Quaternary are ideal time intervals to study these sedimentary bodies; specifically after the Middle Pleistocene Transition (MPT), high-amplitude (ca. 120 m) fluctuations caused variations in sediment supply and played a crucial role in continental margin outbuilding (Somoza et al., 1997). These fluctuations forced systematic shifts in the position of the shoreline across the continental

\* Corresponding author.

E-mail address: [m.rovere@ismar.cnr.it](mailto:m.rovere@ismar.cnr.it) (M. Rovere).

<https://doi.org/10.1016/j.marpetgeo.2020.104767>

Received 6 February 2020; Received in revised form 9 October 2020; Accepted 14 October 2020

shelves, resulting in progradational, retrogradational and aggradational stratal stacking patterns (Patruño and Helland-Hansen, 2018). In these contexts, clinoforms and clinothem (clinoform-bounded sedimentary units) represent fundamental building blocks of the margin characterized by different geometric elements with a topset (low angle, shallow sector), a foreset (steepest angle and dip seaward) and a bottomset (low angle, deep sector) (Steel and Olsen, 2002). In addition, the MPT was likely accompanied by a global reorganization of the thermohaline circulation (Pena and Goldstein, 2014) with enhanced deposition of contourite systems after the MPT, as documented along the Atlantic-Mediterranean water mass exchange, with the more saline Mediterranean Water Outflow affecting the Algarve margin in the Gulf of Cádiz (Roque et al., 2012) and the Cantabrian margin in the NE Atlantic (Van Rooij et al., 2010). Similarly, in the Mediterranean Sea, thermohaline circulation enhanced contourite deposition after the MPT in the Corsica Trough (Miramontes et al., 2016), the southwestern Adriatic margin (Pellegrini et al., 2016) and the Balearic Promontory (Vandorpe et al., 2011).

The higher rates of sediment accumulation during the Pleistocene resulted in high rates of deposition and caused mass movement of sediments that were deposited too rapidly to allow for stable accumulation along the slopes. While submarine mass failures are indeed well-known along the fronts of rapidly prograding depositional systems from deltas to continental slope settings (Thöle et al., 2016), other studies have investigated the relationships between contourite deposits and MTDs (Laberg and Camerlenghi, 2008; Martorelli et al., 2016; Miramontes et al., 2018; Stoker and Hafliðason, 2005). However, the role of contourite deposits on margin stability is not yet fully understood.

Here, we document the case of a sector of the Mediterranean

continental margin, the Gela Basin (GB), characterized by the deposition of clinothem, contourite deposits and MTDs through the Plio-Quaternary. The added value in studying the GB is threefold: 1) its location in the Strait of Sicily is a key area of water masses circulation and exchange between the Atlantic Ocean and the eastern and western Mediterranean Sea; 2) its limited extent (90 km along-strike) offers the opportunity to study the variability of stratal geometries and margin morphology; 3) it has relatively high sedimentation rates which allow to study the effect of long-term climate change on different depositional systems.

In this study, we focus on the eastern side of the basin and document: 1) the predominance of tectonics as a predisposing factor for margin instability during the Pliocene; 2) the onset of contourite deposits and their role in favouring slope instability from the Late Pliocene, as an additional predisposing factor for slope failure; and 3) climate variability as the main driver of stratigraphic architecture and margin instability after the MPT.

## 2. Background

### 2.1. Geodynamic and tectonic setting of the Gela Basin

The Gela Basin (GB), located in the northern Strait of Sicily (Fig. 1), represents the Pliocene-Quaternary foredeep of the Maghrebic fold-and-thrust belt, which developed at the subduction-collisional boundary between the European and African plates (Colantoni et al., 1975). In the north, the GB was overthrustured during the late Pliocene–early Pleistocene by the southern movement of the Gela Nappe, the southernmost migrating thrust wedge of the Maghrebic chain (Argnani,

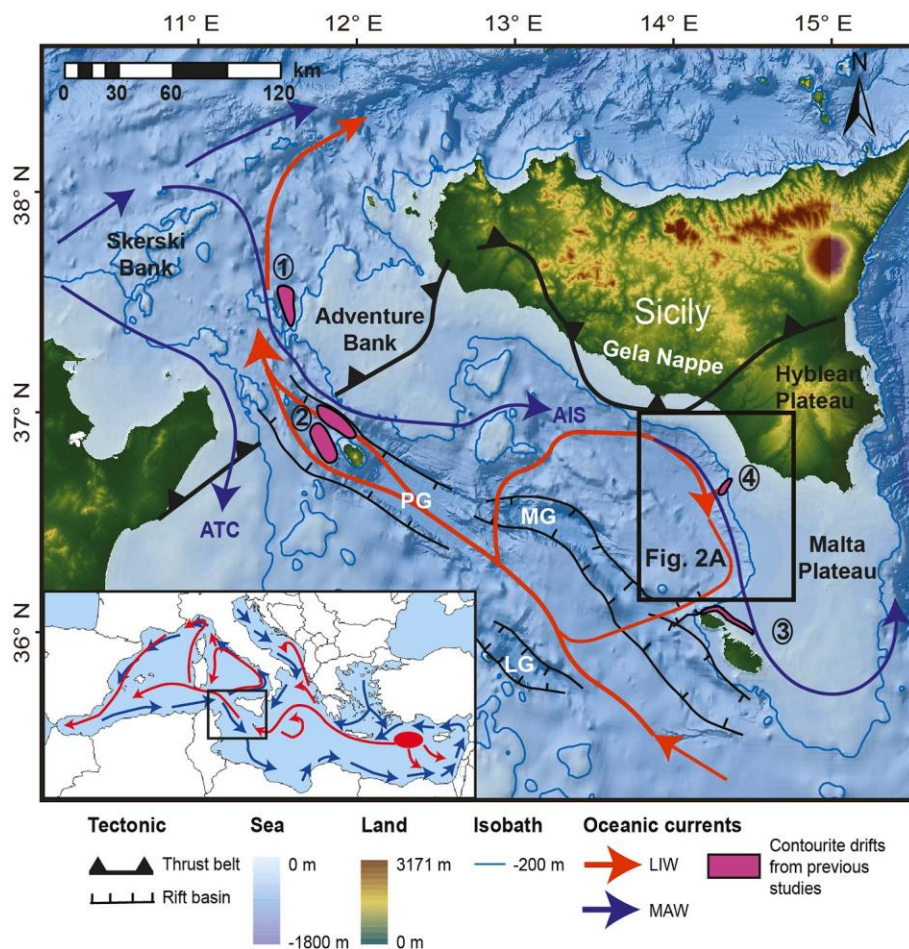


**Fig. 1.** Relief and bathymetric map of the Strait of Sicily; red and blue arrows represent the Levantine Intermediate Water (LIW) and the Modified Atlantic Water (MAW) (adapted from Lermusiaux and Robinson, 2001). 1–4 = previously studied contourite deposits: 1 = Marani et al. (1993), 2 = Martorelli et al. (2011), 3 = Micallef et al. (2013) and 4 = Verdicchio and Trincardi (2008). AIS = Atlantic Ionian Stream, ATC = Atlantic Tunisian Current, PG = Pantelleria Graben, MG = Malta Graben, LG = Linosa Graben. Inset: general oceanographic circulation in the Mediterranean Sea. (For interpretation of the references to colour in this figure legend, the reader is referred to the Web version of this article.)

1987; Butler et al., 1992). The Maghrebian fold-and-thrust belt reached its current position during the middle–late Pleistocene, concomitantly to a general uplift of the Hyblean Plateau (Ghielmi et al., 2012). The GB is delimited in the south and southwest by a NW–SE trending extensional rift system comprised of banks and grabens (Finetti, 1984, Fig. 1). The rift system formed in the late Miocene to early Pliocene, continued through the Quaternary forming the deep (> 1000 m) Pantelleria, Malta, and Linosa grabens (Gardiner et al., 1995, Fig. 1). Normal faults belonging to the same extensional system extend across the GB, where they are buried below the late Pliocene–Quaternary sediment infill (Argnani, 1987; Ghisetti et al., 2009).

The GB is rimmed by a narrow (8 km) continental shelf in the north, broadening to several tens of kilometres in the 100–150 m deep Malta Plateau, a structural horst of the Pelagian African foreland (Bishop and Debono, 1996). Following the Africa–Europe collision, moderate inversion tectonics affected the Malta Plateau (Argnani and Torelli, 2001), and regional uplift occurred in late Pliocene between Malta and SE Sicily, generating NE-trending normal faults (Gardiner et al., 1995). The uplift may have favoured the development of westward-prograding Quaternary wedges observed on the western sector of the Malta Plateau (Ghielmi et al., 2012; Minisini et al., 2007).

## 2.2. Oceanographic circulation

The Mediterranean Sea is a semi-enclosed basin connected to the Atlantic Ocean through the Strait of Gibraltar (inset of Fig. 1). The oceanographic circulation in the Mediterranean Sea is mainly composed of the Modified Atlantic Water (MAW), a relatively fresh and light water from the Atlantic and the Levantine Intermediate Water (LIW), saltier and relatively warmer formed in the Levantine Sea (Béranger et al., 2004). The flow of these two water masses generates oceanic currents across the Strait of Sicily: the MAW, directed eastward at 0–200 m water depths (w.d.) and the LIW, flowing westward between 200 and 500 m w. d. (Lermusiaux and Robinson, 2001; Astraldi et al., 2001). On the western side of the Strait of Sicily, the MAW is partially deviated northward by the Skerki Bank and then split into three main branches (Astraldi et al., 2001, Fig. 1). The first branch directly flows into the Tyrrhenian Sea along the northern coast of Sicily, while the remaining two turn southward (Astraldi et al., 2001, Fig. 1). The Atlantic Tunisian Current (ATC) flows south of the study area at the edge of the Tunisian shelf along the 200 m isobath, while the Atlantic Ionian Stream (AIS) circulates in the GB and Malta Plateau (Lermusiaux and Robinson, 2001, Fig. 1). The path of the LIW is influenced by the seafloor morphology and, due to Bernoulli’s effect, its flow speed in the Strait of Sicily

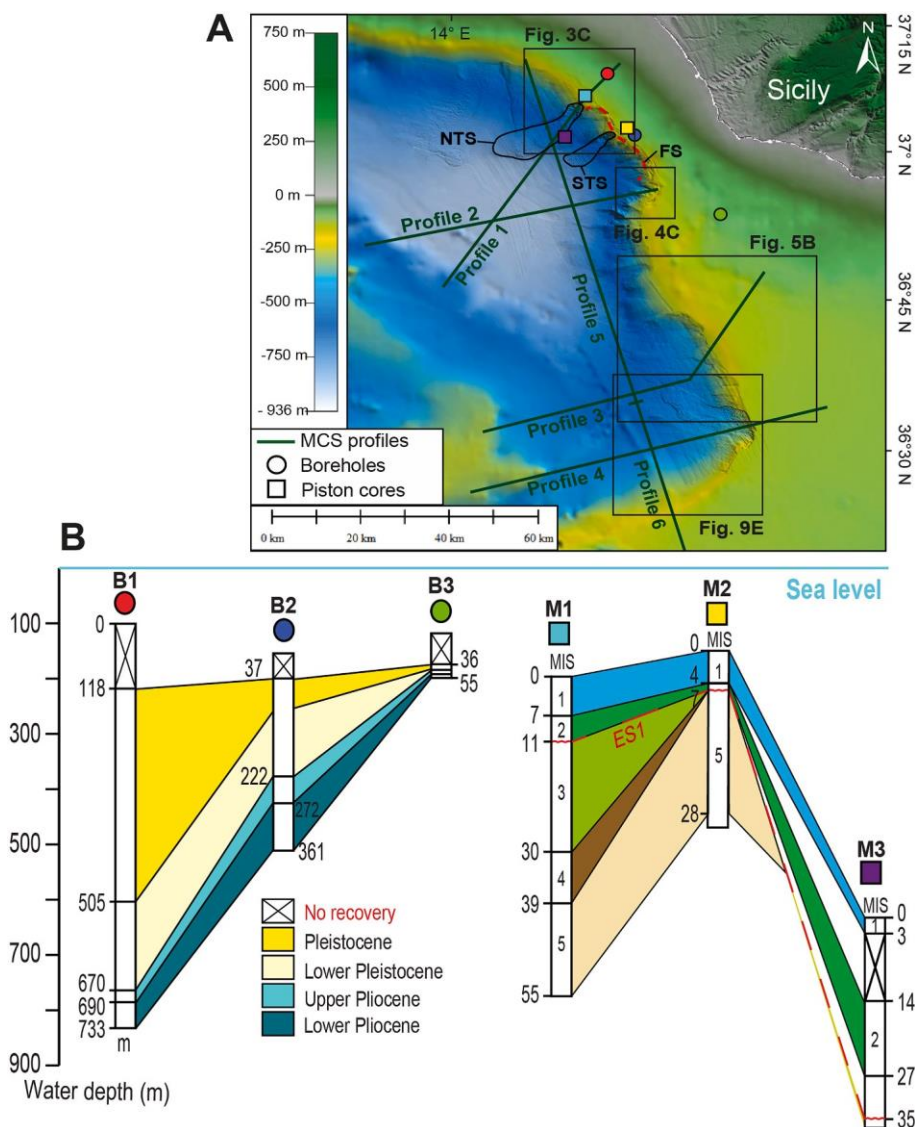


**Fig. 2.** A. The eastern Gela Basin bathymetric map showing the location of the MCS profiles (green lines), deep boreholes (circles) and piston cores (squares) used in this study. The deep boreholes cross section is on depositional strike, whether the piston core cross section is on depositional dip. NTS: Northern Twin Slide, STS: Southern Twin Slide, FS: Father Slide. B. Regional stratigraphic correlation between the boreholes B1–B3 and the piston cores M1–M3. See also Table 1. (For interpretation of the references to colour in this figure legend, the reader is referred to the Web version of this article.)

(Astraldi et al., 2001) increases in the GB (Lermusiaux and Robinson, 2001).

### 2.3. Stratigraphy and late Quaternary depositional sequences

A widespread shallow-water carbonate platform covered the Malta Plateau since the late Triassic and until the Oligocene. Since the Oligocene, clastic sediments started to spread over the Malta Plateau from the emerging Maghrebian fold-and-thrust belt. During the Messinian Salinity Crisis, when a regional desiccation event led to basin-wide accumulation of evaporitic and post-evaporitic deposits, a marked erosional unconformity formed across the margin (Base Pliocene in this study), overlain by 2.5 km of shallowing-upward Pliocene-Quaternary marine sediments (Colantoni et al., 1975).

Seismic stratigraphic analysis carried out in the western GB revealed several unconformity-bounded depositional sequences consisting of Pliocene and Pleistocene deposits up to 1.9 km thick in the deepest part of the basin (Di Stefano et al., 1993). On the shelf, well-developed prograding complexes correlating to turbidites in the basin characterize Pleistocene deposits (Di Stefano et al., 1993).

Two piston cores, 55 m and 27 m long, located at the shelf edge and on the slope of the northern GB (Fig. 2A), sampled almost entirely the sedimentary succession emplaced during the last 100 kyr glacio-eustatic cycle, spanning from Marine Isotope Stage 5 (MIS 5) to the Holocene (Kuhlmann et al., 2015 and Fig. 2B). Radiocarbon dates bracket the hiatus associated with the Erosional Surface (ES1) between the Last Glacial Maximum (LGM) and ~30 kyr cal BP (Kuhlmann et al., 2015). Seismic reflection profiles across the coring sites indicate that the last phase of clinothem aggradation occurred during MIS 5. To explain the enhanced sediment accumulation rates (SAR) of up to 200 cm kyr<sup>-1</sup> during highstand conditions, an intensification of LIW activity associated with the flooding of the Malta Plateau and highlighted by the presence of contourite deposits was invoked (Kuhlmann et al., 2015).

### 2.4. Contourite deposits in the Gela Basin

Within the Strait of Sicily, Marani et al. (1993) first described contourite deposits along the Adventure Bank (Fig. 1). Small, mounded drifts and irregular patch drifts as well as zones of scours were described within the deep rift basins (Reeder et al., 2002) and around Pantelleria Island (Martorelli et al., 2011, Fig. 1). Shallow contourite deposits (< 300 m w. d.) were discovered in the upper slope of the northern GB (Verdicchio and Trincardi, 2008a, b; Fig. 1) and along the northern coast of Malta (Micallef et al., 2013). Well-defined contour-parallel elongated moats (700 m wide and 50 m deep) possibly developed in response to the LIW flow along the shelf edge (Verdicchio and Trincardi, 2008a).

### 2.5. Mass-transport deposits in the Gela Basin

Several mass-transport deposits (MTDs) were highlighted by previous studies in the northern part of the basin. The Gela Slide, with a thickness of 700 m and an inferred volume of 1050 km<sup>3</sup>, was probably emplaced 600 ka (Di Stefano et al., 1993), likely involving the surface slope of the frontal area of the Gela Nappe (Trincardi and Argnani, 1990).

Slope instability after the early Pleistocene affected progradational sequences characterized by a progressive steepening (Minisini and Trincardi, 2009). A large MTD (18.9 km<sup>3</sup>), named Father Slide (FS in Fig. 2A), was emplaced ~87 ka and involved MIS 5e to MIS 5c sedimentary units. The Father Slide was followed by eight major slope failure events with a ~10 kyr return frequency (Kuhlmann et al., 2017). In particular, during the late Holocene, frequent failures affected post-glacial unconsolidated deposits with the emplacement of two larger MTDs: the Northern Twin Slide with a volume of 0.57 km<sup>3</sup> and the Southern Twin Slide with a volume of 0.36 km<sup>3</sup> (Minisini et al., 2007; Minisini and Trincardi, 2009, Fig. 2A). In the late Holocene, mudflows

have also been observed in bathymetric data affecting the downslope flank of contourite deposits along the northern slope of the basin (Verdicchio and Trincardi, 2008a, b; Fig. 1).

Preferential failure planes for the largest MTDs are provided by surfaces at the base of the lowstand progradational wedge or at the base of the post-glacial contourite deposits (Minisini and Trincardi, 2009). Occasionally, they include volcanic ash layers (Kuhlmann et al., 2017). Rapid deposition of Quaternary units and progressively increasing slope angles of prograding units explain the frequent recurrence of slope failures in the Gela Basin (Kuhlmann et al., 2017).

## 3. Material and methods

### 3.1. Boreholes and sediment cores

Three deep industry boreholes located on the shelf (Fig. 2A) were used for core-seismic correlation, together with the information from three published long piston cores (M1 and M2 from Kuhlmann et al., 2015; M3 from Kuhlmann et al., 2017) (Fig. 2B, Table 1). The log data of the boreholes (Plinio Sud 001, Pellicano Ovest 001 and Merluzzo Mare 001; B1–B3 in Fig. 2B) recovered along the northern shelf (accessible online at <http://www.videpi.com/videpi/progetto.asp>) reached the Mesozoic by drilling 4332 m, 4524 m and 2906 m, respectively. In this study, we used the stratigraphic information from the Base of Pliocene, which represents the marine sedimentation after the Messinian Salinity Crisis; for sub-epochs, we used the informal spatial subdivision i.e. Lower, Middle, Upper (Haile, 1987; Pearson et al., 2017). Borehole “Plinio Sud 001” (B1 in Fig. 2) allowed us to correlate three key seismic reflections corresponding to: Lower Pliocene, Upper Pliocene and Lower Pleistocene. The reported taxa *Globorotalia bononiensis*, *G. puncticulata*, *G. margaritae* (rare), and *Sphaeroidinellopsis Sphaeroidinellopsis* sp. *Globogerinoides obliquus*, *G. extremus*, *G. sacculifer* (frequent), *G. trilobus*, *Orbulina universa* was equated to the time interval spanning the Mediterranean Pliocene (MPI) 1 (5.33 Ma) – MPI 4a (3.57 Ma) biozones (Lower to Early Middle Pliocene). The taxa *G. crassaformis*, *G. aemiliana*, *G. extremus*, *G. obliquus* are planktonic key taxa present in this interval, indicating an age not older than MPI 4b biozone (3.57 Ma) and not younger than MPI 5b biozone (2.09 Ma) (Upper Pliocene to Lower Pleistocene after Gibbard et al., 2010), according to Lirer et al. (2019) and references therein. The taxa *G. inflata* (frequent) and *G. extremus* (rare) correspond to MPI 6 biozone (2.09–1.79 Ma) (Lower Pleistocene after Gibbard et al., 2010) according to Lirer et al. (2019) and references therein. The last interval between 505 and 470 m shows planktonic taxa (*G. pachyderma*, *G. truncatulinoides*, *G. inflata*) of Pleistocene age, from MPI 6b (2 Ma) to MPI e2e2 (present) biozone, according to the updated biochronology (Lirer et al., 2019).

### 3.2. Multi-channel seismic (MCS) reflection profiles

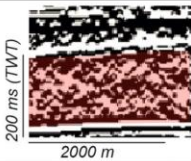
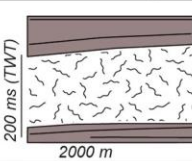
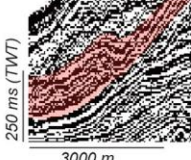
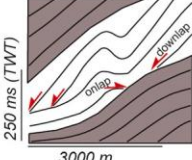
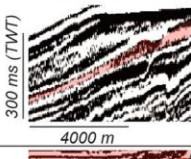
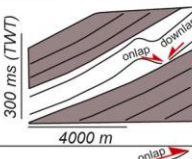
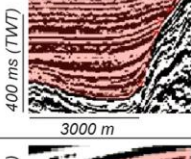
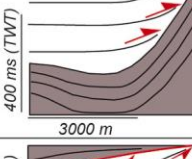
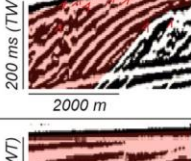
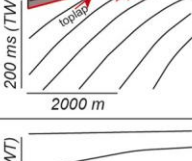
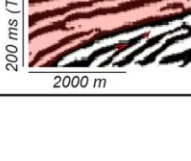
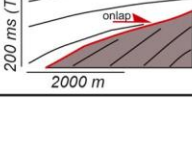
A set of unpublished MCS profiles (Fig. 2A) was made available by Eni S.p.A. and accessed through the virtual data room at their premises in San Donato Milanese (Italy). The interpretation software package used was Halliburton-Landmark Decision Space® G1 Edition. To interpret the stratigraphy of the margin, we identified reflection configurations and terminations, described the seismic facies (Table 2) and selected key unconformities in MCS profiles. On the shelf, these unconformities show an erosional character highlighted by top-lapping reflections and for this reason have been labelled Erosional Surfaces (ESs) in earlier works (ES1 and ES2; Kuhlmann et al., 2015; Minisini et al., 2007). Eight erosional surfaces (ES1–ES8) were thus identified on the topsets with ES8 coinciding with the MPT horizon traced and correlated at 800 ka in the northern GB by Di Stefano et al. (1993). The sequences above the erosional surfaces show onlapping terminations on the upper slope and pass basinward to correlative conformities (Fig. 6A).

The term clinoform denotes surfaces which gently prograde seawards (Rich, 1951) characterized by three geometric elements (topset,

**Table 1**  
Boreholes and sediment piston cores used in this study.

Core/ Borehole	Type	Total drilling depth (m)	Map key	Coordinates		Year	Operator	Water depth (m)	Length used (m)	Stratigraphy	comments	Reference
				Latitude	Longitude							
Plinio Sud 001	Well	4332	B1	36° 53.607' N	14° 16.232' E	1981	AGIP	100	733	Plio- Quaternary	missing Upper Quaternary	website Videpi
Pellicano Ovest 001	Well	4524	B2	36° 47.46' N	14° 19.042' E	1973	AGIP	145	370	Plio- Quaternary	missing Upper Quaternary	website Videpi
Merluzzo Mare 001	Well	2906	B3	36° 39.387' N	14° 27.83' E	1982	ELF	94	79	Plio- Quaternary	missing Upper Quaternary	website Videpi
GeoB14403	Piston core	55	M1	36° 51.410' N	14° 13.910' E	2010	MARUM	182	55	MIS 1 - MIS 2 - MIS 3 - MIS 4 - MIS 5		<a href="#">Kuhlmann et al. (2015)</a>
GeoB14414	Piston core	27	M2	36° 48.130' N	14° 18.170' E	2010	MARUM	146	27	MIS 1 - MIS 2 - MIS 5		
GeoB14401	Piston core	36	M3	36° 47.20' N	14° 11.90' E	2010	MARUM	613	36	MIS 1 - MIS 2	no recovery 3–15 m	<a href="#">Kuhlmann et al. (2017)</a>

**Table 2**  
Seismic facies F1 to F5 observed in MCS profiles, complemented with illustrative images, sketches, facies descriptions and inferred sedimentary processes.

Name	Image	Line drawing	Description	Sediment processes	Interpretation
F1			High/Low Amplitude Discontinuous and chaotic seismic (HADCh/LADCh) reflections	Rapid sediment accumulation, deformed internal structure, brittle to plastic deformation/laminar flow	Mass Transport deposits
F2 (a)			High Amplitude Continuous and Mounded (HACM) reflections	Reworking of sediments by along-slope bottom currents	Mounded Contourite deposits
F2 (b)			High Amplitude Continuous and Elongated (HACE) reflections		Plastered Contourite deposits
F3			High-Amplitude Continuous and Parallel (HACP) reflections with onlap terminations	Rapid sediment accumulation, turbulent flow	Turbidite deposits
F4			HACP and oblique reflections with toplap terminations	Sediment eroded due to relative sealevel fall	Progradation-degradation
F5			HACP reflection on top of a progradation-degradation facies	Sediment accumulation on the shelf/upper-slope related to high stand of sealevel	Progradation-aggradation

foreset and bottomset), separated by morphological breaks in the slope (points of maximum curvature) called rollover points (Pirmez et al., 1998). Clinotherm characterization was performed following the nomenclature and parameters proposed in Pellegrini et al. (2020) and was integrated with shelf-edge trajectory analysis that was originally proposed by Helland-Hansen and Martinsen (1996).

Isobath maps of two key reflections (Base Pliocene and ES5; Fig. 9A and B) were obtained from contour maps of the traveltimes to the seismic reflections, depth-converted using an inferred seismic velocity of  $1500 \text{ m s}^{-1}$ , and interpolated using algorithms available in the package Halliburton-Landmark Decision Space® G1 Edition. Isopach maps display lines of equal thickness in the stratigraphic units measured perpendicular to the layer boundaries Base Pliocene – ES5 (Fig. 9C), ES5 – seabed reflection (Fig. 9D) and were automatically calculated from the

depth-converted contour maps. Whereas, the depocenter thickness map between Base Pliocene and seabed reflection was obtained with ESRI ArcGIS 10.5.1 by importing the ASCII points of the respective contour maps, that were interpolated into surface rasters using the kriging algorithm and processed using a cut/fill calculation (Fig. 9E).

### 3.3. Sub-bottom seismic reflection (SBS) profiles

SBS profiles were collected with a Teledyne Benthos CHIRP-III system, composed of a 16 hull-mounted transducer array, using a 2–20 kHz sweep-modulated bandwidth and 4 kW power per-channel, which allows a vertical resolution of about 50 cm and shallow penetration (< 100 m). Profiles were acquired during several surveys on board R/V Urania between 2005 and 2009. An additional SBS profile (RSM line in

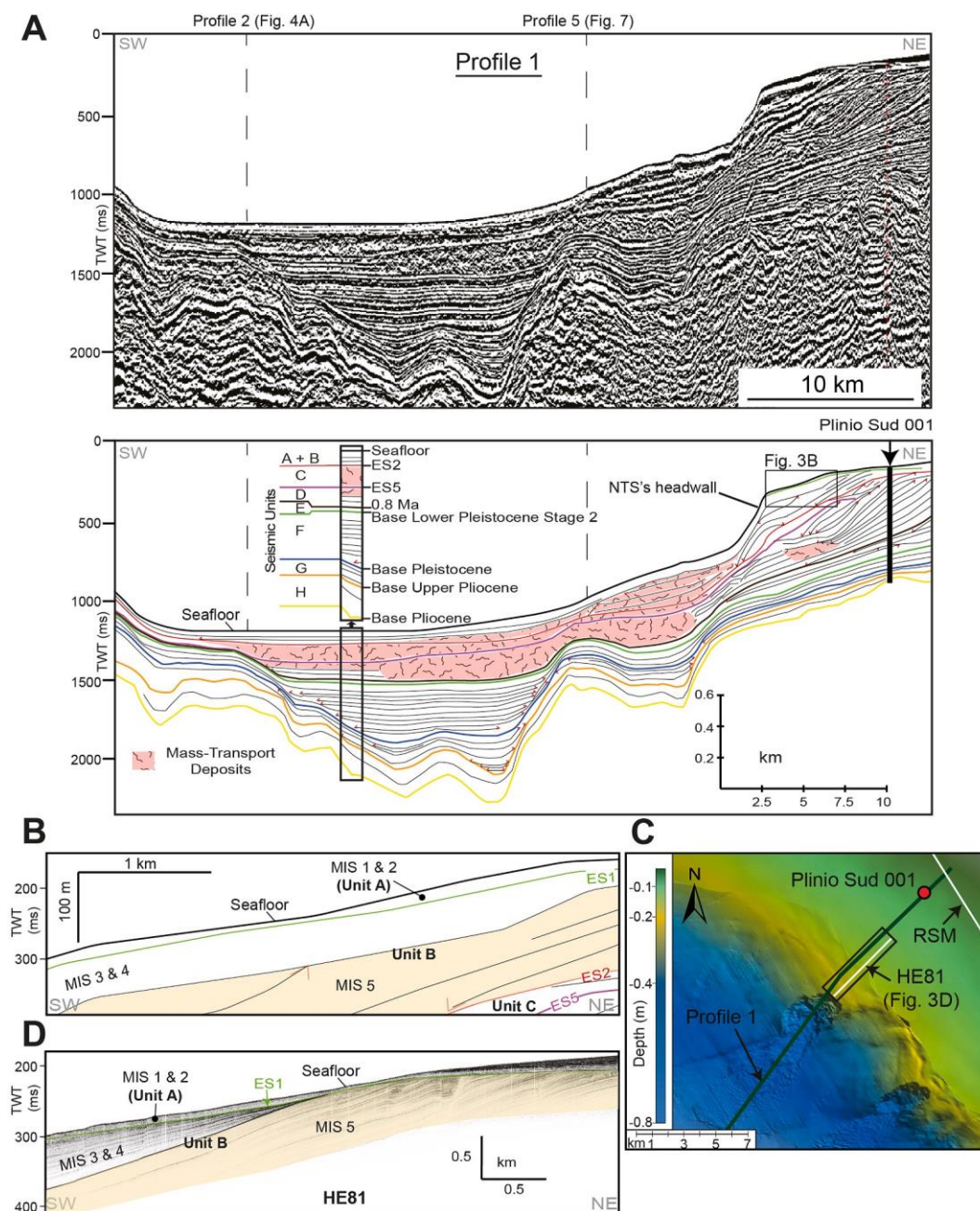


**Fig. 3.** A. Original seismic section and line drawing of MCS profile 1 crossing the borehole “Plinio Sud 001” (location in Fig. 2A). B. Enlargement of the prograding shelf-edge of MCS profile 1. C. Bathymetric map showing the location of B (black rectangle) and of SBS profile (white line) shown in D. D. Interpretation of SBS profile “HE81” showing the geometry of the seismic units A and B (Table 3) at the shelf edge. This profile was used to correlate the unconformity ES1 on MCS profile 1.

Fig. 7B), acquired with a similar system, was obtained from RINA Consulting S.p.A. All SBS profiles were post-processed with Geo Marine Survey Systems, Version 2.6. SBS profiles allowed to map ES1 (~30 kyr cal. BP; Kuhlmann et al., 2015) and ES2 (predating MIS 5e; Kuhlmann et al., 2015) that were correlated with MCS profiles (Figs. 3A, 4A and 5A). Isopach maps were obtained for stratigraphic units bounded by ES2 and ES1 (Fig. 9F), ES1 and the seabed reflection (Fig. 9G) with ESRI ArcGIS 10.5.1 and the same methodology described above. In addition, SBS profiles helped to characterize different surficial seismic facies, including contourite deposits and MTDs (Fig. 10).

3.4. Bathymetric data

The swath bathymetry data used in this work derive from several

surveys undertaken on board R/V Urania with different multibeam systems, including: 30 kHz Kongsberg-Simrad EM300, 50 kHz Reson Seabat® 8160, 70–100 kHz Kongsberg EM710, the latter used in 2007 during the MAKROS-CORSARO survey. The swath bathymetry data was merged with the 1/8 x 1/8 arc minutes resolution EMODnet compilation, where areas are not covered by actual soundings (EMODnet Bathymetry Consortium, 2016). From a 20-m-resolution swath bathymetry DTM (Fig. 11A), we obtained a slope gradient map (Fig. 11B), a slope aspect map (Fig. 11C) and a curvature map (Fig. 11D) using the tools provided in ESRI ArcGIS 10.5.1.

4. Results

The eastern side of the Gela Basin can be subdivided into three

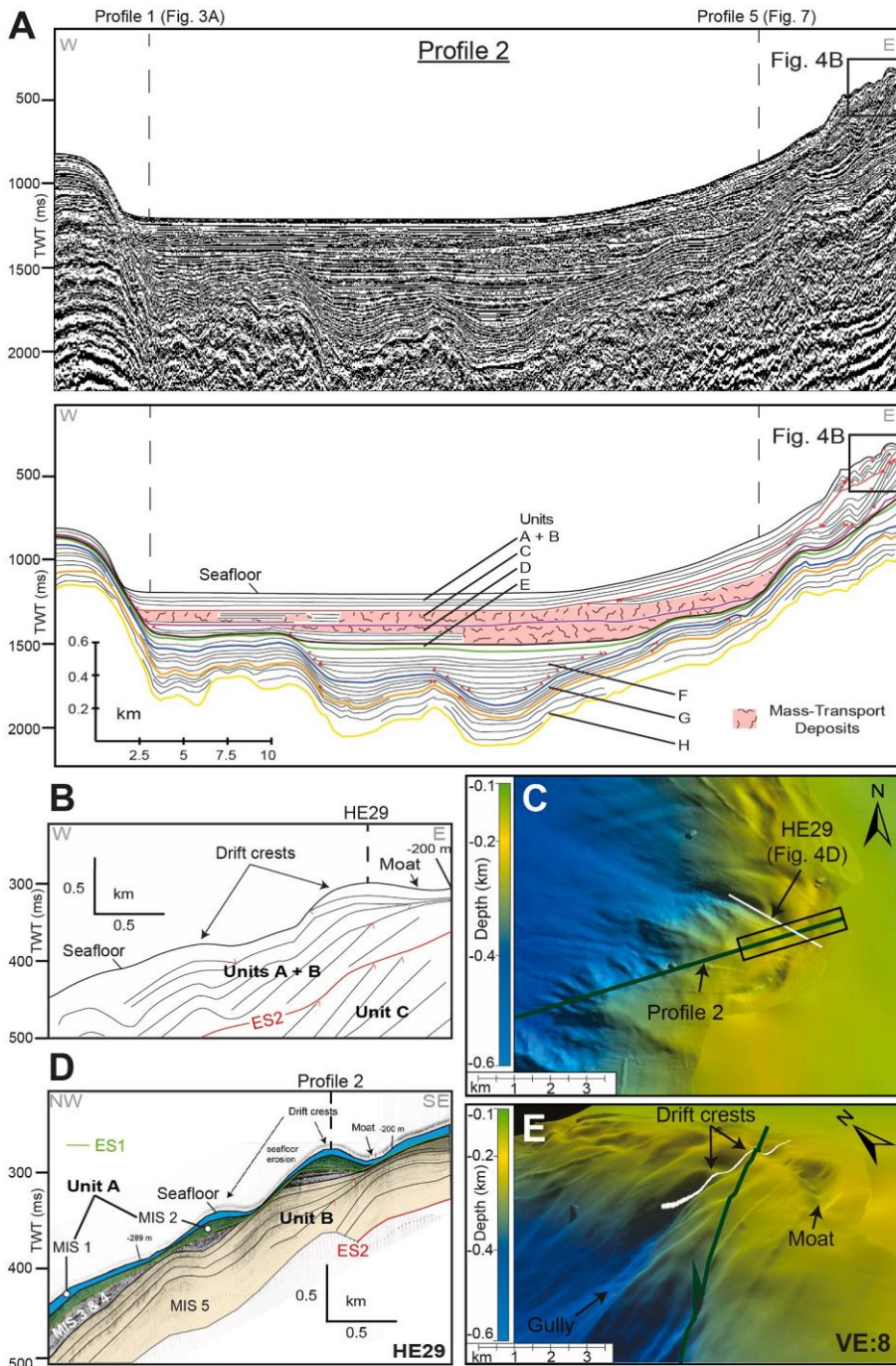
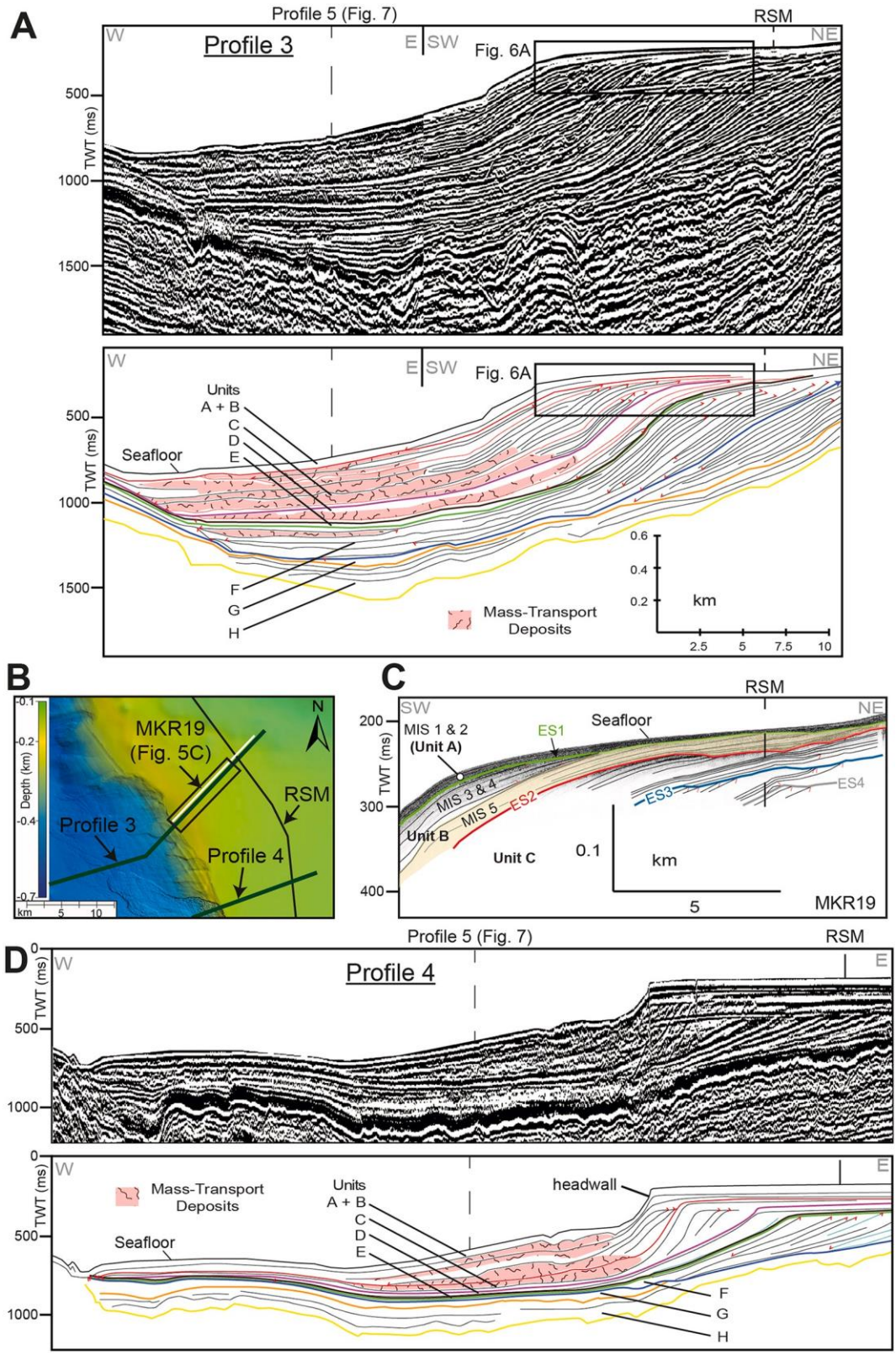
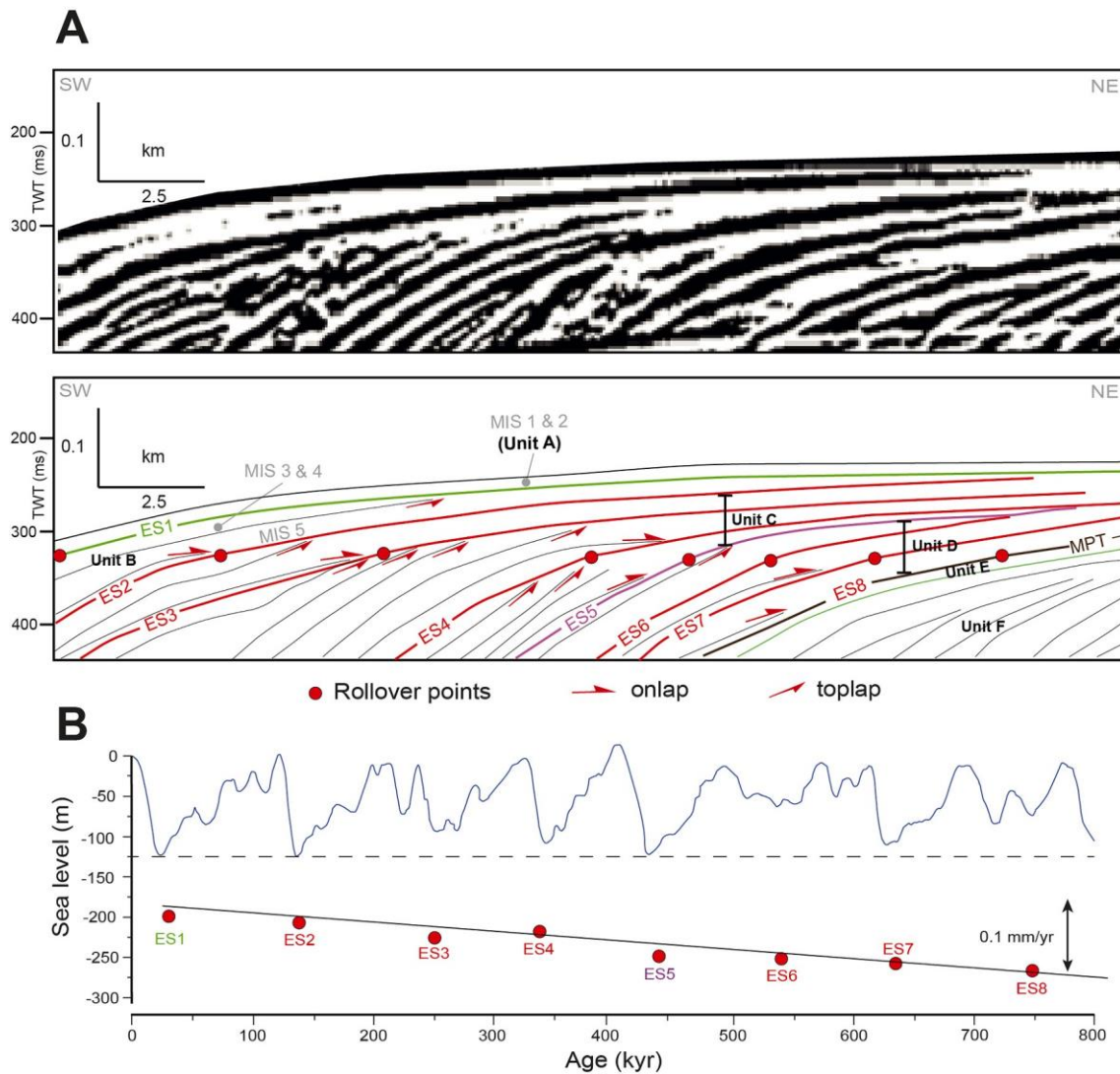


Fig. 4. A. Original seismic section and line drawing of MCS profile 2 highlighting the initiation of contourite deposits during the Upper Pliocene and their evolution through time. B. Enlargement of the prograding shelf-edge of MCS profile 2. C. Bathymetric map showing the location of B (black rectangle) and of SBS profile (white line) shown in D. D. Interpretation of SBS “HE29” highlighting the timing of contourite growth in Sector 1. E. 3D bathymetric view of the area in C. See Fig. 3A and Table 3 for the description and interpretation of seismic units.



**Fig. 5.** A. Original seismic section and line drawing of MCS profile 3 showing the largest prograding set of the eastern Gela Basin. B. Bathymetric map showing the location of the enlarged area in Fig. 6A (black rectangle) and of SBS profile (white line) shown in C. C. Interpretation of SBS “MKR19” showing seismic units A, B and C (Table 3). D. Original seismic section and line drawing of MCS profile 4 showing oblique clinofolds during the Pliocene, top truncated strata and a net change in shelf aggradation after the MPT; same vertical and horizontal scales as in Fig. 5A. See Fig. 3A and Table 3 for the description and interpretation of the seismic units.



**Fig. 6.** A. Enlargement of the shelf-edge clinothems of MCS profile 3 of Fig. 5A bounded by the last eight erosional unconformities and highlighted by toplaps and onlaps (red arrows), showing a descending shelf-edge trajectory. B. Sea-level curve adapted from Spratt and Lisiecki (2006) with the corresponding rollover point for each erosional surface. Given the depth of rollover points (shoreline position) on the seismic profile, we estimated an average tectonic component of 0.1 mm/yr after the MPT, except for the last sea-level cycle when the tectonic vertical component is estimated at 2.5 mm/yr. (For interpretation of the references to colour in this figure legend, the reader is referred to the Web version of this article.)

sectors along a NW–SE direction, based on the Pliocene morphology (Fig. 9A). The map of the horizon corresponding to the Base of the Pliocene in fact shows two sub-basins up to 2.7 km deep located in Sector 1 (Fig. 9A), a headland at the shelf edge in Sector 2 and a bowl-shaped sub-basin in Sector 3 confined to the east by the Malta Plateau. The Pliocene–Quaternary sedimentary succession reached up to 2.4 km in thickness in Sector 1 and up to 1.2 km in Sector 3 (Fig. 9E) and can be subdivided in the units described in the following paragraphs.

#### 4.1. Seismostratigraphic units

A total of eight seismostratigraphic units from Lower Pliocene (Unit H) to MIS 1 (Unit A) were recognized between each key reflection in MCS and SBS profiles (Figs. 3–8 and 10), and were characterized by distinctive seismic facies (Table 2).

##### 4.1.1. Unit H (Base Pliocene – Upper Pliocene)

The H unit is characterized by a sheet drape external geometry at the base of the Pliocene–Quaternary succession (Fig. 7). From foresets to bottomsets, the unit increases in thickness reaching a maximum

thickness of 225 m in the bottomsets (Fig. 5A). In the along-strike profile, a decreasing in thickness is observed towards the south (Fig. 7). Overall, unit H shows a dominance of seismic facies F3 (Table 2) characterized by onlapping terminations in the two sub-basins of Sector 1 (Figs. 7A and 9A). Seismic facies F3 in the unit include both high and low amplitude reflections of interbedded layers (Table 2). The onlapping deposits of facies F3 reach a volume of almost 300 km<sup>3</sup> in Sector 1 for unit H (Figs. 3A and 4A and Table 4).

##### 4.1.2. Unit G (Upper Pliocene – base Pleistocene)

The G unit shows an overall sheet drape external geometry (Fig. 4A) and is characterized on the topsets by a sigmoid configuration (Fig. 5A). The unit has a maximum thickness of 250 m in the bottomsets (Fig. 3A) and is up to 220 m deep in the topsets (Fig. 5A). The G unit is mainly characterized by seismic facies F3 (Fig. 5A, Table 2).

##### 4.1.3. Unit F (Base Pleistocene – Lower Pleistocene)

The F unit shows an oblique tangential progradational configuration with a descending shelf-edge trajectory (Fig. 5A). The unit has a variation in thickness along the dip-oriented profile 1 from 100 m in the

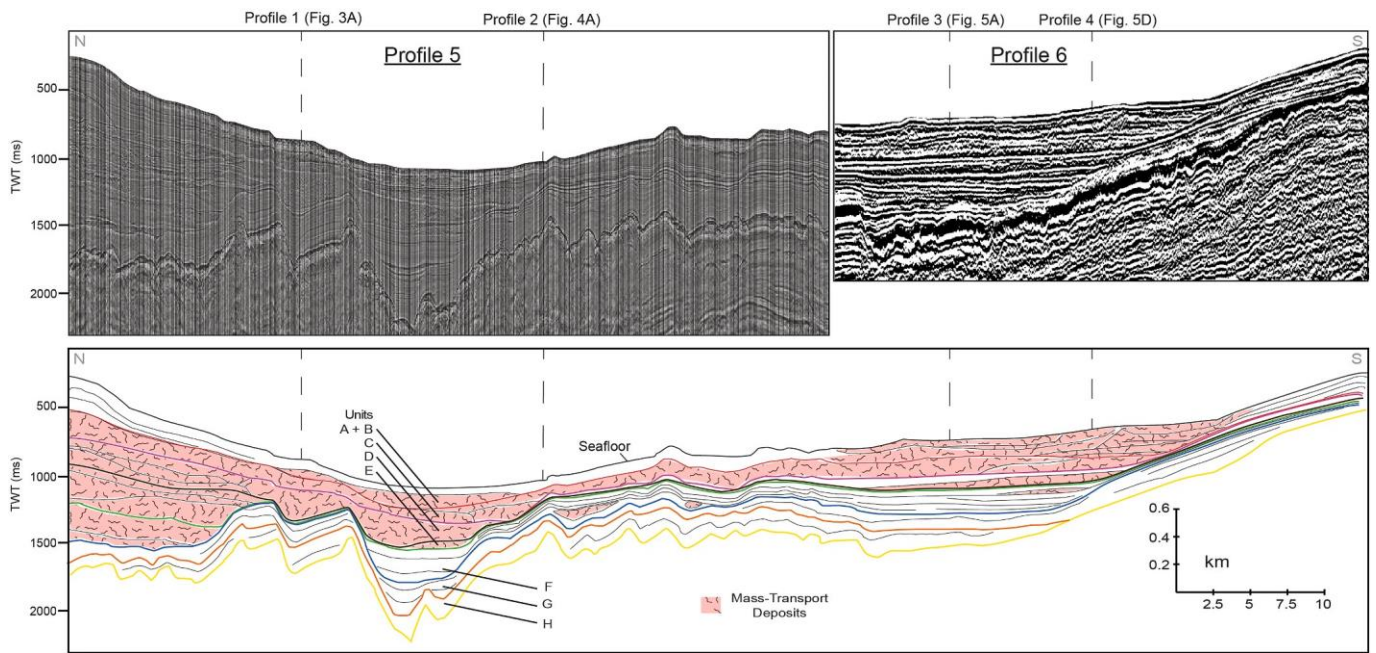


**Fig. 7. A.** Original seismic section and line drawing of MCS profiles 5 and 6 showing the along-strike variability (NW-SE direction) of the Pliocene-Pleistocene succession. See Fig. 2A for location.

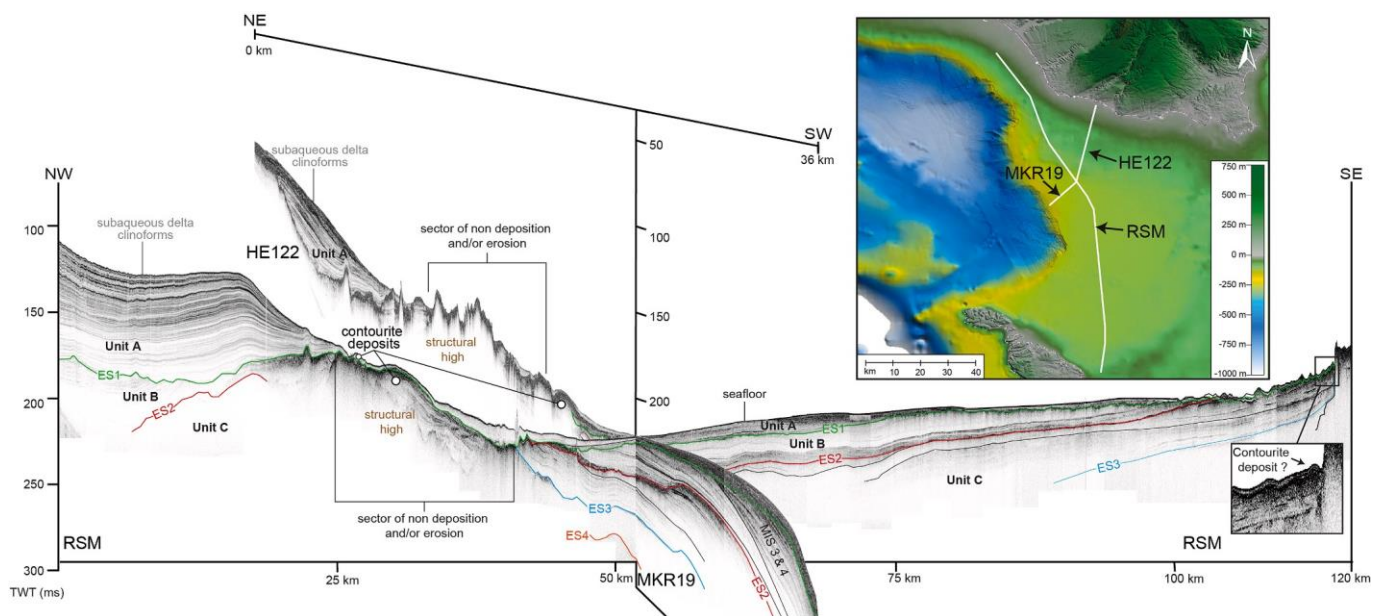


**Fig. 8.** SBS profile “RSM” which shows the younger clinothem (units A and B) crossed by SBS profiles “HE122” and “MKR19” (NE-SW direction) to highlight the changes in clinothem thickness along the shelf and the overall along-strike variability of the margin.

topsets to 350 m in the bottomsets (Figs. 3A and 4A). The topsets display also a lateral variability along the strike of the basin reaching up to 400 m thick towards the south (Fig. 5A). The unit is characterized by seismic facies F4 in the upper foresets (Fig. 5A) and by seismic facies F3 in the bottomsets (Fig. 3A, Table 2). Overall, onlapping deposits of seismic facies F3 have volumes of 4 km<sup>3</sup> in unit F (Table 4). In Sector 1, the unit is characterized by seismic facies F1 in the bottomsets, which corresponds to MTDs (Table 2) as thick as 200 m (Fig. 7).

#### 4.1.4. Unit E (Lower Pleistocene – MPT ~ 800 ka)

The E unit shows an overall sheet drape external geometry (e.g. Fig. 5D) and develops only in the north of the basin, where it reaches a

maximum thickness of 260 m in the foresets (Fig. 7). The unit is characterized by seismic facies F3 in the topsets-foresets (Fig. 3A) and seismic facies F1 in the bottomsets (Fig. 7, Table 2). The unit marks a change in the overall stacking pattern of the margin, with the appraisal in the foresets of seismic facies F2a, characterized by mounded reflections (Fig. 4A, Table 2).

#### 4.1.5. Unit D (MPT ~ 800 ka – ES5)

The D unit is represented by a complex sigmoid-oblique prograding reflection configuration with an ascending shelf-edge trajectory and reaches a maximum thickness of 350 m in the foresets (Fig. 3A). On the along-strike profile, the D unit shows a lateral variability in thickness

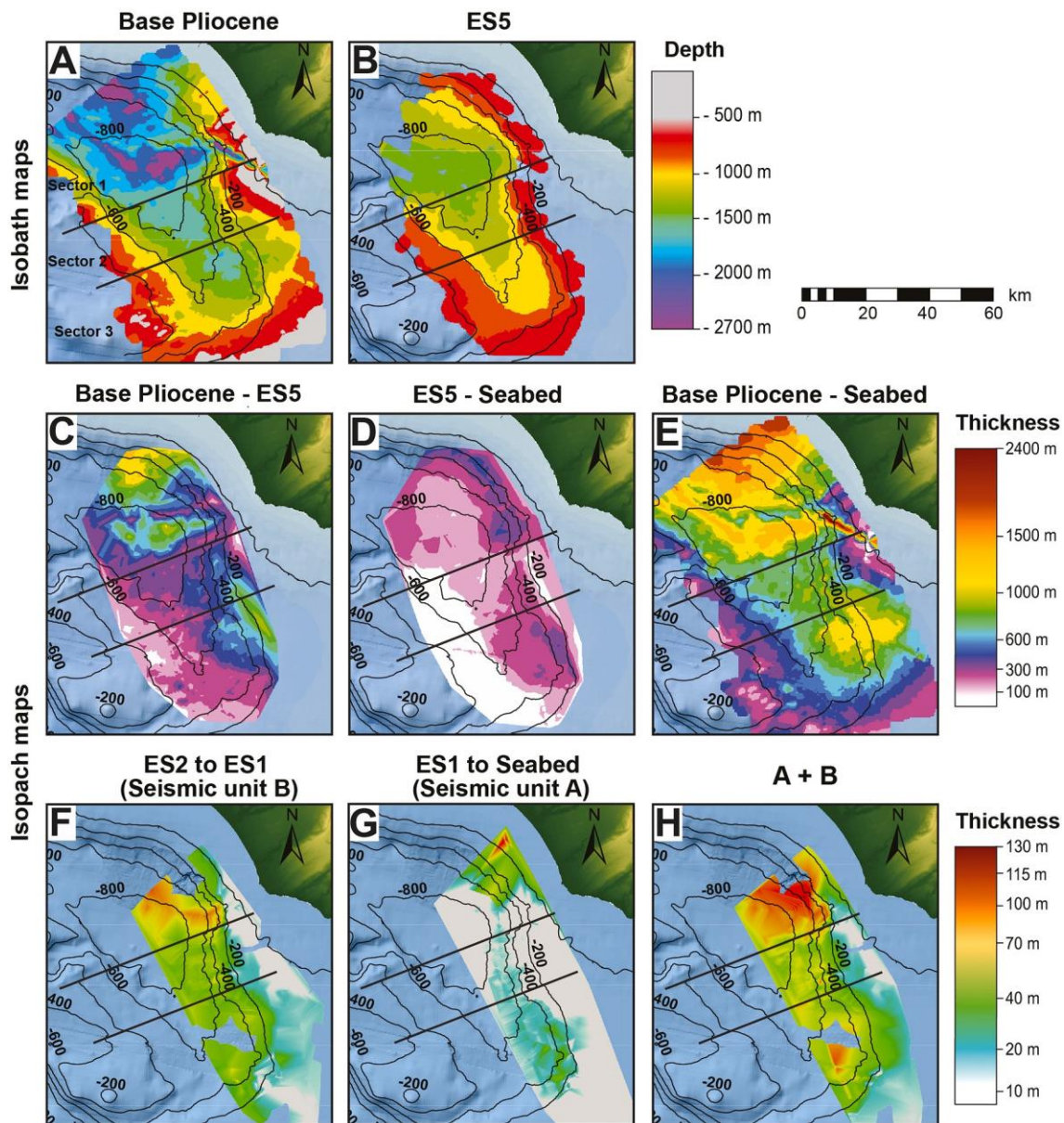


**Fig. 9.** Isobath maps (A and B) of key stratigraphic horizons and isopach maps (C, D, E, F, G) of significant stratigraphic units in the study area. C shows evidence of three sub-basins in Sector 1. D shows that sediment deposition was limited to the shelf edge during the corresponding time interval. E represents the overall Plio-Quaternary deposition showing maximum thickness in Sector 1. F and G are the sedimentation thickness between ES2 and ES1 and between ES1 and the seabed. H represents the sediment accumulation since ES2 until today (seismostratigraphic units A + B, Table 3) where it concentrated mainly on the slope of sectors 1 and 3.

with higher values in the north (Fig. 7). The unit is characterized by seismic facies F3 in the topsets (Fig. 5A), by seismic facies F2a in the foresets (Fig. 4A) and by seismic facies F3 and F1 in the bottomsets (Table 2, Figs. 3A, 4A and 5A, 5D and 7).

The isobath map of the ES5 reflection shows that the depocenters in the bottomsets of Sector 1 were partially filled during the Upper Pliocene and Lower Pleistocene (Fig. 9B), and depositional thickness reached up to 1.5 km in the two depocenters in the north and up to 1 km in the depocenter in the southeast (Fig. 9C). The shelf edge migrated < 5 km in Sector 1, < 1 km in Sector 2 and more than 20 km in Sector 3, before reaching the current position (Fig. 9B).

#### 4.1.6. Unit C (ES5 – ES2)

The C unit presents a stack of prograding clinoform sets that from north to south can be described as oblique (Fig. 4A), complex sigmoid-oblique with alternation of descending and ascending shelf-edge

trajectories (Fig. 5A), and oblique to complex sigmoid-oblique reflection configurations (Fig. 5D). The descending trajectories are highlighted by top truncated reflections at the outer shelf, whereas ascending trajectories are associated with minimum aggradation of the topsets (in the order of 10 ms; Figs. 5C and 8). The unit shows a maximum thickness of up to 385 m in the foresets (Fig. 5D, Table 3). In the basin, the unit is characterized both by seismic facies F1 (Figs. 3A, 4A and 5A, 5D and 7) and F3 (Fig. 5A and D, Table 2). The thickness between ES5 and the seabed is up to 450 m in Sector 1 and 400 m in Sector 3 (Fig. 9D).

#### 4.1.7. Unit B (ES2 – ES1 ~ 30 ka)

The B unit shows a complex sigmoid-oblique reflection configuration (Fig. 3A) and an increase in thickness in the lower foresets, where it reaches more than 200 m (Figs. 3A and 7B). The B unit is characterized by seismic facies F4 in the topsets (Fig. 3D) and seismic facies F3 in the bottomsets passing laterally to seismic facies F1 at the base of the slope

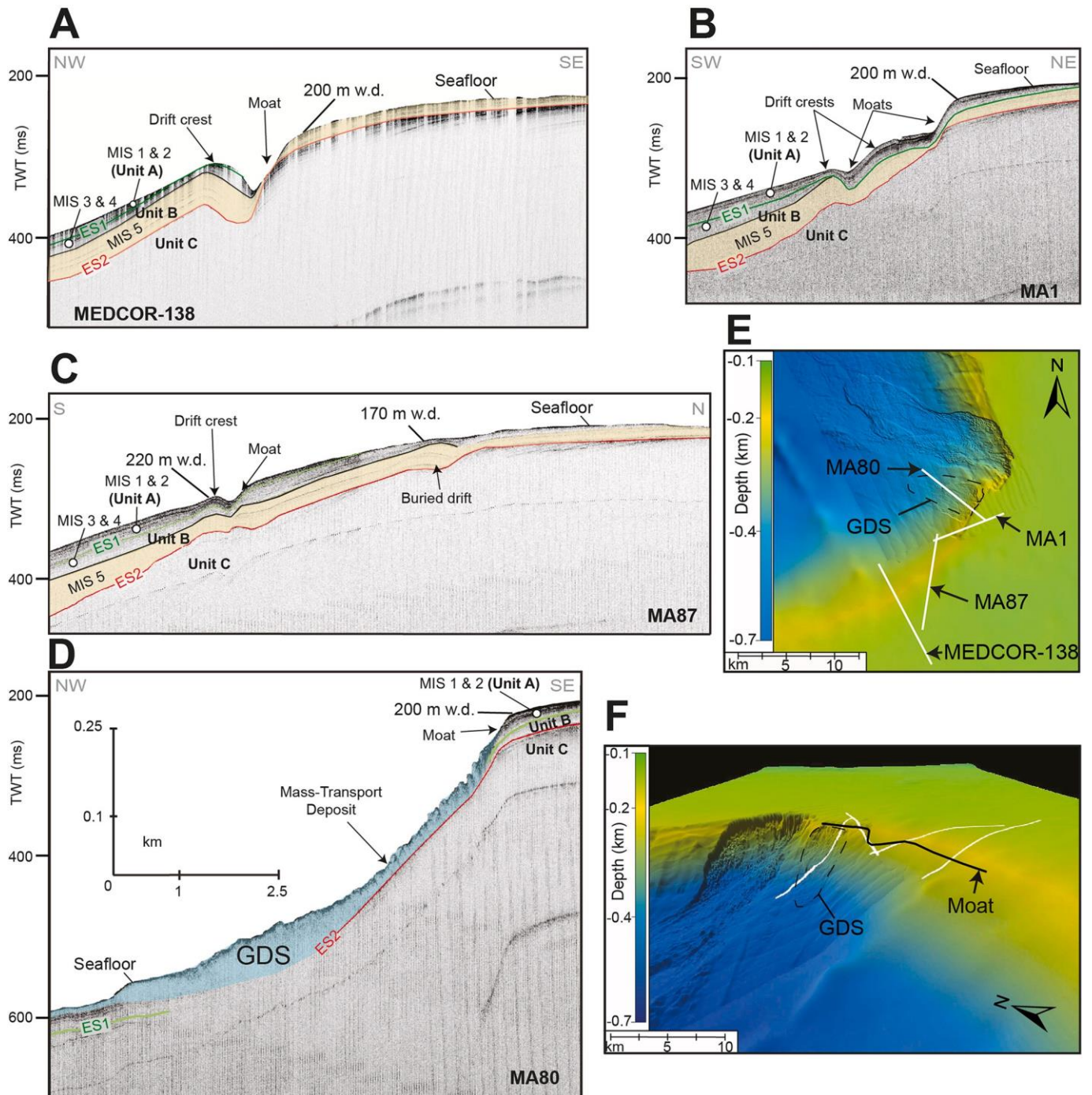


**Fig. 10.** A. SBS profile “MEDCOR-138” showing the internal structures of the most prominent contourite deposit in the upper slope of Sector 3. Seismic units A and B show that the deposition of the drift crests occurred mainly during MIS 5 (see also Table 3). B. SBS profile “MA1” showing the continuity of the contourite deposits along the shelf edge and upper slope. C. SBS “MA1” showing the presence of a buried drift developed on top of ES2. D. SBS “MA80” shows a moat and the Gela Drift Slide (GDS) gliding on top of the erosional surface ES2. E. Bathymetric map with location of the seismic profiles shown in A, B, C and D. F. 3D bathymetric view showing the GDS deposit located downslope the failed drift crests. Horizontal and vertical scales of SBS profiles are given in Fig. 10D.

(Figs. 3A, 5A and 5D, Table 2).

From ES2 to ES1, sedimentation is limited in the foresets and bottomsets with a deposition thickness up to 100 m (Fig. 9G). MIS 5 deposits are 150 m thick in the topsets, however SBS profiles penetrated the deposit until the rollover point between the foresets and topsets and ES2 is not visible.

4.1.8. Unit A (ES1 ~ 30 ka – present)

The A unit shows an overall sheet drape external geometry in the

topsets (Figs. 3D and 5C) with a sigmoidal configuration (Fig. 8) which, along with the continuous coastal seismic reflections, suggest the presence of a mud belt up to 50 m thick (Fig. 8). On the dip-oriented profile, the A unit increases in thickness towards the lower foresets reaching up to 40 m in the south (Fig. 10A). Here, the A unit is characterized by the occurrence of moats oriented along the contours (Fig. 10). The unit is characterized by seismic facies F3 in the topsets (Fig. 8) and the lower foresets (Fig. 10D) and by seismic facies F2b in the upper foresets (Figs. 4 and 10). This unit exhibits two depocenters, a 50 m thick depocenter

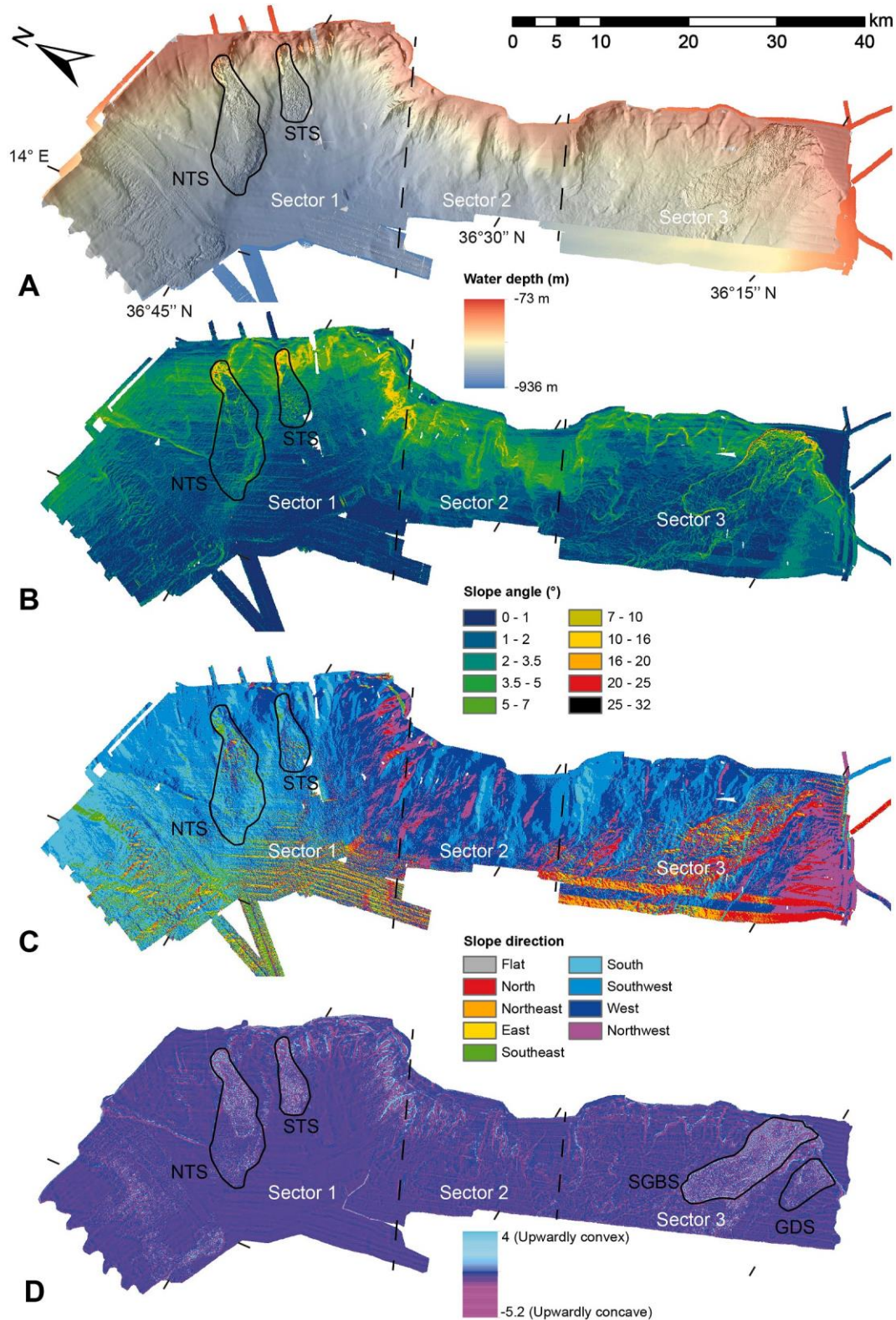


**Fig. 11.** A. Shaded-relief map of the 25-m-resolution DTM of the eastern margin of the Gela Basin subdivided in three sectors and highlighting the mass-transport deposits (MTDs) described in previous studies (Northern Twin Slide–NTS and Southern Twin Slide–STS). B. Slope gradient map showing an average gradient of 2.1° and up to 32° at the shelf edge of sectors 1 and 3. C. Aspect map showing a southern direction in Sector 1 and an N–NW direction in sectors 2 and 3. D. Curvature map revealing hummocky surfaces corresponding to the MTDs discovered by this study (Southern Gela Basin Slide–SGBS and Gela Drift Slide–GDS).

**Table 3**

Details of seismic units A to H identified in the seismic profiles and correlated with borehole and sediment core data. For the descriptions of seismic facies refer to Table 2.

Seismic units	Lower boundary	Upper boundary	Age			Thickness range (m)	Seismic facies	Description	Interpretation
A	ES1	Seafloor	MIS 1	MIS 2		0–119	HACP and HADCh	Sheet drape	Low sedimentation since last sea-level lowstand
B	ES2	ES1	MIS 3	MIS 4	MIS 5	50–250	HACP and HADCh	Complex sigmoid-oblique configuration with toplap terminations and chaotic reflections in the basin	Changes in relative sea level and presence of MTDs
C	ES5	ES2	Middle Pleistocene - Stage 2			0–385	HACP and HADCh	Complex sigmoid-oblique configuration with alternation of descending and ascending trajectories along with chaotic reflections in the basin	Changes in relative sea level and presence of MTDs
D	MPT	ES5	Middle Pleistocene - Stage 1			10–350	HACP, HACM and HADCh	Complex sigmoid-oblique configuration with ascending trajectories and onlap terminations along with chaotic reflections in the basin	Growth of contourite deposits and presence of MTDs
E	Lower Pleistocene	MPT	Lower Pleistocene - Stage 2			0–260	HACP, LADCh and HACM	Sheet drape and mounded reflections along with chaotic reflections in the basin	Initiation of contourite deposits and presence of MTDs
F	Base Pleistocene	Lower Pleistocene	Lower Pleistocene - Stage 1			0–400	HACP and LADCh	Complex sigmoidal to oblique tangential configuration with descending trajectories along with chaotic reflections in the basin	Relative sea-level fall and presence of MTDs
G	Upper Pliocene	Base Pleistocene	Upper Pliocene			0–250	HACP	Sheet drape and sigmoid configuration	End of the Zanclean flood and initiation of the progradation
H	Base Pliocene	Upper Pliocene	Lower Pliocene			0–225	HACP and HAD	Sheet drape and onlap terminations	Start of sedimentation after the Zanclean flood

located in the topsets in Sector 1, and a 40 m thick depocenter in the foresets in Sector 3 (Fig. 9G). Inside unit A, sediments deposited after ES2 mostly occur along the slope of sectors 1 and 3 (Fig. 9H).

4.2. Seafloor morphology and seismic facies

The high-resolution bathymetry shows a shelf edge at 200 m w.d. and a basin as deep as 936 m w.d. in Sector 1 (Fig. 11A). The average slope gradient is 2.1° with maximum local values of 32° at the headwall

scars of the Twin Slides (NTS and STS in Fig. 11A) and in the south of Sector 3 (Fig. 11B). The slope angle is 1–10° in sectors 2 and 3 (Fig. 11B), and both sectors display changes in the slope direction from SSW to NNW (Fig. 11C), forming a curvature of the margin and creating large amphitheatre-like morphologies, characterized by upwardly convex and concave structures (Fig. 11D).

The short-distance changes in slope direction and gradient define the contourite moats located in 200 m w.d. in Sector 1 (Fig. 4C and E) and in Sector 3 (Fig. 10F). The moats are 3.5 long and 40 m deep (Fig. 4D) in

**Table 4**

MTDs and turbidite deposits observed in the seismic profiles available in the study area, accompanied by their inferred recurrence times, dimensions, source directions, location along the margin sectors and likely controlling factors.

Time	Seismic Unit	Type	Recurrence (Myr)	Area (km <sup>2</sup> )	Thickness (km)	Volume (km <sup>3</sup> )	Source Sector	Name	Controlling factors	
<b>Upper Pleistocene-Holocene</b>	<b>A b B</b>	MTD	0.1	15.5	0.037	0.5735	NE	1	NTS	Eustasy
		MTD	0.1	14.4	0.025	0.36	NE	1	STS	Eustasy
		MTD	0.1	8	0.05	0.4	SE	3	GDS	Oceanographic
		MTD	0.1	350	0.05	17.5	NE	1	FS	Oceanographic
		MTD	0.1	100	0.05	5	NE	1		Oceanographic
		MTD	0.1	120	0.05	6	NE	1		Oceanographic
		MTD	0.1	580	0.04	20	SE	3		Eustasy
<b>Middle Pleistocene-Stage 2</b>	<b>C</b>	MTD	0.35	800	0.12	96	N	1		Tectonic
		MTD	0.1	48	0.05	2.4	SE	3		Eustasy
		MTD	0.1	26	0.05	1.3	SE	3		Eustasy
		MTD	0.1	47	0.05	2.35	SE	3		Eustasy
		MTD	0.1	25	0.05	1.25	SE	3		Eustasy
		MTD	0.1	760	0.12	91	SE	2/3		Eustasy
<b>Middle Pleistocene-Stage 1</b>	<b>D</b>	MTD	0.3	375	0.12	45	NE	1		Oceanographic
		MTD	0.1	286	0.04	11.44	SE	3		Eustasy
		MTD	0.1	550	0.066	30	N	1		Tectonic
		MTD	0.1	550	0.066	35	N	1		Tectonic
		MTD	0.1	550	0.066	40	N	1		Tectonic
<b>Lower Pleistocene-Stage 2</b>	<b>E</b>	MTD	0.6	1032	0.1	100	N	1		Tectonic
		MTD	0.6	1032	0.1	120	N	1		Tectonic
		MTD	0.6	1032	0.1	80	N	1		Tectonic
		MTD	1.8	119	0.04	4.76	E	1		Oceanographic
<b>Lower Pleistocene-Stage 1</b>	<b>F</b>	MTD	0.5	1032	0.1	110	N	1		Tectonic
		MTD	0.5	1032	0.1	90	N	1		Tectonic
		Turbidite	1	411	0.34	139.74	E	1		
<b>Upper Pliocene</b>	<b>G</b>	Turbidite	1.7	1740	0.17	295.8	NE	1		

Sector 1 and 9 km long and 70 m deep (Fig. 10A) in Sector 3. Contourite deposits display mounded reflections in SBS profiles that highlight the internal structures of the drift crests in Sector 1 (Fig. 4B and D) and Sector 3 (Fig. 10). Drift crests that developed on top of ES2 are mainly composed of sediments deposited during MIS 5 with a 60 m thick accumulation in Sector 3 (Fig. 10A).

In Sector 1 the Twin Slides deposits show a southern slope direction while areas in the south of Sector 3 show a northern and eastern slope direction, which contrast with the main NW slope direction of sectors 2 and 3 (Fig. 11C). Upward convex or concave features are observed downslope steep headwalls and are thus interpreted as mass-transport deposits (MTDs) and named South Gela Basin Slide (SGBS) and Gela Drift Slide (GDS; Figs. 10D and 11D). Their headwall scars reach lengths of 12.1 km and 3.6 km, respectively. The GDS in particular is characterized by transparent to chaotic seismic facies and reaches a maximum thickness of 50 m with an estimated volume of 0.41 km<sup>3</sup> (Fig. 10D and Table 4).

## 5. Discussion

### 5.1. The Pliocene–Quaternary stratigraphic architecture of the Gela Basin

The Pliocene–Quaternary stratigraphic architecture of the Gela Basin

records two main phases of margin outbuilding characterized by changes in depositional patterns as well as a drastic change in sediment accumulation rates.

#### 5.1.1. Progradational phase (Pliocene – MPT)

The Lower Pliocene was characterized by the deposition of parallel strata draping the uneven pre-existing morphology and marking the inundation of the Mediterranean Sea from the Atlantic Ocean after the opening of the Gibraltar Strait (Zanclean flood in Table 3; Garcia-Castellanos et al., 2009). The inherited uneven morphology, characterized by two deep sub-basins, determined the position of the Plio-Quaternary depocenters. Above sub-parallel strata, a 300-m-thick sediment wedge deposited during the Upper Pliocene recording a basinward migration of the shelf edge of ca. 10 km in Sector 3 (Fig. 5A), and with the concomitant infilling of the structural sub-basins in sectors 1 and 3 by onlapping strata ascribed to turbidite deposits by Ghielmi et al. (2012) (Figs. 3A, 7 and 13). In the Pleistocene, progradation extended to the south with the emplacement of oblique shelf-edge clinothems (Fig. 5D). The top truncated strata of these clinothems coupled with the flat to slightly descending shelf-edge trajectory may reflect the Lower Pleistocene uplift of the Malta Plateau documented by Gardiner et al. (1995) (Fig. 12). From Pliocene to MPT, the sediment wedge increased in thickness by 150 m/Myr, with the main depocenters located in Sector 1

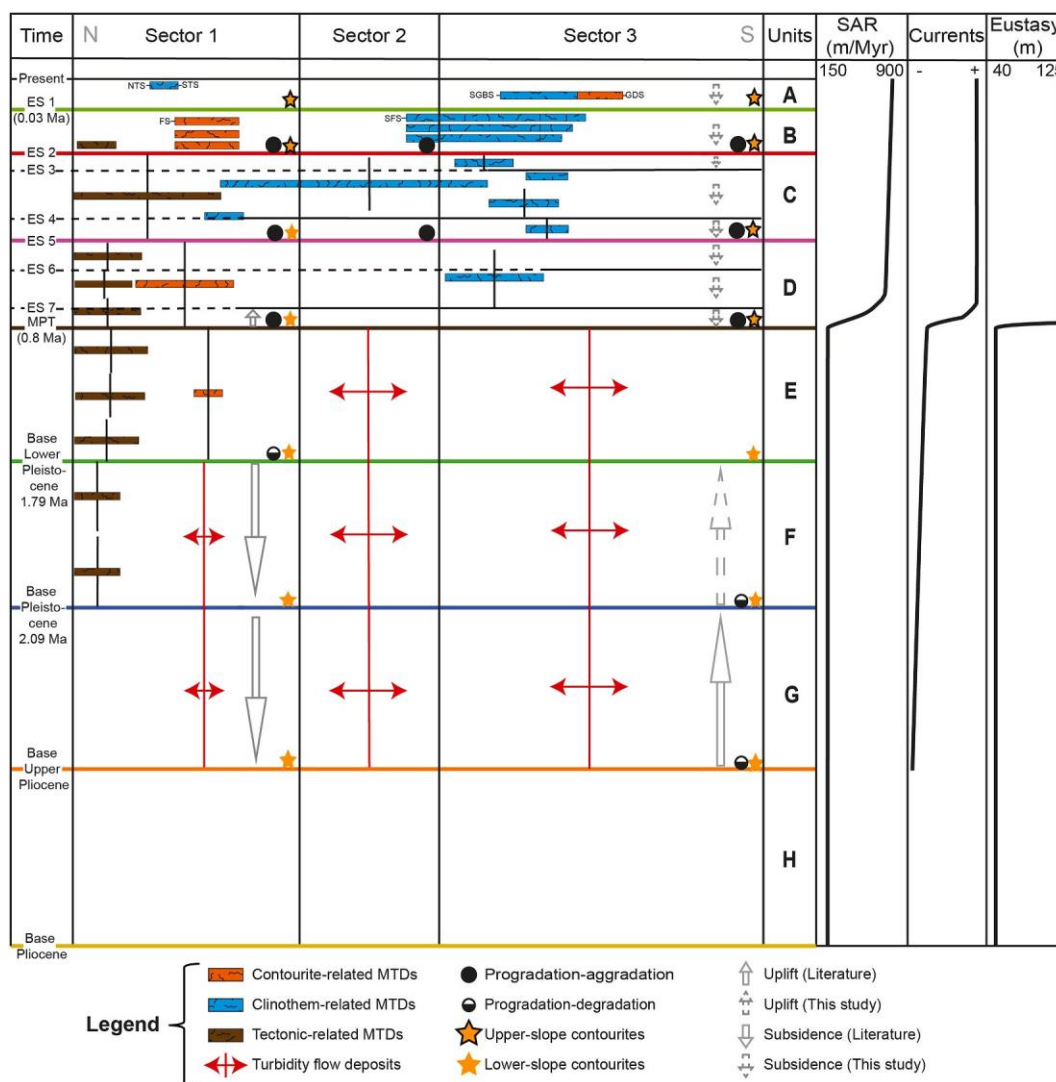
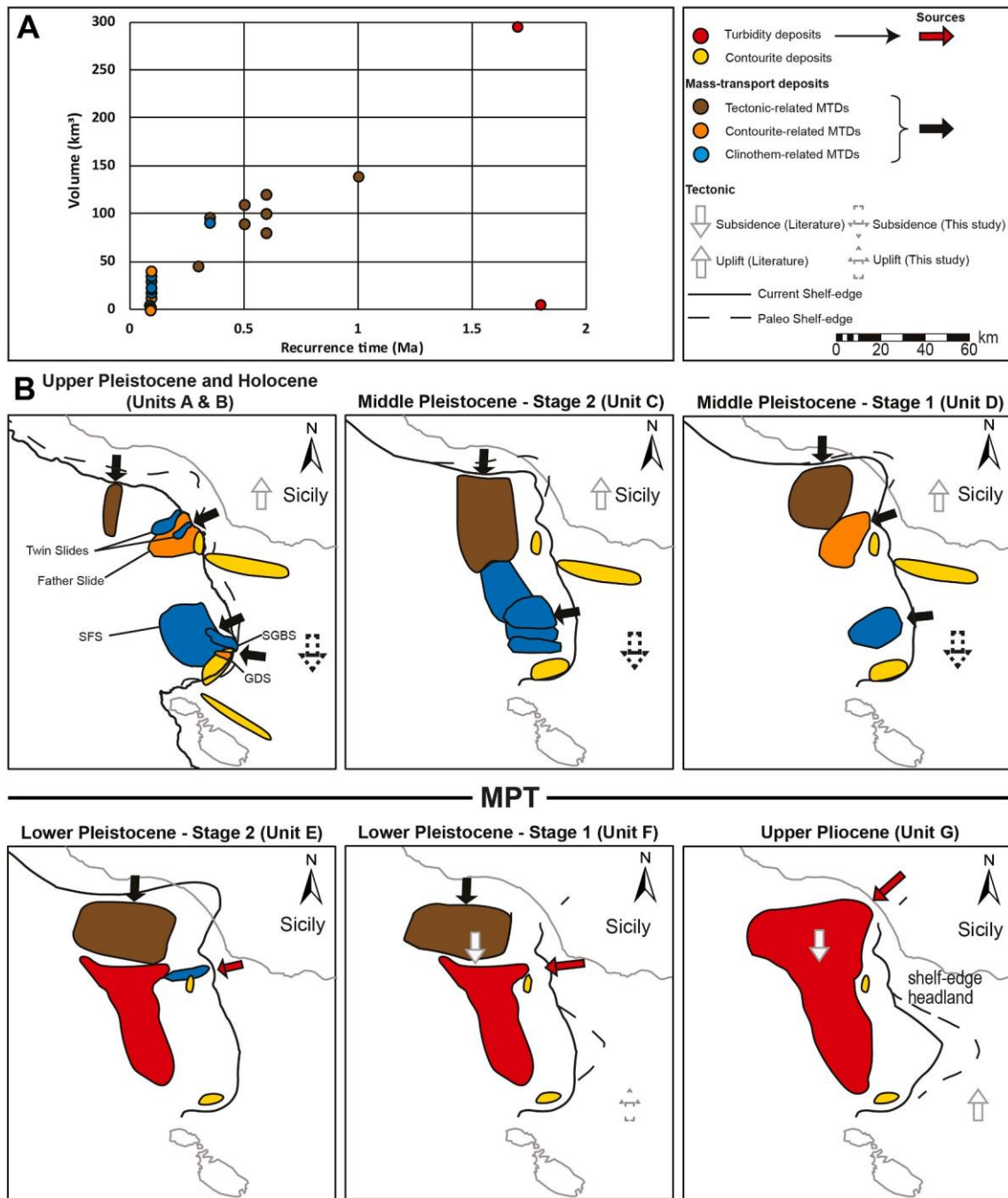


Fig. 12. N–S oriented chronostratigraphic cross-section summarizing the evolution of the eastern Gela Basin since the Pliocene. The temporal distribution of the deposits is schematic. SAR: sediment accumulation rate.



**Fig. 13.** A. Recurrence time plotted against reconstructed volumes of mass-transport deposits (MTDs) and turbidite deposits mapped in the eastern Gela Basin since the Pliocene (see also Table 4). B. Time sketch of the eastern Gela shelf-edge margin growth (black lines) for the Pliocene to Quaternary along with the distribution of sedimentary bodies and MTDs.

and in the east of Sector 3 (Fig. 12).

5.1.2. Progradational-aggradational (MPT – present)

The MPT horizon (Table 3) coincided with a general reorganization of the margin growth and of the stratigraphic architecture (Fig. 12). The margin outbuilding evolved from a progradational to a progradational with strongly aggradational motif (e.g. Fig. 5A), suggesting an overall increase in accommodation on the continental shelf accompanied by an increased sediment flux in all three sectors of the margin (Fig. 13). Like other continental margins (Ercilla et al., 1994; Fatoke and Bhattacharya, 2010; Gong et al., 2016), the deposition of thick sedimentary bodies after the MPT was accompanied by the increased occurrence of MTDs

and the Gela Basin recorded the destabilization of the entire eastern slope with the emplacement of several submarine landslides (Figs. 10, 11D and 15B).

The sedimentation rate of the progradation-aggradation phase reached 900 m/Myr, likely contributing to increased sediment load and causing subsidence of the shelf. The subsidence was previously documented by Gardiner et al. (1993), however they attributed the sinking to normal faulting. From the comparison with the underlying Pliocene–Lower Pleistocene progradational phase, a six-fold increase in the rate of margin outbuilding occurred after the MPT. This finding has implications for the geological time recorded by clino-stratified successions, and suggests that the physical scale of the lithosomes recorded

in the stratigraphic succession is unrelated to the time elapsed during their deposition as observed on other margins (Miall, 2016; Pellegrini et al., 2017a; Smith et al., 2015).

### 5.1.3. Slope instability and different types of MTDs

We analysed the morphology of the accumulation areas of MTDs, the orientation and shape of their headwall scars and their volumes to infer which predisposing factor (tectonics, shelf progradation, bottom currents) was predominant in their mobilization during the Pliocene and Pleistocene (Table 4). In the north (Sector 1), tectonic vertical movements were prevailing until the MPT, likely reflecting the proximity of the Maghrebian fold-and-thrust belt (Fig. 1) and the Messinian deformation that initiated the general uplift and exhumation of the accretionary wedge while the Hyblean Plateau locally forced uplift at the orogenic front (Henriquet et al., 2020). Transtensional movements concentrated during Late Miocene to Pliocene, resulting in a N–S extension in the Pantelleria Graben (PG in Fig. 1; Martinelli et al., 2019), with minimum effects in the study area. MTDs linked to extensional tectonics have distinct signatures, including blocks, debris-flow deposits and chaotic volumes from turbidites (Alves and Gamboa, 2019). The MTDs emplaced in the Upper Pliocene and Lower Pleistocene in the study area have prominent headwall scars, blocky to chaotic seismic facies and are sourced from the north (Table 4, Figs. 12 and 13), similar to the Gela Slide, which was triggered by the uplift of the Gela Nappe (Trincardi and Argnani, 1990). These tectonic-related MTDs are in the range 30–120 km<sup>3</sup> and have been deposited roughly every 400 kyr (Table 4, Fig. 13A).

After the MPT, only minor local subsidence on the Malta Plateau (Gardiner et al., 1993) and regional uplift in the Hyblean Plateau (Ghielmi et al., 2012) occurred, with no significant impact on sediment supply. In sectors 2 and 3, contourite-related MTDs formed downslope of contourite deposits involving volumes from 0.4 km<sup>3</sup> to 45 km<sup>3</sup> with a recurrence possibly influenced by the 100 kyr glacial/interglacial timescale climate variability (Figs. 10D, 12 and 13, Table 4).

In sectors 1 and 3, the high sediment accumulation rate at the shelf edge caused an increase of the slope gradient, which contributed to the margin instability, as previously suggested by Minisini and Trincardi (2009). Clinothem-related MTDs were thus emplaced where the margin had the highest sediment input, possibly related to the occurrence of river networks as suggested by Kuhlmann et al. (2015), coupled with the activity of persistent bottom currents (Fig. 8). The clinothem-related MTDs have volumes averaging at about 23 km<sup>3</sup> and reflect an eustatic control with a pacing similar to the contourite-related MTDs (Table 4, Figs. 12 and 13).

## 5.2. Contourite deposits as key markers of stratigraphic architecture

### 5.2.1. Onset of contourite deposits

Despite having been described in previous studies (Marani et al., 1993; Martorelli et al., 2001; Micallef et al., 2013; Verdicchio and Trincardi, 2008a,b), the timing of the onset of contourite deposits in the Strait of Sicily remains elusive. Our data show that the Upper Pliocene horizon marks the onset of contourite deposition on the lower slope of sectors 1 and 3 of GB, where mounded and plastered drifts (*sensu* Stow and Faugères, 2008, Table 2) developed, respectively (Figs. 12 and 13). The mounded drifts onset at the toe of the slope and progressively migrated upslope (Figs. 4B and 12). We ascribe the presence of thicker contourite drifts in Sector 1 (Fig. 4B and D) to the activity of a paleo bottom current interacting with the uneven topography inherited since the base of the Pliocene (see the structural high in Figs. 8, 9A and 9E). Integrated sedimentological and oceanographic analyses have recently shown that such mounded drifts typically characterize slope sectors where deceleration of bottom current promotes deposition, whereas plastered drifts tend to form in sediment-starved margin sectors (Miramontes et al., 2018). In our case, the presence of the structural high with a pronounced shelf-edge bulge (Fig. 8) led to the deposition of

contourite deposits on its up- and down-current sides (Fig. 13) as discussed elsewhere by Falcini et al. (2016) and Rovere et al. (2019).

### 5.2.2. Evolution of contourite deposits

After the MPT, the accelerated growth of contourite deposits along the whole margin (Figs. 12 and 13) implies the enhanced activity of near-seafloor water masses along the slope similar to the modern LIW, as suggested in other basins of the Mediterranean Sea (Amelio and Martorelli, 2008; Miramontes et al., 2016; Pellegrini et al., 2016). A bottom current should have a speed range > 10–12 cm s<sup>-1</sup> and < 20 cm s<sup>-1</sup> to initiate erosion and subsequent deposition of mounded sediment drifts in fine-grained sediments (e.g. McCave and Hall, 2006; Stow et al., 2009). The LIW circulates in the Strait of Sicily with a velocity of 13 cm s<sup>-1</sup> (Lermusiaux and Robinson, 2001), but may undergo intensity fluctuations, as observed in the Corsica Channel, possibly influenced by climatic changes on Milankovitch timescales (Toucanne et al., 2012).

### 5.2.3. Bottom currents strength and sea level variations

In an attempt to define when and where contourite deposits grow in relation to sea-level variations, Verdicchio and Trincardi (2008a) inferred an increased strength of the LIW during interglacials in the Central Mediterranean, while Miramontes et al. (2016) inferred faster bottom currents during cold intervals in the Corsica Channel. Our SBS profiles indeed show that the most recent growth of contourite deposits occurred during late MIS 2 and MIS 5 (Figs. 4D, 8 and 10) in the Gela Basin, supporting the action of bottom currents during both late glacial and interglacial periods, as envisaged in other contexts (e.g. Brack-enridge et al., 2011).

High sediment accumulation rates (200 cm kyr<sup>-1</sup>) in the prograding clinothems during MIS 5 in Sector 1 were observed in previous studies (Kuhlmann et al., 2015). Our data show a thickness decrease of MIS 5 deposits proceeding southward from Sector 1 to Sector 2 (Fig. 8). However, MIS 5 deposits increase their thickness in Sector 3 with a sediment accumulation rate at 100 cm kyr<sup>-1</sup>, where contourite drifts formed (Fig. 10). This evidence seems to indicate that sediments bypassed Sector 2 along a seaward bulge of the shelf edge (headland) and accumulated downcurrent in Sector 3, under the action of the LIW (Fig. 1).

### 5.2.4. Contourites and erosional surfaces as predisposing factors to margin instability

In the Gela Basin, the growth of contourite deposits is concomitant with an increase in the occurrence and decrease in the size of MTDs in the basin (Figs. 12 and 13). This finding suggests a causal relation between the development of contourites and the emplacement of MTDs. Since the growth of contourite deposits on the slope, large sectors of the slope destabilized, involving in some cases the entire stratigraphic succession (Fig. 12) and promoting an increase in the number of MTDs, with volumes ranging from 0.5 to 40 km<sup>3</sup>, named contourite-related MTDs (Fig. 13A). In Sector 3, the Gela Drift Slide (GDS) affected a large extent of a contourite drift with the Erosional Surface ES2 at its base, possibly acting as a glide plane (Fig. 10D). Previous studies suggested that weak layers such as intercalated volcanoclastic layers (Kuhlmann et al., 2017) create a basal change in mechanical properties which, together with increased pore pressure induced by rapid deposition (Urlaub et al., 2013) and higher slope gradient (Miramontes et al., 2018) as in the case of contourites, may favour the initiation of margin destabilization. In the case of the GDS, we suggest that the ES2 might have acted as a weak layer, due to a change in grain size, as reflected by the change in acoustic impedance in the seismic profiles (Fig. 10D). Contourite deposits are comprised of fine-grained sediments in the Gela Basin, alike in the Mediterranean Sea due to the average limited availability of coarser grained deposits on the shelf (Mulder et al., 2008), and differ in grain size from sediments deposited during lowstands. This mechanism has been suggested also for the Brazilian margin (Alves, 2010) and is supported by the evidence that, since the MPT, MTDs in the Gela Basin

consistently develop atop of regional lowstand unconformities (Fig. 5A).

5.3. Climate as main driver of clinothem architecture and margin instability after the MPT

We analysed reflection terminations to define sequence boundaries and related depositional sequences reconstructing timing of sediment delivery in the Gela Basin. There commonly are, however, a variety of erosional surfaces of different duration and lateral extents observable on shelves that can be interpreted potentially as sequence boundaries (e.g.

Pellegrini et al., 2017b; Madof et al., 2017, 2019). Sequence-stratigraphic models refer to the formation of a sequence boundary either at the beginning (e.g. Posamentier et al., 1992) or the end of the eustatic fall (e.g. Hunt and Tucker, 1992). Following the classic definition of sequence boundary by Mitchum et al. (1977), we were able to distinguish sequence boundaries from other erosional surfaces by differentiating the types and extents of their toplaps and onlaps at the shelf and on the slope, respectively (Figs. 5A, 6 and 14). We analysed the character of these surfaces along a ca. 100 km stretch of the Gela Basin (Figs. 5A, 6 and 14) and observed: i) the flat to slightly

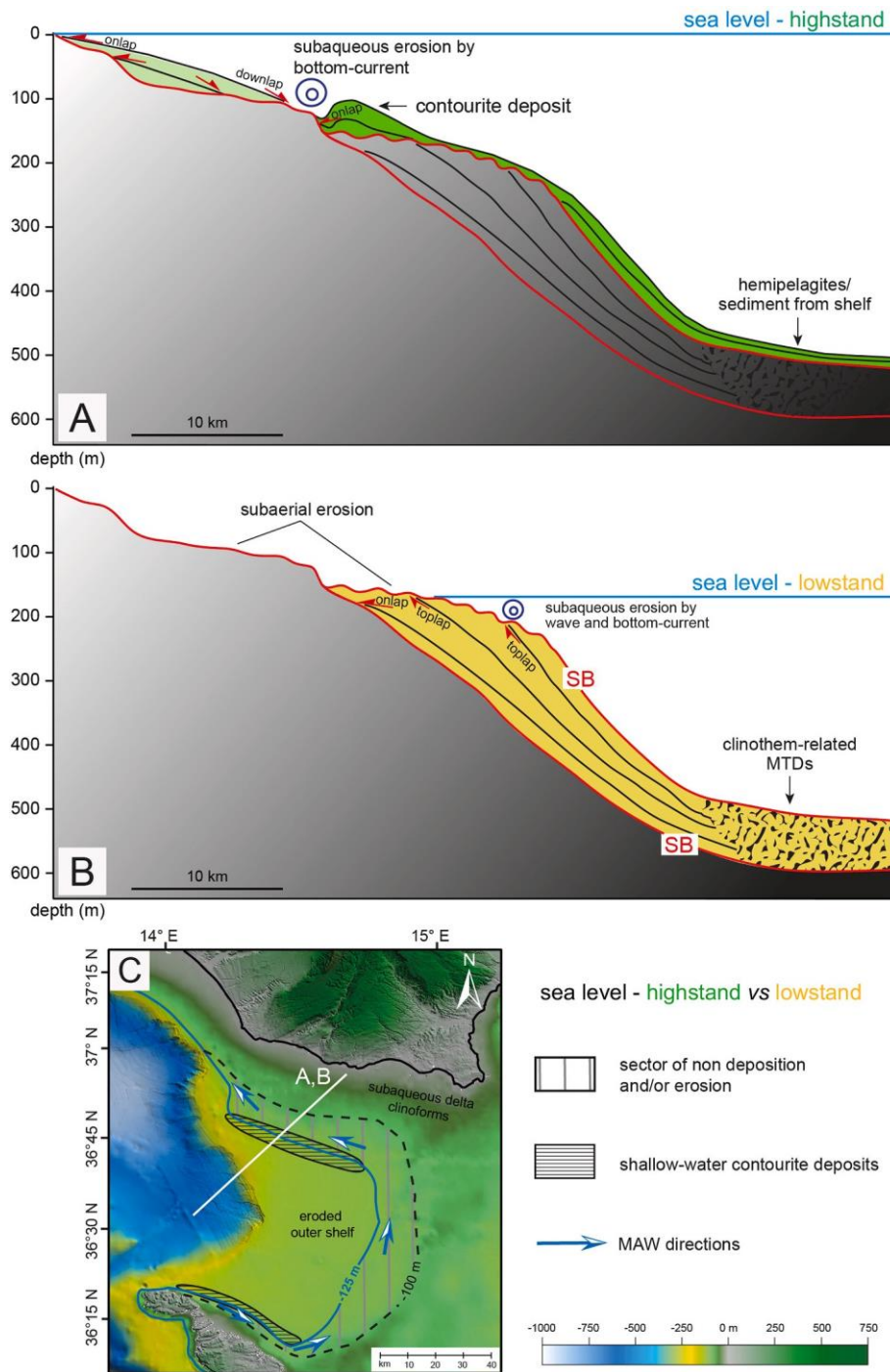


**Fig. 14.** Along-dip shelf stratigraphic reconstructions illustrating the changes in sediment deposition during the current Holocene highstand (A) and the Last Glacial Maximum (B). C. The occurrence of an elongated area of non-deposition adjacent to contourite deposits on the Malta Plateau indicates the path of bottom currents flowing at around 100 m w.d.

descending shelf-edge trajectory of the clinothems bracketed between ES1 and ES8 unconformities; ii) no evidence of relevant tectonic activity after the MPT (Fig. 12). ES1-ES8 unconformities therefore represent the sequence boundaries formed until the end of each eustatic fall (Fig. 6B). Independently constrained calibration of the youngest (ES1) and oldest (ES8) unconformities, dated at 30 kyr BP (Kuhlmann et al., 2015) and ca. 800 ka (Di Stefano et al., 1993), respectively, support this interpretation (Fig. 6B). Clinothems above the sequence boundaries show onlap terminations on the slope and have erosional topsets (highlighted by toplap terminations; Fig. 6A), and correlative MTDs in the basin and on the slope, here named clinothem-related MTDs (Fig. 14B). The erosional nature of their topsets can be explained by a fluvial system docked at the shelf edge, as documented in tank experiments (Martin et al., 2009). The depths of the rollover points of each sequence boundary indicate a quasi-steady subsidence rate of 0.1 mm/yr (Fig. 6B) and suggest, like in the western Adriatic Sea (Maselli et al., 2010), the formation of these erosional surfaces by subaerial exposure as reported in Kuhlmann et al. (2015) in the adjacent study area. However, the presence of ES1 rollover point at 200 m w. d. on the Malta Plateau (Figs. 6A, 8) and 75 m below the position of sea level during the last eustatic lowstand, would imply a subsidence rate of 2.5 mm/yr solely in the last 30 kyr. Instead, we suggest that ES1 can be the result of subaerial erosion during the last lowstand on the inner and mid shelf and of subaqueous erosion on the outer shelf, presumably by waves and bottom currents (Fig. 14B). The subaqueous erosion on the outer shelf may have further contributed to the emplacement of MTDs in the basin (Fig. 14B). The clinothems prograded at the shelf edge until further sea-level rise brought about the flooding of the continental shelf. During flooding phases and highstands, the shoreline shifted landward accompanied by: i) the formation of a condensed succession in the basin detected as single and laterally continuous reflections observed in MCS profiles (Fig. 14A). These reflections can be interpreted as hemipelagites and shelf-derived sediments as reported elsewhere in similar contexts (e.g. Paumard et al., 2020); ii) the deposition of sediment drifts on the outer shelf (Fig. 14A and C). We indeed found evidence of contourite deposits as shallow as 100 m w.d. on the Malta Plateau (inset of Fig. 8), similar to those suggested close to Malta by Micallef et al. (2013) (Fig. 1). We thus infer the presence of bottom currents constrained in their paths by the structural highs of the Malta Plateau during highstands suggesting an along-contour sediment redistribution, under the influence of the MAW from north to south along the shelf edge (Fig. 14C). Overall, this evidence suggest that sea level was the main driver in determining the position of the depocenters with a systematic shift of the depocenters towards the shelf edge during glacial periods. Therefore, sea-level variations concur in promoting margin destabilization under high-amplitude glacio-eustatic fluctuations (Fig. 12). This implies orbitally-controlled climatic cycles as the key predisposing factor of margin instability after the MPT, with clinothem-MTDs paced roughly at 100 kyr cycles (Table 4).

## 6. Conclusions

The Pliocene–Quaternary stratigraphic succession of the Gela Basin results from the stacking of three main types of sedimentary bodies: clinothems, contourite deposits and mass-transport deposits (MTDs). Altogether, the stratal stacking pattern records variations in tectonic activity, climate (affecting sediment flux from the continent and eustasy), and changes in the oceanographic regime at Milankovitch and sub-Milankovitch time scales.

Tectonic-related MTDs are the least recurrent gravity-flow deposits in the Gela Basin but the largest in volumes until the Lower Pleistocene in the north of the basin. The outbuilding of the margin changed drastically along the Middle Pleistocene Transition (MPT, 0.8 Ma) from a shelf-edge progradational phase with an accumulation of 700 m in ca. 4.5 Myr, to a progradational-aggradational phase with a comparable volume of sediment accumulated in a much shorter time span. This high

sediment accumulation rate promoted the emplacement of MTDs favoured by significantly increased slope gradients of the foresets of prograding clinofolds. Therefore, shelf-edge clinothems and their associated MTDs were paced at Milankovitch cyclicity and resulted in the systematic shift of the shoreline to the shelf edge during glacial periods, revealing sea-level change as the main driver in determining the position of the depocenters along the shelf-edge and indirectly favoring margin destabilization after the MPT.

Following the MPT, contourite deposits, confined to the lower slope since the Upper Pliocene, progressively migrated upslope, under the action of enhanced bottom currents with a flow pattern likely similar to that of the modern LIW. Contourite drifts formed on the up and down-current side of a shelf-edge headland inherited from the Pre-Pliocene morphology of the margin, which probably accelerated bottom currents locally. Markedly different sediment accumulation rates north and south along the margin during interglacial periods (e.g. MIS 5) further suggest a re-organization in the sediment dispersal along the shelf, with sediment by-pass around the shelf-edge headland. In this context, MTDs generated from failed, contourite deposits are systematically found above erosional surfaces, which probably acted as glide planes.

Overall, these findings suggest that:

1. The contourite- and clinothem-related MTDs are smaller in size compared to the tectonic-related MTDs but more recurrent and reflect sea-level fluctuations, changes in sediment supply and dispersal by bottom currents.
2. Contourite deposits emplaced over erosional unconformities are prone to failure thereby acting as a major control on the architecture of the margin.
3. The physical scale of the lithosomes recorded in the stratigraphic succession has no implications on the time elapsed during their deposition, as already observed in other margins.

## CRediT authorship contribution statement

**Tugdual Gauchery:** Investigation, Visualization, Software, Writing - original draft. **Marzia Rovere:** Conceptualization, Methodology, Writing - original draft, Writing - review & editing, Supervision. **Claudio Pellegrini:** Conceptualization, Methodology, Writing - original draft, Writing - review & editing. **Antonio Cattaneo:** Methodology, Supervision. **Elisabetta Campiani:** Data curation, Software. **Fabio Trincardi:** Writing - review & editing.

## Declaration of competing interest

The authors declare that they have no known competing financial interests or personal relationships that could have appeared to influence the work reported in this paper.

## Acknowledgments

The authors wish to thank Eni S.p.A., in particular Luca Aleotti and Alessandro Fattorini for granting the access to the virtual data room at their premises in San Donato Milanese (Italy) and Claudio Cattaneo for his kind technical assistance. Alessandra Asioli helped to interpret the biozones of the boreholes. Francesca Zolezzi helped a lot in putting together and analysing the seismic data during T.G.'s several stays at Rina Consulting S.p.A. The comments and suggestions by Victorien Paumard, Andrew S. Madof and Tiago M. Alves greatly improved the paper. The PhD of Tugdual Gauchery is funded by the European Union's Horizon 2020 research and innovation programme under the Marie-Sklodowska-Curie grant via project ITN SLATE (grant agreement No 721403). This work is dedicated to the memory of our beloved colleague Elisabetta Campiani.

## References

- Alves, T.M., 2010. A 3-D morphometric analysis of erosional features in a contourite drift from offshore SE Brazil. *Geophys. J. Int.* 183 (3), 1151–1164. <https://doi.org/10.1111/j.1365-246X.2010.04827.x>.
- Alves, T.M., Gamboa, D., 2019. Mass-transport deposits as markers of local tectonism in extensional basins. In: Ogata, K., Festa, A., Pini, G.A. (Eds.), *Submarine Landslides Subaqueous Mass Transport Deposits from Outcrops to Seismic Profiles*. Geoph. Monog. Series 246. AGU, pp. 71–90. <https://doi.org/10.1002/9781119500513.ch5>.
- Amelio, M., Martorelli, E., 2008. Seismo-stratigraphic characters of paleocontourites along the calabro-tyrrhenian margin (southern Tyrrhenian Sea). *Mar. Geol.* 252, 141–149. <https://doi.org/10.1016/j.margeo.2008.03.011>.
- Anell, I., Midtkandal, I., 2017. The quantifiable clinothem – types, shapes and geometric relationships in the Plio-Pleistocene Giant Foresets Formation, Taranaki Basin, New Zealand. *Basin Res.* 29 (S1), 277–297. <https://doi.org/10.1111/bre.12149>.
- Argnani, A., 1987. The Gela nappe: evidence of accretionary melange in the maghrebien foredeep of sicily. *Memorie Società Geologica Italiana* 38, 419–428.
- Argnani, A., Torelli, L., 2001. The Pelagian Shelf and its graben system (Italy/Tunisia). *Memoir. Mus. Natl. Hist.* 186, 529–544.
- Astraldi, M., Gasparini, G.P., Gervasio, L., Salusti, E., 2001. Dense water dynamics along the Strait of sicily (Mediterranean Sea). *J. Phys. Oceanogr.* 31, 3457–3475. [https://doi.org/10.1175/1520-0485\(2001\)031<3457:DWDATS>2.0.CO;2](https://doi.org/10.1175/1520-0485(2001)031<3457:DWDATS>2.0.CO;2).
- Béranger, K., Mortier, L., Gasparini, G.P., Gervasio, L., Astraldi, M., Crépon, M., 2004. The dynamics of the Sicily Strait: a comprehensive study from observations and models. *Deep-Sea Res. Pt. II* 51 (4–5), 411–440. <https://doi.org/10.1016/j.dsr2.2003.08.004>.
- Bishop, W.F., Debono, G., 1996. The hydrocarbon geology of southern offshore Malta and surrounding regions. *J. Petrol. Geol.* 19, 129–160. <https://doi.org/10.1111/j.1747-5457.1996.tb00422.x>.
- Brackenridge, R., Stow, D.A.V., Hernández-Molina, F.J., 2011. Contourites within a deep-water sequence stratigraphic framework. *Geo Mar. Lett.* 31, 343–360. <https://doi.org/10.1007/s00367-011-0256-9>.
- Butler, R.W.H., Grasso, M., La Manna, F., 1992. Origin and deformation of the neogene-recent maghrebien foredeep at the Gela nappe, SE sicily. *J. Geol. Soc.* 149 (4), 547–556. <https://doi.org/10.1144/gsjgs.149.4.0547>.
- Colantoni, P., Del Monte, M., Gallignani, P., Zarudkzi, E.F.K., 1975. Il Banco Graham: un vulcano recente del Canale di Sicilia. *Giorn. Geol.* 40, 141–162.
- Di Stefano, E., Infuso, S., Scarantino, S., 1993. Plio-Pleistocene sequence stratigraphy of south western offshore Sicily from well logs and seismic sections in a high resolution calcareous plankton biostratigraphic framework. In: Max, M.D., Colantoni, P. (Eds.), *Geological Development of the Sicilian-Tunisian Platform*. Reports in Marine Science, vol. 58. UNESCO, pp. 37–42.
- EMODnet Bathymetry Consortium, 2016. EMODnet Digital Bathymetry (DTM). The European Marine Observation and Data Network. <https://doi.org/10.12770/c7b53704-999d-4721-b1a3-046ec60c87238>.
- Ercilla, G., Farran, M., Alonso, B., Diaz, J.I., 1994. Pleistocene progradational growth pattern of the northern Catalonia continental shelf (northwestern Mediterranean). *Geo Mar. Lett.* 14, 264–271. <https://doi.org/10.1007/BF01274062>.
- Falcini, F., Martorelli, E., Chiocci, F.L., Salusti, E., 2016. A general theory for the effect of local topographic unevenness on contourite deposition around marine capes: an inverse problem applied to the Italian continental margin (Cape Suvero). *Mar. Geol.* 378, 74–80. <https://doi.org/10.1016/j.margeo.2016.01.004>.
- Fatoke, O.A., Bhattacharya, J.P., 2010. Controls on depositional systems and sequence stratigraphy of the Pliocene-Pleistocene strata of eastern Niger delta, Nigeria. AAPG (Am. Assoc. Pet. Geol.) Convention, Denver, Colorado. June 7–10, 2009. [http://www.searchanddiscovery.com/documents/2010/10220fatoke/ndx\\_fatoke.pdf](http://www.searchanddiscovery.com/documents/2010/10220fatoke/ndx_fatoke.pdf).
- Faugères, J.C., Stow, D.A.V., Imbert, P., Viana, A., 1999. Seismic features diagnostic of contourite drifts. *Mar. Geol.* 162, 1–38. [https://doi.org/10.1016/S0025-3227\(99\)00068-7](https://doi.org/10.1016/S0025-3227(99)00068-7).
- Finetti, I., 1984. Geophysical study of the sicily channel rift zone. *Boll. Geofis. Teor. Appl.* 26, 3–28.
- García-Castellanos, D., Estrada, F., Jiménez-Munt, I., Gorini, C., Fernández, M., Vergés, J., De Vicente, R., 2009. Catastrophic flood of the Mediterranean after the Messinian salinity crisis. *Nature* 462, 778–781. <https://doi.org/10.1038/nature08555>.
- Gardiner, W., Grasso, M., Sedgely, D., 1993. Plio-Pleistocene stratigraphy and recent movements of the Malta platform. In: Max, M.D., Colantoni, P. (Eds.), *Geological Development of the Sicilian-Tunisian Platform*. Reports in Marine Science, vol. 58. UNESCO, pp. 111–116.
- Gardiner, W., Grasso, M., Sedgely, D., 1995. Plio-pleistocene fault movement as evidence for mega-block kinematics within the Hyblean—Malta Plateau, Central Mediterranean. *J. Geodyn.* 19, 35–51. [https://doi.org/10.1016/0264-3707\(94\)00006-9](https://doi.org/10.1016/0264-3707(94)00006-9).
- Ghielmi, M., Amore, M.R., Bolla, E.M., Carubelli, P., Knezaurek, G., Serraino, C., 2012. The Pliocene to pleistocene succession of the hyblean foredeep (sicily, Italy). October 23–26, 2011 AAPG (Am. Assoc. Pet. Geol.) Internat. Conf. Exhib. Milan, Italy. [http://www.searchanddiscovery.com/documents/2012/30220ghielmi/ndx\\_giemi.pdf](http://www.searchanddiscovery.com/documents/2012/30220ghielmi/ndx_giemi.pdf).
- Ghisetti, F.C., Gorman, A.R., Grasso, M., Vezzani, L., 2009. Imprint of foreland structure on the deformation of a thrust sheet: the Plio-Pleistocene Gela nappe (southern Sicily, Italy). *Tectonics* 28, 1–16. <https://doi.org/10.1029/2008TC002385>.
- Gibbard, P.L., Head, M.J., Walker, M.J.C., 2010. The subcommission on quaternary stratigraphy, formal ratification of the quaternary system/period and the pleistocene series/epoch with a base at 2.58 Ma. *J. Quat. Sci.* 25 (2), 96–102. <https://doi.org/10.1002/jqs.1338>.
- Gong, C., Steel, R.J., Wang, Y., Lin, C., Olariu, C., 2016. Shelf-margin architecture variability and its role in sediment-budget partitioning into deep-water areas. *Earth Sci. Rev.* 154, 72–101. <https://doi.org/10.1016/j.earscirev.2015.12.003>.
- Gong, C., Blum, M.D., Wang, Y., Lin, C., Xu, Q., 2018. Can climatic signals be discerned in a deep-water sink?: an answer from the Pearl River source-to-sink sediment-routing system. *Geol. Soc. Am. Bull.* 130, 661–677. <https://doi.org/10.1130/B31578.1>.
- Haile, N.S., 1987. Time and age in geology the use of Upper/Lower, late/early in stratigraphic nomenclature. *Mar. Petrol. Geol.* 4, 255–257. [https://doi.org/10.1016/0264-8172\(87\)90048-1](https://doi.org/10.1016/0264-8172(87)90048-1).
- Helland-Hansen, W., Martinsen, O.J., 1996. Shoreline trajectories and sequences: description of variable depositional-dip scenarios. *J. Sediment. Res.* 66, 670–688. <https://doi.org/10.1306/d42683dd-2b26-11d7-8648000102c1865d>.
- Henriquet, M., Dominguez, S., Barreca, G., Malavielle, J., Monaco, C., 2020. Structural and tectono-stratigraphic review of the Sicilian orogen and new insights from analogue modeling. *Earth Sci. Rev.* 208, 103257. <https://doi.org/10.1016/j.earscirev.2020.103257>.
- Hunt, D., Tucker, M.E., 1992. Stranded parasequences and the forced regressive wedge systems tract: deposition during base-level fall. *Sediment. Geol.* 81, 1–9. [https://doi.org/10.1016/0037-0738\(92\)90052-S](https://doi.org/10.1016/0037-0738(92)90052-S).
- Johannessen, E.P., Steel, R.J., 2005. Shelf-margin clinoforms and prediction of deepwater sands. *Basin Res.* 17, 521–550. <https://doi.org/10.1111/j.1365-2117.2005.00278.x>.
- Kuhlmann, J., Asioli, A., Trincardi, F., Klügel, A., Huhn, K., 2015. Sedimentary response to Milankovitch-type climatic oscillations and formation of sediment undulations: evidence from a shallow-shelf setting at Gela Basin on the Sicilian continental margin. *Quat. Sci. Rev.* 108, 76–94. <https://doi.org/10.1016/J.QUASCIREV.2014.10.030>.
- Kuhlmann, J., Asioli, A., Trincardi, F., Klügel, A., Huhn, K., 2017. Landslide frequency and failure mechanisms at NE Gela Basin (Strait of sicily). *J. Geophys. Res.-Sol. Ea.* 122, 2223–2243. <https://doi.org/10.1002/2017JF004251>.
- Laberg, J.S., Camerlenghi, A., 2008. The significance of contourites for submarine slope stability. In: Rebesco, M., Camerlenghi, A. (Eds.), *Contourites*. Developments in Sedimentology 60. Elsevier Science, pp. 537–556. [https://doi.org/10.1016/S0070-4571\(08\)10025-5](https://doi.org/10.1016/S0070-4571(08)10025-5).
- Lermusiaux, P.F.J., Robinson, A.R., 2001. Features of dominant mesoscale variability, circulation patterns and dynamics in the Strait of Sicily. *Deep-Sea Res. Pt. I* 48 (9), 1953–1997. [https://doi.org/10.1016/S0967-0637\(00\)00114-X](https://doi.org/10.1016/S0967-0637(00)00114-X).
- Lirer, F., Foresi, L.M., Iaccarino, S.M., Salvarin, G., Turco, E., Cosentino, C., Sierro, F. J., Caruso, A., 2019. Mediterranean Neogene planktonic foraminifer biozonation and Biochronology. *Earth Sci. Rev.* 196, 102869. <https://doi.org/10.1016/j.earscirev.2019.05.013>.
- Llave, E., Matias, H., Hernández-Molina, F.J., Ercilla, G., Stow, D.A.V., Medialdea, T., 2011. Pliocene-Quaternary contourites along the northern Gulf of Cadiz margin: sedimentary stacking pattern and regional distribution. *Geo Mar. Lett.* 31, 377–390. <https://doi.org/10.1007/s00367-011-0241-3>.
- Madof, A.S., Christie-Blick, N., Anders, M.H., Febo, L.A., 2017. Unreciprocated sedimentation along a mud-dominated continental margin, Gulf of Mexico, USA: implications for sequence stratigraphy in muddy settings devoid of depositional sequences. *Mar. Petrol. Geol.* 80, 492–516. <https://doi.org/10.1016/j.marpetgeo.2016.12.022>.
- Madof, A.S., Harris, A.D., Baumgardner, S.E., Sadler, P.M., Laugier, F.J., Christie-Blick, N., 2019. Stratigraphic aliasing and the transient nature of deep-water depositional sequences: revisiting the Mississippi Fan. *Geology* 47 (6), 545–549. <https://doi.org/10.1130/G46159.1>.
- Marani, M., Argnani, A., Roveri, M., Trincardi, F., 1993. Sediment drifts and erosional surfaces in the central Mediterranean: seismic evidence of bottom-current activity. *Sediment. Geol.* 82, 207–220. [https://doi.org/10.1016/0037-0738\(93\)90122-L](https://doi.org/10.1016/0037-0738(93)90122-L).
- Martin, J., Paola, C., Abreu, V., Neal, J., Sheets, B., 2009. Sequence stratigraphy of experimental strata under known conditions of differential subsidence and variable base level. AAPG (Am. Assoc. Pet. Geol.) Bull. 93 (4), 503–533. <https://doi.org/10.1306/12110808057>.
- Martinelli, M., Bistacchi, A., Balsamo, F., Meda, M., 2019. Late Oligocene to Pliocene extension in the Maltese islands and implications for geodynamics of the Pantelleria rift and pelagian platform. *Tectonics* 38, 3394–3415. <https://doi.org/10.1029/2019TC005627>.
- Martorelli, E., Petroni, G., Chiocci, F.L., 2011. Contourites offshore Pantelleria Island (sicily channel, Mediterranean Sea): depositional, erosional and biogenic elements. *Geo Mar. Lett.* 31, 481–493. <https://doi.org/10.1007/s00367-011-0244-0>.
- Martorelli, E., Bosman, A., Casalbone, D., Falcini, F., 2016. Interaction of down-slope and along-slope processes off Capo Vaticano (southern Tyrrhenian Sea, Italy), with particular reference to contourite-related landslides. *Mar. Geol.* 378, 43–55. <https://doi.org/10.1016/j.margeo.2016.01.005>.
- Maselli, V., Trincardi, F., Cattaneo, A., Ridente, D., Asioli, A., 2010. Subsidence pattern in the central Adriatic and its influence on sediment architecture during the last 400 kyr. *J. Geophys. Res.-Sol. Ea.* 115, B12106. <https://doi.org/10.1029/2010JB007687>.
- McCave, I.N., Hall, I.R., 2006. Size sorting in marine muds: processes, pitfalls, and prospects for paleoflow-speed proxies. *G-cubed* 7, Q10N05. <https://doi.org/10.1029/2006GC001284>.
- Miall, A.D., 2016. The evaluation of unconformities. *Earth Sci. Rev.* 163, 22–71. <https://doi.org/10.1016/j.earscirev.2016.09.011>.
- Micallef, A., Fogliani, F., Le Bas, T., Angeletti, L., Maselli, V., Pasuto, A., Taviani, M., 2013. The submerged paleolandscapes of the Maltese Islands: morphology, evolution and relation to Quaternary environmental change. *Mar. Geol.* 335, 129–147. <https://doi.org/10.1016/J.MARGEO.2012.10.017>.

- Minisini, D., Trincardi, F., 2009. Frequent failure of the continental slope: the Gela Basin (Sicily channel). *J. Geophys. Res.-Earth* 114, 1–17. <https://doi.org/10.1029/2008JF001037>.
- Minisini, D., Trincardi, F., Asioli, A., Canu, M., Fogliani, F., 2007. Morphologic variability of exposed mass-transport deposits on the eastern slope of Gela Basin (Sicily channel). *Basin Res.* 19, 217–240. <https://doi.org/10.1111/j.1365-2117.2007.00324.x>.
- Miramontes, E., Cattaneo, A., Jouet, G., Th ereau, E., Thomas, Y., Rovere, M., Cauquil, E., Trincardi, F., 2016. The pianosa contourite depositional system (northern Tyrrhenian Sea): drift morphology and plio-quaternary stratigraphic evolution. *Mar. Geol.* 378, 20–42. <https://doi.org/10.1016/j.margeo.2015.11.004>.
- Miramontes, E., Garziglia, S., Sultan, N., Jouet, G., Cattaneo, A., 2018. Morphological control of slope instability in contourites: a geotechnical approach. *Landslides* 15, 1085–1095. <https://doi.org/10.1007/s10346-018-0956-6>.
- Mitchum Jr., R.M., Vail, P.R., Sangree, J.B., 1977. Seismic stratigraphy and global changes of sea level, Part 6: stratigraphic interpretation of seismic reflection patterns in depositional sequences, section 2: application of seismic reflection configuration to stratigraphic interpretation. *AAPG (Am. Assoc. Pet. Geol.) Memoir* 26, 117–133. <https://doi.org/10.1306/M26490C8>.
- Mulder, T., Faug eres, J.-T., Gonthier, E., 2008. Mixed turbidite-contourite systems. In: *Rebesco, M., Camerlenghi, A. (Eds.), Contourites. Developments in Sedimentology* 60. Elsevier, pp. 435–456. [https://doi.org/10.1016/S0070-4571\(08\)10021-8](https://doi.org/10.1016/S0070-4571(08)10021-8).
- Patruno, S., Helland-Hansen, W., 2018. Clinoform systems: review and dynamic classification scheme for shorelines, subaqueous deltas, shelf-edges and continental margins. *Earth Sci. Rev.* 185, 202–233. <https://doi.org/10.1016/j.earscirev.2018.05.016>.
- Paumard, V., Bourget, J., Payenberg, T., George, A.D., Ainsworth, R.B., Lang, S., 2019. From quantitative 3D seismic stratigraphy to sequence stratigraphy: insights into the vertical and lateral variability of shelf-margin depositional systems at different stratigraphic orders. *Mar. Petrol. Geol.* 110, 797–831. <https://doi.org/10.1016/j.marpetgeo.2019.07.007>.
- Paumard, V., Bourget, J., Payenberg, T., George, A.D., Ainsworth, R.B., Lang, S., Posamentier, H.W., 2020. Controls on deep-water sand delivery beyond the shelf edge: accommodation, sediment supply, and deltaic process regime. *J. Sediment. Res.* 90 (1), 104–130. <https://doi.org/10.2110/jsr.2020.2>.
- Pearson, P.N., Wade, B.S., Backman, J., Raffi, I., Monechi, S., 2017. Sub-series and sub-epochs are informal units and should continue to be omitted from the International Chronostratigraphic Chart. *Episodes* 40 (1), 5–7. <https://doi.org/10.18814/epiugs/2017v40i1/017002>.
- Pellegrini, C., Maselli, V., Trincardi, F., 2016. Pliocene–Quaternary contourite depositional system along the south-western Adriatic margin: changes in sedimentary stacking pattern and associated bottom currents. *Geo Mar. Lett.* 36, 67–79. <https://doi.org/10.1007/s00367-015-0424-4>.
- Pellegrini, C., Maselli, V., Gamberi, F., Asioli, A., Bohacs, K.M., Drexler, T.M., Trincardi, F., 2017a. How to make a 350-m-thick lowstand systems tract in 17,000 years: the Late Pleistocene Po River (Italy) lowstand wedge. *Geology* 45 (4), 327–330. <https://doi.org/10.1130/G38848.1>.
- Pellegrini, C., Bohacs, K.M., Drexler, T.M., Gamberi, F., Rovere, M., Trincardi, F., 2017b. Identifying the sequence boundary in over- and under-supplied contexts: the case of the late Pleistocene adriatic continental margin. In: *Hart, B., Rosen, N.C., West, D., D'Agostino, A., Messina, C., Hoffman, M., Wild, R. (Eds.), Sequence Stratigraphy: the Future Defined. Proceedings of the 36<sup>th</sup> Annual Perkins-Rosen Research Conference*, pp. 160–182. <https://doi.org/10.5724/gcs.17.160>. Houston, Texas.
- Pellegrini, C., Patruno, S., Helland-Hansen, W., Steel, R.J., Trincardi, F., 2020. Clinoforms and clinothem: fundamental elements of basin infill. *Basin Res.* 32, 187–205. <https://doi.org/10.1111/bre.12446>.
- Pena, L.D., Goldstein, S.L., 2014. Thermohaline circulation crisis and impacts during the mid-Pleistocene transition. *Science* 345, 318–322. <https://doi.org/10.1126/science.1249770>.
- Pirmez, C., Pratson, L.F., Steckler, M.S., 1998. Clinoform development by advection-diffusion of suspended sediment: modeling and comparison to natural systems. *J. Geophys. Res.-Sol. Ea.* 103, 24141–24157. <https://doi.org/10.1029/98jb01516>.
- Posamentier, H.W., Allen, G.P., James, D.P., Tesson, M., 1992. Forced regressions in a sequence stratigraphic framework: concepts, examples, and exploration significance (1). *AAPG (Am. Assoc. Pet. Geol.) Bull.* 76, 1687–1709. <https://doi.org/10.1306/BDF8AA6-1718-11D7-8645000102C1865D>.
- Reeder, M.S., Rothwell, G., Stow, D.A.V., 2002. The Sicilian gateway: anatomy of the deep-water connection between East and West Mediterranean basins. *Geol. Soc. Mem.* 22, 171–189. <https://doi.org/10.1144/GSL.MEM.2002.022.01.13>.
- Rich, J.L., 1951. Three critical environments of deposition, and criteria for recognition of rocks deposited in each of them. *GSA Bull.* 62, 1–20. [https://doi.org/10.1130/0016-7606\(1951\)62\[1:TCEODA\]2.0.CO](https://doi.org/10.1130/0016-7606(1951)62[1:TCEODA]2.0.CO) accessed day-2.
- Roque, C., Duarte, H., Terrinha, P., Valadares, V., Noiva, J., Cach ao, M., Ferreira, J., Legoinha, P., Zitellini, N., 2012. Pliocene and Quaternary depositional model of the Algarve margin contourite drifts (Gulf of Cadiz, SW Iberia): seismic architecture, tectonic control and paleoceanographic insights. *Mar. Geol.* 303–306, 42–62. <https://doi.org/10.1016/j.margeo.2011.11.001>.
- Rovere, M., Pellegrini, C., Chiggiato, J., Campiani, E., Trincardi, F., 2019. Impact of dense bottom water on a continental shelf: an example from the SW Adriatic margin. *Mar. Geol.* 408, 123–143. <https://doi.org/10.1016/j.margeo.2018.12.002>.
- Smith, D.G., Bailey, R.J., Burgess, P.M., Fraser, A.J., 2015. Strata and time: probing the gaps in our understanding. *Geol. Soc. Spec. Publ.* 404 (1), 1–10. <https://doi.org/10.1144/SP404.16>.
- Somoza, L., Hern andez-Molina, F.J., De Andres, J.R., Rey, J., 1997. Continental shelf architecture and sea-level cycles: late Quaternary high-resolution stratigraphy of the Gulf of C adiz, Spain. *Geo Mar. Lett.* 17, 133–139. <https://doi.org/10.1007/s003670050018>.
- Spratt, R.M., Lisiecki, L.E., 2006. A late Pleistocene sea level stack. *Clim. Past* 12, 1079–1092. <https://doi.org/10.5194/cp-12-1079-2016>.
- Steckler, M.S., Mountain, G.S., Miller, K.G., Christie-Blick, N., 1998. Reconstruction of Tertiary progradation and clinoform development on the New Jersey passive margin by 2-D backstripping. *Mar. Geol.* 154, 399–420. [https://doi.org/10.1016/S0025-3227\(98\)00126-1](https://doi.org/10.1016/S0025-3227(98)00126-1).
- Steel, R., Olsen, T., 2002. Clinoforms, clinoform trajectories and deepwater sands. In: *Armentrout, J.M., Rosen, N.C. (Eds.), Sequence Stratigraphic Models for Exploration and Production: Evolving Methodology, Emerging Models, and Application Histories. Proceedings of 22<sup>nd</sup> Annual Gulf Coast Section SEPM Foundation Bob F. Perkins Research Conference*, pp. 367–380. <https://doi.org/10.5724/gcs.02.22.0367>. Houston, Texas.
- Stoker, M.S., Hafidason, H., 2005. Contourites and their relevance for mass wasting along the Mid-Norwegian Margin. *Mar. Petrol. Geol.* 22, 85–96. <https://doi.org/10.1016/j.marpetgeo.2004.10.012>.
- Stow, D.A.V., Faug eres, J.-C., 2008. Contourite facies and the facies model. In: *Rebesco, M., Camerlenghi, A. (Eds.), Contourites. Developments in Sedimentology* 60. Elsevier Science, pp. 223–256. [https://doi.org/10.1016/S0070-4571\(08\)10013-9](https://doi.org/10.1016/S0070-4571(08)10013-9).
- Stow, D.A.V., Hern andez-Molina, F.J., Llave, E., Sayago-Gil, M., D iaz-del R io, V., Branson, A., 2009. Bedform-velocity matrix: the estimation of bottom current velocity from bedform observations. *Geology* 37, 327–330. <https://doi.org/10.1130/G25259A.1>.
- Thi eblement, A., Hern andez-Molina, F.J., Miramontes, E., Raison, F., Penven, P., 2019. Contourite depositional systems along the Mozambique channel: the interplay between bottom currents and sedimentary processes. *Deep-Sea Res. Pt. I* 147, 79–99. <https://doi.org/10.1016/j.dsr.2019.03.012>.
- Th ole, H., Kuhlmann, G., Lutz, R., Gaedicke, C., 2016. Late Cenozoic submarine slope failures in the southern North Sea - evolution and controlling factors. *Mar. Petrol. Geol.* 75, 272–290. <https://doi.org/10.1016/j.marpetgeo.2016.04.028>.
- Toucanne, S., Jouet, G., Ducassou, E., Bassetti, M.A., Dennielou, B., Angue Minto'o, C.M., Lahmi, M., Touyet, N., Charlier, K., Lericolais, G., Mulder, T., 2012. A 130,000-year record of levantine intermediate water flow variability in the Corsica Trough, western Mediterranean Sea. *Quat. Sci. Rev.* 33, 55–73. <https://doi.org/10.1016/j.quascirev.2011.11.020>.
- Trincardi, F., Argnani, A., 1990. Gela submarine slide: a major basin-wide event in the Plio-quaternary foredeep of Sicily. *Geo Mar. Lett.* 10, 13–21. <https://doi.org/10.1007/BF02431017>.
- Tziperman, E., Gildor, H., 2003. On the mid-Pleistocene transition to 100-kyr glacial cycles and the asymmetry between glaciation and deglaciation times. *Paleoceanography* 18 (1), 1001. <https://doi.org/10.1029/2001PA000627>.
- Urliab, M., Talling, P.J., Masson, D.G., 2013. Timing and frequency of large submarine landslides: implications for understanding triggers and future geohazard. *Quat. Sci. Rev.* 72, 63–82. <https://doi.org/10.1016/j.quascirev.2013.04.020>.
- Van Rooij, D., Iglesias, J., Hern andez-Molina, F.J., Ercilla, G., Gomez-Ballesteros, M., Casas, D., Llave, E., De Hauwere, A., Garcia-Gil, S., Acosta, J., Henri et, J.P., 2010. The le danois contourite depositional system: interactions between the mediterranean Outflow water and the upper cantabrian slope (north iberian margin). *Mar. Geol.* 274, 1–20. <https://doi.org/10.1016/j.margeo.2010.03.001>.
- Vandorpe, T.P., Van Rooij, D., Stow, D.A.V., Henri et, J.-P., 2011. Pliocene to Recent shallow-water contourite deposits on the shelf and shelf edge off south-western Mallorca, Spain. *Geo Mar. Lett.* 31, 391–403. <https://doi.org/10.1007/s00367-011-0248-9>.
- Verdicchio, G., Trincardi, F., 2008a. Mediterranean shelf-edge muddy contourites: examples from the Gela and south adriatic basins. *Geo Mar. Lett.* 28, 137–151. <https://doi.org/10.1007/s00367-007-0096-9>.
- Verdicchio, G., Trincardi, F., 2008b. Shallow-water contourites. In: *Rebesco, M., Camerlenghi, A. (Eds.), Contourites. Developments in Sedimentology* 60. Elsevier Science, pp. 409–433. [https://doi.org/10.1016/S0070-4571\(08\)10020-6](https://doi.org/10.1016/S0070-4571(08)10020-6).



### Take-Home Messages

- The Middle Pleistocene Transition (MPT) represents a drastic change in morphology and an increasing accumulation rate of the outbuilding of the Gela Basin
- Before the MPT, few but large MTDs controlled to tectonic activity
- After the MPT, many but small MTDs controlled by climate (Milankovitch cyclicity).
- Increasing amplitude of the sea level changes favoured the emplacement of clinothems-related MTDs paced at Milankovitch cyclicity;
- Contributed to the presence of erosional surfaces acting as glide planes, increased the changes in oceanographic circulation, which together favoured the emplacement of contourite-related MTDs.



# Chapter 5. Tsunamis from submarine collapses along the eastern slope of the Gela Basin

---

“Tsunamis from submarine collapses along the eastern slope of the Gela Basin (Strait of Sicily)”

- Authors:
- Filippo Zaniboni (University of Bologna, Italy)
  - Gianluca Pagnoni (University of Bologna, Italy)
  - Maria A. Paparo<sup>1</sup>(University of Bologna, Italy)
  - Tugdual Gauchery (University of Bologna, Italy; *Istituto di Scienze Marine, CNR di Bologna, Italy*)
  - Marzia Rovere (*Istituto di Scienze Marine, CNR di Bologna, Italy*)
  - Andrea Argnani (*Istituto di Scienze Marine, CNR di Bologna, Italy*)
  - Alberto Armigliato (University of Bologna, Italy)
  - Stefano Tinti (University of Bologna, Italy)

- Objectives:
- Identification of the critical characterization of the MTDs in the Gela Basin
  - Assess the tsunamigenic potential of two MTDs present in the Gela Basin at relatively shallow water and their hazards for the coasts of Sicily and Malta.





# Tsunamis From Submarine Collapses Along the Eastern Slope of the Gela Basin (Strait of Sicily)

Filippo Zaniboni<sup>1,2\*</sup>, Gianluca Pagnoni<sup>1</sup>, Maria Ausilia Paparo<sup>1</sup>, Tugdual Gauchery<sup>3,4</sup>, Marzia Rovere<sup>3</sup>, Andrea Argnani<sup>3</sup>, Alberto Armigliato<sup>1</sup> and Stefano Tinti<sup>1</sup>

<sup>1</sup>Department of Physics and Astronomy "Augusto Righi", University of Bologna, Bologna, Italy, <sup>2</sup>National Institute of Geophysics and Volcanology, Bologna, Italy, <sup>3</sup>Institute of Marine Sciences, National Research Council, Bologna, Italy, <sup>4</sup>Department of Civil, Chemical, Environmental and Materials Engineering, University of Bologna, Bologna, Italy

## OPEN ACCESS

Edited by:

Jörn Behrens,  
University of Hamburg, Germany

Reviewed by:

Roger Urgeles,  
Consejo Superior de Investigaciones  
Científicas (CSIC), Spain  
Juan Horrillo,  
Texas A&M University College Station,  
United States

\*Correspondence:

Filippo Zaniboni  
filippo.zaniboni@unibo.it

Specialty section:

This article was submitted to  
Geohazards and Georisks,  
a section of the journal  
Frontiers in Earth Science

Received: 02 September 2020

Accepted: 20 November 2020

Published: 20 January 2021

Citation:

Zaniboni F, Pagnoni G, Paparo MA,  
Gauchery T, Rovere M, Argnani A,  
Armigliato A and Tinti S (2021)  
Tsunamis From Submarine Collapses  
Along the Eastern Slope of the Gela  
Basin (Strait of Sicily).  
Front. Earth Sci. 8:602171.  
doi: 10.3389/feart.2020.602171

Geophysical surveys in the eastern slope of the Gela Basin (Strait of Sicily, central Mediterranean) contributed to the identification of several episodes of sediment mass transport, recorded by scars and deposits of various dimensions within the Pleistocene succession. In addition to a huge failure called Gela Slide with volume exceeding 600 km<sup>3</sup>, the most studied events show volumes estimated between 0.5 and 1.5 km<sup>3</sup>, which is common to many other submarine landslide deposits in this region and that can therefore be considered as a characteristic value. In this work, the tsunamigenic potential of two of such landslides, the so-called Northern Twin Slide and South Gela Basin Slide located about 50 km apart along the eastern slope of the Gela Basin, are investigated using numerical codes that describe the onset and motion of the slide, as well as the ensuing tsunami generation and propagation. The results provide the wave height of these tsunami events on the coast of southern Sicily and Malta and can be taken as representative of the tsunamigenic potential of typical landslides occurring along the slope of the Gela Basin.

Keywords: margin instability, landslide dynamics, tsunamis, numerical simulation, geo-marine hazard

## INTRODUCTION

Continental margins are one of the most favorable environments for the generation of relevant landslide-tsunamis (Masson et al., 2006; Tappin, 2010; Kawamura et al., 2014), due to many factors. Amongst these, one very relevant is the continuous supply of unconsolidated sediments from rivers, which may be activated in a submarine landslide by both seismic shaking and gravitational load. When the collapse starts from relatively shallow water the tsunami generation is particularly efficient: the perturbation is more easily transmitted to the whole water column, and the sliding mass soon attains high velocities, due to the steep slope typical of such environments, that can exceed 10°.

The most adopted approach in the description of mass transport deposits (MTD) along submarine slopes considers the size distribution and their frequency, providing in this way an assessment of the potential hazard connected to these occurrences. This has been repeatedly applied for the hazard analysis in several margins around the world, mainly in North America: the United States Atlantic margin (Chaytor et al., 2009; ten Brink et al., 2014); the United States Pacific coast (McAdoo et al., 2000; Greene et al., 2006); the Puerto Rico northern platform (ten Brink et al., 2006); the Gulf of Mexico (Pampell-Manis et al., 2016; Fan et al., 2020); Alaska (Sawyer et al., 2017). The Norway margin (North-East Atlantic Ocean) as well, has been object of investigation from this point of view (Solheim et al., 2005).

TABLE 1 | List of submarine landslides with volumes comparable to the NTS and the SGBS whose tsunamigenic potential has been explored in literature.

Name	Location	Headwall depth (m)	Deposit depth (m)	Initial volume (km <sup>3</sup> )	Deposit volume (km <sup>3</sup> )	References
Thasos slide	Aegean sea	~375		1.85	3.8	Janin et al. (2019)
	Papua New Guinea	1,420			6.4	Tappin et al. (2008)
	Alboran sea	700–800		0.5	2.2–5.6	Rodriguez et al. (2017)
Al-Borani	Alboran sea	70	800		1	Macias et al. (2015)
	Atsumi escarpment near Namkai Trough, Japan				1.26	Harbitz et al. (2014)
Assi slide	Offshore southern Calabria				1.85	Ceramicola et al. (2014)
	Southern Adriatic	560	700		0.03	Argnani et al. (2011)
Gaviota mudflow	Santa Barbara channel, Southern California	380	500		0.2	Fisher et al. (2005)

In the Mediterranean Sea, the tsunami hazard connected to continental slopes is still poorly constrained. The comprehensive study by Urgeles and Camerlenghi (2013) represents the first step toward the characterization of MTDs in the whole basin. In total, 696 events have been mapped and described, spanning wide area and volume ranges, ( $10^{-3}$ – $10^5$  km<sup>2</sup>) and ( $10^{-4}$ – $10^4$  km<sup>3</sup>) respectively. Among these, 28 events are reported to have generated tsunamis, both by direct observations and by

deposits characterization. While it is not surprising the presence in this subset of huge masses (9 events in the volume range  $10$ – $100$  km<sup>3</sup>, 3 exceeding  $100$  km<sup>3</sup>), it is significant the incidence in terms of tsunami generation of smaller occurrences: 9 between 1 and  $10$  km<sup>3</sup>, and 7 below  $1$  km<sup>3</sup>. Such typology of MTD is scarcely considered in the study of non-seismic tsunami hazard, since in general they generate considerable waves only when occurring in shallow water and in proximity of the coast.

One of the main characteristics of the Mediterranean Sea is the high recurrence of the combination of these two elements: mass wasting features (scars, headwalls, canyons) are recognizable along several margins close to populated coastal communities. Some of them are here recalled:

- The Balearic Sea, where one of the most impressive underwater sliding bodies has been found along the Ebro margin, the so-called BIG'95 (Lastras et al., 2005; Lastras et al., 2007), whose tsunamigenic potential has been explored through numerical modeling (Iglesias et al., 2012; Zaniboni et al., 2014a; Løvholt et al., 2014).
- The margin of the Ligurian Sea (French-Italian Riviera), with very steep slopes and relatively frequent seismicity that can mobilize sediments (Ioualalen et al., 2014), such as the case of the 1979 Nice tsunami (Assier-Rzadkiewicz et al., 2000).
- The Tyrrhenian and Ionian margins, where many mass wasting processes covering different spatial scales have been mapped in the framework of the Italian project MaGIC (Chiocci and Ridente, 2011; Casalbore et al., 2014; Rovere et al., 2014; Casalbore et al., 2019). Among the many potential occurrences, numerical simulations for the study of the generated tsunamis have been performed for the 1977 Gioia Tauro event (Zaniboni et al., 2014b), on the Tyrrhenian Calabrian side, with an estimated volume of approximately  $0.005$  km<sup>3</sup> volume. On the Ionian side of Calabria, the Assi landslide (Ceramicola et al., 2014), has

been object of investigation (see Table 1 for details). Also, the area of Crotona, Calabria, is worth of mention, with the (indeed still questioned) homonymous potential megalandslide involving a very thick sedimentary sequence (Zecchin et al., 2018).

- The southern Adriatic Margin, where structures favoring mass transport such as the Bari Canyon (Trincardi et al., 2007) are found and pieces of evidence of vast movements exist, such as the large Gondola slide, a complex of events mobilizing deposits in the order of tens of km<sup>3</sup> (Ridente et al., 2008). The tsunamigenic potential of small landslides on the eastern margin has been investigated as well (see Table 1; Argnani et al., 2011).
- The Hyblean-Malta Escarpment (Ionian coast of Sicily), where many canyons and scars are evident (Micallef et al., 2014), and the potential for tsunami generation has been examined (Paparo et al., 2017). To mention also that the possibility of a  $5$  km<sup>3</sup> submarine landslide occurring in the occasion of the 1,693 earthquake, that might have enhanced considerably the effects of the earthquake-tsunami at a local scale (Argnani et al., 2012).
- The margins close to the coasts of Crete and Cyprus (Papadopoulos et al., 2007b; Papadopoulos et al., 2014) and along the Corinth Gulf, where on 1963 a coastal slump generated relevant waves (Papadopoulos et al., 2007a; Tinti et al., 2007).
- The African coast of the Mediterranean, that is still scarcely investigated. Some indications of collapses have been reported in Loncke et al. (2009), describing mass wasting processes covering a large volume range (from  $1$  km<sup>3</sup> to around  $500$  km<sup>3</sup>) along the Nile river submarine fan, offshore the town of Alexandria (Egypt).
- The Levantine Basin is a place of large mass transport complexes, ranging from  $35$  to  $94$  km<sup>3</sup>, occurring along the continental margin off Israel and Lebanon (see Eruteya et al., 2016, and references therein).

The above list constitutes only a subset of the potential margins that are prone to sliding in the Mediterranean Sea and can potentially generate tsunamis. In this paper, we consider the Gela Basin eastern slope (GBES from now on) that is found in the northern part of the Strait of Sicily and extends from the shelf-edge at relatively shallow water ( $\sim 200$  m) rapidly deepening to about  $900$  m depth. Studies based on

morpho-bathymetric data show that the GBES has been extensively affected by submarine mass wasting during the Late Quaternary, involving volumes of sediments in the order of magnitude of 1 km<sup>3</sup> (e.g., Minisini et al., 2007; Kuhlmann et al., 2017).

Among the recorded landslide events, we select two as representative of potential scenarios along the GBES. To evaluate their tsunamigenic potential, a comprehensive investigation through numerical codes is performed, mainly consisting into three phases: the simulation of the landslide dynamics; the computation of the tsunamigenic impulse, that is time-dependent; the simulation of wave propagation, with the assessment of the tsunami hazard for the neighboring coasts of Sicily and Malta. The analysis is limited to the effects of the tsunami on a regional scale, leaving the study of inland flooding for future publications.

The study of these two landslide scenarios along the GBES has been performed in the framework of the Italian project SPOT (Sismicità Potenzialmente innesabile Offshore e Tsunami; Antoncicchi et al., 2020), aiming at assessing the tsunamigenic potential of earthquakes and landslides possibly triggered by hydrocarbon production offshore the Italian coasts.

## THE GELA BASIN EASTERN SLOPE

### Geological Setting

The Gela Basin is a bathymetric depression of limited water depth (up to 936 m) located south of central Sicily. It represents the foreland basin of the Maghrebian thrust belt of Sicily (Argnani et al., 1987; Lickorish et al., 1999), and is filled by up to 2000 m of turbidites and pelagic sediments of Pliocene-Quaternary age. The sedimentation rate from Pliocene to Middle Pleistocene (800 ka) was 150 m/Myr and reached 900 m/Myr in the last 800 kyr (Gauchery et al., 2021). The upper part of the sedimentary fill is characterized by abundant mass transport deposits. The northern margin of the basin is partly shaped by the arcuate front of the Gela Nappe (Argnani, 1987), which represents the most recent Maghrebian thrust front (Figure 1). A sedimentary prograding set, fed from the north, developed on top of the Gela Nappe. This prograding set extends eastward, away from the thrust front, fringing the Hyblean Plateau. The most recent cliniform of this prograding set represents the northern and eastern bathymetric slope of the Gela Basin.

The eastern slope, denoted as GBES here, has been the site of several mass transport events, as evidenced by the abundant slide scars which are visible on the morpho-bathymetry map (see Figures 1B,C), and as reported in detailed studies of selected sectors (e.g., Minisini et al., 2007). The morphological evidence indicates that complex and recurrent sediment failures affected the GBES during the Late Quaternary.

### Mass Failures Along the GBES

Mass transport events characterize the whole extent of the GBES, and in some cases, the reconstruction of the sliding mechanism and sequence is quite difficult, due to the superposition of different occurrences.

Starting from the north, the first occurrence is the Gela Slide (GS, see Figure 1A), a 630 km<sup>3</sup> landslide affecting an area of more than 1,500 km<sup>2</sup>, characterized by a few km downslope movement and occurred presumably in the Late Pleistocene. First described in the geological work by Trincardi and Argnani (1990), this collapse has been taken as one of the scenarios in the study of tsunami hazard on the coasts of the Malta archipelago by Mueller et al. (2020). According to their tsunami simulations, the flow depth exceeded 10 m on the island of Gozo, which was hit around 18 min after onset of the landslide.

Moving to the east of the GS, several other landslides have been recognized by Trincardi and Argnani (1990) and in more recent investigations (Minisini and Trincardi, 2009; Kuhlmann et al., 2017). The most interesting cases are the so-called Twin Slides located about 30 km far from the GS (see Figure 1B). These collapses, that occurred probably simultaneously in Late Holocene, are characterized by well-defined scars (see the headwalls, Figure 1B), deepening from 200 to 500 m water depth with well-recognizable deposits of comparable size at the toe (enclosed within the dashed-red and dashed-green boundaries respectively), down to 700 m b.s.l. The estimated volume is slightly less than 0.5 km<sup>3</sup> for both slides. The Northern and Southern Twin Slides (NTS and STS) have been interpreted as the final stage of a very complex sliding sequence, tentatively reconstructed in Kuhlmann et al. (2017), that started with a larger “Father Slide” (black line in Figure 1B) 87 ka ago and that repeats periodically about every 10 kyr.

Another submarine slide is placed southward, about 40 km north of the Malta archipelago (Figure 1C). In this work, it is named South Gela Basin Slide (SGBS) according to Gauchery et al. (2021). Pieces of evidence of collapse are very clear: a large scar at the shelf-edge, more than 5 km long (blue line in Figure 1C), with a 5° average slope from 200 to 500 m water depth; a large deposit, easily recognizable at the toe of the slope (350–550 m water depth), covering an area of more than 50 km<sup>2</sup> (delimited by the dashed-blue contour in Figure 1C).

In this paper, we have opted to compute the tsunamis produced by two slides out of the many that have been identified along the GBES, namely the NTS and the SGBS. Although there is not any direct piece of evidence of the occurrence and the effects of such tsunamis, nonetheless exploring these scenarios is important mainly because 1) the involved volumes are the most frequently observed in the Mediterranean Sea (see the frequency distribution in Urgeles and Camerlenghi, 2013) and 2) landslides with comparable volumes are known to produce relevant (though local) waves, which stresses the need to systematically include also such sources in tsunami hazard evaluation. Some interesting examples of tsunami studies from this kind of landslides are listed in Table 1.

## NUMERICAL METHODS

The study of the tsunamis associated with submarine mass movements along the GBES is performed through a well-

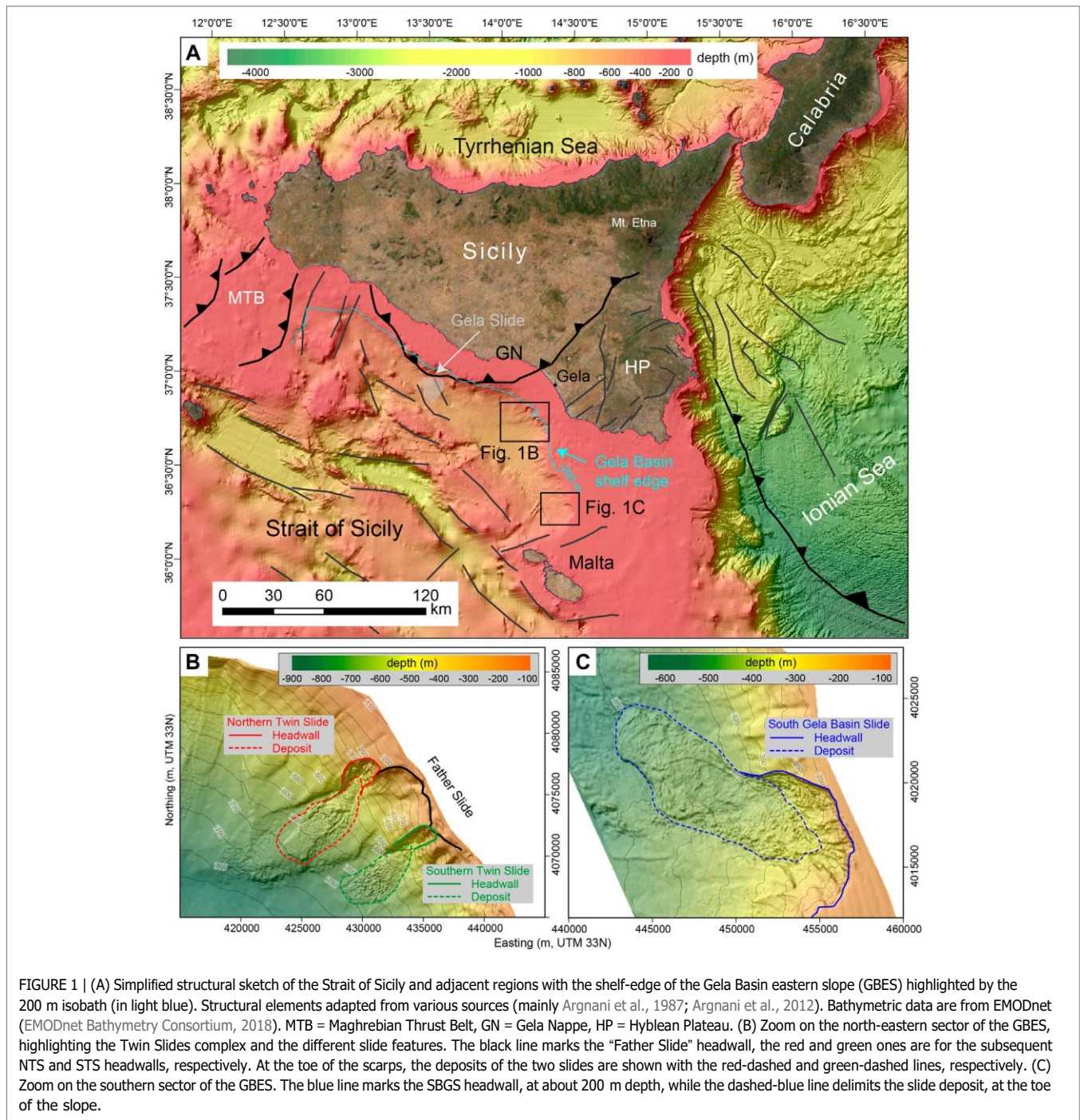


FIGURE 1 | (A) Simplified structural sketch of the Strait of Sicily and adjacent regions with the shelf-edge of the Gela Basin eastern slope (GBES) highlighted by the 200 m isobath (in light blue). Structural elements adapted from various sources (mainly Argnani et al., 1987; Argnani et al., 2012). Bathymetric data are from EMODnet (EMODnet Bathymetry Consortium, 2018). MTB = Maghrebian Thrust Belt, GN = Gela Nappe, HP = Hylean Plateau. (B) Zoom on the north-eastern sector of the GBES, highlighting the Twin Slides complex and the different slide features. The black line marks the “Father Slide” headwall, the red and green ones are for the subsequent NTS and STS headwalls, respectively. At the toe of the scarps, the deposits of the two slides are shown with the red-dashed and green-dashed lines, respectively. (C) Zoom on the southern sector of the GBES. The blue line marks the SBGS headwall, at about 200 m depth, while the dashed-blue line delimits the slide deposit, at the toe of the slope.

tested numerical procedure that has been developed in-house and applied to several cases of landslide-generated tsunamis (Zaniboni et al., 2014b; Ceramicola et al., 2014; Zaniboni and Tinti, 2014; Zaniboni et al., 2016; Zaniboni et al., 2019; Gallotti et al., 2020; Triantafyllou et al., 2020). Under the assumption that the submarine slope will fail, the simulation sequence covers the whole process including 1) the dynamics of the sliding motion, 2) the tsunamigenic impulse caused by the movement of the mass along the sea bottom, and 3) the propagation of the tsunami over the computational domain.

## Landslide Dynamics

When the sliding body reaches instability conditions, it starts moving along the slope. The dynamics of such motion is computed through the code UBO-BLOCK1, which implements a Lagrangian approach. The sliding body is partitioned into a set of interacting blocks, whose centers of mass (CoMs) motion is determined by the interaction with the surrounding environment, i. e., by the body forces (gravity, buoyancy), the surface stresses (basal friction, water drag on the exposed surfaces), and the internal interactions between blocks. The blocks conserve their

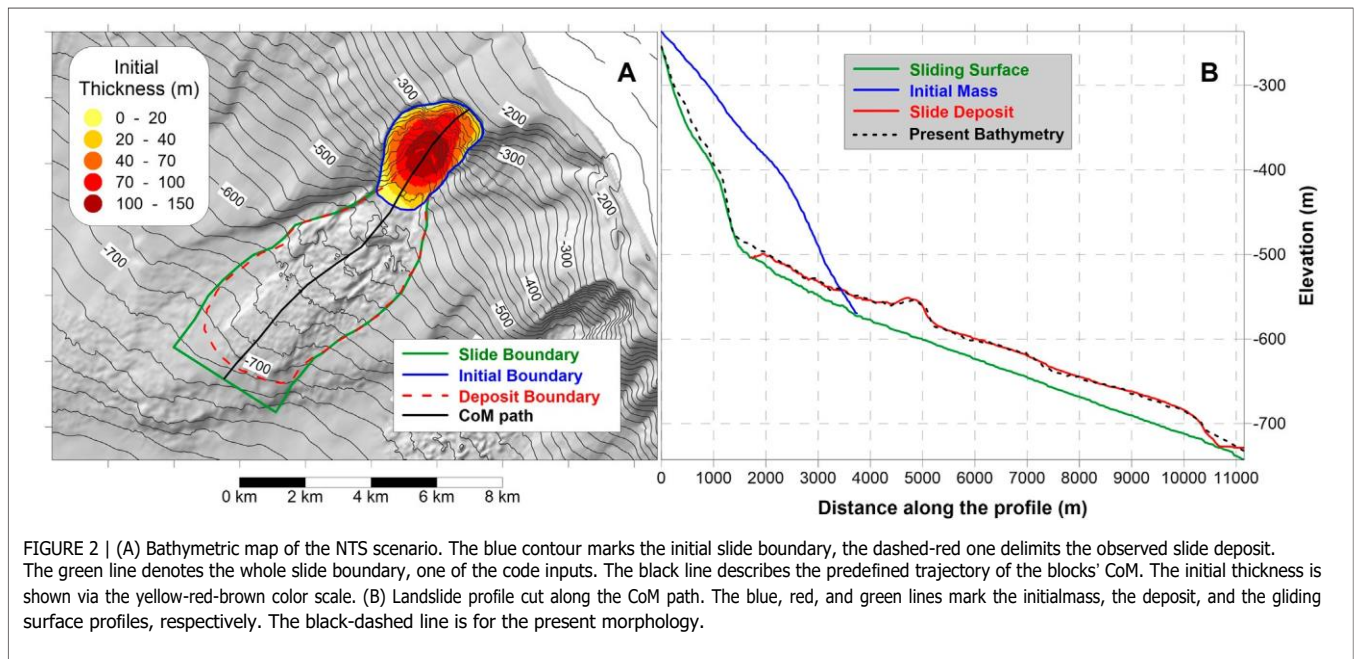


FIGURE 2 | (A) Bathymetric map of the NTS scenario. The blue contour marks the initial slide boundary, the dashed-red one delimits the observed slide deposit. The green line denotes the whole slide boundary, one of the code inputs. The black line describes the predefined trajectory of the blocks' CoM. The initial thickness is shown via the yellow-red-brown color scale. (B) Landslide profile cut along the CoM path. The blue, red, and green lines mark the initial mass, the deposit, and the gliding surface profiles, respectively. The black-dashed line is for the present morphology.

mass and cannot penetrate nor superimpose with each other. This approach allows one to quantify how much the slide changes its shape during its descent, a crucial factor in tsunami generation. The simulation is stopped when the mass exits the computational domain, or when the mean velocity lowers a predefined threshold.

The application of UBO-BLOCK1 requires as input:

- i. The undisturbed sliding surface;
- ii. The upper surface of the initial sliding mass;
- iii. The predefined CoM trajectory;
- iv. The lateral boundaries of the sliding surface.

Further details on the code can be found in Tinti et al. (1997).

## Tsunami Generation and Propagation

The motion of the sliding body on the sea bottom changes the sea depth and mobilizes the whole water column, generating a perturbation that propagates throughout the water body. The tsunami impulse provided by the slide is not instantaneous, since the time scale of the two phenomena (landslide motion – wave propagation) is comparable, in contrast to the process of earthquake-generated waves, where the source can be considered instantaneous.

The tsunamigenic impulse is computed as the time history of the seabed change due to the passage of the mass, over each node of the tsunami computational grid. This perturbation is filtered with the water depth through a function cutting higher frequencies. These tasks are performed by a specific code, named UBO-TSUIMP, which is described in full detail in Tinti et al. (2006).

The wave propagation is modeled by the application of the classic non-linear shallow-water equations (SWE), that are solved by a finite difference approach (leap-frog numerical scheme) implementing the staggered grids technique. When the computational grid boundary is the open sea, a pure transparency condition is imposed, while the

interaction with the coast is handled in two possible ways: in case of land inundation, the model implements the moving boundary technique, considering the flooded inland cells as part of the bathymetry; when the no-inundation condition is selected, the coast is considered as a vertical wall and the wave is reflected seaward. The choice between the two approaches depends on the aims of the investigation. If one wants to evaluate the tsunami hazard at a regional scale over a wide domain, the second is preferable. If the interest is on the effect on coastal communities and buildings, one should select the first option. The two alternatives usually require domains with different characteristics: high resolution to compute inundation, low resolution to simulate propagation in oceanic regions. The code, named UBO-TSUFD, includes also the possibility to manage domains with different spatial steps implementing the nested-grid technique, useful if a heterogeneous resolution is convenient for the simulation.

The input datasets needed to run the code are:

- i. The tsunami computational grid, or set of grids;
- ii. The tsunami initial condition.

This code is more extensively described in Tinti and Tonini (2013). Its applications are reported in the same references cited in the previous section. Besides, one can find an application to a case of an earthquake-tsunami in Loreto et al. (2017).

## BUILDING THE LANDSLIDE SCENARIOS AND THE TSUNAMI COMPUTATIONAL GRID

In this paper we study the NTS and the SGBS since we consider their volume as typical of tsunamigenic mass movements in this region, and, more in general, because events of this size require

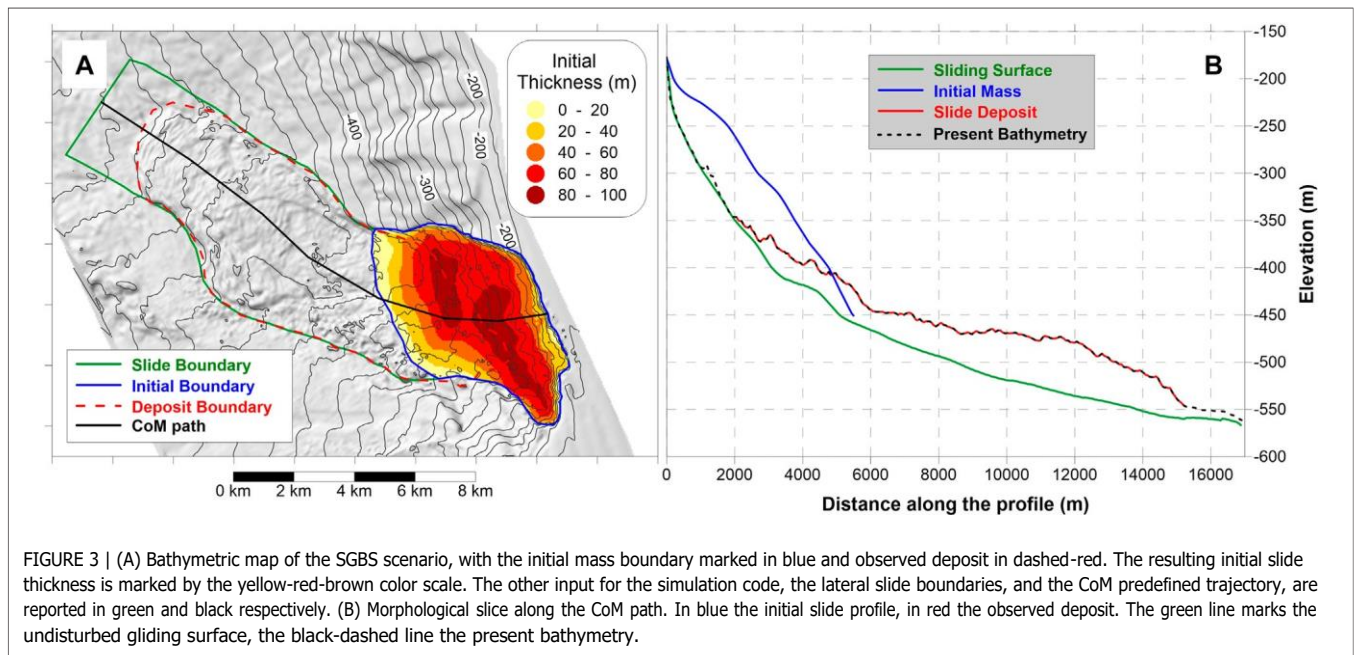


FIGURE 3 | (A) Bathymetric map of the SGBS scenario, with the initial mass boundary marked in blue and observed deposit in dashed-red. The resulting initial slide thickness is marked by the yellow-red-brown color scale. The other input for the simulation code, the lateral slide boundaries, and the CoM predefined trajectory, are reported in green and black respectively. (B) Morphological slice along the CoM path. In blue the initial slide profile, in red the observed deposit. The green line marks the undisturbed gliding surface, the black-dashed line the present bathymetry.

more attention and investigations. The tsunamis from NTS and SGBS are expected to be relevant for the coasts of southern Sicily and the Malta archipelago, and this consideration has guided us in building the grids for tsunami simulations.

### Landslide Scenario for NTS

The simulation of the landslide motion requires the definition of the four elements listed in *Landslide Dynamics* Section. These have been devised mainly on morphological considerations, starting from the present seabed bathymetry given in Figure 2. In the NTS scenario, the sliding surface (green line in Figure 2B) coincides with the slide scar in the steeper part of the margin, uncovered after the sliding event down to 500 m depth. The remaining portion, now hidden by the slide deposit, has been inferred by extending the outer isobaths inside the sliding boundary (green boundary, Figure 2A) since these are supposed to represent the undisturbed surface under the slide deposit. After the sliding surface has been reconstructed, it is straightforward to obtain the sliding deposit, simply by difference with the present bathymetry (red line, Figure 2B). Though not essential for the simulation itself, the observed final distribution of the mass is very useful as a constraint for the parameters governing the sliding model. The initial mass has been obtained simply by filling the scar, again extending the isobaths inside the initial landslide contour (blue line, Figure 2A). The result is a body with volume of  $0.46 \text{ km}^3$ , consistent with the deposit at the toe of the slope, covering an area of almost  $7 \text{ km}^2$ . The initial slide mass distribution, obtained as the difference with the gliding surface, evidences a thicker central part, reaching 150 m (Figure 2A). The CoM path follows the direction of local maximum steepness, while the slide lateral boundaries (Figure 2A, in green) follow the observed slide deposit (red line, Figure 2A).

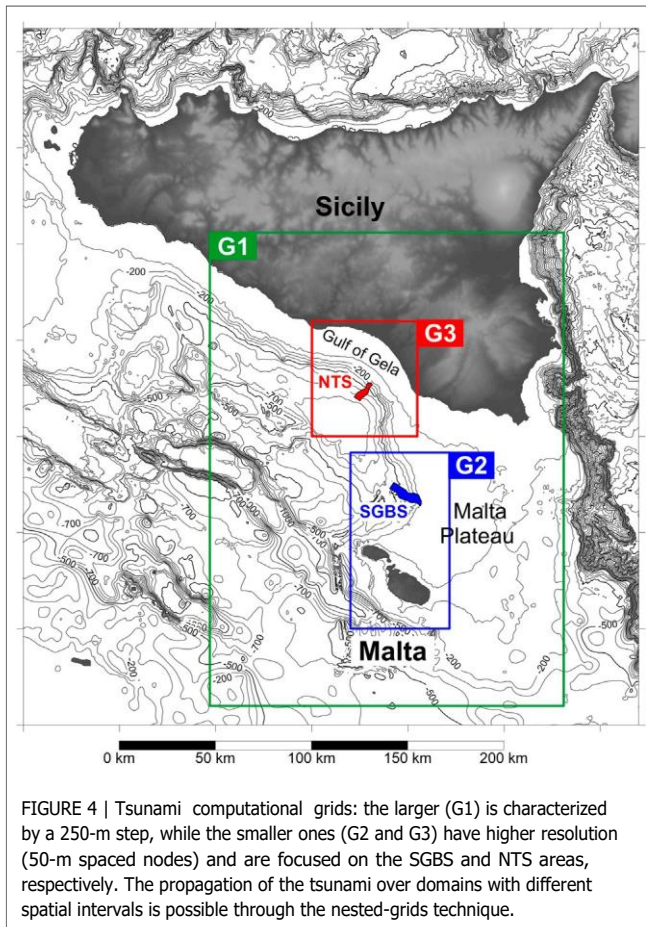
### Landslide Scenario for SGBS

The second landslide scenario selected is placed around 50 km south of the NTS, closer to the Malta archipelago. The same procedure followed for the NTS has been used for the preparation of the SGBS simulation input. The sliding surface follows the uncovered steeper part of the slope and under the present deposit, is inferred by continuity with the outer isobaths (green profile in Figure 3B). The initial mass is obtained by filling the scar inside the respective boundary (blue boundary in Figure 3A), providing an initial sediment body with a volume of  $1.48 \text{ km}^3$  (three times bigger than NTS), over an area of more than  $26 \text{ km}^2$  (four times larger than NTS), implying a smaller thickness (maximum less than 100 m, Figure 3A). The final deposit is obtained by the difference between the present morphology and the sliding surface. As in the previous case, the obtained volume has been used as a further constraint on the reconstruction of the initial mass, since the two amounts have to be compatible.

### Tsunami Computational Grids

The simulations of the landslide-generated tsunamis require a regularly spaced computational grid. The investigated area is shown in Figure 4: the larger grid (G1, in green) covers the southern corner of Sicily, more specifically the SE coast watered by the Strait of Sicily to the south and by the Ionian Sea to the east. This grid has been built with a spatial step of 250 m. The source data come from the EMODnet public database, covering this area with a resolution of about 115 m.

Due to the limited extent of the tsunami sources, that would have been described by too few nodes with the resolution of grid G1, it was necessary to make use of finer domains, covering the two tsunami generation areas. Grid G2, marked in blue in Figure 4, accounts for the SGBS scenario and includes the Malta archipelago as well; grid G3 (in red) covers the NTS case and the coast of the Gulf of Gela. Both computational



grids have been built with a 50 m spatial step by combining a swath bathymetry dataset acquired with 30–100 kHz multibeam systems and an overall 50 m resolution along the slope (Gauchery et al., 2021), with the already cited EMODnet bathymetry used to fill the data gaps.

This grids configuration (a larger 250-m mesh, G1, and two smaller 50-m domains, G2 and G3) allows an acceptable and detailed reconstruction of the landslide dynamics and their tsunamigenic impulse in the source areas, and sufficient coverage of the tsunami propagation in the Strait of Sicily. The simulation with this grid set is possible through the nested-grid technique implemented in the model UBO-TSUF, allowing to account for the passage of the tsunami wave across boundaries of contiguous computational domains with different resolutions.

## LANDSLIDES SIMULATIONS

The code UBO-BLOCK1 provides the complete time-history of the motion of each block composing the landslide mass. As a consequence, the simulation accounts for the mass shape variation during the descent, a factor that deeply influences

the perturbation produced on the water column, necessary to evaluate the time-dependent tsunamigenic impulses associated with the mass moving along the seabed.

The comparison with the observed deposit provides important constraints on the simulation parameters governing the slide motion. Concerning the friction coefficient, a value of 0.03 provided the best fit: this is a typical value for submarine landslides. The drag coefficients have been selected basing on values coming from previous applications, simulating similar failures. For the superficial stress, the value chosen for the drag parameter is  $C_d = 0.2$ ; as for the frontal drag,  $C_f = 0.5$  (for a more detailed description of these coefficients and of their range of values, refer to Tinti et al., 1997). Both sliding bodies are affected by a considerable elongation, as inferable also from the profiles of Figures 2,3: NTS passes from 4 km to more than 8 km at the end of the motion; SGBS from 6 km to more than 12 km. The values adopted for the internal interaction parameters, governing the mass deformation, have been tuned to account for this behavior.

Figure 5 reports some of the motion features of the two scenarios. Panels A and B report the velocity evolution with time: it can be noticed that the two curves are similar, with an initial abrupt acceleration phase followed by a slower deceleration, typical of masses moving along steep margins, and then reaching the flat area at their toe. The NTS reaches the mean velocity peak (15 m/s) after around 100 s, while for SGBS the peak is slightly smaller, and attained at around 200 s. The black dots mark the individual CoM velocity record: notice that there is a generalized spread around the mean values (continuous line, red for NTS, and blue for SGBS), which is a natural consequence of the mass elongation during the descent. The mass comes to rest after almost 700 s for NTS and more than 850 s for SGBS, but it can be noticed that some blocks stop much earlier (already after 300 s for NTS; at 500 s for SGBS), while other have still residual velocity when the simulation is stopped.

The block thickness evolution is represented in Panels C and D of Figure 5: reflecting the elongation and spreading at the end of the motion, the sliding mass gets thinner, passing from an average of 75 m to around 20 m for NTS, and from 58 m to 31 m for SGBS. It is noticeable that in correspondence with the velocity peak, the block thickness increases considerably, especially for the NTS where some blocks reach height values of more than 120 m, with obvious influence on tsunami generation.

A typical indicator of the tsunamigenic efficiency is the Froude number,  $Fr$ . This is computed as the ratio between the horizontal component of the slide velocity and the wave phase speed ( $\sqrt{gh}$  with  $g$  gravity acceleration and  $h$  local depth). When the two quantities are equal, the energy transfer from the slide to the water is maximum, and the resonance condition is attained ( $Fr = 1$ ). For values lower than 1 (subcritical condition, typical of deep slides) the wave moves faster than the slide; for  $Fr > 1$  (supercritical condition, typical of fast subaerial slides entering the water, usually occurring close to the generation area) the mass runs away from the generated wave. In the present cases, one can notice that the motion is always subcritical (panels E and F, Figure 5). The maximum

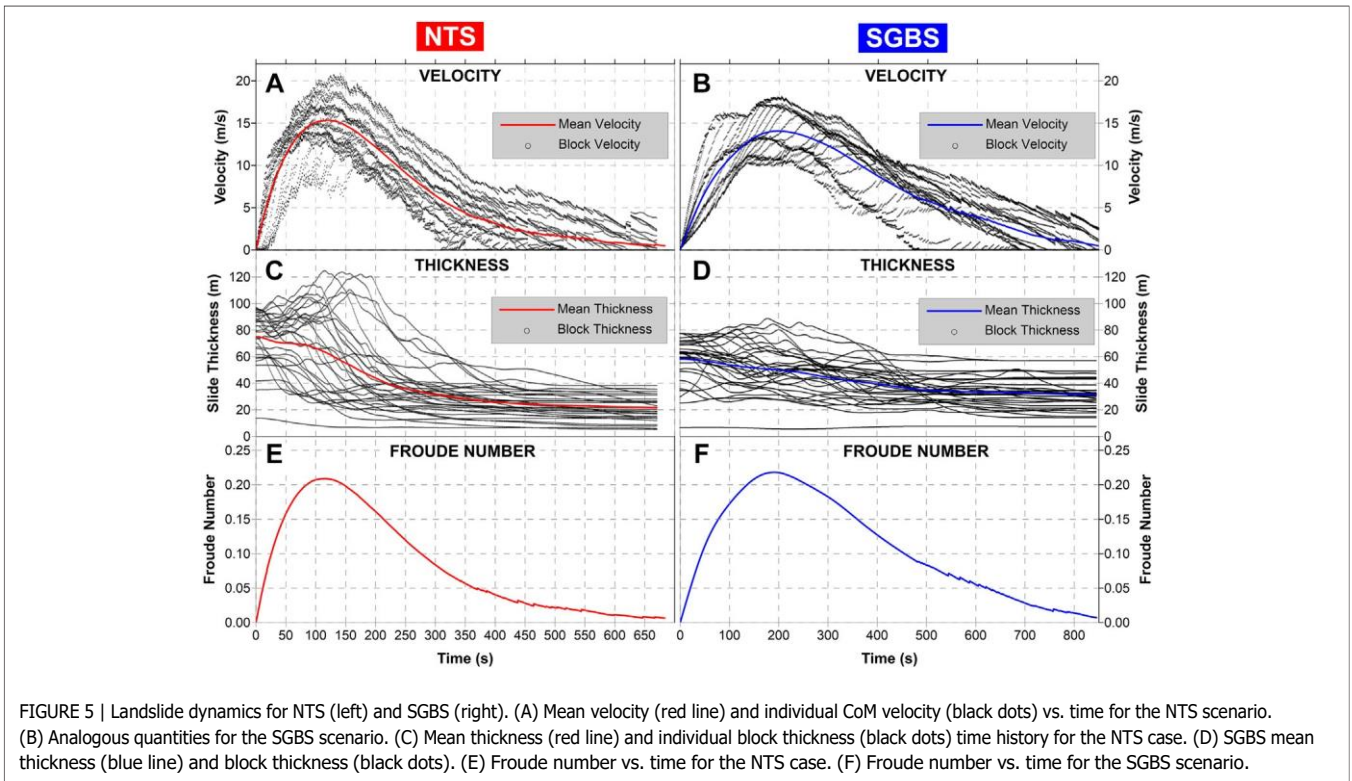


FIGURE 5 | Landslide dynamics for NTS (left) and SGBS (right). (A) Mean velocity (red line) and individual CoM velocity (black dots) vs. time for the NTS scenario. (B) Analogous quantities for the SGBS scenario. (C) Mean thickness (red line) and individual block thickness (black dots) time history for the NTS case. (D) SGBS mean thickness (blue line) and block thickness (black dots). (E) Froude number vs. time for the NTS case. (F) Froude number vs. time for the SGBS scenario.

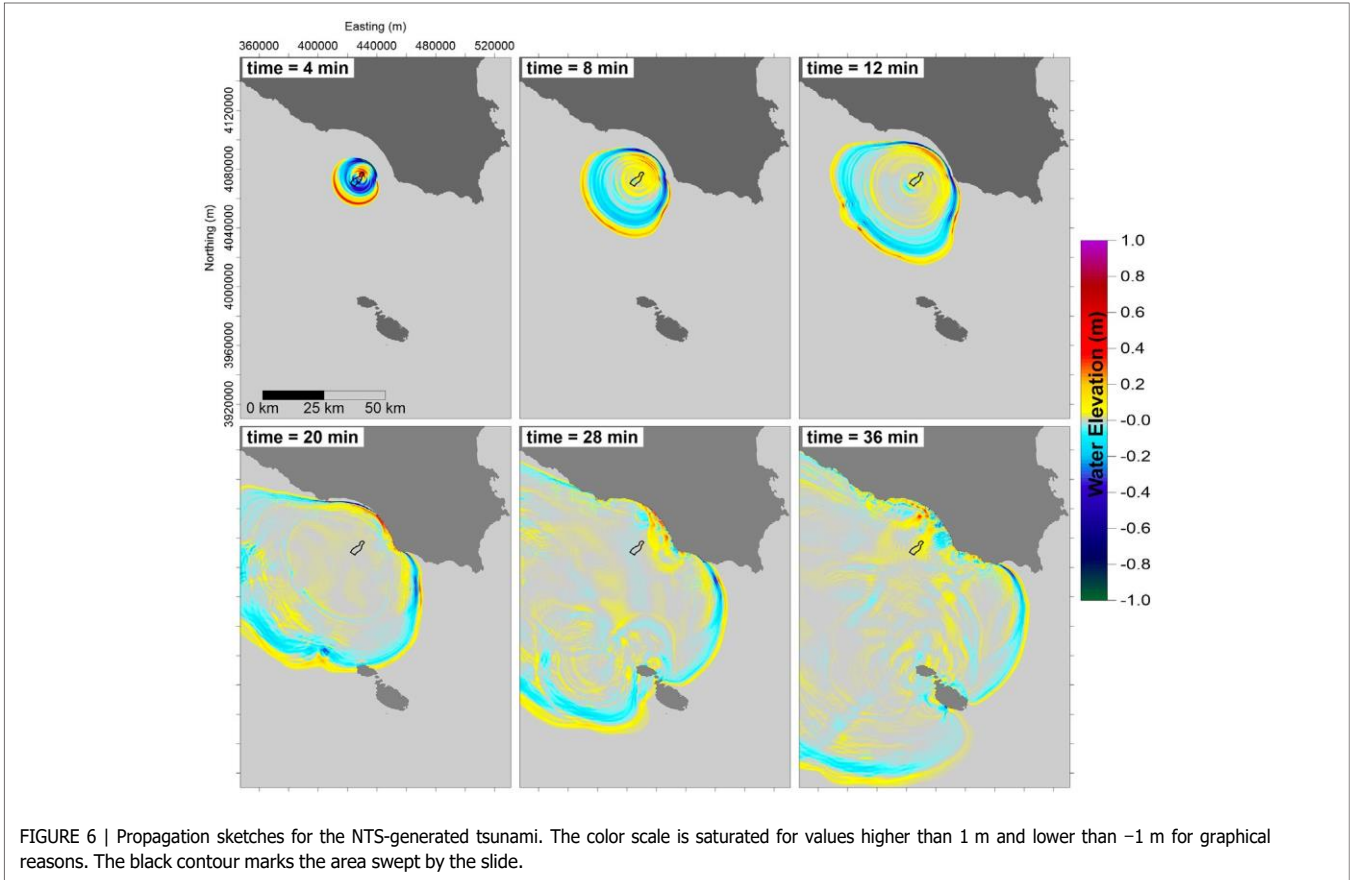
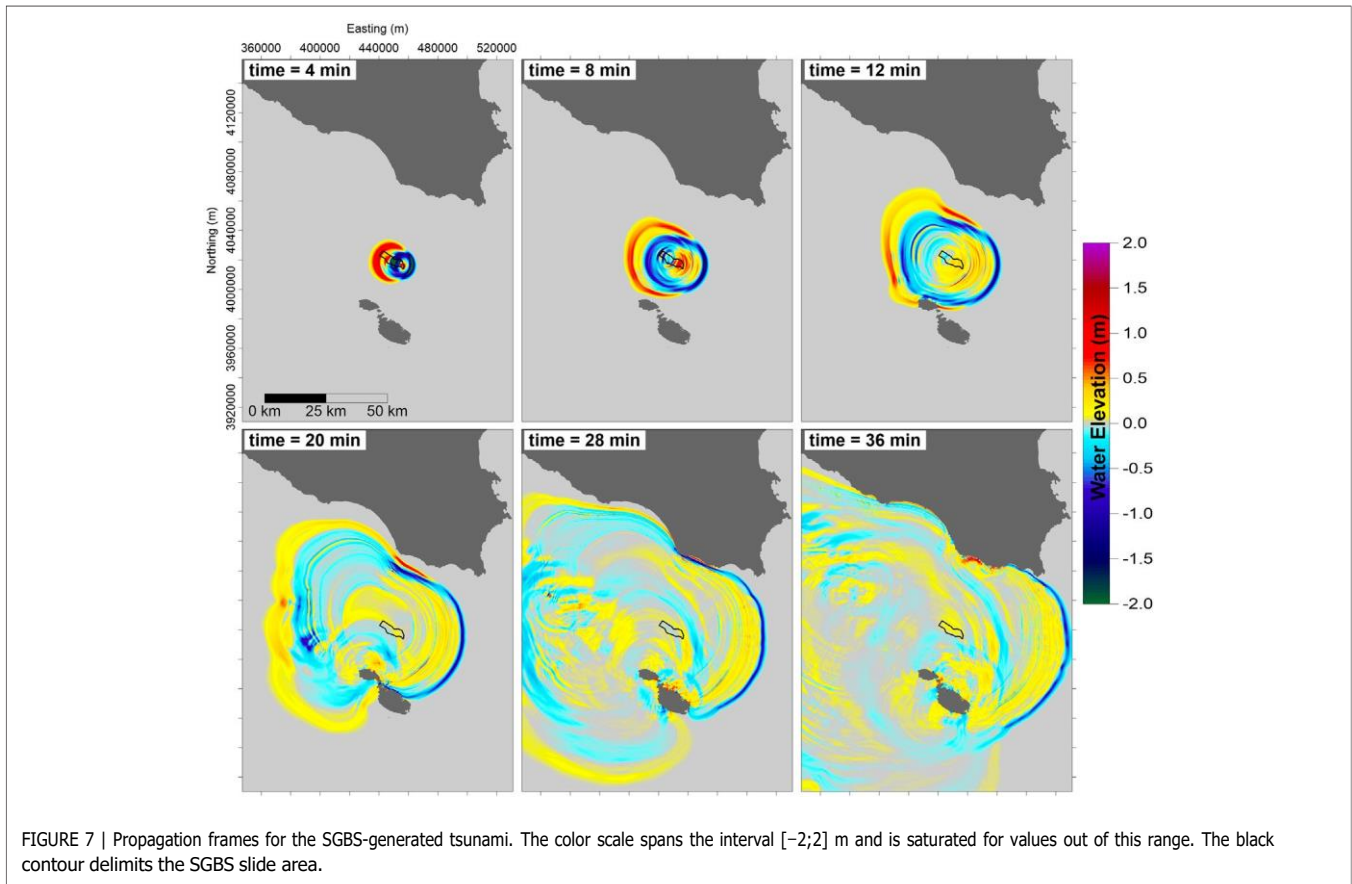


FIGURE 6 | Propagation sketches for the NTS-generated tsunami. The color scale is saturated for values higher than 1 m and lower than -1 m for graphical reasons. The black contour marks the area swept by the slide.



value of  $Fr$  (0.2) is attained in correspondence with the velocity peak for both slides.

## TSUNAMI PROPAGATION

Tsunami simulations have been run with the linear version of the code UBO-TSUFDF, without considering land inundation. Concerning the Malta archipelago where coasts have complex morphology, this task would require more refined grids, to describe better the many small gulfs and inlets characterizing especially the northern coast.

The propagation of the NTS-generated tsunami is shown in Figure 6. In the first frames (4 and 8 min) the typical circular radiation of landslide-tsunamis can be noticed, with a positive front propagating in the same direction as the slide motion (offshore, toward south-west) and a negative signal on the opposite side. This entails that the tsunami firstly manifests with a sea withdrawal at the Sicily coast, a factor that can be important in terms of alert management. The wave hits the coasts after about 12 min, with the negative front, which is soon followed by a positive wave, meaning sea-level increase. Within 20 min the whole Gulf of Gela (see Figure 2 for geographic location) is affected by the wave, the same happens for Gozo (the north-westernmost island of the Malta archipelago), that in contrast to Sicily is hit by a positive

wavefront. Notice that the travel time is very similar to the one obtained in Mueller et al. (2020) for a much bigger mass, the Gela Slide. The 36-min sketch shows that at this time almost the entire Malta islands are affected by the tsunami. Finally, notice the strong deceleration effect of the Malta Plateau, the shallow-water area between Sicily and Malta (whose location is shown in Figure 4 as well), on the wave propagation due to bathymetry and shoaling mechanisms.

The SGBS-tsunami propagation sketches (Figure 7) show some similarities with the NTS case, especially in the first frames, i. e., the circular radiation from the source and the polarity of the wavefront (positive westward, negative eastward). Conversely, the SGBS tsunami is generally higher than the NTS one. Gozo island is attacked by a positive front between 8 and 12 min, and the whole Malta archipelago within 28 min. Considering the Sicily coasts, one can notice that already at the 12 min frame the wavefront tends to deform, due to the interaction with the bathymetry. The first affected coastal stretch is the southern extreme of the Gulf of Gela, between 20 and 28 min. At this time a positive signal reaches the coast. Here the tsunami signal deceleration in the Malta Plateau area is evident as well, with the negative front (in blue) taking several minutes to cross this sea region.

Interesting insights on the tsunami characteristics come from Figure 8, representing the maximum sea surface elevation computed for each node of the tsunami grid, during the whole

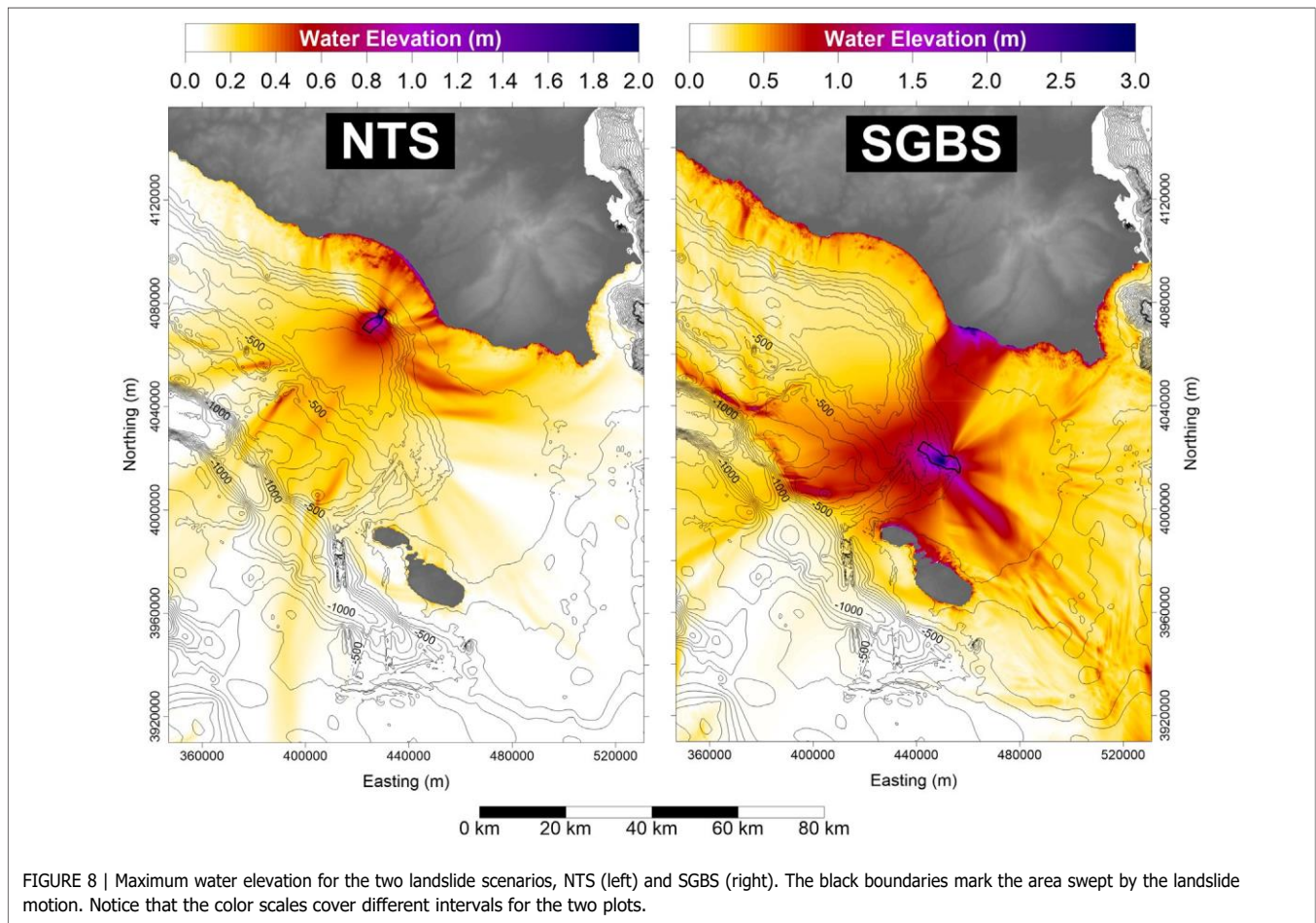


FIGURE 8 | Maximum water elevation for the two landslide scenarios, NTS (left) and SGBS (right). The black boundaries mark the area swept by the landslide motion. Notice that the color scales cover different intervals for the two plots.

tsunami propagation history. This plot provides a useful glance at the spatial distribution of the tsunami energy.

One can notice that most of the tsunami energy in the NTS scenario is captured within the Gulf of Gela. Some tsunami beams are visible, evidencing preferential directions for water maximum elevation. Noticeable are two rays hitting the central part of the gulf, two more affecting its eastern end, and another one moving south-eastward. The Malta archipelago coasts seem scarcely affected by waves generated from the NTS scenario.

Concerning the SGBS (Figure 8 – right panel), the pattern is quite different. The Malta islands are hit by relevant maximum waves, reaching also 2 m. A strong beam heads towards the Malta Plateau, south-east, but the most noticeable feature is the high concentration of energy directing towards the coast of Sicily, east of the Gulf of Gela. Here the water elevation exceeds 3 m. Conversely, the coasts of the gulf itself are moderately protected, since most of the tsunami energy is attracted to the east. The SGBS scenario, though more distant, produces more relevant and diffused effects on the Sicily coasts than the NTS scenario.

These observations are confirmed by Figure 9, representing the maximum water elevation along the coast of Sicily. The water height is computed along the 5-m isobath since the linear version of the simulation code with fixed coastal boundary has been run and no inundation has been computed. Therefore, the results described here

can be considered as underestimations of the effective run-up heights in terms of hazard, also considering that non-linear terms would amplify the waves when approaching the coast.

Figure 9 confirms that the NTS tsunami is mainly confined within the Gela Gulf (between points #1 and #4), where a maximum of 3 m is reached close to Marina di Acate (node #3) and another 2 m peak can be observed around node #4 (Santa Croce Camerina). Out of this coastal stretch, about 80 km long, the wave height rapidly drops below 1 m and is almost negligible west of Licata (#1) and beyond Capo Passero (point #6).

The curve representing SGBS coastal water height, on the other hand, shows the maximum elevations reached between points #4 and #5, i. e., the area towards which the tsunami beam mentioned above (Figure 9) is directed. Here waves reach 3.5 m and remain higher than 2 m for at least 30 km along the coast. Within the Gulf of Gela, the water elevation oscillates around the value of 1.5 m, comparable then to the NTS case. West of Licata (#1) the wave height remains in the range of 1–1.5 m for almost the entire coast. On the east, similar behavior is observed, with oscillations exceeding 1.5 m towards Capo Passero (node #6) and also farther, along the eastern coast of Sicily. In general, the SGBS affects the coast of Sicily with waves exceeding 1 m for almost the whole coastal stretch covered by the simulation, 300 km long, dropping down to 1 m elevation only at the plot borders.

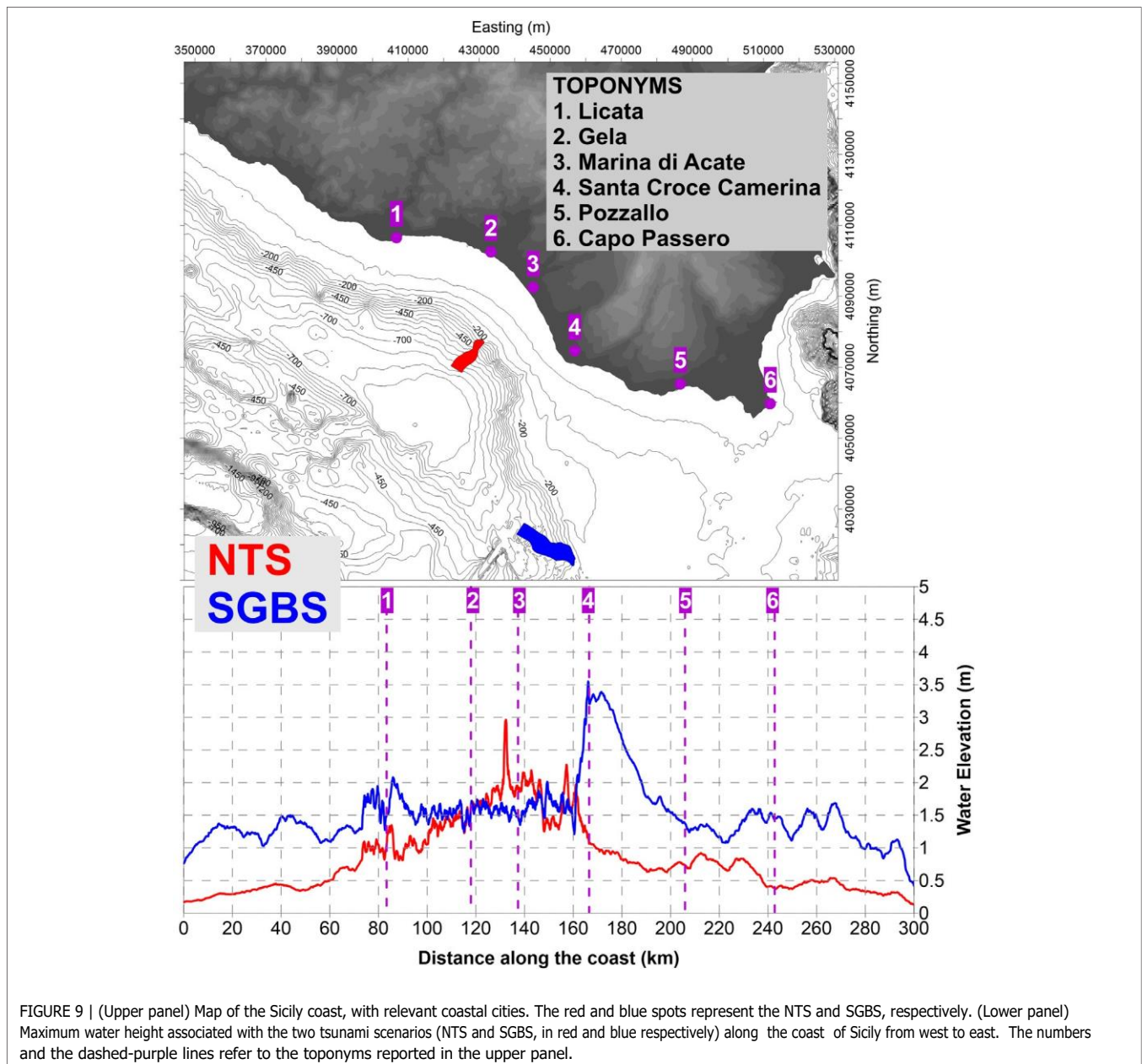


FIGURE 9 | (Upper panel) Map of the Sicily coast, with relevant coastal cities. The red and blue spots represent the NTS and SGBS, respectively. (Lower panel) Maximum water height associated with the two tsunami scenarios (NTS and SGBS, in red and blue respectively) along the coast of Sicily from west to east. The numbers and the dashed-purple lines refer to the toponyms reported in the upper panel.

Focusing the attention on the Malta archipelago, we consider the maximum water elevation along the 20-m isobath rather than along the 5-m isoline (Figure 10). This choice is motivated by the fact that the bathymetry in the shallow coastal zone here is quite complex, being characterized by numberless small inlets, bays, promontories that could be well described only by high-resolution grids, which in turn would require heavier computational costs. The results we will show on the 20-m isoline are expected to be underestimates of the maximum tsunami waves since they do not account for possible resonance amplification nor tsunami energy focusing. Nonetheless, they provide a good basis to evaluate the overall impact of the tsunami on the Malta islands.

The NTS tsunami produces limited effects, mainly on the northern part of the Gozo island, where 0.4 m height is reached.

The inlets along the northern coasts are affected by waves at most of some tens of centimeters, that can be considered negligible in terms of human hazard but can be amplified by resonance effects, producing heavy damage on boats and harbor facilities.

The SGBS source area is closer to the Malta archipelago, producing relevant effects especially along the northern coasts. Gozo island is the most affected, with the north-western coast hit by waves exceeding 2 m. Also, the northern half of the main Malta island is impacted by a wave at least 1.5 m high, with relevant waves entering St. Paul's Bay (point #1 in Figure 10), the most populated town of the island, with a substantial increase of population in the tourist season. Also, the inlet of La Valletta (point #2 in Figure 10) is affected by waves higher than 1 m. All

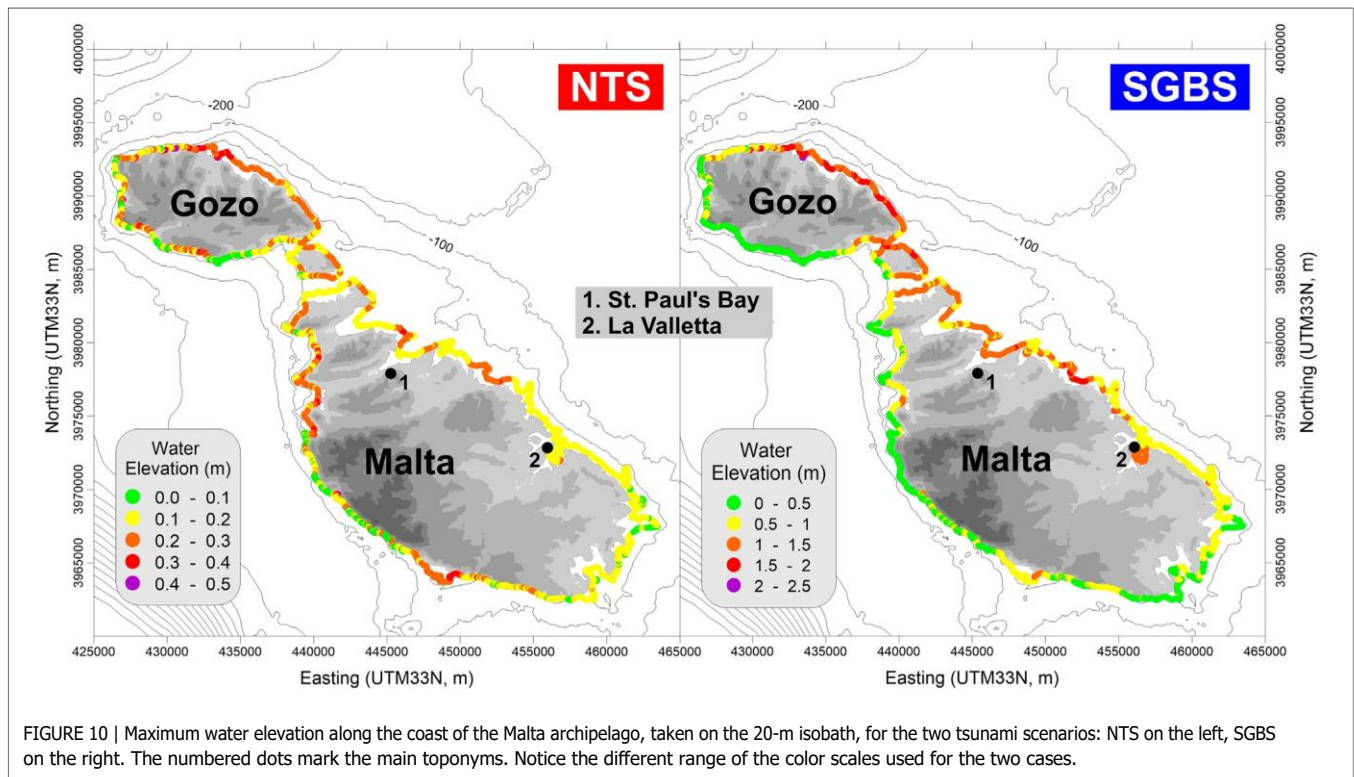


FIGURE 10 | Maximum water elevation along the coast of the Malta archipelago, taken on the 20-m isobath, for the two tsunami scenarios: NTS on the left, SGBS on the right. The numbered dots mark the main toponyms. Notice the different range of the color scales used for the two cases.

the southern coast, on the contrary, seems protected with maximum waves barely reaching half a meter.

## CONCLUSIONS

In this paper, we have studied two cases of tsunamis produced by mass failures along the GBES, selected mainly for two reasons. First, high-quality seafloor geomorphological data are available, accurately describing the scar and the slide deposit, which allows a suitable reconstruction of the landslide sources and provides useful constraints for the simulation model. Moreover, these slides can be considered representative of typical failure episodes along the slope.

In the framework of the SPOT project, aimed at assessing the influence of local earthquakes on tsunami generation and mobilization of sediments, the stability analysis of the two landslide scenarios have been performed (see results in Supplementary Appendix A). They showed that failures in the northern sector of the GBES, where the NTS is located, can be activated with a return period of few thousands of years. More in the south, farther away from the seismic faults, at least according to the present knowledge of the offshore tectonics, failures like the SGBS cannot be explained by invoking seismic load, and other destabilizing causes have to be found, which implies further research efforts.

Mass movements along the GBES require particular attention since they occur in relatively shallow water. Moreover, in the initial stage, they soon attain large velocity, due to the high steepness of the continental slope ( $5^{\circ}$ – $10^{\circ}$ ). The combination of

these two elements (large velocity and shallow water) enhances the tsunamigenic potential in a considerable way.

The tsunami simulations show that masses such as the NTS and the SGBS can produce relevant waves impacting coastal stretches from tens to hundreds of km long. For the NTS, the arrival of the tsunami on the Sicily coasts manifests as a sea withdrawal. In this case, a useful precursor could be the earthquake, destabilizing the underwater body since it anticipates the tsunami arrival by some tens of minutes. This latter kind of phenomenon sometimes called “surprise tsunami” (Ward, 2001) needs increasing attention and continental margins should therefore be more extensively mapped, investigated and possibly monitored, especially off those coasts of the Mediterranean Sea that are densely populated. The continuous supply of sediments by rivers, the diffused seismicity in the whole basin, the presence of other destabilizing phenomena (such as strong submarine bottom currents and volcanoclastic material) are elements contributing to increasing the potential hazard.

## Further Improvements and Perspectives

The GBES is particularly interesting for many reasons. First of all, it is placed in relatively shallow water, connecting a wide shelf at 200 m depth to the deeper sea (800–900 m). This permits the characterization of the morphology in detail, both for the reconstruction of past events and for the recognition of possible future occurrences. Many submarine landslide events can be mapped by high-resolution bathymetric data and described with sufficient accuracy, covering a large spectrum of volumes and return periods, making it possible to apply probabilistic approaches.

The study of the tsunami effects on the coast should also consider land inundation and the impact on coastal communities. This issue was the scope of the Italian project SPOT (Antoncccchi et al., 2020) for the coast of Sicily, but not for the Malta archipelago. It was addressed by employing empirical laws for tsunami flow over coastal 1D transects and the results are left to further publications. As regards the Malta coasts, the inlets along the northern coasts, in particular, favor wave amplifications that should be investigated through more detailed computational grids. The two scenarios explored in this work, together with the ones reported in Mueller et al. (2020), could be integrated into a more comprehensive study of tsunami hazard of the Malta archipelago.

An exhaustive study of the tsunami hazard related to collapses along the GBES would require more scenarios, covering a larger spectrum of volumes, also using a probabilistic approach. Nonetheless, the authors are convinced that the two cases presented here provide interesting insights for the evaluation of the tsunami hazard along the coast of Sicily and Malta and that will stimulate the interest on these phenomena, which should require increasing consideration.

Validation of results from numerical simulations can come from the analysis of tsunami deposits in the sedimentary sequences on land and also offshore. This was the case, for example, of the geological investigations by Pantosti et al. (2008), De Martini et al. (2012) and Smedile et al. (2020), that were able to associate sediment layers found in trenches or cores in eastern Sicily to historical- as well as paleo-tsunami cases. The GBES morphology suggests that mass collapses along the slope repeat cyclically, and the generated tsunami can reach the coasts of Sicily and Malta with potentially relevant waves. The events investigated here are prehistorical. Finding their coastal signature is a hard, but not an impossible task and future research by tsunami geologists could fill this gap.

## DATA AVAILABILITY STATEMENT

The raw data supporting the conclusions of this article will be made available by the authors, without undue reservation.

## AUTHOR CONTRIBUTIONS

FZ realized the datasets describing the landslide scenarios; contributed to develop and maintain the landslide simulation code; performed the landslide dynamics simulations; wrote the first draft of the paper; produced most of the figures in the paper; collected and harmonized all the contributions from coauthors; managed the manuscript progress. GP contributed to develop and

## REFERENCES

Ai, F., Kuhlmann, J., Huhn, K., Strasser, M., and Kopf, A. (2014). Submarine slope stability assessment of the central Mediterranean continental margin: the Gela Basin," in *Submarine mass movements and their consequences. Advances in*

maintain the tsunami simulation code; built the tsunami computational grids; run the simulations of the tsunami propagation. MAP contributed to the definition of the landslide scenarios; contributed to develop and maintain the stability analysis code; performed the slope stability analysis. TG contributed to the definition of the SGBS scenario and the discussion of the collapse triggering factors; performed the literature review on landslide-tsunamis; revised the paper. MR provided bathymetric data for landslide scenarios and tsunami computational grids; contributed to the definition of the landslide scenarios; supervised the geological part of the work; produced Figure 1; contributed to the manuscript revision. AArg: contributed to the definition of the landslide scenarios; supervised the geological part of the work; contributed to the manuscript revision; produced Figure 1. AArm contributed to develop and maintain the tsunami simulation code; supervised the modeling part of the work; revised the paper. ST developed the stability, landslide, and tsunami numerical codes; supervised the whole work; revised the paper.

## ACKNOWLEDGMENTS

The bathymetric metadata and Digital Terrain Model data products have been derived from the EMODnet Bathymetry portal - <http://www.emodnet-bathymetry.eu>. The PGAs in the landslide areas originated by the selected faults were provided by Barbara Borzi and her research team (Eucentre), in the framework of the SPOT project. The SPOT project was funded by the Italian Ministry of Economic Development, Directorate General for Safety—National Mining Office for Hydrocarbons and Georesources (DGS-UNMIG) under the umbrella of the Offshore safety network "Clypea," which is in force since 2014, and was established with bilateral agreements between the Ministry and Research Centres, Governmental Bodies and Universities to increase the safety, also in terms of environmental protection, of offshore plants operations. The Ph.D. of Tugdual Gauchery is funded by the European Union's Horizon 2020 research and innovation program under the Marie-Skłodowska-Curie grant via project ITN SLATE (Grant Agreement No 721403). The authors are indebted to the editor and the reviewers, Roger Urgeles and Juan Horrillo, whose comments and suggestions contributed to considerably improve the manuscript.

## SUPPLEMENTARY MATERIAL

The Supplementary Material for this article can be found online at: <https://www.frontiersin.org/articles/10.3389/feart.2020.602171/full#supplementary-material>.

*natural and technological hazards research*. Editors S. Krastel, et al. (Cham: Springer), Vol. 37. doi:10.1007/978-3-319-00972-8\_20

Antoncccchi, I., Ciccone, F., Dialuce, G., Grandi, S., Terlizze, F., Di Bucci, D., et al. (2020). *Progetto SPOT - Sismicità Potenzialmente innescabile Offshore e Tsunami. Report integrato di fine progetto*, ISBN 9788894366945 (in Italian). doi:10.5281/zenodo.3732887

- Argnani, A. (1987). The Gela Nappe: evidence of accretionary melange in the Maghrebian foredeep of Sicily. *Mem. Società Geol. Italiana* 38, 419-428.
- Argnani, A., Armigliato, A., Pagnoni, G., Zaniboni, F., Tinti, S., and Bonazzi, C. (2012). Active tectonics along the submarine slope of south-eastern Sicily and the source of the 11 January 1693 earthquake and tsunami. *Nat. Hazards Earth Syst. Sci.* 12, 1311-1319. doi:10.5194/nhess-12-1311-2012
- Argnani, A., Cornini, S., Tortelli, L., and Zitellini, N. (1987). Diachronous foredeep system in the neogene-quaternary of the strait of sicily. *Memorie Società Geologica Italiana*. 38, 407-417.
- Argnani, A., Tinti, S., Zaniboni, F., Pagnoni, G., Armigliato, A., Panetta, D., et al. (2011). The eastern slope of the southern Adriatic basin: a case study of submarine landslide characterization and tsunamigenic potential assessment. *Mar. Geophys. Res.* 32, 299-311. doi:10.1007/s11001-011-9131-3
- Assier-Rzadkiewicz, S., Heinrich, P., Sabatier, P. C., Savoye, B., and Bourillet, J. F. (2000). Numerical modelling of a landslide-generated tsunami: the 1979 nice event. *Pure Appl. Geophys.* 157, 1707-1727. doi:10.1007/PL00001057
- Casalbore, D., Bosman, A., Ridente, D., and Chiocci, F. L. (2014). "Coastal and submarine landslides in the tectonically-active tyrrhenian calabrian margin (southern Italy): examples and geohazard implications," in *Submarine mass movements and their consequences. Advances in natural and technological hazards research*. Editors S. Krastel, et al. (Cham, Springer), Vol. 37. doi:10.1007/978-3-319-00972-8\_23
- Casalbore, D., Martorelli, E., Bosman, A., Morelli, E., and Chiocci, F. L. (2019). Failure dynamics of landslide scars on the lower continental slope of the Tyrrhenian Calabrian margin: insights from an integrated morpho-bathymetric and seismic analysis. *Geol. Soc., London, Spec. Publ.* 477, 389-397. doi:10.1144/SP477.16
- Ceramicola, S., Tinti, S., Zaniboni, F., Praeg, D., Planinsek, P., Pagnoni, G., et al. (2014). "Reconstruction and tsunami modeling of a submarine landslide on the Ionian margin of Calabria (Mediterranean Sea)," in *Landslide science for a safer geoenvironment*. Editors K. Sassa, P. Canuti, and Y. Yin (Cham: Springer International Publishing Switzerland), Vol. 3, 557-562. doi:10.1007/978-3-319-04996-0\_85
- Chaytor, J. D., ten Brink, U. S., Solow, A. R., and Andrews, B. D. (2009). Size distribution of submarine landslides along the U.S. Atlantic margin. *Mar. Geol.* 264, 16-27. doi:10.1016/j.margeo.2008.08.007
- Chiocci, F. L., and Ridente, D. (2011). Regional-scale seafloor mapping and geohazard assessment. The experience from the Italian project MaGIC (Marine Geohazards along the Italian Coasts). *Mar. Geophys. Res.* 32, 13-23. doi:10.1007/s11001-011-9120-6
- De Martini, P. M., Barbano, M. S., Pantosti, D., Smedile, A., Pirrotta, C., Del Carlo, P., et al. (2012). Geological evidence for paleotsunami along eastern Sicily (Italy): an overview. *Nat. Hazards Earth Syst. Sci.* 12, 2569-2580. doi:10.5194/nhess-12-2569-2012
- EMODnet Bathymetry Consortium (2018). *EMODnet digital bathymetry (DTM)*. Brussels: The European Marine Observation and Data Network, European Maritime and Fisheries Fund. <http://doi.org/10.12770/18ff0d48-b203-4a65-94a9-5fd8b0ec35f6>
- Eruteya, O. E., Safadi, M., Waldmann, N., Makovsky, Y., and Ben-Avraham, Z. (2016). "Seismic geomorphology of the Israel slump complex in the levant basin (SE Mediterranean)," in *Submarine mass movements and their consequences. Advances in natural and technological hazards research*. Editor G. Lamarche, et al. (Cham: Springer), Vol. 41. doi:10.1007/978-3-319-20979-1\_4
- Fan, W., McGuire, J. J., and Shearer, P. M. (2020). Abundant Spontaneous and dynamically triggered submarine landslides in the gulf of Mexico. *Geophys. Res. Lett.* 47, e2020GL087213. doi:10.1029/2020GL087213
- Fisher, M., Normark, W. R., Gary Greene, H., Lee, H. L., and Sliter, R. W. (2005). Geology and tsunamigenic potential of submarine landslides in Santa Barbara channel, southern California. *Mar. Geol.* 224, 1-22. doi:10.1016/j.margeo.2005.07.012
- Gallotti, G., Passaro, S., Armigliato, A., Zaniboni, F., Pagnoni, G., Wang, L., et al. (2020). Potential mass movements on the Palinuro volcanic chain (southern Tyrrhenian Sea, Italy) and consequent tsunami generation. *J. Volcanol. Geoth. Res.* 404, 107025. doi:10.1016/j.jvolgeores.2020.107025
- Gauchery, T., Rovere, M., Pellegrini, C., Cattaneo, A., Campiani, E., and Trincardi, F. (2021). Factors controlling margin instability during the plio-quaternary in the Gela Basin (Strait of Sicily, Mediterranean Sea). *Mar. Petrol. Geol.*, 123, 104767. doi:10.1016/j.marpetgeo.2020.104767
- Greene, H. G., Murai, L. Y., Watts, P., Maher, N. A., Fisher, M. A., Paull, C. E., et al. (2006). Submarine landslides in the Santa Barbara channel as potential tsunami sources. *Nat. Hazards Earth Syst. Sci.* 6, 63-88. doi:10.5194/nhess-6-63-2006
- Harbitz, C. B., Lovholt, F., and Bungum, H. (2014). Submarine landslide tsunamis: how extreme and how likely? *Nat. Hazards* 72, 1341-1374. doi:10.1007/s11069-013-0681-3
- Iglesias, O., Lastras, G., Canals, M., Olabarrieta, M., Gonzalez, M., Aniel-Quiroga, I., et al. (2012). The BIG'95 submarine landslide-generated tsunami: a numerical simulation. *J. Geol.* 120 (1), 31-48. doi:10.1086/662718
- Ioualalen, M., Larroque, C., Scotti, O., and Daubord, C. (2014). Tsunami mapping related to local earthquakes on the French-Italian Riviera (Western Mediterranean). *Pure Appl. Geophys.* 171, 1423-1443. doi:10.1007/s00024-013-0699-1
- Janin, A., Rodríguez, M., Sakellariou, D., Lykousis, V., and Gorini, C. (2019). Tsunamigenic potential of a Holocene submarine landslide along the North Anatolian Fault (northern Aegean Sea, off Thasos island): insights from numerical modelling. *Nat. Hazards Earth Syst. Sci.* 19, 121-136. doi:10.5194/nhess-19-121-2019
- Kawamura, K., Laberg, J. S., and Kanamatsu, T. (2014). Potential tsunamigenic submarine landslides in active margins. *Mar. Geol.* 356, 44-49. doi:10.1016/j.margeo.2014.03.007
- Kuhlmann, J., Asioli, A., Trincardi, F., Klügel, A., and Huhn, K. (2015). Sedimentary response to Milankovitch-type climatic oscillations and formation of sediment undulations: evidence from a shallow-shelf setting at Gela Basin on the Sicilian continental margin. *Quat. Sci. Rev.* 108, 76-94. doi:10.1016/J.QUASCIREV.2014.10.030
- Kuhlmann, J., Asioli, A., Trincardi, F., Klügel, A., and Huhn, K. (2017). Landslide frequency and failure mechanisms at NE Gela Basin (Strait of Sicily). *J. Geophys. Res.: Earth Surf.* 122, 2223-2243. doi:10.1002/2017JF004251
- Lastras, G., Canals, M., Amblas, D., Frigola, J., Urgeles, R., Calafat, A. M., et al. (2007). Slope instability along the northeastern Iberian and Balearic continental margins. *Geol. Acta.* 5, 35-47. doi:10.1344/105.000000308
- Lastras, G., De Blasio, F. V., Canals, M., and Elverhoi, A. (2005). Conceptual and numerical modeling of the BIG'95 debris flow, Western Mediterranean Sea. *J. Sediment. Res.* 75, 784-797. doi:10.2110/jsr.2005.063
- Lickorish, W. H., Grasso, M., Butler, R. W. H., Argnani, A., and Maniscalco, R. (1999). Structural styles and regional tectonic setting of the Gela Nappe (SE Sicily). *Tectonics* 18, 655-668. doi:10.1029/1999TC900013
- Loncke, L., Gaullier, V., Droz, L., Ducassou, E., Migeon, S., and Mascle, J. (2009). Multi-scale slope instabilities along the Nile deep-sea fan, Egyptian margin: a general overview. *Mar. Petrol. Geol.* 26: 633-646. doi:10.1016/j.marpetgeo.2008.03.010
- Loreto, M. F., Pagnoni, G., Pettenati, F., Armigliato, A., Tinti, S., Sandron, D., et al. (2017). Reconstructed seismic and tsunami scenarios of the 1905 Calabria earthquake (SE Tyrrhenian sea) as a tool for geohazard assessment. *Eng. Geol.* 224, 1-14. doi:10.1016/j.enggeo.2017.04.018
- Løvholt, F., Harbitz, C. B., Vanneste, M., De Blasio, F. V., Urgeles, R., Iglesias, O., et al. (2014). Modeling potential tsunami generation by the BIG'95 landslide," in *Submarine mass movement and their consequences, Advances in natural and technological hazards research*. Editors S. Krastel, J.-H. Behrmann, D. Völker, M. Stipp, C. Berndt, R. Urgeles, et al. (Dordrecht, The Netherlands: Springer), Vol. 37, 507-515. doi:10.1007/978-3-319-00972-8\_45
- Macías, J., Vázquez, J. T., Fernández-Salas, L. M., González-Vida, J. M., Bárcenas, P., Castro, M. J., et al. (2015). The Al-Borani submarine landslide and associated tsunami. A modelling approach. *Mar. Geol.* 361, 79-95. doi:10.1016/j.margeo.2014.12.006
- Masson, D. G., Harbitz, C. B., Wynn, R. B., Pedersen, G., and Løvholt, F. (2006). Submarine landslides: processes, triggers and hazard prediction. *Phil. Trans. R Soc. A* 364, 2009-2039. doi:10.1098/rsta.2006.1810
- McAdoo, B. G., Pratson, L. F., and Orange, D. L. (2000). Submarine landslide geomorphology, US continental slope. *Mar. Geol.* 169, 103-136. doi:10.1016/S0025-3227(00)00050-5
- Meletti, C., and Montaldo, V. (2007). Stime di pericolosità sismica per diverse probabilità di superamento in 50 anni: valori di ag. Progetto DPC-INGV S1, Deliverable D2, <http://esse1.mi.ingv.it/d2.html> (Accessed June, 2018).

- Micallef, A., Georgiopolou, A., Le Bas, T., Mountjoy, J. J., Huvenne, V., and Lo Iacono, C. (2014). "The Malta-Sicily Escarpment: mass movement dynamics in a sediment-undersupplied margin," in *Submarine mass movements and their consequences. Advances in natural and technological hazards research*. Editors S. Krastel, et al. (Cham: Springer), Vol. 37. doi:10.1007/978-3-319-00972-8\_28
- Minisini, D., and Trincardi, F. (2009). Frequent failure of the continental slope: the Gela Basin (Sicily channel), *J. Geophys. Res.* 114, F03014. doi:10.1029/2008JF001037
- Minisini, D., Trincardi, F., Asioli, A., Canu, M., and Fogliini, F. (2007). Morphologic variability of exposed mass-transport deposits on the eastern slope of Gela Basin (Sicily channel). *Basin Res.* 19 (2), 217–240. doi:10.1111/j.1365-2117.2007.00324.x
- Miramontes, E., Garziglia, S., Sultan, N., Jouet, G., and Cattaneo, A. (2018). Morphological control of slope instability in contourites: a geotechnical approach. *Landslides* 15, 1085–1095. doi:10.1007/s10346-018-0956-6
- Mueller, C., Micallef, A., Spatola, D., and Wang, X. (2020). The tsunami inundation hazard of the Maltese islands (central Mediterranean Sea): a submarine landslide and earthquake tsunami scenario study. *Pure Appl. Geophys.* 177, 1617–1638. doi:10.1007/s00024-019-02388-w
- Pampell-Manis, A., Horrillo, J., Shigihara, Y., and Parambath, L. (2016). Probabilistic assessment of landslide tsunami hazard for the northern Gulf of Mexico. *J. Geophys. Res.: Oceans*. 121, 1009–1027. doi:10.1002/2015JC011261
- Pantosti, D., Barbano, M. S., Smedile, A., De Martini, P. M., and Tigano, G. (2008). Geological evidence of paleotsunamis at Torre degli Inglesi (northeast Sicily), *Geophys. Res. Lett.* 35, L05311. doi:10.1029/2007GL032935
- Papadopoulos, G. A., Daskalaki, E., and Fokaeis, A. (2007b). Tsunamis generated by coastal and submarine landslides in the Mediterranean Sea." in *Submarine mass movements and their consequences. Advances in natural and technological hazards research*. Editors V. Lykousis, D. Sakellariou, and J. Locat (Dordrecht: Springer), Vol. 27. doi:10.1007/978-1-4020-6512-5\_43
- Papadopoulos, G. A., Gracia, E., Urgeles, R., Sallares, V., De Martini, P. M., Pantosti, D., et al. (2014). Historical and pre-historical tsunamis in the Mediterranean and its connected seas: geological signatures, generation mechanisms and coastal impacts. *Mar. Geol.* 354, 81–109. doi:10.1016/j.margeo.2014.04.014
- Papadopoulos, G. A., Lobkovsky, L. I., Mazova, R. Kh., Garagash, I. A., Karastathis, V., Kataeva, L. Yu., et al. (2007a). Numerical modeling of sediment mass sliding and tsunami generation: the case of February 7, 1963, in Corinth Gulf, Greece. *Mar. Geodes.* 30, 315–331. doi:10.1080/01490410701568541
- Paparo, M. A., and Tinti, S. (2017). Analysis of seismic-driven instability of Mt. Nuovo in the Ischia Island, Italy. *Bull. Seismol. Soc. Am.* 107 (2), 750–759. doi:10.1785/0120160139
- Paparo, M. A., Armigliato, A., Pagnoni, G., Zaniboni, F., and Tinti, S. (2017). Earthquake-triggered landslides along the Hyblean-Malta Escarpment (off Augusta, eastern Sicily, Italy) – assessment of the related tsunamigenic potential. *Adv. Geosci.* 44, 1–8. doi:10.5194/adgeo-44-1-2017
- Ridente, D., Fracassi, U., Di Bucci, D., Trincardi, F., and Valensise, G. (2008). Middle Pleistocene to Holocene activity of the Gondola fault zone (Southern Adriatic Foreland): deformation of a regional shear zone and seismotectonic implications. *Tectonophysics* 453, 110–121. doi:10.1016/j.tecto.2007.05.009
- Rodríguez, M., Maleuvre, C., Jollivet-Castelot, M., d'Acremont, E., Rabaute, A., Lafosse, M., et al. (2017). Tsunamigenic submarine landslides along the Xauen-Tofiño banks in the Alboran Sea (Western Mediterranean Sea). *Geophys. J. Int.* 209, 266–281. doi:10.1093/gji/ggx028
- Rovere, M., Gamberi, F., Mercorella, A., and Leidi, E. (2014). Geomorphometry of a submarine mass-transport complex and relationships with active faults in a rapidly uplifting margin (Gioia Basin, NE Sicily margin). *Mar. Geol.* 356, 31–43. doi:10.1016/j.margeo.2013.06.003
- Sawyer, D. E., Reece, R. S., Gulick, S. P. S., and Lenz, B. L. (2017). Submarine landslide and tsunami hazards offshore southern Alaska: seismic strengthening versus rapid sedimentation. *Geophys. Res. Lett.* 44, 8435–8442. doi:10.1002/2017GL074537
- Shipboard Scientific Party (1996). "Site 963," in Proceedings of the ocean drilling program, initial reports, Editor K.-C. Emeis, Robertson A. H. F., Richter C. M., M. M. Blanc-Valleron, I. Bouloubassi, H.-J. Brumsac, et al. (Houston, TX: Texas A&M University), 160, 55–84. doi:10.2973/odp.proc.ir.160.104.1996
- Smedile, A., Molisso, F., Chagué, C., Iorio, M., De Martini, P. M., Pinzi, S., et al. (2020). New coring study in Augusta Bay expands understanding of offshore tsunami deposits (Eastern Sicily, Italy). *Sedimentology* 67, 1553–1576. doi:10.1111/sed.12581
- Solheim, A., Bryn, P., Sejrup, H. P., Mienert, J., and Berg, K. (2005). Ormen Lange—an integrated study for the safe development of a deep-water gas field within the Storegga slide complex, NE Atlantic continental margin; executive summary. *Mar. Petrol. Geol.* 22, 1–9. doi:10.1016/j.marpetgeo.2004.10.01
- Tappin, D. R. (2010). "Mass transport events and their tsunami hazard." in *Submarine mass movements and their consequences. Advances in natural and technological hazards research*. Editors D. C. Mosher, et al. (Dordrecht: Springer), Vol. 28. doi:10.1007/978-90-481-3071-9\_54
- Tappin, D. R., Watts, P., and Grilli, S. T. (2008). The Papua New Guinea tsunami of 17 July 1998: anatomy of a catastrophic event. *Nat. Hazards Earth Syst. Sci.* 8, 243–266. doi:10.5194/nhess-8-243-2008
- ten Brink, U. S., Chaytor, J. D., Geist, E. L., Brothers, D. S., and Andrews, B. D. (2014). Assessment of tsunami hazard to the U.S. Atlantic margin. *Mar. Geol.* 353, 31–54. doi:10.1016/j.margeo.2014.02.011
- ten Brink, U. S., Giest, E. L., and Andrews, B. D. (2006). Size distribution of submarine landslides and its implication to tsunami hazard in Puerto Rico. *Geophys. Res. Lett.* 33, L11307. doi:10.1029/2006GL026125
- Tinti, S., and Manucci, A. (2008). A new computational method based on the minimum lithostatic deviation (MLD) principle to analyse slope stability in the frame of the 2D limit-equilibrium theory. *Nat. Hazards Earth Syst. Sci.* 8, 671–683. doi:10.5194/nhess-8-671-2008
- Tinti, S., and Manucci, A. (2006). Gravitational stability through the limit equilibrium method revisited. *Geophys. J. Int.* 164, 1–14. doi:10.1111/j.1365-246X.2005.02796.x
- Tinti, S., and Tonini, R. (2013). The UBO-TSUFID tsunami inundation model: validation and application to a tsunami case study focused on the city of Catania, Italy. *Nat. Hazards Earth Syst. Sci.* 13, 1795–1816. doi:10.5194/nhess-13-1795-2013
- Tinti, S., Bortolucci, E., and Vannini, C. (1997). A block-based theoretical model suited to gravitational sliding. *Nat. Hazards* 16, 1–28. doi:10.1023/A:1007934804464
- Tinti, S., Pagnoni, G., and Zaniboni, F. (2006). The landslides and tsunamis of 30<sup>th</sup> December 2002 in Stromboli analysed through numerical simulations, *Bull. Volcanol.* 68, 462–479. doi:10.1007/s00445-005-0022-9
- Tinti, S., Zaniboni, F., Armigliato, A., Pagnoni, G., Gallazzi, S., Manucci, A., et al. (2007). "Tsunamigenic landslides in the western Corinth gulf: numerical scenarios," in *Submarine mass movements and their consequences III. Advances in natural and technological hazards research*. Editors V. Lykousis, D. Sakellariou, and J. Locat (Springer), Vol. 27, 405–414.
- Triantafyllou, I., Zaniboni, F., Armigliato, A., Tinti, S., and Papadopoulos, G. A. (2020). The large earthquake (\* M7) and its associated tsunami of 8 november 1905 in Mt. Athos, Northern Greece. *Pure Appl. Geophys.* 117, 1267–1293. doi:10.1007/s00024-019-02363-5
- Trincardi, F., and Argnani, A. (1990). Gela submarine slide: a major basin-wide event in the plio-quaternary foredeep of Sicily. *Geo Mar. Lett.* 10, 13–21. doi:10.1007/BF02431017
- Trincardi, F., Fogliini, F., Verdicchio, G., Asioli, A., Correggiari, A., Minisini, D., et al. (2007). The impact of cascading currents on the Bari canyon system, SW-Adriatic margin (Central Mediterranean). *Mar. Geol.* 246, 208–230. doi:10.1016/j.margeo.2007.01.013
- Urgeles, R., and Camerlenghi, A. (2013). Submarine landslides of the Mediterranean Sea: trigger mechanisms, dynamics, and frequency-magnitude distribution. *J. Geophys. Res.: Earth Surf.* 118, 2600–2618. doi:10.1002/2013JF002720
- Urlaub, M., Talling, P. J., and Masson, D. G. (2013). Timing and frequency of large submarine landslides: implications for understanding triggers and future geohazard. *Quat. Sci. Rev.* 72, 63–82. doi:10.1016/j.quascirev.2013.04.020
- Ward, S. N. (2001). Landslide tsunami. *J. Geophys. Res.* 106, 11201–11215. doi:10.1029/2000JB900450
- Zaniboni, F., and Tinti, S. (2014). Numerical simulations of the 1963 Vajont landslide, Italy: application of 1D Lagrangian modelling. *Nat. Hazards* 70, 567–592. doi:10.1007/s11069-013-0828-2
- Zaniboni, F., Armigliato, A., Pagnoni, G., and Tinti, S. (2014b). Continental margins as a source of tsunami hazard: the 1977 Gioia Tauro (Italy) landslide-tsunami investigated through numerical modelling. *Mar. Geol.* 357 (2014), 210–217. doi:10.1016/j.margeo.2014.08.011

- Zaniboni, F., Armigliato, A., and Tinti, S. (2016). A numerical investigation of the 1783 landslide-induced catastrophic tsunami in Scilla, Italy. *Nat. Hazards* 84, 455–470. doi:10.1007/s11069-016-2461-3
- Zaniboni, F., Pagnoni, G., Armigliato, A., Tinti, S., Iglesias, O., and Canals, M. (2014a). “Numerical simulation of the BIG’95 debris flow and of the generated tsunami,” in *Engineering geology for society and territory - Volume 4*. Editors G. Lollino, A. Manconi, J. Locat, Y. Huang, and M. Canals Ardilas (Springer International Publishing Switzerland). doi:10.1007/978-3-319-08660-6\_19
- Zaniboni, F., Pagnoni, G., Gallotti, G., Paparo, M. A., Armigliato, A., and Tinti, S. (2019). Assessment of the 1783 Scilla landslide-tsunami’s effects on the Calabrian and Sicilian coasts through numerical modelling. *Nat. Hazards Earth Syst. Sci.* 19, 1585–1600. doi:10.5194/nhess-19-1585-2019
- Zecchin, M., Accaino, F., Ceramicola, S., Civile, D., Critelli, S., Da Lio, C., et al. (2018). The Crotona Megalandslide, southern Italy: Architecture, timing and tectonic control. *Sci. Rep.* 8, 7778. doi:10.1038/s41598-018-26266-y

**Conflict of Interest:** The authors declare that the research was conducted in the absence of any commercial or financial relationships that could be construed as a potential conflict of interest.

The reviewer RU declared a past co-authorship with one of the authors MR to the handling editor.

*Copyright © 2021 Zaniboni, Pagnoni, Paparo, Gauchery, Rovere, Argnani, Armigliato and Tinti. This is an open-access article distributed under the terms of the Creative Commons Attribution License (CC BY). The use, distribution or reproduction in other forums is permitted, provided the original author(s) and the copyright owner(s) are credited and that the original publication in this journal is cited, in accordance with accepted academic practice. No use, distribution or reproduction is permitted which does not comply with these terms.*

### Take-Home Messages

- The shallow water and high steepness increased considerably the velocity of the MTDs enhancing their tsunamigenic potential
- In one of the MTD (NTS), earthquake can be used as useful precursor for tsunami arrival, which allow an anticipation of the waves by tens of minutes.
- The more distal MTD (SGBS) produced stronger damages and arrived without warnings.
- The SGBS occurring further away from seismogenic faults are difficult to anticipate increasing the number of possible precursors and the necessity for more mapping and more investigations.



# Chapter 6. Post-LGM multi-proxy sedimentary record of bottom-current variability and downslope sedimentary processes in a contourite drift of the Gela Basin

---

“Post-LGM multi-proxy sedimentary record of bottom-current variability and downslope sedimentary processes in a contourite drift of the Gela Basin (Strait of Sicily)”

- Authors:
- Tugdual Gauchery (University of Bologna, Italy; *Istituto di Scienze Marine, CNR di Bologna, Italy*)
  - Marzia Rovere (*Istituto di Scienze Marine, CNR di Bologna, Italy*)
  - Claudio Pellegrini (*Istituto di Scienze Marine, CNR di Bologna, Italy*)
  - Alessandra Asioli (*Istituto di Scienze Marine, CNR di Bologna, Italy*)
  - Tommaso Tesi (*Istituto di Scienze Marine, CNR di Bologna, Italy*)
  - Antonio Cattaneo (*Ifremer, Géosciences Marines, Plouzané, France*)
  - Fabio Trincardi (*Istituto di Scienze Marine, CNR, Bologna, Italy*)
- Objectives:
- Distinguish sediments deposited by along-slope from downslope processes
  - Investigate the key time intervals and destabilization causes responsible for instability
  - Identify the general conditions that favour the emplacement of MTDs in the southeastern Gela Basin.

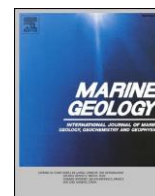




ELSEVIER

Contents lists available at ScienceDirect

## Marine Geology

journal homepage: [www.elsevier.com/locate/margo](http://www.elsevier.com/locate/margo)

# Post-LGM multi-proxy sedimentary record of bottom-current variability and downslope sedimentary processes in a contourite drift of the Gela Basin (Strait of Sicily)

Tugdual Gauchery<sup>a,b</sup>, Marzia Rovere<sup>a,\*</sup>, Claudio Pellegrini<sup>a</sup>, Alessandra Asioli<sup>a</sup>, Tommaso Tesi<sup>c</sup>, Antonio Cattaneo<sup>d</sup>, Fabio Trincardi<sup>a</sup>

<sup>a</sup> Istituto di Scienze Marine (ISMAR), Consiglio Nazionale delle Ricerche, via Gobetti 101, 40129 Bologna, Italy

<sup>b</sup> Dipartimento di Ingegneria Civile, Chimica, Ambientale e dei Materiali, Viale del Risorgimento 2, 40136 Bologna, Italy

<sup>c</sup> Istituto di Scienze Polari, Consiglio Nazionale delle Ricerche, via Gobetti 101, 40129 Bologna, Italy

<sup>d</sup> Institut français de recherche pour l'exploitation de la mer (Ifremer), Géosciences Marines, Z.I Pointe du Diable, BP70 Plouzané, France

## ARTICLE INFO

Editor: Michele Rebesco

## Keywords:

Mediterranean oceanography

Gela Basin

Contourite drifts

Mass-transport deposits

Sedimentary facies

Sortable silt

Bioecozone

Post-LGM

Ichnofacies

## ABSTRACT

Depositional systems accumulating under the combined influence of along-slope currents and downslope sediment-gravity flows are frequent in several continental margins. Despite being well-documented in terms of how these opposing depositional processes shape the margin architecture, many aspects related to their interaction and distinctive characters of resulting sediment accumulations remain elusive. Here we focus on the Gela Basin, the foredeep of the Maghrebian fold-and-thrust belt in the Strait of Sicily, where the Levantine Intermediate Water (LIW) and the Modified Atlantic Water (MAW) are confined by margin morphology, which amplify their velocities. Two sediment cores located on the upper and lower slope of the Gela Basin document the overlapping of along- and downslope processes since the very last phase of the Last Glacial Maximum (LGM). Detailed analysis of several proxies including sedimentary structures, sortable silt, geochemical elemental composition, oxygen and carbon isotopes, ichnofacies and foraminifera assemblages helped to disentangle the sedimentary imprints of contourites (including variations in bottom-current velocity through time) and downslope gravity-driven processes (turbidity currents and mass-transport processes).

The slope experienced exceptionally high sedimentation rates up to 1300 cm kyr<sup>-1</sup> during the last phase of LGM and early phase of Heinrich Stadial 1 (HS1), which rapidly decreased before Heinrich Event 1 (< 100 cm kyr<sup>-1</sup>). The high accumulation rates were driven by a combination of sediment input from the inner and mid shelf and lateral advection promoted by strong bottom-currents under the action of the LIW. An abrupt and brief intensification (+ 7.8 cm<sup>-1</sup>) of the MAW speed during the early phase of HS1 affected the stability of the sediment drifts, which were growing since the previous interglacial and contributed to the emplacement of mass-transport deposits around 17 kyr BP. During the post-glacial sea-level rise pulses, before and during the Heinrich Event 1, the two sediment cores registered contrasting bottom-current velocities, suggesting a progressive shoaling of the LIW and modifications at the interface between the LIW and the MAW, in response to the increased fresh water discharge from the Atlantic. Our findings suggest that sea-level fluctuations can change the thickness and core-depth of the Central Mediterranean water masses, leading to intervals of enhanced bottom-current erosion and margin instability along the outer shelf and upper slope.

## 1. Introduction

Contourite deposits are considered excellent archives for reconstructing paleoceanographic circulation at regional scale as a key aspect of climatic variability (e.g., Hernandez-Molina et al., 2014).

Furthermore, numerous studies use their sedimentary record to reconstruct variations in bottom-current flow strength through time (McCave et al., 1995; Toucanne et al., 2012; Miramontes et al., 2016). Bottom currents can be in fact governed by geostrophic thermohaline circulation and occur with variable intensities that directly influence their

\* Corresponding author.

E-mail address: [m.rovere@ismar.cnr.it](mailto:m.rovere@ismar.cnr.it) (M. Rovere).

<https://doi.org/10.1016/j.margeo.2021.106564>

Received 5 February 2021; Received in revised form 28 June 2021; Accepted 4 July 2021

Available online 10 July 2021

0025-3227/© 2021 The Authors.

Published by Elsevier B.V. This is an open access article under the CC BY-NC-ND license

(<http://creativecommons.org/licenses/by-nc-nd/4.0/>).

ability for inducing lateral advection of sediment (Rebesco et al., 2014; Pellegrini et al., 2016). The signature of contour-currents is relatively well-preserved where current intensity is high and in areas where sea-floor morphology generates lateral flow constriction and this often happens in the upper slope around headlands, volcanic islands, submarine plateaus (Van Rooij et al., 2010; Martorelli et al., 2011; Rovere et al., 2019).

Along-slope contour currents often occur on continental margins where also downslope gravity flows are common. Interactions between contour currents and gravity flows are rarely documented, especially at the sedimentary and seismic facies level, either because the criteria to identify them are sometimes ambiguous in interbedded sedimentary sequences (e.g. Stow and Smillie, 2020) or because gravity flows usually overprint bottom-current sedimentary structures (Mulder et al., 2008). On the other hand, contour currents may in part obliterate sedimentary structures related to turbidity-current deposition through the winnowing of fine grains (e.g. Martín-Chivelet et al., 2008). Therefore, from a sedimentary standpoint, in dynamic environments where along- and downslope processes occur simultaneously during strata deposition, it remains crucial to find diagnostic tools to disentangle strata recording bottom-current activity from strata emplaced by downslope gravity-driven processes (e.g. landslides, turbidity currents, wave-enhanced sediment gravity flows).

Several continental margins dominated by the Atlantic-Mediterranean thermohaline circulation show the interplay between along-slope and downslope processes and have been investigated at the sedimentary body level (Brackenridge et al., 2013; Martorelli et al., 2016; Miramontes et al., 2016), in flume tank experiments (Miramontes et al., 2020), but to a lesser extent at the sedimentary facies level (Beckers et al., 2016). Shallow- and intermediate-water contourites can more frequently record the interplay with gravity flows process, especially during sea-level lowstands when sediment flux from land and downslope transport are usually enhanced (Lee, 2009). In addition, the upper continental slope and shelf-edge areas are directly affected by sea-level fluctuations, as the depth range of the wind-driven surface and intermediate water masses may change as well as their ability to impinge on the sea floor (Miramontes et al., 2016). However, only a minor set of studies focus on the small-scale dynamics of locally confined contourite drifts that develop in response to oceanographic changes such as the lateral shift and vertical migration of water masses (e.g. Hanebuth et al., 2015; Petrovic et al., 2019).

In the Mediterranean Sea, the Strait of Sicily is a relatively-shallow sill separating the much deeper western and eastern basins and represents a 2-layer gateway for Atlantic and Eastern Mediterranean water exchange, where surface and intermediate currents are recorded (Béranger et al., 2004). In the Strait of Sicily, several confined shallow-water contourite deposits have been identified on the shelf and upper slope of the Gela Basin (Verdicchio and Trincardi, 2008; Kuhlmann et al., 2015; Gauchery et al., 2021). Contourites mainly formed by the action of the Levantine Intermediate Water (LIW) during interglacials and sea-level highstands when the intensity of the flow is believed to increase along the eastern slope of the Gela Basin. Contourites forming on the outer shelf are controlled by the displacing action of the Mediterranean Surface Water (MAW) (Gauchery et al., 2021). The presence of rapidly deposited contourite drift deposits in the upper slope that concurred to high sediment accumulation rates (250–330 cm/kyr) since the Last Glacial Maximum (LGM, ~ 19–23 ka) are considered the main factors conducive to recurrent slope failure with the emplacement of several mass-transport deposits (MTDs) in the northern Gela Basin (Minisini and Trincardi, 2009).

This paper presents paleo archives of post-LGM from two sediment piston cores collected in the upper and lower slope of the southern Gela Basin along a sediment drift and downslope of two MTDs, generated by the collapse of the sediment drift itself. Our multi-proxy approach includes seismic stratigraphy, benthic and planktonic foraminifera assemblages, stable isotope geochemistry, geochemical element ratios,

sortable silt grain size to distinguish between strata recording bottom-current activity alone and in combination with other sedimentary processes (e.g. gravity-driven flows). Diagnostic radiographic images of sedimentary structures were integrated with the carbon isotopic fingerprint of plant debris and displaced foraminifera from the shelf to infer the occurrence of downslope transport. The ichnofacies of bio-turbating fauna was analysed to understand bottom oxygen conditions and infer proximity to the bottom-current core.

By reconstructing the depositional history of two sedimentary records of the Gela Basin, this paper aims to: 1) evaluate proxies and criteria to disentangling along- vs downslope processes; 2) reconstruct bottom-current activity during the post-LGM, with particular focus on the stratigraphically-expanded Heinrich Stadial 1; 3) discuss time intervals and predisposing conditions that lead to the failure of sectors of the sediment drifts. Overall, the climatic signal stored in the sedimentary records in the form of variability of the paleo-current activity and intensity enabled us to make inferences on the general Mediterranean circulation, with reference to the post-LGM sea-level fluctuations.

## 2. Background

### 2.1. Geological setting

The Gela Basin is located in the Strait of Sicily and represents the foredeep of the Maghrebian fold-and-thrust belt, is shaped by the most recent arcuate front of the Gela Nappe in the north (Argnani, 1987) and constrained by the 100–150 m deep Malta Plateau in the east (Fig. 1A). The basin reaches the maximum water depth (wd) of 936 m and is filled by turbidites, mass-transport (MTD) and contourite deposits of Pliocene-Quaternary age overlying Messinian evaporites and fine-grained marls of the early Pliocene Trubi Formation. Sediments are represented by clays intercalated with thin-bedded fine-grained sands in distal settings and thicker sand beds on the southern Sicily slope (Ghielmi et al., 2012).

Sedimentary prograding wedges, fed from the north, developed on top of the Gela Nappe starting from the late Pliocene and extended eastward, away from the thrust front, fringing the Hyblean Plateau (Fig. 1B). In the Pleistocene, progradation extended to the south of the basin with the emplacement of oblique shelf-edge clinothems (Gauchery et al., 2021). From Pliocene to the Middle Pleistocene Transition (ca. 800 ka), the sediment wedge increased in thickness by 150 m/Myr. In the last 800 kyr, the margin outbuilding developed a markedly aggradational motif, with sediment accumulation rate reaching 900 m/Myr, suggesting an overall increase in accommodation on the continental shelf accompanied by an increased sediment flux along the eastern margin of the Gela Basin (Gauchery et al., 2021).

Sedimentation rates as low as 11 cm/kyr have been observed for the last 30 kyr BP in the western Gela Basin at ODP site 963 (Shipboard Scientific Party, 1996). On the contrary, sediment cores document accumulation rates up to 200 cm/kyr during the last major interglacial period before the Holocene (MIS 5, 120 to 70 ka) and 100 cm/kyr in the last 18 kyr BP (Kuhlmann et al., 2015) in the eastern Gela Basin. To explain particularly high sedimentation rates during MIS 5 Interglacials and short-lived relative high stands, Kuhlmann et al. (2015) hypothesized the action of intermittent hyperpycnal flows acting during overall arid climate in addition to enhanced thermohaline circulation. The hydrological regime of Sicilian rivers still reflects one of the most arid conditions in the Mediterranean with a discharge of Gela River as low as 0.02 km<sup>3</sup>/yr (Milliman and Farnsworth, 2011; Fig. 1C).

### 2.2. Oceanographic regime since Last Glacial Maximum

The Mediterranean Sea is connected with the Atlantic Ocean via the Strait of Gibraltar where the relatively fresher and warmer ocean waters enter and transform into the Modified Atlantic Water (MAW) (Astraldi et al., 1999). The MAW flows eastward onto the Eastern Mediterranean via the Strait of Sicily with a velocity of 15–30 cm s<sup>-1</sup> between 100 and

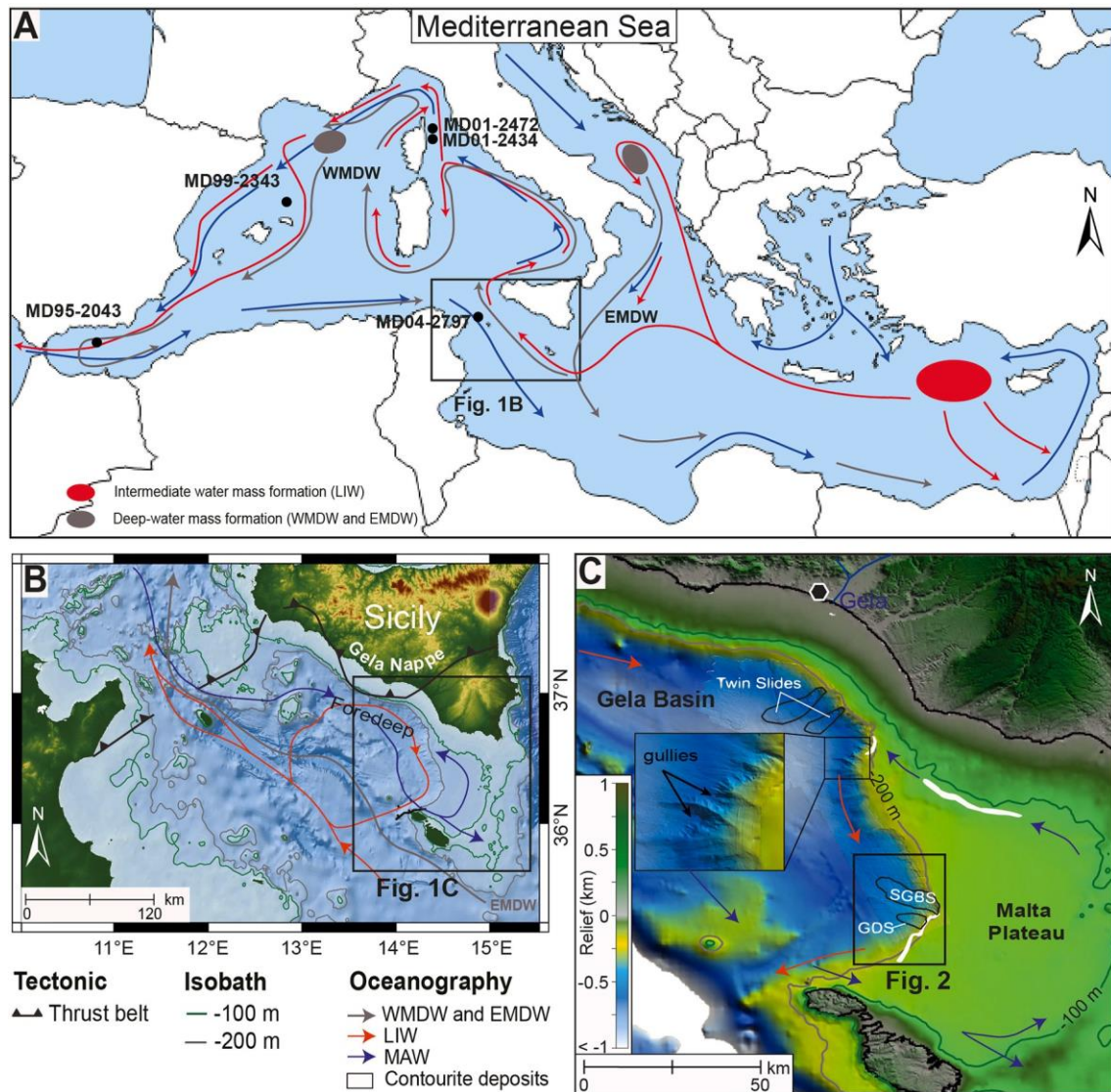


**Fig. 1.** A) Circulation of the surface (Modified Atlantic Water – MAW), intermediate (Levantine Intermediate Water – LIW) and deep-waters (Western and Eastern Mediterranean Deep Water – WMDP and EMDW) in the Mediterranean Sea (modified from [Astraldi et al., 2001](#)). The black circles indicate the location of the reference cores used in this study. B) Relief and bathymetric map of the Strait of Sicily area with superimposed the water mass circulation and the general tectonic framework (modified from [Millot, 1999](#); [Millot and Taupier-Letage, 2005](#)). C) Relief and bathymetric map of the Gela Basin highlighting mass-transport deposits: Twin Slides ([Minisini et al., 2007](#)), Southern Gela Basin Slide (SGBS) and Gela Drift Slide (GDS) ([Gauchery et al., 2021](#)). White polygons indicate contourite deposits ([Verdicchio and Trincardi, 2008](#); [Gauchery et al., 2021](#)).

200 m wd ([Lermusiaux and Robinson, 2001](#); [Millot and Taupier-Letage, 2005](#); [Fig. 1A](#)). The increasing evaporation and temperature from west to east promote vertical mixing during wintertime and result in the formation of the Levantine Intermediate Water (LIW) in the Levantine Basin ([Millot and Taupier-Letage, 2005](#); [Fig. 1A](#)). The LIW flows westward via the Strait of Sicily during summer with a velocity of  $13 \text{ cm s}^{-1}$  between 200 and 600 m wd ([Fig. 1B](#); [Lermusiaux and Robinson, 2001](#); [Sammari et al., 1999](#)). Both LIW and MAW have likely been active through the Quaternary but experienced variations in flow direction and velocity with sea-level fluctuations ([Gauchery et al., 2021](#)). Deep waters form in the Mediterranean due to mixing of cooled surface winter waters and the LIW in the northern Adriatic Sea (Eastern Mediterranean Deep Water; [Astraldi et al., 2001](#)) and in the Gulf of Lions (Western Mediterranean Deep Water; [Millot, 1999](#)) ([Fig. 1A](#)).

During the LGM, sea level was  $\sim 135 \text{ m}$  below the modern position ([Lambeck et al., 2014](#)) and the limited amount of freshwater input through the reduced section of the Gibraltar Gateway contributed to intensify intermediate and deep-water formation, resulting in stronger

bottom currents in the Mediterranean Sea ([Rogerson et al., 2008](#); [Toucanne et al., 2012](#); [Miramontes et al., 2016](#)). Well-mixed and ventilated water masses persisted during Greenland Stadial GS-2a even when massive iceberg melting at the Heinrich Event 1 (HE1) considerably reduced the salinity of the surface Mediterranean waters and caused profound reduction of deep-water formation and thermohaline circulation ([Sierro et al., 2005](#)). Indeed, during HE1 strong LIW dynamics characterized the Western ([Jiménez-Espejo et al., 2015](#)) and Central Mediterranean ([Toucanne et al., 2012](#)), while circulation was sluggish in the Eastern Mediterranean mostly due to reduced water exchange across the Strait of Sicily ([Cornuault et al., 2018](#)).

At the last glacial/interglacial transition during Greenland Interstadial 1 (GI-1) about 15 ka, a drastic reduction of the ventilation and velocity of the LIW was documented in the Corsica Trough ([Toucanne et al., 2012](#)), coinciding with warmer climate (i.e. Bølling-Allerød period) and large eustatic sea-level rise (i.e. Meltwater Pulse 1A, [Deschamps et al., 2012](#)). Moreover, the onset of the African Humid Period (AHP) at 14.8 kyr BP, when gradually increasing Northern

Hemisphere summer insolation drove the intensification and northward migration of the African monsoon (see [Shanahan et al., 2015](#) and references therein), promoted continental runoff from North Africa into the Mediterranean Sea (see [Rohling et al., 2015](#) for a complete review). The excess of freshwater input during pluvial maxima of the AHP acted as an additional forcing to the system and drastically changed the circulation pattern in the Central and Eastern Mediterranean ([Toucanne et al., 2012](#); [Revel et al., 2015](#)), probably through a partial inhibition of the vertical mixing ([Schmiedl et al., 2010](#)).

The intense and short cooling period known as Greenland Stadial 1 (GS-1) was characterized by a decrease in the Atlantic surface temperatures and salinity depletion due to fast southward shift of the polar front ([Cacho et al., 2001](#)). In the Mediterranean Sea, the arid climatic conditions favoured a more intense LIW circulation associated with lower oxygenation and higher productivity ([Toucanne et al., 2012](#); [Jiménez-Espejo et al., 2015](#)).

The transition to warmer conditions (10.8 to 6.8 ka, [Cacho et al., 2001](#)), coupled with enhanced Nile runoff, which led to deposition of Sapropel S1 ([Rohling et al., 2015](#)), significantly slowed down the LIW dynamics in the Western ([Jiménez-Espejo et al., 2015](#); [Dubois-Dauphin et al., 2017](#)) and Eastern Mediterranean ([Toucanne et al., 2012](#); [Tesi et al., 2017](#)), with reduced water exchange at the Strait of Sicily ([Cornuault et al., 2018](#)).

### 2.3. Contourite-derived mass-transport deposits

Contourite deposits are widespread along the shelf-edge and upper slope (~ 200 m wd) of the northern ([Verdicchio and Trincardi, 2008](#))

and southern ([Gauchery et al., 2021](#)) Gela Basin as well as over the shallow-water area of the Malta Plateau (~135 m wd, [Fig. 1C](#)) south of Sicily ([Gauchery et al., 2021](#)). Given the water depth of their occurrence, these contourite deposits reflect the action of intermediate waters (LIW, [Verdicchio and Trincardi, 2008](#)) and surface circulation (MAW, [Gauchery et al., 2021](#)).

In the northern Gela Basin multi-stage and stacked mass-transport deposits (MTDs) have been recorded since 87 kyr BP with ~10 kyr return frequency and involve contourites and clinothem deposits ([Kuhlmann et al., 2017](#)). During LGM, small-scale landslide deposits that are not discernible in seismic reflection profiles are revealed by the presence of displaced foraminifera ([Kuhlmann et al., 2017](#)). The uppermost of these minor stacked mudflow deposits occurred about 8.5 kyr BP and displaced the postglacial rapidly deposited units of the sediment drifts ([Minisini and Trincardi, 2009](#)). On top of the mudflow, the Twin Slides ([Minisini et al., 2007](#)) are the youngest MTD in the region and occurred in the late Holocene ([Fig. 1C](#)).

The contourite deposits located in the upper slope of the southern Gela Basin are composed of fine-grained sediment with well-developed sediment drifts and moats and their most recent phase of growth occurred during MIS 5 and late MIS 2 ([Gauchery et al., 2021](#)). The presence of erosional surfaces downcutting the upper slope combined with oversteepening caused by high sediment accumulation rates favoured the emplacement of the South Gela Basin Slide (SGBS) and the Gela Drift Slide (GDS). These two events reflect changes in sediment supply and dispersal by bottom-currents mainly due to sea-level fluctuations orbitally-controlled by climatic cycles paced at 100 kyr ([Gauchery et al., 2021](#); [Fig. 1C](#)).

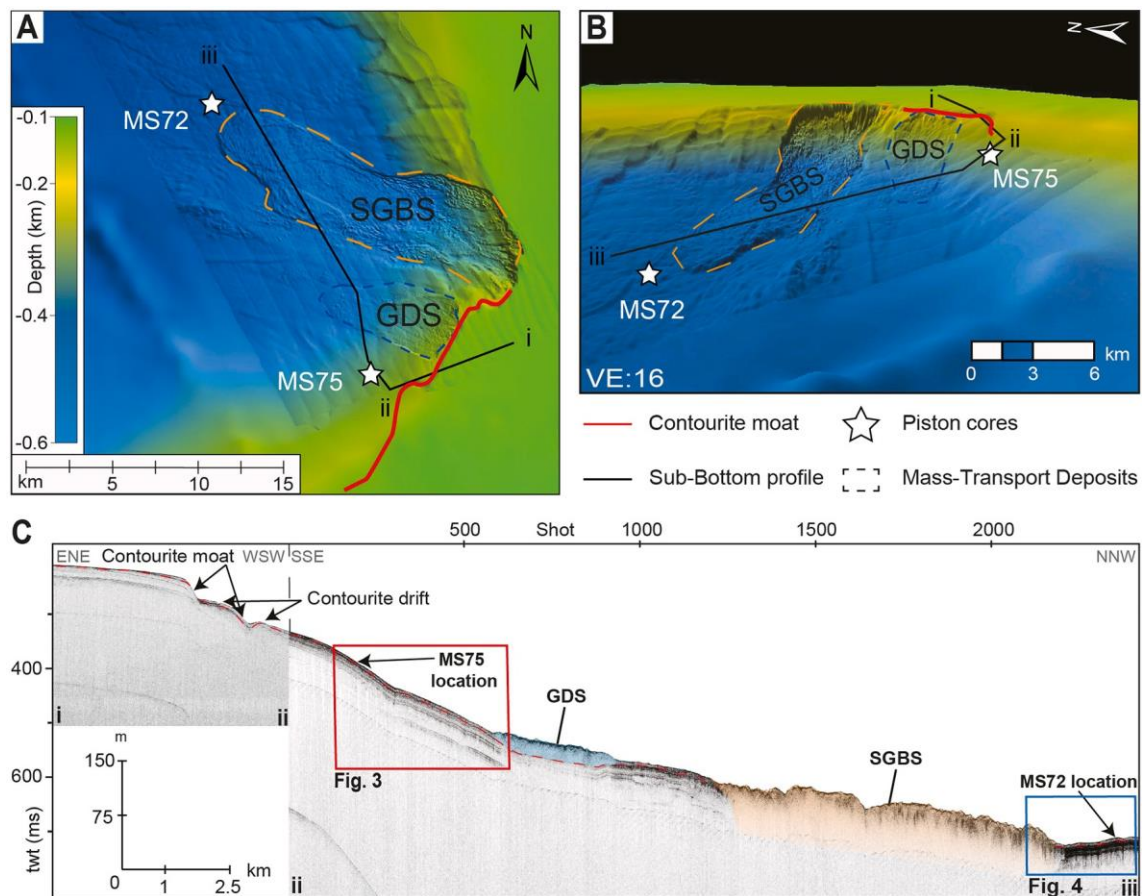


**Fig. 2.** A) 2D and B) 3D bathymetric map with location of cores MS75 and MS72 (white stars). The black line indicates the sub-bottom seismic reflection profile shown in C; the red line outlines a contour-parallel moat located upslope of the mass-transport deposits Southern Gela Basin Slide (SGBS) and Gela Drift Slide (GDS). C) Sub-bottom seismic reflection profile showing the location of cores MS75 and MS72. (For interpretation of the references to colour in this figure legend, the reader is referred to the web version of this article.)

### 3. Materials, methods and approach

#### 3.1. Methods

##### 3.1.1. Hydroacoustic data

Bathymetric maps were obtained from a compilation of a  $1/16 \times 1/16$  arc minutes resolution EMODnet (EMODnet Bathymetry Consortium, 2016) with swath bathymetry data collected with a 50 kHz Reson Seabat® 8160 on board RV Urania in 2006 during the CORSARO survey (Fig. 2).

The sub-bottom seismic reflection profiles (Fig. 2C) were collected using a Teledyne Benthos CHIRP-III system on board RV Urania in 2006 during the MAKROS campaign. The transducer is composed of a 16 hull-mounted array with a sweep-modulated frequency of 2–20 kHz outgoing signal and 4 kW power per-channel enabling a vertical resolution of 0.5 m and shallow penetration (< 100 m).

##### 3.1.2. Sediment cores

Two sediment cores were recovered using a piston corer on board RV Urania in 2007 during the MARCOS cruise (Fig. 2). Core MS75 was collected on the upper slope at 280 m water depth (wd) and is 842.5 cm long (Fig. 3); core MS72 was retrieved at 550 m wd in the lower slope and is 1078.5 cm long (Fig. 4). For stratigraphic correlations, additional reference from long piston cores were used from the literature (Fig. 1A for location).

#### 3.2. Laboratory Analysis on sediment cores

X-ray images of the sediment cores were obtained with a Fuji PRIMA T2 digital acquisition system from Ibis X-rays systems and a Gilardoni cpx-m 160 generator. Magnetic susceptibility was acquired with a Bartington® system mounting an MS2 sensor (range 0.1 SI) and using a 2 cm spacing resolution.

X-ray fluorescence (XRF) data were acquired with a 3rd generation AVAATECH core scanner on split cores equilibrated for room temperature, carefully smoothed to remove surface roughness and covered with a 4 µm Ultralene® film to prevent contamination of the sensor during core logging. The generator is an Oxford 100-W X-Ray source with rhodium anode, while the sensor is a Canberra Silicon Drift Detector with Be window. The XRF data were collected in three separate runs using generator settings: 10 kV with helium flux, 30 kV, 50 kV and 400–450 µA with counting times of 10–35 s every centimetre downcore. Dead times were automatically corrected. Raw spectroscopic data were processed and converted to elemental counts by Iterative Least square software (WIN AXIL) package from Canberra Eurisys. Post-processing of the results indicated that light elements (Al to Fe) were affected by seawater content, with Cl values showing an opposite trend. Thus, light elements from lithogenic sources were replaced by heavier elements when normalizing XRF data (e.g. Fe replaced by Ti) (Hennekam and De Lange, 2012; Tjallingii et al., 2007).

Foraminifera assemblages were examined by means of an optical stereomicroscope to obtain a semi-quantitative micropaleontological analysis on 1 cm thick sediment slices taken every ~10 cm. The sediment samples were dried in oven at 50 °C and sieved at 0.063 mm in advance of the micropaleontology analysis.

Radiocarbon AMS dating were performed on monospecific samples (Table 1), when possible, of planktonic or benthonic foraminifera at the National Ocean Sciences Accelerator Mass Spectrometry Facility (NOSAMS, Woods Hole Oceanographic Institution, USA). Specimens were picked-up under the optical stereomicroscope from the size fraction >0.180 mm, discarding filled, encrusted and broken specimens. The selected specimens underwent an ultrasonic bath in demineralized water before shipping to the laboratory. The calibration was obtained with the Calib 7.1.0 Radiocarbon Calibration Program (Stuiver and Reimer, 1993) and the Marine13 calibration data set (Reimer et al., 2013) applying a reservoir age of  $71 \pm 50$  years according to the Calib

database for Sicily (Kuhlmann et al., 2015; Siani et al., 2000; Table 1).

Oxygen and carbon stable isotope analyses of foraminifera ( $\delta^{13}\text{C}_{\text{for-ams}}$ ) were performed on the planktonic species *Globigerina bulloides* for both cores and on the benthonic taxon *Bulimina marginata* only for core MS72. These two taxa were selected because of their continuous presence in the cores and because they allow a comparison with other Mediterranean records. *G. bulloides* occurs in the Mediterranean Sea, preferentially in the western basin, during winter at water depth 50–200 m (Pujol and Vergnaud-Grazzini, 1995). Twenty-five specimens, where available, were picked-up for both taxa from the size fraction >0.180 mm and they were selected under the optical stereomicroscope to avoid broken, filled or encrusted specimens. The measurements were performed at the Leibniz Laboratory for Radiometric Dating and Stable Isotope Research, University of Kiel, Germany. The analytical precision is  $< \pm 0.05\text{‰}$  ( $^{13}\text{C}$ ) and  $< \pm 0.08\text{‰}$  ( $^{18}\text{O}$ ). The isotopic composition is reported as per mil (‰) deviation with respect to the Vienna Pee Dee Belemnite (VPDB) standard. The data were not corrected for the ice volume effect.

Plant debris was handpicked from the sieved sediment and transferred in silver cups, where samples were acidified with 1.5 M HCl twice. Elemental (organic carbon and total nitrogen) and carbon stable isotope analyses ( $\delta^{13}\text{C}_{\text{oc}}$ ) were performed at ISMAR's premises using a Finnigan DeltaPlus mass spectrometer directly coupled with a FISIONS NA2000 Element Analyzer via a CONFLO interface for continuous flow measurements. The standard deviation is 0.15‰ based on replicates of laboratory internal standards. The isotopic composition is reported as per mil (‰) deviation with respect to the Vienna Pee Dee Belemnite (VPDB) standard.

Grain-size analysis was performed on the carbonate-free fraction of the sediment, which was sampled every 5 cm taking out 5 g for each sample. The decarbonisation was obtained with three consecutive washes with 10 ml of hydrochloric acid (20%) to remove the biogenic carbonate component, which reflects vertical marine sedimentation. Deflocculation of the samples was done by successive washes followed by centrifugation (2 times for 10 min at 3000–3500 tr/mn) to accelerate particles settling and siphoning of the supernatant. The samples were then freeze-dried for 48 h and mechanically stirred to ensure particle dispersion. After treatment, samples were stored in sample vials. A micro sample splitter was used to quarter the samples until reaching a representative quantity of sediment to get an obscuration between 8 and 15% during the analysis. The aliquots (around 100 mg) were mixed with water and stirred for four minutes at 15 Hz and went through ultrasonic bath at 80 Hz until complete disaggregation. Despite repeated sets of ultrasonic bath, some samples still contained larger particles identified as pyrite encrustations. The grain-size distribution was obtained with a Malvern Master Sizer 3000 (0.1–2000 µm) at Ifremer's laboratories with the following settings: particle type opaque (Fraunhofer approximation) and non-spherical. The instrument calculated the percentage of grain size for each group (bin) with 21 bins spanning the sortable-silt fraction (SS, 10–63 µm). For statistical redundancy, each sample was measured three times and the average used as the representative result.

#### 3.3. Data handling

##### 3.3.1. Paleo-flow speed reconstruction by sortable silt

The history of a flow speed can be reconstructed through the quantification and characterization of the sortable silt (e.g. McCave et al., 1995; Toucanne et al., 2012; Voigt et al., 2016; Lebreiro et al., 2018). We calculated the mean size of the sortable silt ( $\overline{SS}$ ) and abundance of sortable silt (SS%) according to formulas provided in McCave and Andrews (2019) to estimate changes in flow speed. With this method, the accuracy of the paleo-velocity calculation can be assessed by the correlation coefficient ( $r$ ) measuring the linear relationship between  $\overline{SS}$  for all samples and their abundance percentage in sortable silt (SS%). The closer ( $r$ ) is to 1 more confidently sediment can be interpreted as

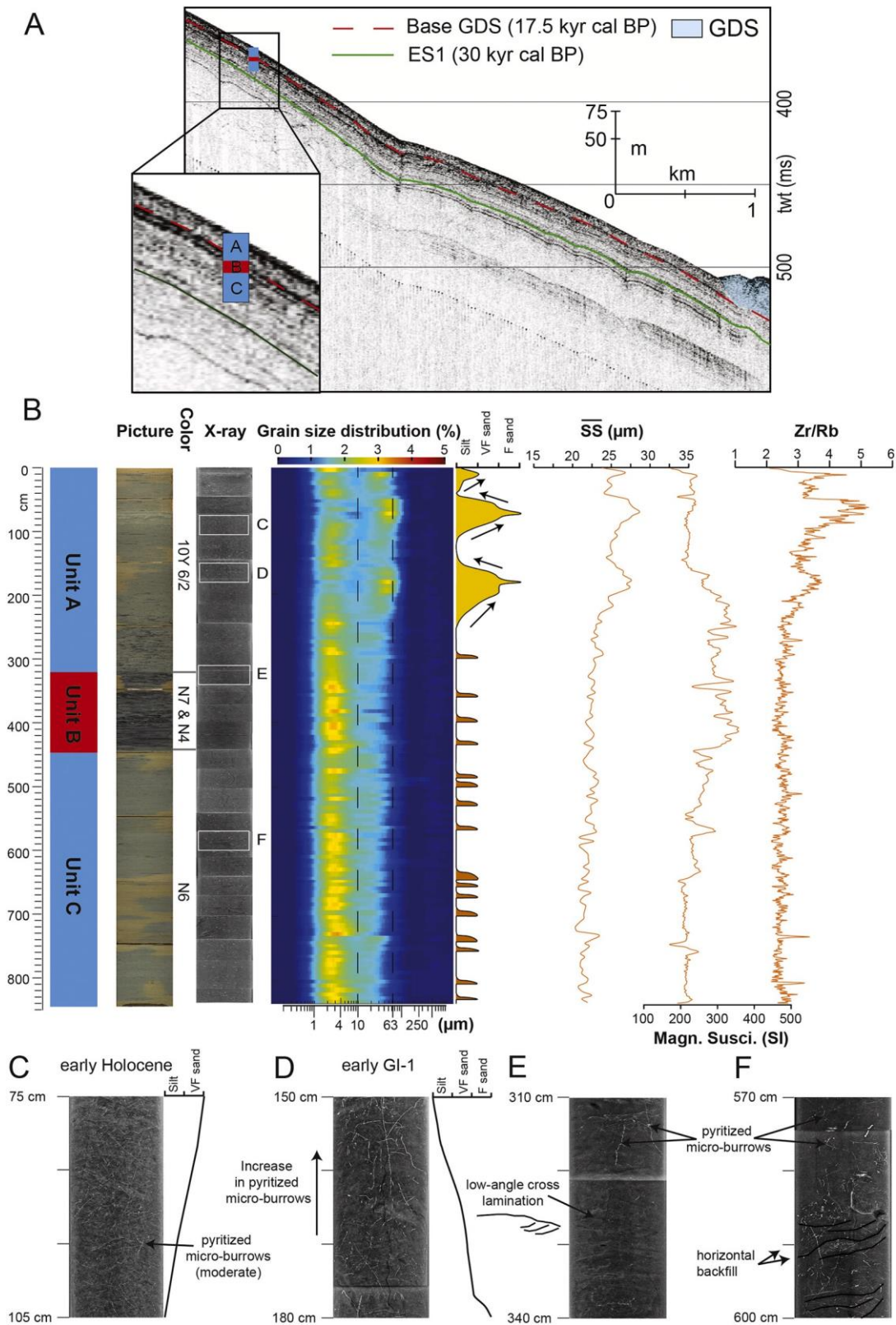


**Fig. 3.** A) Location of core MS75 in sub-bottom seismic reflection profile. Blue = low seismic amplitude (Units A and C), red = high seismic amplitude (Unit B). The Erosional Surface (ES1) is radiocarbon dated between the Last Glacial Maximum (LGM) and ~ 30 kyr cal BP (Kuhlmann et al., 2015) and seismo-stratigraphically correlated in the study area. B) From left to right: seismic units, core photo and colour scale, X-ray core scan, grain-size distribution and log,  $\overline{SS}$ , magnetic susceptibility, Zr/Rb ratio. Zoom of X-ray photos: C) non-parallel lamination and moderate abundance of pyritized micro-burrows. D) Non-parallel lamination and increase in pyritized micro-burrows along with decrease in grain size. E) Non-parallel wavy curved lamination, bioturbation and pyritized micro-burrows. F) Pyritized micro-burrows and back-fill. (For interpretation of the references to colour in this figure legend, the reader is referred to the web version of this article.)

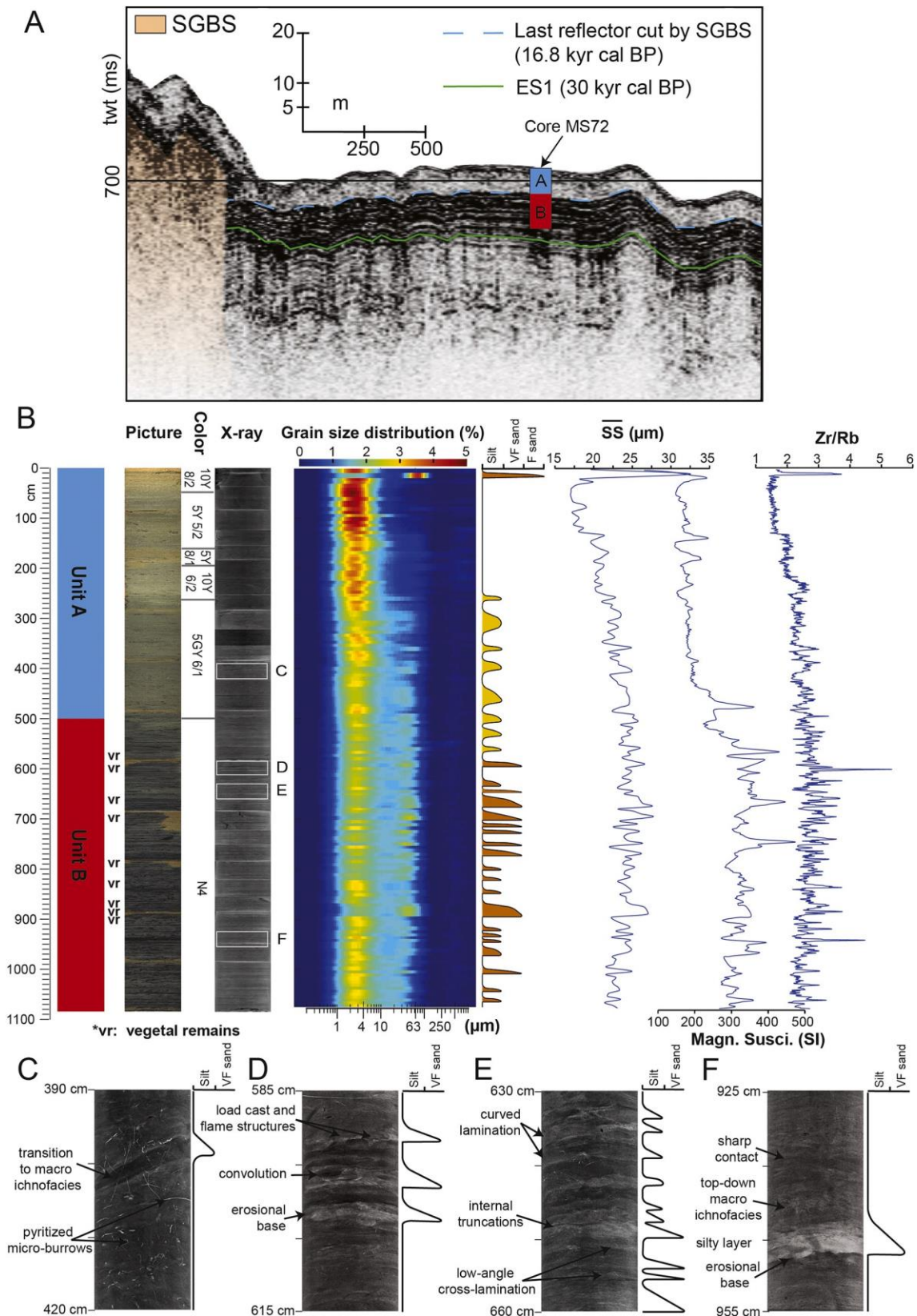


**Fig. 4.** A) Location of core MS72 in the sub-bottom seismic reflection profile. Blue = low seismic amplitude (Unit A), red = high seismic amplitude (Unit B). B) From left to right: seismic units, core photo and colour scale, X-ray core scan, grain-size distribution and log  $\overline{SS}$ , magnetic susceptibility, Zr/Rb ratio. Zoom of X-ray photos: C) change from moderate/high bioturbation by shallow tier structures (pyritized micro-burrows) to macro ichnofacies. D) Intercalations of wavy laminations with low-angle cross-bedding laminations. E) Convolute laminations, load casting and flame structures. F) Lenticular beds characterized by erosional base and sharp contact at the top, close alternation of centimetric silty and muddy layers inside and escaping bioturbating macro fauna. (For interpretation of the references to colour in this figure legend, the reader is referred to the web version of this article.)

**Table 1**  
AMS  $^{14}\text{C}$  and calibrated ages based on monospecific and mixed foraminifera.  
Results are expressed as 2-sigma range.

Core depth (cm)	Age (yr B. P.)	Calibrated age (yr. B.P.) $2\sigma$	Material
Core MS75			
20–21	9220 $\pm$ 35	9697–10,134	<i>Globigerinoides ruber</i> + <i>Globorotalia inflata</i>
71–72	12,600 $\pm$ 50	13,823–14,184	<i>Globigerinoides ruber</i>
96–97	13,550 $\pm$ 95	15,299–16,001	<i>Globigerinoides ruber</i> + <i>Neogloboquadrina incompta</i>
146–147	14,200 $\pm$ 95	16,245–16,951	mixed benthic forams
207–208	14,700 $\pm$ 110	16,949–17,655	<i>Cibicides pachyderma</i>
297.5–298.5	14,850 $\pm$ 120	17,138–17,873	mixed benthic forams
457–458	15,150 $\pm$ 70	17,614–18,081	<i>Globigerinoides ruber</i>
717–718	17,700 $\pm$ 100	20,479–21,095	<i>Globigerinoides ruber</i>
841.5–842.5	15,800 $\pm$ 80	18,369–18,788	<i>Globigerinoides ruber</i> + <i>Neogloboquadrina incompta</i>
Core MS72			
44.3–44.8	5110 $\pm$ 20	5281–5536	<i>Globigerinoides ruber</i>
134–135	10,450 $\pm$ 40	11,219–11,760	<i>Globigerinoides ruber</i>
174–175	11,050 $\pm$ 45	12,295–12,674	<i>Neogloboquadrina incompta</i>
273–274	13,150 $\pm$ 55	14,735–15,306	<i>Neogloboquadrina incompta</i>
393–394	14,050 $\pm$ 100	16,028–16,756	<i>Globigerina bulloides</i> + <i>Neogloboquadrina incompta</i>
493–494	15,400 $\pm$ 120	17,843–18,474	mixed benthic forams
711–712	15,900 $\pm$ 120	18,396–18,932	mixed benthic forams
970–971	16,600 $\pm$ 85	19,162–19,739	<i>Neogloboquadrina incompta</i>
1077–1078	16,250 $\pm$ 85	18,799–19,297	<i>Globigerinoides ruber</i> + <i>Neogloboquadrina incompta</i>

current-sorted and reliable for providing a flow history (McCave et al., 1995; McCave and Hall, 2006). In order to better differentiate along-slope from downslope sedimentary processes, we identified sediments not affected by bottom-current transport using the 9-point correlation method proposed by McCave and Andrews (2019) and excluded these samples to constrain the bottom-velocity calculations. The method uses the Correl function in Microsoft Excel to evaluate the correlation among nine values of SS% plotted against  $\overline{SS}$ . The correlation calculated for each sample is then combined with its mean value of the slope based on the same nine values to determine the correlation coefficients for each sample (see McCave and Andrews, 2019). Finally, we estimated the magnitude of absolute changes in flow speed by multiplying the difference between minimum and maximum downcore values in  $\overline{SS}$  with the sensitivity of the Malvern laser ( $1.33 \text{ cm s}^{-1}/\mu\text{m}$ ; McCave et al., 2017).

### 3.3.2. Paleo-oceanographic reconstruction by sediment elemental ratios

Marine sediments record paleo-environmental changes over time through variations in major and trace element concentrations (Martinez-Ruiz et al., 2015). In particular, in this study, we used the following elemental ratio proxies:

- Zr/Rb as a grain-size proxy, because Zr is mainly hosted in heavy minerals of coarse-grained siliciclastic sediments and Rb in fine-grained siliciclastic sedimentary rocks (Rothwell and Croudace, 2015). In a few works, Zr/Al has been used as indicative of bottom current strength in relation to the winnowing and enrichment in

heavy minerals (e.g. Bahr et al., 2014). However, we decided to use heavy elements for trend reliability.

- Ti/Ca as terrigenous flux proxy, where Ti reflects siliciclastic sediment primarily delivered to the ocean by fluvial transport processes, while Ca reflects changes in the production of calcium carbonate ( $\text{CaCO}_3$ ) by marine plankton (e.g., Piva et al., 2008; Govin et al., 2012). The magnetic susceptibility also can be used to broadly infer the prevalence of marine sedimentation or terrigenous input (Vigliotti et al., 2008).
- Ba/Ti as a paleo-productivity proxy, where the biogenic barium is related to the abundance of organic matter (Jaccard et al., 2010).
- S/Cl and pyrite encrustations as evidence of sub-oxic or anoxic conditions, when high concentrations in sulphur lead to sulphate reduction, formation of authigenic iron sulphate and pyrite (e.g. Revel et al., 2015).

### 3.3.3. Paleo-current and gravity flows identification by sedimentary facies

In addition to the elemental ratios, we used other proxies specifically to distinguish between downslope and along-slope sediment transport: the presence of reworked (e.g. planktonic taxa which are not supposed to be present in that time interval), mixed and broken shells of foraminifera to infer the occurrence of gravity flows and downslope transport. The presence of benthic samples typical of inner-shelf environment (displaced taxa) potentially coeval with other taxa and transported to a deeper environment. Foraminifera assemblages with homogeneous test size were used as proxies of bottom-current sorting.

We searched for sedimentary traction structures in the X-ray images, including horizontal and curved laminae and low-angle cross-laminae, sharp bottom contact (Martín-Chivelet et al., 2008), inverse to normal grading (Stow and Smillie, 2020), as indication of bottom-current fine-grained reworked sediment. We looked into fine-scale sedimentary structures to highlight cross-lamination in normal grading bedding, the presences of loads, flame structures and erosional contacts, lenticular and discontinuous lamination, convolute lamination, water-escape structures, indicative of very rapid deposition under sediment-gravity flows (e.g. Stow and Smillie, 2020).

We used the isotopic fingerprint of plant debris to infer the sediment source area (Tesi et al., 2007; Pedrosa-Pàmies et al., 2015).

Finally, we used ichnofacies of bioturbating fauna to distinguish between: high oxygen levels and intermediate ventilation associated with macro ichnofacies; low oxygen levels and strong bottom currents (Stow and Smillie, 2020) with micro ichnofacies and pyritised micro-burrows (Petrovic et al., 2019). We used the ichnofacies also to broadly infer the distance from the bottom-current core, based on the assumption that sedimentation rates and ecologically stressful conditions are higher in proximal areas where shallow tier tracemakers (micro ichnofacies) are more abundant, while distal settings favour the development of middle and deep tier tracemakers (macro ichnofacies) (Dorador et al., 2019).

## 4. Results

### 4.1. Seismic and sedimentary facies

#### 4.1.1. Core MS75

Distinct seismic facies in sub-bottom seismic reflection profile correspond to the stratigraphic intervals penetrated by core MS75 and allow the identification of three seismic units (Fig. 3A). Unit A (0–320 cm) is characterized by low amplitude and discontinuous reflections and overall transparent seismic facies; unit B (320–450 cm) displays very high amplitude reflections (in red; Fig. 3A); unit C (450–842.5 cm) is characterized by low amplitude almost continuous and parallel reflections.

The seismic units correspond to changes in sediment colour at core scale: pale olive (10Y 6/2) in unit A, medium dark grey (N7) in unit B and medium light grey (N6) in unit C. The X-ray images show wavy to

curved laminations in unit A associated with pyritized micro-burrows (Fig. 3C) that are particularly abundant in the 100–300 cm interval (Fig. 3D). Unit B is characterized by few non-parallel, cross-laminations, whereas pyritized micro-burrows are present only in the uppermost part (Fig. 3E). Unit C shows non-parallel laminations at the top, abundance of pyritized micro-burrows indicating micro-ichnofacies and some horizontal backfill suggesting the presence of transitional ichnofacies (sensu Petrovic et al., 2019) in the bottom part (Fig. 3F) (Table 2).

#### 4.1.2. Core MS72

Two seismic facies characterize the corresponding penetration depth of core MS72 in the sub-bottom seismic reflection profile with a sharp change between low amplitude and discontinuous reflections in unit A (0–500 cm) to high amplitude, continuous and parallel reflections in unit B (500–1078.5 cm) (Fig. 4A).

The striking change in seismic facies corresponds to different sediment colours at core scale: greenish grey in unit A and medium/dark grey in unit B (Fig. 4B). The X-ray images show overall homogenous beds in unit A (Fig. 4B). Abundant macro ichnofacies is present in the upper unit A down to about 250 cm, where is substituted by pyritized micro-burrows (Fig. 4C). Unit B is overall characterized by wavy to curved laminations and moderate macro ichnofacies bioturbation where lamination is less pronounced. Beds characterized by erosional base and convolute lamination, load casting and flame structures are also visible in unit B (Fig. 4D). Closely spaced alternations of laminae broadly curved to wavy at the base and planar upward, showing internal truncations in overall fining-upward beds are present at 600–800 cm (Fig. 4E). Mostly discontinuous, lenticular beds characterize the lower part of unit B, they have an erosional contact, are overlain by rapid alternation of centimetric silty and muddy layers and are topped by a sharp contact. Some burrows truncate the silt layer and the erosional contact at the base (Fig. 4F) (Table 2).

#### 4.2. Grain size distribution

##### 4.2.1. Core MS75

The average grain-size distribution of core MS75 is 70% silt, 24% clay and 6% sand. A slightly higher concentration in sand (8.5%) reflects the bimodal distribution observed in unit A, compared to the unimodal distribution of units B and C (Fig. 3B). In unit A, the bimodal distribution is better defined at 50–90 cm and 150–200 cm with an increase in sand concentration of 13.5% and 10%, respectively (Fig. 3B). Unit A is characterized by  $\overline{SS}$  as high as 27  $\mu\text{m}$ , while units B and C have values at least 3  $\mu\text{m}$  lower (Fig. 3B). The grain-size log shows two large inverse to normal grading beds in unit A and normal grading beds characterized by sharp erosional contacts at their base in units B and C. Zr/Rb ratio is overall higher in unit A with peak intervals that are consistent with  $\overline{SS}$  trend (Fig. 3B). The magnetic susceptibility shows an opposite trend compared to the previous proxies, with low values where Zr/Rb and  $\overline{SS}$  are higher in unit A (Fig. 3B).

**Table 2**

Summary of the seismic and sedimentary proxies of cores MS72 and MS75.

Core	Seismic unit, amplitude	Downcore depth (cm)	Sediment grain size and sorting	Sediment structures	Bioturbating fauna ichnofacies	Distance from bottom-current core
MS75	A, Low	0–320	Increase in silt, bimodal, current-sorted	Wavy to curved lamination	Micro	Proximal
	B, High	320–450	Clay, unimodal, unsorted	Low-angle cross lamination	Micro	Decreasingly distal upward
	C, Low	450–842.5		Non-parallel lamination	Micro and transitional	
MS72	A, Low	0–250	Clay, unimodal, current-sorted	Parallel lamination	Macro	Increasingly distal upward
	B, High	250–500	Increase in silt, bimodal, current-sorted	Wavy, cross and non-parallel lamination, flames and load structures	Micro	Proximal
		500–1078.5			Macro and micro	

#### 4.2.2. Core MS72

The average grain-size distribution of core MS72 is 68% silt, 26% clay and 6% sand. Clay and silt concentrations vary significantly between units A (30% clay, 65% silt) and B (23% clay, 71% silt) (Fig. 4B). The differences in grain-size concentration reflect the unimodal distribution of unit A and the bimodal distribution of unit B (Fig. 4B). Unit A is characterized by  $\overline{SS}$  in the range 17–21.4  $\mu\text{m}$ , while unit B shows values 24–27  $\mu\text{m}$ . The grain-size log shows inverse to normal grading beds in the lower unit A and normal grading beds characterized by sharp erosional contacts intercalated with inverse to normal grading beds within unit B. The magnetic susceptibility and Zr/Rb ratios reflect the change in trend between units A and B (Fig. 4B), with overall higher values and variability in unit B compared to unit A (Fig. 4B).

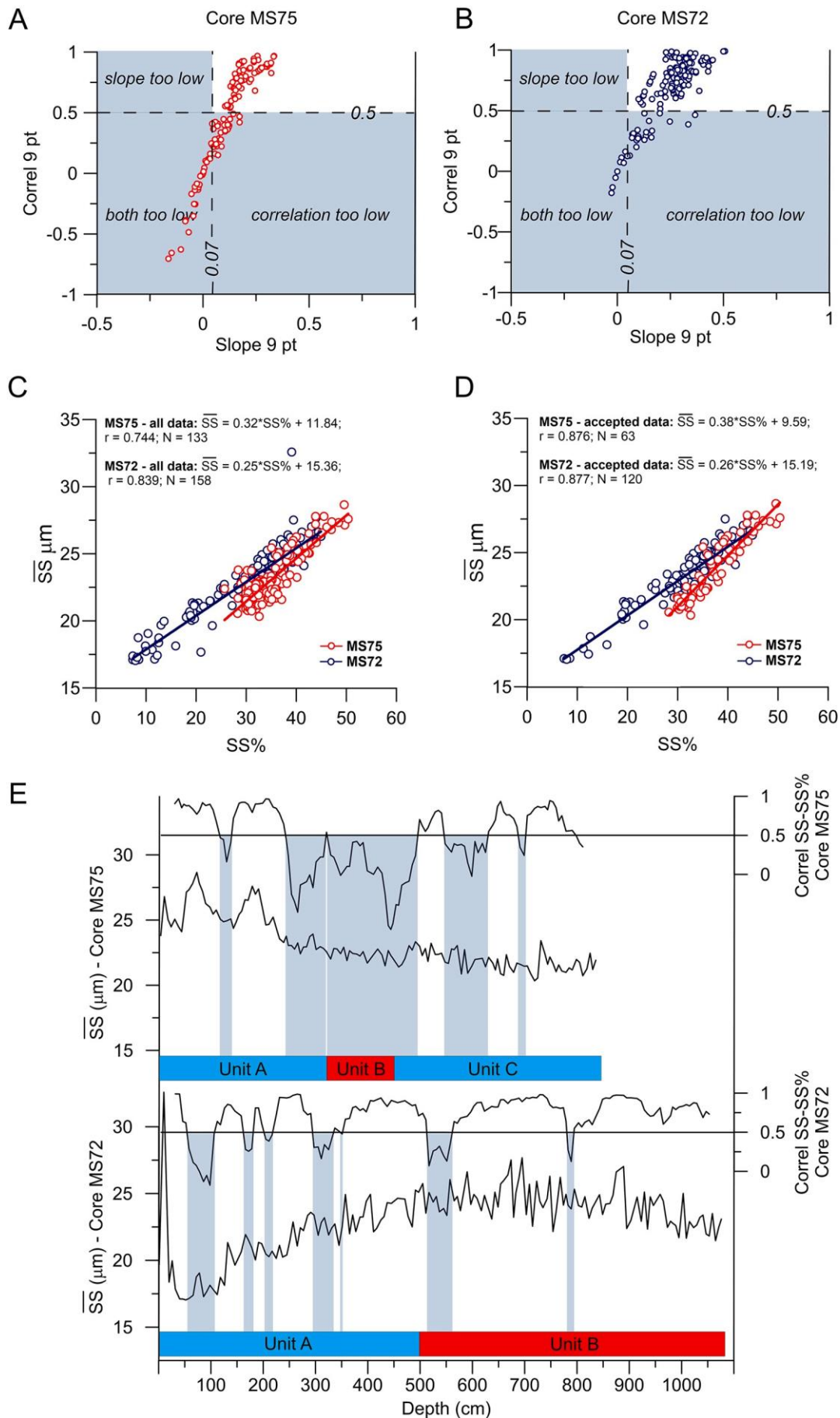
#### 4.3. Paleo-flow reconstruction

The slope and correlation coefficients calculated for core MS75 (Fig. 5A) and core MS72 (Fig. 5B) indicate acceptable values for paleo-flow reconstruction, especially for MS72. However, several sediment layers that are not related to bottom-current transport are present in both cores. Thus, layers with correlation values <0.5 and slope values <0.07 were considered unreliable for paleo-flow reconstruction and rejected, according to the method proposed by McCave and Andrews (2019). The exclusion of the unreliable data led to an increase of the correlation coefficient ( $r$ ) from 0.744 to 0.876 (red circles in Figs. 5C, D) in core MS75, from 0.839 to 0.877 in core MS72 (blue circles in Figs. 5C, D). Therefore, the reliability tests indicate that core MS75 shows optimal values for paleo-flow reconstruction in unit A, while most of units B and C are unreliable for paleo-flow reconstruction (blue bars in Fig. 5E). On the other hand, core MS72 is overall characterized by hydraulically-sorted sediments, though few unreliable intervals for paleo-flow reconstruction are present in both units A and B (blue bars in Fig. 5E) (Table 2).

#### 4.4. Oxygen and Carbon stable isotopes

The  $\delta^{13}\text{C}_{\text{oc}}$  of plant debris collected in unit B of core MS72 are comprised between 16 and 24 per mil and their C/N molar ratios between 40 and 100 (Fig. 6). The  $\delta^{13}\text{C}_{\text{forams}}$  curve of the planktonic taxon *G. bulloides* (core MS72) shows the lower part, more or less corresponding to the lower sub-interval of the  $\delta^{18}\text{O}$  curve of the same species, with frequent oscillations of 0.5 per mil amplitude on average, while the middle part (up to ca. 300 cm) has a steadier trend (Fig. 7). The upper interval displays a general decrease of the values punctuated, between 180 and 130 cm, by a temporary increase of the values. The values increase again starting from ca. 50 cm upward (Fig. 7).

The  $\delta^{18}\text{O}$  curve of the planktonic taxon *G. bulloides* displays, for both cores, a similar trend, which can be divided in three main sub-intervals (Fig. 7). The lower one, from the core bottom up to 680 cm in core MS72 and up to 420 cm in core MS75, shows the heaviest values within an oscillatory trend around +3.5–3.6 per mil. From the top of this interval,



(caption on next page)

**Fig. 5.** Reliability tests of the downcore correlation coefficients on the 9-points window adapted from McCave and Andrews (2019). Plots of correlation vs slope identify the unreliable  $\overline{SS}$  data for cores: A) MS75 and B) MS72 when correlation is  $<0.5$  and slope  $<0.07$ . Plots of  $SS\%$  vs  $\overline{SS}$  to calculate: C) the initial correlation coefficient using all  $\overline{SS}$  data and D) the final correlation coefficient after rejection of unreliable data with their linear regressions. E) Pale blue bars indicate sediment layers where paleo bottom-currents are not the main active sediment-transport mechanism. (For interpretation of the references to colour in this figure legend, the reader is referred to the web version of this article.)

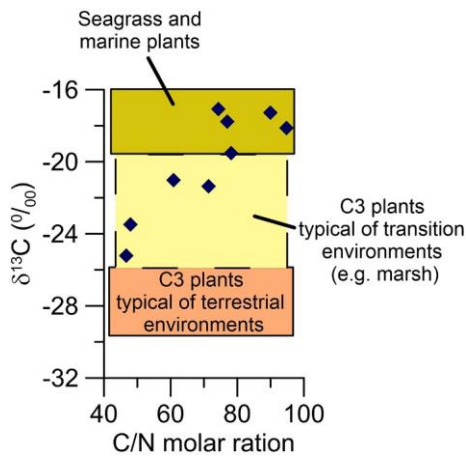


**Fig. 6.** Bulk composition (carbon/nitrogen ratio combined with stable carbon isotopes) of plant debris sampled in core MS72 (see Figs. 4B and 7 for location of the samples, “vr”). End-members  $\delta^{13}\text{C}$  values are from Vizzini et al. (2003) and DeLaune and Lindau (1987).

the two curves are characterized by a general decreasing trend culminating at 130 cm in core MS72 and at 13 cm in core MS75 with values between  $+2.2$  and  $2.5$  per mil. The upper interval shows a further abrupt decrease of the values ( $<1.0$  per mil). The  $\delta^{18}\text{O}$  curve of the benthonic foraminifer *B. marginata*, although represented by a quite minor number of measures because the taxon was lacking in several samples, mimics the general trend described for *G. bulloides*, but with absolute values higher than *G. bulloides* (Fig. 11).

#### 4.5. Foraminifera assemblages and ecozones

The turnovers observed in the foraminifera assemblages in the two cores allowed recognizing planktonic (Pl 1–4) and benthonic (Be 1–4) ecozones (Table 3). However, several samples (green “r” in Fig. 7) included rare specimens of benthonic epiphytic taxa (*Asterigerinata mamilla*, *Elphidium crispum*, *Reussella spinulosa*) or belonging to species typical of inner-middle shelf environment (*Ammonia beccarii*, *Elphidium decipiens*, *Elphidium advenum*, *Elphidium poyeanum*). Other samples were well-sorted and displayed the whole foraminifera assemblage characterized by a quite homogeneous test size (grey “r” in Fig. 7) or by the presence of very rare larger specimens (black “r” in Fig. 7).

#### 4.6. Age-depth model

The chronology of the two cores integrates the results and calibration of radiocarbon dating (Table 1), eco-biostratigraphy (Table 3), oxygen and carbon stratigraphy and allows determining an age-depth model (Table 4).

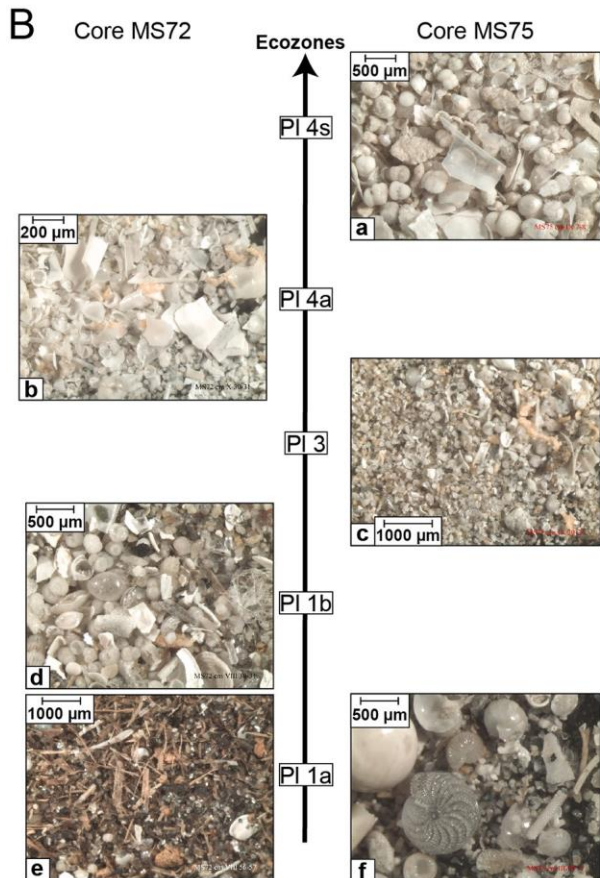
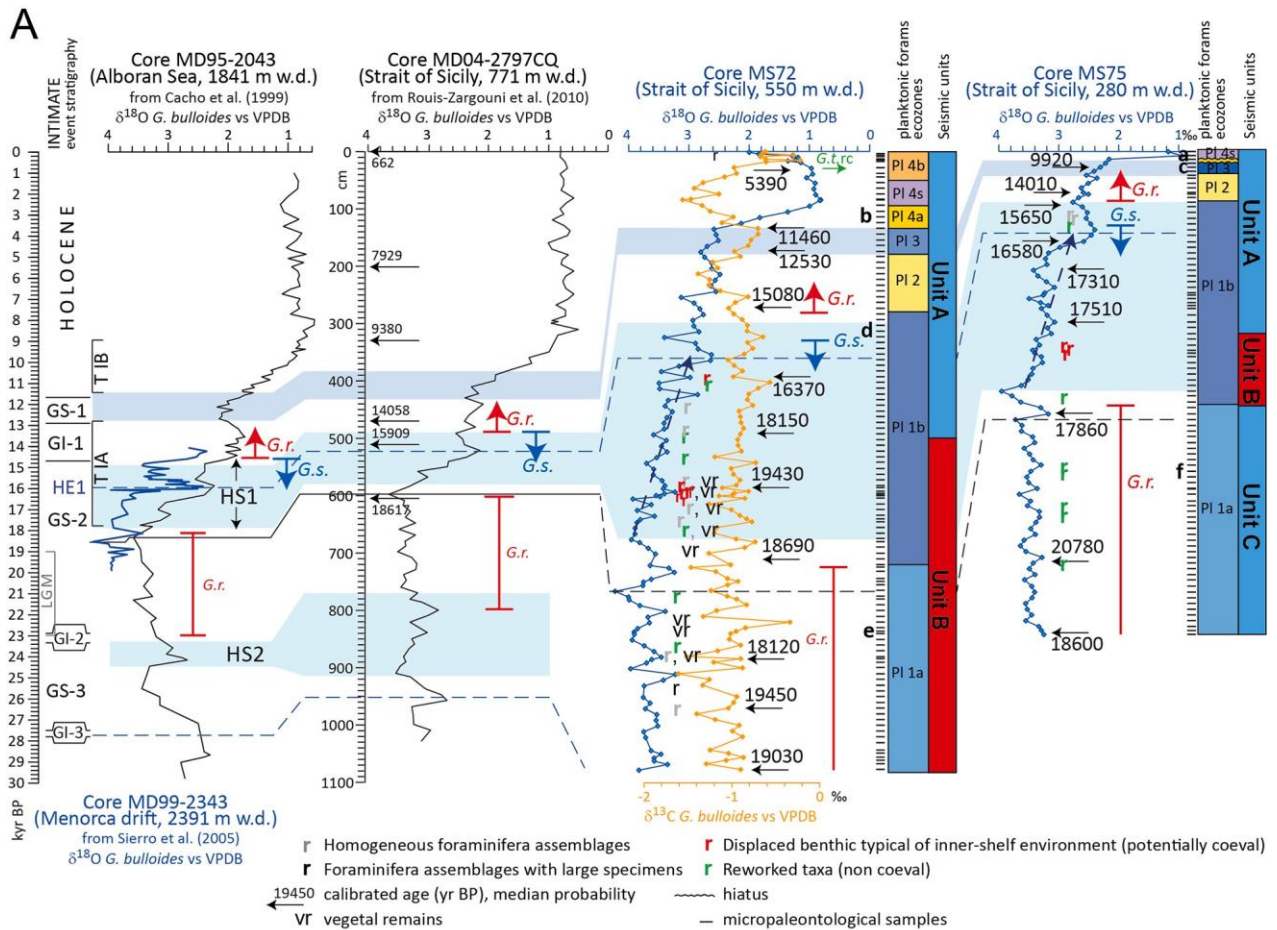
The planktonic foraminiferal ecozones can be compared with similar ecozones described for this area (Vergnaud-Grazzini et al., 1988; Sprovieri et al., 2003; Minisini et al., 2007; Rouis-Zargouni et al., 2010; Ferraro et al., 2018) and in other Mediterranean basins (Asioli et al., 1999; Perez-Folgado et al., 2003; Melki et al., 1999; Lirer et al., 2013; Siani et al., 2010). The paleoenvironmental interpretation of these ecozones provided a sequence of events correlatable with Mediterranean and extra-Mediterranean paleoclimate events during the Late Quaternary (event stratigraphy) (Asioli et al., 2001; Sprovieri et al., 2003).

Moreover, the turnovers observed in the planktonic foraminifera assemblages allowed recognizing the following (temporary) disappearances and/or (re)occurrences of taxa, already reported in the literature.

- Peak of *Globorotalia truncatulinoides* right coiling during the late Holocene. This event was reported in the Strait of Sicily also by Sprovieri et al. (2003), dated at 4300 yr cal. BP ( $4280 \pm 40$   $^{14}\text{C}$  age) by Minisini et al. (2007), at 2500 yr BP by interpolation by Rouis-Zargouni et al. (2010) and Desprat et al. (2013), and at 3600 yr BP ( $4139 \pm 37$   $^{14}\text{C}$  age) by Ferraro et al. (2018). The discrepancy between the calibrated ages by Minisini et al. (2007) and Ferraro et al. (2018) depends on the applied reservoir age ( $\Delta R$  value of  $71 \pm 50$  yr by Minisini et al., 2007 and no  $\Delta R$  correction by Ferraro et al., 2018), as the radiocarbon ages are very close. Here we preferred the calibrated age by Minisini et al. (2007), as based on the reservoir correction available for Strait of Sicily in the Calib dataset, while we rejected the much younger age by Rouis-Zargouni et al. (2010) confirming the age uncertainties for the upper 80 cm of core MD04-2797CQ suggested by Desprat et al. (2013).
- Temporary disappearance of *G. truncatulinoides* (along with a *Globorotalia inflata* frequency minimum) corresponding to the base of Sapropel 1 equivalent (Sprovieri et al., 2003; Minisini et al., 2007). We ascribed the age 10,000 yr cal. BP to this bioevent which detects the base of the S1a interval by Minisini et al. (2007), dated at  $9340 \pm 120$   $^{14}\text{C}$  age (10,052 yr cal. BP median probability). This age is in full agreement with the onset of the Sapropel 1 deposition in the Eastern Mediterranean and Adriatic Sea (Tesi et al., 2017).
- First abrupt increase of *Globigerinoides ruber* and warm species and concurrent last occurrence of *Globorotalia scitula*, marking the beginning of Greenland Interstadial 1 (GI-1)/Bølling-Allerød (Vergnaud-Grazzini et al., 1988; Perez-Folgado et al., 2003; Sprovieri et al., 2003; Minisini et al., 2007; Rouis-Zargouni et al., 2010).

The  $\delta^{18}\text{O}$  *G. bulloides* curve of the two cores have been correlated with other similar Mediterranean records in the Alborán Sea (core MD95–2043 from Cacho et al., 1999), the Western Mediterranean (Menorca drift, core MD99–2343 from Sierro et al., 2005) and the Strait of Sicily (core MD04–2797CQ from Rouis-Zargouni et al., 2010). The second step of the Termination I (T1B) with its characteristic abrupt decrease of the  $\delta^{18}\text{O}$  values, as well as the preceding GS-1 interval, can be detected quite easily in both the studied cores (blue area in Fig. 7). The first step of the Termination I (T1A), which includes the Heinrich Stadial 1 episode (HS 1) (Heinrich, 1988; Bond et al., 1992; Hodell et al., 2017) is also visible, although the progressive decreasing  $\delta^{18}\text{O}$  values culminating in the low peak of  $\delta^{18}\text{O}$  at the Heinrich Event 1 (ca. 16 ka, dashed blue line in Fig. 7) is at least 300 cm thick in both cores. The correlation of the HS1 interval is further constrained by the stratigraphic position of the foraminifera bioevents: first increase of *G. ruber* at the base of GI-1; Last Occurrence (LO) of *G. scitula* just before GI-1; the continuous presence of *G. ruber* between 23 and 18 kyr BP, as also reported by Perez-Folgado et al. (2003) in the Alborán Sea and in the Strait of Sicily by Rouis-Zargouni et al. (2010).

In addition to the oxygen isotope stratigraphy of *G. bulloides*, we also used the  $\delta^{13}\text{C}$  *G. bulloides* record in core MS72 to strengthen the chronology. Indeed, it has been demonstrated that across the Mediterranean the  $\delta^{13}\text{C}$  *G. bulloides* record displays a consistent pattern during the last glacial/post glacial interval with two negative excursions during T1A and IB intercalated by intervals of heavier values during the Younger Dryas (GS-1) and the present time (Vergnaud-Grazzini et al., 1986,



(caption on next page)

**Fig. 7.** A) Stratigraphic correlation of the  $\delta^{18}\text{O}$  record of cores MS72 and MS75 compared with the reference cores from the Alborán Sea, Menorca Drift and Strait of Sicily (see references on top of each core). The stratigraphic position of the main foraminiferal bioevents is reported. The reference INTIMATE event stratigraphy is from Björck et al. (1998) and Blockley et al. (2012). The ages reported for the reference core MD04-2797CQ are calibrated (yr BP) according to Rouis-Zargouni et al. (2010). The data were not corrected for the ice volume effect. G.r. = *Globigerinoides ruber*, G.s. = *Globorotalia scitula*, G. tr. rc = *Globorotalia truncatulinoides* right coiling, GS = Greenland Stadial, GI = Greenland interstadial, HS = Heinrich Stadial, LGM = Last Glacial Maximum chronozone according to Mix et al. (2001). B) Micrographs of foraminifera assemblages and their ecozones: a & b) hemipelagic sample without terrigenous; c) foraminifera with terrigenous; d) cold-water planktonic foraminifera showing different test sizes (no hydraulic selection); e) abundant vegetal debris with fine terrigenous; f) foraminifera assemblage, including taxa typical of inner shelf (*Elphidium crispum*), with fine terrigenous.

1988; Ariztegui et al., 2000). This pattern is visible in core MS72.

Radiocarbon datings help refining the age model, although some of them provide ages slightly older than expected based on the oxygen-isotope stratigraphy, mainly below the relative peak of  $\delta^{18}\text{O}$  of the Heinrich Event 1 at ca. 16 kyr BP, and a few age reversals also occur. The frequent presence of displaced, reworked or sorted foraminifera suggests transport processes possibly shedding sediment of ages not much older than the in situ sediments.

At the top of core MS72  $\delta^{18}\text{O}$  and  $\delta^{13}\text{C}$  *G. bulloides* records show an anomalous trend:  $\delta^{18}\text{O}$  curve has values too high (up to 2 per mil) and  $\delta^{13}\text{C}$  show oscillations too wide. The concurrent presence of reworked foraminifera confirms that the upper part of core MS72 (12 cm) is disturbed. Similarly, the uppermost part of core MS75 shows some inconsistency among  $^{14}\text{C}$  age (9920 yr cal. BP, corresponding to the beginning of the deposition of Sapropel 1 in the Levantine Basin),  $\delta^{18}\text{O}$  values (2.2 per mil, values relatively high and more coherent with the beginning of the Holocene rather than the base of Sapropel 1 deposition) and planktonic ecozone (more relatable with the pre-Boreal than with the GS-1, because of the common presence of *G. ruber*). Therefore, considering the lack of  $\delta^{18}\text{O}$  values typical of the abrupt shift of T IB (recorded in core MS72), sediment erosion is likely present between 7 and 20 cm. Overall, the mean temporal resolution over the deglacial interval is ca. 11–14 yr/cm.

#### 4.7. Sedimentation rates and age of emplacement of MTDs

Based on the reconstructed age-depth model, a linear sedimentation rate (LSR) was calculated for both cores. LSR was obtained from a linear interpolation between the intercepts of the control points that have not been rejected (Table 4). In core MS75, sedimentation rates range from 17 to 114 cm/kyr and briefly peak at 1322 cm/kyr in the early phase of HS1 and 770 cm/kyr in the last phase of LGM (Fig. 8A). In core MS72, sedimentation rates range from 11 to 95 cm/kyr and peak at 230 cm/kyr in the early phase of HS1 and 370 cm/kyr in the last phase of LGM (Fig. 8B).

The age-depth model allowed to constrain the age of significant reflections in the sub-bottom profiles and tentatively dating the age of emplacement of two submarine landslides identified by their chaotic seismic facies: the Gela Drift Slide (GDS in Fig. 3A) and the South Gela Basin Slide (SGBS in Fig. 4A). For GDS, the high amplitude reflection at the base of the slide accumulation correlates with the top of unit B of core MS75 and, according to the age model, corresponds to 17.5 kyr cal. BP (red dashed line, Fig. 3A). Therefore, GDS must have been emplaced after ca. 17.5 ka. For SGBS, the last seismic reflection cut by the slide correlates with the top of unit B of core MS72, which dates at 16.8 kyr cal. BP (blue dashed line in Fig. 4A) suggesting that SGBS must be younger.

#### 4.8. Paleoenvironmental elemental proxies

Based on the reconstructed chronology, the elemental ratio proxies inform on periods of increased/decreased sea-bottom oxygenation, biogenic activity and productivity.

##### 4.8.1. Core MS75

From 18.6 to 18 kyr BP S/Cl ratio shows low values around 0.01, increasing to 0.05 around 18 kyr BP and varying around 0.03 until 8 kyr

BP (Fig. 9).

From 18.5 to 17 kyr BP Ti/Ca ratio shows values  $>0.04$ , decreasing to 0.03–0.04 until 15 kyr BP where a drastic decrease occurs with values nearing 0.01. At 13 kyr BP Ti/Ca increases above 0.02 before decreasing again down to 0.01 around 12.7 ka (Fig. 9).

##### 4.8.2. Core MS72

Ba/Ti, is higher ( $-0.02$ ) from 19 until 12.8 kyr BP along with higher values in S/Cl and stronger variations up to 0.17 from 19 to 15.8 kyr BP (Fig. 10). From 15.08 to 12.8 kyr BP, Ba/Ti stays high while fewer variations are observed in S/Cl. At 12.8 kyr BP, Ba/Ti values drastically decrease ( $-0.09$ ) at the end of GI-1 and S/Cl shows constant values close to zero. From 11.5 to 4 kyr BP Ba/Ti stays low as well as S/Cl.

Since 19 ka Ti/Ca shows high values around 0.05 until 15.08 kyr BP when a drastic decrease down to 0.02 occurs (Fig. 10). Towards the end of GI-1, Ti/Ca ratio increases until reaching values up to 0.03 around 12 ka (GS-1) and keep similar values during the Holocene.

## 5. Discussion

### 5.1. Deciphering along-slope and downslope processes in sedimentary records

Two sediment cores from the upper and lower slope of Gela Basin, Strait of Sicily, were collected along a sediment drift deposited under the activity of the Levantine Intermediate Water (LIW) and provided an unprecedented stratigraphically-expanded sedimentary record spanning the last phase of LGM and early phase of HS1 ( $\sim 19$ –16 kyr BP) for the Central Mediterranean Sea. In particular, the interval 19–18 kyr BP is characterized by exceptionally high linear sedimentation rates in both cores (LSR, Fig. 8). Various proxies allow identifying the sedimentary processes that concur to obtain such deposition.

During 19–16 ka, sediment core MS75 records weak bottom-current velocities (Fig. 12) and prevailing deposition of clay in unimodal grain size distribution (Fig. 3B, Table 2) which exclude the presence of a persistent contour-current regime along the upper slope. The presence of sparse laminations and normal grading beds (Fig. 3B) together with reworked foraminifera (Fig. 7) indicate that moderate downslope sediment transport is taking place in the upper slope. Variations in S/Cl and presence of authigenic pyrites and pyritized micro burrows are all indicative of lack of oxygen/ventilation and stressful conditions at the sea bottom (Fig. 9) whereas transitional ichnofacies seems to indicate less stressful condition, that may be related to sediment-gravity flows coarsely-spaced in time.

On the contrary, during 19–16 ka, in sediment core MS72, high  $\overline{\text{SS}}$  and bimodal grain size distribution (Fig. 4B, Table 2), combined with increased hydraulic sorting of foraminifera (Fig. 7), indicate that strong bottom-currents are actively moving sediments on the lower slope. The seismic facies points to turbidite deposition (Fig. 4A), the grain-size log highlights inverse to normal grading beds typical of contourite deposition intercalated with normal grading beds typical of rapid downslope deposition (Fig. 4B). The sedimentary facies indicate the presence of products of storm waves (tempestites) intercalated with sediment-gravity flows (turbidites) with a combination and overprinting of traction transport and suspended load (Fig. 4D). At the same time, convolute and flame structures seem produced just below the water-sediment interface by a passing current or by downslope sliding on the

Table 3

Foraminifera ecozones and inferred paleoenvironments for cores MS72 and MS75 along with the corresponding time intervals/events to which the ecozones were equated. Bolded and underlined names define the abundant and common species, respectively.

Ecozones	Depth	Assemblage	Environment	References	Time interval
Pl 4b	MS72 = 0–54 cm, not recognized in MS75	<i>Globigerinoides ruber</i> , <i>Globorotalia inflata</i> , <i>Globorotalia truncatulinoides</i> (in MS72, <u><i>r.c.</i></u> dominates at cm 28–29 in MS72, while <i>l.c.</i> dominates cm 0–28). <i>Globigerinoides sacculifer</i> , <i>Orbulina universa</i> , <i>Globigerinella siphonifera</i> , <i>Globigerina bulloides</i> , <i>Turborotalita quinqueloba</i> , <i>Globigerinella calida</i> , <i>Globoturborotalita rubescens</i>	Warm water assemblage with deep dwellers (winter mixing)	Vergnaud-Grazzini et al. (1988), Sprovieri et al. (2003), Minisini et al. (2007), Rouis-Zargouni et al. (2010), Ferraro et al. (2018)	Late Holocene (0–6 kyr BP)
Pl 4 s	MS72 = 54–94 cm, MS75 = 0–8 cm	<i>G. ruber</i> (including <i>G. ruber</i> pink variety with thin and inflated test), <i>O. universa</i> , <i>G. sacculifer</i> , <i>G. siphonifera</i> , <i>G. bulloides</i> , <i>T. quinqueloba</i> , <i>G. rubescens</i> , <i>G. inflata</i>	Warm water assemblage with strong decrease of deep dwellers (weak winter mixing)	Vergnaud-Grazzini et al. (1988), Sprovieri et al. (2003), Minisini et al. (2007), Rouis-Zargouni et al. (2010)	Holocene (Sapropel 1 deposition) (6–10 kyr BP)
Pl 4a	MS72 = 94–134 cm, MS75 = 13–14 cm	<i>G. ruber</i> , <i>G. inflata</i> , <i>G. truncatulinoides</i> , <i>G. glutinata</i> , <i>G. bulloides</i> , <i>T. quinqueloba</i> , <i>Neogloboquadrina incompta</i>	Temperate water assemblage with deep dwellers (winter mixing)	as above	Early Holocene (pre-Boreal) (10–11.5 kyr BP)
Pl 3	MS72 = 134–180 cm, MS75 = 20–41 cm	<i>G. bulloides</i> , <i>N. incompta</i> , <i>T. quinqueloba</i> , <i>G. glutinata</i> , <i>G. inflata</i> , <i>G. ruber</i> RR/absent	Cold and productive water assemblage	as above	Late Pleistocene (GS-1) (11.5–12.8 kyr BP)
Pl 2	MS72 = 180–280 cm, MS75 = 41–88 cm	<i>G. ruber</i> , <i>G. inflata</i> , <i>T. quinqueloba</i> , <i>G. bulloides</i> , <i>N. incompta</i> , <i>Orbulina universa</i> , <i>G. glutinata</i> , <i>Globorotalia truncatulinoides</i>	Temperate water assemblage, DCM developed, winter mixing	as above	Late Pleistocene (GI-1) (12.8–14.7 kyr BP)
P 1b	MS72 = 280–720 cm, MS75 = 88–442 cm	<i>T. quinqueloba</i> , <i>N. incompta</i> and <i>G. bulloides</i> , <i>Globorotalia scitula</i> , <i>G. glutinata</i>	Cold and productive water assemblage	as above	Late Pleistocene (GI-1) (14.5–18 kyr BP)
Pl 1a	MS72 = 720–1079 cm, MS75 = 442–842 cm	<i>T. quinqueloba</i> , <i>N. incompta</i> , <i>G. bulloides</i> , <i>G. scitula</i> , <i>G. glutinata</i> , <i>G. ruber</i> (continuous presence)	cold and productive water assemblage	Sprovieri et al. (2003), Rouis-Zargouni et al. (2010)	Late Pleistocene > 18 kyr BP
Be 4	MS72 = 0–54 cm and 94–134 cm, MS75 = 8–14 cm	assemblage not very rich; <i>Uvigerina mediterranea</i> , <i>Gyroidinoides altiformis</i> , <i>Hyalinea balthica</i> , <i>Melonis barleeanum</i> , <i>Bulimina marginata</i> , <i>Cibicides pachyderma</i> , <i>Cassidulina laevigata carinata</i> , <i>Bigenerina nodosaria</i> , <i>Pseudoclavulina crustata</i> , <i>Bulimina costata</i> , <i>Amphycorinae scalaris</i> , <i>Planulina wuellerstorfi</i> , <i>Lenticulina stellata</i> , <i>Lenticulina peregrina</i> , <i>Gyroidinoides</i> spp., <i>Glomospira charoides</i> , miliolids ( <i>Biloculinella labiata</i> , <i>Sigmoilinita tenuis</i> , <i>Sigmoilopsis schlumbergeri</i> , <i>Quinqueloculina seminulum</i> )	upper slope (mesotrophic environment)	Jorissen (1987), De Stigter et al. (1998), De Rijk et al. (1999), Schmiel et al. (2010), Minisini et al. (2007)	Holocene (0–11.7 kyr BP) except Sapropel 1 interval
Be 4 s	MS72 = 54–94 cm, MS75 = 0–8 cm	foraminifera scarce or rare; <i>U. mediterranea</i> , <i>G. altiformis</i> , <i>M. barleeanum</i> , <i>Uvigerina peregrina</i> , <i>Chilostomella mediterraneensis</i> , <i>Sphaeroidina bulloides</i> , <i>C. laevigata carinata</i> , <i>B. nodosaria</i> , <i>P. crustata</i> , <i>A. scalaris</i> , <i>Lenticulina</i> spp., miliolids ( <i>Biloculinella globula</i> , <i>Pyrgo depressa</i> , <i>Triloculina trigonula</i> , <i>Spiroloculina</i> spp., <i>S. schlumbergeri</i> )	upper slope (mesotrophic environment, with more organic matter accumulation and lower bottom ventilation)	Jorissen (1999), De Rijk et al. (1999), Minisini et al. (2007)	Holocene (Sapropel 1 deposition) (6–10 kyr BP)
Be 3	MS72 = 134–180 cm, MS75 = 20–41 cm	<i>U. mediterranea</i> , <i>Brizalina dilatata</i> , <i>C. laevigata carinata</i> , <i>G. altiformis</i> , <i>H. balthica</i> , <i>M. barleeanum</i> , <i>B. marginata</i> , <i>C. pachyderma</i> , <i>Bolivina albatrossi</i> , <i>Globobulimina affinis</i> , <i>Bulimina inflata</i> , <i>B. costata</i> , <i>Hanzawaia boueana</i> , <i>S. bulloides</i> , <i>Gyroidinoides</i> spp., <i>Hoeglundina elegans</i> , <i>G. altiformis</i> , <i>P. crustata</i> , <i>Pyrgo bulloides</i> , <i>P. depressa</i> , <i>Spiroloculina</i> spp., <i>S. tenuis</i> , <i>S. schlumbergeri</i> , <i>Q. seminulum</i> , <i>Triloculina tricarinata</i>	upper slope	Vergnaud-Grazzini et al. (1988), Minisini et al. (2007)	Late Pleistocene (GS-1) (11.5–12.8 kyr BP)
Be 2	MS72 = 180–280 cm, MS75 = 41–88 cm	<i>C. laevigata carinata</i> , <i>U. mediterranea</i> , <i>U. peregrina</i> , <i>B. dilatata</i> , <i>G. altiformis</i> , <i>H. balthica</i> , <i>M. barleeanum</i> , <i>S. bulloides</i> , <i>B. marginata</i> , <i>C. pachyderma</i> , <i>G. affinis</i> , <i>C. mediterraneensis</i> , <i>B. costata</i> , <i>H. boueana</i> , <i>Gyroidinoides</i> spp., <i>H. elegans</i> , <i>Planulina ariminensis</i> , <i>P. bulloides</i> , <i>Spiroloculina</i> spp., <i>S. tenuis</i> , <i>S. schlumbergeri</i> , <i>Q. seminulum</i> , <i>Quinqueloculina padana</i> , <i>Articulina tubulosa</i>	upper slope	as above	Late Pleistocene (GI-1) (12.8–14.7 kyr BP)
Be 1b	MS72 = 280–720 cm, MS75 = 88–442 cm	<i>B. dilatata</i> , <i>Brizalina aenariensis</i> , <i>Brizalina alata</i> , <i>C. laevigata carinata</i> , <i>B. albatrossi</i> , <i>H. balthica</i> , <i>M. barleeanum</i> , <i>S. bulloides</i> , <i>B. inflata</i> , <i>Nonion depressulus</i> , <i>B. nodosaria</i> , <i>B. marginata</i> , <i>U. peregrina</i> , <i>Trifarina angulosa</i> , <i>G. affinis</i> , <i>C. pachyderma</i> , <i>G. altiformis</i> , <i>Hanzawaia boueana</i> , <i>P. bulloides</i> , <i>P. depressa</i> , <i>Spiroloculina</i> spp., <i>Cycloforina tenuicollis</i> , <i>S. tenuis</i> , <i>S. schlumbergeri</i> , <i>Q. seminulum</i> , <i>Biloculinella</i> spp., <i>A. tubulosa</i> in core MS72 and <i>Sigmoilina sellii</i> in core MS75	upper slope (mesotrophic environment, with low bottom ventilation)	as above	Late Pleistocene 14.5–18 kyr BP
Be 1a					

(continued on next page)

Table 3 (continued)

Ecozones	Depth	Assemblage	Environment	References	Time interval
MS72 = 720–1079 cm, MS75 = 442–842 cm		rich assemblage; <i>B. aenariensis</i> , <i>B. alata</i> , <i>B. dilatata</i> , <i>M. barleeianum</i> , <i>Valvulineria</i> <i>complanata</i> , <i>C. laevigata carinata</i> and <i>H. balthica</i> and <i>B. marginata</i> (MS75), <i>S. bulloides</i> , <i>B. inflata</i> , <i>G. affinis</i> , <i>C. pachyderma</i> , <i>U. peregrina</i> , <i>B.</i> <i>nodosaria</i> , <i>P. bulloides</i> , <i>Spiroloculina</i> spp., <i>Miliolinella subrotunda</i> , <i>S. tenuis</i> , <i>S. schlumbergeri</i> , <i>Q. seminulum</i> , <i>Q. padana</i> , <i>A. tubulosa</i> (MS75),	upper slope (mesotrophic environment, with low bottom ventilation)	<a href="#">Sprovieri et al. (2003)</a> , <a href="#">Rouis- Zargouni et al. (2010)</a>	Late Pleistocene > 18 kyr BP

Table 4  
Age-depth model adopted in this study.

Core depth (cm)	Control point (yr BP)	Source	Note
Core MS75			
10	8000	Ecozone PI 1 s	
13	11,700	top ecozone PI 2 (GS-1)	
20.5	9920	$^{14}\text{C}$ AMS (median probability)	rejected
41	12,900	base ecozone PI 2 (GS-1)	
71.5	14,010	$^{14}\text{C}$ AMS (median probability)	
96.5	15,650	$^{14}\text{C}$ AMS (median probability)	
136.5	16,000	$\delta^{18}\text{O}$ negative peak HS1 core MD99–2343 ( <a href="#">Sierro et al., 2005</a> )	
146.5	16,580	$^{14}\text{C}$ AMS (median probability)	
207.5	17,310	$^{14}\text{C}$ AMS (median probability)	
298	17,510	$^{14}\text{C}$ AMS (median probability)	
417	17,600	$\delta^{18}\text{O}$ positive peak base HS1 core MD99–2343 ( <a href="#">Sierro et al., 2005</a> )	
457.5	17,860	$^{14}\text{C}$ AMS (median probability)	rejected
457.5	18,100	$\delta^{18}\text{O}$ negative peak below HS1 core MD99–2343 ( <a href="#">Sierro et al., 2005</a> )	
717.5	20,780	$^{14}\text{C}$ AMS (median probability)	rejected
842	18,600	$^{14}\text{C}$ AMS (median probability)	
Core MS72			
13.5	4300	peak <i>G. truncatulinoidea</i> r.c. ( <a href="#">Mimisini et al., 2007</a> )	
44.5	5390	$^{14}\text{C}$ AMS (median probability)	
94	10,000	Base ecozone PI 1 s	
134.5	11,460	$^{14}\text{C}$ AMS (median probability)	
174.5	12,530	$^{14}\text{C}$ AMS (median probability)	
273.5	15,080	$^{14}\text{C}$ AMS (median probability)	
360	16,000	$\delta^{18}\text{O}$ negative peak HS1 core MD99–2343 ( <a href="#">Sierro et al., 2005</a> )	
393.5	16,370	$^{14}\text{C}$ AMS (median probability)	
493.5	18,150	$^{14}\text{C}$ AMS (median probability)	rejected
587.5	19,430	$^{14}\text{C}$ AMS (median probability)	rejected
676	17,600	$\delta^{18}\text{O}$ positive peak base HS1 core MD99–2343 ( <a href="#">Sierro et al., 2005</a> )	
711.5	18,690	$^{14}\text{C}$ AMS (median probability)	rejected
733	18,100	$\delta^{18}\text{O}$ negative peak below HS1 core MD99–2343 ( <a href="#">Sierro et al., 2005</a> )	
885.5	18,120	$^{14}\text{C}$ AMS (median probability)	rejected
970.5	19,450	$^{14}\text{C}$ AMS (median probability)	rejected
1077.5	19,030	$^{14}\text{C}$ AMS (median probability)	

unconsolidated mud (e.g. [Potter et al., 2005](#)). Therefore, the load structures can be a direct sign of the high sedimentation rates recorded in the lower slope during the last phase of LGM and early HS1 ([Fig. 4E](#)). Furthermore, the presence of bioturbating fauna, characterized by macro ichnofacies signal, that tend to rework the upper parts of a bed while leaving the lower parts unaffected ([Fig. 4F](#)), are indicative of turbidites interbedded with less energetically accumulated contourites (e.g. [Stow and Smillie, 2020](#)).

Overall, intermediate characteristics between silty-muddy turbidites and muddy contourites are thus apparent in the lower slope and suggest the activity of contour currents during or shortly after turbidite deposition, as proposed for margins where the interplay between downslope and along-slope processes is more frequent ([Fig. 4F](#); [Massé et al., 1998](#); [Fonnesu et al., 2020](#)). The concomitant presence of both displaced (e.g. *Elphidium decipiens*) and hydraulically-sorted foraminifera confirm the

overlap of two transport mechanisms. Furthermore, the presence of plant debris from shallow water marine domain (e.g. *Posidonia oceanica*) and transitional domains (e.g. marsh, [Fig. 6](#)) strengthen the evidence of sediment input from the inner-mid shelf through the action of persistent gravity flows active until at least 17.5 ka ([Figs. 4, 11](#)). The high sedimentation rate associated with downslope sediment transport superimposed by sustained lateral advection caused overall low oxygen conditions, as testified by the presence of sediments rich in iron sulphate and benthic foraminifera resistant to low oxygen stressful conditions induced by rapid burial. Furthermore, shallow tier structures left by bioturbating fauna are indicative that the bottom-current core was located near the lower slope ([Table 2](#)).

During sea-level low stands and glacial periods, the shoreline is closer to the shelf edge and sediment input to the slope increases, this has been observed particularly in the last phase of LGM when also several submarine landslides are believed to have been emplaced along the continental margins (e.g. [Lee, 2009](#)). High sedimentation rates

during glacial periods are thus normal, however strong bottom-currents active along a specific continental margin imply an even larger sediment availability along the slope to counterbalance bottom erosion ([Miramontes et al., 2016](#)). Marked increase in sedimentation rates during glacial periods, 2–7 times those in interglacials, are often considered a function of reduction of vegetation cover during arid conditions, resulting in increased erosion and basin sediment flux (e.g. [McNeill et al., 2019](#)). Furthermore, frequency and magnitude of hyperpycnal flows are known to increase during arid climate when relative sea level rises in areas with a wide continental shelf ([Mulder et al., 2003](#)), as is the case of the Malta Plateau. The sea level was rising with rates of ca. 12 m/kyr between 19 and 17.5 ka ([Lambeck et al., 2014](#)) and the scattered plot of Zr/Rb indicating high Zr content could be correlated with flood events carrying greater coarse-grain sediment loads (e.g. [Wang et al., 2011](#)). High LSR observed in the northern Gela Basin were explained by the occurrence of intermittent hyperpycnal flows ([Kuhlmann et al., 2015](#)). However, in the southern Gela Basin the presence along the slope of epiphytic benthic taxa ([Fig. 11](#)) and the source apportionment of the plant debris ([Fig. 6](#)) suggest a sediment provenance from the inner and middle shelf. Therefore, all data including terrigenous proxy (Ti/Ca) concur to exclude a direct riverine sediment source and indicate that sediment was sourced from shelf erosion during low stands of sea level and moderate sea-level rise.

The presence of gullies on the northern slope of the Gela Basin ([Fig. 1C](#)) may have represented preferential sediment by-pass from shelf to basin, as elsewhere envisaged ([Ricketts and Evenchick, 1999](#)), together with along-slope sediment transport from north to south sustained by strong bottom currents concomitantly active at the seafloor in the lower slope. The sediment by-pass may have shut down at 18–17.5 ka, when the two sediment cores face a drastic drop of LSR and bottom-current velocities peak maximum intensity in the lower slope ([Figs. 10 and 12](#)). Moreover, the significant change in magnetic susceptibility trend between units A and B of core MS72 ([Fig. 4B](#)) may indicate different sources with sediment supply from downslope gravity flows before 17.5 ka and prevailing marine deposition afterwards. The drastic reduction in sedimentation rate can thus be explained by a combination of factors: prevailing erosion over deposition by bottom-current action, reduced along-slope apportionment of sediment from the north together with

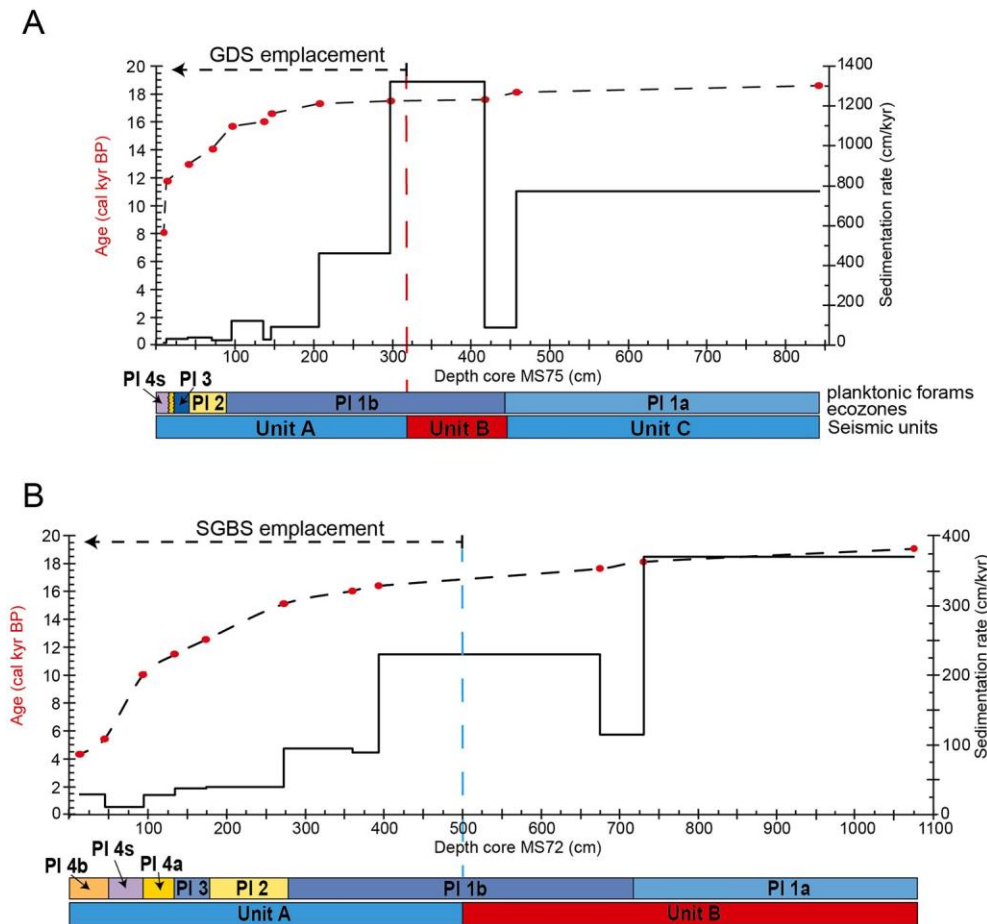


**Fig. 8.** Linear sedimentation rates (LSR) of cores MS72 (A) and MS75 (B). Red dots indicate the  $^{14}\text{C}$  calibrated ages. Planktonic foraminifera ecozones and seismic units are displayed below the age-depth plot. The dashed vertical lines identify the estimated age of emplacement of mass-transport deposits GDS and SGBS. (For interpretation of the references to colour in this figure legend, the reader is referred to the web version of this article.)

reduced sediment input from sediment-gravity flows in the southern slope of the Gela Basin.

### 5.2. LIW intensity and interface variations in the Gela Basin during deglaciation

By excluding both the stratigraphic intervals deposited under downslope processes (tempestites and turbidites, Fig. 4B) and those with evidence of reworking/displacement/hydraulic selection of foraminifera (yellow stripes in Fig. 11) of core MS72, we are able to reconstruct the post-LGM bottom current dynamics in the Gela Basin and making inferences about the thermohaline Mediterranean circulation.

During the last phase of LGM and early HS1 (19.4–18 kyr cal. BP)  $\delta^{13}\text{C}_{\text{forams}}$  and  $\delta^{18}\text{O}$  (Fig. 11) and planktonic assemblages are typical of cold and productive waters, benthic assemblages are dominated by species expected in mesotrophic environment with low bottom ventilation (ecozones PI 1a and Be 1a in Table 3, respectively). The  $\overline{\text{SS}}$  increases by 4–6  $\mu\text{m}$  with an increase in current velocity by 4  $\text{cm s}^{-1}$  (Fig. 12). Therefore, benthic assemblages and grain-size data support the presence of an active Levantine Intermediate Water (LIW) during MIS 2 in the Gela Basin, impacting the benthic communities, in agreement with the intense Mediterranean thermohaline circulation recorded in the Western Mediterranean Sea for the same time interval (e.g. Sierrro et al., 2005; Cacho et al., 2007).

During the lower phase of HS1 (18–16.3 kyr BP), the  $\overline{\text{SS}}$  constantly decreases although still indicates fast bottom-currents (Fig. 12). Planktonic assemblages are still representative of cold and productive water

(PI 1b, Table 3), whereas benthic assemblages are dominated by infaunal species resistant to low oxygen conditions (e.g. De Rijk et al., 1999; Goineau et al., 2012) (Be 1b in Table 3). In particular, the *B. marginata*  $\delta^{13}\text{C}_{\text{forams}}$  shows a slight increase of the mean values in comparison with the previous interval. This trend may suggest a decrease of organic flux to the seafloor. In fact, a change in the micro-habitat by *B. marginata* as response to variations of oxygen/food supply (e.g. vertical migration towards the sediment-water interface, Jorissen et al., 1995) is not plausible, because the benthic assemblage does not show major changes in the most abundant/dominant taxa between ecozones (Be 1a and Be 1b in Table 3). More importantly, the observed  $\delta^{13}\text{C}$  increase does not match with the general abrupt decreasing trend, which starts at 18 ka and culminates during the HE1 event, displayed by the  $\delta^{13}\text{C}$  record of the epibenthic taxa *C. pachyderma* in the western Mediterranean Sea (Cacho et al., 1999, 2007), Menorca drift (Sierro et al., 2005) and Strait of Sicily (Vergnaud-Grazzini et al., 1988) (Fig. 11). Therefore, the progressive weakening of the Western Mediterranean Deep Water (Cacho et al., 1999, 2007; Sierrro et al., 2005) and slowdown of the vertical mixing of water masses in the Strait of Sicily (Vergnaud-Grazzini et al., 1988) is not registered in the high-resolution sedimentary record of core MS72 with the same intensity and pace during this time interval.

During the upper phase of HS1 (16.3–15 kyr BP) the  $\delta^{13}\text{C}$  of *B. marginata* and *G. bulloides* finally start showing a marked decreasing trend just below the  $\delta^{18}\text{O}$  minimum peak related to the HE1 event (Fig. 11), pointing to enhanced water mass stratification and productivity, in agreement with increased Ba/Ti (Fig. 10). The  $\overline{\text{SS}}$  further

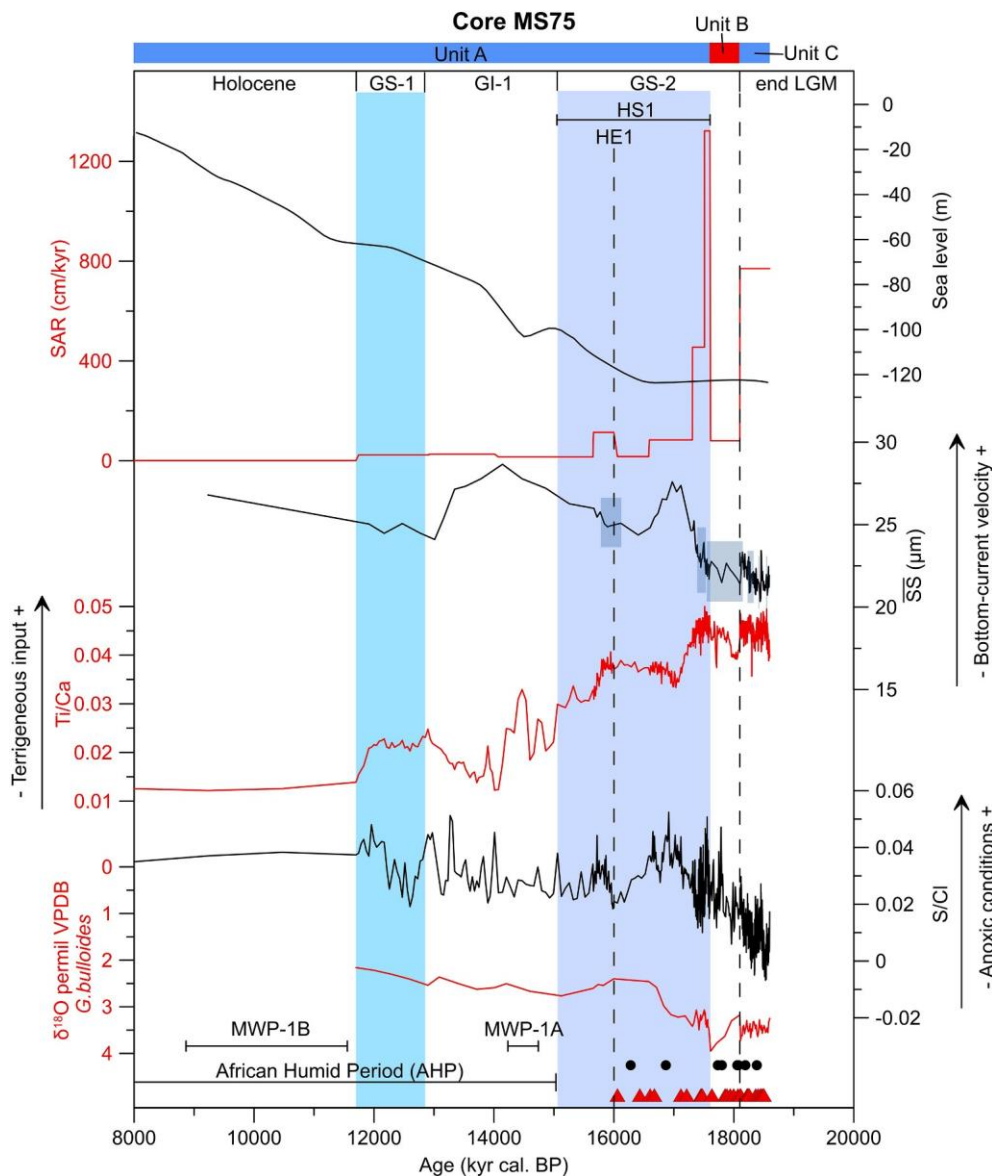


**Fig. 9.** Isotopic stratigraphy ( $\delta^{18}\text{O}$ ), geochemical element composition (S/Cl, Ca/Ti), sortable silt mean size ( $\overline{SS}$ ) and LSR of core MS75 displayed in age. Sea-level curve from Lambeck et al. (2014). Reworked foraminifera = black circles, pyrites = red triangles. GS-1 = Glacial Stadial 1 (sky blue bar), GI-1 = Glacial Interstadial 1, HS1 = Heinrich Stadial 1 (dark blue bar), HE1 = Heinrich Event 1, LGM = Last Glacial Maximum. Pale blue rectangles on  $\overline{SS}$  data represent sediments unsorted by bottom currents. (For interpretation of the references to colour in this figure legend, the reader is referred to the web version of this article.)

decreases highlighting an overall decreasing in current speed of  $6 \text{ cm s}^{-1}$  since the base of the HS1 (Fig. 12). Transitional ichnofacies appear around HE1 (Fig. 4C), suggesting a change to intermediate ventilation and reduced stress at the seafloor. Overall, the data suggest that only in the late HS1 the Gela Basin slope was progressively affected by the weakening of the bottom currents accompanied by increase of water stratification and organic flux to the sea-bottom, in agreement with similar observations in the Western Mediterranean (Cacho et al., 2007) and Strait of Sicily (Vergnaud-Grazzini et al., 1988) (Fig. 1). However, this slow-down is in striking contrast with observations made in the Corsica Trough where the LIW's speed increases during HE1 in association with minimal sea-surface temperatures recorded throughout the Mediterranean Sea (Toucanne et al., 2012, Fig. 12). The stratigraphically-expanded sedimentary succession of the Gela Basin thus reveals, for the first time, the short-term variability of the LIW in the Central Mediterranean Sea during HS1. Our data suggest that the decisive weakening of the LIW began 16.3–16.5 kyr BP, ca. 1000 years before what has been previously suggested by Toucanne et al. (2012) and does not coincide with the amelioration of the atmospheric circulation at the beginning of the interstadial (i.e. GI-1 warm period). This difference can be the result of small-scale oceanographic differences in

circulation pattern between the Corsica Trough and Gela Basin, which can be ascribed both to the quite different morphological settings and the connection with the Western Mediterranean. The Corsica Trough consists of a linear narrow corridor well connected with the surface circulation of the Western Mediterranean, to whose changes responds promptly. On the other hand, the Gela Basin is a bowl-shaped basin, which better reflects the oceanographic changes of the eastern Mediterranean and in particular the LIW's dynamics. In summary, our sediment cores seem capable of better disentangling the different circulation patterns between the Western and the Eastern Mediterranean at a centennial time-scale.

Subsequently, during the Greenland Interstadial 1 (GI-1, 15 kyr–12.8 kyr cal. BP)  $\delta^{18}\text{O}$  show trends similar to the rest of the Mediterranean (e.g. Desprat et al., 2013, Fig. 11),  $\overline{SS}$  data indicate the continued weakening of the LIW on the lower slope. The concurrent drastic Ti/Ca drop associated with very low LSR support low lateral advection during GI-1, resulting in the deposition of sediments relatively high in biogenic Ca on the lower slope. These overall conditions are in agreement with observations made in the reference studies (Fig. 12). On the contrary,  $\overline{SS}$  data of core MS75 show a large increase of the flow velocities from 16.5 ka (+5.7  $\text{cm s}^{-1}$ , Fig. 12). This large flow increase is supported by grain-size

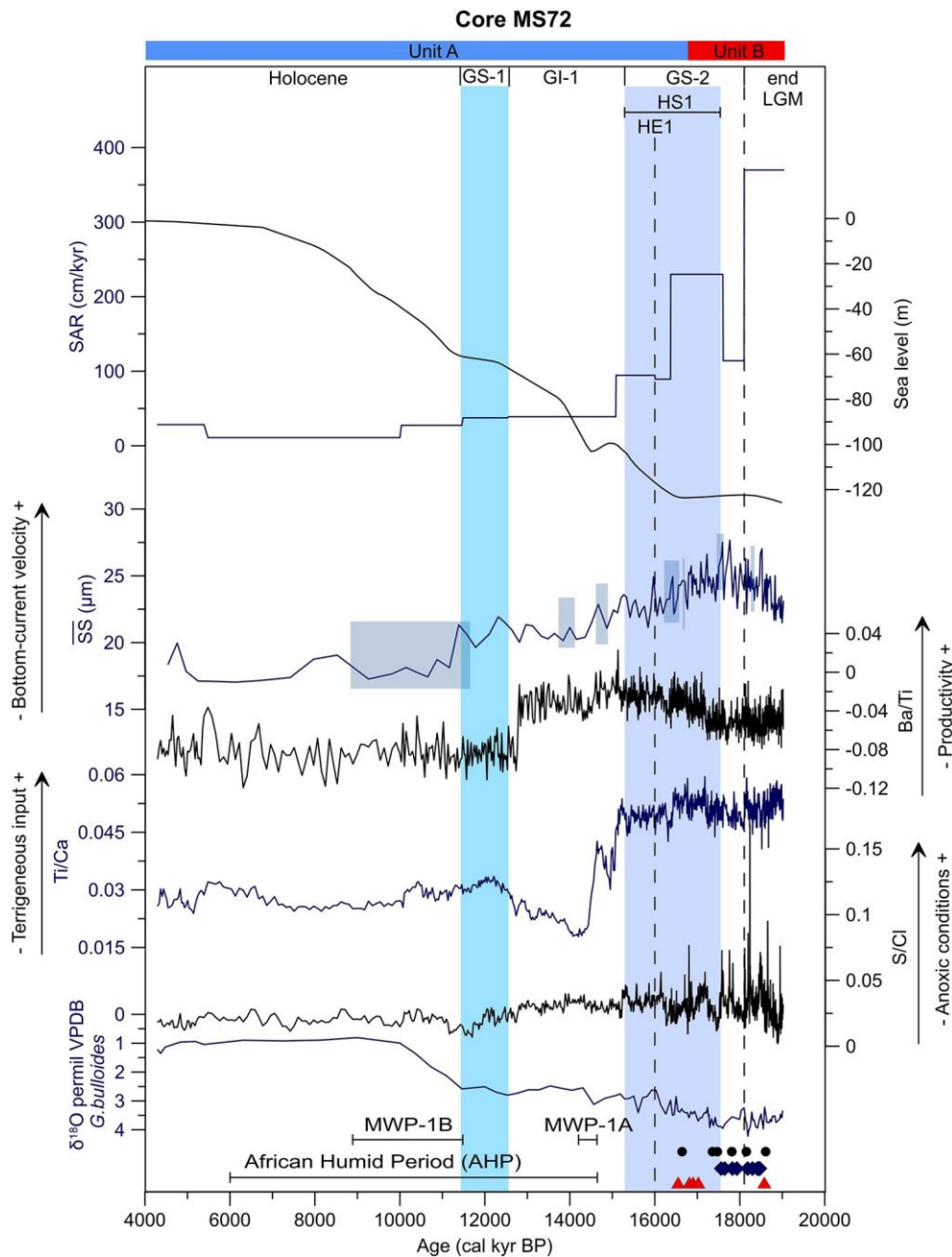


**Fig. 10.** Isotopic stratigraphy ( $\delta^{18}\text{O}$ ), geochemical element composition (S/Cl, Ca/Ti, Ba/Ti), sortable silt mean size ( $\overline{SS}$ ), and LSR of core MS72 displayed in age. Sea-level curve from Lambeck et al. (2014). Reworked foraminifera = black circles, pyrites = black triangles, plant debris = blue diamonds. See Fig. 9 for other symbols and abbreviations. (For interpretation of the references to colour in this figure legend, the reader is referred to the web version of this article.)

bimodal distribution, inverse to normal grading and high Zr/Rb (Fig. 3B), which constrain the activity of a current able to mobilize coarse grains on the upper slope. Active bottom currents are also shown by increasing presence of micro-ichnofacies indicative of stressful conditions at the seafloor (Fig. 3D). Overall, GI-1 marks an abrupt warming associated with an extremely rapid sea-level rise up to 20 m between 14.3 and 12.8 ka caused by Meltwater Pulse-1A (Stanford et al., 2011, Fig. 9). The widened cross-section of the Strait of Gibraltar promotes Atlantic freshwater discharge with consequent salinity decrease of the Mediterranean Sea (Rogerson et al., 2012). We thus suggest an upward vertical shift of the LIW during GI-1 in response to enhanced water column density gradient, caused by the presence of dense Atlantic water masses at shallower depths and surface freshening in the Mediterranean. Supporting the idea of a lighter LIW during sea-level rise, the  $\delta^{18}\text{O}$

*G. bulloides* signal shows progressive depletion around mid GI-1 in the Gela Basin (Fig. 7). Indeed, sea-level variations seem capable of controlling the buoyancy of saline waters, as for example in the Gulf of Cádiz, where the density gradient promoted the Mediterranean Outflow Water (MOW) shoaling during the last deglaciation (Jiménez-Espejo et al., 2015) while increased salinity during sea-level lowstands might have produced a downslope shift of a denser MOW (Kaboth et al., 2015). Furthermore, the onset of the African Humid Period (AHP) around the same time may have added another forcing that hampered the ventilation in the Eastern Mediterranean, which would concur to explain the drastic reduction of the density of the LIW on the lower slope of the Gela Basin. On the same line of reasoning, Toucanne et al. (2012) notice the progressive shoaling of the LIW from 20 to 12 ka in the Corsica Trough, they interpret the benthic  $\delta^{18}\text{O}$  record as reflecting significant density

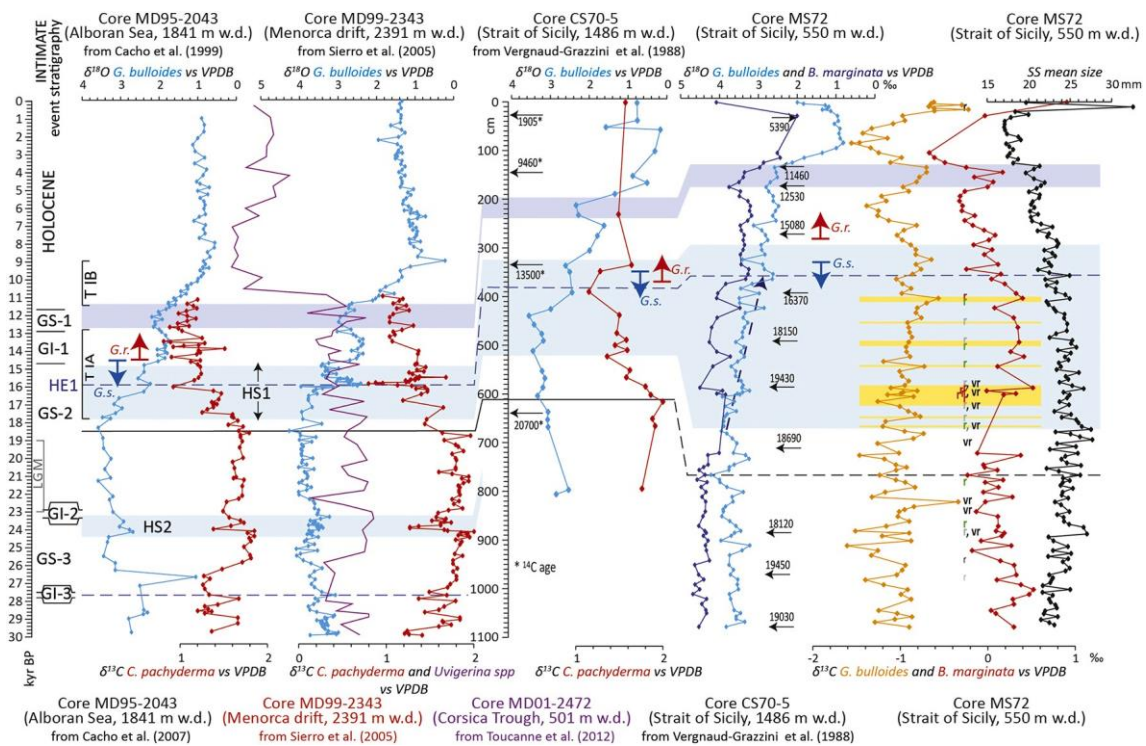


**Fig. 11.** Basin-wide correlation of benthonic and planktonic  $\delta^{13}\text{C}$  and  $\delta^{18}\text{O}$  records of core MS72 and the reference cores of the Mediterranean (see references on top of each core). The ages are calibrated (yr BP). The yellow stripes represent the intervals with evidence of major reworking/displacement of foraminifera. See Fig. 7 for a detailed explanation of symbols and abbreviations. (For interpretation of the references to colour in this figure legend, the reader is referred to the web version of this article.)

changes of the LIW in relation to climate stadial/interstadial cycles (Toucanne et al., 2012). However, sedimentary records in the Corsica Trough have no sufficient resolution during HS1 and are located only in the deeper part of the basin and are thus not ideal to highlight different bottom-current behaviours along different depths of the slope. The  $\overline{\text{SS}}$  data of core MS75 indicate that reconstructed paleo-flow velocities drastically decrease starting from 12.8 kyr BP when the return of the domination of *G. bulloides* and *N. incompta* with the rare presence of *G. ruber* mark the inception of the Greenland Stadial 1 (GS-1) at ca. 12.65–12.9 kyr BP. The appraisal of cooler temperatures is reflected also by rapid Ti/Ca increase observed in both cores, most probably related to the attenuated biogenic activity. We thus possibly constrain the timing of the shoaling phase of the LIW between 16.5 and 12.8 ka in the Gela Basin, which coincides with the time interval of enhanced sea-level rise (Fig. 12).

Finally, during GS-1, significant intensification of the LIW activity has been observed in the Mediterranean (e.g. McCulloch et al., 2010) and particularly in the Corsica Trough (Fig. 12). On the contrary, slight increases of  $\overline{\text{SS}}$  in core MS72 and even more subtle in core MS75 (Fig. 12) suggest smaller bottom-current acceleration in the Gela Basin. Comparing the depths of the sediment cores collected in the Gela Basin and Corsica Trough with bottom-current velocities, we infer that the LIW was flowing at maximum speed between 210 and 430 m wd in the Gela Basin (Fig. 12), possibly in relation to the pause in sea-level rise during GS-1.

### 5.3. Predisposing conditions to slope instability

The multi-proxy sedimentary records of the Gela Basin allow to better constraining the timing of erosion/deposition along the shelf edge and the identification of conditions that promote failure of drifts deposits.

Around 16.5 ka planktonic taxa characteristic of MIS 5 or older

(*G. truncatulinoides*) are present in sediment core MS72 (red “r” in Fig. 7), suggesting the reworking of sediments through MTDs. Our data show that two submarine landslides, the South Gela Basin Slides (SGBS) and the Gela Drift Slide (GDS) have been emplaced around the same time interval from the wasting of sediment drifts that were growing since MIS 5 (Gauchery et al., 2021).

Shortly before, between 17.5 and 17 ka, a short-living but decisive increase in bottom-current strength in the upper slope and shelf-edge area is constrained by reliable data for paleo-flow reconstructions of core MS75 (Fig. 9). The increase in flow velocity is accompanied by LSR peaking to 1320 cm/kyr (ca. 17.5–17.2 ka) and plummeting soon after, when velocities reach their maximum speed. Furthermore, the velocity increase mirrors the drastic decrease in Ti/Ca, which can be related to the sudden change in the strength of lateral advection in the upper slope (Figs. 9, 12). This brief episode of acceleration appears disjointed by sea-level variations and climate forcing, because sea level was steadily rising by 12 cm/kyr during this time interval (Lambeck et al., 2014) and is uncoupled from the activity and dynamics of the LIW. We therefore suggest that sediment remobilization is related to the action of bottom currents under the influence of the surface water mass (MAW). On the other hand, the presence of bottom currents displacing sediments on the outer shelf and constrained in their paths by the structural highs of the Malta Plateau during flooding phases was already hypothesized by Gauchery et al. (2021), based on geophysical data only. Therefore, we suggest that the MAW accelerated along the shelf of the Gela Basin at the beginning of deglaciation in combination with local topographic constraints on the shelf. The erosion of the outer shelf may have been enhanced by the action of storm waves compatible with the path of atmospheric circulation characterized by southerlies during LGM (Kuhlemann et al., 2008).

Storm waves and bottom currents, the latter governed by surface-water circulation, triggered the instability of the contourite drifts that at the time were as shallow as 100 m water depth. In the literature,

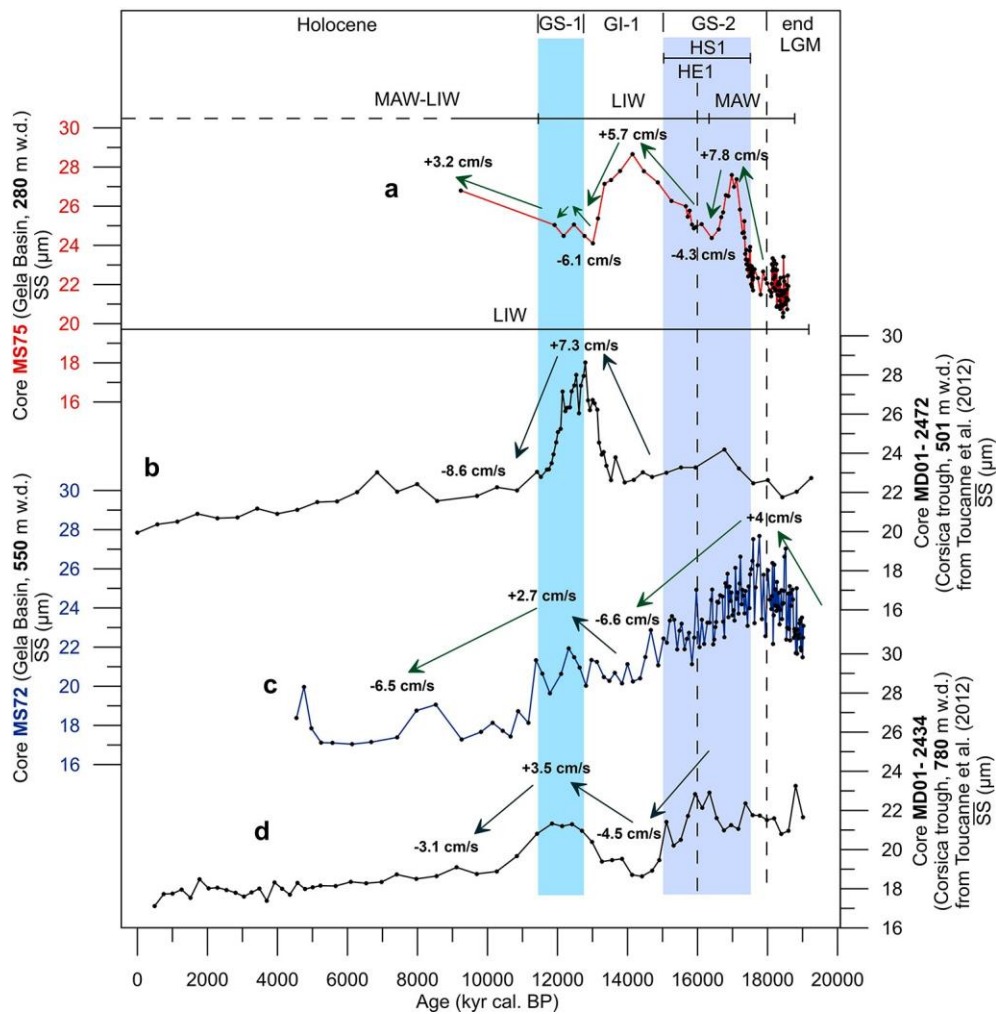


**Fig. 12.** Sortable silt mean size ( $\overline{SS}$ ) in the Gela Basin (A and C) compared to the Corsica Trough (B and D) over the last 19 kyr BP. The green arrows indicate the increases and decreases in flow speed ( $\text{cm s}^{-1}$ ). The deepest cores (all but MS75) registered fluctuations of the intermediate water mass (LIW). The shallower core (MS75) shows contrasting values compared to the other cores, which possibly reflect changes in the depth of the upper boundary of the LIW due to sea-level rise pulses and the activity of the surface water (MAW) at the beginning of deglaciation. (For interpretation of the references to colour in this figure legend, the reader is referred to the web version of this article.)

several reasons are identified to explain the occurrence of failure in contourite deposits, including the oversteepening caused by the mounded geometry itself and the high sedimentation rates in well-sorted sediments that promote overloading combined with low shear strength (e.g. [Rebesco et al., 2014](#)). Furthermore, seismic triggering has been excluded for the specific case of SGBS based on the margin stability analysis carried out with the minimum lithostatic deviation method which accounts for peak ground acceleration estimated along the continental margin (see [Zaniboni et al., 2021](#)). We thus suggest that a further predisposing condition to failure for shallow-water contourites is provided by rapid changes of bottom-current velocities in the upslope of contourite drifts.

Another increase ( $\pm 3.2 \text{ cm s}^{-1}$ ) of the flow velocity ([Fig. 12](#)), accompanied by high Zr/Rb ([Fig. 9](#)), is visible in core MS75 after the end of GS-1. The increase lasts until the core top, which is chronologically constrained at 8 kyr cal. BP. The velocity increase is associated with a continuous decrease of the sedimentation rate from the early Holocene ([Fig. 9](#)). This further increase in bottom current activity in the upper slope is timely related to the discharge of Atlantic freshwater during Meltwater Pulse-1B, which was a multi-millennial interval of enhanced rates of sea-level rise between 11.5 ka and 8.8 ka BP ([Stanford et al., 2011](#)). This prolonged freshwater discharge may have induced significant differences in density between the surface and intermediate water masses with the creation of internal waves oscillating along the interface between the LIW and the MAW. Internal waves are capable of sediment mobilization in shallow slope settings and promote long-term downslope transport (e.g. [Ma et al., 2016](#)). The sediment hiatus corresponding

to the last 8 kyr BP suggests that erosion may have taken place in the upper slope seafloor of the Gela Basin as also revealed by the seismic facies of the sub-bottom profiles ([Fig. 3A](#)). The slight increase of current strengths in the upper slope may have promoted seabed erosion in the southern Gela Basin in the early Holocene, which is around the time when mudflows were emplaced (ca. 8.5 ka) in the northern Gela Basin ([Kuhlmann et al., 2017](#)). This would infer that changes in sea level and variations in water-mass interface may favour erosion of the shelf edge and upper slope and can contribute to the instability of shallow-water contourite drifts.

## 6. Conclusions

Extensive sediment drifts developed on the upper and lower slope of Gela Basin, in the Strait of Sicily, which is a topographically complex region that allows surface and intermediate water exchange between the eastern and the western Mediterranean basins. Two sediment cores span the post-LGM and are characterized by exceptionally high sedimentation rates in the last phase of LGM and the early Heinrich Stadial 1 (~19 kyr–16 kyr BP) that provide an excellent record to reconstruct the fine-scale variability of the paleoceanographic circulation and sedimentary processes in the Central Mediterranean. The multi-proxy sedimentary records allow to: 1) distinguish sedimentary processes controlled by along-slope currents from downslope sediment-gravity flows; 2) reconstruct the variability of the paleo-current activity and intensity in relation to sea-level fluctuations; 3) identify genetic links between contourite deposits and MTDs suggesting key time intervals and

predisposing conditions that lead to the failure of part of the sediment drifts. In particular, the expanded sedimentary records allowed us to perform a semi-quantitative analysis of displaced foraminifera and stranded plant debris in sediment layers, which were not defined as current-sorted by the sortable silt method, to diagnose downslope sedimentary processes.

During the post-LGM lowstand and first phases of sea-level rise, sediment was supplied to the lower slope from the inner-middle shelf, where erosion was caused by storm waves and/or bottom currents. Strong intermediate water bottom-currents caused lateral advection from north to south and enhanced sediment accumulation in the mid-lower slope. Here, the sedimentary facies show an overprinting of lateral traction transport and sediment load structures proving the concurrent presence of along-slope and downslope processes active at the same time. This implies that sediment fluxes from land are not necessarily accountable for high sedimentation rates on margins dominated by intense bottom-water circulation.

The stratigraphically-expanded sedimentary succession of the Gela Basin allowed predating the progressive weakening of the Levantine Intermediate Water (LIW) at 16.3 kyr BP. Thus, the LIW slow-down seems independent of climate forcing related to atmospheric temperatures and position of the northern polar fronts, contrary to what was previously suggested from core sediment evidence in the Corsica Trough, in the Central Mediterranean. Rather, the slow-down of the LIW was affiliated with sea-level rise pulses, consequent increased Atlantic fresh water discharge at the Strait of Gibraltar and Mediterranean surface freshening. In particular, the change in salinity gradient caused the progressive shoaling of the LIW upper boundary between 16.5 and 12.8 ka. Thus, sea-level fluctuations have a direct impact on the buoyancy of the bottom-currents inducing density gradients that may change the depth interface of water masses and therefore their capability of mobilizing sea-bottom sediments.

The action of persisting bottom currents in the upslope of shallow-water sediment drifts, driven by surface water masses that respond to sea-level fluctuations, combined with drastic changes in sedimentation rates, seem to create predisposing conditions to the failure of sediment drifts. In the Gela Basin, in particular, enhanced instability of sediment drifts that accumulated since the previous interglacial period occurred during two key-time intervals. 1) The lower phase of HS1, around 17 ka, when brief acceleration of wind-driven water masses and storm waves caused erosion on the outer shelf; 2) the early Holocene, when prolonged sea-level rise and freshwater discharge caused changes in density at the interface between the Modified Atlantic Water and the Levantine Intermediate Water, which promoted sediment erosion and downslope transport.

#### Data availability

Bathymetric data used in this research work are downloadable from the EMODnet compilation at <https://portal.emodnet-bathymetry.eu/>. All other raw and processed data such as core photos, X-ray images of the cores and grain-size analysis are available upon request to the corresponding author.

#### Declaration of Competing Interest

The authors declare that they have no known competing financial interests or personal relationships that could have appeared to influence the work reported in this paper.

#### Acknowledgments

The first author wishes to thank Samuel Toucanne for the raw sediment core data of the Corsica Trough used in Fig. 12 and for the guidance on the methodology of the grain-size analysis. Grain-size analyses were performed at Ifremer during TG's several stays (secondments)

with the SLATE project. We thank Jeremie Gouriou for his kind assistance in the sedimentology laboratory. Authors are grateful to two anonymous reviewers for their valuable comments. The PhD of Tugdual Gauchery was funded by the European Union's Horizon 2020 research and innovation programme under the Marie-Sklodowska-Curie grant via project ITN SLATE (grant agreement N° 721403).

#### References

- Argnani, A., 1987. The Gela nappe: evidence of accretionary melange in the maghrebian foredeep of sicily. *Memorie Societ a Geologica Italiana* 38, 419–428.
- Ariztegui, D., Asiola, A., Lowe, J.J., Trincardi, F., Vigliotti, L., Tamburini, F., Chondrogianni, C., Accorsi, C.A., Bandini Mazzanti, M., Mercuri, A.M., Van der Kaars, S., McKenzie, J.A., Oldfield, F., 2000. Paleoclimate and the formation of sapropel S1: inferences from late Quaternary lacustrine and marine sequences in the Central Mediterranean region. *Palaeoceanogr. Palaeoclimatol. Palaeoecol.* 158, 215–240. [https://doi.org/10.1016/S0031-0182\(00\)00051-1](https://doi.org/10.1016/S0031-0182(00)00051-1).
- Asioli, A., Trincardi, F., Lowe, J.J., Oldfield, F., 1999. Short-term climate changes during the last Glacial–Holocene transition: comparison between Mediterranean records and the GRIP event stratigraphy. *J. Quat. Sci.* 14, 373–381. [https://doi.org/10.1002/\(SICI\)1099-1417\(199907\)14:4<373::AID-JQS472>3.0.CO;2-T](https://doi.org/10.1002/(SICI)1099-1417(199907)14:4<373::AID-JQS472>3.0.CO;2-T).
- Asioli, A., Trincardi, F., Lowe, J.J., Ariztegui, D., Langone, L., Oldfield, F., 2001. Submillennial scale climatic oscillations in the central Adriatic during the Late glacial: palaeoceanographic implications. *Quat. Sci. Rev.* 20, 1201–1221. [https://doi.org/10.1016/S0277-3791\(00\)00147-5](https://doi.org/10.1016/S0277-3791(00)00147-5).
- Astraldi, M., Balopoulos, S., Candela, J., Font, J., Gacic, M., Gasparini, G.P., Manca, B., Theoharis, A., Tintor , J., 1999. The role of straits and channels in understanding the characteristics of Mediterranean circulation. *Prog. Oceanogr.* 44 (1–3), 65–108. [https://doi.org/10.1016/S0079-6611\(99\)00021-X](https://doi.org/10.1016/S0079-6611(99)00021-X).
- Astraldi, M., Gasparini, G.P., Gervasio, L., Salusti, E., 2001. Dense water dynamics along the Strait of Sicily (Mediterranean Sea). *J. Phys. Oceanogr.* 31, 3457–3475. [https://doi.org/10.1175/1520-0485\(2001\)031<3457:DWDATS>2.0.CO;2](https://doi.org/10.1175/1520-0485(2001)031<3457:DWDATS>2.0.CO;2).
- Bahr, A., Jim nez-Espejo, F., Kolasinac, N., Grunert, P., Hern andez-Molina, F., R hl, U., Voelker, A., Escutia, C., Stow, D., Hodell, D., Zarkikian, C., 2014. Deciphering bottom current velocity and paleoclimate signals from contourite deposits in the Gulf of C diz during the last 140 kyr: an inorganic geochemical approach. *Geochem. Geophys. Res.* 15 <https://doi.org/10.1002/2014GC005356>.
- Beckers, A., Beck, C., Hubert-Ferrari, A., Tripanas, E., Crouzet, C., Sakellariou, D., Papatheodorou, G., De Batist, M., 2016. Influence of bottom currents on the sedimentary processes at the western tip of the Gulf of Corinth, Greece. *Mar. Geol.*
- Beranger, K., Mortier, L., Gasparini, G.P., Gervasio, L., Astraldi, M., Crepon, M., 2004. The dynamics of the Sicily Strait: a comprehensive study from observations and models. *Deep-Sea Res. Pt. II* 51 (4–5), 411–440. <https://doi.org/10.1016/j.dsr2.2003.08.004>.
- Bj rck, S., Walker, M.J.C., Cwynar, L., Johnsen, S.J., Knudsen, K.L., Lowe, J.J., Wohlfarth, B., 1998. An event stratigraphy for the last termination in the North Atlantic region based on the Greenland Ice Core record: a proposal by the INTIMATE group. *J. Quat. Sci.* 13, 283–292. [https://doi.org/10.1002/\(SICI\)1099-1417\(199807/08\)13:4<283::AID-JQS386>3.0.CO;2-A](https://doi.org/10.1002/(SICI)1099-1417(199807/08)13:4<283::AID-JQS386>3.0.CO;2-A).
- Blockley, S.P.E., Lane, C.S., Hardiman, M., Rasmussen, S., Seierstad, I., Steffensen, J.P., Svensson, A., Lotter, A.F., Turney, C.S., Ramsey, C.B., 2012. Synchronisation of palaeoenvironmental records over the last 60,000 years, and an extended INTIMATE event stratigraphy to 48,000 b2k. *Quat. Sci. Rev.* 36, 2–10. <https://doi.org/10.1016/j.quascirev.2011.09.017>.
- Bond, G., Bond, G.C., Heinrich, H., Broecker, W., Labeyrie, L., McManus, J., Andrews, J., Huon, S., Jantschik, R., Clasen, S., Simet, C., Tedesco, K., Klas, M., Bonani, G., Ivy, S., 1992. Evidence for massive discharges of icebergs into the glacial northern Atlantic. *Nature* 360, 245–249. <https://doi.org/10.1038/360245a0>.
- Brackneridge, R.E., Hern andez-Molina, F.J., Stow, D.A.V., Llave, E., 2013. A Pliocene mixed contourite-turbidite system offshore the Algarve margin, Gulf of Cadiz: Seismic response, margin evolution and reservoir implications. *Mar. Pet. Geol.* 46, 36–50. <https://doi.org/10.1016/j.marpetgeo.2013.05.015>.
- Cacho, I., Grimalt, J.O., Pelejero, C., Canals, M., Sierro, F.J., Flores, J.A., Shackleton, N. J., 1999. Dansgaard-Oeschger and Heinrich event imprints in the Alboran Sea paleotemperatures. *Paleoceanography* 14, 698–705. <https://doi.org/10.1029/1999PA900044>.
- Cacho, I., Grimalt, J.O., Canals, M., Sbaifi, L., Shackleton, N.J., Sch nfeld, J., Zahn, R., 2001. Variability of the western Mediterranean Sea surface temperature during the last 25,000 years and its connection with the northern hemisphere climatic changes. *Paleoceanography* 16, 40–52. <https://doi.org/10.1029/2000PA000502>.
- Cacho, I., Shackleton, N., Elderfield, H., Sierro, F., Grimalt, J., 2007. Glacial rapid variability in deep-water temperature and  $\delta^{18}O$  from the Western Mediterranean Sea. *Quat. Sci. Rev.* 25, 3294–3311. <https://doi.org/10.1016/j.quascirev.2006.10.004>.
- Cornuault, M., Tachikawa, K., Vidal, L., Guihou, A., Siani, G., Deschamps, P., Bassinot, F., Revel, M., 2018. Circulation changes in the eastern Mediterranean Sea over the past 23,000 years inferred from authigenic Nd isotopic ratios. *Paleoceanogr. Palaeoclimatol.* 33, 264–280. <https://doi.org/10.1002/2017PA003227>.
- De Rijk, S., Troelstra, S.R., Rohling, E.J., 1999. Benthic foraminiferal distribution in the Mediterranean Sea. *J. Foram. Res.* 29, 93–103. <https://doi.org/10.2113/jsjfr.29.2.93>.

- De Stigter, H.C., Jorissen, F.J., Van der Zwaan, G.J., 1998. Bathymetric distribution and microhabitat partitioning of live (Rose Bengal stained) benthic foraminifera along a shelf to deep sea transect in the southern Adriatic Sea. *J. Foram. Res.* 28, 40–65.
- DeLaune, R.D., Lindau, C.W., 1987.  $\delta^{13}\text{C}$  signature of organic carbon in estuarine bottom sediment as an indicator of carbon export from adjacent marshes. *Biogeochemistry* 3, 225–230.
- Deschamps, P., Durand, N., Bard, E., Hamelin, B., Camoin, G., Thomas, A.L., Henderson, G.M., Okuno, J., Yokoyama, Y., 2012. Ice-sheet collapse and sea-level rise at the Bølling warming 14,600 years ago. *Nature* 483, 559–564. <https://doi.org/10.1038/nature10902>.
- Desprat, S., Combourieu-Nebout, N., Essallami, L., Sicre, M.A., Dormoy, I., Peyron, O., Siani, G., Bout Roumazeilles, V., Turon, J.L., 2013. Deglacial and Holocene vegetation and climatic changes in the southern Central Mediterranean from a direct land-sea correlation. *Clim. Past* 9, 767–787. <https://doi.org/10.5194/cp-9-767-2013>.
- Dorador, J., Tovar, F., Mena, A., Francés, G., 2019. Lateral variability of ichnological content in muddy contourites: Weak bottom currents affecting organisms' behavior. *Sci. Rep.* 9, 17713. <https://doi.org/10.1038/s41598-019-54246-3>.
- Dubois-Dauphin, Q., Montagna, P., Giuseppe, S., Douville, E., Wienberg, C., Hebbeln, D., Liu, Z., Kallel, N., Dapigny, A., Revel Pons-Branchu, E., Taviani, M., Colin, C., 2017. Hydrological variations of the intermediate water masses of the western Mediterranean Sea during the past 20 ka inferred from neodymium isotopic composition in foraminifera and cold-water corals. *Clim. Past* 13, 17–37. <https://doi.org/10.5194/cp-2016-64>.
- EMODnet Bathymetry Consortium, 2016. EMODnet Digital Bathymetry (DTM). The European Marine Observation and Data Network. <https://doi.org/10.12770/c7b53704-999d-4721-b1a3-04ec6087238>.
- Ferraro, S., Sulli, A., Di Stefano, E., Giaramita, L., Incarbona, A., Graham Mortyn, P., Sprovieri, M., Sprovieri, R., Tonielli, R., Vallefucio, M., Zizzo, E., Tranchida, G., 2018. Late Quaternary palaeoenvironmental reconstruction of sediment drift accumulation in the Malta Graben (Central Mediterranean Sea). *Geo-Mar. Lett.* 38, 241–258. <https://doi.org/10.1007/s00367-018-0534-x>.
- Fonnesu, M., Palermo, D., Galbiati, M., Marchesini, M., Bonamini, E., Bendias, D., 2020. A new world-class deep-water play-type, deposited by the syndepositional interaction of turbidity flows and bottom currents: the giant Eocene Coral Field in northern Mozambique. *Mar. Pet. Geol.* 111, 179–201. <https://doi.org/10.1016/j.marpetgeo.2019.07.047>.
- Gauchery, T., Rovere, M., Pellegrini, C., Cattaneo, A., Campiani, E., Trincardi, F., 2021. Factors controlling margin instability during the Plio-Quaternary in the Gela Basin (Strait of Sicily, Mediterranean Sea). *Mar. Petrol. Geol.* 123, 104767. <https://doi.org/10.1016/j.marpetgeo.2020.104767>.
- Ghielmi, M., Amore, M.R., Bolla, E.M., Carubelli, P., Knezarek, G., Serrano, C., 2012. The Pliocene to pleistocene succession of the hyblean foredeep (sicily, Italy). October 23–26, 2011. In: AAPG (Am. Assoc. Pet. Geol.) Internat. Conf. Exhib. Milan, Italy. [http://www.searchanddiscovery.com/documents/2012/30220ghielmi/ndx\\_ghielmi.pdf](http://www.searchanddiscovery.com/documents/2012/30220ghielmi/ndx_ghielmi.pdf).
- Goineau, A., Fontanier, C., Jorissen, F., Buscail, R., Kerhervé, P., Cathalot, C., Pruski, A. M., Lantoiné, F., Bourgeois, S., Metzger, E., Legrand, E., Rabouille, C., 2012. Temporal variability of live (stained) benthic foraminiferal faunas in a river-dominated shelf – Faunal response to rapid changes of the river influence (Rhône prodelta, NW Mediterranean). *Biogeosciences* 9, 1367–1388. <https://doi.org/10.5194/bg-9-1367-2012>.
- Govin, A., Holzwarth, U., Heslop, D., Ford Keeling, L., Zabel, M., Mulitza, S., Collins, J. A., Chiessi, C.M., 2012. Distribution of major elements in Atlantic surface sediments (36°N–49°S): imprint of terrigenous input and continental weathering. *Geochem. Geophys. Geosyst.* 13, 1–23. <https://doi.org/10.1029/2011GC003785>.
- Hanebuth, T., Zhang, W., Hofmann, A., Löwemark, L., Schwenk, T., 2015. Oceanic density fronts steering bottom-current induced sedimentation deduced from a 50 ka contourite-drift record and numerical modeling (off NW Spain). *Quat. Sci. Rev.* 112, 207–225. <https://doi.org/10.1016/j.quascirev.2015.01.027>.
- Heinrich, H., 1988. Origin and consequences of cyclic ice rafting in the Northeast Atlantic Ocean during the past 130,000 years. *Quat. Res.* 29, 142–152. [https://doi.org/10.1016/0033-5894\(88\)90057-9](https://doi.org/10.1016/0033-5894(88)90057-9).
- Hennekam, R., De Lange, G., 2012. X-ray fluorescence core scanning of wet marine sediments: methods to improve quality and reproducibility of high-resolution paleoenvironmental records. *Limnol. Oceanogr. Methods* 10, 991–1003. <https://doi.org/10.4319/lom.2012.10.991>.
- Hernandez-Molina, F.J., Llave, E., Preu, B., Ercilla, G., Fontan, A., Bruno, M., Serra, N., Gomis, J.J., Brackenridge, R.E., Sierro, F.J., Stow, D.A.V., García, M., Juan, C., Sandoval, N., Arnaiz, A., 2014. Contourite processes associated to the Mediterranean Outflow Water after its exit from the Strait of Gibraltar: Global and conceptual implications. *Geology* 42 (3), 227–230. <https://doi.org/10.1130/G35083.1>.
- Hodell, D.A., Nicholl, J.A., Bontognali, T.R.R., Danino, S., Dorador, J., Dowdeswell, J.A., Einsle, J., Kuhlmann, H., Martrat, B., Mlenek-Vautravers, M.J., Rodríguez-Tovar, F. J., Röhl, U., 2017. Anatomy of Heinrich Layer 1 and its role in the last deglaciation. *Paleoceanogr.* 32, 284–303. <https://doi.org/10.1002/2016PA003028>.
- Jaccard, S.L., Galbraith, E.D., Sigman, D.M., Haug, G.H., 2010. A pervasive link between Antarctic icecore and subarctic Pacific sediment records over the past 800 kyr. *Quat. Sci. Rev.* 29, 206–212. <https://doi.org/10.1016/j.quascirev.2009.10.007>.
- Jiménez-Espejo, F.J., Pardo-Gené, M., Martínez-Ruiz, F., García-Alix, A., van de Fliedert, T., Toyofuku, T., Bahr, A., Kreissig, K., 2015. Geochemical evidence for intermediate water circulation in the westernmost Mediterranean over the last 20 kyr BP and its impact on the Mediterranean Outflow. *Glob. Planet. Change* 135, 38–46. <https://doi.org/10.1016/j.gloplacha.2015.10.001>.
- Jorissen, F.J., 1987. The distribution of benthic foraminifera in the Adriatic Sea. *Mar. Micropaleontol.* 12, 21–48.
- Jorissen, F.J., 1999. Benthic foraminiferal microhabitats below the sediment-water interface. In: Sen Gupta, B.K. (Ed.), *Modern Foraminifera*. Kluwer Academic Publishers, Great Britain, pp. 161–179. [https://doi.org/10.1007/0-306-48104-9\\_10](https://doi.org/10.1007/0-306-48104-9_10).
- Jorissen, F.J., de Stigter, H.C., Widmark, J.G.V., 1995. A conceptual model explaining benthic foraminiferal microhabitats. *Mar. Micropaleontol.* 22, 3–15.
- Kaboth, S., Bahr, A., Reichart, G.J., Jacobs, B., Lourens, L.J., 2015. New insights into upper MOW variability over the last 150 kyr from IODP 339 Site U1386 in the Gulf of Cadiz. *Mar. Geol.* 377, 136–145. <https://doi.org/10.1016/j.margeo.2015.08.014>.
- Kuhlemann, J., Rohling, E.J., Krumrei, I., Kubik, P., Ivy-Ochs, S., Kucera, M., 2008. Regional synthesis of Mediterranean atmospheric circulation during the last Glacial Maximum. *Science* 321, 1338–1340. <https://doi.org/10.1126/science.1157638>.
- Kuhlmann, J., Asioli, A., Trincardi, F., Klügel, A., Huhn, K., 2015. Sedimentary response to Milankovitch-type climatic oscillations and formation of sediment undulations: evidence from a shallow-shelf setting at Gela Basin on the Sicilian continental margin. *Quat. Sci. Rev.* 108, 76–94. <https://doi.org/10.1016/j.quascirev.2014.10.030>.
- Kuhlmann, J., Asioli, A., Trincardi, F., Klügel, A., Huhn, K., 2017. Landslide frequency and failure mechanisms at NE Gela Basin (Strait of sicily). *J. Geophys. Res. Sol. Ea.* 122, 2223–2243. <https://doi.org/10.1002/2017JF004251>.
- Lambeck, K., Rouby, H., Purcell, A., Sun, Y., Sambridge, M., 2014. Sea level and global ice volumes from the last Glacial Maximum to the Holocene. *Proc. Natl. Acad. Sci.* 111 (43), 15296–15303. <https://doi.org/10.1073/pnas.1411762111>.
- Lebreiro, S.M., Antón, L., Reguera, I., Marzocchi, A., 2018. Paleocceanographic and climatic implications of a new Mediterranean Outflow branch in the southern Gulf of Cadiz. *Quat. Sci. Rev.* 197, 92–111. <https://doi.org/10.1016/j.quascirev.2018.07.036>.
- Lee, H.J., 2009. Timing of occurrence of large submarine landslides on the Atlantic Ocean margin. *Mar. Geol.* 264, 53–64. <https://doi.org/10.1016/j.margeo.2008.09.009>.
- Lermusiaux, P.F.J., Robinson, A.R., 2001. Features of dominant mesoscale variability, circulation patterns and dynamics in the Strait of Sicily. *Deep Sea Res. Part I Oceanogr. Res. Pap.* 48, 1953–1997. [https://doi.org/10.1016/S0967-0637\(00\)00114-X](https://doi.org/10.1016/S0967-0637(00)00114-X).
- Lirer, F., Sprovieri, M., Ferraro, L., Vallefucio, M., Capotondi, L., Cascella, A., Petrosino, P., Insinga, D.D., Pelosi, N., Tamburrino, S., Lubritto, C., 2013. Integrated stratigraphy for the Late Quaternary in the eastern Tyrrhenian Sea. *Quat. Int.* 292, 71–85. <https://doi.org/10.1016/j.quaint.2012.08.2055>.
- Ma, X., Yan, J., Hou, Y., Lin, F., Zheng, X., 2016. Footprints of obliquely incident internal solitary waves and internal tides near the shelf break in the northern South China Sea. *J. Geophys. Res. Ocean.* 121, 6762–6778. <https://doi.org/10.1002/2016JC012009>.
- Martín-Chivelet, J., Fregenal-Martínez, M.A., Chacón, B., 2008. Traction Structures in Contourites. *Dev. Sedimentol.* 60, 159–182. [https://doi.org/10.1016/S0070-4571\(08\)10010-3](https://doi.org/10.1016/S0070-4571(08)10010-3).
- Martínez-Ruiz, F., Kastner, M., Gallego-Torres, D., Rodrigo-Gámiz, M., Nieto-Moreno, V., Ortega-Huertas, M., 2015. Paleoclimate and paleoceanography over the past 20,000 yr in the Mediterranean Sea Basins as indicated by sediment elemental proxies. *Quat. Sci. Rev.* 107, 25–46. <https://doi.org/10.1016/j.quascirev.2014.09.018>.
- Martorelli, E., Petroni, G., Chiochi, F.L., Pantelleria Sci, P., 2011. Contourites offshore Pantelleria Island (Sicily Channel, Mediterranean Sea): depositional, erosional and biogenic elements. *Geo-Mar. Lett.* 31, 481–493. <https://doi.org/10.1007/s00367-011-0244-0>.
- Martorelli, E., Bosman, A., Casalbore, D., Falcini, F., 2016. Interaction of down-slope and along-slope processes off Capo Vaticano (southern Tyrrhenian Sea, Italy), with particular reference to contourite-related landslides. *Mar. Geol.* 378, 43–55. <https://doi.org/10.1016/j.margeo.2016.01.005>.
- Massé, L., Faugères, J.C., Hrovatin, V., 1998. The interplay between turbidity and contour current processes on the Columbia Channel fan drift, Southern Brazil Basin. *Sediment. Geol.* 115, 111–132. [https://doi.org/10.1016/S0037-0738\(97\)00089-4](https://doi.org/10.1016/S0037-0738(97)00089-4).
- McCave, I.N., Andrews, J.T., 2019. Distinguishing current effects in sediments delivered to the ocean by ice. I. Principles, methods and examples. *Quat. Sci. Rev.* 212, 92–107. <https://doi.org/10.1016/j.quascirev.2019.03.031>.
- McCave, I.N., Hall, I.R., 2006. Size sorting in marine muds: processes, pitfalls, and prospects for paleoflow-speed proxies. *Geochem. Geophys. Geosyst.* 7 (10) <https://doi.org/10.1029/2006GC001284>.
- McCave, I.N., Manighetti, B., Robinson, S.G., 1995. Sortable silt and fine sediment size/composition slicing: parameters for paleocurrent speed and paleoceanography. *Paleoceanogr. Paleoclim.* 10, 593–610. <https://doi.org/10.1029/94PA03039>.
- McCave, I.N., Thornalley, D.J.R., Hall, I.R., 2017. Relation of sortable silt grain-size to deep-sea current speeds: calibration of the 'Mud Current Meter'. *Deep Sea Res. Oceanogr. Res. Pap.* 127, 1–12. <https://doi.org/10.1016/j.dsr.2017.07.003>.
- McCulloch, M., Taviani, M., Montagna, P., Lopez Correa, M., Remia, A., Mortimer, G., 2010. Proliferation and demise of deep-sea corals in the Mediterranean during the Younger Dryas. *Earth Planet. Sci. Lett.* 298, 143–152. <https://doi.org/10.1016/j.epsl.2010.07.036>.
- McNeill, L.C., Shillington, D.J., Carter, G.D.O., Everest, J.D., Gawthorpe, R.L., Miller, C., Phillips, M.P., Collier, R.E.L., Cvetkoska, A., De Gelder, G., Diz, P., Doan, M.L., Ford, M., Geraga, M., Gillespie, J., Helmsdal, R., Herrero-Bervera, E., Ismael, M., Janikian, L., Kouli, K., Le Ber, E., Li, S., Maffione, M., Mahoney, C., Machlus, M.L., Michas, G., Nixon, C.W., Oflaz, S.A., Omale, A.P., Panagiotopoulos, K., Pechlivanidou, S., Sauer, S., Seguin, J., Sergiou, S., Zakharova, N.V., Green, S., 2019. High-resolution record reveals climate-driven environmental and sedimentary changes in an active rift. *Sci. Rep.* 9, 1–11. <https://doi.org/10.1038/s41598-019-40022-w>.
- Melki, T., Kallel, N., Jorissen, F.J., Guichard, F., Dennielou, B., Berné, S., Labeyrie, L., Fontugne, M., 1999. Abrupt climate change, sea surface salinity and

- palaeoproductivity in the Western Mediterranean (Gulf of Lion) during the last 28 kyr. *Palaeogeogr. Palaeoclimatol. Palaeoecol.* 279, 96–113. <https://doi.org/10.1016/j.palaeo.2009.05.005>.
- Milliman, J., Farnsworth, K., 2011. *River Discharge to the Coastal Ocean: A Global Synthesis*. Cambridge University Press, p. 24. <https://doi.org/10.1017/CBO9780511781247>.
- Millot, C., 1999. Circulation in the Western Mediterranean Sea. *J. Mar. Syst.* 20 (1–4), 423–442. [https://doi.org/10.1016/S0924-7963\(98\)00078-5](https://doi.org/10.1016/S0924-7963(98)00078-5).
- Millot, C., Taupier-Letage, I., 2005. Circulation in the Mediterranean Sea. In: Salot, A. (Ed.), *The Mediterranean Sea*. Springer Berlin Heidelberg, Berlin, Heidelberg, pp. 29–66. <https://doi.org/10.1007/b107143>.
- Minisini, D., Trincardi, F., 2009. Frequent failure of the continental slope: the Gela Basin (Sicily channel). *J. Geophys. Res. Earth* 114, 1–17. <https://doi.org/10.1029/2008JF001037>.
- Minisini, D., Trincardi, F., Asioli, A., Canu, M., Fogliani, F., 2007. Morphologic variability of exposed mass-transport deposits on the eastern slope of Gela Basin (Sicily channel). *Bas. Res.* 19, 217–240. <https://doi.org/10.1111/j.1365-2117.2007.00324.x>.
- Miramontes, E., Cattaneo, A., Jouet, G., Th ereau, E., Thomas, Y., Rovere, M., Cauquil, E., Trincardi, F., 2016. The Pianosa Contourite Depositional System (Northern Tyrrhenian Sea): drift morphology and Plio-Quaternary stratigraphic evolution. *Mar. Geol.* 378, 20–42. <https://doi.org/10.1016/j.margeo.2015.11.004>.
- Miramontes, E., Eggenhuisen, J.T., Jacinto, R.S., Poneti, G., Pohl, F., Normandeau, A., Campbell, D.C., Hern andez-Molina, F.J., 2020. Channel-levee evolution in combined contour current-turbidity current flows from flume-tank experiments. *Geology* 48 (4), 353–357. <https://doi.org/10.1130/G47111.1>.
- Mix, A.C., Bard, E., Schneider, R., 2001. Environmental processes of the ice age: Land, oceans, glaciers (EPiLOG). *Quat. Sci. Rev.* 20, 627–657. [https://doi.org/10.1016/S0277-3791\(00\)00145-1](https://doi.org/10.1016/S0277-3791(00)00145-1).
- Mulder, T., Syvitski, J.P.M., Migeon, S., Faug eres, J.C., Savoye, B., 2003. Marine hyperpycnal flows: Initiation, behaviour and related deposits. A review. *Mar. Pet. Geol.* 20, 861–882. <https://doi.org/10.1016/j.margeo.2003.01.003>.
- Mulder, T., Faug eres, J.-T., Gonthier, E., 2008. Mixed turbidite-contourite systems. In: Rebesco, M., Camerlenghi, A. (Eds.), *Contourites*. Developments in Sedimentology 60. Elsevier, pp. 435–456. [https://doi.org/10.1016/S0070-4571\(08\)10021-8](https://doi.org/10.1016/S0070-4571(08)10021-8).
- Pedrosa-P amies, R., Parinos, C., Sanchez-Vidal, A., Gogou, A., Calafat, A., Canals, M., Bouloubassi, I., Lampadariou, N., 2015. Composition and sources of sedimentary organic matter in the deep eastern Mediterranean Sea. *Biogeosciences* 12, 7379–7402. <https://doi.org/10.5194/bg-12-7379-2015>.
- Pellegrini, C., Maselli, V., Trincardi, F., 2016. Pliocene–Quaternary contourite depositional system along the south-western Adriatic margin: changes in sedimentary stacking pattern and associated bottom currents. *Geo-Marine Lett.* 36, 67–79. <https://doi.org/10.1007/s00367-015-0424-4>.
- Perez-Folgado, M., Sierro, F.J., Flores, J.A., Cacho, I., Grimalt, J.O., Zahn, R., Shackleton, N., 2003. Western Mediterranean planktonic foraminifera events and millennial climatic variability during the last 70 kyr. *Mar. Micropaleontol.* 48, 49–70. [https://doi.org/10.1016/S0377-8398\(02\)00160-3](https://doi.org/10.1016/S0377-8398(02)00160-3).
- Petrovic, A., Lantzsch, H., Schenk, T., Marquardt, J., Tischack, J., Hanebuth, T.J.J., 2019. Post-LGM upward shift of the Mediterranean Outflow Water recorded in a contourite drift off NW Spain. *Mar. Geol.* 407, 334–379. <https://doi.org/10.1016/j.margeo.2018.11.015>.
- Piva, A., Asioli, A., Schneider, R.R., Trincardi, F., Andersen, N., Colmenero-Hidalgo, E., Dennielou, B., Flores, J.-A., Vigliotti, L., 2008. Climatic cycles as expressed in sediments of the PROMESS1 borehole PRAD1–2, central Adriatic, for the last 370 ka: 1. Integrated stratigraphy. *Geochem. Geophys. Geosyst.* 9, Q01R01 <https://doi.org/10.1029/2007GC001713>.
- Potter, P.E., Maynard, J.B., Depetris, P.J., 2005. *Mud and Mudstones*. Springer-Verlag, Berlin Heidelberg.
- Pujol, C., Vergnaud-Grazzini, C., 1995. Distribution patterns of live planktic foraminifers as related to regional hydrography and productive systems of the Mediterranean Sea. *Mar. Micropaleontol.* 25, 187–217. [https://doi.org/10.1016/0377-8398\(95\)00002-1](https://doi.org/10.1016/0377-8398(95)00002-1).
- Rebesco, M., Hern andez-Molina, F.J., Van Rooij, D., W ahlin, A., 2014. Contourites and associated sediments controlled by deep-water circulation processes: State-of-the-art and future considerations. *Mar. Geol.* 352, 111–154. <https://doi.org/10.1016/j.margeo.2014.03.011>.
- Reimer, P.J., Bard, E., Bayliss, A., Beck, J.W., Blackwell, P.G., Bronk Ramsey, C., Buck, C. E., Cheng, H., Edwards, R.L., Friedrich, M., Grootes, P.M., Guilderson, T.P., Hafliadason, H., Hajdas, I., Hatt e, C., Heaton, T.J., Hogg, A.G., Hughen, K.A., Kaiser, K.F., Kromer, B., Manning, S.W., Niu, M., Reimer, R.W., Richards, D.A., Scott, E.M., Southon, J.R., Turney, C.S.M., van der Plicht, J., 2013. *IntCal13 and MARINE13 radiocarbon age calibration curves 0–50000 years cal BP*. *Radiocarbon* 55 (4), 1869–1887. [https://doi.org/10.2458/azu\\_js\\_rc.55.16947](https://doi.org/10.2458/azu_js_rc.55.16947).
- Revel, M., Ducassou, E., Skonieczny, C., Colin, C., Bastian, L., Bosh, D., Migeon, S., Mascle, J., 2015. 20,000 years of Nile River dynamics and environmental changes in the Nile catchment area as inferred from Nile upper continental slope sediments. *Quat. Sci. Rev.* 130, 200–221. <https://doi.org/10.1016/j.quascirev.2015.10.030>.
- Ricketts, B.D., Evenchick, C., 1999. Shelfbreak gullies: products of sea-level lowstand and sediment failure: examples from Bowser Basin, northern British Columbia. *J. Sediment. Res.* 69 (6), 1232–1240. <https://doi.org/10.2110/jsr.69.1232>.
- Rogerson, M., Cacho, I., Jimenez-Espejo, F., Reguera, M.I., Sierro, F.J., Mart nez-Ruiz, F., Frigola, J., Canals, M., 2008. A dynamic explanation for the origin of the western Mediterranean organic-rich layers. *Geochem. Geophys. Geosyst.* 9, Q07U01 <https://doi.org/10.1029/2007GC001936>.
- Rogerson, M., Rohling, E.J., Bigg, G.R., Ramirez, J., 2012. Paleooceanography of the Atlantic-Mediterranean exchange: overview and first quantitative assessment of climatic forcing. *Rev. Geophys.* 50, RG2003 <https://doi.org/10.1029/2011RG000376>.
- Rohling, E., Marino, G., Grant, K.M., 2015. Mediterranean climate and oceanography, and the periodic development of anoxic events (sapropels). *Earth Sci. Rev.* 143, 62–97. <https://doi.org/10.1016/j.earscirev.2015.01.008>.
- Rothwell, R.G., Croudace, I.W., 2015. Twenty years of XRF Core Scanning Marine Sediments: What do Geochemical Proxies tell Us? In: Croudace, I.W., Rothwell, R.G. (Eds.), *Micro-XRF Studies of Sediment Cores*, Dev. Paleoenvironmental. Res., Vol. 17, pp. 25–103. [https://doi.org/10.1007/978-94-017-9849-5\\_2](https://doi.org/10.1007/978-94-017-9849-5_2).
- Rouis-Zargouni, L., Turon, J.L., Londeix, L., Essallami, L., Kallel, N., Sicre, M.A., 2010. Environmental and climatic changes in the Central Mediterranean Sea (Siculo-Tunisian Strait) during the last 30 ka based on dinoflagellate cyst and planktonic foraminifera assemblages. *Palaeogeogr. Palaeoclimatol. Palaeoecol.* 285, 17–29. <https://doi.org/10.1016/j.palaeo.2009.10.015>.
- Rovere, M., Pellegrini, C., Chiggiato, J., Campiani, E., Trincardi, F., 2019. Impact of dense bottom water on a continental shelf: an example from the SW Adriatic margin. *Mar. Geol.* 408, 123–143. <https://doi.org/10.1016/j.margeo.2018.12.002>.
- Sammari, C., Millot, C., Taupier-Letage, I., Stefani, A., Brahim, M., 1999. Hydrological characteristics in the Tunisia–Sardinia–Sicily area during spring 1995. *Deep Sea Res. Part I Oceanogr. Res. Pap.* 46, 1671–1703. [https://doi.org/10.1016/S0967-0637\(99\)00026-6](https://doi.org/10.1016/S0967-0637(99)00026-6).
- Schmiedl, G., Kuhnt, T., Ehrmann, W., Emeis, K.C., Hamann, Y., Kotthoff, U., Dulski, P., Pross, J., 2010. Climatic forcing of Eastern Mediterranean deep-water formation and benthic ecosystems during the past 22,000 years. *Quat. Sci. Rev.* 29, 3006–3020. <https://doi.org/10.1016/j.quascirev.2010.07.002>.
- Shanahan, T.M., McKay, N.P., Hughen, K.A., Overpeck, J.T., Otto-Bliesner, B., Heil, C.W., King, J., Schulz, C.A., Peck, J., 2015. The time-transgressive termination of the African Humid period. *Nat. Geosci.* 8, 140–144. <https://doi.org/10.1038/NNGEO2329>.
- Shipboard Scientific Party, 1996. Site 963. In: Emeis, K.-C., Robertson, A.H.F., Richter, C., et al. (Eds.), *Proceedings of the Ocean Drilling Program, Initial Reports*. 160. Texas A&M University, Houston, Texas, pp. 55–84. <https://doi.org/10.2973/odp.proc.ir.160.104.1996>.
- Siani, G., Paterne, M., Arnold, M., Bard, E., M etivier, B., Tisnerat, N., Bassinot, F., 2000. Radiocarbon reservoir ages in the Eastern Mediterranean Sea and Black Sea. *Radiocarbon* 42, 271–280. <https://doi.org/10.1017/S0033822200059075>.
- Siani, G., Paterne, M., Colin, C., 2010. Late glacial to Holocene planktic foraminifera bioevents and climatic record in the South Adriatic Sea. *J. Quat. Sci.* 25 (5), 808–821. <https://doi.org/10.1002/jqs.1360>.
- Sierro, F.J., Hodell, D.A., Curtis, J., Flores, J.A., Reguera, I., Colmenero-Hidalgo, E., Barcana, M.A., Grimalt, J., Canals, M., 2005. Impact of iceberg melting during Heinrich events on Mediterranean thermohaline circulation. *Paleoceanography* 20, PA2019. <https://doi.org/10.1029/2004PA001051>.
- Sprovieri, R., Di Stefano, E., Incarbona, A., Gargano, M.E., 2003. A high-resolution record of the last deglaciation in the Sicily Channel based on foraminifera and calcareous nannofossil quantitative distribution. *Palaeogeogr. Palaeoclimatol. Palaeoecol.* 202, 119–142. [https://doi.org/10.1016/S0031-0182\(03\)00632-1](https://doi.org/10.1016/S0031-0182(03)00632-1).
- Stanford, J.D., Hemingway, R., Rohling, E.J., Challenor, P.G., Medina-Elizalde, M., Lester, A.J., 2011. Sea-level probability for the last deglaciation: a statistical analysis of far-field records. *Glob. Planet. Change* 79, 193–203. <https://doi.org/10.1016/j.gloplacha.2010.11.002>.
- Stow, D., Smillie, Z., 2020. Distinguishing between deep-water sediment facies: Turbidites, contourites and hemipelagites. *Geosci.* 10 <https://doi.org/10.3390/geosciences10020068>.
- Stuiver, M., Reimer, P.J., 1993. Extended <sup>14</sup>C database and revised CALIB radiocarbon calibration program. *Radiocarbon* 35, 215–230. <https://doi.org/10.1017/S0033822200013904>.
- Tesi, T., Miserocchi, S., Goni, M., Langone, L., 2007. Source, transport and fate of terrestrial organic carbon on the western Mediterranean Sea, Gulf of Lions, France. *Mar. Chem.* 105, 101–117. <https://doi.org/10.1016/j.marchem.2007.01.005>.
- Tesi, T., Asioli, A., Minisini, D., Maselli, V., Dalla Valle, G., Gamberi, F., Langone, L., Cattaneo, A., Montagna, P., Trincardi, F., 2017. Large-scale response of the Eastern Mediterranean thermohaline circulation to African monsoon intensification during sapropel S1 formation. *Quat. Sci. Rev.* 159, 139–154. <https://doi.org/10.1016/j.quascirev.2017.01.020>.
- Tjallingii, R., R ohl, U., K olling, M., Bickert, T., 2007. Influence of the water content on X-ray fluorescence core-scanning measurements in soft marine sediments. *Geochem. Geophys. Geosyst.* 8, Q02004 <https://doi.org/10.1029/2006GC001393>.
- Toucanne, S., Jouet, G., Ducassou, E., Bassetti, M.-A., Dennielou, B., Angue Minto'o, C. M., Lahmi, M., Touyet, N., Charlier, K., Lericolais, G., Mulder, T., 2012. A 130,000-year record of Levantine Intermediate Water flow variability in the Corsica Trough, western Mediterranean Sea. *Quat. Sci. Rev.* 33, 55–73. <https://doi.org/10.1016/j.quascirev.2011.11.020>.
- Van Rooij, D., Iglesias, J., Hern andez-Molina, F.J., Ercilla, G., Gomez-Ballesteros, M., Casas, D., Llave, E., De Hauwere, A., Garcia-Gil, S., Acosta, J., Henri et, J.P., 2010. The Le Danois Contourite Depositional System: Interactions between the Mediterranean Outflow Water and the upper Cantabrian slope (North Iberian margin). *Mar. Geol.* 274, 1–20. <https://doi.org/10.1016/j.margeo.2010.03.001>.
- Verdicchio, G., Trincardi, F., 2008. Mediterranean shelf-edge muddy contourites: examples from the Gela and South Adriatic basins. *Geo-Mar. Lett.* 28, 137–151. <https://doi.org/10.1007/s00367-007-0096-9>.
- Vergnaud-Grazzini, C., Devaux, M., Znaidi, J., 1986. Stable isotope "anomalies" in Mediterranean Pleistocene records. *Mar. Micropaleontol.* 10, 35–69. [https://doi.org/10.1016/0377-8398\(86\)90024-1](https://doi.org/10.1016/0377-8398(86)90024-1).
- Vergnaud-Grazzini, C., Borsetti, A.M., Cati, F., Colantoni, P., D'Onofrio, S., Sali e, J.F., Sartori, R., Tampieri, R., 1988. Paleooceanographic record of the last deglaciation in

- the Strait of Sicily. *Mar. Micropaleontol.* 13, 1–21. [https://doi.org/10.1016/0377-8398\(88\)90010-2](https://doi.org/10.1016/0377-8398(88)90010-2).
- Vigliotti, L., Verosub, K.L., Cattaneo, A., Trincardi, F., Asioli, A., Piva, A., 2008. Palaeomagnetic and rock magnetic analysis of Holocene deposits from the Adriatic Sea: Detecting and dating short-term fluctuations in sediment supply. *The Holocene* 18 (1), 141–152. <https://doi.org/10.1177/0959683607085605>.
- Vizzini, S., Sarà, G., Mateo, M.A., Mazzola, A., 2003.  $\delta^{13}\text{C}$  and  $\delta^{15}\text{N}$  variability in *Posidonia oceanica* associated with seasonality and plant fraction. *Aquat. Bot.* 76 (3), 195–202. [https://doi.org/10.1016/S0304-3770\(03\)00052-4](https://doi.org/10.1016/S0304-3770(03)00052-4).
- Voigt, I., Chiessi, C., Piola, A., Henrich, R., 2016. Holocene changes in Antarctic Intermediate Water flow strength in the Southwest Atlantic. *Palaeogeogr. Palaeoclimatol. Palaeoecol.* 463, 60–67. <https://doi.org/10.1016/j.palaeo.2016.09.018>.
- Wang, M., Zheng, H., Xie, X., Fan, D., Yang, S., Zhou, Q., Wang, K., 2011. A 600-year flood history in the Yangtze River drainage: comparison between a subaqueous delta and historical records. *Chin. Sci. Bull.* 56, 188–195. <https://doi.org/10.1007/s11434-010-4212-2>.
- Zaniboni, F., Pagnoni, G., Paparo, M.A., Gauchery, T., Rovere, M., Argnani, A., Armigliato, A., Tinti, S., 2021. Tsunamis from Submarine Collapses along the Eastern Slope of the Gela Basin (Strait of Sicily). *Front. Earth Sci.* 8, 602171. <https://doi.org/10.3389/feart.2020.602171>.

### Take-Home Messages

- Very high sedimentation rates revealed during the Heinrich Stadial I
- Instability occurred during the deglaciation (after 17.5 kyr cal. BP)
- Sea-level rise pulses induced changes in the interface's water depth of the water masses.
- Margin instability is related to erosion by bottom currents over the shelf and rapid sea-level rise.



# Chapter 7. Synthesis, Conclusions and Perspectives

---

## 7.1 Synthesis

Submarine landslides can occur in oceans (Moscardelli and Wood, 2016 and references therein), seas (e.g. Urgeles and Camerlenghi, 2013 and references therein) and lakes (Sammartini et al., 2019 and references therein). Submarine landslides are globally distributed along continental margin slopes (i.e. fjords, active river deltas, submarine canyon-fan systems, volcanic island flanks). The sedimentary bodies of submarine landslides, MTDs, tend to be located on low slope angles with a worldwide average of  $5^\circ$  (Moscardelli and Wood, 2016). In the Mediterranean Sea, the average slope angle is even lower ( $<2^\circ$ ; Urgeles and Camerlenghi, 2013). Similarly, the water depth interval in which failures tend to be generated is 300 to 900 m shallower in the Mediterranean Sea compared to world oceans. The water depth interval may be further decreased by retrogressive erosion which tends to extend the failure upslope towards the shelf (e.g. Badhani et al., 2020b). Concerning the average volume of MTDs, the Mediterranean Sea is composed of MTDs with volumes 3 to 60 times lower than in the Atlantic Ocean depending on the slope angle (Urgeles and Camerlenghi, 2013). Hühnerbach and Masson (2004) reported larger MTDs (average =  $30 \text{ km}^3$ ) on lower slope gradients ( $2.2^\circ$ ) and smaller MTDs (average =  $1.4 \text{ km}^3$ ) on steeper slope gradients ( $4.5^\circ$ ). The slope angle seems to play a role in the volume of sediments displaced and in their runout as submarine landslides tend to have shorter runout in the Mediterranean Sea (average = 45 km) than in other ocean realms (average = 64 km). In general, submarine landslides have 1 order of magnitude larger volumes and longer runout compared to subaerial landslides (Urgeles and Camerlenghi, 2013).

In the Mediterranean Sea, Urgeles and Camerlenghi (2013) reported more than 700 MTDs from blocky slides to mud-flows covering more than 18% of the seafloor ( $\sim 450\,000 \text{ km}^2$ ). The multiple types of MTDs observed in the Mediterranean Sea depends mostly on the sediment composition leading to different internal and surface deformation, which inform on the type of movements and the material transported. These MTDs were classified into different typologies based on the deformation observed. MTDs can have relative coherent mass (Block slide; e.g. Trincardi and Argnani, 1990) with rotational movements (Slump; e.g. Cattaneo et al., 2014) to cohesionless movements with individual rock fragment (Debris slide; e.g. Bell et al., 2013) or be heterogeneous (Debris flow; e.g. Dan et al., 2007).

The varied seafloor morphology of the Mediterranean Sea, composed of narrow and shallow passages, banks, deltas, volcanic islands and basins, creates accommodation space for the accumulation of sediments where MTDs are present (e.g. Alonso et al., 2014; Spatola et al., 2018). Debris flows and slumps have been reported near the Strait of Gibraltar and the Nile Delta (e.g. Ducassou et al., 2013; Garfunkel, 1985) and block slides in the Strait of Sicily and along the shelves of the Ionian and Levantine Basins (e.g. Trincardi and Argnani, 1990; Alves, 2015 and references therein). The deepest Mediterranean basins (Algerian, Ionian and Levantine) host the accumulation of sediments from megaturbidites (Urgeles and Camerlenghi, 2013 and references therein; Cattaneo et al., 2019).

The particular morphology of the Mediterranean Sea is due to its development at the boundary of three tectonic plates (Africa, Eurasia and Arabia). Remnant of a large ocean, the Tethys Ocean, the Mediterranean Sea owes his closure to the counterclockwise rotation of Africa towards Eurasia, which formed a semi-enclosed basin reducing its connection with the Atlantic Ocean (Faccenna et al., 2001 and references therein). The African-Eurasian convergence controls the evolution of the Mediterranean and the southern retreat of the slab rollback led to the opening of several basins (Alboran Sea, the Liguro-Provencal basin, the Tyrrhenian Sea and the Aegan Sea) (Jolivet et al., 2006; Faccenna, et al., 2011). The latest migration of the contractional front (S/SE) of the African/Eurasian plates boundary during Pliocene resulted in the formation of the Gela Basin in the Strait of Sicily (Ghielmi et al., 2012). In the similar time lap, the initiation of the rift, responsible of the deep graben formation in the Strait of Sicily, constrained the southern Gela Basin with extensional movements while compressional movements increase the water depth in the north.

The limited water connection of the Mediterranean Sea to the Atlantic Ocean via the Strait of Gibraltar and the shallow water depth of the Strait of Sicily resulted in the formation of shallow (MAW, 100-200 m w.d.), intermediate (LIW; 200-600 m w.d.) and deep water masses (EMDW and WMDW, > 600 m w.d.). This connection is primordial due to the arid climate at these latitudes resulting in intense evaporation and explaining its higher salinity content ( $\geq 38$  psu; Skliris et al., 2018). The strong water exchange, high evaporation and strong and cold winds in winter drive the thermohaline circulation in the Mediterranean Sea. The encounter of cold winds with warm and saline water increase the density of the water masses and decrease the temperature sinking the water masses. These mechanisms lead to the formation of the LIW in the Levantine basin from the MAW and the deep water masses in the Adriatic

Sea and in the Gulf of Lions from the LIW (Astraldi et al., 2001; Millot, 1999; Millot and Taupier-Letage, 2005). The shallow depth of the Strait of Sicily allow the circulation of the surface (eastward) and intermediate water masses (westward). The high-velocity thermohaline circulation close to the seafloor, controlled by the seafloor morphology and the climate, in turn controls particle transport and deposition on geological time scales and has produced contourite deposits along the main bottom current path (Cattaneo et al., 2017 and references therein).

Contourite deposits are sediments deposited or substantially reworked by the persistent action of bottom-currents and classified based on their lithological, sedimentological and morphological characteristics (Rebesco et al., 2005; 2014). The lithological content of contourite deposits consists of clastic and/or calcareous sediments (from clay to gravel) and can be composed of biogenic, terrigenous and volcanoclastic materials (Stow and Faugères, 2008; Rebesco et al., 2014). The depositional area is known as *contourite drift* and can be bounded on one or both sides by non-depositional or erosional channels called *contourite moats* (Rebesco et al., 2008). The contourite drifts can be characterized by mounded (mounded drift) or low-relief features (plastered drift), extend by ten to hundreds of kilometers, cover large areas (i.e. 1,000,000 km<sup>2</sup>) and increase the relief from tens to hundreds of meters above the surrounding seafloor (Faugères et al., 1993b; e.g. Hernández-Molina et al., 2016b; Preu et al., 2013). The type of contourite drifts indicates the bottom-current velocity and the sediment supply. Mounded drifts indicate locations where deceleration of bottom current promotes deposition while plastered drifts tend to form in sediment-starved margin sectors with low bottom-current velocities (Miramontes et al., 2019). Contourite deposits can be formed anywhere along margins from shelf to basin (e.g. Vandorpe et al., 2011; Miramontes et al., 2016) and migrate through time (e.g. Pellegrini et al., 2016). Sedimentation rates in contourites are much higher than in pelagic sediments (Stow and Smillie, 2020), which can reach themselves remarkable values in the Mediterranean Sea (i.e. 40 cm/kyr: Stow et al., 2013), providing enhanced temporal resolution archives to reconstruct the past oceanography and climate (e.g. Toucanne et al., 2012; Bahr et al., 2014). In addition, the higher sedimentation rate of contourite deposits implies higher water content, resulting in under-consolidation strata and decreased sediment shear strength, which together with excess pore-pressure and steep downslope gradients make them prone to failure (Laberg and Camerlenghi, 2008; Miramontes et al., 2018; e.g. Verdicchio and Trincardi, 2008; Gatter et al., 2020). Therefore, contourite deposits can contribute to large-scale failures in the Mediterranean Sea (Miramontes et al., 2018; e.g. Dalla Valle et al., 2014).

Submarine landslides may contribute to the accumulation of gas and hydrocarbon reservoirs (Shanmugam et al., 2009) however, they mostly represent a major geohazard in the marine realm capable to damage coastal and offshore infrastructures (L'Heureux et al., 2012; Kopf et al., 2012) and generate tsunamis (Tappin et al., 2010; e.g. Macías et al., 2015). The amount of energy induced by submarine landslides, which depends on the volume of sediment displaced, the initial water depth and the acceleration velocity based on the type of sediments and the slope gradients, controls the possible tsunamis formation and their sizes (Ward, 2001; Harbitz et al., 2005). Despite a smaller average volume of the MTDs in the Mediterranean Sea, many tsunami-landslides have been reported (Papadopoulos et al., 2007 and references therein) including large-size (e.g. >10 m; Mueller et al., 2020; Perissoratis and Papadopoulos, 1999).

The Mediterranean Sea is a natural laboratory for submarine landslides research being characterized by the presence of many varied MTDs emplaced in various morphologic, geodynamic and oceanographic contexts. Within the Mediterranean Sea, the Strait of Sicily represents a particular area where water-mass exchange between the eastern and the western Mediterranean Sea registers the past climate and oceanographic circulation. Therefore, the sedimentary record of the Gela Basin, located between Malta and Sicily (Italy), register not only the oceanographic exchanges leading to the formation of contourite deposits (Verdicchio and Trincardi, 2008) but also the tectonic activity and high sedimentation rates resulting in the emplacement of multiple exposed, partially overlapping and stacked MTDs (Trincardi and Argnani, 1990; Minisini et al., 2007; Kuhlmann et al., 2017).

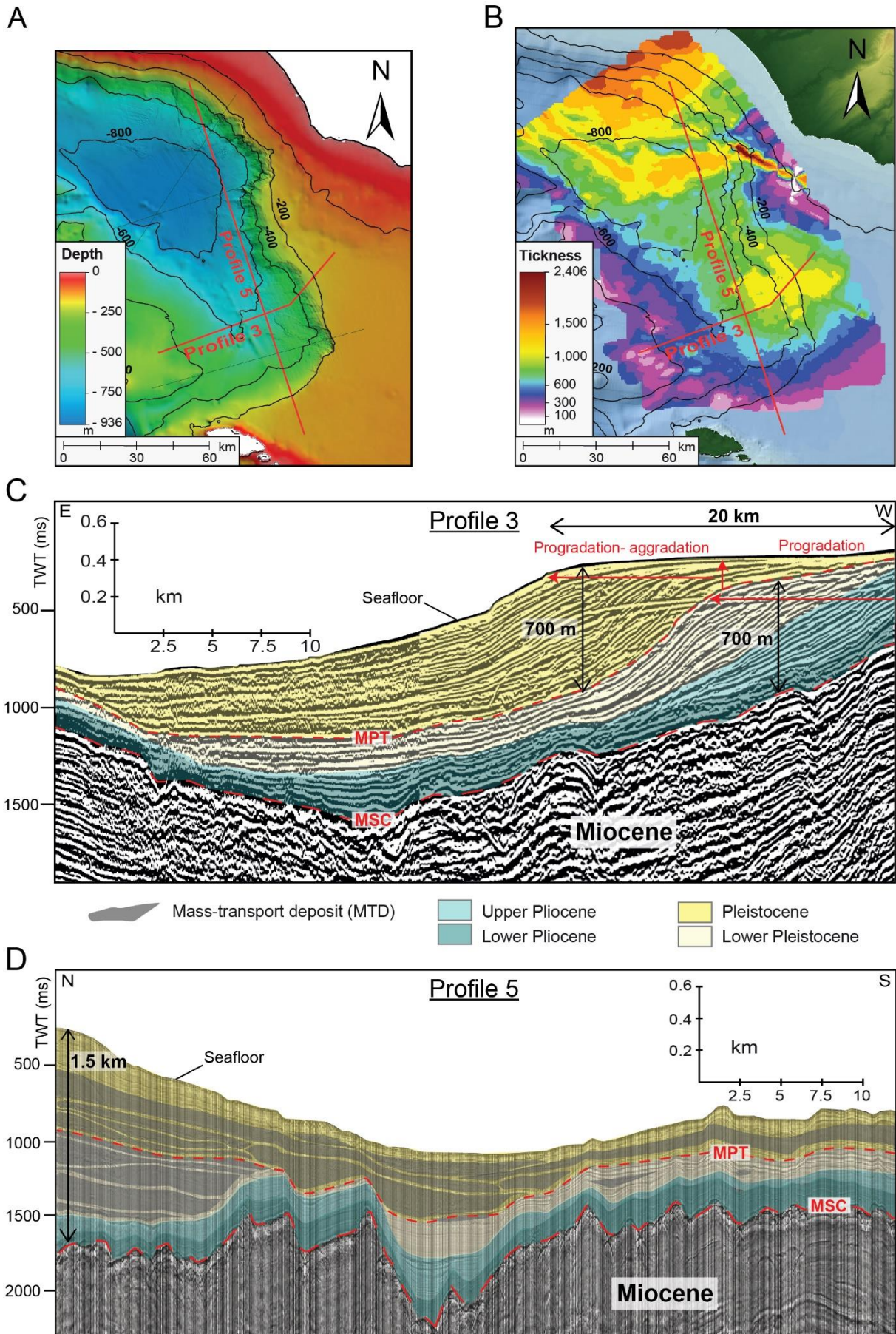
#### Pliocene-Quaternary evolution of the Gela Basin

The access to large- (deep boreholes logs and industrial multi-channel seismic reflection profiles) and small-scale dataset with high-resolution (CHIRP sonar seismic profiles and swath bathymetry) gave the opportunity to: 1) understand the interaction between tectonic activity, climate change and shifts in oceanographic regime in the Gela Basin and 2) identify when and where MTDs were emplaced within the global change.

The interpretation of the multi-channel seismic profiles (MCS), which was obtained via the correlation of the deep boreholes, permitted to identify the age of key seismic reflections (Lower and Upper Pliocene, Lower Pleistocene and Pleistocene) and highlight the main phases of the margin growth after the desiccation of the Mediterranean Sea. Our results show that the Gela Basin recorded up to 2.4 km-thick Pliocene and Quaternary sediments infilling the uneven

pre-existing morphology with up to 20 km seaward migration of the shelf-edge clinothems. The margin outbuilding was characterized by a progradational phase until the transition from Lower Pleistocene to Pleistocene, aged at 0.8 Ma corresponding to the Middle Pleistocene Transition (MPT), followed by an equivalent sediment wedge accumulation with a progradation phase and strong aggradational motif (Figs. 7.1A, B and C). The margin experienced a drastic increase of the prograding rate from 150 m/Myr to 900 m/My (multiplied by 6) at the MPT inferring that geological time cannot be related to the physical scale of the wedge and resulting in the formation of a wide prograding wedge on the Malta Plateau.

In addition, the MCS profiles are characterized by the presence of multiple buried MTDs and contourite deposits. The chaotic facies used to identify MTDs were age-constrained by the key seismic reflections. The data highlights a change in MTDs spatial distribution emplaced before and after the MPT. Before the MPT, MTDs are sourced from the north with volumes ranging between 30 to 120 km<sup>3</sup> (Fig. 7.1D) similar to the Gela Slide that is likely related to the uplift and exhumation of last front of the Maghrebian fold-and thrust belt (Trincardi and Argnani, 1990). The signature of the MTDs (prominent headwall and blocky to chaotic seismic facies) permitted to reject the influence of the transtensional movement of the Pantelleria Graben affecting the northern Gela Basin stability (Fig. 7.1D). After the MPT, the data shows a clear increase in the number of MTDs along the eastern Gela Basin but a decrease in size (0.4 - 45 km<sup>3</sup>, Fig. 7.1D) when the margin experienced a drastic increase in sedimentation rate. Their higher recurrence may be associated to the 100 kyr glacial-interglacial climate variability (Tziperman and Gildor, 2003) as only minor local subsidence and regional uplift occurred with no significant impact on the sediment supply during that time interval (Gardiner et al., 1993; Ghielmi et al., 2012). The transition from tectonic to climatic and sea-level changes influence has been recorded by the Gela Basin at the MPT, similarly to observations made in the Gulf of Cadiz (Llave et al., 2007).



(caption on next page)

*Figure 7.1: A) Bathymetric map showing the location of profiles 3 and 5. B) Isopach map representing the overall Pliocene-Quaternary deposition in the Gela Basin and showing the extension of the largest (north) and thickest (east) progradation sets highlighted by profiles 3 and 5, respectively. C) Interpreted multi-channel seismic profile 3 showing the largest progradation set of the Gela Basin and its increasing rate at the Middle-Pleistocene Transition (MPT). D) Interpreted multi-channel seismic profile 5 highlighting the thickest progradation set of the Gela Basin and the changes of the along-strike spatial distribution of the MTDs emplaced in the Gela Basin at the MPT. MSC: Messinian Salinity Crisis.*

Additionally, older contourite deposits were identified in the northern Gela Basin where seafloor-emergent contourite deposits were previously studied by Verdicchio and Trincardi (2008), while in the southern Gela Basin contourite deposits were identified at the seafloor by CHIRP sonar seismic profiles. The internal structures of the seismic reflections, interpreted as contourite drift based on Rebesco and Stow (2001) classification and constrained by the key seismic reflections, indicates an onset of contourite deposition on the lower slope during the Pliocene followed by a growth and up-slope migration after the MPT as observed in the Adriatic Sea (Pellegrini et al., 2015) and in the Corsica Trough (Miramontes et al., 2016). The types of the buried contourite deposits could only be recognized based on the MCS profiles in which their resolution permitted to analyse their morphological characteristics. However, the extension of the buried contourite deposits could not be estimated based on the MCS profiles. Similarly, the extension of the southern contourite deposits, recognized by the CHIRP sonar seismic profiles, could not be confirmed by the bathymetry in the southern Gela Basin due to the limited acquisition of the high-resolution swath bathymetry along the eastern Gela Basin. Nevertheless, the resolution of the CHIRP profiles permitted the identification and correlation of other key seismic reflections (i.e. erosional surfaces ES2 and ES1) highlighting the failure of a contourite deposit in the southern Gela Basin (Gela Drift Slide – GDS) with ES2 as its base, which suggests erosional surfaces to act as weak layers due to the change in grain size from sediments deposited during lowstands.

### 7.1.1 Tsunamigenic potential in the Gela Basin

Among the multiple MTDs identified in the Gela Basin, two recently emplaced MTDs (the South Gela Basin Slide-SGBS and the North Twin Slide-NTS) were chosen to determine if they can generate a tsunami and estimate the tsunamigenic potential in the Gela Basin (Fig. 7.2). The NTS (0.5 km<sup>3</sup>) and the SGBS (1.5 km<sup>3</sup>) have relatively small volumes compared to other MTDs emplaced in the Gela Basin but their volumes and depth range make them among representative of the most frequently observed MTDs in the Mediterranean Sea (Urgeles and

Camerlenghi, 2014; Fig. 7.2). In addition, the high-resolution swath bathymetry allowed to reconstruct the pre-failure margin morphology in order to estimate their tsunamigenic potential.

As said, the data (swath bathymetry and CHIRP sonar seismic profiles) allowed to identify the slide parameters (undisturbed slope, top initial surface and predefined centre of mass) and compute the landslide motions via in-house coding. The computed sliding motions provided the velocity of the slides including accelerations and decelerations. These information are necessary for the tsunami simulation to estimate the size, speed and propagation of the tsunami waves generated by the sliding motions. The simulations are based on splitting the landslide mass into independent and interactive portions that can change shape but not their volumes (e.g. Zaniboni and Tinti, 2014 and references therein).

Based on these estimations, results show that both landslide-tsunamis from the SGBS and NTS hit the coast of Sicily and Malta within only a few minutes. Interestingly, the computed tsunamis show that in both cases, the energy of the tsunami wave focuses towards the coast of Sicily with more relevant and diffused effects from the farthest landslide, the SGBS. Despite a propagation efficiency limited compared to earthquakes-triggered tsunamis (Okal and Synolakis, 2003), the tsunami simulation reveals that both scenarios are capable of impacting coastal stretches from tens to hundreds of kilometers long.

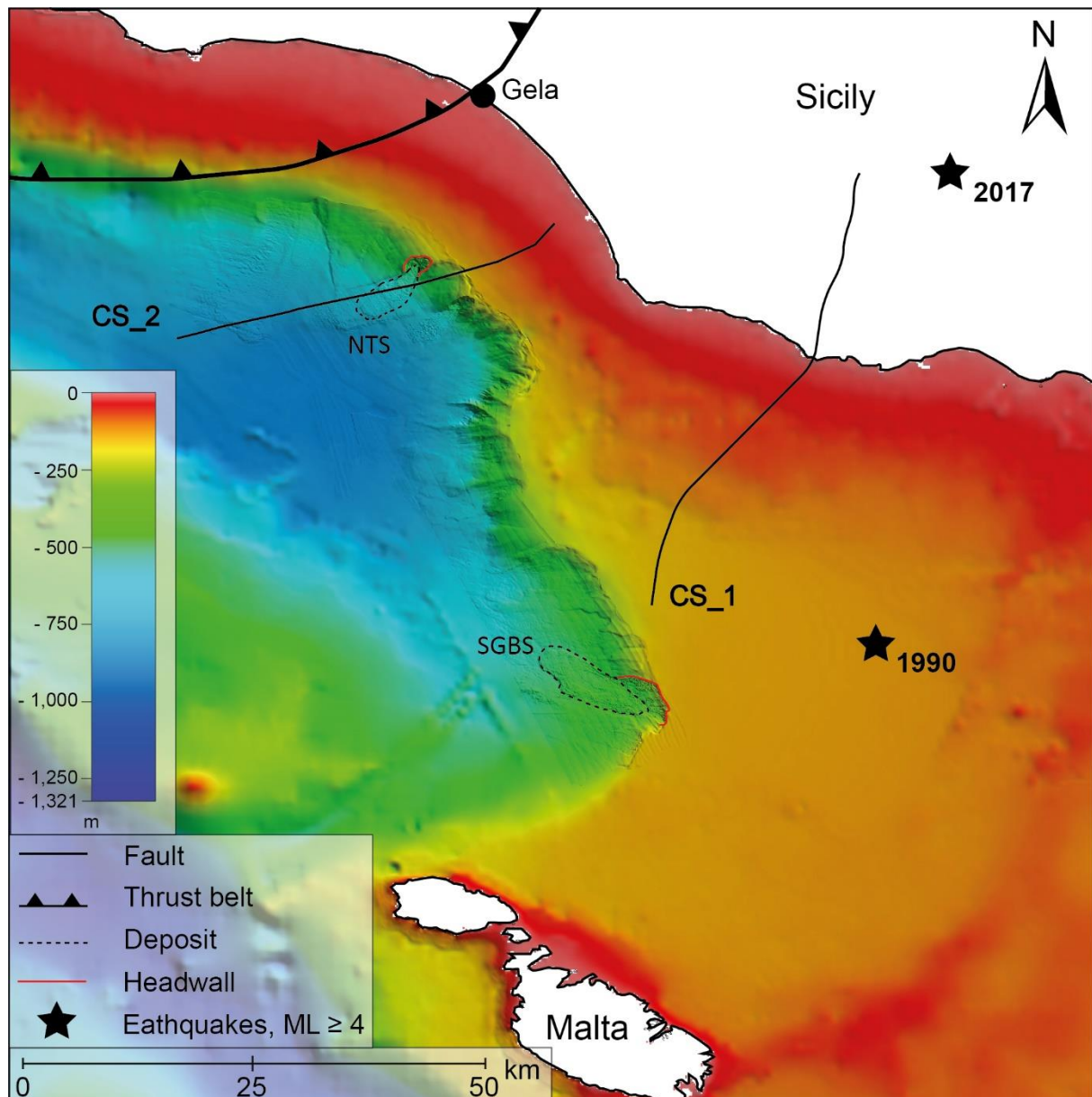


Figure 7.2: Bathymetric map showing the location of the North Twin Slide (NTS) and South Gela Basin Slide (SGBS) and the location of the recent seismic sequences registered near the Gela Basin as well as the positioning of the faults (CS\_1 and CS\_2) used in the stability analysis based on Antoncicchi et al. (2020). CS\_01 represents the offshore continuation of the Scicli-Ragusa fault where a few NE-SW small fault segments until 8 km were identified in the near offshore area (Azzaro and Barbono, 2000). CS\_2 is a normal fault offsetting the Meso-Cenozoic sedimentary succession until Top Messinian at the Gela Nappe front and possibly reactivated in compression.

A stability analysis was performed along the slope close to both SGBS and NTS by applying different Peak Ground Acceleration (PGA), which are expressed as a fraction of the gravity acceleration “g”. The maximum PGAs that could have affected the stability of the eastern slope of the Gela Basin were computed based on a structural analysis from which two possible faults are located close to the SGBS and NTS (CS\_01 and CS\_02; Antoncicchi et al.,

2020). Two seismic sequences (1990 and 2017) were registered in proximity of CS\_01 and little evidence of deformation was appreciated in the Plio-Quaternary succession where CS\_02 is located relatively nearby NTS (Fig. 7.2). The purpose was to test if seismic shaking could have been responsible for the instabilities of the NTS and SGBS and estimate the seismic intensity necessary to make the slope unstable (e.g. Strasser et al., 2007; Strozyk et al., 2010; Robert et al., 2012). The calculated maximum PGA values were equivalent to an earthquake intensity of 6.5 in magnitude and the different PGAs applied on both landslides gave access to the safety factor. The results show that only the NTS could get unstable with that magnitude of seismic shaking while even the highest PGA applied on SGBS from CS\_02 was insufficient to make unstable any profiles along its initial sliding mass.

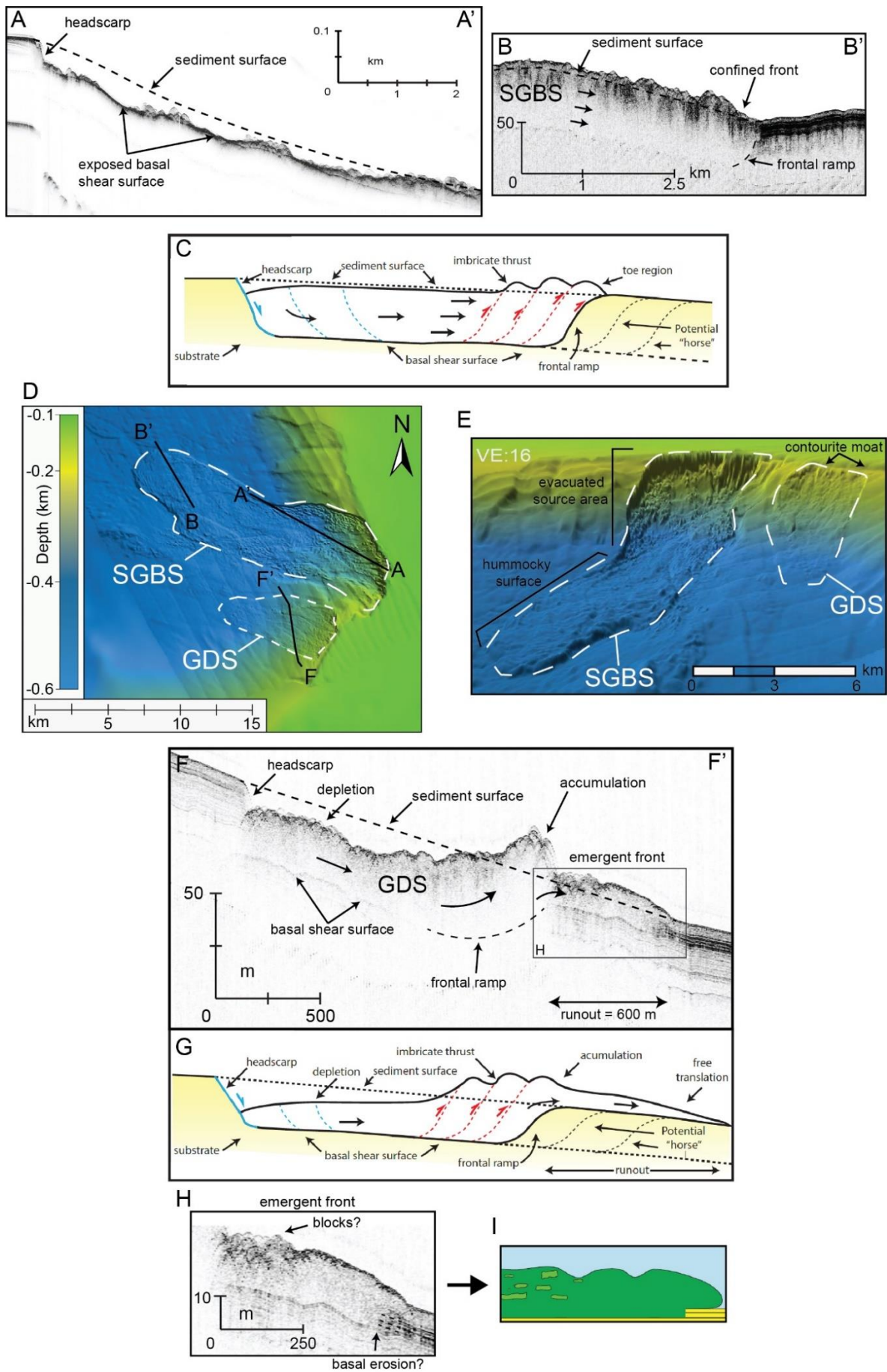
This difference in pre-conditioning mechanisms between two submarine landslides only 80 km apart within the same sedimentary basin reveals the diversity and complexity of the basin (e.g. Talling et al., 2014; Becker et al., 2017; Kremer et al., 2017). In the case of the NTS, a useful precursor for tsunami arrival would be an earthquake (tens of minutes ahead) in the northern Gela Basin but the SGBS may have been triggered by multiple and aseismic factors making it difficult to anticipate any margin instability (e.g. high sedimentation rate: Laberg and Camerlenghi, 2008; bottom currents: Miramontes et al., 2018; volcanoclastic materials: Masson et al., 2002).

### 7.1.2 Along- and down-slope processes in the Gela Basin

The accessibility of two piston cores recovered in the southern Gela Basin near the SGBS permitted, along with swath bathymetry and CHIRP sonar seismic profiles, to investigate the paleo-sedimentary processes and constrain the ages and pre-conditioning factors of the SGBS and GDS (the contourite-related MTD) emplacements.

The SGBS and GDS, exposed or shallowly buried, could be analysed by high-resolution (but low penetration) CHIRP sonar seismic profiles. The data show distinct but different structures between the SGBS and the GDS, which were used to designate the type of flows and in turn the type of material transported as well as the sediment concentration. The SGBS is characterized by an evacuated well-defined amphitheatre-like source area exposing the erosional base, hyperbolic reflections interpreted as isolated rock debris (Figs. 7.3A and E) and a confined front (Sensu Frey-Martinez et al., 2006; Figs. 7.3B and C). The latter, meaning a bulldozing of the foreland, and the evacuated source area suggest a catastrophic collapse, when

a rapid acceleration of the landslide at the failure initiation due to the relatively high slope gradient ( $> 5^\circ$ ) was simulated (Zaniboni et al., 2021), resulting in the formation of a new frontal ramp basinward (Scarselli, 2020). In addition, the swath bathymetry reveals a hummocky surface on the depositional area where the CHIRP profiles indicate the presence of blocks (Figs. 7.3B and D). These information, similar to other studied MTDs (e.g. Bell et al., 2013; Masson et al., 2002), suggests the SGBS to be a debris slide. In the case of the GDS, a prominent headscarp with a depletion is visible at the source area while a 25 m accumulation above the pre-failure sediment surface is present on top of a curved frontal ramp at the toe domain and is accompanied by a 600 m long emergent front (Sensu Frey-Martinez et al., 2006; Figs. 7.3F and G). The missing high- and low- amplitude reflectors at the emergent front but present basinward of the GDS suggest a basal erosion of the substrate 9 m below the sediment surface (Sobiesiak et al., 2018; Figs. 7.3H and I). The sharp change into undeformed strata is interpreted as discontinuous no-slip flows possibly due to the presence of rafted blocks in mostly clayey material (Sobiesiak et al., 2018), which could explain the thick accumulation at its toe domain (Fig. 7.3F). The chaotic to transparent reflections on a curved glide plane with a backward rotation of the slide, as seen in Perissoratis and Papadopoulos (1999) and Shanmugam (2006), infers the GDS to be a slump. The rafted blocks present at the toe domain suggest their origin from the erosion of the substrate but the presence of heterogeneous blocks assemblage in the SGBS depositional and source area infer the disaggregation of the failed MTD (Sobiesiak et al., 2018). This difference in the type of MTDs, only a few km apart, may be explained by the presence of a contourite deposit upslope the GDS where reworked sediment, high sedimentation rates and well-sorted grain size, result in abrupt lithological changes and higher shear strength contrast with the substrate (Rebesco et al., 2014 and references therein; Gatter et al., 2020).



(caption on next page)

*Figure 7.3: CHIRP profiles highlighting A) the SGBS evacuated source area and B) the confined toe domain compared to C) the schematic drawing representing a frontally-confined mass flow from Sobiesiak et al. (2018). Note that no deformation are visible in front and within the toe domain of the SGBS. D) Bathymetric map with location of the CHIRP profiles shown in A, B and F. E) 3D bathymetric view showing the evacuated amphitheatre-like source area of the SGBS and its hummocky depositional area as well as the GDS deposit located downslope the failed drift crest. F) CHIRP profiles representing the GDS cross-section and showing the depletion near the headscarp as well as the concentrated accumulation at the toe domain with an emergent front inducing a backward rotation. G) Schematic drawing of the frontally-emergent mass flow from Sobiesiak et al. (2018) used to compare the GDS depositional area based on its morphology and internal structures. H) Enlargement of the GDS emergent front showing the possible presence of blocks and a basal erosion as represented in I) the cartoon modified after Sobiesiak et al. (2018) inducing no-slip flows.*

---

The sediment piston cores, recovered at the toe of the SGBS (MS72) and the flank of GDS (MS75), contain sediments from the lower (-550 m w.d.) and upper slope (-280 m w.d.), respectively. The piston cores were analysed via multi-proxies run on the whole (magnetic susceptibility) and open cores (X-ray images and XRF data) as well as on samples (grain size, foraminifera assemblages and plant debris). The  $\delta^{18}\text{O}$ ,  $\delta^{13}\text{C}$  and radiocarbon dates, obtained from the foraminifera analysis, permitted to make age models and correlate the piston cores with other cores in the Strait of Sicily (Rouis-Zargouni et al., 2010) and the Mediterranean Sea (Cacho et al., 1999). However, the very variable sedimentation rates of the cores complicated the age-depth relationship with a few age reversals. The identification of foraminiferal ecozones was used to correlate the cores and calibrate the age-depth model. After calibration of the age models, the cores revealed sediment from the post-Glacial with a stratigraphically expanded record of Heinrich Stadial 1 (HS1), which represents the termination of the last glacial period characterized by major and rapid climate changes (Allard et al., 2021; Camuera et al., 2021). The penetration depth of the piston cores (8.42 m for MS75 and 10.72 m for MS72) made accessible sediments from the high amplitude reflector located at the base of GDS and from the last seismic reflection cut by the SGBS. In both cases, the age models indicate that the MTDs were likely emplaced during or after HS1, which corresponds to a time interval when most of the submarine landslides occurred in the last 100 kyr within the Mediterranean Sea (Urgeles and Camerlenghi, 2013; Fig. 7.4).

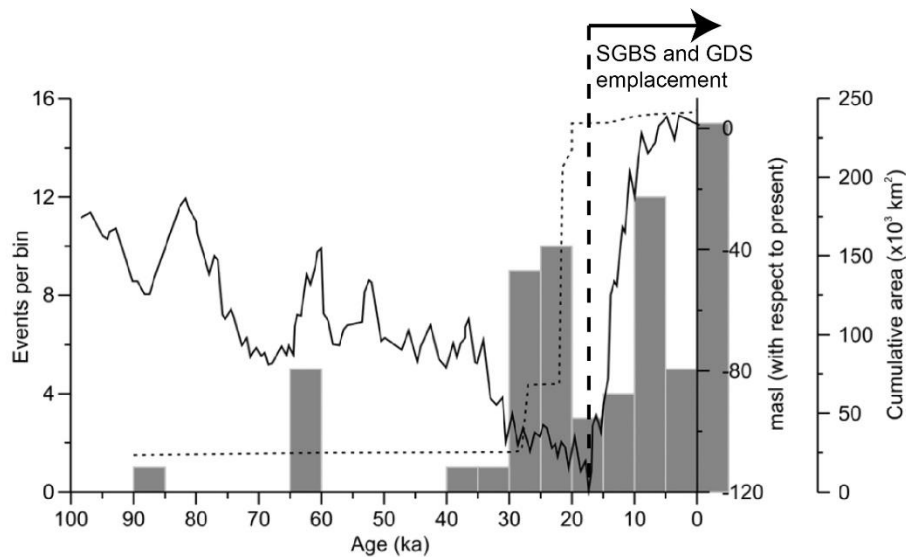


Figure 7.4: Representation of the number of MTDs found in the Mediterranean Sea with respect to their age constrained plotted versus the sea level curve of the last 100 kyr. Figure modified from Urgeles and Camerlenghi (2013).

Cores MS72 and MS75 indicate, based on the foraminifera analysis, the presence of reworked, sorted and displaced foraminifera suggesting the occurrence of downslope and along-slope sedimentary processes (Culver et al., 2012, Fentimen et al., 2020). In order to determine the processes responsible for the failures of the SGBS and GDS, a multi-proxy approach was used on the sediment cores including sediment structures, grain size and terrigenous concentration to distinguish the two processes (Tab. 7.1).

Table 7.1: List of proxies used to identify along- and down-slope processes based on literatures.

Proxies	Down-slope transport	Along-slope transport	References
Foraminifera	Reworked/displaced/mixed/broken	homogeneous test size	e.g. Culver et al., 2012
Sediment structure	Cross-lamination, loads, flames, erosional contacts, lenticular, discontinuous, convolute.	Horizontal, curved, low-angle, inverse to normal grading	e.g. Martín-Chivelet et al., 2008; Stow and Smillie, 2020
Grain size	Low $\overline{SS}$ , unimodal distribution, high correlation coefficient (R)	High $\overline{SS}$ , bimodal distribution, high Zr/Rb, low R	e.g. Bahr et al., 2014; McCave et al., 1995; McCave and Andrews, 2019; Toucanne et al., 2012;
Terrigenous flux	High Ti/Ca	Low Ti/Ca, low S/Cl	e.g. Piva et al., 2008; Revel et al., 2015

The data reveal strong changes in lateral advection on the upper-slope before and during HS1, which may have further predisposed the slope to failure. The different environments

recorded between the upper- and lower-slope were compared to another studied area from the western Mediterranean Sea (Corsica Trough; Toucanne et al., 2012) and suggest this difference to be due to the influence of different water masses on the upper slope of the Gela Basin (MAW and LIW). The influence of different water masses in the upper slope and in particular at core MS75's location, which is controlled by the LIW at the current stand of sea level (Millot and Taupier-Letage, 2005), infer changes in their buoyancy. The different buoyancy of the water masses impacting Gela Basin eastern slope were associated to sea-level variations based on the various changes in bottom current velocity recorded by the core during periods of rapid sea-level rises (i.e. MWP-1A). This phenomenon was explained by the higher freshwater input from the Atlantic Ocean when sea-level rises decreased the salinity of the Mediterranean Sea and in turn increased the water column density gradient (e.g. Jiménez-Espejo et al., 2015). Previous research suggested the density changes of water masses due to climate change (e.g. Toucanne et al., 2012). An increasing in density contrast between the LIW and the MAW can create internal waves capable of eroding and remobilizing sediments in the upper slope (Droghei et al., 2016) and hence, could explain the emplacement of the Twin Slides after 8.5 ka (Kuhlmann et al., 2017) and the missing last 8 kyr in core MS75 soon after the MWP-1B.

## 7.2 Conclusions

The Gela Basin represents an ideal research laboratory for the studies of MTDs within the Mediterranean Sea where tectonic activity, oceanographic circulation and climate forcing together influenced and rhythmized the margin outbuilding along with its instabilities. This research permitted to answer the following scientific questions:

- *What are the pre-conditioning and triggering factors responsible for the emplacement of submarine landslides in the Gela Basin?*

Multiple failures occurred in the Gela Basin during the outbuilding of the margin within Pliocene and Pleistocene. During Pliocene and Early Pleistocene, mass-transport deposits (MTDs) are mostly constrained in the northern Gela Basin and come from the north where their headwalls are located, similarly to the Gela Slide. Their emplacement was probably related to the uplift of the Gela Nappe. The spatial distribution of the MTDs changed radically after the Middle-Pleistocene Transition (MPT) with a widening of the surface area affected by MTDs. The accelerated margin outbuilding (multiplied by 6) is concomitant with the increasing number of submarine landslides after the MPT, a condition which makes possible to infer high-sedimentation rates, controlled by sea-level fluctuations, as pre-conditioning factor. This hypothesis was confirmed with the analysis of contourite deposits present along the shelf-edge where important sedimentation rate fluctuations were associated to sea-level pulses, independent to climate forcing, which overall increased the relief and promoted slope instabilities.

- *How frequency and size of the submarine landslides emplaced in the Gela Basin evolved through the Pliocene-Pleistocene?*

In addition to the changes in spatial distribution of the MTDs at the MPT in the Gela Basin, the drastic development of the margin outbuilding led to changes in the volumes and frequencies of the submarine landslides. Before the MPT, a few but large and stacked MTDs (30-120 km<sup>3</sup>) were emplaced giving an estimated recurrence of around 400 kyr based on the time interval of deposition. After the MPT, the large tectonic-related MTDs were subdued by smaller (0.4-45 km<sup>3</sup>) but more frequent MTDs. The systematic emplacement of MTDs above erosional surfaces, inferring a sea-level fluctuations control, suggest a frequency paced at Milankovitch cyclicity (ca. 100 kyr).

- *What were the key time intervals for the emplacement of submarine landslides and their relationship with climate and/or sea-level change?*

MTDs were emplaced in the northern Gela Basin during major uplift of the Gela Nappe and more recent seismic activity. The slope stability analysis made along the headwalls of a MTD present in the northern basin confirmed the influence of seismicity as a factor capable of mobilizing upper slope sediment. However, even strong seismic shaking ( $M=6.5$ ) was insufficient to mobilize an MTD located in the southern Gela Basin. This MTD, called the Southern Gela Basin Slide (SGBS), was emplaced downslope of a contourite deposit during or after the Heinrich Stadial 1 ( $\leq 17.5$  kyr cal. BP) when strong bottom-current fluctuations occurred along the shelf-edge explaining the variations in sedimentation rates. The periods of changes in bottom-current velocities were associated with periods of rapid sea-level rises and/or high river discharges as both promoted freshwater input which increased the water column density gradient and the salinity contrast between the MAW and the LIW. This increased contrast in density gradient may explain instability after 8 kyr cal. BP by generating internal waves capable of remobilizing sediments.

- *What threat pose submarine landslides on the offshore and coastal infrastructures around the Gela Basin?*

The MTDs emplaced during the post-Glacial in the Gela Basin are rather small compared to other MTDs emplaced worldwide but are very representative of the average volume displaced in the Mediterranean Sea. Their tsunamigenic analysis show that even small submarine landslides ( $0.5 - 1.5 \text{ km}^3$ ) are capable of generating high-waves (up to 3 m) tsunamis and damage distant coastal cities. This demonstrates the geohazard potential and threat that represent submarine landslides in the Mediterranean Sea where numerous and small MTDs ( $\sim 1 \text{ km}^3$ ) were emplaced, and the importance to study them due to the growing economic interest of the seabed and the coastline urbanization, especially in the very densely populated Mediterranean region.

### 7.3 Perspectives

This research contributes to the study of submarine landslides and shows the potential for contourite deposits to contribute in the remobilization of important volumes of sediments capable of generating tsunamis. The quality and resolution of the data show how more spatially distributed cores along different water depths of the slope may help to highlight different bottom-current behaviours and therefore, better constrain the oceanographic dynamics influencing the margin. Additional sediment cores would be beneficial for the study of MTDs in the southern Gela Basin (SGBS and GDS) to improve the characterization of sediments mobilized in the SGBS and GDS, long sediment drilling cores reaching to the glide plane would confirm the existence of changes in grain size and lithological characteristics that make erosional surfaces potential weak layers. Additional coverage of high-resolution swath bathymetry data along the southern margin would give a better idea of the continuity of the southern contourite deposits where other MTDs are possibly emplaced and failed along similar weak layers. In the tsunami simulation of the submarine landslides, the tsunami heights may be underestimated along the coast of Malta due to the lack of high-resolution bathymetry for the computation. The presence of many little bays represents a potential hazard where the reflected waves may lead to the superposition of two identical waves with the same frequency and the same amplitudes moving in opposite direction and hence, forming higher waves heights (= constructive interference). Once included, the integration of high-resolution topographic data in the simulation would permit the analysis of the waves' propagation inland and refine the tsunami hazard zone for the coast of Malta and Sicily.

# Bibliography

---

Allard, J.L., Hughes, P.D., Woodward, J.C., 2021. Heinrich Stadial aridity forced Mediterranean-wide glacier retreat in the last cold stage. *Nat. Geosci.* 14, 197–205. <https://doi.org/10.1038/s41561-021-00703-6>

Alonso, B., Ercilla, G., García, M., Vazquez, J.-T., Juan, C., Casas, D., Estrada, F., d'Acremont, E., Gorini, C., El Moumni, B., Farran, M., 2014. Quaternary Mass-Transport Deposits on the North-Eastern Alboran Seamounts (SW Mediterranean Sea). pp. 561–570. <https://doi.org/10.1007/978-3-319-00972-8>

Alves, T.M., 2010. A 3-D morphometric analysis of erosional features in a contourite drift from offshore SE Brazil. *Geophys. J. Int.* 183, 1151–1164. <https://doi.org/10.1111/j.1365-246X.2010.04827.x>

Alves, T.M., 2015. Submarine slide blocks and associated soft-sediment deformation in deep-water basins: A review. *Mar. Pet. Geol.* 67, 262–285. <https://doi.org/10.1016/j.marpetgeo.2015.05.010>

Alves, T.M., Cartwright, J.A., 2010. The effect of mass-transport deposits on the younger slope morphology, offshore Brazil. *Mar. Pet. Geol.* 27, 2027–2036. <https://doi.org/10.1016/j.marpetgeo.2010.05.006>

Ambias, D., Gerber, T.P., De Mol, B., Urgeles, R., Garcia-Castellanos, D., Canals, M., Pratson, L.F., Robb, N., Canning, J., 2012. Survival of a submarine canyon during long-term outbuilding of a continental margin. *Geology* 40, 543–546. <https://doi.org/10.1130/G33178.1>

Amelio, M., Martorelli, E., 2008. Seismo-stratigraphic characters of paleocontourites along the Calabro-Tyrrhenian margin (Southern Tyrrhenian Sea). *Mar. Geol.* 252, 141–149. <https://doi.org/10.1016/j.margeo.2008.03.011>

Amos, J., 2020. Mapping quest edges past 20% of global ocean floor. *BBC News*, June 21<sup>st</sup>, 2020. <https://www.bbc.com/news/science-environment-57530394>

Antoncecchi, I., Ciccone, F., Dialuce, G., Grandi, S., Terlizze, F., Di Bucci, D., et al. (2020). Progetto SPOT – Sismicità Potenzialmente innesabile Offshore e Tsunami. Report integrato di fine progetto, ISBN 9788894366945 (in Italian). <https://doi.org/10.5281/zenodo.3732887>

Astraldi, M., P. Gasparini, G., Gervasio, L., Salusti, E., 2001. Dense Water Dynamics along the Strait of Sicily (Mediterranean Sea). *J. Phys. Oceanogr.* 31, 3457–3475. [https://doi.org/10.1175/1520-0485\(2001\)031<3457:DWDATS>2.0.CO;2](https://doi.org/10.1175/1520-0485(2001)031<3457:DWDATS>2.0.CO;2)

Badhani, S., Cattaneo, A., Collico, S., Urgeles, R., Dennielou, B., Leroux, E., Colin, F., Garziglia, S., Rabineau, M., Droz, L., 2020a. Integrated geophysical, sedimentological and geotechnical investigation of submarine landslides in the Gulf of Lions (Western Mediterranean). *Geol. Soc. London, Spec. Publ.* 500, 359–376. <https://doi.org/10.1144/SP500-2019-175>

Badhani, S., Cattaneo, A., Dennielou, B., Leroux, E., Colin, F., Thomas, Y., Jouet, G., Rabineau, M., Droz, L., 2020b. Morphology of retrogressive failures in the Eastern Rhone interfluvium during the

last glacial maximum (Gulf of Lions, Western Mediterranean). *Geomorphology* 351, 106894. <https://doi.org/10.1016/j.geomorph.2019.106894>

Bahr, A., Jiménez-Espejo, F.J., Kolasinac, N., Grunert, P., Hernández-Molina, F.J., Röhl, U., Voelker, A.H.L., Escutia, C., Stow, D.A.V., Hodell, D., Alvarez-Zarikian, C.A., 2014. Deciphering bottom current velocity and paleoclimate signals from contourite deposits in the Gulf of Cádiz during the last 140 kyr: An inorganic geochemical approach. *Geochemistry, Geophys. Geosystems* 15, 3145–3160. <https://doi.org/10.1002/2014GC005356>

Baltzer, A., Axel, E., Carine, R., Souron, A., Cordier, C., Clouet, H., Dubois, S., 2014. Geophysical exploration of an active pockmark field in the Bay of Concarneau, southern Brittany, and implications for resident suspension feeders. *Geo-Marine Lett.* 34, 215–230. <https://doi.org/10.1007/s00367-014-0368-0>

Barber, P.M., 1981. Messinian subaerial erosion of the proto-Nile Delta. *Mar. Geol.* 44, 253–272. [https://doi.org/10.1016/0025-3227\(81\)90053-0](https://doi.org/10.1016/0025-3227(81)90053-0)

Beaubouef, R.T., Abreu, V., 2010. MTCs of the Brazos-Trinity Slope System; Thoughts on the Sequence Stratigraphy of MTCs and Their Possible Roles in Shaping Hydrocarbon Traps, in: Mosher, D.C., Shipp, R.C., Moscardelli, L., Chaytor, J.D., Baxter, C.D.P., Lee, H.J., Urgeles, R. (Eds.), *Submarine Mass Movements and Their Consequences*. Springer Netherlands, Dordrecht, pp. 475–490. [https://doi.org/10.1007/978-90-481-3071-9\\_39](https://doi.org/10.1007/978-90-481-3071-9_39)

Bechle, A.J., Wu, C.H., 2014. The Lake Michigan meteotsunamis of 1954 revisited. *Nat. Hazards* 74, 155–177. <https://doi.org/10.1007/s11069-014-1193-5>

Beckers, A., Hubert-Ferrari, A., Beck, C., Papatheodorou, G., de Batist, M., Sakellariou, D., Tripsanas, E., Demoulin, A., 2018. Characteristics and frequency of large submarine landslides at the western tip of the Gulf of Corinth. *Nat. Hazards Earth Syst. Sci.* 18, 1411–1425. <https://doi.org/10.5194/nhess-18-1411-2018>

Bell, K., Carey, S., Nomikou, P., Sigurdsson, H., Sakellariou, D., 2013. Submarine evidence of a debris avalanche deposit on the eastern slope of Santorini volcano, Greece. *Tectonophysics* 597–598, 147–160. <https://doi.org/10.1016/j.tecto.2012.05.006>

Benjamin, J., Rovere, A., Fontana, A., Furlani, S., Vacchi, M., Inglis, R.H., Galili, E., Antonioli, F., Sivan, D., Miko, S., Mourtzas, N., Felja, I., Meredith-Williams, M., Goodman-Tchernov, B., Kolaiti, E., Anzidei, M., Gehrels, R., 2017. Late Quaternary sea-level changes and early human societies in the central and eastern Mediterranean Basin: An interdisciplinary review. *Quat. Int.* 449, 29–57. <https://doi.org/10.1016/j.quaint.2017.06.025>

Beta Analytic, 2021. <https://www.radiocarbon.com/ams-dating-forams.htm> (accessed 21 March 2021)

Bishop, W.F., Debono, G., 1996. The hydrocarbon geology of southern offshore Malta and surrounding regions. *J. Pet. Geol.* 19, 129–160. <https://doi.org/10.1111/j.17475457.1996.tb00422.x>

Bol'shakov, V.A., 2015. On the mechanism of the Middle Pleistocene Transition. *Stratigr. Geol. Correl.* 23, 536–550. <https://doi.org/10.1134/S0869593815050019>

Bouma, A.H., 1964. Notes on X-ray interpretation of marine sediments. *Mar. Geol.* 2, 278–309. [https://doi.org/10.1016/0025-3227\(64\)90045-3](https://doi.org/10.1016/0025-3227(64)90045-3)

Bouma, A.H., 2000. Coarse-grained and fine-grained turbidite systems as end member models: applicability and dangers. *Mar. Pet. Geol.* 17, 137–143. [https://doi.org/10.1016/S0264-8172\(99\)00020-3](https://doi.org/10.1016/S0264-8172(99)00020-3)

Breitzke, M., Wiles, E., Krockner, R., Watkeys, M.K., Jokat, W., 2017. Seafloor morphology in the Mozambique Channel: evidence for long-term persistent bottom-current flow and deep-reaching eddy activity. *Mar. Geophys. Res.* 38, 241–269. <https://doi.org/10.1007/s11001-017-9322-7>

Broecker, W., Mix, A., Andree, M., Oeschger, H., 1984. Radiocarbon measurements on coexisting benthic and planktic foraminifera shells: potential for reconstructing ocean ventilation times over the past 20 000 years. *Nucl. Instruments Methods Phys. Res. Sect. B Beam Interact. with Mater. Atoms* 5, 331–339. [https://doi.org/10.1016/0168-583X\(84\)90538-X](https://doi.org/10.1016/0168-583X(84)90538-X)

Bryn, P., Berg, K., Forsberg, C.F., Solheim, A., Kvalstad, T.J., 2005. Explaining the Storegga Slide. *Mar. Pet. Geol.* 22, 11–19. <https://doi.org/10.1016/j.marpetgeo.2004.12.003>

Bugge, T., Befring, S., Belderson, R.H., Eidvin, T., Jansen, E., Kenyon, N.H., Holtedahl, H., Sejrup, H.P., 1987. A giant three-stage submarine slide off Norway. *Geo-Marine Lett.* 7, 191–198. <https://doi.org/10.1007/BF02242771>

Bull, S., Cartwright, J., Huuse, M., 2009. A review of kinematic indicators from mass-transport complexes using 3D seismic data. *Mar. Pet. Geol.* 26, 1132–1151. <https://doi.org/10.1016/j.marpetgeo.2008.09.011>

Byrne, R. H., Duxbury, A.C., Mackenzie, F. T., 2020. Seawater. *Encyclopedia Britannica*, <https://www.britannica.com/science/seawater>. Accessed 27 February 2021.

Cacho, I., Grimalt, J. O., Pelejero, C., Canals, M., Sierro, F. J., Flores, J. A., Shackleton, N. J., 1999. Dansgaard-Oeschger and Heinrich event imprints in the Alboran Sea paleotemperatures. *Paleoceanography* 14, 698-705. <https://doi.org/10.1029/1999PA900044>

Cacho, I., Grimalt, J.O., Canals, M., Saffi, L., Shackleton, N.J., Schönfeld, J., Zahn, R., 2001. Variability of the western Mediterranean Sea surface temperature during the last 25,000 years and its connection with the Northern Hemisphere climatic changes. *Paleoceanography* 16, 40–52. <https://doi.org/10.1029/2000PA000502>

Camargo, J.M.R., Silva, M.V.B., Ferreira Júnior, A. V, Araújo, T.C.M., 2019. Marine Geohazards: A Bibliometric-Based Review. *Geosciences* 9. <https://doi.org/10.3390/geosciences9020100>

Camuera, J., Jiménez-Moreno, G., Ramos-Román, M.J., García-Alix, A., Jiménez-Espejo, F.J., Toney, J.L., Anderson, R.S., 2021. Chronological control and centennial-scale climatic subdivisions of the Last Glacial Termination in the western Mediterranean region. *Quat. Sci. Rev.* 255, 106814. <https://doi.org/10.1016/j.quascirev.2021.106814>

Capotondi, L., Maria Borsetti, A., Morigi, C., 1999. Foraminiferal ecozones, a high resolution proxy for the late Quaternary biochronology in the central Mediterranean Sea. *Mar. Geol.* 153, 253–274. [https://doi.org/10.1016/S0025-3227\(98\)00079-6](https://doi.org/10.1016/S0025-3227(98)00079-6)

Capponi, M., Glavich, E., Sampietro, D., 2020. Map of the Plio-Quaternary sediment depths in the Mediterranean Sea. *Boll. Geofis. Teor. Appl.* 61, 421-432. <https://doi.org/10.4430/bgta0320>

Carter, L., Milliman, J.D., Talling, P.J., Gavey, R., Wynn, R.B., 2012. Near-synchronous and delayed initiation of long run-out submarine sediment flows from a record-breaking river flood, offshore Taiwan. *Geophys. Res. Lett.* 39. <https://doi.org/10.1029/2012GL051172>

Casalbore, D., Bosman, A., Casas, D., Chiocci, F., Martorelli, E., Ridente, D., 2019. Morphological Variability of Submarine Mass Movements in the Tectonically–Controlled Calabro–Tyrrhenian Continental Margin (Southern Italy). *Geosciences* 9, 43. <https://doi.org/10.3390/geosciences9010043>

Casas, D., Chiocci, F., Casalbore, D., Ercilla, G., de Urbina, J.O., 2016. Magnitude-frequency distribution of submarine landslides in the Gioia Basin (southern Tyrrhenian Sea). *Geo-Marine Lett.* 36, 405–414. <https://doi.org/10.1007/s00367-016-0458-2>

Cattaneo, A., Jouet, G., Charrier, S., Théreau, E., Riboulot, V., 2014. Chapter 39 Submarine Landslides and Contourite Drifts Along the Pianosa Ridge (Corsica Trough, Mediterranean Sea), in: Krastel, S., Behrmann, J.-H., Völker, D., Stipp, M., Berndt, C., Urgeles, R., Chaytor, J., Huhn, K., Strasser, M., Harbitz, C.B. (Eds.), *Submarine Mass Movements and Their Consequences: 6th International Symposium*, Springer International Publishing, Cham, pp. 435–445. [https://doi.org/10.1007/978-3-319-00972-8\\_39](https://doi.org/10.1007/978-3-319-00972-8_39)

Cattaneo, A., Miramontes, E., Samalens, K., Garreau, P., Caillaud, M., Marsset, B., Corradi, N., Migeon, S., 2017. Contourite identification along Italian margins: The case of the Portofino drift (Ligurian Sea). *Mar. Pet. Geol.* 87, 137–147. <https://doi.org/10.1016/j.marpetgeo.2017.03.026>

Cattaneo, A., Badhani, S., Caradonna, C., Bellucci, M., Leroux, E., Babonneau, N., Garziglia, S., Poort, J., Akhmanov, G.G., Bayon, G., Dennielou, B., Jouet, G., Migeon, S., Rabineau, M., Droz, L., Clare, M., 2020. The Last Glacial Maximum Balearic Abyssal Plain megabed revisited. *Geol. Soc. London, Spec. Publ.* 500, 341–357. <https://doi.org/10.1144/SP500-2019-188>

Ceramicola, S., Tinti, S., Zaniboni, F., Praeg, D., Planinsek, P., Pagnoni, G., Forlin, E., 2014. Reconstruction and Tsunami Modeling of a Submarine Landslide on the Ionian Margin of Calabria (Mediterranean Sea), in: Sassa, K., Canuti, P., Yin, Y. (Eds.), *Landslide Science for a Safer Geoenvironment*. Springer International Publishing, Cham, pp. 557–562. [https://doi.org/10.1007/978-3-319-04996-0\\_85](https://doi.org/10.1007/978-3-319-04996-0_85)

Chalk, T.B., Capron, E., Drew, M., Panagiotopoulos, K., 2017. Interglacials of the 41 ka-world and the Mid-Pleistocene Transition. *Past Global Changes Magazine* 25, 155. <https://doi.org/10.22498/pages.25.3.155>

Clare, M., Chaytor, J., Dabson, O., Gamboa, D., Georgiopoulou, A., Eady, H., Hunt, J., Jackson, C., Katz, O., Krastel, S., León, R., Micallef, A., Moernaut, J., Moriconi, R., Moscardelli, L., Mueller, C., Normandeau, A., Patacci, M., Steventon, M., Urlaub, M., Völker, D., Wood, L., Jobe, Z.,

2019. A consistent global approach for the morphometric characterization of subaqueous landslides. *Geol. Soc. London, Spec. Publ.* 477, 455 LP-477. <https://doi.org/10.1144/SP477.15>

Clark, P.U., Archer, D., Pollard, D., Blum, J.D., Rial, J.A., Brovkin, V., Mix, A.C., Pisias, N.G., Roy, M., 2006. The middle Pleistocene transition: characteristics, mechanisms, and implications for long-term changes in atmospheric pCO<sub>2</sub>. *Quat. Sci. Rev.* 25, 3150–3184. <https://doi.org/10.1016/j.quascirev.2006.07.008>

Clarke, J.E.H., 2012. Optimal Use of Multibeam Technology in the Study of Shelf Morphodynamics. *Sediments, Morphol. Sediment. Process. Cont. Shelves*, Wiley Online Books. <https://doi.org/10.1002/9781118311172.ch1>

Clauzon, G., 1978. The Messinian Var canyon (Provence, southern France) — Paleogeographic implications. *Mar. Geol.* 27, 231–246. [https://doi.org/10.1016/0025-3227\(78\)90033-6](https://doi.org/10.1016/0025-3227(78)90033-6)

Colantoni, P., Del Monte, M., Gallignani, P., Zarudzki, E.F.K., 1975. Il Banco Graham: un vulcano recente del Canale di Sicilia. *Giorn. Geol.* 40, 141–162.

Coleman, J.M., Walker, H.J., Grabau, W.E., 1998. Sediment instability in the Mississippi River Delta. *J. Coast. Res.* 14, 872–881.

Colman, S.M., Baucom, P.C., Bratton, J.F., Cronin, T.M., McGeehin, J.P., Willard, D., Zimmerman, A.R., Vogt, P.R., 2002. Radiocarbon Dating, Chronologic Framework, and Changes in Accumulation Rates of Holocene Estuarine Sediments from Chesapeake Bay. *Quat. Res.* 57, 58–70. <https://doi.org/10.1006/qres.2001.2285>

Culver, S., Camp, R., Walsh, J.P., Hayward, B., Corbett, D., Alexander Jr, C., 2012. Distribution of Foraminifera of the Poverty Continental Margin, New Zealand: Implications for Sediment Transport. *J. Foraminifer. Res.* 42, 305–326. <https://doi.org/10.2113/gsjfr.42.4.305>

Dalla Valle, G., Gamberi, F., Rocchini, P., Minisini, D., Errera, A., Baglioni, L., Trincardi, F., 2013. 3D seismic geomorphology of mass transport complexes in a foredeep basin: Examples from the Pleistocene of the Central Adriatic Basin (Mediterranean Sea). *Sediment. Geol.* 294, 127–141. <https://doi.org/10.1016/j.sedgeo.2013.05.012>

Dalla Valle, G., Campiani, E., Foglini, F., Gamberi, F., Trincardi, F., 2014. Mass Transport Complexes from Contourite and Shelf-Edge Deposits Along the South-Western Adriatic Margin (Italy), in: *Advances in Natural and Technological Hazards Research*. pp. 447–457. [https://doi.org/10.1007/978-3-319-00972-8\\_40](https://doi.org/10.1007/978-3-319-00972-8_40)

Dan, G., Sultan, N., Savoye, B., 2007. The 1979 Nice harbour catastrophe revisited: Trigger mechanism inferred from geotechnical measurements and numerical modelling. *Mar. Geol.* 245, 40–64. <https://doi.org/10.1016/j.margeo.2007.06.011>

Dannowski, A., Kopp, H., Klingelhoefer, F., Klaeschen, D., Gutscher, M.-A., Krabbenhoft, A., Dellong, D., Rovere, M., Graindorge, D., Papenberg, C., Klauke, I., 2019. Ionian Abyssal Plain: a window into the Tethys oceanic lithosphere. *Solid Earth* 10, 447–462. <https://doi.org/10.5194/se-10-447-2019>

- Davies, R.J., Clark, I.R., 2006. Submarine slope failure primed and triggered by silica and its diagenesis. *Basin Res.* 18, 339–350. <https://doi.org/10.1111/j.1365-2117.2006.00297.x>
- Del Bianco, F., Gasperini, L., Giglio, F., Bortoluzzi, G., Kljajic, Z., Ravaioli, M., 2014. Seafloor morphology of the Montenegro/N. Albania Continental Margin (Adriatic Sea—Central Mediterranean). *Geomorphology* 226, 202–216. <https://doi.org/10.1016/j.geomorph.2014.08.006>
- Dellong, D., Klingelhoefer, F., Kopp, H., Graindorge, D., Margheriti, L., Moretti, M., Murphy, S., Gutscher, M.-A., 2018. Crustal Structure of the Ionian Basin and Eastern Sicily Margin: Results From a Wide-Angle Seismic Survey. *J. Geophys. Res. Solid Earth* 123, 2090–2114. <https://doi.org/10.1002/2017JB015312>
- Desprat, S., Combourieu-Nebout, N., Essallami, L., Sicre, M.A., Dormoy, I., Peyron, O., Siani, G., Bout Roumazeilles, V., Turon, J.L., 2013. Deglacial and holocene vegetation and climatic changes in the southern central Mediterranean from a direct land-sea correlation. *Clim. Past* 9, 767–787. <https://doi.org/10.5194/cp-9-767-2013>
- Dey, R., Hawlader, B.C., Phillips, R., Soga, K., 2016. Numerical modelling of submarine landslides with sensitive clay layers. *Géotechnique* 66, 454–468. <https://doi.org/10.1680/jgeot.15.P.111>
- Dilek, Y., 2006. Collision tectonics of the Mediterranean region: Causes and consequences, in: Dilek, Y., Pavlides, S. (Eds.), *Postcollisional Tectonics and Magmatism in the Mediterranean Region and Asia*. Geological Society of America 409, pp. 1-13. [https://doi.org/10.1130/2006.2409\(01\)](https://doi.org/10.1130/2006.2409(01))
- Dingle, R.V., 1977. The anatomy of a large submarine slump on a sheared continental margin (SE Africa). *J. Geol. Soc. London.* 134, 293–310. <https://doi.org/10.1144/gsjgs.134.3.0293>
- Dingle, R.V., 1980. Large allochthonous sediment masses and their role in the construction of the continental slope and rise off southwestern Africa. *Mar. Geol.* 37, 333–354. [https://doi.org/10.1016/0025-3227\(80\)90109-7](https://doi.org/10.1016/0025-3227(80)90109-7)
- Donnarumma, A., Revellino, P., Grelle, G., Guadagno, F.M., 2013. Slope Angle as Indicator Parameter of Landslide Susceptibility in a Geologically Complex Area, in: Margottini, C., Canuti, P., Sassa, K. (Eds.), *Landslide Science and Practice: Volume 1: Landslide Inventory and Susceptibility and Hazard Zoning*. Springer Berlin Heidelberg, Berlin, Heidelberg, pp. 425–433. [https://doi.org/10.1007/978-3-642-31325-7\\_56](https://doi.org/10.1007/978-3-642-31325-7_56)
- Dott, R., 1963. Dynamics of Subaqueous Gravity Depositional Processes. *Am. Assoc. Pet. Geol. Bull.* 47, 104–128.
- Driscoll, N., Weissel, J., Goff, J., 2000. Potential for large-scale submarine slope failure and tsunami generation along the U.S. mid-Atlantic coast. *Geology* 28, 407–410. [https://doi.org/10.1130/0091-7613\(2000\)028<0407:PFLSSS>2.3.CO;2](https://doi.org/10.1130/0091-7613(2000)028<0407:PFLSSS>2.3.CO;2)
- Droghei, R., Falcini, F., Casalbore, D., Martorelli, E., Mosetti, R., Sannino, G., Santoleri, R., Chiocci, F.L., 2016. The role of Internal Solitary Waves on deep-water sedimentary processes: the case of up-slope migrating sediment waves off the Messina Strait. *Sci. Rep.* 6, 36376. <https://doi.org/10.1038/srep36376>

Ducassou, E., Migeon, S., Capotondi, L., Mascle, J., 2013. Run-out distance and erosion of debris-flows in the Nile deep-sea fan system: Evidence from lithofacies and micropalaeontological analyses. *Mar. Pet. Geol.* 39, 102–123. <https://doi.org/10.1016/j.marpetgeo.2012.09.006>

Ducrocq, V., Drobinski, P., Gualdi, S., Raimbault, P., 2016. The water cycle in the Mediterranean, in: Moatti, J., Thiébaud, S. (Eds.), *The Mediterranean Region under Climate Change: A Scientific Update*. IRD Éditions. pp. 73–81. <https://doi.org/10.4000/books.irdeditions.23073>

Embley, R., Jacobi, R., 1977. Distribution and morphology of large submarine sediment slides and slumps on Atlantic continental margins. *Mar. Georesources Geotechnol.* 2, 205–228. <https://doi.org/10.1080/10641197709379780>

Emeis, K.-C., Weissert, H., 2009. Tethyan–Mediterranean organic carbon-rich sediments from Mesozoic black shales to sapropels. *Sedimentology* 56, 247–266. <https://doi.org/10.1111/j.1365-3091.2008.01026.x>

Ercilla, G., Baraza, J., Alonso, B., Estrada, F., Casas, D., Farrán, M., 2002. The Ceuta Drift, Alboran Sea, southwestern Mediterranean. *Geol. Soc. London, Mem.* 22, 155 LP-170. <https://doi.org/10.1144/GSL.MEM.2002.022.01.12>

Ercilla, G., Juan, C., Hernández-Molina, F.J., Bruno, M., Estrada, F., Alonso, B., Casas, D., Farran, M. I., Llave, E., García, M., Vázquez, J.T., D’Acremont, E., Gorini, C., Palomino, D., Valencia, J., Moumni, B. El, Ammar, A., 2016. Significance of bottom currents in deep-sea morphodynamics: An example from the Alboran Sea. *Mar. Geol.* 378, 157–170. <https://doi.org/10.1016/j.margeo.2015.09.007>

Faccenna, C., Becker, T.W., Lucente, F.P., Jolivet, L., Rossetti, F., 2001. History of subduction and back arc extension in the Central Mediterranean. *Geophys. J. Int.* 145, 809–820. <https://doi.org/10.1046/j.0956-540x.2001.01435.x>

Faccenna, C., Molin, P., Orecchio, B., Olivetti, V., Bellier, O., Funiciello, F., Minelli, L., Piromallo, C., Billi, A., 2011. Topography of the Calabria subduction zone (southern Italy): Clues for the origin of Mt. Etna. *Tectonics* 30, 1–20. <https://doi.org/10.1029/2010TC002694>

Faccenna, C., Becker, T.W., Auer, L., Billi, A., Boschi, L., Brun, J.P., Capitanio, F.A., Funiciello, F., Horvath, F., Jolivet, L., Piromallo, C., Royden, L., Rossetti, F., Serpelloni, E., 2014. Mantle dynamics in the Mediterranean. *Rev. Geophys.* 52, 283–332. <https://doi.org/10.1002/2013RG000444>

Faugères, J.-C., Stow, D.A. V, 1993a. Bottom-current-controlled sedimentation: a synthesis of the contourite problem. *Sediment. Geol.* 82, 287–297. [https://doi.org/10.1016/0037-0738\(93\)90127-Q](https://doi.org/10.1016/0037-0738(93)90127-Q)

Faugères, J.C., Mézerais, M.L., Stow, D.A. V, 1993b. Contourite drift types and their distribution in the North and South Atlantic Ocean basins. *Sediment. Geol.* 82, 189–203. [https://doi.org/10.1016/0037-0738\(93\)90121-K](https://doi.org/10.1016/0037-0738(93)90121-K)

Felix, M., Peakall, J., 2006. Transformation of debris flows into turbidity currents: mechanisms inferred from laboratory experiments. *Sedimentology* 53, 107–123. <https://doi.org/10.1111/j.1365-3091.2005.00757.x>

Fentimen, R., Lim, A., Rüggeberg, A., Wheeler, A.J., Van Rooij, D., Foubert, A., 2020. Impact of bottom water currents on benthic foraminiferal assemblages in a cold-water coral environment: The Moira Mounds (NE Atlantic). *Mar. Micropaleontol.* 154, 101799. <https://doi.org/10.1016/j.marmicro.2019.101799>

Fernández, M., Torne, M., Vergés, J., Casciello, E., Macchiavelli, C., 2019. Evidence of Segmentation in the Iberia–Africa Plate Boundary: A Jurassic Heritage? *Geosciences* 9, 343. <https://doi.org/10.3390/geosciences9080343>

Festa, A., Ogata, K., Pini, G.A., Dilek, Y., Alonso, J.L., 2016. Origin and significance of olistostromes in the evolution of orogenic belts: A global synthesis. *Gondwana Res.* 39, 180–203. <https://doi.org/10.1016/j.gr.2016.08.002>

Fine, I. V., Rabinovich, A.B., Bornhold, B.D., Thomson, R.E., Kulikov, E.A., 2005. The Grand Banks landslide-generated tsunami of November 18, 1929: preliminary analysis and numerical modeling. *Mar. Geol.* 215, 45–57. <https://doi.org/10.1016/j.margeo.2004.11.007>

Finetti, I., 1984. Geophysical study of the sicily channel rift zone. *Boll. Geofis. Teor. Appl.* 26, 3–28.

Fisher, R. V., 1983. Flow transformations in sediment gravity flows. *Geology* 11, 273. [https://doi.org/10.1130/0091-7613\(1983\)11<273:FTISGF>2.0.CO;2](https://doi.org/10.1130/0091-7613(1983)11<273:FTISGF>2.0.CO;2)

Flemings, P.B., Long, H., Dugan, B., Germaine, J., John, C.M., Behrmann, J.H., Sawyer, D., 2008. Pore pressure penetrometers document high overpressure near the seafloor where multiple submarine landslides have occurred on the continental slope, offshore Louisiana, Gulf of Mexico. *Earth Planet. Sci. Lett.* 269, 309–325. <https://doi.org/10.1016/j.epsl.2007.12.005>

Frey Martinez, J., Cartwright, J., Hall, B., 2005. 3D seismic interpretation of slump complexes: examples from the continental margin of Israel. *Basin Res.* 17, 83–108. <https://doi.org/10.1111/j.1365-2117.2005.00255.x>

Frey-Martinez, J., Cartwright, J., James, D., 2006. Frontally confined versus frontally emergent submarine landslides: A 3D seismic characterisation. *Mar. Pet. Geol.* 23, 585–604. <https://doi.org/10.1016/j.marpetgeo.2006.04.002>

Frizon de Lamotte, D., Raulin, C., Mouchot, N., Wrobel-Daveau, J.-C., Blanpied, C., Ringenbach, J.-C., 2011. The southernmost margin of the Tethys realm during the Mesozoic and Cenozoic: Initial geometry and timing of the inversion processes. *Tectonics* 30. <https://doi.org/10.1029/2010TC002691>

Froude, M.J., Petley, D.N., 2018. Global fatal landslide occurrence from 2004 to 2016. *Nat. Hazards Earth Syst. Sci.* 18, 2161–2181. <https://doi.org/10.5194/nhess-18-2161-2018>

Gamberi, F., Rovere, M., Marani, M., 2011. Mass-transport complex evolution in a tectonically active margin (Gioia Basin, Southeastern Tyrrhenian Sea). *Mar. Geol.* 279, 98–110. <https://doi.org/10.1016/j.margeo.2010.10.015>

Gamberi, F., Dalla Valle, G., Foglini, F., Rovere, M., Trincardi, F., 2019. Submarine Landslides on the Seafloor, in: Ogata, K., Festa, A., Pini, G.A. (Eds.), Submarine Landslides, Geophysical Monograph Series. pp. 339–356. <https://doi.org/10.1002/9781119500513.ch20>

Garcia-Castellanos, D., 2011a. The Messinian Salinity Crisis (1/3) - 1-km salt layer over most of the Mediterranean. <http://retosterricolas.blogspot.com/2011/10/messinian-salinity-crisis-13-salt-all.html>. Accessed on 04/03/2021.

Garcia-Castellanos, D., Villaseñor, A., 2011b. Messinian salinity crisis regulated by competing tectonics and erosion at the Gibraltar arc. *Nature* 480, 359–363. <https://doi.org/10.1038/nature10651>

Garcia-Castellanos, D., Estrada, F., Jiménez-Munt, I., Gorini, C., Fernández, M., Vergés, J., De Vicente, R., 2009. Catastrophic flood of the Mediterranean after the Messinian salinity crisis. *Nature* 462, 778–781. <https://doi:10.1038/nature08555>

Garcia-Castellanos, D., Micallef, A., Estrada, F., Camerlenghi, A., Ercilla, G., Perriáñez, R., Abril, J.M., 2020. The Zanclean megaflood of the Mediterranean – Searching for independent evidence. *Earth-Science Rev.* 201, 103061. <https://doi.org/10.1016/j.earscirev.2019.103061>

Garfunkel, Z., 1984. Large-scale submarine rotational slumps and growth faults in the Eastern Mediterranean. *Mar. Geol.* 55, 305–324. [https://doi.org/10.1016/0025-3227\(84\)90074-4](https://doi.org/10.1016/0025-3227(84)90074-4)

Gargani, J., Rigollet, C., Scarselli, S., 2010. Isostatic response and geomorphological evolution of the Nile valley during the Messinian salinity crisis. *Bull. la Société Géologique Fr.* 181, 19–26. <https://doi.org/10.2113/gssgfbull.181.1.19>

Gatter, R., Clare, M.A., Hunt, J.E., Watts, M., Madhusudhan, B.N., Talling, P.J., Huhn, K., 2020. A multi-disciplinary investigation of the AFEN Slide: the relationship between contourites and submarine landslides. *Geol. Soc. London, Spec. Publ.* 500, 173–193. <https://doi.org/10.1144/SP500-2019-184>

Gee, M.J.R., Masson, D.G., Watts, A.B., Allen, P.A., 1999. The Saharan debris flow: an insight into the mechanics of long runout submarine debris flows. *Sedimentology* 46, 317–335. <https://doi.org/10.1046/j.1365-3091.1999.00215.x>

Gee, M.J.R., Uy, H.S., Warren, J., Morley, C.K., Lambiase, J.J., 2007. The Brunei slide: A giant submarine landslide on the North West Borneo Margin revealed by 3D seismic data. *Mar. Geol.* 246, 9–23. <https://doi.org/10.1016/j.margeo.2007.07.009>

Geertsema, M., Schwab, J.W., Blais-Stevens, A., Sakals, M.E., 2009. Landslides impacting linear infrastructure in west central British Columbia. *Nat. Hazards* 48, 59–72. <https://doi.org/10.1007/s11069-008-9248-0>

Genesseeux, M., Burollet, P., Winnock, E., 1998. Thickness of the Plio-Quaternary sediments (IBCM-PQ). *Boll. Geofis. Teor. Appl.* 39, 243-284.

Georgiopoulou, A., Krastel, S., Finch, N., Zehn, K., McCarron, S., Huvenne, V.A.I., Haughton, P.D.W., Shannon, P.M., 2019. On the Timing and Nature of the Multiple Phases of Slope Instability on Eastern Rockall Bank, Northeast Atlantic. *Geochemistry, Geophys. Geosystems* 20, 594–613. <https://doi.org/10.1029/2018GC007674>

Geostar Survey 2009. High Resolution Seismic Surveys, <http://geostar-surveys.com/methodology - High Resolution Seismic surveys.html>

Gerber, T.P., Pratson, L.F., Kuehl, S., Walsh, J.P., Alexander, C., Palmer, A., 2010. The influence of sea level and tectonics on Late Pleistocene through Holocene sediment storage along the high-sediment supply Waipaoa continental shelf. *Mar. Geol.* 270, 139–159. <https://doi.org/10.1016/j.margeo.2009.10.002>

Ghielmi, M., Amore, M.R., Bolla, E.M., Carubelli, P., Knezaurek, G., Serraino, C., 2012. The Pliocene to pleistocene succession of the hyblean foredeep (sicily, Italy). October 23-26, 2011 AAPG (Am. Assoc. Pet. Geol.) Internat. Conf. Exhib. Milan, Italy. [http://www.searchanddiscovery.com/documents/2012/30220ghielmi/ndx\\_ghie lmi.pdf](http://www.searchanddiscovery.com/documents/2012/30220ghielmi/ndx_ghie lmi.pdf)

Glade, T., Anderson, M.G., Crozier, M.J., 2005. *Landslide Hazard and Risk*. West Sussex, UK: John Wiley & Sons.

Govers, R., 2009. Choking the Mediterranean to dehydration: The Messinian salinity crisis. *Geology* 37, 167–170. <https://doi.org/10.1130/G25141A.1>

Govin, A., Holzwarth, U., Heslop, D., Ford Keeling, L., Zabel, M., Mulitza, S., Collins, J.A., Chiessi, C.M., 2012. Distribution of major elements in Atlantic surface sediments (36°N–49°S): Imprint of terrigenous input and continental weathering. *Geochem. Geophys. Geosy.* 13, 1–23. <https://doi.org/10.1029/2011GC003785>

Grant, K.M., Grimm, R., Mikolajewicz, U., Marino, G., Ziegler, M., Rohling, E.J., 2016. The timing of Mediterranean sapropel deposition relative to insolation, sea-level and African monsoon changes. *Quat. Sci. Rev.* 140, 125–141. <https://doi.org/10.1016/j.quascirev.2016.03.026>

Greene, H.G., Maher, N.M., Paull, C.K., 2002. Physiography of the Monterey Bay National Marine Sanctuary and implications about continental margin development. *Mar. Geol.* 181, 55-82. [https://doi.org/10.1016/S0025-3227\(01\)00261-4](https://doi.org/10.1016/S0025-3227(01)00261-4)

Greene, H.G., Murai, L.Y., Watts, P., Maher, N.A., Fisher, M.A., Paull, C.E., Eichhubl, P., 2006. Submarine landslides in the Santa Barbara Channel as potential tsunami sources. *Nat. Hazards Earth Syst. Sci.* 6, 63–88. <https://doi.org/10.5194/nhess-6-63-2006>

Haflidason, H., Lien, R., Sejrup, H.P., Forsberg, C.F., Bryn, P., 2005. The dating and morphometry of the Storegga Slide. *Mar. Pet. Geol.* 22, 123–136. <https://doi.org/10.1016/j.marpetgeo.2004.10.008>

Hage, S., Cartigny, M.J.B., Sumner, E.J., Clare, M.A., Hughes Clarke, J.E., Talling, P.J., Lintern, D.G., Simmons, S.M., Silva Jacinto, R., Vellinga, A.J., Allin, J.R., Azpiroz-Zabala, M., Gales, J.A., Hizzett, J.L., Hunt, J.E., Mozzato, A., Parsons, D.R., Pope, E.L., Stacey, C.D., Symons, W.O., Vardy, M.E., Watts, C., 2019. Direct Monitoring Reveals Initiation of Turbidity Currents From Extremely Dilute River Plumes. *Geophys. Res. Lett.* 46, 11310–11320. <https://doi.org/10.1029/2019GL084526>

Hampton, M.A., Lee, H.J., Locat, J., 1996. Submarine landslides. *Rev. Geophys.* 34, 33–59. <https://doi.org/10.1029/95RG03287>

- Haq, B., Gorini, C., Baur, J., Moneron, J., Rubino, J.-L., 2020. Deep Mediterranean's Messinian evaporite giant: How much salt? *Glob. Planet. Change* 184, 103052. <https://doi.org/10.1016/j.gloplacha.2019.103052>
- Harbitz, C., Løvholt, F., Pedersen, G., Masson, D., 2006. Mechanisms of tsunami generation by submarine landslides: A short review. *Nor. J. Geol.* 86, 255–264. <http://nora.nerc.ac.uk/id/eprint/142982>
- Harbitz, C.B., Løvholt, F., Bungum, H., 2014. Submarine landslide tsunamis: how extreme and how likely? *Nat. Hazards* 72, 1341–1374. <https://doi.org/10.1007/s11069-013-0681-3>
- Harders, R., Kutterolf, S., Hensen, C., Moerz, T., Brueckmann, W., 2010. Tephra layers: A controlling factor on submarine translational sliding? *Geochemistry, Geophys. Geosystems* 11, Q05S23. <https://doi.org/10.1029/2009GC002844>
- Harders, R., Ranero, C.R., Weinrebe, W., Behrmann, J.H., 2011. Submarine slope failures along the convergent continental margin of the Middle America Trench. *Geochemistry, Geophys. Geosystems* 12, Q05S32. <https://doi.org/10.1029/2010GC003401>
- Harrison, J. V., Falcon, N.L., 1938. An Ancient Landslip at Saidmarreh in Southwestern Iran. *J. Geol.* 46, 296–309. <https://doi.org/10.1086/624654>
- Haughton, P., Davis, C., McCaffrey, W., Barker, S., 2009. Hybrid sediment gravity flow deposits – Classification, origin and significance. *Mar. Pet. Geol.* 26, 1900–1918. <https://doi.org/10.1016/j.marpetgeo.2009.02.012>
- Heezen, B.C., Hollister, C., 1964. Deep-sea current evidence from abyssal sediments. *Mar. Geol.* 1, 141–174. [https://doi.org/https://doi.org/10.1016/0025-3227\(64\)90012-X](https://doi.org/https://doi.org/10.1016/0025-3227(64)90012-X)
- Heffernan, O., 2019. Seabed mining is coming - bringing mineral riches and fears of epic extinctions. *Nature* 571, 465–468. <https://doi.org/10.1038/d41586-019-02242-y>
- Heijnen, M.S., Clare, M.A., Cartigny, M.J.B., Talling, P.J., Hage, S., Lintern, D.G., Stacey, C., Parsons, D.R., Simmons, S.M., Chen, Y., Sumner, E.J., Dix, J.K., Hughes Clarke, J.E., 2020. Rapidly-migrating and internally-generated knickpoints can control submarine channel evolution. *Nat. Commun.* 11, 3129. <https://doi.org/10.1038/s41467-020-16861-x>
- Henkel, S., Strasser, M., Schwenk, T., Hanebuth, T.J.J., Hüsener, J., Arnold, G.L., Winkelmann, D., Formolo, M., Tomasini, J., Krastel, S., Kasten, S., 2011. An interdisciplinary investigation of a recent submarine mass transport deposit at the continental margin off Uruguay. *Geochemistry, Geophys. Geosystems* 12. <https://doi.org/10.1029/2011GC003669>
- Hernández-Molina, J., Llave, E., Somoza, L., Fernández-Puga, M.C., Maestro, A., León, R., Medialdea, T., Barnolas, A., García, M., del Río, V.D., Fernández-Salas, L.M., Vázquez, J.T., Lobo, F., Dias, J.M.A., Rodero, J., Gardner, J., 2003. Looking for clues to paleoceanographic imprints: A diagnosis of the Gulf of Cadiz contourite depositional systems. *Geology* 31, 19–22. [https://doi.org/10.1130/0091-7613\(2003\)031<0019:LFCTPI>2.0.CO;2](https://doi.org/10.1130/0091-7613(2003)031<0019:LFCTPI>2.0.CO;2)
- Hernández-Molina, F.J., Llave, E., Preu, B., Ercilla, G., Fontan, A., Bruno, M., Serra, N., Gomiz, J.J., Brackenridge, R.E., Sierro, F.J., Stow, D.A. V., García, M., Juan, C., Sandoval, N., Arnaiz, A., 2014. Contourite processes associated with the Mediterranean Outflow Water after its exit from the

Strait of Gibraltar: Global and conceptual implications. *Geology* 42, 227–230. <https://doi.org/10.1130/G35083.1>

Hernández-Molina, F.J., Sierro, F.J., Llave, E., Roque, C., Stow, D.A. V., Williams, T., Lofi, J., Van der Schee, M., Arnáiz, A., Ledesma, S., Rosales, C., Rodríguez-Tovar, F.J., Pardo-Igúzquiza, E., Brackenridge, R.E., 2016a. Evolution of the gulf of Cadiz margin and southwest Portugal contourite depositional system: Tectonic, sedimentary and paleoceanographic implications from IODP expedition 339. *Mar. Geol.* 377, 7–39. <https://doi.org/10.1016/j.margeo.2015.09.013>

Hernández-Molina, F.J., Soto, M., Piola, A.R., Tomasini, J., Preu, B., Thompson, P., Badalini, G., Creaser, A., Violante, R.A., Morales, E., Paterlini, M., De Santa Ana, H., 2016b. A contourite depositional system along the Uruguayan continental margin: Sedimentary, oceanographic and paleoceanographic implications. *Mar. Geol.* 378, 333–349. <https://doi.org/10.1016/j.margeo.2015.10.008>

Hill, P.R., Moran, K.M., Blasco, S.M., 1982. Creep deformation of slope sediments in the Canadian Beaufort Sea. *Geo-Marine Lett.* 2, 163. <https://doi.org/10.1007/BF02462758>

Hooper, J.R., Suhayda, J.N., 2005. Hurricane Induced Seafloor Failures in the Mississippi Delta: 2005 Offshore Hurricane Readiness and Recovery Conference, American Petroleum Institute, Houston, Texas, July 26–27, 2005. <http://www.bsee.gov/Research-and-Training/Technology-Assessment-and-Research/tarprojects/500-599/559/559AC2.aspx>

Hopkins, T.S., 1985. Physics of the sea. In: Margalef, R. (Ed.), *Key Environments: West Mediterranean*. Pergamon Press, New York, pp. 100–125.

Hsu, H.-H., Dong, J.-J., Hsu, S.-K., Su, C.-C., 2018. Back analysis of an earthquake-triggered submarine landslide near the SW of Xiaoliuqi. *Terr. Atmos. Ocean. Sci.* 29, 77–85. <https://doi.org/10.3319/TAO.2017.05.08.01>

Hsü, K.J., Ryan, W.B.F., Cita, M.B., 1973. Late Miocene desiccation of the Mediterranean. *Nature* 242, 240–244. <https://doi.org/10.1038/242240a0>

Hughes, P.D., Gibbard, P.L., Ehlers, J., 2013. Timing of glaciation during the last glacial cycle: evaluating the concept of a global “Last Glacial Maximum” (LGM). *Earth-Science Rev.* 125, 171–198. <https://doi.org/10.1016/j.earscirev.2013.07.003>

Huhn, K., Kock, I., Kopf, A., 2006. Comparative numerical and analogue shear box experiments and their implications for the mechanics along the failure plane of landslides. *Nor. J. Geol.* 86, 209–220.

Hühnerbach, V., Masson, D.G., 2004. Landslides in the North Atlantic and its adjacent seas: An analysis of their morphology, setting and behaviour. *Mar. Geol.* 213, 343–362. <https://doi.org/10.1016/j.margeo.2004.10.013>

Hüneke, H., Mulder, T., 2011. Deep-Sea Sediments. Developments in Sedimentology, 63. Elsevier, New York. 849 pp. [ISBN 978-0-444-53000-4](#)

Ifremer 2020. Acoustic data processing. [https://wwz.ifremer.fr/gm\\_eng/Activities/Cartography-Data-Processing-and-Instrumentation-group-CDPI/Acoustic-data-processing](https://wwz.ifremer.fr/gm_eng/Activities/Cartography-Data-Processing-and-Instrumentation-group-CDPI/Acoustic-data-processing)

Istituto Nazionale di Geofisica e Vulcanologia, Osiride version 1.37.2 <http://terremoti.ingv.it/en> (accessed 13 March 2021)

Jaccard, S.L., Galbraith, E.D., Sigman, D.M., Haug, G.H., 2010. A pervasive link between Antarctic ice core and subarctic Pacific sediment records over the past 800 kyrs. *Quat. Sci. Rev.* 29, 206–212. <https://doi.org/10.1016/j.quascirev.2009.10.007>

Jakob, M., Hungr, O., 2005. Debris-flow Hazards and Related Phenomena. Berlin: Heidelberg, Praxis-Springer, pp. 739.

Jiménez-Espejo, F., Pardos-Gené, M., Martínez-Ruiz, F., García-Alix, A., Flierdt, T., Toyofuku, T., Bahr, A., Kreissig, K., 2015. Geochemical evidence for intermediate water circulation in the westernmost Mediterranean over the last 20kyrBP and its impact on the Mediterranean Outflow. *Glob. Planet. Change* 135. <https://doi.org/10.1016/j.gloplacha.2015.10.001>

Jolivet, L., Faccenna, C., 2000. Mediterranean extension and the Africa-Eurasia collision. *Tectonics* 19, 1095–1106. <https://doi.org/10.1029/2000TC900018>

Jolivet, L., Augier, R., Robin, C., Suc, J.-P., Rouchy, J.M., 2006. Lithospheric-scale geodynamic context of the Messinian salinity crisis. *Sediment. Geol.* 188–189, 9–33. <https://doi.org/10.1016/j.sedgeo.2006.02.004>

Kanamori, H., Kikuchi, M., 1993. The 1992 Nicaragua earthquake - A slow tsunami earthquake associated with subducted sediments. *Nature* 361, 714–716. <https://doi.org/10.1038/361714a0>

Kelley, D.S., Delaney, J.R., Juniper, S.K., 2014. Establishing a new era of submarine volcanic observatories: Cabling Axial Seamount and the Endeavour Segment of the Juan de Fuca Ridge. *Mar. Geol.* 352, 426–450. <https://doi.org/10.1016/j.margeo.2014.03.010>

Kendall, C., Caldwell, E.A., 1998. Chapter 2: Fundamentals of Isotope Geochemistry, in: Kendall, C., McDonnell, J.J. (Eds.), *Isotope Tracers in Catchment Hydrology*. Elsevier Science B.V., Amsterdam, pp. 51-86.

Kennett, J.P., 1982. *Marine Geology*. Prentice-Hall, Englewood Cliffs, N.J. 813 p.

Kidd, R.B., Cita, M.B., Ryan, W.B.F., 1978. Stratigraphy of eastern Mediterranean sapropel sequences recovered during DSDP Leg 42A and their paleoenvironmental significance. *Initial Reports of the Deep-Sea Drilling Project 42A*, 421-443.

Kirschbaum, D.B., Adler, R., Hong, Y., Hill, S., Lerner-Lam, A., 2010. A global landslide catalog for hazard applications: method, results, and limitations. *Nat. Hazards* 52, 561–575. <https://doi.org/10.1007/s11069-009-9401-4>

Kopf, A.J., Kasten, S., Bles, J., 2010. Geochemical Evidence for Groundwater-Charging of Slope Sediments: The Nice Airport 1979 Landslide and Tsunami Revisited, in: Mosher, D.C., Shipp, R.C., Moscardelli, L., Chaytor, J.D., Baxter, C.D.P., Lee, H.J., Urgeles, R. (Eds.), *Submarine Mass Movements and Their Consequences*. Springer Netherlands, Dordrecht, pp. 203–214. [https://doi.org/10.1007/978-90-481-3071-9\\_17](https://doi.org/10.1007/978-90-481-3071-9_17)

Kopf, A., Fleischmann, T., Gauchery, T., Meinecke, G., Renken, J., Spiesecke, U., Stange, N., Völker, D., von Wahl, T., Wenau, S., Wittauer, C., Wu, T.-W., 2016. Report and preliminary results of R/V POSEIDON cruise POS500, LISA, Ligurian Slope AUV mapping, gravity coring and seismic reflection, Catania (Italy) – Malaga (Spain), 25.05.2016 – 09.06.2016. *Berichte, MARUM – Zentrum für Marine Umweltwissenschaften, Fachbereich Geowissenschaften, Universität Bremen*, 312, pp. 58. ISSN 2195-9633.

Korup, O., 2012. Earth's portfolio of extreme sediment transport events. *Earth-Science Rev.* 112, 115–125. <https://doi.org/10.1016/j.earscirev.2012.02.006>

Korup, O., Clague, J.J., Hermanns, R.L., Hewitt, K., Strom, A.L., Weidinger, J.T., 2007. Giant landslides, topography, and erosion. *Earth Planet. Sci. Lett.* 261, 578–589. <https://doi.org/10.1016/j.epsl.2007.07.025>

Kremer, K., Usman, M.O., Satoguchi, Y., Nagahashi, Y., Vadakkepuliambatta, S., Panieri, G., Strasser, M., 2017. Possible climate preconditioning on submarine landslides along a convergent margin, Nankai Trough (NE Pacific). *Prog. Earth Planet. Sci.* 4, 20. <https://doi.org/10.1186/s40645-017-0134-9>

Krijgsman, W., Hilgen, F.J., Raffi, I., Sierro, F.J., Wilson, D.S., 1999. Chronology, causes and progression of the Messinian salinity crisis. *Nature* 400, 652–655. <https://doi.org/10.1038/23231>

Kuhlmann, J., Asioli, A., Strasser, M., Trincardi, F., Huhn, K., 2014. Integrated Stratigraphic and Morphological investigation of the Twin Slide complex offshore southern Sicily, in: *Submarine Mass Movements and Their Consequences*. pp. 583–594. <https://doi.org/10.1007/978-94-010-0093-2>

Kuhlmann, J., Asioli, A., Trincardi, F., Klügel, A., Huhn, K., 2015. Sedimentary response to Milankovitch-type climatic oscillations and formation of sediment undulations: evidence from a shallow-shelf setting at Gela Basin on the Sicilian continental margin. *Quat. Sci. Rev.* 108, 76–94. <https://doi.org/10.1016/J.QUASCIREV.2014.10.030>

Kuhlmann, J., Asioli, A., Trincardi, F., Klügel, A., Huhn, K., 2017. Landslide Frequency and Failure Mechanisms at NE Gela Basin (Strait of Sicily). *J. Geophys. Res. Earth Surf.* 122, 2223–2243. <https://doi.org/10.1002/2017JF004251>

Kvalstad, T.J., Andresen, L., Forsberg, C.F., Berg, K., Bryn, P., Wangen, M., 2005. The Storegga slide: evaluation of triggering sources and slide mechanics. *Mar. Pet. Geol.* 22, 245–256. <https://doi.org/10.1016/j.marpetgeo.2004.10.019>

L'Heureux, J.-S., Hansen, L., Longva, O., Emdal, A., Grande, L., 2010. A multidisciplinary study of submarine landslides at the Nidelva fjord delta, Central Norway - Implications for geohazard assessment. *Nor. J. Geol.* 90, 1–20.

L'Heureux, J.-S., Longva, O., Steiner, A., Hansen, L., Vardy, M.E., Vanneste, M., Haflidason, H., Brendryen, J., Kvalstad, T.J., Forsberg, C.F., Chand, S., Kopf, A., 2012. Identification of Weak Layers and Their Role for the Stability of Slopes at Finneidfjord, Northern Norway, in: Yamada, Y., Kawamura, K., Ikehara, K., Ogawa, Y., Urgeles, R., Mosher, D., Chaytor, J., Strasser, M. (Eds.), *Submarine Mass Movements and Their Consequences*. Springer Netherlands, Dordrecht, pp. 321–330.

Laberg, J.S., Camerlenghi, A., 2008. The Significance of Contourites for Submarine Slope Stability, in: Rebesco, M., Camerlenghi, A. (Eds.), *Contourites, Developments in Sedimentology*. Elsevier, pp. 537–556. [https://doi.org/10.1016/S0070-4571\(08\)10025-5](https://doi.org/10.1016/S0070-4571(08)10025-5)

Lamarche, G., Mountjoy, J., Bull, S., Hubble, T., Krastel, S., Lane, E., Micallef, A., Moscardelli, L., Mueller, C., Pecher, I., Woelz, S., 2016. Submarine Mass Movements and Their Consequences: Progress and Challenges, in: Lamarche, G., Mountjoy, J., Bull, S., Hubble, T., Krastel, S., Lane, E., Micallef, A., Moscardelli, L., Mueller, C., Pecher, I., Woelz, S. (Eds.), *Submarine Mass Movements and Their Consequences: 7th International Symposium*. Springer International Publishing, Cham, pp. 1–12. [https://doi.org/10.1007/978-3-319-20979-1\\_1](https://doi.org/10.1007/978-3-319-20979-1_1)

Lambeck, K., Rouby, H., Purcell, A., Sun, Y., Sambridge, M., 2014. Sea level and global ice volumes from the Last Glacial Maximum to the Holocene. *Proceedings of the National Academy of Sciences* 111, 15296-15303. <https://doi.org/10.1073/pnas.1411762111>

Langone, L., Bergami C., Cargini, D., Covazzi, A., D'Amico, D., Fogliani, F., Gallerani, A., Zeppilli, D., 2005. GELA – 05 cruise report of R/V URANIA, Catania, August 10 – Catania, August 23, 2005. Hotspot Ecosystem Research on the Margins of European Seas – HERMES.

Lastras, G., Canals, M., Hughes-Clarke, J.E., Moreno, A., Batist, M., Masson, D.G., Cochonat, P., 2002. Seafloor imagery from the BIG'95 debris flow, western Mediterranean. *Geology* 30, 871–874. [https://doi.org/10.1130/0091-7613\(2002\)030<0871:SIFTBD>2.0.CO;2](https://doi.org/10.1130/0091-7613(2002)030<0871:SIFTBD>2.0.CO;2)

Ledbetter, M.T., 1979. Fluctuations of Antarctic Bottom Water velocity in the Vema Channel during the last 160,000 years. *Mar. Geol.* 33, 71–89. [https://doi.org/10.1016/0025-3227\(79\)90133-6](https://doi.org/10.1016/0025-3227(79)90133-6)

Ledbetter, M.T., Balsam, W.L., 1985. Paleoceanography of the Deep Western Boundary Undercurrent on the North American continental margin for the past 25 000 yr. *Geology* 13, 181–184. [https://doi.org/10.1130/0091-7613\(1985\)13<181:POTDWB>2.0.CO;2](https://doi.org/10.1130/0091-7613(1985)13<181:POTDWB>2.0.CO;2)

Lee, H.J., Locat, J., Desgagnés, P., Parsons, J.D., McAdoo, B.G., Orange, D.L., Puig, P., Wong, F.L., Dartnell, P. and Boulanger, E. (2007). Submarine Mass Movements on Continental Margins, in: Jarvis, I., Nittrouer, C.A., Austin, J.A., Field, M.E., Kravitz, J.H., Syvitski, J.P.M., Wiberg, P.L. (Eds.), *Continental Margin Sedimentation*. John Wiley & Sons, Ltd, pp. 213–274. <https://doi.org/10.1002/9781444304398.ch5>

Lermusiaux, P.F.J., Robinson, A.R., 2001. Features of dominant mesoscale variability, circulation patterns and dynamics in the Strait of Sicily. *Deep Sea Res. Part I Oceanogr. Res. Pap.* 48, 1953–1997. [https://doi.org/10.1016/S0967-0637\(00\)00114-X](https://doi.org/10.1016/S0967-0637(00)00114-X)

Leynaud, D., Sultan, N., Mienert, J., 2007. The role of sedimentation rate and permeability in the slope stability of the formerly glaciated Norwegian continental margin: the Storegga slide model. *Landslides* 4, 297. <https://doi.org/10.1007/s10346-007-0086-z>

- Li, W., Alves, T.M., Wu, S., Rebesco, M., Zhao, F., Mi, L., Ma, B., 2016. A giant, submarine creep zone as a precursor of large-scale slope instability offshore the Dongsha Islands (South China Sea). *Earth Planet. Sci. Lett.* 451, 272–284. <https://doi.org/10.1016/j.epsl.2016.07.007>
- Lirer, F., Foresi, L.M., Iaccarino, S.M., Salvatorini, G., Turco, E., Cosentino, C., Sierro, F.J., Caruso, A., 2019. Mediterranean Neogene planktonic foraminifer biozonation and biochronology. *Earth-Science Rev.* 196, 102869. <https://doi.org/10.1016/j.earscirev.2019.05.013>
- Lisiecki, L.E., Raymo, M.E., 2009. Diachronous benthic  $\delta^{18}\text{O}$  responses during late Pleistocene terminations. *Paleoceanography* 24, PA3210. <https://doi.org/10.1029/2009PA001732>
- Lisiecki, L.E., Stern, J.V., 2016. Regional and global benthic  $\delta^{18}\text{O}$  stacks for the last glacial cycle. *Paleoceanography* 31, 1368–1394. <https://doi.org/10.1002/2016PA003002>
- Llave, E., Hernández-Molina, F.J., Somoza, L., Stow, D.A. V., Díaz Del Río, V., 2007. Quaternary evolution of the contourite depositional system in the Gulf of Cadiz. *Geol. Soc. London, Spec. Publ.* 276, 49–79. <https://doi.org/10.1144/GSL.SP.2007.276.01.03>
- Lobo, F.J., Ridente, D., 2014. Stratigraphic architecture and spatio-temporal variability of high-frequency (Milankovitch) depositional cycles on modern continental margins: An overview. *Mar. Geol.* 352, 215–247. <https://doi.org/10.1016/j.margeo.2013.10.009>
- Locat, J., Lee, H.J., 2002. Submarine landslides: advances and challenges. *Can. Geotech. J.* 39, 193–212. <https://doi.org/10.1139/t01-089>
- Locat, J., Gardner, J.V., Lee, H., Mayer, L., Hughes Clarke, J., Kammerer, E., 1999. Using multibeam sonar surveys for submarine landslide investigations, in: Yagi, N., Yamagami, T., Jiang, J.-C. (Eds.), *Slope Stability Engineering*. Balkema, pp. 127–134.
- Locat, J., Leroueil, S., Locat, A., Lee, H., 2014. Weak Layers: Their Definition and Classification from a Geotechnical Perspective, in: Krastel, S., Behrmann, J.-H., Völker, D., Stipp, M., Berndt, C., Urgeles, R., Chaytor, J., Huhn, K., Strasser, M., Harbitz, C.B. (Eds.), *Submarine Mass Movements and Their Consequences: 6th International Symposium*. Springer International Publishing, Cham, pp. 3–12. [https://doi.org/10.1007/978-3-319-00972-8\\_1](https://doi.org/10.1007/978-3-319-00972-8_1)
- Loget, N., Van Den Driessche, J., 2006. On the origin of the Strait of Gibraltar. *Sediment. Geol.* 188–189, 341–356. <https://doi.org/10.1016/j.sedgeo.2006.03.012>
- Loncke, L., Gaullier, V., Droz, L., Ducassou, E., Migeon, S., Mascle, J., 2009. Multi-scale slope instabilities along the Nile deep-sea fan, Egyptian margin: A general overview. *Mar. Pet. Geol.* 26, 633–646. <https://doi.org/10.1016/j.marpetgeo.2008.03.010>
- Lonsdal, P., Malfait, B., 1974. Abyssal Dunes of Foraminiferal Sand on the Carnegie Ridge. *GSA Bull.* 85, 1697–1712. [https://doi.org/10.1130/0016-7606\(1974\)85<1697:ADOFSO>2.0.CO;2](https://doi.org/10.1130/0016-7606(1974)85<1697:ADOFSO>2.0.CO;2)
- Lopes, R.P., Kinoshita, A., Baffa, O., Figueiredo, A.M.G., Dillenburg, S.R., Schultz, C.L., Pereira, J.C., 2014. ESR dating of Pleistocene mammals and marine shells from the coastal plain of Rio Grande do Sul state, southern Brazil. *Quat. Int.* 352, 124–134. <https://doi.org/10.1016/j.quaint.2013.07.020>

Løvholt, F., Harbitz, C.B., Haugen, K.B., 2005. A parametric study of tsunamis generated by submarine slides in the Ormen Lange/Storegga area off western Norway. *Mar. Pet. Geol.* 22, 219–231. <https://doi.org/10.1016/j.marpetgeo.2004.10.017>

Ludwig, W., Dumont, E., Meybeck, M., Heussner, S., 2009. River discharges of water and nutrients to the Mediterranean and Black Sea: Major drivers for ecosystem changes during past and future decades? *Prog. Oceanogr.* 80, 199–217. <https://doi.org/10.1016/j.pocean.2009.02.001>

Lusty, P.A., Hein, J.R., Josso, P., 2019. Formation and occurrence of ferromanganese crusts: Earth's storehouse for critical metals. *Elements* 14, 313–318. <https://doi.org/10.2138/gselements.14.5.313>

Macías, J., Vázquez, J.T., Fernández-Salas, L.M., González-Vida, J.M., Bárcenas, P., Castro, M.J., Díaz-del-Río, V., Alonso, B., 2015. The Al-Borani submarine landslide and associated tsunami. A modelling approach. *Mar. Geol.* 361, 79–95. <https://doi.org/10.1016/j.margeo.2014.12.006>

Madof, A.S., Bertoni, C., Lofi, J., 2019. Discovery of vast fluvial deposits provides evidence for drawdown during the late Miocene Messinian salinity crisis. *Geology* 47, 171–174. <https://doi.org/10.1130/G45873.1>

Malinverno, A., Ryan, W.B.F., 1986. Extension in the Tyrrhenian Sea and shortening in the Apennines as result of arc migration driven by sinking of the lithosphere. *Tectonics* 5, 227–245. <https://doi.org/10.1029/TC005i002p00227>

Marani, M., Argnani, A., Roveri, M., Trincardi, F., 1993. Sediment drifts and erosional surfaces in the central Mediterranean: seismic evidence of bottom-current activity. *Sediment. Geol.* 82, 207–220. [https://doi.org/10.1016/0037-0738\(93\)90122-L](https://doi.org/10.1016/0037-0738(93)90122-L)

Martín-Chivelet, J., Fregenal-Martinez, M.A., Chacón, B., 2008. Chapter 10 Traction Structures in Contourites, in: Rebesco, M., Camerlenghi, (Eds.), *Contourites*, Elsevier, pp. 157–182. [https://doi.org/10.1016/S0070-4571\(08\)10010-3](https://doi.org/10.1016/S0070-4571(08)10010-3)

Martinez-Ruiz, F., Kastner, M., Gallego-Torres, D., Rodrigo-Gámiz, M., Nieto-Moreno, V., Ortega-Huertas, M., 2015. Paleoclimate and paleoceanography over the past 20,000 yr in the Mediterranean Sea Basins as indicated by sediment elemental proxies. *Quat. Sci. Rev.* 107, 25–46. <https://doi.org/10.1016/j.quascirev.2014.09.018>

Martinsen, O.J., 1989. Styles of soft-sediment deformation on a Namurian (Carboniferous) delta slope, Western Irish Namurian Basin, Ireland. *Geol. Soc. London, Spec. Publ.* 41, 167–177. <https://doi.org/10.1144/GSL.SP.1989.041.01.13>

Martorelli, E., Petroni, G., Chiocci, F.L., 2011. Contourites offshore Pantelleria Island (Sicily Channel, Mediterranean Sea): depositional, erosional and biogenic elements. *Geo-Marine Lett.* 31, 481–493. <https://doi.org/10.1007/s00367-011-0244-0> Masson, D., Kidd, R., Gardner, J., Huggett, Q., Weaver, P., 1992. Saharan continental rise: Facies distribution and sediment slides, in: Poag, C.W., Graciansky, P.C. (Eds.), *Geologic Evolution of Atlantic Continental Rises*, Van Norstrand Reinhold, New York, pp. 327–343.

Masson, D.G., Van Niel, B., Weaver, P.P.E., 1997. Flow processes and sediment deformation in the Canary Debris Flow on the NW African Continental Rise. *Sediment. Geol.* 110, 163–179. [https://doi.org/10.1016/S0037-0738\(96\)00089-9](https://doi.org/10.1016/S0037-0738(96)00089-9)

Masson, D.G., Watts, A.B., Gee, M.J.R., Urgeles, R., Mitchell, N.C., Le Bas, T.P., Canals, M., 2002. Slope failures on the flanks of the western Canary Islands. *Earth-Science Rev.* 57, 1–35. [https://doi.org/10.1016/S0012-8252\(01\)00069-1](https://doi.org/10.1016/S0012-8252(01)00069-1)

Masson, D.G., Harbitz, C.B., Wynn, R.B., Pedersen, G., Løvholt, F., 2006. Submarine landslides: processes, triggers and hazard prediction. *Philos. Trans. R. Soc. A Math. Phys. Eng. Sci.* 364, 2009–2039. <https://doi.org/10.1098/rsta.2006.1810>

Masson, D.G., Wynn, R.B., Talling, P.J., 2010. Large Landslides on Passive Continental Margins: Processes, Hypotheses and Outstanding Questions, in: Mosher, D.C., Shipp, R.C., Moscardelli, L., Chaytor, J.D., Baxter, C.D.P., Lee, H.J., Urgeles, R. (Eds.), *Submarine Mass Movements and Their Consequences*. Springer Netherlands, Dordrecht, pp. 153–165. [https://doi.org/10.1007/978-90-481-3071-9\\_13](https://doi.org/10.1007/978-90-481-3071-9_13)

Mateos, R.M., Herrera, G., García-Davalillo, J.C., Grandjean, G., Poyiadji, E., Maftai, R., Filipciuc, T.-C., Auflič, M.J., Jez, J., Podolszki, L., Trigila, A., Comerci, V., Raetzo, H., Kociu, A., Przyłucka, M., Kułak, M., Laskowicz, I., Sheehy, M., Kopackova, V., Frei, M., Kuhn, D., Dehls, J.F., Hermanns, R.L., Koulermou, N., Smith, C.A., Engdahl, M., Pagespetit, P.B., González, M., Banks, V., Dashwood, C., Reeves, H., Cigna, F., Liščák, P., Mikulénas, V., Demir, V., Raha, M., Quental, L., Oliveira, D., Dias, R., Sandić, C., 2017. Integration of Geohazards into Urban and Land-Use Planning. Towards a Landslide Directive. The EuroGeoSurveys Questionnaire, in: Mikos, M., Tiwari, B., Yin, Y., Sassa, K. (Eds.), *Advancing Culture of Living with Landslides*. Springer International Publishing, Cham, pp. 1067–1072. [https://doi.org/10.1007/978-3-319-53498-5\\_121](https://doi.org/10.1007/978-3-319-53498-5_121)

Maurizio, W., Cebrian, D., Requena Moreno, S., 2015. Sicily Channel/Tunisian Plateau: Topography, circulation and their effects on biological components. *UNEP-MAP-RAC/SPA*. <https://doi.org/10.13140/RG.2.2.35786.31689>

McAdoo, B.G., Pratson, L.F., Orange, D.L., 2000. Submarine landslide geomorphology, US continental slope. *Mar. Geol.* 169, 103–136. [https://doi.org/10.1016/S0025-3227\(00\)00050-5](https://doi.org/10.1016/S0025-3227(00)00050-5)

McCave, I.N., Hall, I.R., 2006. Size sorting in marine muds: Processes, pitfalls, and prospects for paleoflow-speed proxies. *Geochemistry, Geophys. Geosystems* 7, Q10N05. <https://doi.org/10.1029/2006GC001284>

McCave, I.N., Andrews, J.T., 2019. Distinguishing current effects in sediments delivered to the ocean by ice. I. Principles, methods and examples. *Quat. Sci. Rev.* 212, 92–107. <https://doi.org/10.1016/j.quascirev.2019.03.031>

McCave, I.N., Manighetti, B., Robinson, S.G., 1995. Sortable silt and fine sediment size/composition slicing: Parameters for palaeocurrent speed and palaeoceanography. *Paleoceanography* 10, 593–610. <https://doi.org/10.1029/94PA03039>

McCave, I.N., Thornalley, D.J.R., Hall, I.R., 2017. Relation of sortable silt grain-size to deep-sea current speeds: Calibration of the ‘Mud Current Meter’. *Deep Sea Res. Part I Oceanogr. Res. Pap.* 127, 1–12. <https://doi.org/10.1016/j.dsr.2017.07.003>

McHugh, C.M.G., Damuth, J.E., Mountain, G.S., 2002. Cenozoic mass-transport facies and their correlation with relative sea-level change, New Jersey continental margin. *Mar. Geol.* 184, 295–334. [https://doi.org/10.1016/S0025-3227\(01\)00240-7](https://doi.org/10.1016/S0025-3227(01)00240-7)

Mehta, A.J., Letter, J. V, 2013. Comments on the transition between cohesive and cohesionless sediment bed exchange. *Estuar. Coast. Shelf Sci.* 131, 319–324. <https://doi.org/10.1016/j.ecss.2013.07.001>

Menier, D., Bourillet, J.-F., Proust, J.-N., Perez-Belmonte, L., Goubert, E., Thinon, I., Guennoc, P., Guillocheau, F., Leroy, P., 2006. Morphology and infilling of Quaternary incised valleys on the Armorican margin of the Bay of Biscay. 10<sup>th</sup> International Symposium on Oceanography of the Bay of Biscay, Apr 2006, Vigo, Spain. pp. 99–102

Micallef, A., Foglini, F., Le Bas, T., Angeletti, L., Maselli, V., Pasuto, A., Taviani, M., 2013. The submerged paleolandscape of the Maltese Islands: Morphology, evolution and relation to Quaternary environmental change. *Mar. Geol.* 335, 129–147. <https://doi.org/10.1016/j.margeo.2012.10.017>

Middleton, G.V., Hampton, M.A., 1973. Sediment gravity flows: Mechanics of flow and deposition, in: Middleton, G.V., Bouma, A.H. (Eds.), *Turbidites and deep-water sedimentation*, pp. 1–38. Anaheim, CA: SEPM Pacific section Short Course.

Mienert, J., Berndt, C., Laberg, J., Vorren, T.O., 2002. Submarine landslides on continental margins. *Ocean Margins Syst.* Springer Verlag, 179–193. [https://doi.org/10.1007/978-3-662-05127-6\\_11](https://doi.org/10.1007/978-3-662-05127-6_11)

Milankovitch, M., 1930. Mathematische Klimalehre und astronomische Theorie der Klimaschwankungen, in: Köppen, W., Geiger, R. (Eds.), *Handbuch der Klimatologie*, 1(A). Berlin, Gebrüder Borntraeger, pp.1-176.

Milliman, J.D., Meade, R.H., 1983. World-Wide Delivery of River Sediment to the Oceans. *J. Geol.* 91, 1–21. <http://www.jstor.org/stable/30060512>

Millot, C., 1999. Circulation in the Western Mediterranean Sea. *J. Mar. Syst.* 20, 423–442. [https://doi.org/10.1016/S0924-7963\(98\)00078-5](https://doi.org/10.1016/S0924-7963(98)00078-5)

Millot, C., Taupier-Letage, I., 2005. Circulation in the Mediterranean Sea, in: Saliot, A. (Ed.), *The Mediterranean Sea*. Springer Berlin Heidelberg, Berlin, Heidelberg, pp. 29–66. <https://doi.org/10.1007/b107143>

Minisini, D., Trincardi, F., 2009. Frequent failure of the continental slope: the Gela Basin (sicily channel). *J. Geophys. Res.-Earth* 114, 1–17. <https://doi.org/10.1029/2008JF001037>

Minisini, D., Trincardi, F., Asioli, A., Canu, M., Foglini, F. 2007. Morphologic variability of exposed mass-transport deposits on the eastern slope of Gela Basin (Sicily channel). *Bas. Res.* 19, 217–240. <https://doi.org/10.1111/j.1365-2117.2007.00324.x>

Miramontes, E., Cattaneo, A., Jouet, G., Théreau, E., Thomas, Y., Rovere, M., Cauquil, E., Trincardi, F., 2016. The Pianosa Contourite Depositional System (Northern Tyrrhenian Sea): Drift

morphology and Plio-Quaternary stratigraphic evolution. *Mar. Geol.* 378, 20-42. <https://doi.org/10.1016/j.margeo.2015.11.004>

Miramontes, E., Garziglia, S., Sultan, N., Jouet, G., Cattaneo, A., 2018. Morphological control of slope instability in contourites: a geotechnical approach. *Landslides* 15, 1085–1095. <https://doi.org/10.1007/s10346-018-0956-6>

Miramontes, E., Garreau, P., Caillaud, M., Jouet, G., Pellen, R., Hernández-Molina, F.J., Clare, M.A., Cattaneo, A., 2019. Contourite distribution and bottom currents in the NW Mediterranean Sea: Coupling seafloor geomorphology and hydrodynamic modelling. *Geomorphology* 333, 43–60. <https://doi.org/10.1016/j.geomorph.2019.02.030>

Moscardelli, L., Wood, L., 2016. Morphometry of mass-transport deposits as a predictive tool. *Geol. Soc. Am. Bull.* 128, 47-80. <https://doi.org/10.1130/B31221.1>

Moscardelli, L., Wood, L., Mann, P., 2006. Mass-transport complexes and associated processes in the offshore area of Trinidad and Venezuela. *Am. Assoc. Pet. Geol. Bull.* 90, 1059–1088. <https://doi.org/10.1306/02210605052>

Mountjoy, J., Micallef, A., 2018. Submarine Landslides, in: Micallef, A., Krastel, S., Savini, A. (Eds.), *Submarine Geomorphology*. Springer International Publishing, Cham, pp. 235–250. [https://doi.org/10.1007/978-3-319-57852-1\\_13](https://doi.org/10.1007/978-3-319-57852-1_13)

Mountjoy, J.J., Howarth, J.D., Orpin, A.R., Barnes, P.M., Bowden, D.A., Rowden, A.A., Schimel, A.C.G., Holden, C., Horgan, H.J., Nodder, S.D., Patton, J.R., Lamarche, G., Gerstenberger, M., Micallef, A., Pallentin, A., Kane, T., 2018. Earthquakes drive large-scale submarine canyon development and sediment supply to deep-ocean basins. *Sci. Adv.* 4. <https://doi.org/10.1126/sciadv.aar3748>

Mueller, C., Micallef, A., Spatola, D., Wang, X., 2020. The Tsunami Inundation Hazard of the Maltese Islands (Central Mediterranean Sea): A Submarine Landslide and Earthquake Tsunami Scenario Study. *Pure Appl. Geophys.* 177, 1617–1638. <https://doi.org/10.1007/s00024-019-02388-w>

Mulder, T., Cochonat, P., 1996. Classification of offshore mass movements. *J. Sediment. Res.* 66, 43–57. <https://doi.org/10.1306/D42682AC-2B26-11D7-8648000102C1865D>

Mulder, T., Alexander, J., 2001. The physical character of subaqueous sedimentary density flows and their deposits. *Sedimentology* 48, 269–299. <https://doi.org/10.1046/j.1365-3091.2001.00360.x>

Narcisi, B., Vezzoli, L., 1999. Quaternary stratigraphy of distal tephra layers in the Mediterranean—an overview. *Glob. Planet. Change* 21, 31–50. [https://doi.org/10.1016/S0921-8181\(99\)00006-5](https://doi.org/10.1016/S0921-8181(99)00006-5)

Nieto-Moreno, V., Martínez-Ruiz, F., Giralt, S., Jiménez-Espejo, F., Gallego-Torres, D., Rodrigo-Gámiz, M., García-Orellana, J., Ortega-Huertas, M., de Lange, G.J., 2011. Tracking climate variability in the western Mediterranean during the Late Holocene: a multiproxy approach. *Clim. Past* 7, 1395–1414. <https://doi.org/10.5194/cp-7-1395-2011>

NTL (Novosibirsk Tsunami Laboratory). Web Encyclopedia on Natural Hazards– Historical Tsunami Database for the World Ocean (HTDB/WLD). <http://tsun.sccc.ru/nh/tsunami.php>

Ohlmacher, G., 2001. The Relationship Between Geology and Landslide Hazards of Atchison, Kansas, and Vicinity. *Curr. Res. Earth Sci.* 244 pp.

Okal, E., Synolakis, C., 2003. A Theoretical Comparison of Tsunamis from Dislocations and Landslides. *Pure Appl. Geophys.* 160, 2177–2188. <https://doi.org/10.1007/s00024-003-2425-x>

Pakoksung, K., Suppasri, A., Imamura, F., Athanasius, C., Omang, A., Muhari, A., 2019. Simulation of the Submarine Landslide Tsunami on 28 September 2018 in Palu Bay, Sulawesi Island, Indonesia, Using a Two-Layer Model. *Pure Appl. Geophys.* 176, 3323–3350. <https://doi.org/10.1007/s00024-019-02235-y>

Palomino, D., Vázquez, J.-T., Ercilla, G., Alonso, B., López-González, N., Díaz-del-Río, V., 2011. Interaction between seabed morphology and water masses around the seamounts on the Motril Marginal Plateau (Alboran Sea, Western Mediterranean). *Geo-Marine Lett.* 31, 465–479. <https://doi.org/10.1007/s00367-011-0246-y>

Papadopoulos, G.A., Daskalaki, E., Fokaefs, A., 2007. Tsunamis Generated By Coastal And Submarine Landslides In The Mediterranean Sea, in: Lykousis, V., Sakellariou, D., Locat, J. (Eds.), *Submarine Mass Movements and Their Consequences: 3 International Symposium*, Springer Netherlands, Dordrecht, pp. 415–422. [https://doi.org/10.1007/978-1-4020-6512-5\\_43](https://doi.org/10.1007/978-1-4020-6512-5_43)

Paparo, M., Tinti, S., 2017. Analysis of Seismic-Driven Instability of Mt. Nuovo in the Ischia Island, Italy. *Bull. Seismol. Soc. Am.* 107, 750–759. <https://doi.org/10.1785/0120160139>

Patruno, S., Helland-Hansen, W., 2018. Clinofolds and clinofold systems: Review and dynamic classification scheme for shorelines, subaqueous deltas, shelf edges and continental margins. *Earth-Science Rev.* 185, 202–233. <https://doi.org/10.1016/j.earscirev.2018.05.016>

Patterson, R., Guilbault, J.-P., Thomson, R., Luternauer, J., 1995. Foraminiferal Evidence of Younger Dryas Age Cooling on the British Columbia Shelf. *Géographie Phys. Quat.* 49, 409–427. <https://doi.org/10.7202/033063ar>

Paull, C.K., Talling, P.J., Maier, K.L., Parsons, D., Xu, J., Caress, D.W., Gwiazda, R., Lundsten, E.M., Anderson, K., Barry, J.P., Chaffey, M., O'Reilly, T., Rosenberger, K.J., Gales, J.A., Kieft, B., McGann, M., Simmons, S.M., McCann, M., Sumner, E.J., Clare, M.A., Cartigny, M.J., 2018. Powerful turbidity currents driven by dense basal layers. *Nat. Commun.* 9, 4114. <https://doi.org/10.1038/s41467-018-06254-6>

Pellegrini, C., Maselli, V., Trincardi, F., 2016. Pliocene–Quaternary contourite depositional system along the south-western Adriatic margin: changes in sedimentary stacking pattern and associated bottom currents. *Geo-Marine Lett.* 36, 67–79. <https://doi.org/10.1007/s00367-015-0424-4>

Perissoratis, C., Papadopoulos, G., 1999. Sediment instability and slumping in the southern Aegean Sea and the case history of the 1956 tsunami. *Mar. Geol.* 161, 287–305. [https://doi.org/10.1016/S0025-3227\(99\)00039-0](https://doi.org/10.1016/S0025-3227(99)00039-0)

Petrovic, A., Lantzsch, H., Schwenk, T., Marquardt, J., Titschack, J., Hanebuth, T.J.J., 2019. Post-LGM upward shift of the Mediterranean Outflow Water recorded in a contourite drift off NW Spain. *Mar. Geol.* 407, 334–349. <https://doi.org/10.1016/j.margeo.2018.11.015>

Pinder, D., 2001. Offshore oil and gas: global resource knowledge and technological change. *Ocean Coast. Manag.* 44, 579–600. [https://doi.org/10.1016/S0964-5691\(01\)00070-9](https://doi.org/10.1016/S0964-5691(01)00070-9)

Piper, D.J.W., Shor, A.N., Hughes Clarke, J.E., 1988. The 1929 “Grand Banks” earthquake, slump, and turbidity current, in: Clifton, H.E. (Ed.), *Sedimentologic Consequences of Convulsive Geologic Events*. Geological Society of America, pp. 77-92. <https://doi.org/10.1130/SPE229-p77>

Piper, D.J.W., Cochonat, P., Morrison, M.L., 1999. The sequence of events around the epicentre of the 1929 Grand Banks earthquake: initiation of debris flows and turbidity current inferred from sidescan sonar. *Sedimentology* 46, 79–97. <https://doi.org/10.1046/j.1365-3091.1999.00204.x>

Piper, D., Pirmez, C., Manley, P., Long, D., Flood, Normark, Showers, W., 1997. Mass Transport Deposits of Amazon Fan, in: Flood, R.D., Piper, D.J.W., Klaus, A. (Eds.), *Proceedings of the Ocean Drilling Program, Scientific Results, Vol. 155*. Ocean Drilling Program, College Station, Texas A & M University, pp. 109–146.

Piva, A., Alessandra, A., Schneider, R., Trincardi, F., Andersen, N., Colmenero-Hidalgo, E., Dennielou, B., Flores, J., Vigliotti, L., 2008. Climatic cycles as expressed in sediments of the PROMESSI borehole PRAD1-2, central Adriatic, for the last 370 ka: 1. Integrated stratigraphy. *Geochem. Geophys. Geosy.* 9, Q01R01. <https://doi.org/10.1029/2007GC001713>

Plets, R., Dix, J., Adams, J., Bull, J., Henstock, T., Gutowski, M., Best, A., 2009. The use of a high-resolution 3D Chirp sub-bottom profiler for the reconstruction of the shallow water archaeological site of the Grace Dieu (1439), River Hamble, UK. *J. Archaeol. Sci.* 36, 408–418. <https://doi.org/10.1016/j.jas.2008.09.026>

Pope, E.L., Talling, P.J., Carter, L., 2017. Which earthquakes trigger damaging submarine mass movements: Insights from a global record of submarine cable breaks? *Mar. Geol.* 384, 131–146. <https://doi.org/10.1016/j.margeo.2016.01.009>

Portnov, A., Cook, A.E., Sawyer, D.E., Yang, C., Hillman, J.I.T., Waite, W.F., 2019. Clustered BSRs: Evidence for gas hydrate-bearing turbidite complexes in folded regions, example from the Perdido Fold Belt, northern Gulf of Mexico. *Earth Planet. Sci. Lett.* 528, 115843. <https://doi.org/10.1016/j.epsl.2019.115843>

Posamentier, H.W., Davies, R.J., Cartwright, J.A., Wood, L., 2007. Seismic geomorphology - an overview. *Geol. Soc. London, Spec. Publ.* 277, 1–14. <https://doi.org/10.1144/GSL.SP.2007.277.01.01>

Preu, B., Hernández-Molina, F.J., Violante, R., Piola, A.R., Paterlini, C.M., Schwenk, T., Voigt, I., Krastel, S., Spiess, V., 2013. Morphosedimentary and hydrographic features of the northern Argentine margin: The interplay between erosive, depositional and gravitational processes and its conceptual implications. *Deep Sea Res. Part I Oceanogr. Res. Pap.* 75, 157–174. <https://doi.org/10.1016/j.dsr.2012.12.013>

- Prior, D.B., Bornhold, B.D., Coleman, J.M., Bryant, W.R., 1982. Morphology of a submarine slide, Kitimat Arm, British Columbia. *Geology* 10, 588–592. [https://doi.org/10.1130/0091-7613\(1982\)10<588:MOASSK>2.0.CO;2](https://doi.org/10.1130/0091-7613(1982)10<588:MOASSK>2.0.CO;2)
- Rebesco, M., 2005. Sedimentary Environments: Contourites, in: Selley, R.C., Cocks, L.R.M., Plimer, I.R. (Eds.), *Encyclopedia of Geology*, Elsevier, pp. 513–527. <https://doi.org/10.1016/B0-12-369396-9/00497-4>
- Rebesco, M., Stow, D., 2001. Seismic expression of contourites and related deposits: a preface. *Mar. Geophys. Res.* 22, 303–308. <https://doi.org/10.1023/A:1016316913639>
- Rebesco, M., Camerlenghi, A., 2008. *Contourites*, 1st Edition. Elsevier Science, pp. 688.
- Rebesco, M., Hernández-Molina, F.J., Van Rooij, D., Wåhlin, A., 2014. Contourites and associated sediments controlled by deep-water circulation processes: State-of-the-art and future considerations. *Mar. Geol.* 352, 111–154. <https://doi.org/10.1016/j.margeo.2014.03.011>
- Reeder, M.S., Rothwell, G., Stow, D.A. V., 2002. The Sicilian gateway: anatomy of the deep-water connection between East and West Mediterranean basins. *Geol. Soc. London, Mem.* 22, 171–189. <https://doi.org/10.1144/GSL.MEM.2002.022.01.13>
- Revel, M., Ducassou, E., Skonieczny, C., Colin, C., Bastian, L., Bosch, D., Migeon, S., Mascle, J., 2015. 20,000 years of Nile River dynamics and environmental changes in the Nile catchment area as inferred from Nile upper continental slope sediments. *Quat. Sci. Rev.* 130, 200–221. <https://doi.org/10.1016/j.quascirev.2015.10.030>
- Robert, D.J., Thusyanthan, N.I., Jegandan, S., 2012. An overview of submarine slope stability and runout assessment for deepwater pipelines. *Offshore Site Investigation and Geotechnics: Integrated Technologies - Present and Future*, London, UK, September 2012 <https://doi.org/10.13140/2.1.3421.2645>
- Rohling, E.J., Marino, G., Grant, K.M., 2015. Mediterranean climate and oceanography, and the periodic development of anoxic events (sapropels). *Earth-Science Rev.* 143, 62–97. <https://doi.org/10.1016/j.earscirev.2015.01.008>
- Rohling, E.J., Foster, G.L., Grant, K.M., Marino, G., Roberts, A.P., Tamisiea, M.E., Williams, F., 2014. Sea-level and deep-sea-temperature variability over the past 5.3 million years. *Nature* 508, 477–482. <https://doi.org/10.1038/nature13230>
- Roland, E., Haeussler, P., Parsons, T., Hart, P., 2020. Submarine Landslide Kinematics Derived From High-Resolution Imaging in Port Valdez, Alaska. *J. Geophys. Res. Solid Earth* 125, e2019JB018007. <https://doi.org/10.1029/2019JB018007>
- Roque, C., Duarte, H., Terrinha, P., Valadares, V., Noiva, J., Cachão, M., Ferreira, J., Legoinha, P., Zitellini, N., 2012. Pliocene and Quaternary depositional model of the Algarve margin contourite drifts (Gulf of Cadiz, SW Iberia): Seismic architecture, tectonic control and paleoceanographic insights. *Mar. Geol.* 303–306, 42–62. <https://doi.org/10.1016/j.margeo.2011.11.001>

Rosenbaum, G., Lister, G.S., Duboz, C., 2002. Relative motions of Africa, Iberia and Europe during Alpine orogeny. *Tectonophysics* 359, 117–129. [https://doi.org/10.1016/S0040-1951\(02\)00442-0](https://doi.org/10.1016/S0040-1951(02)00442-0)

Rothwell, R.G., 2004. Deep ocean pelagic oozes, in: Selley, R.C.; Cocks, R.M., Plimer, I.R., (Eds.), *Encyclopedia of Geology*. Oxford, Elsevier, 2750 pp.

Rothwell, R.G., Reeder, M.S., Anastasakis, G., Stow, D.A. V, Thomson, J., Kähler, G., 2000. Low sea-level stand emplacement of megaturbidites in the western and eastern Mediterranean Sea. *Sediment. Geol.* 135, 75–88. [https://doi.org/10.1016/S0037-0738\(00\)00064-6](https://doi.org/10.1016/S0037-0738(00)00064-6)

Rouis-Zargouni, I., Turon, J.L., Londeix, L., Essallami, L., Kallel, N., Sicre, M.A., 2010. Environmental and climatic changes in the central Mediterranean Sea (Siculo-Tunisian Strait) during the last 30 ka based on dinoflagellate cyst and planktonic foraminifera assemblages. *Palaeogeogr. Palaeoclimatol. Palaeoecol.* 285, 17-29. <https://doi.org/10.1016/j.palaeo.2009.10.015>

Rovere, M., Pellegrini, C., Chiggiato, J., Campiani, E., Trincardi, F., 2019. Impact of dense bottom water on a continental shelf: An example from the SW Adriatic margin. *Mar. Geol.* 408, 123-143. <https://doi.org/10.1016/j.margeo.2018.12.002>

Roveri, M., 2002. Sediment drifts of the Corsica Channel, northern Tyrrhenian Sea. *Geol. Soc. London, Mem.* 22, 191-208. <https://doi.org/10.1144/GSL.MEM.2002.022.01.14>

Ruff, L.J., 2003. Some Aspects of Energy Balance and Tsunami Generation by Earthquakes and Landslides. *Pure Appl. Geophys.* 160, 2155–2176. <https://doi.org/10.1007/s00024-003-2424-y>

Ryan, W. B. F., 1973. Geodynamic implications of the Messinian crisis of salinity, in: Drooger, D. W. (Ed.), *Messinian events in the Mediterranean*, Elsevier, Amsterdam, pp. 26-38.

Sammari, C., Millot, C., Taupier-Letage, I., Stefani, A., Brahim, M., 1999. Hydrological characteristics in the Tunisia–Sardinia–Sicily area during spring 1995. *Deep Sea Res. Part I Oceanogr. Res. Pap.* 46, 1671–1703. [https://doi.org/10.1016/S0967-0637\(99\)00026-6](https://doi.org/10.1016/S0967-0637(99)00026-6)

Sammartini, M., Camerlenghi, A., Budillon, F., Insinga, D.D., Zgur, F., Conforti, A., Iorio, M., Romeo, R., Tonielli, R., 2018. Open-slope, translational submarine landslide in a tectonically active volcanic continental margin (Licosa submarine landslide, southern Tyrrhenian Sea). *Geol. Soc. London, Spec. Publ.* 477, 133–150. <https://doi.org/10.1144/SP477.34>

Sammartini, M., Moernaut, J., Anselmetti, F.S., Hilbe, M., Lindhorst, K., Praet, N., Strasser, M., 2019. An Atlas of Mass-Transport Deposits in Lakes, in: *Submarine Landslides*. American Geophysical Union (AGU), pp. 201–226. <https://doi.org/10.1002/9781119500513.ch13>

Sanders, J.E., 1965. Primary Sedimentary Structures Formed by Turbidity Currents and Related Resedimentation Mechanisms, in: Middleton, G.V. (Ed.), *Primary Sedimentary Structures and Their Hydrodynamic Interpretation*, pp. 192-219. SEPM Society for Sedimentary Geology. <https://doi.org/10.2110/pec.65.08.0192>

Satow, C., Tomlinson, E.L., Grant, K.M., Albert, P.G., Smith, V.C., Manning, C.J., Ottolini, L., Wulf, S., Rohling, E.J., Lowe, J.J., Blockley, S.P.E., Menzies, M.A., 2015. A new contribution to

the Late Quaternary tephrostratigraphy of the Mediterranean: Aegean Sea core LC21. *Quat. Sci. Rev.* 117, 96–112. <https://doi.org/10.1016/j.quascirev.2015.04.005>

Sawyer, D.E., DeVore, J.R., 2015. Elevated shear strength of sediments on active margins: Evidence for seismic strengthening. *Geophys. Res. Lett.* 42, 10,216–10,221. <https://doi.org/10.1002/2015GL066603>

Sawyer, D.E., Reece, R.S., Gulick, S.P.S., Lenz, B.L., 2017. Submarine landslide and tsunami hazards offshore southern Alaska: Seismic strengthening versus rapid sedimentation. *Geophys. Res. Lett.* 44, 8435–8442. <https://doi.org/10.1002/2017GL074537>

Scarselli, N., 2020. Chapter 16 - Submarine landslides – architecture, controlling factors and environments. A summary, in: Scarselli, N., Adam, J., Chiarella, D., Roberts, D.G., Bally, A.W. (Eds.), *Regional Geology and Tectonics (Second Edition)*, Elsevier, pp. 417–439. <https://doi.org/10.1016/B978-0-444-64134-2.00015-8>

Schramm, M.V., Livraga, G., 1986. Vega field and the potential of Ragusa basin, offshore Sicily, in: Halbouty, M.T. (Ed.), *Future Petroleum Provinces of the World, Memoir 40*. American Association of Petroleum Geologists, pp. 560–566. <https://doi.org/10.1306/AD461782-16F7-11D7-8645000102C1865D>

Schwab, W.C., Danforth, W.W., Scanlon, K.M., 1993. Tectonic and stratigraphic control on a giant submarine slope failure: Puerto Rico insular slope, in: Schwab, W.C., Lee, H.J., Twichell, D.C. (Eds.), *Submarine landslides: Selected studies in the US exclusive economic zone*, pp. 60–68. Washington, D.C: Government Printing Office, US Geological Survey\_Bulletin 2002.

Schweizer, J., Bruce Jamieson, J., Schneebeli, M., 2003. Snow avalanche formation. *Rev. Geophys.* 41. <https://doi.org/10.1029/2002RG000123>

Scotese, C.R., 2001. *Atlas of Earth History. Paleogeography 1*, PALEOMAP Project, Arlington, Texas, 52 pp.

Shackleton, N.J., Sánchez-Goñi, M.F., Pailler, D., Lancelot, Y., 2003. Marine Isotope Substage 5e and the Eemian Interglacial. *Glob. Planet. Change* 36, 151–155. [https://doi.org/10.1016/S0921-8181\(02\)00181-9](https://doi.org/10.1016/S0921-8181(02)00181-9)

Shaltout, M., Omstedt, A., 2012. Calculating the water and heat balances of the Eastern Mediterranean Basin using ocean modelling and available meteorological, hydrological and ocean data. *Oceanologia* 54, 199–232. <https://doi.org/10.5697/oc.54-2.199>

Shaltout, M., Omstedt, A., 2015. Modelling the water and heat balances of the Mediterranean Sea using a two-basin model and available meteorological, hydrological, and ocean data. *Oceanologia* 57, 116–131. <https://doi.org/10.1016/j.oceano.2014.11.001>

Shanmugam, G., 2000. 50 years of the turbidite paradigm (1950s—1990s): deep-water processes and facies models—a critical perspective. *Mar. Pet. Geol.* 17, 285–342. [https://doi.org/10.1016/S0264-8172\(99\)00011-2](https://doi.org/10.1016/S0264-8172(99)00011-2)

Shanmugam, G., 2006. Deep-water processes and facies models: Implications for sandstone petroleum reservoirs: Amsterdam, Elsevier, Handbook of petroleum exploration and production 5, 476 pp.

Shanmugam, G., 2012. New perspectives on deep-water sandstones: Origin, recognition, initiation, and reservoir quality: Amsterdam, Elsevier, Handbook of petroleum exploration and production 9, 524 pp.

Shanmugam, G., 2013. Slides, Slumps, Debris Flows, and Turbidity Currents, in: Elias, S. A. (Ed.), Reference Module in Earth Systems and Environmental Science. Elsevier Online.

Shanmugam, G., Wang, Y., 2015. The landslide problem. *J. Palaeogeogr.* 4, 109–166. <https://doi.org/10.3724/SP.J.1261.2015.00071>

Shanmugam, G., Shrivastava, S., Das, B., 2009. Sandy Debrites and Tidalites of Pliocene Reservoir Sands in Upper-Slope Canyon Environments, Offshore Krishna-Godavari Basin (India): Implications. *J. Sediment. Res.* 79, 736–756. <https://doi.org/10.2110/jsr.2009.076>

Siani, G., Paterne, M., Colin, C., 2010. Late glacial to Holocene planktic foraminifera bioevents and climatic record in the South Adriatic Sea. *J. Quat. Sci.* 25, 808–821. <https://doi.org/10.1002/jqs.1360>

Sicre, M., Siani, G., Genty, D., Kallel, N., Essallami, L., 2013. Seemingly divergent sea surface temperature proxy records in the central Mediterranean during the last deglacial. *Clim. Past* 9, 1375–1383. <https://doi.org/10.5194/cp-9-1375-2013>

Sierro, F.J., Hodell, D.A., Curtis, J.H., Flores, J.A., Reguera, I., Colmenero-Hidalgo, E., Bárcena, M.A., Grimalt, J.O., Cacho, I., Frigola, J., Canals, M., 2005. Impact of iceberg melting on Mediterranean thermohaline circulation during Heinrich events. *Paleoceanography* 20. <https://doi.org/10.1029/2004PA001051>

Skliris, N., Zika, J.D., Herold, L., Josey, S.A., Marsh, R., 2018. Mediterranean sea water budget long-term trend inferred from salinity observations. *Clim. Dyn.* 51, 2857–2876. <https://doi.org/10.1007/s00382-017-4053-7>

Smit, J., Roep, B., Grajales-Nishimura, J., Bermudez, J., 1996. Coarse-grained, clastic sandstone complex at the K/T boundary around the Gulf of Mexico: Deposition by tsunami waves induced by the Chicxulub impact? *Geol. Soc. Am. Spec. Pap.* 307, pp. 151-182. <https://doi.org/10.1130/0-8137-2307-8.151>

Sobiesiak, M.S., Kneller, B., Alsop, G.I., Milana, J.P., 2018. Styles of basal interaction beneath mass transport deposits. *Mar. Pet. Geol.* 98, 629–639. <https://doi.org/10.1016/j.marpetgeo.2018.08.028>

Sohn, Y.K., Choe, M.Y., Jo, H.R., 2002. Transition from debris flow to hyperconcentrated flow in a submarine channel (the Cretaceous Cerro Toro Formation, southern Chile). *Terra Nov.* 14, 405–415. <https://doi.org/10.1046/j.1365-3121.2002.00440.x>

Solheim, A., Bryn, P., Sejrup, H.P., Mienert, J., Berg, K., 2005. Ormen Lange -- an integrated study for the safe development of a deep-water gas field within the Storegga Slide Complex, NE

Atlantic continental margin; executive summary. *Mar. Pet. Geol.* 22, 1–9. <https://doi.org/10.1016/j.marpetgeo.2004.10.001>

Somoza, L., Hernández-Molina, F.J., Andres, J.R. De, Rey, J., 1997. Continental shelf architecture and sea-level cycles: Late Quaternary high-resolution stratigraphy of the Gulf of Cádiz, Spain. *Geo-Marine Lett.* 17, 133–139. <https://doi.org/10.1007/s003670050018>

Sonnenfeld, P., Finetti, I., 1985. Messinian Evaporites in the Mediterranean: A Model of Continuous Inflow and Outflow, in: Stanley, D.J., Wezel, F.-C. (Eds.), *Geological Evolution of the Mediterranean Basin: Raimondo Selli Commemorative Volume* Springer New York, pp. 347–353. [https://doi.org/10.1007/978-1-4613-8572-1\\_17](https://doi.org/10.1007/978-1-4613-8572-1_17)

Soto-Navarro, J., Criado-Aldeanueva, F., García-Lafuente, J., Sánchez-Román, A., 2010. Estimation of the Atlantic inflow through the Strait of Gibraltar from climatological and in situ data. *J. Geophys. Res. Ocean.* 115. <https://doi.org/10.1029/2010JC006302>

Spatola, D., Micallef, A., Sulli, A., Basilone, L., Ferreri, R., Basilone, G., Bonanno, A., Pulizzi, M., Mangano, S., 2018. The Graham Bank (Sicily Channel, central Mediterranean Sea): Seafloor signatures of volcanic and tectonic controls. *Geomorphology* 318, 375–389. <https://doi.org/10.1016/j.geomorph.2018.07.006>

Steventon, M.J., Jackson, C.A.-L., Hodgson, D.M., Johnson, H.D., 2019. Strain analysis of a seismically imaged mass-transport complex, offshore Uruguay. *Basin Res.* 31, 600–620. <https://doi.org/10.1111/bre.12337>

Stoker, M.S., Pheasant, J.B., Josenhans, H., 1997. Seismic Methods and Interpretation, in: Davies, T.A., Bell, T., Cooper, A.K., Josenhans, H., Polyak, L., Solheim, A., Stoker, M.S., Stravers, J.A. (Eds.), *Glaciated Continental Margins: An Atlas of Acoustic Images*. Springer Netherlands, Dordrecht, pp. 9–26. [https://doi.org/10.1007/978-94-011-5820-6\\_2](https://doi.org/10.1007/978-94-011-5820-6_2)

Stow, D.A. V, Tabrez, A.R., 1998. Hemipelagites: processes, facies and model. *Geol. Soc. London, Spec. Publ.* 129, 317–337. <https://doi.org/10.1144/GSL.SP.1998.129.01.19>

Stow, D.A.V., Faugères, J.-C., 2008. Chapter 13 Contourite Facies and the Facies Model. *Dev. Sedimentol.* 60, 223–256. [https://doi.org/10.1016/S0070-4571\(08\)10013-9](https://doi.org/10.1016/S0070-4571(08)10013-9)

Stow, D., Smillie, Z., 2020. Distinguishing between Deep-Water Sediment Facies: Turbidites, Contourites and Hemipelagites. *Geosciences* 10, 68. <https://doi.org/10.3390/geosciences10020068>

Stow, D.A.V., Reading, H. G., Collinson, J. C., 1996. Deep seas, in: Reading, H. G. (Ed.) *Sedimentary Environments and Facies*. Blackwell Scientific Publications, Oxford, pp. 395–453.

Stow, D.A.V., Hernández-Molina, F.J., Alvarez Zarikian, C.A., and Exp. 339 Scientists (Eds.), 2013. Expedition 339 Summary, IODP Management Internation Inc., Tokyo, 918 pp. <https://doi.org/10.2204/iodp.proc.339.101.2013>.

Strachan, L.J., 2008. Flow transformations in slumps: a case study from the Waitemata Basin, New Zealand. *Sedimentology* 55, 1311–1332. <https://doi.org/10.1111/j.1365-3091.2007.00947.x>

Strasser, M., Stegmann, S., Bussmann, F., Anselmetti, F.S., Rick, B., Kopf, A., 2007. Quantifying subaqueous slope stability during seismic shaking: Lake Lucerne as model for ocean margins. *Mar. Geol.* 240, 77–97. <https://doi.org/10.1016/j.margeo.2007.02.016>

Strozyk, F., Strasser, M., Förster, A., Kopf, A., Huhn, K., 2010. Slope failure repetition in active margin environments: Constraints from submarine landslides in the Hellenic fore arc, eastern Mediterranean. *J. Geophys. Res. Solid Earth* 115. <https://doi.org/10.1029/2009JB006841>

Struglia, M.V., Mariotti, A., Filograsso, A., 2004. River Discharge into the Mediterranean Sea: Climatology and Aspects of the Observed Variability. *J. Clim.* 17, 4740–4751. <https://doi.org/10.1175/JCLI-3225.1>

Strupler, M., Hilbe, M., Kremer, K., Danciu, L., Anselmetti, F.S., Strasser, M., Wiemer, S., 2018. Subaqueous landslide-triggered tsunami hazard for Lake Zurich, Switzerland. *Swiss J. Geosci.* 111, 353–371. <https://doi.org/10.1007/s00015-018-0308-5>

Sulpizio, R., Zanchetta, G., Caron, B., Dellino, P., Mele, D., Giaccio, B., Insinga, D., Paterne, M., Siani, G., Costa, A., Macedonio, G., Santacroce, R., 2014. Volcanic ash hazard in the Central Mediterranean assessed from geological data. *Bull. Volcanol.* 76, 866. <https://doi.org/10.1007/s00445-014-0866-y>

Sultan, N., Cochonat, P., Foucher, J.-P., Mienert, J., 2004. Effect of gas hydrates melting on seafloor slope instability. *Mar. Geol.* 213, 379–401. <https://doi.org/10.1016/j.margeo.2004.10.015>

Talling, P.J., Paull, C.K., Piper, D.J.W., 2013. How are subaqueous sediment density flows triggered, what is their internal structure and how does it evolve? Direct observations from monitoring of active flows. *Earth-Science Rev.* 125, 244–287. <https://doi.org/10.1016/j.earscirev.2013.07.005>

Talling, P.J., Wynn, R.B., Masson, D.G., Frenz, M., Cronin, B.T., Schiebel, R., Akhmetzhanov, A.M., Dallmeier-Tiessen, S., Benetti, S., Weaver, P.P.E., Georgiopoulou, A., Zühlendorff, C., Amy, L.A., 2007. Onset of submarine debris flow deposition far from original giant landslide. *Nature* 450, 541–544. <https://doi.org/10.1038/nature06313>

Talling, P., Clare, M., Urlaub, M., Pope, E., Hunt, J., Watt, S., 2014. Large Submarine Landslides on Continental Slopes: Geohazards, Methane Release, and Climate Change. *Oceanography* 27, 32–45. <https://doi.org/10.5670/oceanog.2014.38>

Tang, C. M. 2018. Tethys Sea. *Encyclopedia Britannica*, <https://www.britannica.com/place/Tethys-Sea>. Accessed 8 March 2021.

Tappin, D.R., 2010. Mass Transport Events and Their Tsunami Hazard, in: Mosher, D.C., Shipp, R.C., Moscardelli, L., Chaytor, J.D., Baxter, C.D.P., Lee, H.J., Urgeles, R. (Eds.), *Submarine Mass Movements and Their Consequences*, Springer Netherlands, Dordrecht, pp. 667–684. [https://doi.org/10.1007/978-90-481-3071-9\\_54](https://doi.org/10.1007/978-90-481-3071-9_54)

Tappin, D.R., 2017. Tsunamis from submarine landslides. *Geol. Today* 33, 190–200. <https://doi.org/10.1111/gto.12200>

Tappin, D.R., Watts, P., McMurtry, G.M., Lafoy, Y., Matsumoto, T., 2001. The Sissano, Papua New Guinea tsunami of July 1998 - offshore evidence on the source mechanism. *Mar. Geol.* 175, 1–23. [https://doi.org/10.1016/S0025-3227\(01\)00131-1](https://doi.org/10.1016/S0025-3227(01)00131-1)

Tappin, D.R., McNeil, L.C., Henstock, T., Mosher, D.C., 2007. Mass Wasting Processes - Offshore Sumatra, in: Lykousis, V., Sakellariou, D., Locat, J. (Eds.), *Submarine Mass Movements and Their Consequences: 3 International Symposium*. Springer Netherlands, Dordrecht, pp. 327–336. [https://doi.org/10.1007/978-1-4020-6512-5\\_34](https://doi.org/10.1007/978-1-4020-6512-5_34)

Tappin, D.R., Grilli, S.T., Harris, J.C., Geller, R.J., Masterlark, T., Kirby, J.T., Shi, F., Ma, G., Thingbaijam, K.K.S., Mai, P.M., 2014. Did a submarine landslide contribute to the 2011 Tohoku tsunami? *Mar. Geol.* 357, 344–361. <https://doi.org/10.1016/j.margeo.2014.09.043>

Ten Brink, U.S., Andrews, B.D., Miller, N.C., 2016. Seismicity and sedimentation rate effects on submarine slope stability. *Geology* 44, 563–566. <https://doi.org/10.1130/G37866.1>

Tesi, T., Miserocchi, S., Goñi, M.A., Langone, L., 2007. Source, transport and fate of terrestrial organic carbon on the western Mediterranean Sea, Gulf of Lions, France. *Mar. Chem.* 105, 101–117. <https://doi.org/10.1016/j.marchem.2007.01.005>

Tilling, R.I., Topinka, L.J., Swanson, D.A., 1990. *Eruptions of Mount St. Helens : Past, present, and future*, General Interest Publication. Reston, VA. <https://doi.org/10.3133/7000008>

Tinti, S., Bortolucci, E., 2000. Energy of Water Waves Induced by Submarine Landslides. *Pure Appl. Geophys.* 157, 281–318. <https://doi.org/10.1007/s000240050001>

Tinti, S., Tonini, R., 2013. The UBO-TSUFDF tsunami inundation model: Validation and application to a tsunami case study focused on the city of Catania, Italy. *Nat. Hazards Earth Syst. Sci.* 13, 1795–1816. <https://doi.org/10.5194/nhess-13-1795-2013>

Torfstein, A., Steinberg, J., 2020. The Oligo–Miocene closure of the Tethys Ocean and evolution of the proto-Mediterranean Sea. *Sci. Rep.* 10, 13817. <https://doi.org/10.1038/s41598-020-70652-4>

Tóth, T., 2011. Single and Multichannel Seismics, in: Gupta, H.K. (Ed.), *Encyclopedia of Solid Earth Geophysics*, Springer Netherlands, Dordrecht, pp. 1366–1373. [https://doi.org/10.1007/978-90-481-8702-7\\_210](https://doi.org/10.1007/978-90-481-8702-7_210)

Toucanne, S., Jouet, G., Ducassou, E., Bassetti, M.A., Dennielou, B., Minto'o, C.M.A., Lahmi, M., Touyet, N., Charlier, K., Lericolais, G., Mulder, T., 2012. A 130,000-year record of Levantine intermediate water flow variability in the Corsica Trough, western Mediterranean Sea. *Quat. Sci. Rev.* 33, 55–73. <https://doi.org/10.1016/j.quascirev.2011.11.020>

Trincardi, F., Argnani, A., 1990. Gela submarine slide: A major basin-wide event in the plioquaternary foredeep of Sicily. *Geo-Marine Lett.* 10, 13–21. <https://doi.org/10.1007/BF02431017>

Tripsanas, E.K., Bryant, W.R., Prior, D.B., Phaneuf, B.A., 2003. Interplay Between Salt Activities and Slope Instabilities, Bryant Canyon Area, Northwest Gulf of Mexico, in: Locat, J., Mienert, J., Boisvert, L. (Eds.), *Submarine Mass Movements and Their Consequences: 1st International*

Symposium. Springer Netherlands, Dordrecht, pp. 307–315. [https://doi.org/10.1007/978-94-010-0093-2\\_34](https://doi.org/10.1007/978-94-010-0093-2_34)

Tziperman, E., Gildor, H., 2003. On the mid-Pleistocene transition to 100-kyr glacial cycles and the asymmetry between glaciation and deglaciation times. *Paleoceanography* 18, 1001. <https://doi.org/10.1029/2001PA000627>

Ünlülata, Ü., Oğuz, T., Latif, M.A., Özsoy, E., 1990. On the Physical Oceanography of the Turkish Straits, in: Pratt, L.J. (Ed.), *The Physical Oceanography of Sea Straits* Springer Netherlands, Dordrecht, pp. 25–60. [https://doi.org/10.1007/978-94-009-0677-8\\_2](https://doi.org/10.1007/978-94-009-0677-8_2)

Urgeles, R., Camerlenghi, A., 2013. Submarine landslides of the Mediterranean Sea: Trigger mechanisms, dynamics, and frequency-magnitude distribution. *J. Geophys. Res. Earth Surf.* 118, 2600–2618. <https://doi.org/10.1002/2013JF002720>

Urgeles, R., Camerlenghi, A., Ercilla, G., Anselmetti, F., Brückmann, W., Canals, M., Gràcia, E., Locat, J., Krastel, S., Solheim, A., 2007. Scientific ocean drilling behind the assessment of geo-hazards from submarine slides, Barcelona, Spain, 25–27 October 2006. *Eos, Trans. Am. Geophys. Union* 88, 192. <https://doi.org/10.1029/2007EO170009>

Urgeles, R., Camerlenghi, A., Garcia-Castellanos, D., De Mol, B., Garcés, M., Vergés, J., Haslam, I., Hardman, M., 2011. New constraints on the Messinian sealevel drawdown from 3D seismic data of the Ebro Margin, western Mediterranean. *Basin Res.* 23, 123–145. <https://doi.org/10.1111/j.1365-2117.2010.00477.x>

Urlaub, M., Talling, P.J., Zervos, A., Masson, D., 2015. What causes large submarine landslides on low gradient (<2°) continental slopes with slow (~0.15 m/kyr) sediment accumulation? *J. Geophys. Res. Solid Earth* 120, 6722–6739. <https://doi.org/10.1002/2015JB012347>

Vandorpe, T.P., Van Rooij, D., Stow, D.A. V, Henriët, J.-P., 2011. Pliocene to Recent shallow-water contourite deposits on the shelf and shelf edge off south-western Mallorca, Spain. *Geo-Marine Lett.* 31, 391–403. <https://doi.org/10.1007/s00367-011-0248-9>

Van Rooij, D., Iglesias, J., Hernández-Molina, F.J., Ercilla, G., Gomez-Ballesteros, M., Casas, D., Llave, E., De Hauwere, A., Garcia-Gil, S., Acosta, J., Henriët, J.-P., 2010. The Le Danois Contourite Depositional System: Interactions between the Mediterranean Outflow Water and the upper Cantabrian slope (North Iberian margin). *Mar. Geol.* 274, 1–20. <https://doi.org/10.1016/j.margeo.2010.03.001>

Verdicchio, G., Trincardi, F., 2008. Mediterranean shelf-edge muddy contourites: examples from the Gela and south Adriatic basins. *Geo Mar. Lett.* 28, 137–151. <https://doi.org/10.1007/s00367-007-0096-9>

Verri, G., Pinardi, N., Oddo, P., Ciliberti, S.A., Coppini, G., 2018. River runoff influences on the Central Mediterranean overturning circulation. *Clim. Dyn.* 50, 1675–1703. <https://doi.org/10.1007/s00382-017-3715-9>

Vigliotti, L., Verosub, K., Cattaneo, A., Trincardi, F., Alessandra, A., Piva, A., 2008. Palaeomagnetic and rock magnetic analysis of Holocene deposits from the Adriatic Sea: Detecting and dating short-term fluctuations in sediment supply. *The Holocene* 18, 141–152. <https://doi.org/10.1177/0959683607085605>

Waage, M., Bünz, S., Landrø, M., Plaza-Faverola, A., Waghorn, K.A., 2018. Repeatability of high-resolution 3D seismic data. *GEOPHYSICS* 84, B75–B94. <https://doi.org/10.1190/geo2018-0099.1>

Wang, F., Polcher, J., 2019. Assessing the freshwater flux from the continents to the Mediterranean Sea. *Sci. Rep.* 9, 8024. <https://doi.org/10.1038/s41598-019-44293-1>

Ward, S.N., 2001. Landslide tsunamis. *J. Geophys. Res.* 106, 11201–11215. <https://doi.org/10.1029/2000JB900450>

Wentworth, C.K., 1922. A scale of grade and class terms for clastic sediments. *Journal of Geology*, 30, 377–392.

WHOI 2020. Piston Corer. <https://www.whoi.edu/what-we-do/explore/instruments/instruments-sensors-samplers/piston-corer/sensors-samplers/piston-corer/>

Wiemer, G., Moernaut, J., Stark, N., Kempf, P., De Batist, M., Pino, M., Urrutia, R., de Guevara, B.L., Strasser, M., Kopf, A., 2015. The role of sediment composition and behavior under dynamic loading conditions on slope failure initiation: a study of a subaqueous landslide in earthquake-prone South-Central Chile. *Int. J. Earth Sci.* 104, 1439–1457. <https://doi.org/10.1007/s00531-015-1144-8>

Yegorov, Y., 2007. Tsunami wave generation by the eruption of underwater volcano. *Nat. hazards earth Syst. Sci.* 7, 65–69. <https://doi.org/10.5194/nhess-7-65-2007>

Zaniboni, F., Tinti, S., 2014. Numerical simulations of the 1963 Vajont landslide, Italy: application of 1D Lagrangian modelling. *Nat. Hazards* 70, 567–592. <https://doi.org/10.1007/s11069-013-0828-2>

Zaniboni, F., Armigliato, A., Tinti, S., 2016. A numerical investigation of the 1783 landslide-induced catastrophic tsunamis in Scilla, Italy. *Nat. Hazards* 84, 455–470. <https://doi.org/10.1007/s11069-016-2461-3>

Zaniboni, F., Pagnoni, G., Paparo, M.A., Gauchery, T., Rovere, M., Argnani, A., Armigliato, A., Tinti, S., 2021. Tsunamis From Submarine Collapses Along the Eastern Slope of the Gela Basin (Strait of Sicily). *Front. Earth Sci.* 8, 644. <https://doi.org/10.3389/feart.2020.602171>

Zavatarielli, M., Mellor, G.L., 1995. A Numerical Study of the Mediterranean Sea Circulation. *J. Phys. Oceanogr.* 25, 1384–1414. [https://doi.org/10.1175/1520-0485\(1995\)025<1384:ANSOTM>2.0.CO;2](https://doi.org/10.1175/1520-0485(1995)025<1384:ANSOTM>2.0.CO;2)

Zengaffinen, T., Løvholt, F., Pedersen, G.K., Harbitz, C.B., 2020. Effects of rotational submarine slump dynamics on tsunami genesis: new insight from idealized models and the 1929 Grand Banks event. *Geol. Soc. London, Spec. Publ.* 500, 41–61. <https://doi.org/10.1144/SP500-2019-201>



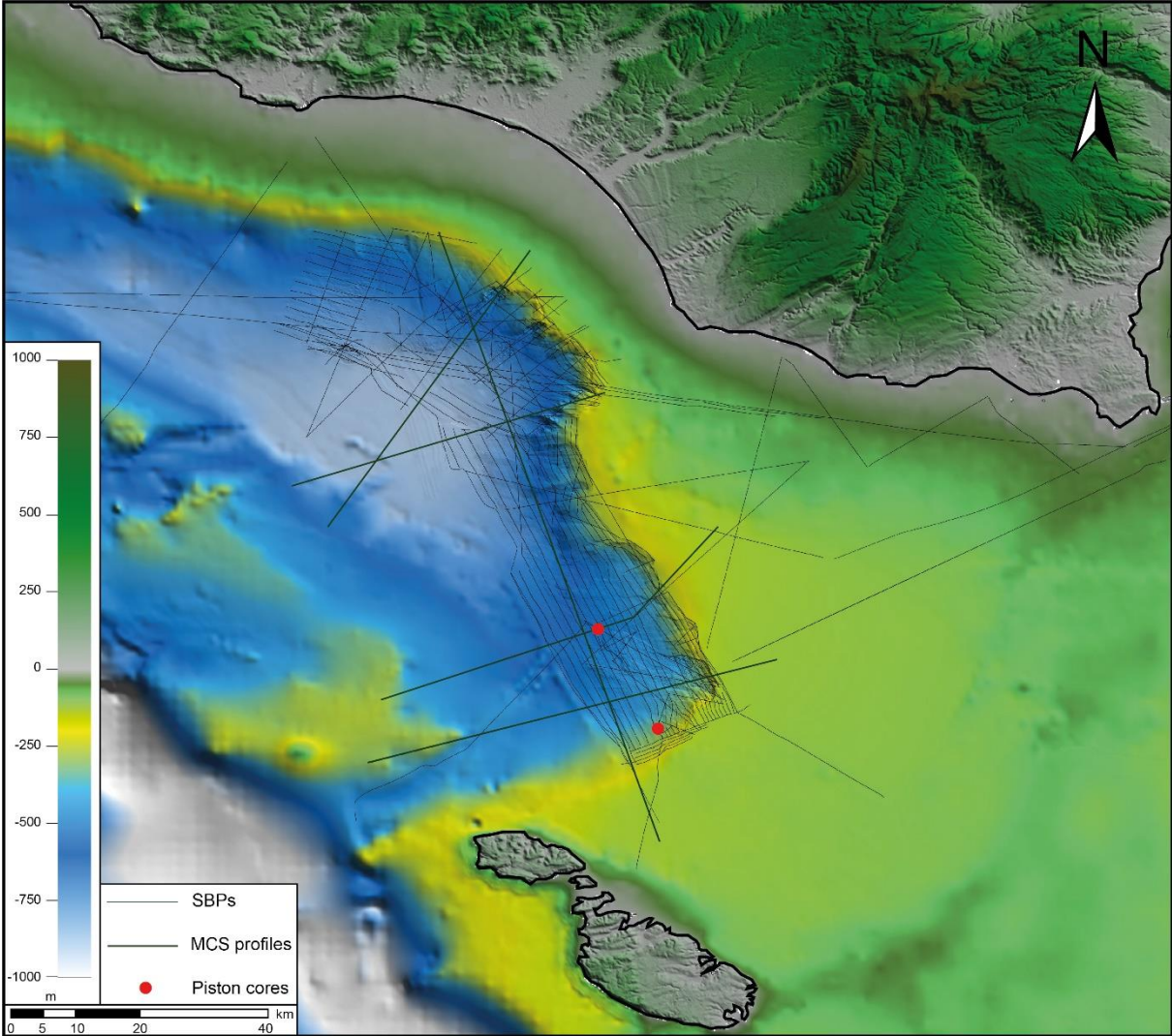
# Annexes

Annexe 1: List of secondments, research stays, courses and seminars, conferences and outreach attended

SECONDMENTS					
START	END	TIME (days)	INSTITUTE	SUPERVISION	AIMS
20/09/18	05/10/18	16	IFREMER, Brest	A. Cattaneo	Grain size analysis, interpretation and advance on the publication
16/04/19	15/05/19	30	IFREMER, Brest	A. Cattaneo	Coaching for 1st manuscript
15/07/19	19/07/19	5	RINA Consulting	F. Zolezzi	Software training and data uploading
01/08/19	31/08/19	31	IFREMER, Brest	A. Cattaneo	Coaching for 1st manuscript writing
06/11/19	30/11/19	25	IFREMER, Brest	A. Cattaneo	Laboratory analyses; tutoring for second manuscript writing
02/12/19	06/12/19	5	RINA Consulting	F. Zolezzi	Completion of data interpretation and comparison with previous data
06/02/20	21/02/20	16	IFREMER, Brest	A. Cattaneo	Grain size analysis and start interpretation
RESEARCH STAYS					
21/05/18	25/05/18	5	Eni, Milan, Italy	C. Cattaneo	Access to industrial MCS profiles to know if they can be usefull for the objectives of the thesis + software training
15/10/18	31/10/18	17	Eni, Milan, Italy	C. Cattaneo	Identification and picking of key seismic reflectors
COURSES AND SEMINARS					
			LOCATION	ORGANISER	TITLE
26/10/17	14/12/17	50	University of Bologna	University of Bologna	English Academic Writing (once a week)
17/01/18	19/01/18	3	ISMAR, Bologna, Italy	ISMAR	GIS training
14/02/18	14/03/18	29	University of Bologna	University of Bologna	Matlab (once a week)
28/02/18	02/05/18	64	University of Bologna	University of Bologna	Ocean and Coastal Engineering (once a week)
23/04/18	27/04/18	5	MARUM, Bremen, Germany	ECORD	ECORD training course
10/05/18	11/05/18	2	Victoria, Canada	IOS	Introduction to Geohazards Assessment: An Energy Industry Perspective
11/06/18	13/06/18	3	Around Bologna	ISMAR	Carbonate conduits linked to the hydrocarbon-enriched fluid escape (3-day field trip)
CONFERENCES					
		LOCATION - MEDIA	CONTRIBUTION TITLE / LINK		
08/04/18	13/04/18	EGU, Vienna, Austria - Poster	Geomorphology of Multi-Stage Submarine Landslides along the South Eastern Slope of the Gela Basin in the Strait of Sicily (Central Mediterranean Sea) / <a href="https://ui.adsabs.harvard.edu/abs/2018EGUGA..2013453G/abstract">https://ui.adsabs.harvard.edu/abs/2018EGUGA..2013453G/abstract</a>		
07/05/18	09/05/18	ISSMMTC, Victoria, Canada - Poster	Triggering factors and stratigraphic reconstruction of multi-stage failures in the southeastern slope of the Gela Basin in the Strait of Sicily (Central Mediterranean Sea) / <a href="https://drive.google.com/open?id=1DZro05Z3NOMAFY0PY9JSpS30oCPu8k_zIu6srIUq9s">https://drive.google.com/open?id=1DZro05Z3NOMAFY0PY9JSpS30oCPu8k_zIu6srIUq9s</a>		
02/09/18	07/09/18	ESC, Valetta, Malta - Poster (co-author)	A large submarine collapse along the Gela Basin margin (Strait of Sicily) and its consequences on the coasts of Sicily and Malta / <a href="http://www.itn-slate.eu/wp-content/uploads/2019/06/ESR_3_TugdualGauchery-Abstract-ESC2018-Posterco-author.pdf">http://www.itn-slate.eu/wp-content/uploads/2019/06/ESR_3_TugdualGauchery-Abstract-ESC2018-Posterco-author.pdf</a>		
07/04/19	12/04/19	EGU, Vienna, Austria - Talk	Contourite deposits and landslides in the south-eastern Gela Basin (Strait of Sicily, Central Mediterranean Sea), relationships and contributory causes / <a href="https://meetingorganizer.copernicus.org/EGU2019/EGU201918698-1.pdf">https://meetingorganizer.copernicus.org/EGU2019/EGU201918698-1.pdf</a>		
10/09/19	13/09/19	IAS, Rome, Italy - Talk	Novel evidence from the Pliocene-Quaternary succession of the southeastern Gela Basin (Strait of Sicily, Central Mediterranean Sea): onset and evolution of contourite deposits / <a href="http://www.itn-slate.eu/wp-content/uploads/2019/10/ESR_2_TugdualGaucheryAbstract-IAS2019.pdf">http://www.itn-slate.eu/wp-content/uploads/2019/10/ESR_2_TugdualGaucheryAbstract-IAS2019.pdf</a>		
OUTREACH					
DATE	LOCATION	DESCRIPTION			
22/11/19	Quimper, France	Present the world of marine geosciences in front of high-school students.			
27/09/19	Bologna, Italy	Present to the public how to study submarine landslides during the European Researchers' Night			
22/05/19	Bologna, Italy	Present my research to Master students from the University of Milan visiting the marine research centre			
02/12/17	Beauvais, France	Present the world of research during Saint Barbara to undergraduate students and their parents thanks to a round table with other PhD students.			



Annexe 2: Location of the data (seismic profiles and piston core) within the Gela Basin accessed and interpreted during this PhD





Annexe 3: High-resolution seismic image of the Gela Basin along-strike variability







In the frame of a European Marie Skłodowska-Curie Actions Training Network program on Submarine Landslides and Their impact on European continental margins (SLATE), this research concentrated on submarine landslides in the central Mediterranean Sea. Commonly found in marine and lacustrine environments, submarine landslides represent one of the main mechanisms of sediment transport along continental margins, their volumes can be far larger than any terrestrial landslides and have potential to produce far-reaching tsunamis that can rival those produced by earthquakes. However, many uncertainties remain concerning their preconditioning factors, triggering mechanisms, return frequencies and relationship with climate change as well as their geohazard potential, which vary depending on their location.

Newly identified submarine landslides emplaced in the Gela Basin (GB; south of Sicily, central Mediterranean Sea) were investigated where the particular geodynamic and oceanographic context and the limited extent basin is ideal for submarine landslides research. The investigation through multiple data types including deep boreholes, multi-channel and subbottom seismic profiles, sediment cores and swath bathymetry revealed the emplacement of multiple submarine landslides during the margin outbuilding in the Pliocene-Quaternary with a drastic transition in their volumes and emplacement location at the Middle-Pleistocene Transition (MPT). This change, accompanied by an accelerated margin outbuilding from 150 to 900 m/kyr and growth of the contourite deposits, has been related to the decreasing tectonic activity at the southern front of the Maghrebian fold-and-thrust belt and the climatic changes linked to the switch to the 100-kyr Milankovitch cyclicity. Numerical in-house codes used for the reconstruction of two small-size MTDs located at the ends of the GB show similar potential of generating high-wave tsunamis that can impact the coasts of Malta and Sicily but different triggering mechanisms based on the stability analysis. A multiproxy approach made on these sediment cores revealed that strong bottom currents and very-high sedimentation rate fluctuations, associated with sea-level changes, affected the stability of contourite deposits and contributed to the recurrent emplacement of MTDs.

**Keywords:** Submarine landslides, preconditioning factors, triggering mechanisms, return frequencies, Gela Basin, Middle Pleistocene Transition, Milankovitch cyclicity, contourite deposits, very-high sedimentation rate



DIPARTIMENTO

INGEGNERIA CIVILE, CHIMICA, AMBIENTALE  
E DEI MATERIALI - DICAM

